COMPUMAG 2003

Conference on the Computation of Magnetic Fields

Saratoga Springs, New York
July 13–17, 2003

Volume III

COMPUMAG

14th Conference on the Computation of Magnetic Fields

July 13-17, 2003
Saratoga Springs, New York USA

Record of the 14th COMPUMAG Conference
on the Computation of Magnetic Fields

Volume III: Wednesday, July 16

COMPUMAG 2003

14th Conference on the Computation of Magnetic Fields
Saratoga Springs, New York, USA
July 13-17, 2003

Compumag 2003 Committee:

Prof. Sheppard J. Salon, Chairman
Rensselaer Polytechnic Institute, Troy, NY USA
Philippe Wendling, Vice Chairman
Magsoft Corporation, Troy, NY USA
David Burow, Secretariat
Genfo, Inc., Troy, NY USA

Local Organizing Committee:

M. DeBortoli K. Sivasubramaniam
M. Lean M. Shah
I. Mayergoyz S. Babic
U. Deshpande

Editorial Board Chairmen:

J. Webb, McGill University, Montreal, Quebec Canada
D. Giannacopoulos, McGill University, Montreal, Quebec Canada
Email: edboard.compumag2003@mcgill.ca

Correspondence:

Compumag 2003
1223 Peoples Ave
Troy, NY 12180 USA
Email : secretariat@compumag2003.com

Lodging Arrangements Made By:

Sherie Klein, Carlson Wagonlit/Albany Travel
30 Corporate Drive, Clifton Park, NY 12065 USA
Phone: +1 (518) 292-9000
Email: corporate@albanytravel.com

COMPUMAG 2003 Chairman's Welcome

Welcome to COMPUMAG 2003, the 14th Conference on the Computation of Electric and Magnetic Fields!

In the 27 years since the first COMPUMAG Conference in 1976 at Oxford, we have seen the society and the conference continue to grow in numbers, in significance and in international renown and respect. We are honored, therefore, to carry on what has become a well-established tradition of presenting the leading research and thought in the area of computational electromagnetics.

Because of its high standards and rigorous review process, the Conference has become the place to present in our field. This year 429 papers were approved for presentation in 8 oral sessions and 32 poster sessions. The contributors represent 30 different countries. Our deep thanks go to the editorial board and to the co-chairs Jon Webb and Dennis Giannacopoulos, who did an outstanding job.

And welcome to Saratoga Springs, New York! Those of us fortunate to live and work in New York's Capital District can take advantage of some of the best opportunities in the United States for research and education; cultural, historical and recreational resources; and small cities and towns where neighbors still don't lock their doors. Nearby research institutions and universities include Rensselaer, GE Global Research Laboratories, Knolls Atomic Power Laboratory, IBM Research Laboratory and others. New York City, Boston, and Montreal, with their rich historical and cultural resources, are all within a few hours' drive. Finally, there is the peace and friendliness of smaller towns and villages, like Saratoga Springs, where you are sure to enjoy the activities we have planned; we hope you will also take time to explore on your own.

COMPUMAG 2003 offers lively scientific exchange to charm the intellect and convivial activities to warm the heart. Welcome!

Prof. Sheppard J. Salon
COMPUMAG 2003 Chairman

City of Saratoga Springs

Kenneth Klotz, Mayor
Hank Kuczynski, Deputy Mayor

July, 2003

Welcome!

On behalf of the entire City of Saratoga Springs, I would like to welcome the ***14th Conference on the Computation of Electromagnetic Fields*** to Saratoga Springs!

As you know, Saratoga Springs is a world-class resort destination, which offers cosmopolitan amenities without the drawbacks of a typical metropolitan area. Our city takes great pride in its hospitality to visitors. We offer world-class attractions, wonderful restaurants, unique shops and a host of related activities that your attendees are sure to enjoy!

Saratoga Springs looks forward to hosting the ***14th Conference on the Computation of Electromagnetic Fields and its attendees.***

Once again, Welcome to our City, where we invite you to.....***Experience Saratoga!***

Sincerely,

Kenneth Klotz
Mayor

City Hall, Saratoga Springs, New York 12866-2296
518/587-3550 • 518/587-1688 fax

COMPUMAG 2003 Editorial Board

Chairmen: J. Webb, D. Giannacopoulos

Raffaele Albanese
Salvatore Alfonzetti
Piergiorgio Alotto
Zoran Andjelic
Carlos F. Lemos Antunes
Abdul-Rahman Arkadan
Michel Aubourg
Zsolt Badics
Bernard Bandelier
Istvan Bardi
João P. Assumpção Bastos
Jean Bigeon
Oszkar Bíró
Carlo Angelo Borghi
Frédéric Bouillault
Hartmut Brauer
John R. Brauer
Noël Burais
François Buret
Andreas Cangellaris
Ermanno Cardelli
José Roberto Cardoso
Zoltan Cendes
Zhiguang Cheng
Mario Chiampi
Charles T. M. Choi
Kyung Choi
Markus Clemens
Enzo Coccorese
Jean-Louis Coulomb
Xiang Cui
Kent R. Davey
Herbert De Gersem
João A. De Vasconcelos
Edward Deeley
Edward Della Torre
Andrzej Demenko
Paolo Di Barba
Bernice Dillon
Alistair Duffy
Fabrizio Dughiero
Patrick Dular
Derek Dyck
Romanus Dyczij-Edlinger
Chris R.I. Emson
Mauro Feliziani
Paolo Fernandes
Gilles Fillion
Raymond Findlay
Virgiliu Fireteanu
Behzad Forghani
Minya Gavrilovic
Dennis Giannacopoulos
Andrew Gibson
Roberto Graglia
Stanislaw Gratkowski
Miklos Gyimesi
Johan Gyselinck
Song-yop Hahn
Kay Hameyer
Florea Ioan Hantila
Nathan Ida
Hajime Igarashi
Kazuhisa Ishibashi
Amália Iványi
Rick Janssen
Jianming Jin
Hyun-Kyo Jung
Manfred Kaltenbacher
Akihisa Kameari
Yasushi Kanai
Manfred Kasper
Yoshihiro Kawase
Leo Kempel
Lauri Kettunen
Ahmed Kishk
Fumio Kojima
Arnulf Kost
Laurent Krähenbühl
Andrzej Krawczyk
Patrick Kuo-Peng
Stefan Kurz
Ioan E. Lager
Hong Cheng Lai
Meng H. Lean
Luiz Lebensztajn
Robert Lee
Jin-Fa Lee
Paul John Leonard
Dominique Lesselier
David Lowther
Valérie Madrangeas
Christian Magele
Yves Maréchal
Marlene Marinescu
Iliana Marinova
Raffaele Martone
Daniel Mayer
Isaak Mayergoyz
Steven McFee
Jan Melkebeek
Frantisek Melkes
Renato Mesquita
Gérard Meunier
Pavel Mintchev
Osama A. Mohammed
Paolo Molfino
Giorgio Molinari
Vikass Monebhurrun
Francesco Carlo Morabito
Irina Munteanu
Silvio Ikuyo Nabeta
Ryszard Nawrowski
Mario Nervi
Alain Nicolas
Laurent Nicolas
Keijo Nikoskinen
Isoharu Nishiguchi
W Toby Norris
Dzevat Omeragic
Jozsef Pavo
Giuseppe Pelosi
Ilaria Perugia
Lionel Pichon
Francis Piriou
Milica Popovic
Kurt Preis
Thomas William Preston
Mirco Raffetto
Adroaldo Raizer
Jaime Ramirez
Liyun Rao
Adel Razek
Zhuoxiang Ren
Werner Renhart
Maurizio Repetto
Gilbert Reyne
Christopher Riley
Françoise Rioux-Damidau
Dave Rodger
Guglielmo Rubinacci
Wolfgang M. Rucker
Stephan Russenschuck
Nelson Sadowski
Pierre Saguet
Magdalena Salazar-Palma
Carlos Sartori
Antonio Savini
Imre Sebestyén
Jan Sikora
John Simkin
Andrea Stella
Saku Suuriniemi
Jan K. Sykulski
Toshiyuki Takagi
Norio Takahashi
Tadasu Takuma
Antonello Tamburrino
Renyuan Tang
Takashi Todaka
Bill Trowbridge
Theodoros Tsiboukis
Igor Tsukerman
Larry R. Turner
Lalita Udpa
Satish Udpa
Hermann Uhlmann
Ursula Van Rienen
Patrick Vaudon
Serge Verdeyme
Fabio Villone
John L. Volakis
Christian Vollaire
Shinji Wakao
Simon Walker
Zanming Wang
Jonathan P. Webb
Thomas Weiland
Slawomir Wiak
Hideo Yamashita
Katsumi Yamazaki
Ivan Yatchev
Traianos Yioultsis
Jiansheng Yuan
Kazimierz Zakrzewski
Ping Zhou

COMPUMAG 2003 Program at a Glance

	July 13 Sunday	July 14 Monday	July 15 Tuesday	July 16 Wednesday	July 17 Thursday	
7:00		Continental Breakfast Buffet	Continental Breakfast Buffet	Continental Breakfast Buffet	Continental Breakfast Buffet	7:00
8:00		Formulations Saratoga Ballroom	Devices Saratoga Ballroom	Quasistatic Saratoga Ballroom	Inverse Problems Saratoga Ballroom	8:00
10:15		Coffee Break	Coffee Break	Coffee Break	Coffee Break	10:15
10:45		Numerical Techniques I Coupled Problems I Devices I Statics I	Numerical Techniques II Coupled Problems II Machines II Statics II	Numerical Techniques III Coupled Problems III Devices III Software	Numerical Techniques IV Coupled Problems IV Machines IV Devices IV	10:45
12:00		Lunch: Grand Ballroom – High Rock	Lunch: Grand Ballroom – High Rock	Lunch: Grand Ballroom – High Rock	Lunch: Grand Ballroom – High Rock	12:00
1:30		Optimization I Waves I Machines I Quasistatic I	Optimization II Waves II Devices II Quasistatic II	Optimization III EMC Machines IIII Materials I	Optimization IV Materials II Education – TEAM Quasistatic III	1:30
2:45		Afternoon Break	Afternoon Break	Afternoon Break	Afternoon Break	2:45
3:15	Registration* 2:00 – 6:00 p.m.	Methodologies Saratoga Ballroom	Materials Saratoga Ballroom	Waves Saratoga Ballroom	Optimization Saratoga Ballroom	3:15
5:30		Enjoy Saratoga!	5:00 Short Break (no refreshments)		Have a safe and pleasant journey home!	5:30
			5:15 Panel Session: Topic To Be Announced Saratoga Ballroom			
6:30	Evening Reception Saratoga Ballroom		6:15 Enjoy Saratoga!	Banquet at the Canfield Casino		6:30

* Registration will also be available each day from 7:00 AM to 12:00 noon and from 1:30 to 2:45 PM.

COMPUMAG 2003 Technical Program

Wednesday, July 16, 2003

	8:00 – 10:15
Oral Session	
	Quasistatic Saratoga Ballroom
	10:45 – 12:00
Poster Session	
	Numerical Techniques III: Hybrid Methodologies and Edge Elements
	Coupled Problems III: Devices and Applications
	Devices III: Induction Heating and Superconductivity
	Software
	1:30 – 2:45
Poster Session	
	Optimization III
	EMC
	Machines III: Permanent Magnet
	Materials I: Hysteresis
	3:15 – 5:30
Oral Session	
	Waves Saratoga Ballroom

Quasistatic Chairman
Wednesday, July 16, 8:00am - 10:15am Dr. Michael P. Perry

Numerical Techniques III: Hybrid Methods and Edge Elements Chairman
Wednesday, July 16, 10:45am - 12:00pm Dr. Wolfgang Rucker

Devices III: Induction Heating and Superconductivity
Wednesday, July 16, 10:45am - 12:00pm
Chairmen
Prof. Jan Sykulski
Dr. Stephan Russenschuck

Software Chairman
Wednesday, July 16, 10:45am - 12:00pm Dr. Zhuoxiang Ren

Optimization III Chairman
Wednesday, July 16, 1:30pm - 2:45pm Dr. Piergiorgio Alotto

EMC Chairman
Wednesday, July 16, 1:30pm - 2:45pm Dr. Laurent Nicolas

Machines III: PM Chairman
Wednesday, July 16, 1:30pm - 2:45pm

Materials I: Hysteresis Chairman
Wednesday, July 16, 1:30pm - 2:45pm Dr. Yasushi Kanai

Waves Chairman
Wednesday, July 16, 3:15pm - 5:30pm Jin-Fa Lee

COMPUMAG Saratoga Springs, New York USA
July 13 - 17, 2003

Nonconforming Mixed Finite Element Approximations to Time-Harmonic Eddy Current Problems

P. Houston[1], I. Perugia[2] and D. Schötzau[3]

Abstract— **We present nonconforming mixed finite element methods for the discretization of time-harmonic eddy current problems. These methods are based on a discontinuous Galerkin approach, where the unknowns are approximated by discontinuous piecewise polynomials. In particular, we consider a stabilized mixed formulation involving equal-order $\mathbb{P}^\ell - \mathbb{P}^\ell$ elements, and a non-stabilized variant employing mixed-order $\mathbb{P}^\ell - \mathbb{P}^{\ell+1}$ elements.**

I. Introduction

In recent years, there has been considerable interest, especially in the context of fluid-dynamics, in nonconforming finite element methods that are based on discontinuous piecewise polynomial approximation spaces. Such approaches are referred to as discontinuous Galerkin (DG) methods (for a recent overview, see [1]). The main advantages of these methods lie in their conservation properties, their ability to treat a wide range of problems within the same unified framework, and their great flexibility in the mesh-design. Indeed, DG methods can easily handle non-matching grids and non-uniform, even anisotropic, polynomial approximation degrees. Moreover, orthogonal bases can easily be constructed which lead to diagonal mass matrices; this is particularly advantageous in unsteady problems. Finally, DG methods can easily be parallelized.

This paper deals with DG discretizations of mixed field and potential-based formulations of eddy current problems in the time-harmonic regime. For the electric field formulation, the divergence-free constraint within non-conductive regions is imposed by means of a Lagrange multiplier. This allows for the correct capturing of edge and corner singularities in polyhedral domains; in contrast, additional Sobolev regularity must be assumed in the DG formulations [2] and [3], when regularization techniques are employed. In particular, we present a mixed method involving discontinuous $\mathbb{P}^\ell - \mathbb{P}^\ell$ elements, which includes a normal jump stabilization term, and a non-stabilized variant employing discontinuous $\mathbb{P}^\ell - \mathbb{P}^{\ell+1}$ elements. The first formulation, introduced in [4], delivers optimal convergence rates for the vector-valued unknowns in a suitable energy norm. The second formulation, which can be viewed as a DG version of the mixed method of [5], is new; this latter scheme is designed to yield optimal convergence rates in both the L^2–norm, as well as in a suitable energy norm.

II. Model Problem

Given $\Omega \subset \mathbb{R}^3$, a simply connected bounded Lipschitz polyhedron with connected boundary $\partial\Omega$, we consider the following problem: find the vector field $\boldsymbol{u}$ and the scalar field p such that

$$\begin{aligned} \nabla \times (\mu^{-1} \nabla \times \boldsymbol{u}) + \eta_1 \boldsymbol{u} + \eta_2 \nabla p &= \boldsymbol{f} \quad \text{in } \Omega, \\ \nabla \cdot (\eta_3\, \boldsymbol{u} + \eta_4 \nabla p) &= 0 \quad \text{in } \Omega, \end{aligned} \tag{1}$$

with suitable boundary conditions, where $\boldsymbol{f}$ is a given source field, and the coefficients μ and η_i, $i = 1, \ldots, 4$, are real functions (in all the cases below, μ is the magnetic permeability).

For $\eta_i = j\omega\sigma$, $i = 1, \ldots, 4$, where ω is a given frequency and σ the electric conductivity, problem (1) represents the $\boldsymbol{A} - V$ formulation of the time-harmonic eddy current problem [6] ($\boldsymbol{u} \equiv \boldsymbol{A}$, the magnetic vector potential, and $p \equiv V$, the electric scalar potential). For $\eta_1 = j\omega\sigma$, $\eta_4 = 0$ and $\eta_2 = \eta_3 = -\varepsilon\chi_{\Omega_0}$, where ε is the electric permittivity and χ_{Ω_0} the characteristic function of the non-conducting subregion $\Omega_0 \subseteq \Omega$, problem (1) is a mixed electric field formulation of the time-harmonic eddy current problem ($\boldsymbol{u} \equiv \boldsymbol{E}$ and p is the Lagrange multiplier related to the divergence-free constraint in Ω_0). For $\eta_1 = \eta_4 = 0$ and $\eta_2 = \eta_3 = 1$, (1) is a mixed magnetic vector potential formulation of the magnetostatic problem with Coulomb's gauge.

III. DG Formulations

We present two DG methods for the discretization of problem (1). For simplicity, we set $\eta_1 = \eta_4 = 0$, $\mu = \eta_2 = \eta_3 = 1$, and impose $\boldsymbol{n} \times \boldsymbol{u} = \boldsymbol{0}$ and $p = 0$ on $\partial\Omega$. The key difficulties in the numerical treatment of the more general problem (1) are present in this particular case.

A. Meshes, finite element spaces and trace operators

We consider shape regular meshes $\mathcal{T}_h$ that partition Ω into tetrahedra, with possible hanging nodes. We denote by h_K the diameter of $K \in \mathcal{T}_h$ and set $h = \max_K h_K$. An *interior face* of $\mathcal{T}_h$ is the (non-empty) two-dimensional interior of $\partial K^+ \cap \partial K^-$, where K^+ and K^- are two adjacent elements, not necessarily matching. A *boundary face* of $\mathcal{T}_h$ is the (non-empty) two-dimensional interior of $\partial K \cap \partial\Omega$, where K is a boundary element. We denote by $\mathcal{E}_h^{\mathcal{I}}$ and $\mathcal{E}_h^{\mathcal{D}}$ the union of all interior and boundary faces, and set $\mathcal{E}_h = \mathcal{E}_h^{\mathcal{I}} \cup \mathcal{E}_h^{\mathcal{D}}$. We define the *local meshsize* function $\mathtt{h}$ on $\mathcal{E}_h$ by setting $\mathtt{h}(\boldsymbol{x}) = \min\{h_{K^+}, h_{K^-}\}$, if $\boldsymbol{x}$ is in the interior of $\partial K^+ \cap \partial K^-$, and $\mathtt{h}(\boldsymbol{x}) = h_K$, if $\boldsymbol{x}$ is in the interior of $\partial K \cap \partial\Omega$.

The generic discontinuous finite element space is

$$P^\ell(\mathcal{T}_h) := \{u \in L^2(\Omega) : \, u|_K \in \mathbb{P}^\ell(K) \;\; \forall K \in \mathcal{T}_h\},$$

where $\mathbb{P}^\ell(K)$ is the space of polynomials of degree $\leq \ell$ on K.

For $e \subset \mathcal{E}_h^{\mathcal{I}}$ shared by two elements K^+ and K^- with outward unit normals $\boldsymbol{n}^\pm$, respectively, we define, with obvious notation, the *jumps* across e by $[\![\boldsymbol{v}]\!]_T = \boldsymbol{n}^+ \times \boldsymbol{v}^+ + \boldsymbol{n}^- \times \boldsymbol{v}^-$, $[\![\boldsymbol{v}]\!]_N = \boldsymbol{v}^+ \cdot \boldsymbol{n}^+ + \boldsymbol{v}^- \cdot \boldsymbol{n}^-$, $[\![q]\!]_N = q^+\boldsymbol{n}^+ + q^-\boldsymbol{n}^-$, and the *averages* by $\{\!\{\boldsymbol{v}\}\!\} = (\boldsymbol{v}^+ + \boldsymbol{v}^-)/2$ and $\{\!\{q\}\!\} = (q^+ + q^-)/2$. On $e \subset \mathcal{E}_h^{\mathcal{D}}$, we set $[\![\boldsymbol{v}]\!]_T = \boldsymbol{n} \times \boldsymbol{v}$, $[\![q]\!]_N = q\,\boldsymbol{n}$ and $\{\!\{\boldsymbol{v}\}\!\} = \boldsymbol{v}$.

[1]Department of Maths. & Computer Science, University of Leicester, Leicester LE1 7RH, UK. Email: Paul.Houston@mcs.le.ac.uk
(Funded by the EPSRC: Grant GR/R76615)
[2]Dipartimento di Matematica, Università di Pavia, Via Ferrata 1, 27100 Pavia, Italy. Email: perugia@dimat.unipv.it
[3]Department of Mathematics, University of Basel, Rheinsprung 21, 4051 Basel, Switzerland. Email: schotzau@math.unibas.ch

B. Discontinuous Galerkin discretizations

For the finite element spaces $\boldsymbol{V}_h = P^\ell(\mathcal{T}_h)^3$ and $Q_h = P^m(\mathcal{T}_h)$ with $\ell, m \geq 1$, we introduce the following DG methods for problem (1): find $(\boldsymbol{u}_h, p_h) \in \boldsymbol{V}_h \times Q_h$ such that

$$\begin{aligned} a_h(\boldsymbol{u}_h, \boldsymbol{v}) + b_h(\boldsymbol{v}, p_h) &= f_h(\boldsymbol{v}) \qquad \forall\, \boldsymbol{v} \in \boldsymbol{V}_h, \\ b_h(\boldsymbol{u}_h, q) \ -c_h(p_h, q) &= 0 \qquad \forall\, q \in Q_h. \end{aligned}$$

Here, a_h, b_h, c_h and f_h are defined, respectively, by

$$\begin{aligned} a_h(\boldsymbol{u}, \boldsymbol{v}) &= \int_\Omega \nabla_h \times \boldsymbol{u} \cdot \nabla_h \times \boldsymbol{v}\, d\boldsymbol{x} \\ &\quad - \int_{\mathcal{E}_h} \Big([\![\boldsymbol{u}]\!]_T \cdot \{\!\{\nabla_h \times \boldsymbol{v}\}\!\} + [\![\boldsymbol{v}]\!]_T \cdot \{\!\{\nabla_h \times \boldsymbol{u}\}\!\} \Big)\, ds \\ &\quad + \int_{\mathcal{E}_h} \mathtt{a}\, [\![\boldsymbol{u}]\!]_T \cdot [\![\boldsymbol{v}]\!]_T\, ds + \int_{\mathcal{E}_h^{\mathcal{I}}} \mathtt{b}\, [\![\boldsymbol{u}]\!]_N [\![\boldsymbol{v}]\!]_N\, ds, \\ b_h(\boldsymbol{v}, p) &= -\int_\Omega \boldsymbol{v} \cdot \nabla_h p\, d\boldsymbol{x} + \int_{\mathcal{E}_h} \{\!\{\boldsymbol{v}\}\!\} \cdot [\![p]\!]_N\, ds, \\ c_h(p, q) &= \int_{\mathcal{E}_h} \mathtt{c}\, [\![p]\!]_N \cdot [\![q]\!]_N\, ds, \qquad f_h(\boldsymbol{v}) = \int_\Omega \boldsymbol{f} \cdot \boldsymbol{v}\, d\boldsymbol{x}, \end{aligned}$$

with ∇_h denoting the elementwise "nabla" operator. The parameters $\mathtt{a}$ and $\mathtt{c}$ are strictly positive and proportional to $1/\mathtt{h}$; $\mathtt{b}$ is a non-negative parameter used to penalize normal jumps of $\boldsymbol{u}$.
Method I (stabilized): we choose $\mathtt{b} > 0$ and proportional to $\mathtt{h}$, and $m = \ell$ (equal-order polynomial spaces).
Method II (non-stabilized): we choose $\mathtt{b} = 0$, and $m = \ell + 1$ (mixed-order polynomial spaces), to ensure stability.

Both methods are well-posed and deliver optimal convergence rates for the unknown $\boldsymbol{u}$ in the DG energy norm given by $\|\boldsymbol{u}\|_{\mathrm{DG}}^2 = \|\nabla_h \boldsymbol{u}\|_{L^2(\Omega)}^2 + \|\mathtt{a}^{\frac{1}{2}}\, [\![\boldsymbol{u}]\!]_T\|_{L^2(\mathcal{E}_h)}^2 + \|\mathtt{b}^{\frac{1}{2}}\, [\![\boldsymbol{u}]\!]_N\|_{L^2(\mathcal{E}_h^{\mathcal{I}})}^2$. In fact, on regular meshes we have the a-priori error bound

$$\|\boldsymbol{u} - \boldsymbol{u}_h\|_{\mathrm{DG}} \leq C h^{\min\{s,\ell\}} \big[\|\boldsymbol{u}\|_{H^s(\Omega)} + \|\nabla \times \boldsymbol{u}\|_{H^s(\Omega)} \big],$$

for $s > 1/2$. This result was derived for Method I in [4], together with optimal estimates for the error in p_h.

IV. Numerical Results

We select $\Omega \subset \mathbb{R}^2$ to be the L–shaped domain with vertices $(1,0)$, $(1,1)$, $(-1,1)$, $(-1,-1)$, $(0,-1)$ and $(0,0)$. Furthermore, we set $\mathbf{f} = \mathbf{0}$ and impose $\boldsymbol{n} \times \boldsymbol{u} = \boldsymbol{g}$ and $p = 0$ on $\partial\Omega$, where $\boldsymbol{g}$ is chosen so that $\boldsymbol{u}(x,y) = \nabla(r^{4/3} \sin(4\vartheta/3))$, in terms of the polar coordinates (r, ϑ). Fig. 1 presents a comparison of $\|\boldsymbol{u} - \boldsymbol{u}_h\|_{\mathrm{DG}}$ using the stabilized method ($\mathtt{a} = 10\ell^2/\mathtt{h}$, $\mathtt{b} = \mathtt{h}$, $\mathtt{c} = 1/\mathtt{h}$) with the (square root of the) number of degrees of freedom in $\boldsymbol{V}_h \times Q_h$, for $\ell = 1, 2$. Here, both uniform square and adaptively refined quadrilateral meshes with hanging nodes are considered. The adaptive meshes are constructed by employing the fixed fraction strategy (ref.: 25%, deref.: 0%) with a simple error indicator based on the gradient of the numerical approximation, cf. [4]. We observe that $\|\boldsymbol{u} - \boldsymbol{u}_h\|_{\mathrm{DG}}$ converges to zero at the optimal rate $\min(s, \ell)$, $s = 4/3 - \varepsilon$, $\varepsilon > 0$; cf. Section III-B. We note that the adaptive meshes with hanging nodes are easily handled by the DG approach. Analogous results hold for the non-stabilized method on uniform and adaptively refined triangular meshes; for brevity, these numerics are omitted.

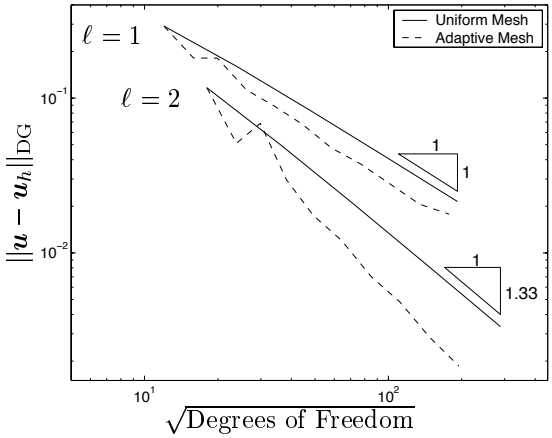

Fig. 1. Method I: Convergence of $\|\boldsymbol{u} - \boldsymbol{u}_h\|_{\mathrm{DG}}$.

Table I highlights the optimality of Method II in the L^2-norm, cf. [4] for the corresponding performance of Method I. Here, we approximate (1) on the same domain as above, but with a smooth exact solution $\boldsymbol{u}$, cf. [4]. For $\ell = 1, 2$, we show the L^2-errors and the convergence rates obtained on a sequence of uniformly refined triangular meshes with n elements ($\mathtt{a} = 10\ell^2/\mathtt{h}$ and $\mathtt{c} = 1/\mathtt{h}$); optimal rates of order $\ell + 1$ are clearly observed.

	$\ell = 1$		$\ell = 2$	
n	$\|\boldsymbol{u} - \boldsymbol{u}_h\|_{L^2(\Omega)}$	rate	$\|\boldsymbol{u} - \boldsymbol{u}_h\|_{L^2(\Omega)}$	rate
96	0.1910E-01	-	0.6586E-03	-
384	0.4866E-02	1.97	0.8210E-04	3.00
1536	0.1227E-02	1.99	0.1024E-04	3.00

TABLE I
Method II: Convergence of $\|\boldsymbol{u} - \boldsymbol{u}_h\|_{L^2(\Omega)}$.

V. Conclusions

Based on the DG methodology, we have considered two nonconforming mixed finite element methods for the discretization of time-harmonic eddy current problems. We have highlighted the advantages of these methods by illustrating the performance of the stabilized scheme on adaptively refined meshes with hanging nodes. The *a-priori* error analysis of Method II will be presented in a forthcoming article. Future work will include extensions to *hp*–adaptive finite element methods.

References

[1] B. Cockburn, G.E. Karniadakis, and C.-W. Shu, eds. *Discontinuous Galerkin Methods. Theory, Computation and Applications*, vol. 11 of *Lect. Notes Comput. Sci. Eng.* Springer–Verlag, 2000.

[2] I. Perugia and D. Schötzau. The *hp*-local discontinuous Galerkin method for low-frequency time-harmonic Maxwell's equations. To appear in *Math. Comp.*

[3] P. Houston, I. Perugia, and D. Schötzau. *hp*-DGFEM for Maxwell's equations. Tech. Rep. 02-02, Dept. of Mathematics, University of Basel, 2002.

[4] P. Houston, I. Perugia, and D. Schötzau. In preparation.

[5] L. Demkowicz and L. Vardapetyan. Modeling of electromagnetic absorption/scattering problems using *hp*–adaptive finite elements. *Comput. Meth. Appl. Mech. Engrg.*, vol. 152, pp. 103-124, 1998.

[6] O. Biro. Edge element formulations of eddy current problems. *Comput. Methods Appl. Mech. Engrg.*, vol. 169, pp. 391-405, 1999.

High-Order Adaptive Time-Domain Solution of Nonlinear Coupled Electromagnetic-Thermal Problems

Zsolt Badics **Bogdan Ionescu** **Zoltan J. Cendes**
Ansoft Corporation
Four Station Square Suite 200
Pittsburgh PA 15219 U.S.A.
badics@ansoft.com, bionescu@ansoft.com, zol@ansoft.com

***Abstract*—An adaptive time-integration algorithm is described for the solution of nonlinear one-way coupled electromagnetic (EM)–thermal problems. The thermal excitations are time-varying thermal loads or/and EM losses due to DC or AC excitation sequences. The equations are discretized in time by an implicit one-step Rosenbrock method. No Newton iteration is required in a time step; only one linear equation system with multiple right hand sides has to be solved. High order integration is achieved by incorporating the Jacobian into the time-integration formula. An induction hardening problem is solved to illustrate the efficiency of the algorithm.**

Model Description

Coupled EM-thermal problems often involve EM systems where the duration of EM transient processes is negligible compared to the time constant of the thermal problem. Assuming that the material properties are relatively constant with respect to temperature, one can solve the EM field distribution and from this compute the loss distribution. The temperature $\vartheta(t,\vec{x})$ resulting from this loss is determined by the nonlinear initial boundary value problem

$$\rho c \partial_t \vartheta = -\nabla\cdot\vec{q} + Q_v(t,\vec{x}), \qquad \vec{q} = -\mathbf{k}(\vartheta)\nabla\vartheta \qquad \text{in } \Omega \quad (1)$$

$$\vartheta(0,\vec{x}) = \vartheta_0(\vec{x}) \qquad \text{in } \Omega \quad (2)$$

$$\vec{q}\cdot\hat{n} = q_C(\vartheta) = h(\vartheta)(\vartheta - \vartheta_r) \qquad \text{on } \Gamma \quad (3)$$

where ρ is the mass density, c is the specific heat, $\mathbf{k}(\vartheta)$ is the nonlinear anisotropic thermal conductivity, and $\vec{q}$ denotes the heat flux density [1]. $\vartheta_0(\vec{x})$ is a given consistent initial temperature distribution. $h(\vartheta)$ and ϑ_r represent convection and/or radiation heat transfer coefficients and the corresponding reference temperatures, respectively.

The volumetric thermal load density Q_v in (1) is either a given function of time or a loss distribution sequence. Consecutive time intervals of an EM loss sequence are generated by different DC or AC excitation states. Figure 1 presents a pictorial representation of the coupled problem with a piecewise constant excitation sequence.

Temporal Discretization

In this work, we discretize in time first, then in space following [2, 3]. Write (1)-(3) as an abstract Cauchy problem

$$\rho c \partial_t \vartheta = F(t,\vartheta(t)), \qquad \vartheta(0) = \vartheta_0, \qquad 0 < t \le t_{END} \qquad (4)$$

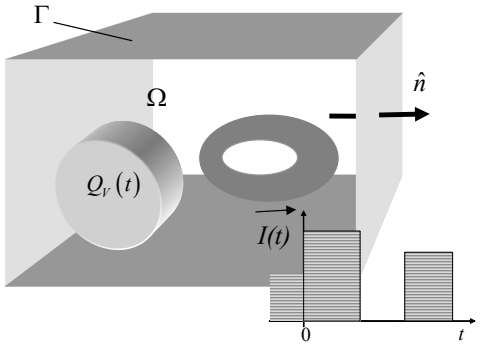

Figure 1. A coupled EM-thermal problem with a varying levels of excitation

We apply a Rosenbrock time-integration strategy that is a *diagonally implicit implicit Runge-Kutta* (DIRK) one-step integration scheme [4, 5]. Suppose that at t_n the temperature is ϑ_n and the selected time step is τ_n. Then, the *M*-stage Rosenbrock scheme estimates ϑ_{n+1} at $t_{n+1} = t_n + \tau_n$ in the form

$$\vartheta_{n+1} = \vartheta_n + \sum_{s=1}^{M} m_s \varphi_{ns} \qquad (5)$$

where φ_{ns} are the stage-variables computed by a set of *M* recursive formulas. The coefficients m_s are suitably selected to obtain desired properties detailed in [4, 5].

The local truncation error r_{n+1} is approximated as

$$r_{n+1} = \vartheta_{n+1} - \hat{\vartheta}_{n+1}; \qquad \hat{\vartheta}_{n+1} = \vartheta_n + \sum_{s=1}^{M} \hat{m}_s \varphi_{ns} \qquad (6)$$

where $\hat{\vartheta}_{n+1}$ is another approximation of ϑ whose order is lower than the order of ϑ_{n+1}. After selecting a suitable error norm $\|\bullet\|$, the quantity $\|r_{n+1}\|$ represents the global temporal error accurately. Figure 2 shows the flow chart of the time-integration algorithm where the time step control implementation is based on the idea introduced in [6].

Spatial Discretization

We can write the *M*-stage Rosenbrock formulas that yield the stage variables φ_{ns} as a set of boundary value problems

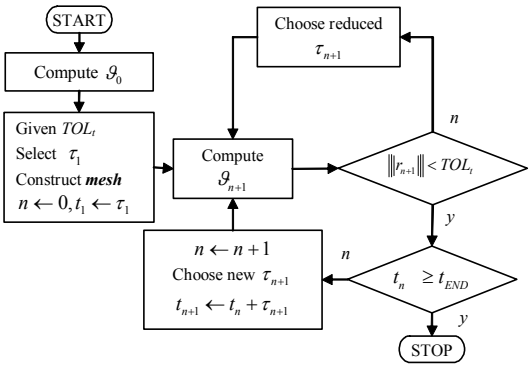

Figure 2. Implementation of the Rosenbrock time integration scheme

$$\frac{\rho c}{\tau_n \gamma}\varphi_{ns} - \nabla\cdot\left(\mathbf{k}\nabla\varphi_{ns}\right) = \nabla\cdot\left(\mathbf{k}\nabla\vartheta_s\right) + Q_v\left(t_s\right) \quad \text{in } \Omega \quad (7)$$
$$+\tau_n\gamma_s\partial_t Q_v\left(t_n\right) - \sum_{j=1}^{s-1}\frac{c_{sj}\rho c}{\tau_n}\varphi_{nj}; \quad s = 1,\ldots,M$$

$$\mathbf{k}\nabla\varphi_{ns}\cdot\hat{n} + \partial_\vartheta q_C\left(\vartheta_n\right)\varphi_{ns} = -q_C\left(\vartheta_s\right) - \mathbf{k}\nabla\vartheta_s\cdot\hat{n} \quad \text{on } \Gamma \quad (8)$$

where $t_s = t_n + \alpha_s\tau_n$ and $\vartheta_s = \vartheta_n + \sum_{j=1}^{s-1} a_{sj}\varphi_{nj}$. The coefficients γ, γ_s, c_{sj}, α_s, and a_{sj} are suitably selected to obtain desired properties detailed in [4, 5]. For the sake of brevity, we consider only linear anisotropic thermal conductivity in (7) and (8). The discretization of the weak form of (7) and (8) is performed by the Galerkin finite element method. Notice that Newton iteration is not required; the Jacobian is incorporated into the time integration formula. Thus, we have to solve *M* sets of linear equations with the same coefficient matrix.

Test Problem

In the problem in Figure 3, the goal is to generate a sudden temperature increase due to eddy currents at the *target area*. The coil current is 2.5 kA (rms) at 270 kHz. The electric and thermal conductivities of the specimen are 9.2E5 S/m and 24.3 W/mK. The heat capacity ρc is 4.8 MJ/m^{3}K. We consider a combination of radiation and convection boundary conditions on the specimen surface.

Figure 4 *(a)* shows the temperature rise resulting from a current step. According to the designers' observation, the average temperature of the target area is between 900 C and 1000 C at 0.8 second. Our result, 939 C, agrees with the observation. Figure 4 *(b)* illustrates the efficiency of our time-step control algorithm. At the beginning, a couple of very small time steps are necessary because of the abrupt appearance of the EM losses. Then, the algorithm quickly increases the step size for a short period until the radiation effect kicks in when step-size reduction is again necessary. As the stationary stage is approached, the step size is increasing gradually.

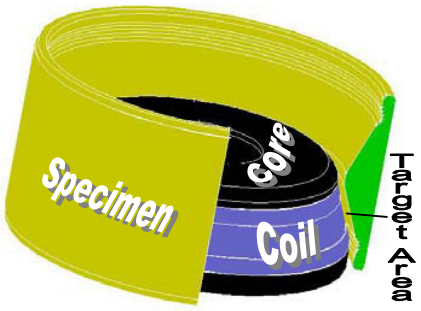

Figure 3. Induction hardening problem: a coil with a ferromagnetic core generates eddy currents and as a result, heat in the specimen. The bulk of the heat is concentrated at the *target area*, which is the part of the inner surface area of the specimen directly facing the coil.

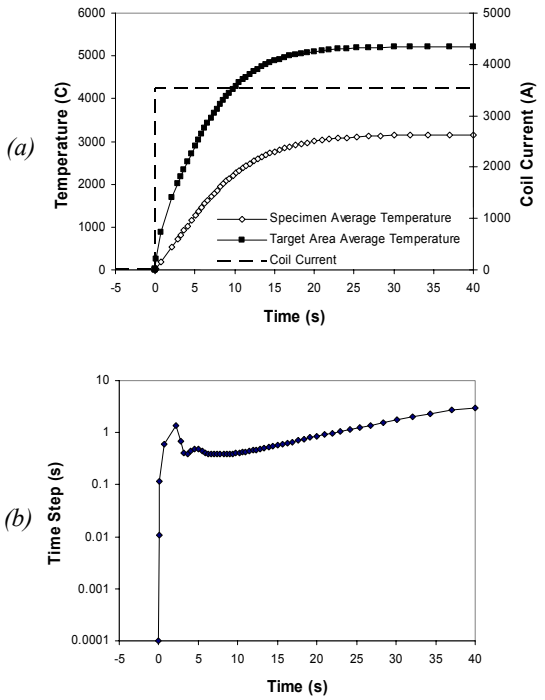

Figure 4. *(a)* Coil current, average temperatures, and *(b)* time steps vs. time

References

[1] J.N. Reddy, D.K. Gartling, *The Finite Element Method in Heat Transfer and Fluid Dynamics*, CRC Press, Boca Raton, 1994.

[2] Bornemann, F. A., "An adaptive multilevel approach to parabolic equations. I. General theory and 1D implementation," IMPACT of Comput. In Sci. and Engrg., 2, pp. 279-317, 1990.

[3] J. Lang, "Adaptive FEM for Reaction-Diffusion Equations," Appl. Numer. Math., 26, pp. 105-116, 1998.

[4] Rosenbrock, H. H., "Some general implicit processes for the numerical solution of differential equations," Computer J., 5, pp. 329-331, 1963.

[5] K.E. Brenan, S.L. Campbell, and L.R. Petzold, *Numerical Solution of Initial-Value Problems in Differential-Algebraic Equations*, SIAM Classics in Applied Mathematics 14, North-Holland, New York, 1996.

[6] K. Gustafsson, "Control-theoretical techniques for step size selection in implicit Runge-Kutta methods," ACM Trans. Math. Software, 20, pp. 496-517, 1994.

COMPUMAG Saratoga Springs, New York USA
July 13 - 17, 2003

Fast Multipole Acceleration of the Hybrid Finite Element-Boundary Element Analysis of 3D Eddy Current Problems

R. V. Sabariego, J. Gyselinck, P. Dular, C. Geuzaine and W. Legros

Department of Electrical Engineering, Institut Montefiore, University of Liège,
Sart Tilman Campus, Building B28, B-4000 Liège, Belgium, r.sabariego@ulg.ac.be

Abstract **– This paper deals with the acceleration of the hybrid finite element – boundary element analysis of 3D eddy current problems by means of the fast multipole method. An adaptive truncation scheme for the multipole expansion of the 3D Laplace Green function is proposed. As an application example, the TEAM workshop problem 28 is considered.**

Introduction

Hybrid finite element – boundary element (FE-BE) models are particularly suited for solving open electromagnetic field problems that comprise movement, nonlinear media and eddy currents [1]. However, the BE part of the hybrid model generates dense blocks in the system matrix and significantly limits the problem size. The fast multipole method (FMM) [2] can be employed to overcome this limitation, reducing both the memory requirements and the computation time. It has been successfully applied to BE models in both the high frequency and the low frequency domain [3]. With regard to hybrid FE-BE models, the FMM has been solely used in scattering applications. This paper deals with its application to a hybrid FE-BE model of low frequency eddy current problems. As test case, the TEAM workshop problem 28 is considered [4].

3D Hybrid FE-BE model

We consider a magnetodynamic problem in $\mathbb{R}^3$. The FE method is used in a domain Ω with boundary Γ while the BE method takes into account the space exterior to Ω. The eddy current conducting part of Ω is denoted Ω_c and the non-conducting one Ω_c^C. Source conductors, with a given current density $\underline{j}_s$, are comprised in $\Omega_s \subset \Omega_c^C$.

Adopting the magnetic field formulation, the general expression of the magnetic field $\underline{h}$ in Ω is

$$\underline{h} = \underline{h}_s + \underline{h}_r - \mathrm{grad}\phi, \tag{1}$$

with $\underline{h}_s$ a source field satisfying $\mathrm{curl}\,\underline{h}_s = \underline{j}_s$, $\underline{h}_r$ the reaction field in Ω_c, and ϕ the reaction magnetic scalar potential in Ω_c^C.

The $\underline{h} - \phi$ magnetodynamic formulation is obtained from the weak form of the Faraday equation:

$$\partial_t(\mu\underline{h}, \underline{h}')_\Omega + (\sigma^{-1}\mathrm{curl}\,\underline{h}, \mathrm{curl}\,\underline{h}')_{\Omega_c} + (\sigma^{-1}\underline{j}_s, \mathrm{curl}\,\underline{h}')_{\Omega_s} + \partial_t\langle\underline{n}\cdot\underline{b}, \phi'\rangle_\Gamma = 0, \quad \forall\,\underline{h}' \in F_{h\phi}(\Omega), \tag{2}$$

where μ is the magnetic permeability, σ is the electric conductivity; $\underline{n}$ is the unit normal vector on Γ pointing into Ω; $(\cdot,\cdot)_\Omega$ and $\langle\cdot,\cdot\rangle_\Gamma$ denote a volume integral in Ω and a surface integral on Γ of the product of its arguments; $F_{h\phi}(\Omega)$ is the function space defined on Ω and containing the basis functions for $\underline{h}$ (coupled to ϕ) as well as for the test function $\underline{h}'$ [5].

The research has been carried out in the frame of the Inter-University Attraction Poles IAP P5/34 funded by the Belgian federal goverment. P. Dular is a Research Associate with the Belgian National Fund for Scientific Research (F.N.R.S.).

The coupling with the BE model is done through the surface integral in (2). We define the following integral operator:

$$\mathcal{P}(q) = \int_\Gamma q\,G\,\mathrm{d}\Gamma \quad \text{with} \quad G(\rho) = \frac{1}{4\pi\rho}, \tag{3}$$

where q is an equivalent magnetic charge on Γ and $G(\rho)$ is the 3D Laplace Green function, ρ being the distance between a source point $\underline{r}_s$ (on Γ) and an observation point $\underline{r}_o$ (in $\mathbb{R}^3\backslash\Omega$). The normal derivative of (3a) in a point on Γ is given by

$$\underline{n}\cdot\mathrm{grad}\,\mathcal{P}(q) = \frac{1}{2}q + \int_\Gamma \underline{n}\cdot\mathrm{grad}\,G\,q\;\mathrm{d}\Gamma. \tag{4}$$

The scalar potential and its normal derivative in a point on Γ can be expressed as

$$\phi(\underline{r}) = \mu^{-1}\,\mathcal{P}(q)\,, \qquad \underline{n}\cdot\mathrm{grad}\,\phi(\underline{r}) = \mu^{-1}\underline{n}\cdot\mathrm{grad}\,\mathcal{P}(q)\,. \tag{5}$$

The surface term in (2) thus becomes

$$\partial_t\langle\underline{n}\cdot\underline{b}, \phi'\rangle_\Gamma = -\partial_t\langle\underline{n}\cdot\mathrm{grad}\,\mathcal{P}(q), \phi'\rangle_\Gamma + \partial_t\langle\mu\underline{n}\cdot\underline{h}_s, \phi'\rangle_\Gamma\,. \tag{6}$$

The weak form of (5a) reads:

$$\langle\phi, q'\rangle_\Gamma = \langle\mu^{-1}\mathcal{P}(q), q'\rangle_\Gamma, \quad \forall q' \in F_q(\Gamma)\,, \tag{7}$$

where $F_q(\Gamma)$ is the function space defined on Γ.

Fast Multipole Method

The fast multipole method (FMM) decomposes the boundary Γ into $\#g$ groups of elements, $\Gamma = \bigcup_{g=1}^{\#g}\Gamma_g$, and determines the interactions between distant groups by means of the multipole expansion of the Green function. Let Γ_s be

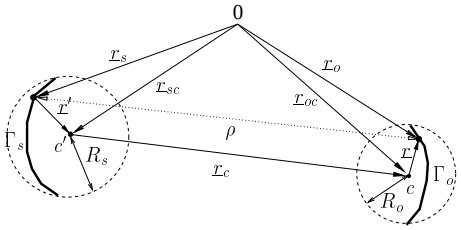

Fig. 1: Distant groups Γ_s and Γ_o on the contour Γ with centers c' and c

a source group with center $\underline{r}_{sc}$ and a source point $\underline{r}_s$, and Γ_o an observation group with center $\underline{r}_{oc}$ and an observation point $\underline{r}_o$. We define the vectors $\underline{r} = \underline{r}_o - \underline{r}_{oc} = (r,\theta,\phi)$, $\underline{r}_c = \underline{r}_{oc} - \underline{r}_{sc} = (r_c,\theta_c,\phi_c)$ and $\underline{r}' = \underline{r}_{sc} - \underline{r}_s = (r',\theta',\phi')$ as shown in Fig. 1. Omitting the factor $1/4\pi$, the 3D Laplace Green function (3b), with $\rho = |\underline{r}_o - \underline{r}_s|$, is expanded as [2]:

$$\frac{1}{\rho} = \Re\Big(\sum_{m=0}^{\infty}\sum_{n=-m}^{m}\sum_{u=0}^{\infty}\sum_{v=-u}^{u}\mathcal{D}_{m,n}\,\mathcal{T}_{m+u,n+v}\,\mathcal{A}_{u,v}\Big) \text{ with} \tag{8}$$

$$\mathcal{D}_{m,n}\,(\underline{r}) = \frac{r^m\,\mathcal{L}_n^m(\theta,\phi)}{(m+n)!}\,, \quad \mathcal{A}_{u,v}\,(\underline{r}') = \frac{r'^u\,\mathcal{L}_u^v(\theta',\phi')}{(u+v)!}\,, \tag{9}$$

$$\mathcal{T}_{m+u,n+v}\left(\underline{r}_c\right) = \frac{(m+u-(n+v))!}{r_c^{m+u+1}}\,\mathcal{L}_{m+u}^{n+v}(\theta_c,-\phi_c)\,, \quad (10)$$

where $\mathcal{L}_n^m(\theta,\phi) = P_m^n(\cos\theta)\,e^{-\imath n\phi}$, P_m^n being the Legendre function of degree m and order n. The imaginary number is denoted $\imath$ and $\Re$ indicates the real part.

In practice, the multipole expansion (8) must be truncated by considering $0 \le m \le p$ and $0 \le u \le p$, where the truncation number p must be sufficiently large to limit the error to a prescribed value ε. In most cases, the conventional choice $p = \log_2(1/\varepsilon)$ [2] is too conservative. Indeed, if $r' \ll r_c$ and $r \ll r_c$, a smaller number of terms suffices. A more economic law takes those distances into account. Let us consider $R_s = \max_{\Gamma_s}(r')$, $R_o = \max_{\Gamma_o}(r)$ and $d = r_c$. The minimum value of p as a function of R_o/d and R_s/d for $\varepsilon = 10^{-6}$ is depicted in Fig. 2.

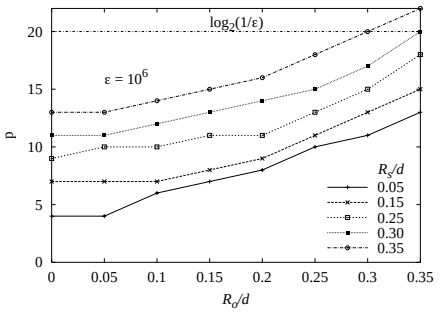

Fig. 2: Truncation number $p(R_o/d, R_s/d)$ for $\varepsilon = 10^{-6}$

The expansion of $\operatorname{grad} G$ is required as well. It can be straightforwardly obtained by deriving (9a) with respect to the coordinates of the observation point.

Application of the FMM

For demonstrating the FMM, let us consider the dense block $\boldsymbol{M}$ in the system matrix due to right handside of (7). The block $\boldsymbol{M}$ can be formally written as

$$\boldsymbol{M} \;\approx\; \boldsymbol{M}^{near} + \boldsymbol{M}^{far} \;=\; \boldsymbol{M}^{near} + \underbrace{\sum_{o=1}^{\#g}\sum_{s=1}^{\#g}}_{\Gamma_o,\,\Gamma_s \text{ far}} \boldsymbol{M}_{o,s}^{far}\,. \quad (11)$$

Let us consider the degrees of freedom q_k and q_l of q with associated basis functions $\beta_k(\underline{r}_o)$ and $\beta_l(\underline{r}_s)$ that are nonzero on the respective far groups Γ_o and Γ_s. Substituting (8) in (7), the contribution to the corresponding element $\left(\boldsymbol{M}_{o,s}^{far}\right)_{k,l}$ in $\boldsymbol{M}^{far}$ is given by

$$\Re\left(\sum_{m=0}^{p}\sum_{n=-m}^{m}\boldsymbol{M}_{o,k,m,n}^{\mathcal{D}}\sum_{u=0}^{p}\sum_{v=-u}^{u}\boldsymbol{M}_{m+u,n+v}^{\mathcal{T}}\,\boldsymbol{M}_{s,l,u,v}^{\mathcal{A}}\right), \quad (12)$$

with

$$\boldsymbol{M}_{o,k,m,n}^{\mathcal{D}} = \int_{\Gamma_o}\beta_k\mathcal{D}_{m,n}\,\mathrm{d}\Gamma\,, \quad \boldsymbol{M}_{s,l,u,v}^{\mathcal{A}} = \int_{\Gamma_s}\beta_l\mathcal{A}_{u,v}\,\mathrm{d}\Gamma\,, \quad (13)$$

$$\boldsymbol{M}_{m+u,n+v}^{\mathcal{T}} = \frac{1}{4\pi\mu}\mathcal{T}_{m+u,n+v}\,. \quad (14)$$

The aim of the formal decomposition (12) is speeding up the multiplication of $\boldsymbol{M}^{far}$ by a trial vector $\boldsymbol{Q}$, required for the iterative solution of the system of algebraic equations. Group by group, the field produced by the equivalent charge in the considered group is aggregated into its center by (13b). This aggregated field is then subsequently translated to the centers of all the far groups by (14), and finally the aggregated and translated field is disaggregated into the degrees of freedom of the far groups thanks to (13a).

Application Example

The TEAM workshop problem 28 [4] is chosen as test case (see Fig. 3). It concerns a cylindrical aluminium plate located above two coaxial coils carrying imposed sinusoidal currents. For the time being, the linear eddy current problem is solved for a fixed position, adopting the complex formalism. In the extended paper, the motion of the plate will be taken into account as well. The source magnetic field $\underline{h}_s$ is calculated by means of the Biot-Savart law. The FE domain Ω can be thus restricted to the conducting plate Ω_c.

The system of algebraic equations is solved by means of the iterative solver GMRES with ILU-preconditioning on a 400 MHz MIPS R12000 Processor. In case of FMM acceleration, the preconditioning is based on the sparse matrix comprising the complete FE contribution but only the BE near-field interactions.

The hybrid FE-BE discretisation yields 6344 complex unknowns: 5000 for the FE part and 1344 for the BE part. The solution of the system was obtained after 31473 s and 8980 s for the non-accelerated and the accelerated model respectively. With regard to the memory requirements, the FMM acceleration reduces them from 260 MByte to 128 MByte.

More results and further discussion on the computational cost will be included in the extended paper.

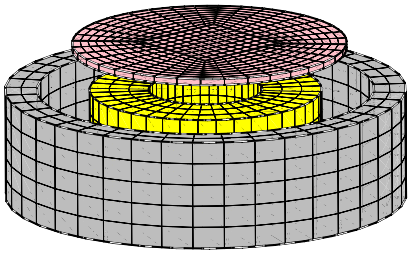

Fig. 3: Levitation device model

References

[1] S. Kurz, J. Fetzer, G. Lehner and W. M. Rucker, "A novel formulation for 3D eddy current problems with moving bodies using a lagrangian description and BEM-FEM coupling," *IEEE Transactions on Magnetics*, vol. 34, no. 5, pp. 3068–3073, Sept. 1998.

[2] V. Rokhlin, "Rapid solution of integral equations of classical potential theory," *Journal of Computational Physics*, vol. 60, no. 2, pp. 187–207, 1985.

[3] A. Buchau, C. J. Huber, W. Rieger and W. M. Rucker, "Fast BEM computations with the adaptive multilevel fast multipole method," *IEEE Transactions on Magnetics*, vol. 36, no. 4, pp. 680–684, July 2000.

[4] H. Karl, J. Fetzer, S. Kurz, G. Lehner and W. M. Rucker, "Description of TEAM workshop problem 28: An electrodynamic levitation device," `http://ics.ec.lyon.fr/team.html`.

[5] P. Dular, C. Geuzaine, W. Legros, "A natural method for coupling magnetodynamic h-formulation and circuit equations," *IEEE Transactions on Magnetics*, vol. 35, no. 3, pp. 1626–1629, May 1999.

COMPUMAG Saratoga Springs, New York USA
July 13 - 17, 2003

Efficient parallel solution of time-stepped multi-slice eddy current induction motor models

Andrew M. Knight
Dept of Electrical and Computer Engineering, University of Alberta
Edmonton, AB. T6G 2V4, Canada
knight@ee.ualberta.ca

Abstract— **An approach to model skewed induction motors using multi-slice two dimensional eddy current FEA is presented. Using the transmission line modeling method to model nonlinear material properties, domain decomposition may be applied to the solution of combined field and circuit equations. As a result, the simulation may be readily parallelized. Test results are presented, indicating that the proposed technique accurately predicts motor performance. Timing data clearly show that the technique scales well with increasing number of processors.**

Keywords— **Finite Element Analysis, Induction Motor, Parallel Computation**

Introduction

Two-dimensional time-stepped finite element analysis of is becoming a commonly used tool in the design of induction motors. One limitation of the two-dimensional approach is the ability to model skewed machines. Skewing the rotors of small to medium size induction motors is a common practise to reduce harmonic components of torque and currents. Unfortunately, from the modeling perspective, skewed machines are inherently three dimensional. Using a multi-slice approach [1], [2] it is possible to approximate skew with a series of two-dimensional models. This approach works well, but as the number of slices increases, the simulation times rapidly reaches the point where the approach is not feasible for practical machine design. One option to reduce design times is to solve long finite element simulations in parallel. However, time-stepped FEA is essentially a serial problem requiring the repeated solution of sparse nonlinear matrices, which in turn are poorly suited to parallelization. In this paper, the numerical technique used is well suited to parallelization, and the results presented indicate that this parallel approach scales well with an increasing number of processors.

Modeling Approach

There are two well known approaches to the simulation of induction machine performance using two-dimensional time-stepped FEA: the coupled circuit approach and the eddy-current approach. Both techniques have been applied to the solution of skewed induction motors by using time-stepped, two-dimensional, multi-slice methods to approximate variation along the length of the machine [1], [2]. It has been shown [3], [4] that when modeling small induction motors the eddy current approach is significantly faster than the coupled circuit approach. In the eddy current approach, the two dimensional field equation:

$$\frac{\partial}{\partial x}\left(\nu\frac{\partial A}{\partial x}\right)+\frac{\partial}{\partial y}\left(\nu\frac{\partial A}{\partial y}\right)-J \tag{1}$$

may be written as follows:

$$\frac{\partial}{\partial x}\left(\nu\frac{\partial A}{\partial x}\right)+\frac{\partial}{\partial y}\left(\nu\frac{\partial A}{\partial y}\right) = 0 \tag{2}$$

$$\nu\frac{\partial^2 A}{\partial x^2}+\nu\frac{\partial^2 A}{\partial y^2} = -J \tag{3}$$

$$\nu\frac{\partial^2 A}{\partial x^2}+\nu\frac{\partial^2 A}{\partial y^2} = -\sigma\left(\frac{V_b}{l}-\frac{\partial A}{\partial t}\right) \tag{4}$$

where (2) corresponds to iron regions, (3) corresponds to stranded conductors and (4) corresponds to solid conductors. In many nonlinear FE simulations (2) is linearized using the Newton-Raphson approach. In this work, the nonlinearity is handled using the transmission line modelling (TLM) method [5]. This method incorporates nonlinearity using a nonlinear forcing function, with constant reluctivity ν_{init} in the left hand side of the finite element equations. Effectively, (2) may be re-written as:

$$\nu_{init}\frac{\partial^2 A}{\partial x^2}+\nu_{init}\frac{\partial^2 A}{\partial y^2} = -J_{TLM} \tag{5}$$

This technique, solving (5) iteratively with nonlinear J_{TLM} has been used to good effect in machines modeling [4], [6], [7]. When using the eddy current approach to model an unskewed motor the field equations are combined with external circuit equations to obtain a matrix equation of the form in (6).

$$\begin{bmatrix} \mathbf{S_f} & \mathbf{S_{fs}} & \mathbf{S_{frv}} & \mathbf{0} \\ \mathbf{S_{sf}} & \mathbf{S_s} & \mathbf{0} & \mathbf{0} \\ \mathbf{S_{frv}} & \mathbf{0} & \mathbf{S_{rv}} & \mathbf{S_{rvri}} \\ \mathbf{0} & \mathbf{0} & \mathbf{S_{rirv}} & \mathbf{S_{ri}} \end{bmatrix} \begin{bmatrix} \mathbf{A} \\ \mathbf{I_s} \\ \mathbf{V_r} \\ \mathbf{I_r} \end{bmatrix} = \begin{bmatrix} \mathbf{F_f} \\ \mathbf{F_i} \\ \mathbf{F_{rv}} \\ \mathbf{F_{ri}} \end{bmatrix} \tag{6}$$

In (6) subscripts f, s, rv, ri denote field, stator current, rotor voltage and rotor current terms respectively. $\mathbf{F}$ are forcing terms. It should be noted that the current terms contain the necessary dummy variables to ensure that the stiffness matrix is positive definite. Using $\mathbf{C}$ to denote circuit variables,(6) may be re-written as follows.

$$\begin{bmatrix} \mathbf{S_f} & \mathbf{S_{fc}} \\ \mathbf{S_{cf}} & \mathbf{S_c} \end{bmatrix} \begin{bmatrix} \mathbf{A} \\ \mathbf{C} \end{bmatrix} = \begin{bmatrix} \mathbf{F_f} \\ \mathbf{F_c} \end{bmatrix} \tag{7}$$

In the case where two slices are used to approximate a skewed rotor (7) may be rewritten as

$$\begin{bmatrix} \mathbf{S_{f_1}} & \mathbf{0} & \mathbf{S_{fc_1}} \\ \mathbf{0} & \mathbf{S_{f_2}} & \mathbf{S_{fc_2}} \\ \mathbf{S_{cf_1}} & \mathbf{S_{cf_2}} & \mathbf{S_{c_{sk}}} \end{bmatrix} \begin{bmatrix} \mathbf{A_1} \\ \mathbf{A_2} \\ \mathbf{C_{sk}} \end{bmatrix} = \begin{bmatrix} \mathbf{F_{f_1}} \\ \mathbf{F_{f_2}} \\ \mathbf{F_{c_{sk}}} \end{bmatrix} \tag{8}$$

It is important to note that the bar voltages will differ from slice to slice. Continuity of current from slice to slice

is ensured by the inclusion of rotor bar currents in the simultaneous equations.

The system of equations described by (8) would not normally lend itself to efficient parallelization. However, using the TLM method, the LHS of this system of equations is constant at each rotor position. Using domain decomposition, (8) may be rewritten as:

$$\mathbf{S_{dd}C_{sk}} = \mathbf{F_{dd}} \quad (9)$$

$$\mathbf{S_{dd}} = \mathbf{S_{c_{sk}}} - \mathbf{S_{fc_1}S_{f_1}^{-1}S_{fc_1}} - \mathbf{S_{fc_2}S_{f_2}^{-1}S_{fc_2}} \quad (10)$$

$$\mathbf{F_{dd}} = \mathbf{F_{c_{sk}}} - \mathbf{S_{fc_1}S_{f_1}^{-1}F_{f_1}} - \mathbf{S_{fc_2}S_{f_2}^{-1}F_{f_2}} \quad (11)$$

In the form of (9), the contributions from each slice may be calculated independently. In the example case of two slices computed using two processors, each processor calculates the field contribution to $\mathbf{S_{dd}}$ at the start of a time-step, when LU decomposition of $\mathbf{S_{dd}}$ is carried out. At each iteration, the nonlinear field forcing terms are independently calculated and passed to the 'root' process. Once (9) has been solved for currents and voltages, this information is sent to each process to recreate the magnetic vector potentials on each slice.

$$\mathbf{A} = \mathbf{S_f^{-1}}\left[\mathbf{F_f} - \mathbf{S_{fc}C_{sk}}\right] \quad (12)$$

During the iterative process, the only terms that need be passed between processors are the circuit forcing terms and the circuit variable solutions. i.e. the message passing requirement is very low.

Results

The approach presented was tested on a 208V 3-phase 2hp induction motor with rotor skew of one slot pitch. Table I presents a summary of measured torque and currents at rated load, together with predictions for an unskewed simulation, and ones using 4 or 7 slices. Torque predictions were calculated using an air gap element [8]. Figure 1 presents the predicted line current for the unskewed and 7 slice simulations. Table I demonstrates the suitability of this type of model for accurate performance predictions. Together with Fig. 1, these results clearly indicate the excessive harmonic content predicted when an unskewed simulation is used

TABLE I
Comparison of Simulation and Test Results, 1730 rpm

	Test	Slices		
		1	4	7
Steady torque(Nm)	8.29	8.24	8.30	8.29
Torque Ripple pk-pk (Nm)	N/A	2.91	0.603	0.570
Line 1 current(A)	6.48	6.50	6.36	6.36
Line 2 current(A)	6.55	6.53	6.35	6.35
Line 3 current(A)	6.53	6.42	6.37	6.37

The primary aim of this paper is to present a method of solving skewed machine problems in the minimum elapsed time, efficiently using parallel processing. Figure 2 presents timing data for serial and parallel solutions for up to 7 slices. For comparison, the total CPU requirement of the parallel solutions, (elapsed time multiplied by processors used), is also plotted. It is clear from this Fig. 2 that the approach presented in this paper is very scalable.

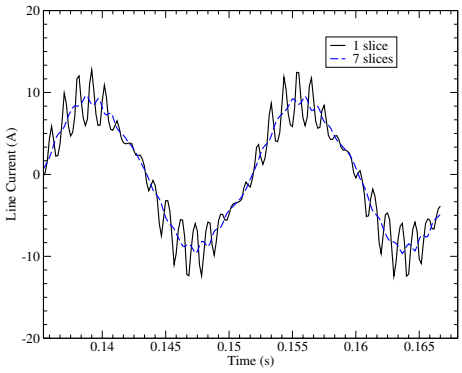

Fig. 1. Line current predictions

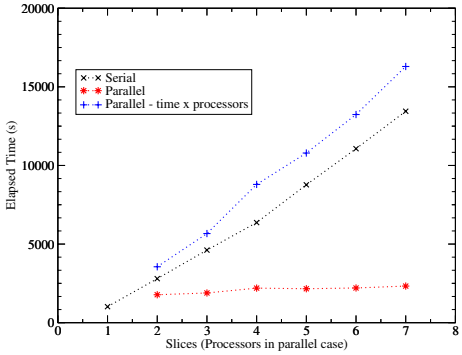

Fig. 2. Simulation Times

References

[1] S. Williamson, T.J. Flack, and A.F. Volschenk, "Representation of skew in timestepped two dimensional finite element models of electrical machines.," *IEEE Transactions on Industry Applications*, vol. 31, no. 5, pp. 1009–1015, Sep/Oct 1995.

[2] A. Tenhunen and A Arkkio, "Modelling of induction machines with skewed rotor slots," *IEE Proceedings on Electric Power Applications*, vol. 148, no. 1, pp. 45–50, 2001.

[3] C.I. McClay and van der Toornm G.T., "A comparison of time-stepped finite element techniques for the calculation of losses in cage induction motors," in *Ninth International Conference on Electrical Machines and Drives*. September 1999, pp. 35–39, IEE.

[4] A Knight, "A comparison of time-stepped finite element modelling methods for induction motor analysis," in *Proc.1st IEE Conference on Power Electronics, Machines and Drives (PEMD02)*. IEE, 2002, pp. 375–380.

[5] J. Lobry, J. Trecat, and c. Broche, "The transmission line modeling (tlm) method as a new iterative technique in nonlinear 2-d magnetostatics," *IEEE Transactions on Magnetics*, vol. 32, no. 2, pp. 559–566, March 1996.

[6] T.J. Flack and R.E. Knight, "On the domain decomposition and transmission line modelling finite element method for time-domain induction motor analysis," *IEEE Transactions on Magnetics*, vol. 35, no. 3, pp. 1290–1293, May 1999.

[7] R.E. Knight and T.J. Flack, "Application of domain decomposition and transmission line modelling techniques to 2d, time domain, finite element problems," *IEEE Transactions on Magnetics*, vol. 35, no. 3, pp. 1478–1481, May 1999.

[8] A.A. Abdel-Razek, J.L. Coulomb, M. Felachi, and J.C. Sabonnadiere, "The calculation of electromagnetic torque in saturated electric machines within combined numerical and analytical solutions of the field equations," *IEEE Transactions on Magnetics*, vol. 17, no. 6, pp. 1250–3252, November 1981.

Voltage Driven Coils in Finite Element Formulations Using a Current Vector and a Magnetic Scalar Potential

O. Bíró, K. Preis
IGTE
Graz University of Technology
Kopernikusgasse 24, A-8010 Graz, Austria
email: biro@igte.tu-graz.ac.at, preis@igte.tu-graz.ac.at

G. Buchgraber
VA TECH ELIN Transformatoren GmbH & Co
Elingasse 3, A-8160 Weiz, Austria
email: gerhard.buchgraber@vatechetg.at

I. Tičar
Faculty of Electrical Engineering and Computer Science
University of Maribor
Smetanova ul. 17, 2000 Maribor, Slovenia
email: ticar@uni-mb.si

***Abstract*— Finite element formulations using a current vector and a magnetic scalar potential are presented for low frequency electromagnetic problems involving voltage driven coils. Windings both with and without skin effect are treated. The voltage constraint is directly incorporated into the finite element equations system. A numerical example is also presented.**

INTRODUCTION

Taking account of voltage driven coils when using a magnetic scalar potential, Φ, and, in case of appreciable skin effect, an additional current vector potential, **T**, to describe the magnetic and electric field is not straightforward. It is the coil current that can be used as a natural excitation in such formulations [1], [2], [3]. In linear problems, it is conceivable to carry out several current driven analyses (as many as the number of voltage driven coils) to obtain the admittance matrix and hence determine the unknown currents. This option is rather time consuming and is obviously not available in the nonlinear case. The aim of this paper is to propose finite element formulations in terms of **T** and Φ that directly incorporate the voltage drive.

For coils without skin effect, a method has been proposed in [4] using a total and a reduced scalar potential. If a reduced scalar potential is used only with the impressed current vector potential represented by edge elements as in [2], the equations are considerably simplified as shown in the present paper.

Skin effect in the coils can be taken into account by introducing an additional current vector potential to describe the electric and magnetic fields [3], [5]. A **T**,Φ-formulation with the voltage of the coils explicitly appearing is introduced in this paper.

COILS WITHOUT SKIN EFFECT

If no skin effect is to be taken into account, it suffices to describe the magnetic field intensity, **H**, in terms of a reduced magnetic scalar potential as

$$\mathbf{H} = \mathbf{T}_0 - grad\,\Phi \qquad (1)$$

where $\mathbf{T}_0$ is an impressed current vector potential represented by edge basis functions. Its curl equals the current density of the coils. For the sake of simplicity, one single coil is assumed in the following, $\mathbf{T}_0$ can then be written as $i\mathbf{t}_0$ where i is the current of the coil. The Galerkin equations are

$$-\int_\Omega grad N_k \cdot \mu\, grad\,\Phi^{(n)} d\Omega + i\int_\Omega grad N_k \cdot \mu \mathbf{t}_0 d\Omega = 0\,,$$

$$k=1, 2, \ldots n \qquad (2)$$

where Ω is the problem region, n is the number of nodes with their potential unknown, μ is the permeability and $\Phi^{(n)}$ is the approximation of Φ in terms of the shape functions N_k. Obviously, $curl\mathbf{t}_0$ is the turn density of the coil, hence the given voltage, u, can be written as

$$u = iR + \int_\Omega \mathbf{E}\, curl\mathbf{t}_0 d\Omega \qquad (3)$$

[4] where R is the resistance of the coil, **E** is the electric field intensity and the integration can be extended over the entire problem region, since $curl\mathbf{t}_0$ is zero outside the coil. Following [4], the integral in (3) can be rewritten as

$$\int_\Omega \mathbf{E}\cdot curl\mathbf{t}_0 d\Omega = \int_\Omega \mathbf{t}_0 \cdot curl\mathbf{E} d\Omega + \oint_{\partial\Omega} (\mathbf{t}_0 \times \mathbf{E})\cdot \mathbf{n} d\Gamma\,. \qquad (4)$$

The surface integral vanishes on symmetry planes and also on far boundaries where the tangential component of $\mathbf{t}_0$ can be assumed to be zero. Using Faraday's law to write

$$curl\mathbf{E} = -\frac{\partial \mathbf{B}}{\partial t} = -\frac{\partial}{\partial t}\mu\left(i\mathbf{t}_0 - grad\,\Phi^{(n)}\right) \qquad (5)$$

and, as in [4], integrating (3) with respect to time, it becomes

$$\int u dt = R\int i dt - i\int_\Omega \mu \mathbf{t}_0 \cdot \mathbf{t}_0 d\Omega + \int_\Omega \mu \mathbf{t}_0 \cdot grad\,\Phi^{(n)} d\Omega\,. \qquad (6)$$

Supplementing (2) by the additional equation (6), a symmetric equations system is obtained.

COILS WITH SKIN EFFECT

If eddy currents are present within the coil, **H** and the current density, **J**, can be written as

$$\mathbf{H} = \mathbf{T_0} + \mathbf{T} - grad\Phi\,, \tag{7}$$

$$\mathbf{J} = curl\mathbf{T_0} + curl\mathbf{T} \tag{8}$$

where $curl\mathbf{T_0}$ represents a current density whose net current equals i [1]. Again, $\mathbf{T_0}$ can be written as $i\mathbf{t_0}$.

The finite element Galerkin equations are

$$\int_{\Omega_c}\left[curl\mathbf{N}_k\cdot\frac{1}{\sigma}curl\mathbf{T}^{(e)} + \mathbf{N}_k\cdot\frac{\partial}{\partial t}\mu\left(\mathbf{T}^{(e)} - grad\Phi^{(n)}\right)\right]d\Omega$$

$$+\int_{\Omega_c}\left[icurl\mathbf{N}_k\cdot\frac{1}{\sigma}curl\mathbf{t_0} + \mathbf{N}_k\cdot\mathbf{t_0}\frac{\partial}{\partial t}(i\mu)\right]d\Omega = 0,$$

k=1, 2, ..., e, (9)

$$\int_{\Omega_c+\Omega_n} gradN_k\cdot\frac{\partial}{\partial t}\mu\left(grad\Phi^{(n)} - \mathbf{T}^{(e)}\right)d\Omega$$

$$-\int_{\Omega_c+\Omega_n} gradN_i\cdot\mathbf{t_0}\frac{\partial}{\partial t}(i\mu)\,d\Omega = 0\,, \qquad k\text{=}1, 2, ..., n \tag{10}$$

where e is the number of edges with unknown circulation of $\mathbf{T}$, σ is the conductivity and $\mathbf{T}^{(e)}$ is the approximation of $\mathbf{T}$ in terms of the edge shape functions $\mathbf{N}_k$.

Following [3], the total power of the coil is

$$p = ui = \int_{\Omega_c}\mathbf{E}\cdot\mathbf{J}d\Omega + \int_{\Omega_c+\Omega_n}\frac{\partial\mathbf{B}}{\partial t}\cdot\mathbf{H}d\Omega \tag{11}$$

where Ω_c is the eddy current region and Ω_n is the eddy current free region where $\mathbf{T} = \mathbf{0}$. Hence, using Poynting's theorem as well as (7):

$$ui = -\oint_{\partial\Omega_c}\left(\mathbf{E}\times\mathbf{H}\right)\cdot\mathbf{n}d\Gamma + \int_{\Omega_n}\frac{\partial\mathbf{B}}{\partial t}\cdot\left(i\mathbf{t_0} - grad\Phi\right)d\Omega\,. \tag{12}$$

The surface integral vanishes on the symmetry planes $\partial\Omega_c - \Gamma_{nc}$ (Γ_{nc} is the interface between Ω_c and Ω_n). Taking account of the fact that the tangential component of $\mathbf{T}$ is zero on Γ_{nc}, (7) yields:

$$-\oint_{\partial\Omega_c}\left(\mathbf{E}\times\mathbf{H}\right)\cdot\mathbf{n}d\Gamma = -\int_{\Gamma_{nc}}\left[\mathbf{E}\times\left(i\mathbf{t_0} - grad\Phi\right)\right]\cdot\mathbf{n}_c d\Gamma\,. \tag{13}$$

Furthermore, using Gauss' theorem and Faraday's law:

$$-\int_{\Omega_n}\frac{\partial\mathbf{B}}{\partial t}\cdot grad\Phi d\Omega = \oint_{\partial\Omega_n}\Phi curl\mathbf{E}\cdot\mathbf{n}d\Gamma\,. \tag{14}$$

This surface integral vanishes on the symmetry planes $\partial\Omega_n - \Gamma_{nc}$, so, in view of the fact that either Φ or $\mathbf{E}\times\mathbf{n}$ is zero along $\partial\Gamma_{nc}$,

$$-\int_{\Omega_n}\frac{\partial\mathbf{B}}{\partial t}\cdot grad\Phi d\Omega = -\int_{\Gamma_{nc}}\left(\mathbf{E}\times grad\Phi\right)\cdot\mathbf{n}_c d\Gamma\,. \tag{15}$$

Setting (13) and (15) into (12):

$$ui = -i\int_{\Gamma_{nc}}\left(\mathbf{E}\times\mathbf{t_0}\right)\cdot\mathbf{n}_c d\Gamma + i\int_{\Omega_n}\mathbf{t_0}\cdot\frac{\partial\mathbf{B}}{\partial t}d\Omega\,. \tag{16}$$

The surface integral can be extended over $\partial\Omega_c$, so, using Gauss' theorem and Faraday's law again, the voltage of the coil is

$$u = \int_{\Omega_c}\mathbf{E}\cdot curl\mathbf{t_0}d\Omega + \int_{\Omega_c+\Omega_n}\mathbf{t_0}\cdot\frac{\partial\mathbf{B}}{\partial t}d\Omega\,. \tag{17}$$

Using (7), (8) and the approximations of the potentials:

$$u = i\int_{\Omega_c}curl\mathbf{t}_0\cdot\frac{1}{\sigma}curl\mathbf{t_0}d\Omega + \int_{\Omega_c+\Omega_n}\mathbf{t_0}\cdot\mathbf{t_0}\frac{\partial}{\partial t}(i\mu)\,d\Omega$$

$$+\int_{\Omega_c}\left[curl\mathbf{t_0}\cdot\frac{1}{\sigma}curl\mathbf{T}^{(e)} + \mathbf{t_0}\cdot\frac{\partial}{\partial t}\left(\mu\mathbf{T}^{(e)}\right)\right]d\Omega$$

$$-\int_{\Omega_c+\Omega_n}\mathbf{t_0}\cdot\frac{\partial}{\partial t}\left(\mu grad\Phi^{(n)}\right)d\Omega\,. \tag{18}$$

Supplementing (9) and (10) by this equations, a symmetric system is obtained.

NUMERICAL EXAMPLE

A 3-D model of the axisymmetric, time harmonic problem of [1] has been analysed with the voltage given as 1V peak. The problem has also been solved by a 2D-code using a single component magnetic vector potential. The current of the winding is 117.15-j1061.5 A in the 2D model and 116.47-j1057.5 A in the 3D model using the formulation of the paper. Fig. 1 shows the model and the maximal value of the current density in the windings.

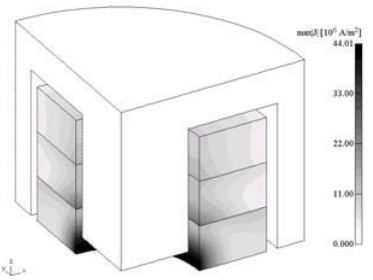

Fig. 1. Current density in the windings

REFERENCES

[1] O. Biro, K. Preis, W. Renhart, G. Vrisk and K.R. Richter, "Computation of 3D current driven skin effect problems using a current vector potential", *IEEE Transactions on Magnetics,* vol. 29, pp. 1325-1328, March 1993.

[2] O. Biro, K. Preis, G. Vrisk, K.R. Richter and I. Ticar, "Computation of 3D magnetostatic fields using a reduced scalar potential", *IEEE Transactions on Magnetics,* vol. 29, pp. 1329-1332, March 1993.

[3] O. Bíró, P.Böhm, K. Preis and G. Wachutka, "Edge finite element analysis of transient skin effect problems", *IEEE Transactions on Magnetics,* vol. 36, pp. 835-839, July 2000.

[4] P.J. Leonard and D. Rodger, "Modelling voltage forced coils using the reduced scalar potential method," *IEEE Transactions on Magnetics,* vol. 28, pp. 1615-1618, March 1992.

[5] K. Preis, I. Bárdi, O. Bíró, K.Richter, K. Papp and H. Reisinger, "Nonlinear periodic eddy currents in single and multiconductor systems", *IEEE Transactions on Magnetics,* vol. 32, pp. 780-783, May 1996.

A 3D Fast Multipole Method for Eddy Current Computations

G. Rubinacci, A. Tamburrino, S. Ventre, F. Villone
Ass. EURATOM/ENEA/CREATE, DAEIMI, Università di Cassino, Via Di Biasio 43, I-03043, Cassino (FR), Italy

Abstract — **The adaptive fast multipole method is combined with a 3D eddy-current integral formulation using edge-element-based shape functions to reduce the computational complexity and the memory requirements from order N^2 to nearly order N where N is the number of edges related unknowns. The effectiveness of this approach is verified with reference to the analysis of some 3D problems of practical interest.**

INTRODUCTION

The solution of electromagnetic problems in complex 3D geometries requires in general a huge number of discrete unknowns to be solved. In order to increase the maximum allowable dimension of treatable problems, several techniques have been developed during the last years. In particular, a number of fast methods and related numerical algorithms have been studied for computing N-body interactions [1], the number N being related to the discretization of the original problem. All these methods allow the computation of the potential due to N charges at the N charge locations in $O(N)$ or $O(N\log N)$ operations instead of the $O(N^2)$ operations required by a direct approach.

One of the most promising technique is the adaptive Fast Multipole Method (FMM), that has been shown to be competitive also in the presence of highly non uniform *3D* charge distributions encountered in applications [2, 3].

It is well known that the solution of the dense system of N equations arising after discretization requires the generation, storage and inversion of dense matrices with computational costs that soon could become prohibitively high. In fact, direct solvers require $O(N^3)$ operations for the inversion of the dense $N\times N$ matrix; on the other hand the computational cost of $O(N^2)$ per iteration required by an iterative solver could be still to high for an efficient solution of 3D problems encountered in applications.

Fast computational methods such as FMM allow to reduce this cost to $O(N)$ per iteration and to avoid forming dense matrices. Many papers have been devoted to improve the numerical algorithms for the efficient implementation of FMM since its introduction in the 1980s. Despite of the big theoretical advantages inherent in this approach, only few examples of applications in low frequency computational electromagnetism can be found in the literature. We recall in particular the studies related to the solution of electrostatic problems [4, 5, 6]. On the other hand, to our knowledge only few extensions to the magneto- quasi-stationary case [6, 7] have been accounted so far. Hence, one of the main objectives of this paper is to report on the numerical experience in the implementation and use of this approach to the solution of large scale eddy current problems such as those encountered in Electromagnetic Non Destructive Evaluation, Electromagnetic Compatibility and Nuclear Fusion reactors engineering. Indeed, although the related numerical schemes have good asymptotic computational cost estimates, the three dimensional versions could provide only modest speedups at high precision or only limited accuracy, if the steps involved in the algorithm are not carefully optimized [3]. In addition, the computation of capacitances and inductances has been shown to be very successful because it is well known that the error on such global parameters (related to energies) can be much less than the computational error in the corresponding local quantities, as charge or current distributions. According to Greengard and Rokhlin [2], "since most real-world problems are three-dimensional, it can be said that analysis-based fast methods are a promising group of techniques, but that they have not yet lived up to all their expectation".

FMM is not the only possible way of tackling the problem. For instance, there is also another class of approaches based on the Precorrected Fast Fourier Trasform Method (PFFT) that has been successfully applied in the past to static [8] and eddy current problems [9,10]. In this approach the large distance interactions are computed by projecting the current densities on a regular grid and exploiting the translation invariance of the discretized integral operator on a regular grid in conjunction with the efficient FFT treatment of the resulting convolution product.

In this paper we will also give some indications about the relative merits of the FMM and of the PFFT approaches.

MATHEMATICAL MODEL AND NUMERICAL FORMULATION

We refer to a conductive body V_c in the free space, where eddy currents are induced by a time-varying source given by the vector potential $\mathbf{A}_s$ The weak formulation for time-harmonic fields in the magneto-quasi-stationary limit is [11]:

$$\text{Find } \mathbf{J}\in Q \text{ such that } j\omega\frac{\mu_0}{4\pi}\int_{V_c}\int_{V_c}\frac{\mathbf{J}(\mathbf{r}')\cdot\mathbf{w}(\mathbf{r})}{|\mathbf{r}-\mathbf{r}'|}dV'dV +$$

$$+\int_{V_c}\eta\mathbf{J}\cdot\mathbf{w}\,dV=-j\omega\int_{V_c}\mathbf{A}_s\cdot\mathbf{w}\,dV,\quad\forall\mathbf{w}\in Q \text{ where} \qquad (1)$$

$Q=\{\mathbf{q}\in L^2_{div}(V_c)\,|\,\nabla\cdot\mathbf{q}=0,\hat{\mathbf{n}}\cdot\mathbf{q}=0\ on\ \partial V_c\}$ is the functional space of admissible solutions, and $\mathbf{L}^2_{div}(V_c)=\{\mathbf{a}\in\mathbf{L}^2(V_c)\,|\,\nabla\cdot q\in L^2(V_c)\}$.

Introducing the electric vector potential $\mathbf{T}$ ($\mathbf{J}=\nabla\times\mathbf{T}$) and expanding $\mathbf{T}$ in terms of edge-element-based shape functions $\mathbf{N}_k$ satisfying the boundary conditions $\hat{\mathbf{n}}\cdot\nabla\times\mathbf{N}_k=0$ on ∂V_c as $\mathbf{T}(\mathbf{r})=\sum_{k=1}^{N}\hat{I}_k\mathbf{N}_k(\mathbf{r})$ and using the Galerkin method we obtain the linear system $(\mathrm{R}+j\omega\mathrm{L})\hat{\mathbf{I}}=\hat{\mathbf{V}}$ where $\hat{\mathbf{I}}$ is the column vector of the $\hat{I}_k s$ and

$$R_{i,j}=\int_{V_c}\eta\nabla\times\mathbf{N}_i\cdot\nabla\times\mathbf{N}_j\,dV,\qquad V_i=-j\omega\int_{V_s}\mathbf{A}_s\cdot\nabla\times\mathbf{N}_i\,dV$$

$$L_{i,j}=\frac{\mu_0}{4\pi}\int_{V_c}\int_{V_c}\frac{\nabla\times\mathbf{N}_i(\mathbf{r}')\cdot\nabla\times\mathbf{N}_j(\mathbf{r})}{|\mathbf{r}-\mathbf{r}'|}dV'\,dV \qquad (3)$$

The gauge assuring the uniqueness of $\mathbf{T}$ is imposed directly in the discrete approximation using the tree-cotree decomposition of the edges of the mesh [11]. We note that L is a full matrix whereas R is a sparse matrix.

A complete description of the fast adaptive multipole algorithm can be found in [3]. Here we recall the main basic ideas. The *i*-th element of the product $\mathrm{L}\hat{\mathbf{I}}$, is the scalar product of the vector potential due to the current density distribution associated to $\hat{\mathbf{I}}$, with $\nabla\times\mathbf{N}_i$. Let us consider a current density distribution **J** localized inside a sphere of radius *R*. The vector potential due to **J** outside the sphere can be represented as:

$$\mathbf{A}(r,\theta,\phi)\cdot\hat{\mathbf{i}}_j=\sum_{n=0}^{p}\sum_{m=-n}^{n}(M_n^m)_j\frac{Y_n^m(\theta,\phi)}{r^{n+1}}+O\left(\frac{R^{p+1}}{(r-R)r^{p+1}}\right) \qquad (5)$$

where $\hat{\mathbf{i}}_j$ identifies the unit vector along each coordinate direction *j=x,y,z*, *p* is the expansion order, r,θ and ϕ are the spherical coordinates with respect to the multipole expansion's origin, $Y_n^m(\theta,\phi)$'s are the surface spherical harmonics, $(M_n^m)_j$ are the multipole coefficients associated to the j-th current density component.

If the vector potential must be evaluated in a cluster of points located at a distance from the centre of the sphere that is much greater than *R*, then only a small number of multipoles is required to achieve a given accuracy. Consequently, the computational cost can be significantly lower than for a direct evaluation of the vector potential.

In the fast adaptive multipole algorithm the computational cost can be further reduced by means of a hierarchical subdivision of the body and suitable linear transformations allowing either to translate the reference point of the multipole expansion or to convert a multipole expansion into a (local) solid harmonics expansion.

This allows the application of such algorithms to real 3D cases.

PRELIMINARY RESULTS

Here we present as a test case a shield with a hole, discretized with a coarse mesh (5152 elements, 10418 nodes, 5097 scalar unknowns) and a fine mesh (14076 elements, 28338 nodes, 13985 scalar unknowns) represented in Fig. 1. Using *p*=3 a relative error of 5.00e-3 and 8.06e-3 was obtained in the computation of the product $\mathrm{L}\hat{\mathbf{I}}$, for the coarse and fine mesh, respectively. Note that in the case involving the fine mesh, because of the size of the problem, the product with the direct procedure was evaluated via a parallel Beowulf system consisting of 16 nodes and the time needed for the product was extrapolated. The speedup with respect to the direct computation achieved in the product was 3.04 and 11.4, for the coarse and fine mesh, respectively.

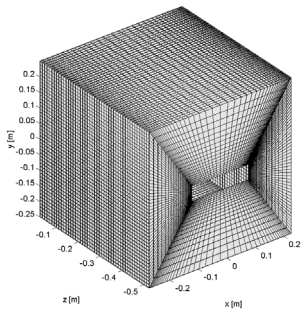

Fig. 1. The fine mesh of the shield with a hole

This work was supported in part by Italian MIUR.

REFERENCES

[1] L. Greengard and V. Rokhlin, 'A fast algorithm for particle simulations', *J. Comput. Phys.* **73**, 325-348(1987).

[2] L. Greengard and V: Rokhlin, A new version of the Fast Multipole Method for the Laplace equation in three dimensions, *Acta Numerica*, 229-269(1997).

[3] H. Cheng, L. Greengard and V. Rokhlin, A Fast Adaptive Multipole Algorithm in Three Dimensions, *J. Comput. Phys.*, **155**, 468-498(1999).

[4] K. Nabors, F. T. Korsmeyer, F. Leighton, J. White, Preconditioned, adaptive, multipole-accelerated iterative methods for three-dimensional first-kind integral equations of potential theory, *SIAM J. Sci. Comput.*, Vol. 15, No. 3, 713-735(1994).

[5] A. Buchau and W. M. Rucker, ' Preconditioned Fast Adaptive Multipole Boundary-Element Method, *IEEE Trans. Magn.,* Vol. 38, pp 461 464, 2002.

[6] S. Kapur, D. E. Long, IES^3: Efficient Electrostatic and Electromagnetic Simulation, *IEEE Computational Science & Engineering*, 5, 60-67,1998

[7] M. Kamon, M.J. Tsuk, J. K. White, FASTHENRY: A Multiple-Accelerated 3-D Inductance Extraction Program, *IEEE Trans. Microwave Theory and Techniques*, Sept. 1994, pp. 1750-1758.

[8] J. R. Phillips, J. K. White, "A precorrected-FFT method for electrostatic analysis of complicated 3d structures", *IEEE Trans. Computer-Aided Design of Integrated Circuits*, Vol. 16, pp. 1059-1072 (1997)

[9] G. Rubinacci, A. Tamburrino, S. Ventre, F. Villone, A Fast Algorithm for Solving 3D Eddy Current Problems with Integral Formulations, *IEEE Trans. Magn*., Vol. 37, pp 3099-3103, 2001.

[10] G. Rubinacci, A. Tamburrino, S. Ventre, F. Villone, Fast Computational Methods for Large-Scale Eddy-Currents Computation, *IEEE Trans. Magn*., Vol. 38, pp 529-532, 2002.

[11] R. Albanese, G. Rubinacci, *Adv. Imag. El. Phys*, **102**, pp. 1-86 (1998)

Degenerate Hexahedral Edge Elements Using Singular Value Decomposition

C.S.Biddlecombe, J.Simkin
Vector Fields Ltd., 24 Bankside, Kidlington, Oxford, OX5 1JE, UK.

Abstract –**This paper extends the formulation of non-conforming hexahedral edge elements to degenerate hexahedra. Using Singular Value Decomposition, shape functions can be calculated for any degeneracy of element without having to analyse which nodes are coincident. These element shape functions have been used to solve models meshed with tetrahedra with all the elements represented by degenerate hexahedra.**

INTRODUCTION

The derivation of edge element shape functions for hexahedra was proposed by van Welij [1]. His formulae start from isoparametric nodal shape functions to develop vector shape functions which perform well for rectangular elements but give less accurate results for any non-rectangular brick. An alternative derivation using "non-conforming" edge element shape functions works even when the elements are non-rectangular [2]. It involves solving a matrix of order 12 for each element. For degenerate elements, the matrices are singular although it is possible to achieve a solution for specific orientations and degeneracies by systematically reducing the degrees of freedom [3].

This paper extends the non-conforming edge elements to degenerate hexahedra by using singular value decomposition to extract solutions from the singular matrices. A simplification of the patch test is proposed to check whether elements are capable of representing linearly varying fields.

SIMPLIFIED PATCH TEST

The simplified patch test which has been used during the investigation of different shape function formulae is based on the assertion that the element should be capable of interpolating a linear field and returning its curl at any point within the element. This test has been implemented using a single element – a unit cube, which has been distorted by moving some corners towards others, eventually forming a tetrahedron. Edge values have been assigned to represent a vector such as (y, $-x$, z) and the interpolated value of the vector and its curl have been calculated at the centroid of the element.

VAN WELIJ ELEMENTS

Van Welij's edge elements are based on isoparametric brick nodal shape functions which are given in terms of the local co-ordinates within the element by

$$N_i = \tfrac{1}{8}(1-\eta_i)(1-\zeta_i)(1-\xi_i) \qquad (1)$$

On an edge i between nodes m and n the edge shape function is

$$\mathbf{E}_i = N_m \nabla N_n - N_n \nabla N_m \qquad (2)$$

The simplified patch test gives the correct answers only for the cube. The values of the vector are wrong by a factor of 4 and the curl by a factor of 2 for the degenerate hexahedron which is a tetrahedron. Worse errors exist closer to the degenerate nodes, where the curl is singular.

NON-CONFORMING ELEMENTS

The major difference with non-conforming elements is in the continuity of vector and its derivatives between adjacent elements. While van Welij elements have tangential continuity of the vectors and normal continuity of the curl across element faces, non-conforming elements only maintain continuity in the area integral of the curl. This might lead to a loss of accuracy.

The non-conforming element edge shape functions are derived using global rather than local co-ordinates. For an edge i the shape function has the form

$$\begin{aligned}\mathbf{E}_i &= (a_{ix} + b_{ix}y + c_{ix}z + d_{ix}yz)\mathbf{1}_x \\ &+ (a_{iy} + b_{iy}z + c_{iy}x + d_{iy}zx)\mathbf{1}_y \\ &+ (a_{iz} + b_{iz}x + c_{iz}y + d_{iz}xy)\mathbf{1}_z\end{aligned} \qquad (3)$$

Thus there are 12 unknown parameters for each edge vector. The parameters can be evaluated using the conditions that the integral of a shape function along its own edge should be 1 and the integral along all other edges should be zero:

$$\int \mathbf{E}_i . \mathbf{dl}_j = \delta_{ij} \qquad (4)$$

This leads to 12 equations in 12 unknowns which can be solved to obtain the parameters for the edge vector. If the coefficients of the equations are expressed as a matrix (there is only one matrix for an element) the parameters for each edge are the columns of the inverse matrix.

The simplified patch test gives the correct answers for all distortions of the cube as long as the corners are distinct. However, for any edges that have zero length, all the equation coefficients are zero and for any edges which are identical the equations are also identical. This makes the matrix singular for any type of degeneracy.

Shape functions for some degeneracies can be formed by restricting the degrees of freedom in (3)[3]. However, the choice of which coefficients should be omitted depends on which nodes are degenerate and on the orientation of the element with respect to the global co-ordinate system. Both these factors make a general implementation of degeneracy by restricting degrees of freedom impossible.

However, when it is singular, the matrix of equations can be solved using Singular Value Decomposition (SVD).

Singular Value Decomposition

SVD is a set of techniques for solving sets of equations where the number of equations is not the same as the number of unknowns [4]. In our case we have less equations than unknowns since the all coefficients of some equations are zero. For such a coefficient matrix, **A**, SVD generates 3 further matrices:

$$\mathbf{A} = \mathbf{U}.\mathbf{V}.\mathbf{W}^T \tag{5}$$

where **U** and **V** are orthogonal matrices and **W** is diagonal. This decomposition is possible, even for singular matrices. The inverse of **A** is given by

$$\mathbf{A}^{-1} = \mathbf{V}.\mathbf{W}^{-1}.\mathbf{U}^T \tag{6}$$

and if we are solving

$$\mathbf{A}.\mathbf{x} = \mathbf{b} \tag{7}$$

the solution is given by

$$\mathbf{x} = \mathbf{V}.\mathbf{W}^{-1}.(\mathbf{U}^T.\mathbf{b}) \tag{8}$$

Because **A** is singular, some of the diagonals of **W** are zero or very small. However, SVD gives the solution **x** with the smallest length if the diagonal entries in $\mathbf{W}^{-1}$ are replaced by zero if the corresponding diagonal of **W** is zero (or very small). Of the infinite number of possible solutions, the one with the minimum $|\mathbf{x}|^2$ would seem to be a good one to choose.

Using SVD to solve the equations for the edge shape function parameters gives the correct answers for the simplified patch test for any degeneracy of element.

Numerical Tests

While the simplified patch test gives some indication of the quality of the non-conforming edge shape functions, it is also necessary to test the elements in a finite element mesh and the test chosen is to find the fundamental resonant frequency of a cylindrical cavity since an analytical solution is available [6],

$$\omega_0 = 2.405\frac{c}{r} \tag{9}$$

The cylinder has a radius of 0.1m and a length of 0.025m giving a frequency f_0=1.141 GHz. Three models have been made, each resulting in approximately 3500 degrees of freedom. The first consists of non-degenerate hexahedra; the second contains some prism elements; the third is entirely tetrahedra treated as degenerate hexahedra. Each model has been solved twice, with van Velij shape functions and with non-conforming shape functions. The resulting fundamental frequencies are given in Table I.

TABLE I. FREQUENCIES FOR DIFFERENT MESHES AND SHAPE FUNCTIONS

Mesh	DoF	f_0(VW) GHz	f_0(NC) GHz
Hexahedra	3427	1.149	1.148
Some prisms	3267	1.150	1.149
Tetrahedra	3549	1.596	1.187

The error in the resonant frequency is very large for the model using tetrahedra treated as degenerate van Welij hexahedra. The effect of the degeneracy in van Welij elements shows more clearly when the curl of the solution is examined. Even using the interpolation of fields averaged from neighbouring elements, the variation of the field is non-physical.

Conclusions

A method for generating edge element shape functions for degenerate hexahedral elements has been described. This enables the solution of meshes which might include degenerate elements with any degree of degeneracy and any orientation with respect to the global coordinate system without the treat each element differently. It has been shown that these non-conforming elements show little effect from being "non-conforming" and give better answers than the van Welij elements especially when the degeneracy is extreme, although, it must be said, in many cases van Welij elements perform together much better than the analysis on a single element would suggest.

References

[1] J. S. van Welij, "Calculation of Eddy Currents in terms of H on Hexahedra", IEEE Trans. Mag. Vol. MAG-21, No. 6, pp. 2239-2241, 1985

[2] M. Gyimesi, D. Ostergaard, "Non-Cnforming Hexahedral Finite Elements for Magnetic Analysis", IEEE Trans. Mag. Vol. 34, No. 5, pp. 2481-2484, 1998

[3] D. Ostergaard, M. Gyimesi "Mixed Shaped Non-Conforming Edge Elements", IEEE Trans. Mag. Vol. 35, No. 3, pp. 1406-1409, 1999

[4] W. H. Press, B. P. Flannery, S. A. Teukolsky, W. T. Vetterling, "Numerical Recipes, The Art of Scientific Computing", Cambridge University Press, 1986.

[5] R. P. Feynman, "The Feynman Lectures on Physics", Vol. 2, Addison-Wesley Publishing Company, 1972.

A Hybrid Charge Method For Electric Field Problems With Floating Electrodes

K.Palaniswamy and K.Udayakumar
High Voltage Division, Anna University,
Chennai - 600025, India.
E-mail: palsy48@hotmail.com

Abstract- **This paper describes the application of a Hybrid Charge Method for electric field problems with floating electrodes. This method has been evolved, by combining the two popular methods, the Charge Simulation Method and the Surface Charge Simulation Method for accurate results. It gives satisfactory results to many electric field problems, some of which are difficult to solve with Charge Simulation Method or Surface Charge Simulation Method. This hybrid method has been applied to some axi-symmetric floating electrode problems and the results obtained are given in this paper.**

I. Introduction

Design of high voltage equipments is highly complicated due to non-uniformity of electric stress in insulating materials. It requires a very accurate computation of electric field to determine the effectiveness of the stress control techniques (like provision of floating electrodes) that are adopted to reduce stress in these equipments. The potential level of a floating electrode depends on many factors, such as the shape and size of the electrode, its location, the relative positions and sizes of other materials and also their potential levels and dielectric constants (in case of insulating materials). Hence an integrated study has to be made, taking into account all these factors, for satisfactory design. The accuracy of the field so computed is one of the critical factors influencing the performance of these equipments.

All the popular methods, like Finite Element Method, Boundary Element Method, Charge Simulation Method (CSM) and Surface Charge Simulation Method (SSM) (known as Indirect Boundary Element Method) have some deficiencies and no single method is powerful enough to effectively solve all types of electric field problems.

CSM [1] gives accurate results but its application to asymmetric problems or thin regions is very limited. In CSM, discrete charges are simulated inside the electrode surface and on both sides of dielectric interfaces, to represent the free and bound charges. In multi-dielectric field studies, charges simulated inside a region requiring solution are ignored and thus singularity is eliminated. Improvement to CSM suggested in [2] for problems with more than two regions is also applied in this study for better results.

SSM [3] can be applied to thin regions and asymmetric problems. It gives accurate results, but it may lead to singularity at locations close to the boundaries. It should be ensured that the methods adopted to treat this singularity do not lead to errors in computation. SSM requires more computation-time due to the integration of distributed charges with varying charge densities at the boundaries.

II. Hybrid Charge Method

The Hybrid Charge Method described in this paper, is a combination of CSM and SSM; it has all the advantages of its constituent methods. The purpose of this method is to reduce the computation time, to simulate thin regions and solve asymmetric problems effectively and to avoid the chances of singularities.

In Hybrid method, each boundary in a problem is identified and categorized on the basis of whether its simulation could be better (i) with discrete charges or (ii) with distributed charges. Boundaries identified for distributed charges are subdivided into many sections. To apply boundary conditions at any contour point, potential component or normal field component is calculated, for each of the discrete charges simulated for the first category of boundaries, as in CSM and also the corresponding component due to the integrated effect of the distributed charges on each subdivided section of the second category of boundaries. The problem of singularity due to distributed charges is treated with the method suggested in [4].

Floating electrode is simulated as a dielectric [5] with dielectric constant ε_r in the range of 10^3 or above, to suppress the tangential fields at its surface. This method yields good results. Another method adopted by some authors is to equate the sum of all the charge quantities simulated at or inside their surfaces to zero [6,7]. But it is difficult to apply this method, if discrete charges are employed in a multi-dielectric system.

III. Application of Hybrid Charge Method

Fig. 1 shows two high voltage support insulators (a) and (b), each with a grading ring and a high voltage electrode. The size and dielectric constant ε_r (=6) of the insulator columns and the applied potential (1 unit volt) on the electrodes are the same for both the cases, while the electrode shape differs. The mean diameter C of the grading ring, its thickness J and its height G from the ground are varied to study the influence of the ring and the electrode on the electric field pattern along the insulator.

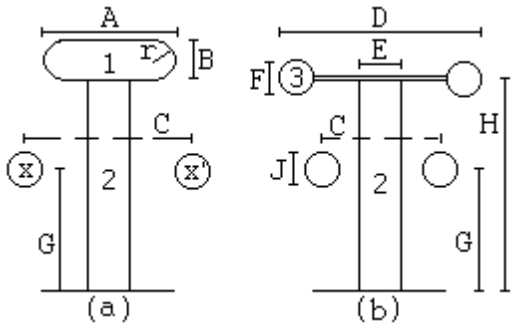

Fig. 1. HV insulators with electrodes and grading rings (a) with a thick electrode and (b) with a thin electrode with its edge shaped to a ring: Dimensions: A =6, B =2, D = 8.5, E =2, F =1.5, H =12, r =1, all in meters

A. Case- study for the configuration in Fig. 1(a)

Simulation of electrode surfaces with distributed charges always gives better results. Hence the configuration in Fig 1(a) was simulated with Hybrid method with distributed charges for HV electrode surface and discrete charges for other boundaries. Results are shown in Fig. 2. Curve 1 is the field pattern along the insulator surface without grading ring, with a maximum field of 0.195 V(p.u.)/m. For the rest of the studies, the position and size of the grading ring (in meters), induced voltage V_R (per unit) at the ring and the maximum field E_m at the insulator surface are given in Table I. A study with CSM with these data gave results almost close to that of Hybrid method, with a difference less than 0.4%.

For the same set of data, results with SSM were found to vary slightly (within 3%) from that of Hybrid method. But the computation time for SSM was more than that of Hybrid method by about 50% and more than ten times that of CSM.

TABLE I. RESULTS FROM HYBRID METHOD

S.No	C	G	J	V_R	E_m	Curve
1	7	7.75	2.5	0.3	0.213	Curve 2
2	7	9.75	2.5	0.46	0.220	Curve 3
3	5	7.75	2.5	0.34	0.215	Curve 4
4	5	7.75	1.5	0.34	0.201	------

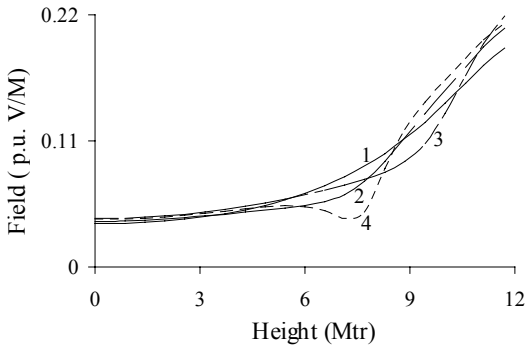

Fig. 2 Field plot for the configuration in Fig. 1 (a)

Maximum potential errors in the above studies with Hybrid method, CSM and SSM were 0.018%, 0.027% and 0.009% respectively. Field errors were found slightly higher.

B. Case- study for the configuration in Fig. 1(b)

The thin HV electrode in Fig. 1 (b) could be simulated only with distributed charges. Simulating its surface with distributed charges and other boundaries with discrete charges, Hybrid method was applied. Without floating electrode, the maximum field at the insulator surface was 0.125 V(p.u.)/m, a markedly lesser value compared to that of Fig. 1(a), due to the electrode shape. The value increased to 0.130 with a grading ring, with the values for C, G and J at 5, 7.5 and 1.5 meters respectively. The induced voltage at the ring in this case was 0.42, as against 0.34 in the case of Fig. 1(a), as shown in item 4 in Table I. This is due to increase in inter-electrode capacitance because of the increased area of the HV electrode.

IV. DISCUSSION

With grading ring as a floating electrode to HV insulators, the non-uniform pattern of electric field is aggravated. This is due to the effect of the vast area of the earth, causing more ground-capacitance effect. However the reverse effect could occur in indoor insulators, due to the effect of roof and walls. Increasing the area of HV electrodes with suitable shapes reduces the maximum field in insulators. Hybrid Charge Method could be applied to accurately determine the effect of HV electrodes and grading rings.

V. CONCLUSION

In this paper, the advantages of the application of Hybrid Charge Method for electric field problems and the influence of the floating electrodes on the field pattern are discussed.

REFERENCES

[1] H.Singer, H.Steinbigler and P.Weiss, 'A charge simulation method for the calculation of high voltage fields', IEEE Trans. PAS, Vol. 93, pp.1660-1668, 1974.

[2] K. Palaniswamy, K. Udayakumar and M.A. Panneer Selvam, 'Application of Improved Charge Simulation Method for Multi-dielectric Field Problems', Intl. Symposium on H V Engg, 1-21, Aug.2001.

[3] Shuji Sato, 'Effective Three-Dimentional Electric Field Analysis by Surface Charge Simulation Method', Doctoral thesis, Swiss Federal Institute of Technology, 1987

[4] Novel Techniques for Treating Singularity Problems in the Boundary Element method Applied to Electric Field Evaluation Within the Tank of a Power Transformer', IEEE Trans. Power Delivery,Vol-15,No.2., Apr.2000.

[5] N.O.Morales, E.S.Asenjo and J.L.Inostroza, 'Calculation of 3-dimensional Fields in a Medium with Several Dielectrics', IEEE Trans. Dielec & Elec. Ins., Vol. 4, No. 2, pp. 172-176, Apr. 1997.

[6] Tadasu Takuma and Tadashi Kawamoto, 'Numerical Calculation of Electric Fields with a Floating Conductor', IEEE Trans. Diele. & Elec. Ins., Vol. 4, No. 2, pp. 177-181, Apr. 1997.

COMPUMAG Saratoga Springs, New York USA
July 13 - 17, 2003

Matrix Properties of a Vector Potential Cell Method for Magnetostatics

P. Alotto[1] and I. Perugia[2]

Abstract—**In this paper a proof of the symmetry of the system matrix arising in a class of vector potential cell methods with non-symmetric material matrices is presented. Some remarks on how the symmetry can be exploited to increase the computational efficiency of cell methods and how to construct other schemes with symmetric system matrices are also presented.**

I. Introduction

In recent years *cell methods* have been gaining increasing popularity in the computational electromagnetics community due to their simple derivation from experimental facts and to their analogy with well-known circuit equations. Efforts are now being devoted to highlighting links with other numerical methods (FE, FV) and to clarify the properties of cell methods from a mathematical point of view. This paper contributes to such efforts. In particular, it is proven that the system matrices arising in a class of vector potential cell method are symmetric, like in analogous FE formulations.

II. A vector potential cell method for Magnetostatics

In this section we recall the derivation of a discrete vector potential formulation of the magnetostatic problem on a dual mesh complex.

A. Dual mesh complex

Consider a three-dimensional dual complex of meshes, $\mathcal{T}$ and $\widetilde{\mathcal{T}}$, that tile a bounded region Ω of $\mathbb{R}^3$, where, to fix the ideas, the primal one, $\mathcal{T}$, is made of tetrahedra, and its volumes coincide with these tetrahedra plus the unbounded region $\mathbb{R}^3 \setminus \Omega$. For simplicity, we assume that Ω is simply connected and has no cavities. Extension to more general cases can be dealt with.

The set of nodes of the dual mesh $\widetilde{\mathcal{T}}$ contains one interior point (say, the center) for each volume of the primal one. An edge of $\widetilde{\mathcal{T}}$ is a curve (say, a piecewise straight line) connecting two dual nodes and passing through and interior point (say, the center) of the face of $\mathcal{T}$ shared by the primal volumes the two connected dual nodes are associated with. This procedure naturally establishes a one-to-one correspondence between primal faces and dual edges. The dual faces are surfaces bounded by loops of dual edges, so that each of them intersects one and only one primal edge, and the dual volumes are regions bounded by loops of dual faces, so that each of them surrounds one and only one primal node. Denote by e, f and v the numbers of edges, faces and tetrahedra, respectively, of $\mathcal{T}$, and by $\widetilde{e}$ and $\widetilde{f}$ the numbers of edges and faces, respectively, of $\widetilde{\mathcal{T}}$. The identities $\widetilde{e} = f$ and $\widetilde{f} = e$ hold true.

[1]Department of Electrical Engineering, University of Genoa, Via Opera Pia 11a, 16145, Genoa, Italy. E-mail: alotto@die.unige.it.
[2]Department of Mathematics, University of Pavia, Via Ferrata 1, 27100, Pavia, Italy. E-mail: perugia@dimat.unipv.it.

B. Magnetostatic prolem

We introduce the connectivity (incidence) matrices

$C_{f\times e}$ faces–edges of $\mathcal{T}$,
$D_{v\times f}$ tetrahedra–faces of $\mathcal{T}$,
$\widetilde{C}_{\widetilde{f}\times\widetilde{e}}$ faces–edges of $\widetilde{\mathcal{T}}$,

which also take into account the orientation of the involved entities. The primal faces and the corresponing dual edges have to be consistently numbered and consistently oriented [1]. It is easy to see that $\widetilde{C} = C^T$ and $DC = 0$.

Denote by $\boldsymbol{b}$ the vector of size f, whose components are the fluxes of the magnetic induction field through the faces of $\mathcal{T}$, and by $\widetilde{\boldsymbol{h}}$ the vector of size $\widetilde{e} = f$, whose components are the line integrals of the magnetic field along the edges of $\widetilde{\mathcal{T}}$. Faraday's and Ampere's laws can be written as

$$D\,\boldsymbol{b} = \boldsymbol{0} \qquad\qquad \widetilde{C}\,\widetilde{\boldsymbol{h}} = \widetilde{\boldsymbol{i}},$$

where $\widetilde{\boldsymbol{i}}$ is the vector of size $\widetilde{f}$, whose components are the fluxes of a current density field, that satisfies $\widetilde{D}\,\widetilde{\boldsymbol{i}} = \boldsymbol{0}$. The constitutive law can be written as

$$\widetilde{\boldsymbol{h}} = N\,\boldsymbol{b},$$

where N is a matrix of size $\widetilde{e}\times f$ (i.e., $f\times f$) which represents material properties and the grid transfer (Hodge) operator. The cell method does not prescribe how N should be constructed. The way of assembling N is not unique, and different choices lead to different numerical schemes. In this paper we consider the following natural and quite common choice [2], [3]:

$$N(i,j) = \sum_{K\in\mathcal{T}} N_K(i,j) = \sum_{K\in\mathcal{T}} s(i)\,\nu_K \int_{\ell_i} \boldsymbol{w}_j \cdot \boldsymbol{t}_i\, dl, \quad (1)$$

where ℓ_i is the portion in K of the dual edge corresponding to the primal face f_i, $s(i) = \pm 1$ depending on the outward or inward orientation of ℓ_i with respect to K, ν_K is the restriction to K of the reluctivity (assumed to be constant within each K), $\boldsymbol{w}_j$ is the *face* shape function associated with the primal face f_j, and $\boldsymbol{t}_i$ is the tangent unit vector to ℓ_i pointing outside K. Notice that N is not symmetric.

C. Vector potential formulation

It can be shown that $D\,\boldsymbol{b} = \boldsymbol{0}$ implies that there exists a vector $\boldsymbol{a}$ of size e such that $\boldsymbol{b} = C\,\boldsymbol{a}$, whose components can be interpreted as the line integrals of a magnetic vector potential [2]. Since $\widetilde{C} = C^T$, the problem amounts to solving

$$C^T N\, C\,\boldsymbol{a} = \widetilde{\boldsymbol{i}}.$$

In order to efficiently solve this positive semidefinite (singular) linear system, appropriate combinations of iterative solvers and preconditioners have to be selected. Obviously, these combinations depend on the properties of the system matrix $C^T N\, C$. In

particular, as proven in the following section, if N is constructed according to (1), $C^T N\, C$ turns out to be symmetric. This property is usually exploited in the solution of the associated linear system, but its proof has not been published yet, at least in the authors' knowledge.

III. Symmetry of $C^T N\, C$

Theorem 1: The matrix $C^T N\, C$, with N constructed according to (1), is symmetric.

Proof: We only have to prove that if $\boldsymbol{p}$ and $\boldsymbol{q}$ are two different columns of C, then

$$\boldsymbol{q}^T N \boldsymbol{p} = \boldsymbol{p}^T N \boldsymbol{q}. \tag{2}$$

Denote by e_p and e_q the primal edges associated with $\boldsymbol{p}$ and $\boldsymbol{q}$, respectively; notice that $\boldsymbol{p}$ and $\boldsymbol{q}$ have nonzero entries only in correspondence to the faces containing e_p and e_q, respectively. We start by showing that, if e_p and e_q do not belong to the same element, then $\boldsymbol{q}^T N \boldsymbol{p} = \boldsymbol{p}^T N \boldsymbol{q} = 0$.

To this end, let $\boldsymbol{r}$ be any row of N and let f_r be the primal face corresponding to the dual edge associated with $\boldsymbol{r}$. Since $\boldsymbol{r}$ can have nonzero entries only in correspondence to the faces belonging to the two tetrahedra sharing f_r, the scalar product $\boldsymbol{r} \cdot \boldsymbol{p}$ can be different form zero only if e_p belongs to one of the two tetrahedra sharing f_r, or, in other words, if e_p and f_r belong to the same tetrahedron. This implies that the vector $N\boldsymbol{p}$ can have nonzero entries only in correspondence to faces that belong to an element containing e_p. Consequently, $\boldsymbol{q}^T N \boldsymbol{p} \neq 0$ only if at least one of the faces containing e_q belongs to a tetrahedron contaning e_p, i.e., only if e_p and e_q belong to the same tetrahedron. The same can be seen for $\boldsymbol{p}^T N \boldsymbol{q}$, with a specular reasoning.

Now, we only need to focus on the case where e_p and e_q belong to the same tetrahedron. More precisely, either there is only one tetrahedron they belong to (this is the case where they do not lie on the same face), or they belong to two adjacent tetrahedra (this is the case where they lie on the same face). Let K be an element containing both e_p and e_q. We have to prove that K gives the same contributions $\boldsymbol{q}^T N_K \boldsymbol{p}$ and $\boldsymbol{p}^T N_K \boldsymbol{q}$ to $\boldsymbol{q}^T N \boldsymbol{p}$ and $\boldsymbol{p}^T N \boldsymbol{q}$, respectively.

Since we need to compute $\boldsymbol{q}^T N \boldsymbol{p}$, we only need to consider the entries in the vector $N\boldsymbol{p}$ corresponding to the (two) faces f_{k_1} and f_{k_2} in K on which e_q lies. Let f_{k_3} and f_{k_4} be the two faces in K to which e_p belongs. The pairs (f_{k_1}, f_{k_2}) and (f_{k_3}, f_{k_4}) can coincide (trivial case), may share one element or be distinct. We do not need to distinguish among these cases.

The contribution from K to the k_i–th component of the vector $N\boldsymbol{p}$, $i = 1, 2$, is given by

$$[N_K \boldsymbol{p}](k_i) = N_K(k_i, k_3)\, \boldsymbol{p}(k_3) + N_K(k_i, k_4)\, \boldsymbol{p}(k_4).$$

Therefore,

$$\begin{aligned} \boldsymbol{q}^T N_K \boldsymbol{p} =& \boldsymbol{q}(k_1)\, N_K(k_1, k_3)\, \boldsymbol{p}(k_3) + \boldsymbol{q}(k_1)\, N_K(k_1, k_4)\, \boldsymbol{p}(k_4) \\ &+ \boldsymbol{q}(k_2)\, N_K(k_2, k_3)\, \boldsymbol{p}(k_3) + \boldsymbol{q}(k_2)\, N_K(k_2, k_4)\, \boldsymbol{p}(k_4). \end{aligned} \tag{3}$$

Analogously,

$$\begin{aligned} \boldsymbol{p}^T N_K \boldsymbol{q} =& \boldsymbol{p}(k_3)\, N_K(k_3, k_1)\, \boldsymbol{q}(k_1) + \boldsymbol{p}(k_4)\, N_K(k_4, k_1)\, \boldsymbol{q}(k_1) \\ &+ \boldsymbol{p}(k_3)\, N_K(k_3, k_2)\, \boldsymbol{q}(k_2) + \boldsymbol{p}(k_4)\, N_K(k_4, k_2)\, \boldsymbol{q}(k_2). \end{aligned} \tag{4}$$

From (1),

$$N_K(k_i, k_j) = s(k_i)\, \nu_K \int_{\ell_{k_i}} \boldsymbol{w}_{k_j} \cdot \boldsymbol{t}_{k_i}\, dl.$$

We recall that the orientation of a primal face is consistent with the orientation of the corresponding dual edge. We observe that

$$\boldsymbol{w}_{k_j} = \frac{1}{3\,|K|}(\boldsymbol{x} - \boldsymbol{v}_{k_j}),$$

where $|K|$ is the volume of K, $\boldsymbol{x} = (x_1, x_2, x_3)$ and $\boldsymbol{v}_{k_j}$ is the coordinate vector of the vertex opposite to face f_{k_j}. Denoting by $\boldsymbol{c}_K$ the coordinate vector of the center of K and $\boldsymbol{c}_{k_j}$ the coordinate vector of the center of face f_{k_j}, owing to the fact that

$$\boldsymbol{c}_{k_j} - \boldsymbol{v}_{k_j} = 4\,(\boldsymbol{c}_{k_j} - \boldsymbol{c}_K),$$

we have

$$\int_{\ell_{k_i}} \boldsymbol{w}_{k_j} \cdot \boldsymbol{t}_{k_i}\, dl = \frac{1}{6\,|K|}|\boldsymbol{c}_{k_j} - \boldsymbol{c}_K|^2 + \frac{1}{9\,|K|}(\boldsymbol{c}_K - \boldsymbol{v}_{k_i}) \cdot (\boldsymbol{c}_K - \boldsymbol{v}_{k_j}).$$

Taking into account that $s(k_1)\, \boldsymbol{q}_{k_1} = s(k_2)\, \boldsymbol{q}_{k_2}$ and $s(k_3)\, \boldsymbol{p}_{k_3} = s(k_4)\, \boldsymbol{p}_{k_4}$, simple algebraic manipulation gives that $\boldsymbol{q}^T N_K \boldsymbol{p} = \boldsymbol{p}^T N_K \boldsymbol{q}$, and (2) is proven. ■

Remark 1: It is clear from the previous proof that formulas (3) and (4) hold for any possible scheme where the non-zero entries of any row of N are only in the columns related to the seven primal faces of the two tetrahedra in which the dual edge corresponding to the considered row is embedded. Therefore, checking the symmetry of $C^T N\, C$ for those methods reduces to checking that the right-hand sides of (3) and (4) coincide.

Remark 2: The elemental contribution to the entry (i, j) of $C^T N\, C$ is given by (3), $\boldsymbol{p}$ and $\boldsymbol{q}$ being the j–th and i–th columns of C, respectively. Owing to this explicit formula, the proven symmetry can be exploited to construct and store only half of the entries of $C^T N\, C$.

IV. Conclusions

In this paper the symmetry of the system matrix arising in a class of vector potential cell methods with non-symmetric material matrices was proven. Comments on how the symmetry can be exploited to increase the computational efficiency of cell methods and how to construct other schemes with symmetric system matrices were given. The construction of appropriate preconditioned iterative solvers is subject of ongoing research efforts and results will be presented in the extended version of this paper.

References

[1] E. Tonti, "Finite Formulation of the Electromagnetic Field", *PIER 32 (Special Volume on Geometrical Methods for Comp. Electromagnetics)*, p. 1–44, 2001.

[2] T. Tarhasaari and L. Kettunen, "Some Realizations of a Discrete Hodge Operator: A Reinterpretation of Finite Element Techniques", *IEEE Trans. Magn.*, Vol. 35, No. 3, p. 1494–1497, 1999.

[3] M. Repetto and F. Trevisan, "3D Magnetostatic With the Finite Formulation", *Proc. of X IEEE CEFC Conference, 16-19 June 2002, Perugia, Italy*, p. 37, 2002.

Coupled Programming : "finite elements" – "dynamical hysteresis flux tubes" for non-homogeneous circuits modelling

F.Sixdenier, B.Ducharne, J.P.Masson, L.Morel, M.A. Raulet
CEGELY, C.N.R.S. UMR 5005, Université Claude Bernard , Bât. 721
43 Bd du 11-11-1918, 69622 Villeurbanne Cedex., France.

Abstract- **A new dynamic modelling and simulation method of magnetic circuits using "dynamical hysteresis flux tubes" and "finite elements" is presented. The "dynamical hysteresis flux tube" model can determine hysteresis loops of a material in case of homogeneous magnetic circuits. In order to increase the accuracy when an air-gap is introduced, we use a FEM near the air-gap area. The both methods can be coupled to obtain both the influence of material laws and local information in high gradient area. The aim of this paper is to present briefly the "dynamical hysteresis flux tube" model and the coupling method. The results will be compared with experimental values on a device designed for this purpose.**

INTRODUCTION

These last years, the advent of numerical methods has allowed an important development for sizing tools for electrical machines. The consequence is that the manufacturers are more and more interested concerning accuracy and robustness of used models. Thus phenomenon such as magnetic hysteresis which were considered as second order problems a few years earlier present now a real interest if we want to be close to the physical reality of the phenomenon.

Electromagnetic phenomenon are ruled by "Maxwell's equations", however if we want to know the temporal evolution of the fields within magnetic materials, dynamical hysteresis phenomenon must be taken into account.

The coupling of finite element method and magnetic material's law leads to long computation time, big storage capacity and numerical problems and so is not now available.

The solution presented here is based on the coupling of a calculation finite elements and flux tubes. This solution seems to be a good alternative to solve this kind of problem.

PRESENTATION OF THE TEST DEVICE

In order to test as an example the method, we choose a simple geometry device. The aim of this work is to define the assumptions which lead to a coupling between the two methods as simple as possible.

We have chosen a rolled circuit excited by a coil of N turns supplied by a sine wave current "Fig (1)". The mean length "lm" is 335 mm and the air-gap is 0.65mm. Two windings are used to measure the flux density and an Hall effect probe measures the field near the material surface. (Equivalent field to the internal tangential excitation field) .

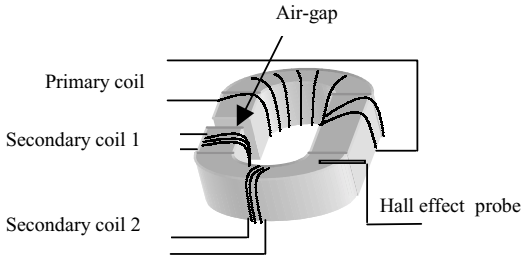

Fig.1 Test device

DYNAMICAL HYSTERESIS FLUX TUBE MODELING

In order to obtain a good representation of the dynamical magnetic hysteresis phenomena, the CEGELY laboratory has developed a model based on the integral resolution of the second Maxwell's equation, this means the conservation of the flux Φ through the element called « flux tube »[1].

This global modelling is described by the following differential equation (1):

$$\frac{d\phi}{dt} = \frac{1}{\gamma}[H - Hstat(B)] * lm \quad (1)$$

This equation signifies that for a given flux density value B, the variation of the flux within the tube is equivalent to the difference between the dynamic excitation field supplied by the source H and a fictitious quantity Hstat(B) evaluated on the quasi-static characteristic B(H). This difference is divided by a parameter γ which is a characteristic of the magnetic circuit.

This temporal resolution of this equation requires the simultaneous evolution of a static hysteresis model. The static model is based on a 2D interpolation matrix dH/dB(B, H). The static model hypothesis is that each point B(H) read on the static hysteresis loop is associated to a peculiar slope, the slope depends on the excitation field H and the induction B.

The calculation is performed using the Matlab/Simulink software. In order to simplify the implementation, we present the model in its electric circuit version. To do this, we have to make an analogy between electric magnitudes and magnetic magnitudes. Thus a mmf NI becomes a current source and dΦ/dt becomes a voltage source. Figure (2) shows the magnetic and electric circuit coupling for the test device, i.e. a constant magnetic circuit section with an air-gap. The air-gap is modelised by a current source wich value is calculated by FEM.

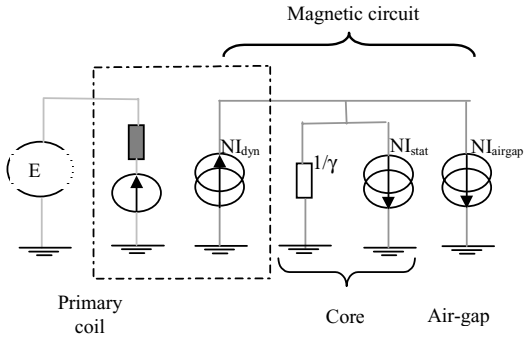

Fig. 2 Full electrical model

The equation in this particular case can be written as (2):

$$\gamma \frac{d\phi}{dt} = NI_{dyn} - NI_{stat} - NI_{airgap} \quad (2)$$

IV. THE FINITE ELEMENT AREA MODELING

In a magnetostatic problem, the flux passing through a section S is expressed by the relation (6) :

$$\phi = \iint_S \vec{B}.d\vec{S} \quad (6) \qquad \text{so} \qquad \phi = Rot\vec{A}.d\vec{S} = \oint \vec{A}.d\vec{\lambda} \quad (7)$$

If the geometry has a constant depth, we can write (8)

$$\phi = \lambda.(A_1 - A_2) \quad (8)$$

λ: depth of the section S

If we imposes $A_2 = 0$, then we can write (9)

$$A_1 = \frac{\phi}{\lambda} \quad (9)$$

The figure (3) represents the whole device and the meshed area. The dimensions don't match with reality. The meshed area is limited with dot lines.

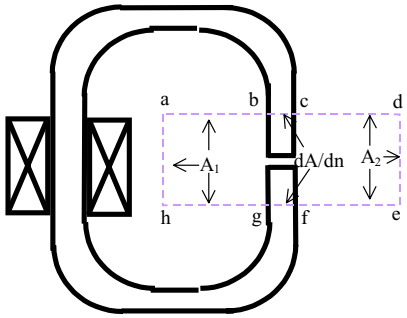

Fig. 3 : Whole device and meshed area

We suppose that the system is without magnetic leakages, so the boundary conditions on [bc] and [gf] are Neumann conditions. Dirichlet condition A_1 is on [ab], [ah] and [hg]. Dirichlet condition A_2 is on [cd], [de] and [ef]. This method allows to reduce the meshed area to adeh domain.

Once the boundary conditions transmitted, we can make the resolution itself. This resolution allows to determine the term NI_{airgap} needed for the resolution of the equation (2).

RESULTS

The results presented in this article were measured using a multi-channel characterization bench.

Two types of results seem to be particularly interesting. The first one shows in figure (4a) the mean induction across the section of the core versus the excitation field. The second one shows in figure (4b) the same mean induction versus the surface magnetic field on the material. Both tests are performed with the same 200Hz sine wave current excitation.

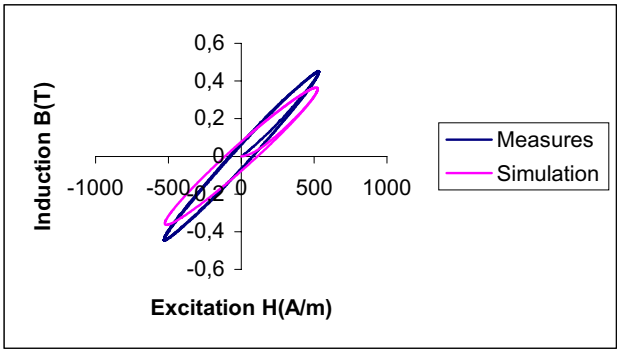

Fig 4a :Mean induction versus excitation field

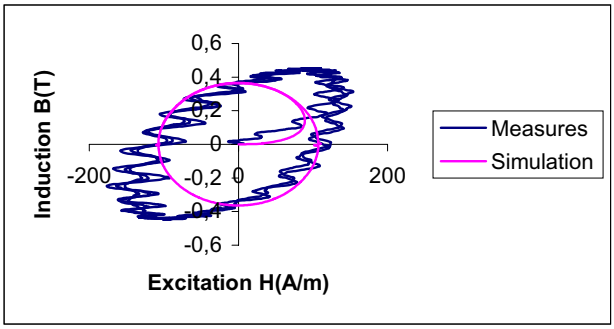

Fig 4b: Mean induction versus surface magnetic excitation field

We can say that the dimensions of the test device doesn't fit to the 2D modelling requirements. Nevertheless the simulations are in accordance with measurements.

CONCLUSION

A new kind of modelling is presented coupling two methods. This new way of modelling can offer great possibilities as a good knowledge of the magnetic losses when an air-gap is present. We work at the optimisation of this model in term of accuracy and calculation time.

REFERENCES

[1] J.P.Masson, J.J. Rousseau, J.P.Chante. Dynamical measurement of magnetic properties of industrial ferromagnetic materials. ICEM 1988 PISE Italy

[2] The MATHWORKS, "Partial Differential Equation User's Guide", Version 1, copyright 1984-1997 by the Mathworks Inc

[3] F.Marthouret, J.P. Masson, H. Fraisse, Modeling of a non-linear conductive magnetic circuit. IEEE Transaction on magnetics, Vol 31 n°6. Nov 1995

Vector finite element method: from edge to nodal values

Christian Vollaire[(1)], François Musy[(2)]
[(1)] CEGELY – UMR CNRS 5005, [(2)] MAPLY – UMR CNRS 5585
Ecole Centrale de Lyon, 36, Avenue Guy de Collongue, 69134 Ecully Cedex, France
christian.vollaire@ec-lyon.fr, francois.musy@ec-lyon.fr

Abstract –**New techniques to obtain representative nodal values from edge finite element values are presented. They are based on a least squares formulation leading to a sparse matrix system to be solved. These methods are compared in terms of accuracy and CPU time.**

INTRODUCTION

Edge-based finite elements (FE) are useful in modeling electromagnetic phenomena because of their right physical sense. Furthermore, it has been shown that better approximation of the solution may be obtained [1]. The degrees of freedom are the circulations of the unknown field along the edges. However the knowledge of the nodal field values remains necessary. First, since maximal values are located at the interfaces, then they are required to predict possible electric breakdown. Second, post-processors are generally based on the nodal representation of the fields. Third, these nodal values may be necessary to achieve some additional computation: induced currents in the conductors, dual field,… Up to now, nodal values inside the elements are generally computed from the edges values. However this method does not allow to obtain the field on the boundary of each element in the mesh, namely on the vertices.

The objective of this paper is to propose a method to compute accurate nodal values from edge values. A FE formulation for open boundary – frequency domain problems is used to validate the approach. Spatial discretization is achieved using incomplete first order tetrahedral edge elements [2].

REFERENCE METHOD

A first and simple method consists in computing local node values on each element of the mesh from the known edge values by means of the local edge basis. A value at a node is then obtained as an arithmetic mean on the elements containing the node. For a node at the interface between two regions, two values are obtained by averaging the field values separately in each region. This method is taken as reference in the further (method 1).

NEW APPROACH

Let a complex vector field $\widetilde{\mathrm{E}}$ be obtained from a computation with H(curl; Ω)-conforming finite elements on a tetrahedral mesh $\boldsymbol{\tau}_h$ of a bounded domain Ω of $\mathbb{R}^3$. We are interested to find a "good representation" of $\widetilde{\mathrm{E}}$ by a continuous vector field **E*** on $\boldsymbol{\tau}_h$. This problem may be formalised by introducing the least squares problem:

$$\begin{aligned} &\textit{Find a vector field } \mathbf{E}^* \in \mathrm{V}_h \\ &\textit{which minimizes } \left\| \widetilde{\mathbf{E}} - \mathbf{E} \right\| \textit{for all } \boldsymbol{E} \textit{ in } \mathrm{V}_h , \end{aligned} \tag{1}$$

where V_h is the nodal conforming FE space of degree 1 defined on $\boldsymbol{\tau}_h$ and $\| \ \|$ is a norm induced by a scalar product in H(curl; Ω). $\widetilde{\mathrm{E}}$ is given from incomplete first order edge elements with circulation along edges as degrees of freedom.

Then in the edge basis denoted $(\mathrm{w}_e)\, e \in \varepsilon_h$, $\widetilde{\mathrm{E}}$ can be decomposed as:

$$\widetilde{\mathbf{E}} = \sum_{e \in \varepsilon_h} \widetilde{\alpha}_e \mathbf{w}_e \text{ with } \widetilde{\alpha}_e = \int_e \widetilde{\mathbf{E}}.\mathbf{t}\, d\Gamma \tag{2}$$

where **t** is an oriented tangent vector. So it seems appropriate to introduce the following scalar product:

$$\left\langle \mathrm{E}, \mathrm{E}' \right\rangle = \theta_1 \int_\Omega \mathrm{E}.\overline{\mathrm{E}'} d\Omega + \theta_2 \sum_{e \in \varepsilon_h} \left(\int_e \mathrm{E}.t d\Gamma \right) \left(\int_e \overline{\mathrm{E}'}.t d\Gamma \right) \tag{3}$$

with θ_1 and θ_2 some non-negative weights.

By definition of the norm induced by a scalar product, the distance between vector fields $\widetilde{\mathrm{E}}$ and **E** is then given by

$$\left\| \widetilde{\mathrm{E}} - \mathrm{E} \right\| = \left[\theta_1 \int_\Omega \left| \widetilde{\mathrm{E}} - \mathrm{E} \right|^2 d\Omega + \theta_2 \sum_{e \in \varepsilon_h} \left| \int_e (\widetilde{\mathrm{E}} - \mathrm{E}).t d\Gamma \right|^2 \right]^{1/2} \tag{4}$$

By minimizing $\left\| \widetilde{\mathrm{E}} - \mathrm{E} \right\|$, according to the choice of the weights θ_1 and θ_2, good approximation **E*** of $\widetilde{\mathrm{E}}$ in each tetrahedron as well as preserving of the circulation along the edges may be expected. Then it is well known that the solution **E*** to the minimization problem is the orthogonal projection of the field $\widetilde{\mathrm{E}}$ into the space V_h. The unknown field **E*** can be decomposed as $\mathbf{E}^* = \sum_{i=1}^{N_h} \xi_i^* \mathrm{v}_i$ where (v_i) is the nodal vector basis of the FE space $\mathbf{V}_h$, and the unknown vector $\xi^* = (\xi_i^*)$ contains the values of each component of

the field **E*** on the nodes of the mesh τ_h. Writing that $\mathbf{E}-\tilde{E}$ is orthogonal to any test function v_i allows to obtain ξ^* as solution to the linear system: $\mathbf{A}\xi=\mathbf{b}$. The matrix **A** is the Gram matrix associated to the scalar product $<.,.>$. The vector **b** is given by $\mathbf{b}_i=<\tilde{\mathbf{E}}, \mathbf{v}_i>$. **A** is real symmetric and positive semi-definite. In the particular case where $\theta_2=0$, the linear system reduces to $R\xi = f$. The matrix R has a block diagonal structure with mass matrices on the diagonal. Then an explicit but approximate solution of the least squares problem can be obtained by a classical mass-lumping.

RESULTS AND DISCUSSIONS

In the following, method 1 (local averaging) is the reference method, method 2 (global energy approximation) is obtained with $\theta_1=1$ and $\theta_2=0$, method 3 (global circulation approximation) corresponds to $\theta_1=0$ and $\theta_2=1$, method 4 (global mixing) is obtained with $\theta_1=1$ and $\theta_2=1$, and method 5 (energy approximation with lumping) corresponds to $\theta_1=1$ and $\theta_2=0$ with the mass lumping strategy. For methods 2, 3, 4, the QMR solver with SSOR preconditioning is used to solve the system matrix $\mathbf{A}\xi=\mathbf{b}$. The accuracy and the time required for each post processing method are compared.

Numerical accuracy of the methods

Numerical results are compared with analytical solutions of scattering of a plane wave by a sphere [3]. A 100 mm radius - sphere is meshed with 100 nodes, the frequency of the incident plane wave is 1 GHz. Absorbing boundary condition is located at one wavelength from the sphere. To estimate the discretization error, circulations on the edges of the sphere are deduced from the analytical nodal values and compared with the corresponding numerical values given by the FE-code. Nodal values on the whole domain are then calculated from the numerical edge values for different strategies and compared on the surface of the sphere with the analytical nodal solution (tables I and II).

In the first example, the sphere is modeled as a perfect electrical conductor (PEC). The problem is meshed with 28161 edges (294 edges on the PEC sphere). The edge values error on the sphere is about 0.067. The total solving time (assembling and solving of the matrix system) with the FE code is about 300s on a HP J5000 (217 iterations of PQMR).

In the second example, the sphere is magnetic, leading to a field discontinuity at the surface of the sphere. It is meshed with 28805 edges and the total time for FE solving is about 436 s (537 iterations of the PQMR). The post processing is made in the region 1 (air) according to the analytical solution. The edge values error on the sphere is about 0.149.

Normal and tangential components on interfaces

The same spherical geometry is used in a third academic example. Circulations on the edges of a radial field of magnitude equal to 1 in the region 1 and to 100 in the region 2 are set in the whole domain. Nodal values are computed from these edge values with the different methods (table III).

TABLE I. COMPARISON OF THE PROPOSED STRATEGIES ON A PEC SPHERE. (RELATIVE ERROR IN %)

Method	Error on 3 components	Error on tangential component	Error on normal component	Iterations	Time (in s)
1	0.238	0.012	0.020	/	2
2	0.190	0.008	0.017	7	11
3	0.130	0.007	0.010	22	21
4	0.133	0.007	0.011	19	20
5	0.255	0.016	0.020	/	1

TABLE II. COMPARISON ON A MAGNETIC SPHERE ($\mu_r = 3$) (RELATIVE ERROR IN %)

Method	Error on 3 components	Error on tangential component	Error on normal component	Iterations	Time (in s)
1	0.265	0.0133	0.023	/	2
2	0.188	0.0098	0.016	7	9
3	0.127	0.0092	0.008	20	19
4	0.129	0.0089	0.009	18	19
5	0.289	0.0129	0.026	/	1

TABLE III. COMPARISON ON THE SPHERE FOR A GIVEN RADIAL FIELD

Method	Normal component (region 1)	Normal component (region 2)	Tangential component (region 1)	Tangential component (region 2)	Iterations
1	1.2	71	0.019	0.081	
2	1.1	87	0.002	0.177	8
3	1.0	100	3.10^{-14}	8.10^{-12}	23
4	1.0	98	1.10^{-5}	0.004	20
5	1.2	70	0.003	0.108	

CONCLUSION

As shown from Tables I, II and III, the most accurate solutions are obtained with the third and fourth methods (global circulation approximation and global mixing). Theses methods are the most CPU consuming. However, the time required for the post processing remains very small compared to the total FE solving time. Better accuracy is then obtained with a very small additional computation time.

REFERENCES

[1] J. P. Webb, "Edge element and what they can do for you," *IEEE Trans. On Magn*., vol. 29, No. 2, pp. 1460-1465, March 1993.

[2] C. Vollaire and L. Nicolas, "Implementation of a finite element and absorbing boundary conditions package on a parallel shared memory computer," *IEEE Trans. On Magn*., vol. 34, No. 5, pp. 3343-3346, September 1998.

[3] R.F. Harrington, "Field Computation by Moment Methods," MacMillan, New-York, 1968.

COMPUMAG

Hybrid Finite Difference-Mode Matching Method for the Efficient Analysis of Waveguide Discontinuity Problems

Zhongxiang Shen and Zhenhai Shao
School of Electrical and Electronic Engineering
Nanyang Technological University , Singapore 639798

Erping Li
Institute of High Performance Computing
1 Science Park II, Singapore 117528

Email: ezxshen@ntu.edu.sg

***Abstract*—A hybrid mode matching (MM) finite difference (FD) method is presented for efficient analysis of waveguide discontinuity problems. The electromagnetic fields in the regular domain and the waveguide port region are expanded into the summation of their modal functions. The irregular coupling region is then discretized using a local mesh refinement algorithm for the finite difference method in the frequency domain. These two methods are then combined to enforce the boundary condition that tangential electric and magnetic field components must be continuous along the regional interfaces. This hybrid technique retains the high numerical efficiency of the MM method and the versatility of the FD method. Numerical results for two examples are in good agreement with those by measurement and other methods.**

***Index Terms*—Hybrid technique, finite-difference method, mode matching method, waveguide discontinuity.**

I. INTRODUCTION

TO meet the rapidly increasing demand for advanced microwave components and antennas in wireless terrestrial and satellite communications [1, 2, 3], accurate and efficient modeling tools are highly desirable. The mode-matching method [4] appears the most accurate and efficient technique for waveguide discontinuity problems though it is limited to waveguides of regular shape. Hybrid techniques such as the contour-integral mode-matching method (CIMMT) [4], the combined mode-matching finite-difference method [5], the hybrid mode-matching finite element method [6] were proposed to handle regions of irregular shape.

This paper presents a hybrid mode matching-finite difference (MM-FD) method for efficient analysis of waveguide discontinuity problems. Unlike the combined mode-matching finite difference method in [5], which only dealt with two-dimensional problems, we use a local mesh refinement algorithm based on a polygonal grid [7, 8] to evaluate the eigen-values and field distributions of an arbitrary waveguide. Generalized scattering matrix for a waveguide junction involving a section of arbitrarily shape waveguide can be obtained using the standard mode-matching process. Two numerical examples are provided to show the efficiency and versatility of the described MM-FD technique.

II. THEORY

As an example, we consider an arbitrary iris of finite thickness between rectangular and circular wavguides. There are three regions: 1, 2, and 3. Regions 1 and 2 are of regular shape and are modeled by the mode-matching method. Region 3 is of arbitrary shape and is discretized by the finite difference method.

Using the mode-matching method, the transverse electromagnetic fields in waveguides 1 and 2 can be written as

$$\vec{E}_{(1)} = \sum_{i=1}^{N_1} [A_{1i}^{-} e^{-\gamma_{1i} z} + A_{1i}^{+} e^{+\gamma_{1i} z}] \vec{e}_{1it} \tag{1a}$$

$$\vec{H}_{(1)} = \sum_{i=1}^{N_1} [A_{1i}^{-} e^{-\gamma_{1i} z} - A_{1i}^{+} e^{+\gamma_{1i} z}] Y_{1i} (\hat{z} \times \vec{e}_{1it}) \tag{1b}$$

$$\vec{E}_{(2)} = \sum_{j=1}^{N_2} [A_{2j}^{+} e^{-\gamma_{2j} z} + A_{2j}^{-} e^{+\gamma_{2j} z}] \vec{e}_{2jt} \tag{2a}$$

$$\vec{H}_{(2)} = \sum_{j=1}^{N_2} [A_{2j}^{+} e^{-\gamma_{2j} z} - A_{2j}^{-} e^{+\gamma_{2j} z}] Y_{2j} (\hat{z} \times \vec{e}_{2jt}) \tag{2b}$$

where A_{1i}^{+} , A_{1i}^{-} and A_{2i}^{+} , A_{2i}^{-} are the modal amplitude coefficients of the incident and reflected waves in waveguides 1 and 2, respectively; γ_{1i} (γ_{2j}) and Y_{1i} (Y_{2j}) are the propagation constant and mode admittance of the i th (j th) mode in guide 1 (2), $\vec{e}_{1it}$ and $\vec{e}_{2jt}$ are the normalized transverse components of the electric field for the i-th mode in guide 1 and the j-th mode in guide 2.

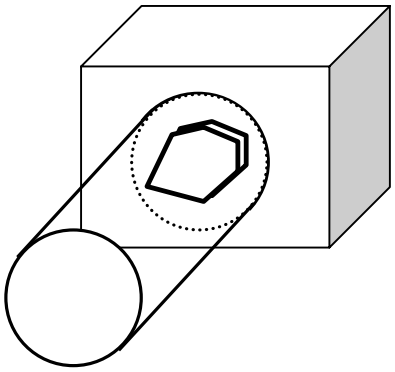

Fig. 1: Junction between two waveguides with an arbitrary iris.

The eigen modes in an arbitrarily shaped waveguide (Region 3) can be determined using the finite difference method based on the polygonal grid. Once all the modal functions in all the three regions are available, the standard mode-matching process is carried out at the regional interfaces to derive the generalized scattering matrix. Line-integral formulation [9] is employed in the hybrid MM-FD technique.

III. Numerical Examples

The first example considered is a rectangular waveguide loaded with a side-rounded iris [10]. The scattering parameters of this waveguide junction are given in Fig. 2. It is seen that our computed results using the described FD-MM method are in excellent agreement with carefully measured data.

The second example is to study the coupling between two rectangular waveguides through a circular aperture on the broad-wall. The mode-matching method is used for the two straight rectangular waveguides, while the coupling region is modeled by the finite difference method. Numerical results for the scattering parameters of this coupling structure are shown in Fig.3. It can be seen that our FD-MM results agree very well with those obtained by Ansoft's HFSS. It should be mentioned that our FD-MM hybrid technique is much more efficient than the finite element method employed in HFSS. The computation time for this coupling structure using our FD-MM method is 8 seconds for a 50-frequency point sweep, compared to 10 minutes required by HFSS on the same computer (1.7GHz Pentium IV).

IV. Conclusion

An efficient hybrid MM-FD technique has been presented for waveguide discontinuity problems. Two numerical examples have been solved by the hybrid FD-MM technique: rectangular waveguide with an iris of arbitrary shape and coupling between two rectangular waveguides through an arbitrary aperture on the broad-wall. Numerical results are in good agreement with those obtained by measurement or other methods. The efficient and versatile hybrid technique will be very useful for various guided-wave problems.

References

[1] G. L. Matthaei, L. Young, and E. M. T. Jones, *Microwave Filters, Impedance-Matching Networks, and Coupling Structures*, Dedham, MA: Artech House, 1980.

[2] C. Kudsia, R. Cameron, and W. C. Tang, "Innovations in microwave filters and multiplexing networks for communication satellite systems," *IEEE Trans. Microwave Theory Tech.*, vol. MTT-40, pp.1133-1149, Jun. 1992.

[3] J. Uher, J. Bornemann, and U. Rosenberg, *Waveguide Components for Antenna Feed Systems: Theory and CAD*, Artech House, MA: Norwood, 1993

[4] F. Arndt, R. Beyer, J. M. Reiter, T. Sieverding, and T. Wolf, "Automated design of waveguide components using hybrid mode-matching/numerical EM building-blocks in optimization-oriented CAD frameworks-State-of-the-art and recent advances," *IEEE Trans. On Microwave Theory Tech.*, vol. MTT-45, pp.747-760, 1997.

[5] M. Mongiardo and R. Sorrentino, "Efficient and versatile analysis of microwave structures by combined mode matching and finite difference methods,'' *IEEE Microwave and Guided Wave Letters, vol.3, no.8, pp. 241-243, 1993.*

[6] R. Beyer and F. Arndt, "Efficient modal analysis of waveguide filters including the orthogonal mode coupling elements by an MM/FE method," *IEEE Microwave and Guided Wave Letters, vol.5, no.1, pp. 9-11, 1995.*.

[7] H. Klingbeil, K. Beilenhoff, and H.L. Hartnagel, "A local mesh refinement algorithm for the FDFD method using a polygonal grid,'' *IEEE Microwave and Guided Wave Letters*, vol.6, no.1, pp.52-54, 1996.

[8] H. Klingbeil, K. Beilenhoff, and H.L. Hartnagel, "Finite-difference analysis of structures consisting of roundly and rectagnularly shaped domains,'' *IEEE Microwave and Guided Wave Letters*, vol.6, no.8, pp.295-297, 1996.

[9] V. Crino, C. Tomassoni, and M. Mongiardo, "Line-integral formulation of the hybrid MM/FEM technique,'' *IEEE MTT-S Symposium Digest*, pp.2033-2036, 2002.

[10] Z. Shen and X. Lu, "Modal analysis of a rectangular waveguide with rounded sides," *Microwave and Optical Technology Letters*, vol. 33, no. 5, pp.365-368, Jun. 2002.

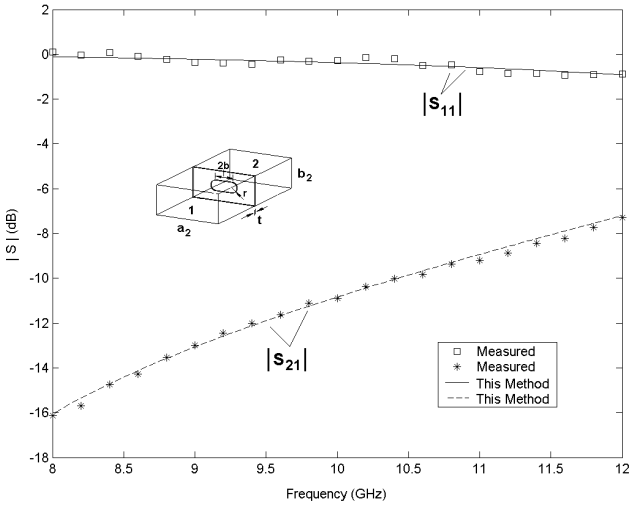

Fig. 2. Scattering parameters of a rectangular waveguide loaded with a horizontal side-rounded rectangular iris (a_2=22.86mm, b_2=10.16mm, r=1.8mm, 2b=6mm, t=0.5mm).

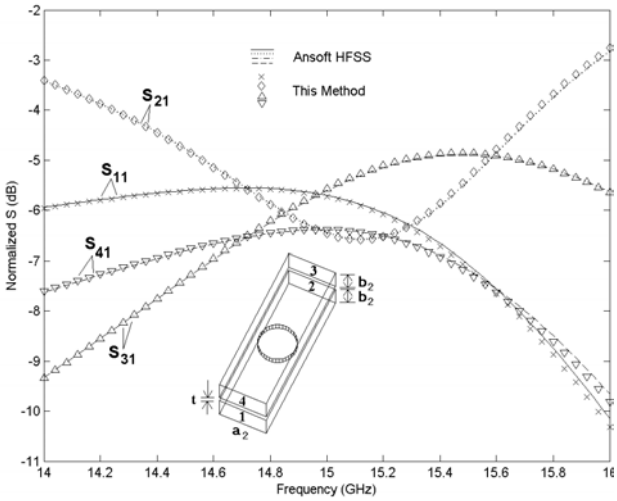

Fig. 3. Scattering parameters of a rectangular waveguide broad-wall coupler with a circular aperture located at the center of the broad wall (a_2=15.799mm, b_2=7.899mm, r=6mm, t=2mm).

Nodal and Edge Boundary Element Methods Applied to Electromagnetic Scattering Problems

M. M. Afonso[(1)], J.A. Vasconcelos[(1)], R. C. Mesquita[(1)], C. Vollaire[(2)], L. Nicolas[(2)]
[(1)] Depto. Eng. Elétrica – Universidade Federal de Minas Gerais (UFMG) – Belo Horizonte – Minas Gerais – Brasil
[(2)] CEGELY - UMR CNRS 5005 Ecole Centrale de Lyon – 69134 Ecully cedex – France
matias@cpdee.ufmg.br, joao@cpdee.ufmg.br, renato@cpdee.ufmg.br, Christian.Vollaire@eea.ec-lyon.fr, Laurent.Nicolas@eea.ec-lyon.fr

Abstract – In this paper both nodal and edge boundary element methods for three-dimensional electromagnetic scattering problems are analyzed. The Galerkin method is applied to discretize edge boundary element formulation and the Whitney elements of second degree are employed to build the vector edges base functions. The scattering of a perfect electric conducting body is computed by both methods.

INTRODUCTION

The boundary element method is commonly used for electromagnetic scattering and radiation computations. This is due to its intrinsic capability to incorporate the Sommerfeld radiation condition when modeling the unbounded free-space problem. It is particularly attractive for two reasons: first, it is an accurate method; second, it reduces the dimension of the problem by one [3].

The earliest discretization used for the boundary elements are scalar where degrees of freedom are associated to the nodes of the elements. In this context, vector field is treated as three coupled scalar fields, with one unknown along each axis of the 3D space, leading to three unknowns per node. This type of element is known as nodal-based element and is still widely used. However, vector fields have a physical and mathematical meanings that goes beyond their representation in any particular coordinate frame. Nodal-based elements fail to take this property into account. Furthermore, they give a safe estimation to the solution but not without an unnatural effort [2, 4].

A possible alternative for the nodal-based elements is the edge-based elements [1, 3]. They have degrees of freedom associated with edges and enforce the tangential continuity H(rot), in the case of curl conforming elements, or enforce the normal continuity H(div) in the case of divergent conforming elements [4, 5]. The Whitney elements of second degree are well suited for 3D scattering problems since they are divergent conform and free of line and charges points. They can be interpreted as a flux density current that leaves each triangle edges, perpendicularly to the edge direction, over the surface of the target [5].

In this paper, the Whitney edge-based elements are employed to build interpolation functions for the boundary element method. Also, the H(div) edge-based elements are compared to classical nodal elements for the solution of 3D scattering problem. Both formulations are first presented. Comparison is performed by solving the scattering of a plane wave by a perfect electric conducting (PEC) body.

NODAL ELEMENT FORMULATION

Consider a PEC body illuminated by a plane wave in the free space. The equation for the surface current density is given by:

$$\frac{\mathbf{J}}{2} = \mathbf{n}\times\mathbf{H}^{inc} + \mathbf{n}\times\int_S \mathbf{J}\times\nabla' \mathbf{G}_0 \mathbf{dS} \qquad (1)$$

where S is the body surface, $\mathbf{n}$ is the unit normal vector over the surface, $\mathbf{H}^{inc}$ is the incident magnetic field. $\mathbf{J}$ is the induced surface current density over the conductor surface, also given by:

$$\mathbf{J} = \mathbf{n}\times\mathbf{H} \qquad (2)$$

The free space Green function and its derivative are given by:

$$G_0(\mathbf{r},\mathbf{r}') = \mathbf{e}^{-jk_0R}/4\pi R \qquad (3)$$

$$\nabla' G_0(\mathbf{r},\mathbf{r}') = (\mathbf{r}-\mathbf{r}')\cdot(1+jkR)\cdot\frac{\mathbf{e}^{-jk_0R}}{4\pi R^3} \qquad (4)$$

where, $R = |\mathbf{r}-\mathbf{r}'|$.

In (3) and (4), $\mathbf{r}$ and $\mathbf{r'}$ correspond to the source and the integration points, respectively. After discretization with N first order triangle elements, (1) is rewritten as:

$$\frac{\mathbf{J}}{2} = \mathbf{n}\times\mathbf{H}^{inc} + \sum_{m=1}^{N}\mathbf{n}\times\int_{S_m}\mathbf{J}_m\times\nabla' G_0\ \mathbf{dS}_m \qquad (5)$$

where S_m is the *mth* first order triangle surface and N is the total number of triangles over the surface of the sphere. On each previous element the current density may be written as:

$$\mathbf{J} = \sum_{n=1}^{3}\lambda_n\mathbf{I}_n \qquad (6)$$

where λ_n stands for the barycentric function and $\mathbf{I}_n$ is the surface current density on the *nth* element node [4].

EDGE ELEMENT FORMULATION

The edge boundary element method formulation is derived from (1) through the application of the Weighted residual - Galerkin methods. The surface of the PEC object is discretized with first order triangular elements and the

edge boundary element formulation is computed for all triangles as following:

$$\int_{S_o} \frac{\mathbf{J}_o \cdot \mathbf{W}_o}{2} dS_o = \int_{S_o} \left(\mathbf{n} \times \mathbf{H}_o^{inc} \right) \cdot \mathbf{W}_o \, dS_o + \int_{S_o} \sum_{m=1}^{N} \left[\mathbf{n} \times \int_{S_m} \mathbf{J}_m \times \nabla' G_0 \, dS_m \right] \cdot \mathbf{W}_o \, dS_o \quad (7)$$

In (7), S_o and S_m are respectively the observer and the *mth* integration elements, $\mathbf{W}_o$ represents the weight function. To build the interpolation vector functions, divergent conforming elements are applied. These elements are well suited to model the current circulation over the conductor surface. They have degrees of freedom associated to the edges and enforce normal vector field continuity [5]. They are defined by:

$$\mathbf{N}_i = \mathbf{n} \times \left(\lambda_j \nabla \lambda_k - \lambda_k \nabla \lambda_j \right) \quad (8)$$

where λ stands for barycentric functions. Based on (8), an approximation of the current over each triangle surface is defined as follow:

$$\mathbf{J} = \sum_{i=1}^{n} \mathbf{N}_i I_i \quad (9)$$

where n stands for the number of edges in an element and I_i is the scalar flux of current that leaves each triangle in a direction perpendicular to its edges.

THE INCIDENT FIELD EVALUATION

The incident field is analytically computed for the nodal formulation as follow:

$$\mathbf{H}^{inc}(\mathbf{r}) = H_o e^{-jk_o \mathbf{r}.\mathbf{k}} \, \mathbf{h} \quad (10)$$

where H_o is the magnetic field amplitude that usually has its module equal to unit, k_o is the free space wave number, and **k** and **h** are, respectively, the unit vectors that indicate the wave and field propagation directions.

For edge elements computations, the incident field can be approximated as:

$$\mathbf{H}^{inc}(\mathbf{r}) = \sum_{i=1}^{3} \mathbf{N}_i h_i \quad (11)$$

$$\mathbf{h}_i = H_o e^{-jk_o \mathbf{r}.\mathbf{k}} \, \mathbf{h} \cdot \mathbf{g}_i \quad (12)$$

where $\mathbf{g}_i$ is the *ith* tangent edge vector.

MAGNETIC FIELD SOLUTIONS

To validate both formulations, scattering of a 1 GHZ plane wave by a 0.1 m radius - PEC sphere, placed in the center of the rectangular coordinates is considered. Nodal discretization leads to 300 nodes and 596 first order triangles elements. Edge discretization leads to 894 degrees of freedom. Fig. 1 shows the solutions for the magnetic field on the points that lies in the intersection of the sphere surface and the z = 0 plane. In this figure, nodal and edge solution are compared with the analytical solution and it is clear that, the edge solution is more closed to the analytical solution.

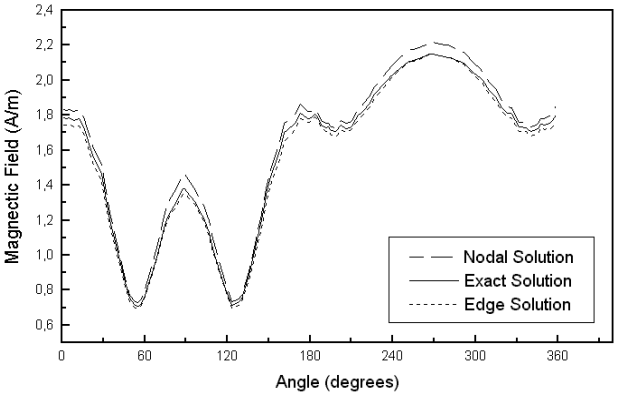

Fig. 1. The magnetic fields solution for PEC equator sphere.

The average error over the PEC sphere surface was calculated by comparing the boundary element solution with the analytical solution by using:

$$\varepsilon = \sqrt{\left(\sum_{sphere} \left| \mathbf{H}_{analytic} - \mathbf{H}_{bem} \right|^2 \right) \cdot \left(\sum_{sphere} \left| \mathbf{H}_{analytic} \right|^2 \right)^{-1}} \quad (14)$$

Table I shows the average error over the sphere surface using (14) for both nodal and edge solutions.

Table I: The average error over the sphere surface.

Kind of Solution	Error (%)
Nodal	2,78
Edge	1,78

CONCLUSION

The edge elements based in Whitney elements of second order were employed to build boundary element interpolation functions. These elements were used successfully to model surface current density. Also, results for nodal-based and edge-based boundary element methods have been compared. Scattering of a PEC sphere shows that the edge-based formulation gives better results.

REFERENCES

[1] C. J. Huber, W. Rieger, M. Haas and W. M. Rucker, "A boundary element formulation using higher order curvilinear edge elements," *IEEE Transactions on Magnetics*, vol. 34, pp. 2441-2444, September 1998.

[2] T. Jacques, L. Nicolas, C. Vollaire, "Electromagnetic scattering with the boundary integral method on MIMD systems", *IEEE Trans. on Magnetics*, vol. 36, n°4, pp.1479-1482, July 2000.

[3] J. Jin, *The finite element method in electromagnetics*, New York, 1993.

[4] J. P. Webb, "Edge elements and what they can do for you ", *IEEE Trans. on Magnetics*, vol. 29, n°2, pp.1460-1465, March 1993.

[5] J. C. Nedelec, "Mixed finite elements in R^3," *Numer. Math*., Vol. 35, pp. 315-341, 1980.

Two Sparse Matrix Open Boundary Methods for Finite-Element Analysis

Wang Xiulian, Tang Renyuan, and Hu Yan
Research Institute of Special Electrical Machines, Shenyang University of Technology
58 Xinghua South Street, Tiexi District
Shenyang, 110023, China
E-mail: tdssyg@mail.sy.ln.cn

***Abstract*---We present comparisons between two sparse matrix open boundary methods in the modeling of low frequencies electromagnetic fields: asymptotic boundary conditions technique, and the use of a geometrical transformation. Asymptotic Boundary Conditions work for rectangle boundaries. Numerical results of two methods obtained for a simple structure are compared**

INTRODUCTION

The finite element method (FEM) has become the most commonly used method for solving electromagnetic-field problems. The use of FEM implies that the domain of study is bounded. The most engineering electromagnetic problems can be regarded as closed boundary problems by means of ferromagnetic material. However, the low permeability material and air can't be regarded as the closed boundary. The open boundary problems need special techniques to represent the outer region in finite element method. Many methods have been proposed to solve this problem. But most of these have the effect of altering the sparsity of the coefficient matrix with resulting in increases compute storage and solution time. Asymptotic boundary conditions (ABCs) provide one of the most attractive alternatives from numerical point of view in unbounded domains because it can preserve the sparsity of the matrix [1,2]. The other technique that can preserve the matrix sparsity is called geometrical transformation method which converting the initial open boundary problem into a closed boundary problem by using a geometrical transformation [3,4].

In this paper, we deal with these two methods. After a brief description of their principle, we shall present some comparisons concerning their numerical solutions.

ASYMPTOTIC BOUNDARY CONDITIONS FOR AXISYMMETRIC MAGNETOSTATIC FIELD PROBLEMS

The governing equation of magnetostatics in terms of the magnetic vector potential **A** can be derived on the basis of Maxwell's equations and is expressed as

$$\nabla\times(\upsilon\nabla\times\mathbf{A})=\mathbf{J} \tag{1}$$

where J is the source current density and υ is the magnetic reluctivity.

The energy-related functional expression for (1) is given by

$$F=\frac{\nu}{2}\int_V B^2 dV-\int_V J\bullet A dV-\oint_S A\times\nu\nabla\times A\bullet dS \tag{2}$$

To solve boundary value problems in an infinite domain by the FEM, it is usual to divide the infinite domain by an artificial boundary Γ into an interior region (where loads, sources etc., may exist) and an exterior region. When using the FEM in the interior region , some boundary condition must be imposed on the boundary Γ. Ideally, the boundary should be at a distance where the field is zero. Any device will look like a dipole at a sufficient distance from the device. The boundary is placed such that the dipole field is negligible in terms of the solution desired.

In axisymmetric problem, all domain values are symmetric and the problem can be considered in the r-z plane. In no source region, the equation of magnetic vector potential **A** in spherical coordinates can be expressed as

$$\nabla^2 A-\frac{1}{r^2\sin^2\theta}A=0 \tag{3}$$

The asymptotic behavior of the magnetic dipole field at a large distance r is

$$\mathbf{A}=\sum_{n=0}^{\infty}\frac{A_n}{r^{n+1}}\sin\theta P_n^{(1)}(\cos\theta) \tag{4}$$

The expansion (4) can be used to derive the ABCs on the artificial boundary Γ. Using (4) we get the following ABCs for the vector potential **A** on a rectangle boundary Γ

$$\frac{\partial A}{\partial r}+\frac{2r^2-z^2}{r^2+z^2}A=0 \qquad (\Gamma: r=r_0) \tag{5}$$

$$\frac{\partial A}{\partial z}+\frac{3z}{r^2+z^2}A=0 \qquad (\Gamma: z=z_0) \tag{6}$$

They are the first-order ABCs for A. The expansion of the

second-order ABCs can be written as:

$$\frac{r^4 - r^2 z^2}{7r^2 - 3z^2}\frac{\partial^2 A}{\partial r^2} + r\frac{\partial A}{\partial r} + \frac{8r^4 - 4r^2 z^2 + 3z^4}{7r^4 + 4r^2 z^2 - 3z^4}A = 0 \qquad (7)$$

$$\frac{r^4 - z^4}{12r^2 - 8z^2}\frac{\partial^2 A}{\partial z^2} + \frac{\partial A}{\partial Z} + \frac{3r^2(r^2 + 3z^2) + 12z^2(r^2 - z^2)}{4r^2(r^2 + z^2) + 8(r^4 - z^4)}A = 0 \qquad (8)$$

GEOMETRIC TRANSFORMATION METHOD FOR FINITE ELEMENT ANALYSIS

The unbounded region model is divided into inner regions and external ones in GTM shown in Fig.1. The infinite region is changed into closed region by means of the geometrical transformation function.

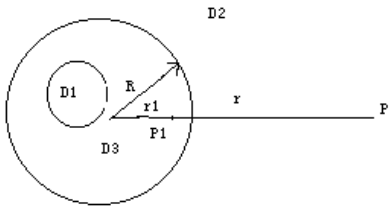

Fig.1 the two regions divided in unbounded region.

where D1 notes inner regions that include the source regions and D2 notes external regions where only includes air. D3 notes the transformation regions.

In no source regions, magnetic scalar u is satisfied with Laplace equation. For axisymmetric case, the expansion of laplace equantion can be written as:

$$\frac{1}{r^2}\frac{\partial}{\partial r}[r^2\frac{\partial^2(\mu_0 u)}{\partial r}] + \frac{1}{r^2\sin\theta}\frac{\partial}{\partial\theta}[\sin\theta\frac{\partial(\mu_0 u)}{\partial\theta}] = 0 \qquad (9)$$

According geometrical transformation, the following relation is satisfied as:

$$r_1 = \frac{R^2}{r} \qquad (10)$$

Using (11) and (12) gives

$$\frac{R^4}{r^5}\{\frac{1}{r_1^2}\frac{\partial}{\partial r_1}[r_1^2\frac{\partial(r\mu_0 u)}{\partial r_1}] + \frac{1}{r_1^2\sin\theta}\frac{\partial}{\partial\theta}[\sin\theta\frac{\partial(r\mu_0 u)}{\partial\theta}] = 0 \qquad (11)$$

Hence in transformation regions,

$$u_1(r_1,\theta) = ru(r,\theta) = \frac{R^2}{r_1}u(r,\theta) \qquad (12)$$

NUMERICAL RESULTS

In order to compare the two methods of open boundary finite-element analysis, a very simple problem is considered. This is the magnetic field of a spiral coil in free space carrying a steady current *I*. The problem is solved numerically. Fig.2 shows the magnetic flux density in the axial line of spiral coil by using ABCs and GTM. The calculating values by ABCs are closer to the analytical solutions in far boundary. Fig.3 shows the magnetic flux density in radial.

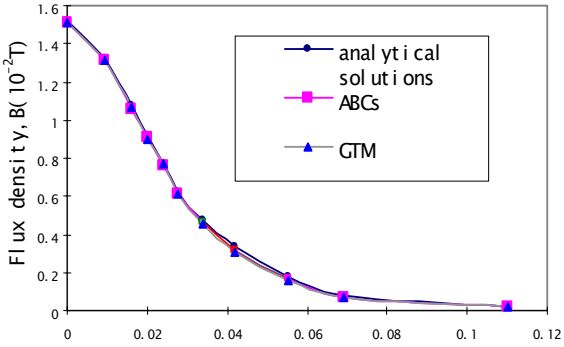

Fig.2 Flux density in axial line of spiral coil

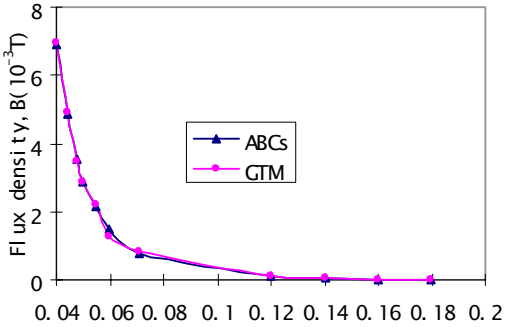

Fig.3 Flux density in radial of spiral coil

CONCLUSION

The two methods preserve the sparsity of the matrix in finite element analysis. But the formulation of the ABCs is simpler than GTM. The transformation functions in GTM are very complicated for actual engineering examples. So we highly recommend using ABCs for open boundary problem from simplicity and accuracy point of view.

REFERENCES

[1]J. R. Brauer, S. M. Schaefer,J. F. lee, and R. Mittra, "Asymptotic boundary condition for three dimensional magnetostatic finite elements"IEEE Trans, Magn., vol. 27, pp.5013-5015, Nov. 1991.

[2]Hu Yan, Tang Renyuan, and Liang Zhenguang. "Geometric Transformation Method of 3D Unbounded Electromagnetic Fields". Proceedings of ICEF'2000. Beijing, China: International Academic Publishers, 2000:51~54.

Problems and solutions for a high−performance coupling between Monte−Carlo and finite element methods

Yannick Eon[(1)], Yves Maréchal[(1)], Philippe Massé[(2)], Alain Glière[(2)]
[(1)] Laboratoire d'Electrotechnique de Grenoble
BP 46
38402 Saint Martin d'Hères, France
yannick.eon@leg.ensieg.inpg.fr
[(2)] Laboratoire d'Electronique, de Technologie de l'Information
DSYS, CEA
38054 Grenoble Cedex 9, France
yannick.eon@cea.fr

***Abstract*−The modelisation of some devices requires to use together continuous models and particulate models. Nevertheless, the coupling of the simulation methods for these two kinds of models leads to many difficulties in terms of efficiency, quality and stability. Some aspects of the realisation of a high−performance coupling between a Monte−Carlo method and a finite element method are proposed.**

INTRODUCTION

For modellers, a compromise have to be found between the physical accuracy of some existing models and the computing efficiency of their simulation methods. Particulate models define the state of a system through the knowledge of individual particle state and their simulation is often time consuming. In opposition, continuous models reduce the system state to the knowledge of few state variables and consequently their validity is restricted by some physical hypothesis.

To treat efficiently problems with complex physical phenomena (highly coupled or out of the validity range of known continuous models) a coupling between particulate and continuous models simulation methods is necessary in order to take into account the localised microscopic effects.

In this article, the Monte−Carlo Method (M.C.M.) and the Finite Element Method (F.E.M.), respectively particulate and continuous models simulation methods, are analysed. Then, we present two examples of coupled (MCM.−FEM.) analysis in order to find out the requirements for an efficient coupling of these two methods.

COMPARISON OF THE TWO METHODS

The Monte−Carlo Method

The Monte−Carlo Method [1] realises a statistical sampling of the repartition of the studied system state densities through the simulation of the stochastic trajectories of a device particle sample.

Particles are governed by a transport phenomenon described by the Boltzmann's equation. It is a differential equation taking into account the deterministic applied forces and the probabilistic interactions on particles with the surrounding media. Interactions with geometrical boundaries are also treated during their movement.

- Materials are linked to the interaction probability laws and characterised by their differential cross sections.
- Characteristic time steps are simply equals to the delay between two consecutive interactions.
- Simulation results are the time evolution of the repartition of the system micro−state densities.

Finite Element Method

In opposition, the finite element method is a deterministic method for which the system state variables are given by an integration of some partial differential equations considering different boundary conditions on the problem description.

- The intrinsic integration method of finite elements imposes the sampling of space and geometry.
- Materials are considered as macroscopic coefficients for the partial differential equation.
- Characteristic time steps are chosen relatively to the evolution of the macroscopic variables and are large in comparison to individual particle dynamics.
- Computed results are the values of the state variables at time and space sample points.

Conclusions

These two simulation methods are different at many description levels (see table I.).

TABLE I. SUMMARY OF DIFFERENCES BETWEEN THE TWO METHODS

Level	Monte−Carlo method	Finite element method
Space	Continuous	Sampled
Physics	Stochastic differential equation	Partial differential equation
Materials	Cross sections	Physical properties
Time steps	Microscopic dynamics	Macroscopic dynamics
Results	Probability densities	Values of state variables

In addition, skills in physical modelisation relative to these two methods are totally different. The coupling is in this way a specific problem that needs a particular study.

The following examples are illustrating two realisations of a coupling between these methods.

ILLUSTRATIVE CASES OF COUPLING

One way coupling: MCM→FEM

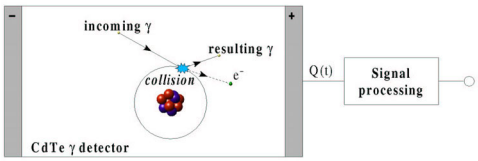

Fig. 1. Detector description

The example is a semiconductor detector for gamma ray image processing [2] (see fig. 1.). The gamma propagation and their interactions with the semiconductor are modelled by a Monte−Carlo method. The electron−hole pairs created by interaction between rays and materials are considered as instant charge sources in the semiconductor derive−diffusion model which is simulated using a boundary integral equation method in order to obtain the output signal of the detector.

Bidirectional coupling: MCM↔FEM

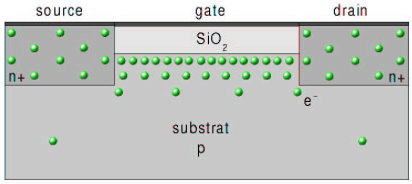

Fig. 2. Device description and charge repartition

The problem is a submicronic MOSFET [1] (see fig 2.). The Monte−Carlo method simulates the charge transport in the semiconductor under the coupled action of electrostatic forces and probabilistic material interactions. The resulting space repartition of charges is introduced as the source part in the resolution of the Poisson's equation by the finite element method in order to get the local values of the electric field. The bidirectional coupling is realised by iterating the two methods until he stationary state is reached.

THE COUPLING SPECIFIC PROBLEM

Summary of the coupling requirements

The previous cases have exhibited, for different modelisation levels, several parameters taking part in information exchange in the coupling of solvers associated to the two methods (see table II.).

TABLE II. EXCHANGE PARAMETERS BETWEEN THE TWO METHODS

Level	Source	Destination	Exchange parameters
Physics	MCM	FEM	Sources
Material	MCM	FEM	Properties
Physics	FEM	MCM	Forces
Material	FEM	MCM	Variables modifying probability laws

The concrete realisation of the method coupling can be carried out as detailed below.

A modular approach

One can try to use two simulation tools in a modular approach and establish a communication protocol for the exchange parameters between methods. The approach is certainly attractive when considering the software engineering aspect but on a numerical point of view it is inefficient for bidirectional coupling cases due to the structural differences between the two methods:

- The different space representations leads to numerical double−interpolation phenomena, thus decreasing the overall simulation quality.
- The localisation of a particle in the finite element grid is very expensive. The safe implementation of the algorithm is a very hard task due to the management of round off errors.
- The post processing of the Monte−Carlo simulation cannot be optimised to the finite element needs, leading to an unacceptable cost.

A global approach

The different aspects mentioned before can be improved by specialising together the two methods for the resolution of coupled problems.

Adapting the Monte−Carlo method to the sampled representation of space used by the finite element method brings two benefits. On the one hand, accuracy issues in the localisation of the particle and its crossing of the boundaries are not so critical. On the other hand, quality and efficiency in the communication process of exchange parameters increase since no more double interpolation is needed.

The vectorisation of the post−processing of the coupling variables is also largely useful to ensure the global efficiency of the coupled method.

CONCLUSION

The structural differences between the Monte−Carlo method and the finite element method are at the origin of the difficulties relative to the coupling of these two methods. An adaptation of the methods in order to realise their coupling is the only way that brings global efficiency in a coupled simulation. Such a realisation will be produced further in the full paper.

REFERENCES

[1] K. Binder, "MonteCarlo Methods in Statistical Physics", Springer−Verlag, New York, 1979.
[2] M. Picone, "Contribution à la simulation tridimensionnelle de détecteurs semiconducteurs en spectrométrie gamma", Thèse de l'Université J. Fourier − Grenoble 1, 2002.
[3] J. Hadji, "Modélisation et simulation tridimensionnelle des composants à semi−conducteurs de taille submicronique", Thèse de Institut National Polytechnique de Grenoble, 1999.

Hybrid PO-MoM Analysis of Large Axi-Symmetric Lens Antennas

Zhongxiang Shen and Duolong Wu
School of Electrical and Electronic Engineering
Nanyang Technological University , Singapore 639798

Erping Li
Institute of High Performance Computing
1 Science Park II, Singapore 117528

Email: ezxshen@ntu.edu.sg

***Abstract*—A hybrid physical optics-method of moments (PO-MoM) technique is described to analyze the radiation characteristics of large axi-symmetric dielectric lens antennas. The procedure combines the method of moments (MoM) for modeling the edge region of the lens and physical optics (PO) for the inner flat region of the lens. Using this technique, the far-field patterns of a lens antenna are obtained from its equivalent surface currents. Numerical results are presented for the radiation pattern of an aperture antenna through a large axi-symmetric lens antenna. The PO-MoM technique proves to be more efficient and accurate than the PO method for solving the large lens antenna radiation.**

***Index Terms*—Lens antennas, hybrid technique, physical optics (PO), method of moments (MoM).**

I. Introduction

The dielectric lens antennas have found wide applications in millimeter-wave and submillimeter-wave frequencies including remote sensing, radio astronomy, radar, mobile and satellite communication systems, and collision avoidance systems for automobiles [1, 2]. The far-field patterns of the lens antennas with various shapes were analyzed with a number of methods by researchers in recent years. The combined ray-optics/diffraction method was presented for an accurate analysis of a homogeneous spherical Tefelon lens antenna [2]. The ray optics method was proposed by Taguchi et al. to analyze the arbitrarily shaped dielectric lens antenna [3]. The ray-optics/field-integration method was used for analysis of an off-axis double-slot antenna on extended hemispherical silicon and quartz lenses [4]. The modal technique that employs separation of variables provided the solution of scattering by spherically stratified microwave lens antennas [5]. The genetic algorithm (GA) optimizer with adaptive cost function was implemented to analyze nonuniform Luneburge two-shell lens antennas [6]. The ray tracing method was employed to estimate ration characteristics of an off-focus feed shaped dielectric lens antenna [7]. The body of revolution finite-difference time-domain (BOR-FDTD) method was recently applied to the analysis of integrated lens antennas [8].

This paper applies the hybrid physical optics-method of moments (PO-MoM) technique [9] to the analysis of large axi-symmetric lens antennas radiating into a free space. Under this technique, the edge region of the lens is modeled using the MoM to take into account its diffraction and multiple interactions, which may be significant. In the inner flat region of the lens, ray techniques in conjunction with physical optics (PO) are used to compute the equivalent currents, which are then combined with the MoM currents at the dielectric boundaries for complete modeling of the lens. Near zone antenna fields are computed at the inner surface of the lens to serve as an excitation source for the MoM and PO currents. Numerical results for the far-field patterns of a large axi-symmetric lens antenna are given.

II. The PO-MoM technique

A typical lens antenna configuration is shown in Fig. 1, consisting of an antenna (reflector, array, etc.) radiating a field upon a dielectric lens and the lens that is made of a homogeneous material. The antenna is placed at the focus point of the lens. A body of revolution (BOR) lens structure is assumed in this paper to further reduce CPU time and memory requirements. Meanwhile, the backward radiation of the antenna is not considered. In order to calculate the equivalent surface currents on the lens, the lens can be divided into two regions: the edge part and the inner flat part, as illustrated in Fig. 1. The inner surface of the lens, close to the antenna, is denoted as S_1, and the outer surface is as S_2. Although the hybrid techniques is described for a lens antenna of one-layer dielectric medium, it can be readily generalized to lens antennas of multilayer homogeneous medium.

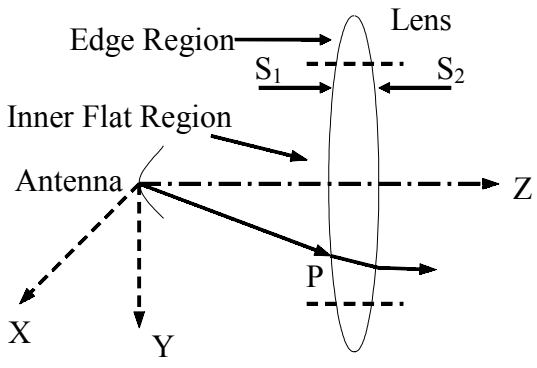

Fig. 1. Geometry of a lens antenna.

The near-zone electrical field of the antenna at the point P on the surface S_1 is given as [9]

$$\vec{E}_p = E_{pr}(z,\phi)\hat{r} + E_{p\theta}(z,\phi)\hat{\theta} + E_{p\phi}(z,\phi)\hat{\phi}. \quad (1)$$

The equivalent electrical and magnetic currents on the surfaces S_1 and S_2 in the edge region are written as $\vec{J}_1^{MM}(\vec{r})$, $\vec{M}_1^{MM}(\vec{r})$ and $\vec{J}_2^{MM}(\vec{r})$, $\vec{M}_2^{MM}(\vec{r})$, respectively. Also, $\vec{J}_1^{PO}(\vec{r})$, $\vec{M}_1^{PO}(\vec{r})$ and $\vec{J}_2^{PO}(\vec{r})$, $\vec{M}_2^{PO}(\vec{r})$ are the equivalent currents on the surfaces S_1 and S_2 in the inner flat region, respectively. Furthermore, the PO currents can be expressed as the following forms

$$\vec{J}_1^{PO}(\vec{r}) = \hat{n}_1 \times (\vec{H}^i + \vec{H}^r) \quad (2)$$

$$\vec{M}_1^{PO}(\vec{r}) = (\vec{E}^i + \vec{E}^r) \times \hat{n}_1 \quad (3)$$

$$\vec{J}_2^{PO}(\vec{r}) = \hat{n}_2 \times \vec{H}^t \quad (4)$$

$$\vec{M}_2^{PO}(\vec{r}) = \vec{E}^t \times \hat{n}_2 \quad (5)$$

where $\hat{n}_1$ and $\hat{n}_2$ are the unit outer-normal vectors on the surfaces S_1 and S_2, and $(\vec{E}^i, \vec{E}^i)$, $(\vec{E}^r, \vec{E}^r)$ and $(\vec{E}^t, \vec{E}^t)$ represent the incident, reflected and transmitted fields on the lens, respectively.

Applying the combined field integral equation (CFIE) and Galerkin's testing in conjunction with BOR principles to the hybrid MoM solution [9], the hybrid PO-MoM matrix equation is generated and the unknown variables can then be determined. From the surface equivalent currents, we can finally calculate the radiation patterns of the lens antenna.

III. Numerical Example

The calculated results for the radiation pattern of a rectangular aperture antenna through a large axi-symmetric dielectric lens using the hybrid PO-MoM are showed in Fig. 2. The aperture of the lens antenna is 30λ, and the aperture antenna is located at the lens' focus. The central 24λ is modeled using the PO, while the two edges of 3λ long each are discretized by the moment method. It can be seen that the agreements are very good for the far-field radiation performance from the above calculated results.

IV. Conclusion

A hybrid physical optics-method of moments (PO-MoM) technique is presented for the analysis of large axi-symmetric lens antennas. Using this technique, the edge region of the lens is modeled with the method of Moments (MoM), and the inner flat region of the lens is analyzed with Physics Optics (PO). The far-field patterns of lens antennas are obtained from the surface equivalent currents, and a computational example is provided. The calculated results are in good agreement with available data in the literature.

References

[1] B. G. Porter, L. L. Rauth, J. R. Mura and S. S. Gearhart, "Dual-polarized slot-coupled path antennas on Duroid with Teflon lenses for 76.5-GHz automotive radar systems", *IEEE Trans. Antenna Propagat.*, vol. AP-47, pp. 1836-1842, 1999.

[2] B. Schoenlinner, X. Wu, J. P. Ebling, G. V. Eleftheriades and G. M. Rebeiz, "Wide-scan spherical-lens antennas for automotive radars", *IEEE Trans. Microwave theory Tech*., vol. 50, pp. 2166-2175, 2002.

[3] M. Taguchi, M. Masuda, H. Shimoda and K. Tanaka, "Analysis of arbitrarily shaped dielectric lens antenna", *Proc. IEEE Antenna Propagat. Int. Symp*., vol. 2, pp. 769-772, 2001.

[4] D. F. Filipovic, G. P. Gauthier, S. Raman, and G. M. Rebeiz, "Off-axi properties of silicon and quartz dielectric lens antennas", *IEEE Trans. Antenna Propagat*., vol. AP-45, pp. 760-766, 1997.

[5] J. R. Sanford, "Scattering by spherically stratified microwave lens antennas", *IEEE Trans. Antenna Propagat*., vol. AP-42, pp. 690-698, 1994.

[6] H. Mosallaei and Y. Rahmat-Samii, "Nonuniform Luneburng and two-shell lens antennas: radiation characteristics and design optimization", *IEEE Trans. Antenna Propagat*., vol. AP-49, pp. 60-69, 2001.

[7] Y. Yamada, S. Sasaki, "Estimations of radiation characteristics of an off-focus feed shaped dielectric lens antenna by a tracing method", Proc. *IEEE Antenna Propagat. Int. Symp*., vol. 4, pp. 398-401, 2002.

[8] M. J. M. van der Vorst and P. J. I. De Maagt, "Efficient body of revolution finite-difference time-domain modeling of integrated lens antennas", *IEEE Microwave and Wireless Components Lett.*, Vol. 12, pp. 258-260, 2002.

[9] M. A. A. Moneum, Z. Shen, J. L. Volakis, and O. Graham, "Hybrid Po-Mom analysis of large axi-symmetric radomes", *IEEE Trans. Antenna Propagat*., vol. AP-49, pp. 1657-1666, 2001.

[10] C. A. Fernandes, "Shaped dielectric lenses for wireless millimeter-wave communications", IEEE Antenna and Propagat. Magzine, vol. 41, pp. 141-150, 1999.

[11] C. J. Sletten, *Reflector and Lens Antennas Analysis and Design Using Personal Computers,* Norwood: Artech House, pp. 215-260, 1988.

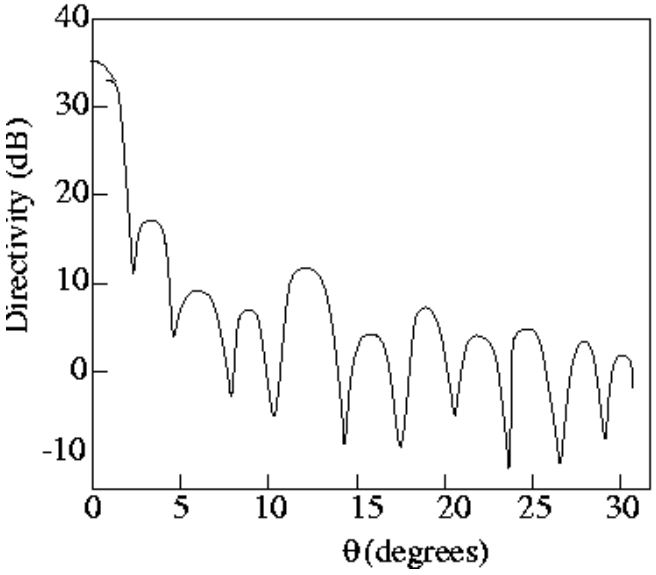

Fig. 2. Field pattern of a rectangular aperture antenna radiating through a large axi-symmetric dielectric lens (D=f=30λ).

DBCI Solution of Helical Scalar Potential Problems in Unbounded Domains

G. Aiello, E. Dilettoso
Dipartimento Elettrico Elettronico e Sistemistico - Università degli Studi di Catania
Viale Andrea Doria 6, Catania
I-95125 - Italy
gaiello@dees.unict.it, edilettoso@dees.unict.it

Abstract — **DBCI (Dirichlet Boundary Condition Iteration) is a hybrid method to solve electromagnetic problems in unbounded domains in conjunction with the standard Finite Element Method. The purpose of the paper is to extend the capabilities of DBCI to compute open-boundary electrical and magnetic scalar potentials exhibiting helical symmetry, and to present some examples of validation and application of the method.**

I. Introduction

Boundary value problems in unbounded domains often need to be solved in all areas of Electrical and Electronic Engineering and a numerical solution can only be obtained by means of a number of widely employed methods used in conjunction with the Finite Element Method (FEM) [1]. In the last decade the authors and their colleagues have developed an iterative hybrid method, called DBCI (Dirichlet Boundary Condition Iteration), for the finite-element solution of several kinds of unbounded electromagnetic problems such as electrostatic, skin effect and eddy current problems [2-3]. A conspicuous decrease in computational effort is achieved by exploiting geometrical symmetry, if any, because it is possible to reduce the dimensions of the problem. Although there are a number of electromagnetic devices which possess helical symmetry, such as solenoids, cables, waveguides, antennas, little attention has been devoted to numerical treatment of this symmetry as compared with translational and axial devices [4]. The aim of the paper is to extend the mathematical formulation of DBCI in order to deal with open-boundary electrical and magnetic scalar potential problems with helical symmetry and to give some examples of validation and application of the method.

II. Mathematical formulation

The solution of a problem exhibiting helical symmetry is conveniently stated in terms of twisted coordinates X,Y,Z or helical polar ones r, ζ, z, because, by virtue of symmetry, the physical quantities depend on the X,Y or r, ζ coordinates respectively, and they can be computed by simple analysis on a plane where Z=const., typically Z=0. The former are related to the Cartesian co-ordinates x,y,z as follows:

$$X=\cos(hz)x+\sin(hz)y \quad Y=-\sin(hz)x+\cos(hz)y \quad Z=z \qquad (1)$$

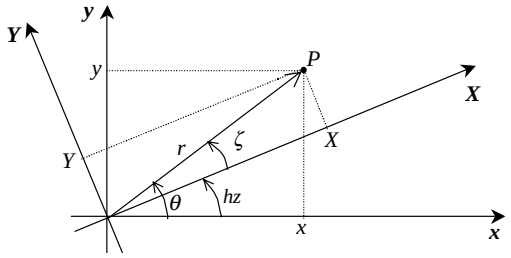

Fig. 1. Twisted X,Y, Z and helical polar r, ζ, Z co-ordinates.

where h (pitch) is equal to $2\pi/p$, p being the period in the Z direction, whereas the latter are identical to the usual polar co-ordinates r, θ, z, except for ζ (see Fig. 1). In this paper X,Y,Z are preferred because they simplify numerical treatment of problem.

First let us consider an electrostatic problem with helical symmetry, in which there are n_C conductors Ω'_k of cross section Ω_k k=1,…,n_C, voltaged with electric potentials φ_k, embedded in a vacuum. The electric scalar potential φ is computed by solving a Laplace equation in an open-boundary domain Ω of the plane Z=0 subjected to Dirichlet $\varphi(P) = \varphi_k \; \forall$ $P \in \partial\Omega_k$ and, if any, Neumann boundary conditions. By dropping all dependence on Z, the Laplace equation in the twisted co-ordinates takes the following form [5]:

$$(1+h^2Y^2)\frac{\partial^2\varphi}{\partial X^2}-2h^2XY\frac{\partial^2\varphi}{\partial X\partial Y}+(1+h^2X^2)\frac{\partial^2\varphi}{\partial Y^2}-h^2\left(X\frac{\partial\varphi}{\partial X}+Y\frac{\partial\varphi}{\partial Y}\right)=0 \qquad (2)$$

The DBCI method starts by choosing an arbitrary fictitious boundary $\partial\Omega_F$ enclosing all Ω_k and imposing on it an initial guess $\boldsymbol{\varphi}^{(0)}_{\mathbf{F}}$ for φ. In this way, a bounded domain $\Omega_F \subset \Omega$ is obtained, and a standard Galerkin finite element method can be used to discretize the boundary value problem. In such a way, a linear equation:

$$\mathbf{A}\boldsymbol{\varphi}^{(0)} = \mathbf{B_0} - \mathbf{A_F}\,\boldsymbol{\varphi}^{(0)}_{\mathbf{F}} \qquad (3)$$

is derived, in which **A** and $\mathbf{A_F}$ are sparse finite element matrices depending on the geometrical discretization, $\mathbf{B_0}$ is the part of the known term due to φ_k, and $\boldsymbol{\varphi}^{(0)}$ the vector of unknown nodal values of the potential inside Ω_F. In order to improve the solution $\boldsymbol{\varphi}^{(0)}$, another equation, relating the potential values on $\partial\Omega_F$ to the charge distribution on $\partial\Omega'_k$, needs to be introduced. This equation is the following:

$$\varphi^{(1)}(P_F) = -\frac{1}{4\pi}\sum_{k=1}^{n_C}\int_{\partial\Omega'_{kp}} \frac{\partial\varphi^{(0)}(P)}{\partial n} g(P,P_F)\,dP \quad (4)$$

where $\partial\Omega'_{kp}$ is the cut helical tube enclosed by one period Ω'_{kp} of the conductor Ω'_k, **n** denotes the outward unit vector of $\partial\Omega'_{kp}$, $P_F \in \partial\Omega_F$ and g is the helical open-boundary Green function having the following expression:

$$g(r_F,\zeta_F,r,\zeta) = -2\log r_> + 4\sum_{m=1}^{+\infty} I_m(mhr_<)K_m(mhr_>)\cos[m(\zeta_F-\zeta)] \quad (5)$$

where $r_> = \max(r_1,r_2)$, $r_< = \min(r_1,r_2)$, I_m and K_m are the m-th modified Bessel functions of the first and second kind, respectively [6]. Note that the surface integrals over the ends of the cut helical tube Ω'_{kp} cancel by periodicity.

The above equation can be recast in a matrix form as:

$$\boldsymbol{\varphi}^{(1)}_{\mathbf{F}} = \boldsymbol{\varphi}_{\mathbf{F0}} + \mathbf{G}\boldsymbol{\varphi}^{(0)} \quad (6)$$

where $\boldsymbol{\varphi}_{\mathbf{F0}}$ represent a vector depending on the conductor potentials and **G** is a sparse matrix, whose entries are calculated by making use of expressions (4) and (5) .

Computing $\boldsymbol{\varphi}^{(1)}_{\mathbf{F}}$ by (6), another guess $\boldsymbol{\varphi}^{(1)}$ can be calculated from (3), and by repeating the above steps, convergence takes place within a few iterations. Note that this approach does not destroy the symmetry and positive definite characters of matrix **A,** allowing (3) to be solved efficiently. Moreover, good accuracy is obtained even if $\partial\Omega_F$ is located close to the conductors or is divided so as to encircle the singles Ω_k. Now consider a system of n_C infinite-length helical symmetric thin solenoids Ω'_k of arbitrary cross section Ω_k, embedded in a vacuum. With minor changes the above formulation is able to compute the magnetic scalar potential in such systems, if we assume a current density vector $\mathbf{J}_k$ on the solenoid surfaces $\partial\Omega'_{kp}$ lying on the Z=constant planes. In fact, although the potential has a discontinuous normal derivative across $\partial\Omega'_{kp}$, equal to $\mu_0 J_k$, μ_0 being the vacuum magnetic permeability, it is harmonic both internally and externally to the solenoids [6]. It can thus be computed by imposing an initial guess $\boldsymbol{\varphi}^{(0)}_{\mathbf{F}}$ on $\partial\Omega_F$, an inhomogeneous Neumann boundary condition on $\partial\Omega'_{kp}$ and by treating the problem in a similar way to a mixed boundary value problem with inhomogeneous "internal" Neumann conditions. Moreover, since $\partial\Omega'_{kp}$ is not equipotential, the computation of $\boldsymbol{\varphi}^{(1)}_{\mathbf{F}}$ must be done by adding the following term to the right hand side of (4):

$$\varphi^{(1)}(P_F) = \frac{1}{4\pi}\sum_{k=1}^{n_C}\int_{\partial\Omega'_{kp}} \varphi^{(0)}(P)\frac{\partial g(P,P_F)}{\partial n}dP \quad (7)$$

In the case of a single solenoid of circular cross section, the following analytical solution is available [6],

$$\varphi(r_F,\zeta_F) = \frac{\mu_0 jh}{4\pi}\int_{-\pi}^{\pi} \frac{r^2(\zeta)b\sin\zeta}{r(\zeta)-b\cos\zeta}\, g(r(\zeta),\zeta,r_F,\zeta_F)\,d\zeta \quad (8)$$

$$r(\zeta) = b\cos\zeta + \sqrt{a^2 - b^2\sin^2\zeta} \quad (9)$$

which has been used to validate the formulation. Figure 2 shows the geometry of the solenoid, whereas Figure 3 shows the magnetic potential contours. The values of the parameters are the following: a=10 cm, b=4 cm, p=10 cm, $J=4\pi/\mu_0 h$ A/m; a fictitious boundary with a radius of 26 cm has been selected. Details of the validation of the method and some examples of application will be given in the full paper.

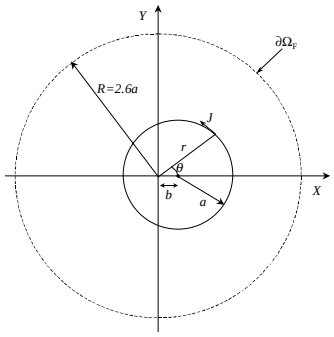

Fig. 2. Geometry of a circular cross section solenoid.

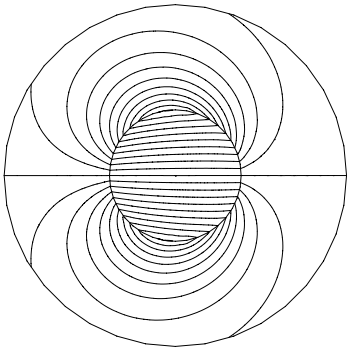

Fig. 3. Magnetic scalar potential contours.

REFERENCES

[1] Q. Chen, A. Konrad "A review of Finite Element Open Boundary Techniques for Static an Quasi Static Electromagnetic Fields Problems", IEEE Trans. On Magnetics, vol. 33, n. 1, January 1997, pp. 663-676.

[2] G. Aiello, S. Alfonzetti, S. Coco, "Charge Iteration: a Procedure for the Finite-Element Computation of Unbounded Electrical Fields", Int. J. Numer. Methods Eng., vol. 37, n. 24, December 1994, pp. 4147-4166.

[3] G. Aiello, S. Alfonzetti, S. Coco, N. Salerno, "Finite-Element Iterative Solution of Skin Effect Problems in Open Boundaries", Int. J. Numer. Modelling, vol. 9, January-April 1996, pp. 125-143.

[4] H. Igarashi, T. Tomna, "BE and FE Solutions to Open Boundary Potential Problems with Helical Symmetry", IEEE Trans. On Magnetics, vol. 28, n. 2, March 1992, pp. 1671-1674.

[5] M. R. Spiegel "Vector Analysis", McGraw-Hill, New York, 1959.

[6] R. L. Dewar, H.J. Gardner, "A Harmonic Expansion for the Magnetic Field of Helical Solenoid", Journal of Computational Physics, vol. 77, pp. 485-500, 1987.

Equivalence Theorem Boundary Conditions for FDTD Formulations

Sami Barmada, Antonino Musolino, Marco Raugi
Dip. Sistemi Elettrici e Automazione, University of Pisa, Via Diotisalvi 2 56126 Pisa, Italy

***Abstract*— In this paper a boundary condition for the truncation of the grid in Finite Difference Time Domain (FDTD) formulations is presented. The proposed technique restricts the computational domain truncating the FDTD grid close to the scattering objects. Following the equivalence theorem the proposed procedure yields a coupling between the region outside the boundary (exterior problem) and inside the boundary (interior problem) numerically solved by a hybrid FDTD-MOM technique. Numerical applications demonstrate the validity of the proposed procedure.**

INTRODUCTION

Among the proposed techniques, to terminate the computational domain in FDTD formulations, Absorbing Boundary Conditions (ABC) and Perfectly Matched Layer (PML) are popular ones that successfully solve the problem. However advantages and disadvantages exists in every technique [1]. In this paper the boundary condition on the termination of the grid is obtained by using the equivalence theorem. A number of fictitious surface enclose the objects splitting the wave propagation problem in a number of interior problem and in an exterior problem coupled together. Unknown distributions of electric current and of tangential electric field on the fictitious surfaces are assumed. Continuity of tangential components of electric and magnetic fields on these surfaces is enforced by Galerkin form of MoM. The interior problems are solved via Yee algorithm; the boundary condition is provided by the electric field distribution on the boundary surfaces. The restriction of the computational domain yields integral equations solved by MOM at the cost of the solution of a dense matrix. If the surface dimension of the boundary yields a high unknowns number the dense matrix can be sparsified adopting a wavelet transformation of the unknowns [2].

MATHEMATICAL FORMULATION

The surfaces S_j that enclose the bodies are boxes with the faces parallel to the coordinate planes. Yee grids are defined in the inner part and terminate on S_j with nodes where tangential components of electric field are defined. Then, the surfaces are discretized in rectangles. Proper basis functions $\boldsymbol{f_n}(\boldsymbol{r})$ for the expansion of currents [3], [4] and pulse basis functions $\boldsymbol{p_{n,E}}(\boldsymbol{r})$, $\boldsymbol{p_{n,H}}(\boldsymbol{r})$ for the tangential components of $\boldsymbol{E}$ and $\boldsymbol{H}$ on S_j are selected. All these basis functions will be briefly described in the full paper. Then, currents, charges and electric and magnetic field distributions can be written as:

$$J(r,t)=\sum_{k=1}^{N_{j,edge}} J_k(t) f_k(r);\quad \frac{\partial}{\partial t}\rho(\boldsymbol{r},t)=-\sum_{k=1}^{N_{j,edge}} J_k(t)\nabla_S\cdot\boldsymbol{f}_k(\boldsymbol{r})$$

$$\boldsymbol{E}_t(\boldsymbol{r},t)=\sum_{k=1}^{N_{j,edge}} E_{t,k}(t)\boldsymbol{p}_{k,E}(\boldsymbol{r});\quad \boldsymbol{H}_t(\boldsymbol{r},t)=\sum_{k=1}^{N_{j,edge}} H_{t,k}(t)\boldsymbol{p}_{k,H}(\boldsymbol{r})$$

We suppose that the free space wavelength of the highest harmonic of the source is much greater than the diagonal of each rectangle on S_j. Let $r_k^{(c)}$ denote the center of the k^{th} rectangle; the time delay $\|r'-r\|/c$ can be approximated with $\Delta t_k=\|r_k^{(c)}-r\|/c$. Electric and magnetic fields can be written from the retarded vector and scalar potentials as:

$$E(r,t)=-\frac{\mu_0}{4\pi}\sum_{k=1}^{N_{j,edge}}\frac{\partial}{\partial t}J_k(t-\Delta t_k)\int_{\Sigma S_k}\frac{f_k(r')}{\|r'-r\|}dr'+$$

$$-\frac{1}{4\pi\varepsilon_0}\sum_{k=1}^{N_{j,face}}\rho_k(t-\Delta t_k)\nabla_r\int_{S_k}\frac{1}{\|r'-r\|}dr'$$

$$H(r,t)=\frac{\mu_0}{4\pi}\sum_{k=1}^{N_{j,edge}}J_k(t-\Delta t_k)\nabla_r\times\int_{\Sigma S_k}\frac{f_k(r')}{\|r'-r\|}dr'$$

where $N_{j,edge}$ is the number of edges on S_j. These expression are inserted in the continuity equations of the tangential component of electric and magnetic fields on S_j:

$$n\times E^S(r,t)+n\times E(r,t)=n\times\boldsymbol{E}_t(\boldsymbol{r},t) \qquad (1a)$$

$$n\times H^S(r,t)+n\times H(r,t)=n\times\boldsymbol{H}_t(\boldsymbol{r},t) \qquad (1b)$$

where $\boldsymbol{n}$ is the outward normal and $E^S(r,t)$ and $H^S(r,t)$ are the incident source fields. MOM is used to enforce the previous equations; the set of weighting function being the same as the basis functions of the current.

With the Yee philosophy in mind ($\boldsymbol{E}$ and $\boldsymbol{H}$ evaluated at halftime steps), the weighted form of (1a) and (1b) are discretized at $t=(n+1/2)\Delta t$ and $t=(n+1)\Delta t$ respectively obtaining (details will be given in the full paper):

$$U_h^{n+1/2}+\sum_{k=1}^{N_{edge}}\left(\frac{A_{h,k}}{\Delta t}+\frac{B_{h,k}\Delta t}{8}\right)J_k^{n+1-d_{h,k}}+\sum_{k=1}^{N_{edge}}\left(\frac{7B_{h,k}\Delta t}{8}-\frac{A_{h,k}}{\Delta t}\right)J_k^{n-d_{h,k}}+$$

$$\sum_{k=1}^{N_{edge}}\frac{B_{h,k}\Delta t}{2}J_k^{n-1-d_{h,k}}+\sum_{k=1}^{N_{edge}}B_{h,k}\int_{-\infty}^{n-1-d_{h,k}}J_k(\tau)d\tau=\sum_{k=1}^{N_{edge}}C_{h,k}E_{t,k}^{n+1/2} \qquad (2a)$$

$$V_h^{n+1}+\sum_{k=1}^{N_{edge}}D_{h,k}J_k^{n+1-d_{h,k}}=\sum_{k=1}^{N_{edge}}F_{h,k}H_{t,k}^{n+1} \qquad (2b)$$

The central difference scheme is used to approximate the derivative of the currents and the trapezoidal rule to approximate the integral. Because of the termination of the Yee grid with tangential component of electric field, the terms $E_{t,k}^{n+1/2}$ are the boundary conditions for the inner problem. Providing them together with the "initial conditions" for $\boldsymbol{E}$ and $\boldsymbol{H}$ at times $t=(n-1/2)\Delta t$ and $t=n\Delta t$

respectively, the Yee algorithm allows evaluating $\boldsymbol{E}$ in the inner points at $t=(n+1/2)\Delta t$ and $\boldsymbol{H}$ everywhere in the grid at $t=(n+1)\Delta t$. To truncate the computational domain the above equations have to be coupled with the FDTD scheme inside S_j. The coupling is achieved by expressing $H_{t,k}^{n+1}$ as a function of $E_{t,k}^{n+1/2}$ by solving the inner problem. This is not straightforward because the tangential components of H are not defined on S_j. $H_{t,k}^{n+1}$ has to be extrapolated as follows. Let us suppose the Yee grid extending in the outer part of S_j for a further half a cell. In these newly obtained points a distribution of $\boldsymbol{H}$ can be defined. In particular, $H_{t,k}^{n+1}$ can be written as: $H_{t,k}^{n+1} = 1/2\left(H_{t,k}^{n+1,\text{int}} + H_{t,k}^{n+1,ext}\right)$ where $H_{t,k}^{n+1,\text{int}}$ is evaluated inside S_j and can be expressed in terms of $\boldsymbol{E}$ at $t=(n+1/2)\Delta t$ and $\boldsymbol{H}$ at $t=n\Delta t$ where $H_{t,k}^{n+1,ext}$ is unknown. An estimate of $\boldsymbol{E}$ at $t=(n+1+1/2)\Delta t$ can be written if we assume a linear profile of $\boldsymbol{E}$ in the time interval $\left[(n-1/2)\Delta t,\ (n+1+1/2)\Delta t\right]$. This assumption can be verified at the subsequent step. Finally we have:

$$H_{t,k}^{n+1} = F(H^n) + G(E^{n-1/2}) + \sum_l \lambda_l E_{t,l}^{n+1/2} \qquad (3)$$

$F(H^n)$ and $G(E^{n-1/2})$ are known quantities and λ_l can be easily evaluated by the procedure above described.

The time marching scheme begins with a standard FDTD technique in the interior regions until the scattered field reaches the boundary. At the boundary, equation (3) is substituted in (2b) and the resulting dense matrix system is solved with respect to J_k^{n+1} and $E_{t,k}^{n+1/2}$. Yee scheme fed with $E_{t,k}^{n+1/2}$ is able to produce $\boldsymbol{E}$ at $t=(n+1/2)\Delta t$ and $\boldsymbol{H}$ at $t=(n+1)\Delta t$. The index n is now incremented and the operations above described are repeated by firstly obtaining $E_{t,k}^{n+1+1/2}$. The assumed linear profile of E in the interval $\left[(n-1/2)\Delta t,\ (n+1+1/2)\Delta t\right]$ can now be verified. If the error is greater than a fixed threshold we can now go back to the previous step and use the newly calculated value of $E_{t,k}^{n+1+1/2}$ to obtain a better estimate of $H_{t,k}^{n+1}$. This iterative procedure rapidly converge and don ot affects the CPU time because the dense matrix needs to be inverted only at the first iteration.

RESULTS

The precision of the proposed procedure has been firstly tested by considering a scattering problem that has an analytical solution available. The normal incidence plane wave scattering by a perfectly electric conducting (PEC) cylinder with TM^z polarization is analysed. The cylinder has radius $a = 0.05m$ and the incident wave is a gaussian pulse of electric field $E(t) = E_0 \exp(-(6\cdot 10^9 t)^2)$, with $E_0 = 1\text{V}$.

The time step is Δt=2e-12 sec while the space step is Δs=2c/Δt. A square boundary with edge L = 1m centred around the cylinder has been considered. The excitation propagates from the left to the right of the x-y plane. The electric field has been calculated at point F=(-0.3,0.0). The analytical time domain solution has been obtained from sinusoidal steady state solution [5] by firstly apply FFT of the input signal, and then inverse transforming by an IFFT.

Figure 1a shows the result obtained by the proposed method and the analytical solution obtained as explained. Good agreement of the two solutions can be observed.

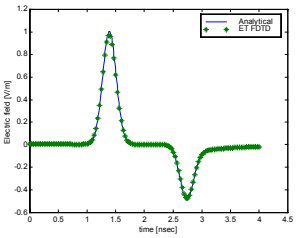

Fig. 1a Comparison between analytical and numerical solution

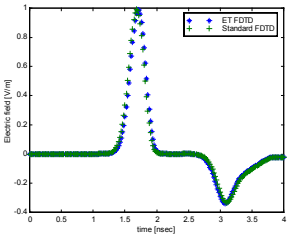

Fig. 1b Comparison between numerical solutions

Then the method has been tested by comparison with a standard FDTD formulation for a practical case. The cylinder has been replaced by a PEC triangle scatterer with vertex in the three points (-0.1,0) (0,0.1) (0,-0.1) with the same boundary of the first test. The same incident pulse of the first case has been considered. The Fig. 1b highlights the same incident pulse but different scattered pulse waveform as expected. The good agreement confirms the efficiency of the proposed method.

CONCLUSIONS

A method using the equivalent theorem to truncate the grid in FDTD scheme by providing proper boundary conditions, evaluated by a rapidly convergent iterative procedure, has been presented. Surfaces S_j can be placed very close to the bodies resulting in FDTD grids of limited extension. Numerical analysis of 2D problems have shown the effectiveness of the proposed procedure.

REFERENCES

[1] A. Taflove, S. C. Hagness, *Computational electrodynamics: The Finite-Difference Time-Domain method*. Norwood, MA: Artech House, 2000.

[2] T.K. Sarkar, C. Su, R. Adve, M. Salazar-Palma, L. Garcia-Castillo, Rafael R. Boix, "A tutorial on wavelets from an electrical engineering perspective Part 1: discrete wavelet techniques," *IEEE Antennas Propagat. Mag.*, vol. 40, pp. 49 – 69. Oct. 1998.

[3] S. M. Rao, D. R. Wilton, A. W. Glisson "Electromagnetic Scattering by Surfaces of Arbitrary Shape", *IEEE Antennas Propagat*. vol. AP-30 pp.409-418. May 1982.

[4] A. W. Glisson, D. R Wilton "Simple and Efficient Numerical Methods for Problems of Electromagnetic Radiation and Scattering form Surfaces", ", *IEEE Antennas Propagat*. vol. AP-28 n° 5 pp.593-603. Sept. 1980.

[5] C. A. Balanis, *Advanced Engineering Electromagnetics*. John Wiley and Sons, 1989.

A New Refinement Algorithm for Electromagnetic Field Computations Based on the Combination of Finite Element and Meshless Methods

S. L. HO[1], Shiyou YANG[2], Guangzheng NI[2], H.C. WONG[3]
[1]EE Department, [3]Industrial Centre, The Hong Kong Polytechnic University, Hong Kong
[2]EE College, Zhejiang University, China

Abstract—A new refinement algorithm for electromagnetic field computations using a combination of finite element and meshless methods is proposed. Bridging scales are proposed to separate the finite element and meshless shape functions to make the refinement hierarchical and to enhance the mathematical properties such as consistency and linear independence of all the bases. Numerical results are reported to demonstrate and validate the applicability and advantages of the proposed algorithms over traditional ones.

THE NEW REFINEMENT ALGORITHM

The meshless method is becoming a very popular numerical technique for solving partial differential equations in engineering. Indeed the absence of complicated meshes offers excellent potentials for field problems where a complicated or variable geometry is to be modeled. However, the inherent approximation characteristics of such algorithms makes them very awkward for enforcing boundary conditions. In order to take the full advantages of both meshless and 'traditional' methods, a new refinement algorithm for the numerical computations of electromagnetic fields using a combination of the Finite Element (FE) and Element Free Galerkin (EFG) methods is proposed in this paper.

Combined Model of FE and Meshless Methods

The general form of the approximation of the solution variable *u(x,y)* using both the FE and EFG shape functions is

$$u(x,y) = \sum_i u_i N_i^{FEM}(x,y) + \sum_j \Phi_j^{EFG}(x,y) c_j \qquad (1)$$

where, $\sum_i u_i N_i^{FEM}(x,y)$ and $\sum_j \Phi_j^{EFG}(x,y) c_j$ are, respectively, the FE and EFG solutions of the solution variable.

To uphold the mathematical properties of the entire bases regarding the consistency and the linear independence, the bridge scales as proposed in [1] is used and (1) becomes

$$u(x,y) = \sum u_i N_i^{FEM}(x,y) + [\Phi_i^{EFG^i}(x,y) - \sum_j N_j^{FEM}(x,y) \Phi_i^{EFG}(x_j,y_j)] c_i \qquad (2)$$

Adaptive Strategy

To take full advantage of both FE and meshless methods in the proposed algorithm, the refinement computation using the EFG method is activated only in regions where high and sharp gradients may occur. In order to overcome the shortcomings of conventional meshless methods in enforcing boundary conditions and in incorporating the interface conditions, standard FEM are used in the proposed algorithm. In other words, the proposed method does not require any special, and generally problematic, techniques to deal with essential and interface conditions as in other meshless methods.

Error Estimation: In the proposed algorithm, one uses an error estimation for each element of the FE solution in order to identify elements that require refinements. Thus a post local error estimation approach, the field difference method [2], is used because of its simplicity in numerical implementations.

Strategy of Refinement: Once the elements are identified, a refinement computation procedure as described below will be executed.

STEP 1. Activate the node addition procedure to add nodes to the identified elements.

STEP 2. Implement the refinement computation.

STEP 3. Termination test. If the test is passed, stop; otherwise, go to STEP 1 for a finer refinement computation.

For triangular elements, the proposed node addition procedure is to determine the number of the total triangles, which are constructed from the nodes of previous step's refinement computation (including both the original FE and the added EFG nodes). A new node is then added onto the geometrical center of every triangle.

Stop Criterion: To stop the refinement process automatically, a criterion based on that for the wavelet solutions as proposed in [3] is extended and used.

Assume that the refinement solutions at some sub-regions at steps *J* and *J+1* are, respectively,

$$u^J(x,y) = \sum_i u_i^J N_i^{FEM}(x,y) + \sum_j \overline{\Phi}_j^{EFG}(x,y) c_j^J, \qquad (3)$$

$$u^{J+1}(x,y) = \sum_i u_i^{J+1} N_i^{FEM}(x,y) + \sum_j \overline{\Phi}_j^{EFG}(x,y) c_j^{J+1}, \qquad (4)$$

the corresponding wavelet solutions are defined as

$$\varphi^J(x,y) = u^{J+1}(x,y) - u^J(x,y) \qquad (5)$$

Then the ratio of the *rms* value of $\varphi^J(x,y)$ to that of the averaged *u(x,y)* in an element is used as an indicator to stop the refinement procedure. Once this value reaches a user specified threshold, the refinement procedure will stop the refinement process in that specific element.

NUMERICAL EXAMPLES

An electrostatic problem, the Laplace equation on an L-shaped region as shown in Fig. 1, is selected as the numerical example to demonstrate the applicability and advantages of

the proposed procedure over the traditional approaches. In the numerical implementation, the fields are firstly determined using only the FE method with a coarse mesh as shown in Fig. 1. The corresponding computed field error distributions under the definition of the field difference method for every element are given in Fig. 2 in per unit values. From this error distribution, a 0.2 threshold value for the errors is used to select the elements where the refinement computations are required. Thirdly, by means of the aforementioned node addition procedure, some nodes are added to the identified elements and the program then repeats the refinement computations until the stop criterion is satisfied. The wavelet solution as defined by (5) under the final and the following final step refinement computations is given in Fig. 3. To compare the performances of the standard FE and the proposed FE+EFG method, this problem is solved repeatedly using standard FE method by successively adjusting the meshes until the same accuracy as that of the FE+EFG method is obtained. The corresponding performance comparison results are given in Table 1. From these numerical results one can see that:

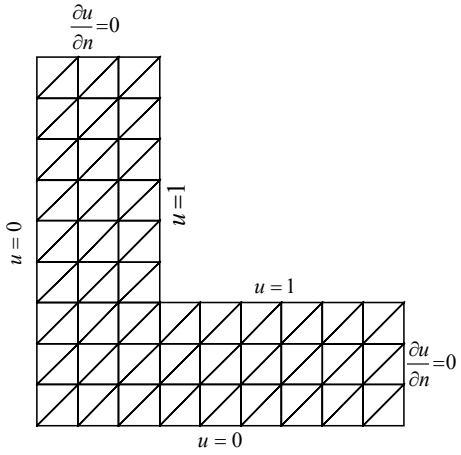

Fig. 1. The L-shaped electrostatic problem showing the finite element mesh.

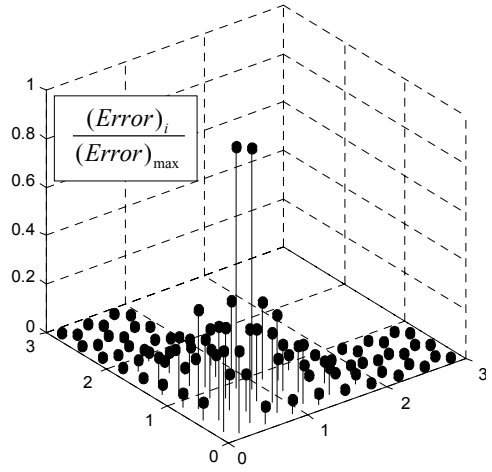

Fig. 2. The error distribution for each element using the field difference method.

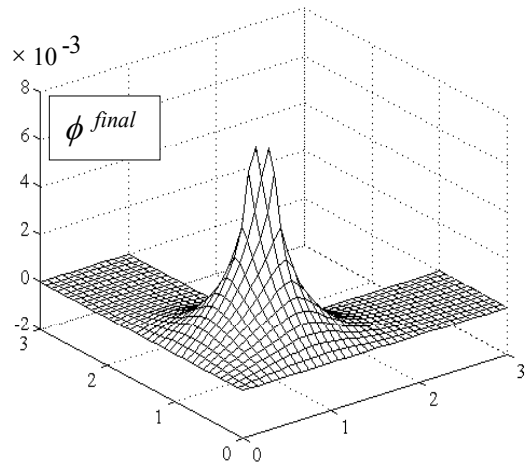

Fig. 3. The wavelet solution of the final and the next-final refinements.

(1) In order to reach the same numerical accuracy, both the degree of freedoms (DoFs) and the solution time for the proposed FE+EFG method are much smaller than those of the standard FE method;

(2) Compared with the traditional FE adaptive computation procedures, the most salient characteristics of the proposed one is that the refinement computation can be carried out by only adding nodes, irrespective of their connectivity, rather than by remeshing the solution domain, thereby allowing the algorithm to be implemented readily;

(3) compared with the purely meshless refinement procedures, the proposed one needs no special techniques to deal with the essential and interface conditions.

(4) Since the situation with respect to the storage technique of the resulting stiffness and the numerical solver for EFG methods is not as satisfactory as that for the FE methods, the reduction in CPU time of the proposed algorithm is not directly proportional to the DoFs.

TABLE 1
PERFORMANCE COMPARISON OF STANDARD FE AND PROPOSED METHODS WITH THE SAME SOLUTION ACCURACY

	DOFs	CPU time (pu)
FEM	224	3.2
FEM+EFG	64*+72**	2.6

*64 is the node number of the original coarse FE mesh of Fig. 2.
**72 is the additional number of nodes of the EFG method in the final step refinements.

REFERENCES

[1] Wagner Greory J. et al., "Hierarchical enrichment for bridging scales and mesh-free boundary conditions," *International Journal for Numerical methods in Engineering,* vol.50, pp.507-524, 2001.

[2] Fernandes, P., Girdinio, P., Molfino, P., Molinari, G., Repetto, M., "A comparison of adaptive strategies for mesh refinement based on "a posteriori" local error estimation procedure," *IEEE Trans. Magn.*, vol. 26, pp. 795-798,1990.

[3] Liu, W.K., Uras, R.A., Chen, Y., "Enrichment of the finite element method with the reproducing kernel particle method," *Journal of Applied Mechanics*, vol. 64, pp. 861-870, 1997.

The 3D transient simulation of the inverter fed linear induction motor

Lech Nowak
Poznań University of Technology
Institute of Industrial Electrical Engineering
ul. Piotrowo 3a, 60-965 Poznań, POLAND
e-mail: lech.nowak@put.poznan.pl

Abstract- **The paper deals with a transient simulation of the linear induction motor supplied with the inverter. The entirely 3D field model of the device has been applied. In order to solve three-dimensional eddy current problem a formulation based on two vector potentials *A* and *T* has been proposed. The equations describing transient electromagnetic field have been coupled to the Kirchhoff's equations of the electric circuits of the device and to the equations of supply system.**

INTRODUCTION

The inverters are very often used for the three-phase electromechanical converters supply. In case of the devices containing solid conducting parts, as for example in linear induction motor, the equivalent resistances and inductances vary during the transient states. Additionally, when the dynamic operation is considered the time-varying electromotive force *E* is generated. The behaviour of the system, especially in dynamic operation, strongly depends on the relations between the actual values of the parameters *R*(*t*), *L*(*t*), *E*(*t*). These parameters have significant influence on the backward diode conduction angles and consequently they determine the shape and value of the output voltage waveforms. Thus, the accuracy of the determination of *R*(*t*), *L*(*t*), *E*(*t*) is very important. Therefore, the entirely 3D field model of the device electromagnetic phenomena is required.

The inverter switching on and switching off processes cause permanently transient states. Consequently, the time-variations of the exciting currents in the winding are not known in advance, i.e. prior to the field calculation. Thus, the equations describing transient electromagnetic field must be supplemented with the Kirchhoff's equations of the device and feeding system.

During the dynamic operation, also the equation of the motion must be included. Algorithm of the simulation of dynamics will be presented in extended version of the paper.

3D EDDY CURRENT FORMULATION

In order to describe the 3D electromagnetic field in conducting regions, different approaches are proposed [1,3]. The most commonly used formulations are $\boldsymbol{A}-V$ or $\boldsymbol{T}-\Omega$ formulations, where $\boldsymbol{A}$ and $\boldsymbol{T}$ are the magnetic and electric vector potentials, respectively, Ω and V are the magnetic and electric scalar potentials. Unfortunately, the pairs of potentials $\boldsymbol{A},V$ and $\boldsymbol{T},\Omega$ are not described uniquely [3]. This is the essential disadvantage of these formulations.

Therefore, in this paper a formulation based on two vector potentials $\boldsymbol{A}$ and $\boldsymbol{T}$ has been proposed. The governing differential equations issue from the independent Ampere's and Faraday's laws. The ***magnetic*** field is described in terms of the magnetic vector potential in the whole region *D*. The ***electric*** vector potential $\boldsymbol{T}$ is computed only in conducting area D_e, which often is relatively small in comparison to *D*.

The ***A-T*** approach is very advantageous also in movement modelling. In case of non-ferromagnetic moving bodies, the matrix of the FEM equations describing the distribution of magnetic potential **A**, which is the largest one, remains unchanged during the successive time steps.

The magnetic vector potential $\boldsymbol{A}$ and electric vector potential $\boldsymbol{T}$ are introduced by putting $\boldsymbol{B}=\operatorname{curl}\mathbf{A}$ and $\boldsymbol{J}=\operatorname{curl}\boldsymbol{T}$. Taking the constitutive properties: $\boldsymbol{H}=\nu\boldsymbol{B}$, $\boldsymbol{J}=\sigma\boldsymbol{E}$, Ampere's law $\operatorname{curl}\boldsymbol{H}=\boldsymbol{J}$ and Faraday's law $\operatorname{curl}\boldsymbol{E}=-\partial\boldsymbol{B}/\partial t$ may be written in the following form:

$$\operatorname{curl}\nu\operatorname{curl}\boldsymbol{A}=\operatorname{curl}\boldsymbol{T}, \tag{1}$$

$$\operatorname{curl}\sigma^{-1}\operatorname{curl}\boldsymbol{T}=-\mathrm{d}(\operatorname{curl}\boldsymbol{A})/\mathrm{d}t, \tag{2}$$

where: ν,σ are the reluctivity and conductivity, respectively.

NUMERICAL IMPLEMENTATION

Numerical implementation of the algorithm is based on the finite element method with triangular prism-shaped elements [2]. The FEM representation of (1) and (2) for the conducting solid area can be represented in the form:

$$\mathbf{S}_\nu\mathbf{A}=\mathbf{Q}\mathbf{T} \tag{3}$$

$$\mathbf{S}_\sigma\mathbf{T}=\mathbf{Q}^{\mathrm{T}}\,\mathrm{d}\mathbf{A}/\mathrm{d}t \tag{4}$$

In order to solve transient problem, the time-stepping Crank-Nicholson algorithm has been applied. After including field sources due to the filamentary coil, the global system of the FEM equations for the *n*-th time step may be written in the following matrix form

$$\begin{bmatrix}\mathbf{S}_\nu & -\mathbf{Q}\\ -\mathbf{Q}^{\mathrm{T}} & -0.5\Delta t\mathbf{S}_\sigma\end{bmatrix}\cdot\begin{bmatrix}\mathbf{A}_n\\ \mathbf{T}_n\end{bmatrix}=\begin{bmatrix}\mathbf{V}_c\,N_c i_n\\ -\mathbf{Q}^{\mathrm{T}}\widetilde{\mathbf{A}}_{n-1}\end{bmatrix}, \tag{5}$$

where: i is the coil current, N_c is the coil "turn density", $\mathbf{V}_c$ is the vector of elementary volume cells within the coil, $\widetilde{\mathbf{A}}_{n-1}=\mathbf{A}_{n-1}+0.5\Delta t(\mathrm{d}\mathbf{A}/\mathrm{d}t)_{n-1}$.

The inconvenience of the ***A-T*** approach is the large

number of nodal unknowns $A_{x1}, A_{x2}, ..., A_{y1}, A_{y2}, ...$ $A_{z1}, A_{z2}, ...$ to be find in each time-step. The number of unknowns T_{xi}, T_{yi}, T_{zi}... is usually much smaller. Therefore, in order to calculate the 3D distributions of the magnetic potential **A**, a special "block-relaxation" iterative procedure has been adopted [2]. The 3D task has been decomposed, i.e. substituted with a sequence of, "quasi-2D" problems. Decomposition consists in: (a) apparent separation of vector potential components and (b) space division into slices. Mutual connections between vector potential components are taken into account iteratively. Each slice consist of one layer of the prism shaped finite elements. The number of nodes in conducting region D_e is usually small enough to calculate vector **T** directly, by using non-iterative method.

In order to solve global 3D transient task (in each time step) the additional, superior "**A – T**" iterations are necessary. The single *m*-th superior iteration includes one iteration for computation the distribution of three components of the potential $\mathbf{A}_m$ on each slice surface and then complete calculations of $\mathbf{T}_m$. In the next iteration (for computation of $\mathbf{A}_{m+1}$), the modified value $\widehat{\mathbf{T}}_{m+1} = \omega\mathbf{T}_m + (1-\omega)\widehat{\mathbf{T}}_m$ is assumed, where $\omega \in (0,1)$ is the sub-relaxation coefficient.

THE FIELD-CIRCUIT MODEL

The flux linked with a single winding composed of filaments can be written in the form: $\psi = N_c \mathbf{V}_c^{\mathrm{T}} \mathbf{A}$. If there are n_c ($n_c > 1$) windings then the vector $\mathbf{V}_c$ should be replaced with matrix $\mathbf{V}$ composed of n_c columns $\mathbf{V}_c$. Then, according to the Cranck-Nicholson scheme, the system of Kirchhoff's equations takes the form

$$2\mathbf{N}^{\mathrm{T}}\mathbf{V}^{\mathrm{T}}\left(\mathbf{A}_n - \widetilde{\mathbf{A}}_{n-1}\right)/\Delta t + \mathbf{R}\mathbf{i}_n = \mathbf{u}_n \tag{6}$$

where $\mathbf{N}$ is the diagonal matrix composed of winding turn densities, $\mathbf{i}_n, \mathbf{u}_n$ are the vectors of currents and voltages.

After branch connection into n_l independent circuit loops, a system of n_l equations is obtained

$$2\mathbf{K}^{\mathrm{T}}\mathbf{N}^{\mathrm{T}}\mathbf{V}^{\mathrm{T}}\left(\mathbf{A}_n - \widetilde{\mathbf{A}}_{n-1}\right)/\Delta t + \mathbf{K}^{\mathrm{T}}\mathbf{R}\mathbf{K}\mathbf{i}_l = \mathbf{u}_{ln} \tag{7}$$

where: $\mathbf{i}_l, \mathbf{u}_l$ are the loop currents and voltages respectively and $\mathbf{K}$ is the incidence matrix describing the connections of branches, such that $\mathbf{i} = \mathbf{K}\mathbf{i}_l$; $\mathbf{u}_l = \mathbf{K}^{\mathrm{T}}\mathbf{u}$.

Thus, the global system of the field-circuit equations for the *n*-th time step can be written as follows

$$\begin{bmatrix} \mathbf{S}_\nu & -\mathbf{Q} & -\mathbf{V}\mathbf{N}\mathbf{K} \\ -\mathbf{Q}^{\mathrm{T}} & -0.5\Delta t\mathbf{S}_\sigma & \mathbf{0} \\ \mathbf{K}^{\mathrm{T}}\mathbf{N}^{\mathrm{T}}\mathbf{V}^{\mathrm{T}} & \mathbf{0} & 0.5\Delta t\mathbf{R}' \end{bmatrix} \cdot \begin{bmatrix} \mathbf{A}_n \\ \mathbf{T}_n \\ \mathbf{i}_{ln} \end{bmatrix} = \begin{bmatrix} \mathbf{0} \\ -\mathbf{Q}^{\mathrm{T}}\widetilde{\mathbf{A}}_{n-1} \\ \mathbf{F}_n \end{bmatrix} \tag{8}$$

where $\mathbf{R}' = \mathbf{K}^{\mathrm{T}}\mathbf{R}\mathbf{K}$, $\mathbf{F}_n = 0.5\Delta t\mathbf{K}^{\mathrm{T}}\mathbf{u}_{ln} + \mathbf{K}^{\mathrm{T}}\mathbf{N}^{\mathrm{T}}\mathbf{V}^{\mathrm{T}}\widetilde{\mathbf{A}}_{n-1}$.

EXAMPLE

Inverter fed linear induction motor has been considered. The ideal characteristics of the semiconductors have been assumed, i.e. their resistances are equal to zero or are infinitive and change without any delays. The connections of phase winding change according to the inverter steps. This means that the incidence matrix in (8) varies: $\mathbf{K} = \mathbf{K}(s)$, where $s = 1,2,...,n_s$ is the number of the inverter step. Total number of steps n_s depends on the conducting angle β. In case of $\beta = \pi$ there are 6 steps. The changes of the circuit structure may be described as follows

$$\begin{bmatrix} U_D & 0 \end{bmatrix}^{\mathrm{T}} = \mathbf{K}_2^{\mathrm{T}}(s)\begin{bmatrix} u_1 & u_2 & u_3 \end{bmatrix}^{\mathrm{T}} \tag{9}$$

where U_D is the d.c. supply voltage, u_1, u_2, u_3 are the output phase voltages. Matrix $\mathbf{K}_2$ has 3 rows and 2 columns; its elements are equal to: -1, 0, 1. For $\beta \in (2/3\pi, \pi)$ there are 12 inverter steps. For odd steps the structure is described by (9). For even steps , the equation is: $U_D = \mathbf{K}_1^{\mathrm{T}}(s)\begin{bmatrix} u_1 & u_2 & u_3 \end{bmatrix}^{\mathrm{T}}$, where $\mathbf{K}_1$ is the one-column matrix.

The computation were made for the period $t \in (0, 60\,\mathrm{ms})$,taking $\beta = \pi$. The time transient variations of phase currents $i_1(t)$, $i_2(t)$, $i_3(t)$ are shown in Fig. 1. The d.c. decaying components of currents can be observed.

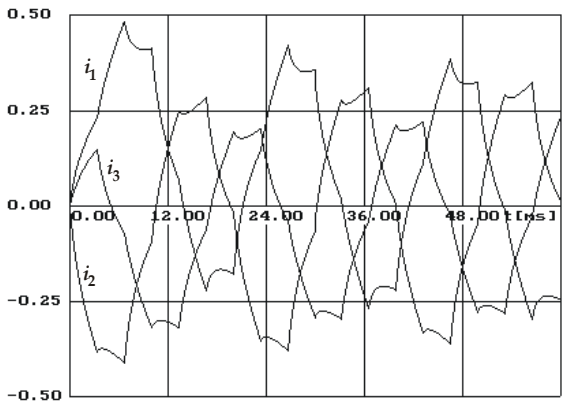

Fig.1. Time variations of phase currents (in Amperes)

REFERENCES

[1] R. Albanese, R. Rubinacci, "Formulation of the eddy-current problem," *IEE Proceeding*, Part A, Vol. 137, No. 1, pp. 16-21, 1990.

[2] L. Nowak, "Iterative procedure for 3D modelling of electromagnetic actuators," *IEEE Transactions on Magnetics*, vol. 31, No. 3, pp.1428-1431, May 1995.

[3] C.W. Trowbridge, "Status of 3D Electromagnetic Field Computation," *Proc. of Beijing International Symposium Electromagnetic Fields in Electrical Engineering*, Beijing (China), pp. 3-81988,.

Current Control For Smoothing of Torque in Single-Phase Permanent Magnet Disc Motor Using 3-D FEM

M. Jagiela[1] and E. A. Mendrela[2]
[1]Technical University of Opole, Department of Electrical Engineering and Automatic Control
PL 45036, ul. Luboszycka 7, Opole, Poland, E-mail: mjagiela@po.opole.pl
[2]Louisiana State University, Department of Electrical and Computer Engineering
Baton Rouge, LA 70803, U.S.A., E-mail: ermen@ece.lsu.edu

Abstract **– A disc-type single-phase permanent magnet motor with salient pole stator is considered. Due to a particular arrangement of the magnets on the rotor disc the motor develops the starting torque. It also is capable to produce a constant, nearly smooth torque by modifying the current waveform. To determine the required current waveform the 3D finite element model is used. To minimize the torque ripple the current is controlled. To analyze the motor performance at this condition, the field model, combined with a circuit model of the motor was applied including the inverter topology.**

INTRODUCTION

Permanent magnet disc motors become very attractive for gearless drives of electric vehicles [1, 3]. Among them are single-phase motors, which are generally susceptible to produce large oscillating torque, so their utilization is limited in particular for the high-speed applications [2]. The disc-type motors are almost never mentioned to be used for such a drive.

The subject of this paper is a single-phase disc-type motor with salient pole stator. The scheme of the motor structure is shown in Fig. 1. To obtain the starting torque in the single-phase motors, various modifications of the magnetic circuit have been proposed [2]. In the motor considered here the starting torque was obtained by rearranging the distribution of the permanent magnets over the surface of one of rotor discs (see Fig. 1). Fig. 2 explains how the starting torque at detent position (angle $\Theta = 0^0, 60^0, 120^0, \ldots$) is developed. If the cogging torque is sinusoidal, the resultant torque, which is the sum of electromagnetic torque components *NS* and *ns,* produced by stator current and "large" permanent magnets on one of the rotor discs and "small" magnets on another disc, is always positive (thick line in Fig. 2). However, the torque

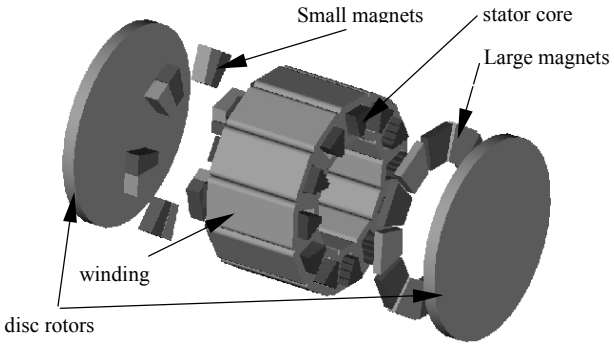

Fig. 1 Structure of a single-phase permanent magnet disc motor

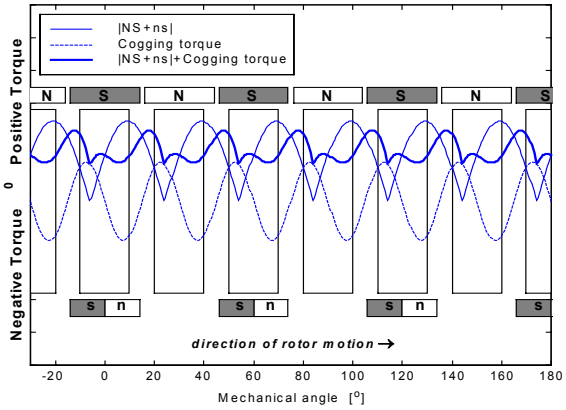

Fig.2 Variation of torque at variable mutual stator and rotor positions, developed by the motor when fed with rectangular current wave

produced by the motor contains a large oscillating component It is caused mainly by the cogging torque. The cogging torque of the real motor is much more deformed from a sinusoidal shape, that was proved experimentally.

The motor, when operating as brushless DC develops high performance, but it produces the large torque ripple. This makes it inapplicable in some type of drives. In the paper the field-based control method is presented, which allows determining such a current waveform, at which the torque ripple is significantly reduced. In this method, the nonlinear materials and armature reaction flux are taken into account.

FINITE ELEMENT MODEL

Due to the complex motor geometry the three-dimensional model should be applied for precise modeling of magnetic field. A 3-D FEM is applied to determine the magnetic field distribution in the motor volume. The motor under study has a symmetric, periodic structure, thus the area of interest for the finite element analysis is only 1/6 of its whole volume. The periodicity conditions and moving band were applied to model the rotor motion. Fig. 3 shows the cogging torque waveform determined from 3D model.

DETERMINATION OF CURRENT WAVEFORM

With the model described above, a series of calculations were performed to obtain the variation of magnetic co-energy

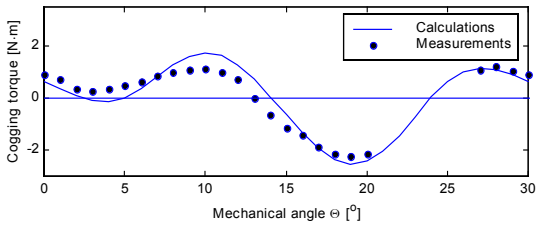

Fig. 3 Cogging torque versus rotational angle characteristic

versus rotational angle Θ and armature current i. Since the variation of magnetic co-energy is known, the optimal current waveform can be determined from this function. If the particular torque T has to be positive and constant in time, the following function must accomplish the minimum:

$$f = T - T_c \ , \tag{1}$$

where T_c is a given value of torque. In a single-phase motor, the magnetic co-energy for each rotor instant is a function of only armature current i. Thus, for a given rotor position $T = T(i)$, and the nonlinear equation (1), can be easily solved using Newton-Raphson procedure. For each time-step the current can be obtained by minimization of function (1) using the following iterative formula:

$$i_{n+1}^k = i_n^k - f\left(i_n^k\right)\left\{\frac{\partial f}{\partial i}\right\}_{i_n^k}^{-1} \ , \tag{2}$$

where k is a number of step in time, and n is an iteration number per one step.

The motor under study is a 12-pole, 600 Watt machine with the surface-mounted magnets. Using the above procedure, the current waveforms were determined for a few values of the torque T_c.

To implement the presented method for the operating conditions close to that of the real object, a circuit-field motor model that considers the inverter topology was applied. In this model the nonlinear co-energy is used to determine the integral parameters of the motor. The equivalent circuit of the voltage inverter possesses the *RL*-type functional models of semiconductors.

The desired current shape was obtained using a control system with hysteresis controller (see Fig. 4). Fig. 5 shows the simulated torque and current of the motor, when it operates as the brushless DC machine, while in Fig. 6 are shown the same quantities when it operates with the optimized current waveform.

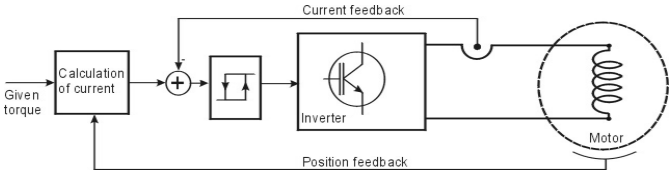

Fig. 4 Diagram of control system for current smoothing

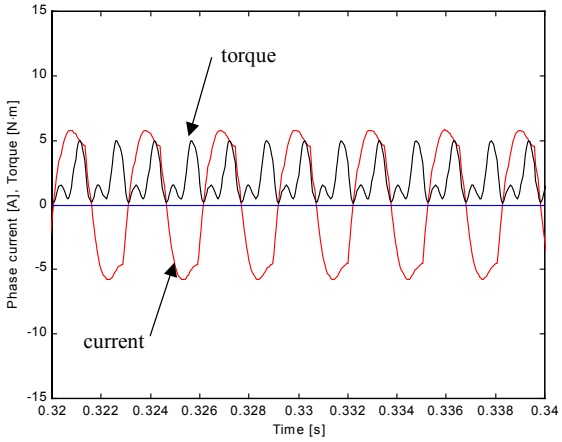

Fig. 5 Current and torque developed by the motor when it operates as a brushless DC machine

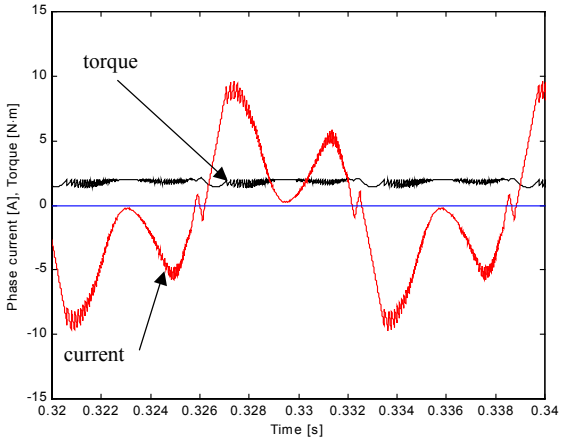

Fig. 6 Current and torque developed by the motor when it operates with optimized current

CONCLUSIONS

The paper presents a preliminary approach for development of DSP-based control system for a single-phase brushless disc motor. Applying a 3D FEM, and considering both: the nonlinearity of motor magnetic circuit and armature reaction, the current waveform was determined, at which the motor develops nearly constant torque.

REFERENCES

[1] C. P. Cho, B. K. Fussel , "Detent Torque and Axial Force Effect in a Dual Air-gap Axial-Field Brushless Motor", *IEEE Trans. on Magnetics*, No. 6, 1993, pp. 2416-2418.

[2] J. S. Mayer, O. Wasynczuk, "Analysis and Modelling of a Single-phase Brush less DC Motor Drive System", *IEEE Trans. on Energy Conversion*, No. 4, 1989, pp. 473-479.

[3] M. Łukaniszyn, R. Wróbel, M. Jagieła: *Reduction of the Torque Ripple in a Brushless DC Torus Motor, International Conference on Electrical Machines*, In proc. of ICEM'2002, Brugge, 2002, p. 403.

Acknowledgment: ***This work has been supported partially by Foundation for Polish Science and partially by National Science Foundation: Project # 0217308.***

Computation of Power Transformers Coupled to Electrical Circuits by Using T-T_0-Ω Formulation

Liang Zhenguang*, Tang Renyuan**, Hu Yan**
*School of Electrical Engineering, Shandong University, Jinan, 250061, China
e-mail: liangzhenguang@yahoo.com.cn
**Research Institute of Special Electrical Machines, Shenyang University of Technology, Shenyang, 110023, China
e-mail: tdssygd@pub.sy.ln.cn

***Abstract*—The T-T_0-Ω formulation of a 3D magnetic field finite element method coupled to electrical circuits is presented in the paper. Validity of the method is shown by comparing its result with that of the A,V-A formulation. The method is used to compute transient processes of a three-phase transformer during its fault procedures. Results show that certain fault current may exceed the maximum value of sudden three phase short-circuit currents.**

INTRODUCTION

Electromagnetic devices, such as transformers, are usually driven by voltage sources. The coupled problem of electromagnetic fields and electrical circuits is often solved by using the formulation based on magnetic vector potentials [1]. However, the use of magnetic vector potentials in the whole domain leads to expensive computaion. Although develpments in computer hardware have resulted in fast computers and large memories, attention will still be focussed on economical and efficient computational techniques. An alternaive approach to solve the coupled problem is using the formulation based on the magnetic scalar potential in the whole domain and the electric vector potential only in the conducting region [2, 3]. The $\boldsymbol{T}$-$\boldsymbol{T}_0$-Ω formulation allows us to save computaion cost, especially when the nonconducing region is main region [3]. When dealing with the problem of multiply connect regions, $\boldsymbol{T}_0$ regions cover holes in conducting regions. In hole regions, cancllation error comes. The error is not serious in fields outside iron parts. However, it is a serious problem in permeable regions where the total field is the sum of two large, but opposing fields. In the computation of a transformer, cuts are used to deal with this problem.

FORMULATION

A. Electromagnetic field formulation

The current density in conducting region V_c is written as

$$\boldsymbol{J} = \nabla \times (\boldsymbol{T} + \boldsymbol{T}_0), \tag{1}$$

where $\boldsymbol{T}$ denotes the unknown electric vector potential and $\boldsymbol{T}_0$ denotes the impressed electric vector potential. $\boldsymbol{T}_0$ describes the arbitrary current distribution with its net current being equal to supplied current in electric circuit.

The magnetic field intensity is as follow

$$\boldsymbol{H} = \boldsymbol{T}_0 + \boldsymbol{T} - \nabla\Omega, \qquad \text{in } V_c. \tag{2}$$

According to the Maxwell equations, and applying the Coulomb gauge, the governing equations are as follows

$$\nabla \times (\rho \nabla \times \boldsymbol{T}) - \nabla(\rho \nabla \cdot \boldsymbol{T}) + \frac{\partial}{\partial t}(\mu \boldsymbol{T}) - \frac{\partial}{\partial t}(\mu \nabla\Omega) = -\frac{\partial}{\partial t}(\mu \boldsymbol{T}_0), \quad \text{in } V_c, \tag{3}$$

$$\nabla \cdot (\mu \boldsymbol{T} - \mu \nabla\Omega) = -\nabla \cdot (\mu \boldsymbol{T}_0), \qquad \text{in } V_c, \tag{4}$$

where Ω denotes magnetic scalar potential, ρ denotes the resistivity and μ denotes the permeability.

The magnetic field intensity in nonconducting regions V_n is

$$\boldsymbol{H} = -\nabla\Omega, \qquad \text{in } V_n. \tag{5}$$

According to the Maxwell equations, the governing equations is as follow

$$\nabla \cdot (\mu \nabla\Omega) = 0, \qquad \text{in } V_n. \tag{6}$$

In nonconducting regions, multiply connect regions are eliminated by using cuts shown in Fig.1.

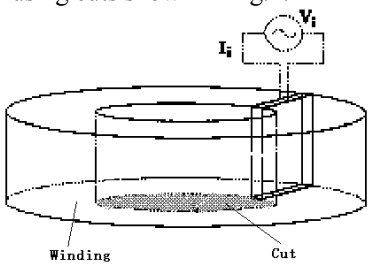

Fig.1. Multiply connect region and cut

The magnetic field intensity in cut regions V_{cut} is

$$\boldsymbol{H} = \boldsymbol{T}_0 - \nabla\Omega, \qquad \text{in } V_{cut}, \tag{7}$$

and the governing equations is as follow

$$\nabla \cdot (\mu \nabla\Omega) = \nabla \cdot (\mu \boldsymbol{T}_0), \qquad \text{in } V_{cut}. \tag{8}$$

In conducting regions and cut regions, $\boldsymbol{T}_0$ exists and is normal to region surface. To a winding, by introducing wire density $\boldsymbol{K}$, $\boldsymbol{T}_0$ is expressed as $\boldsymbol{T}_0 = \boldsymbol{K}\boldsymbol{i}$.

B. Electric circuit equations

In the circuit model, the electric circuit equation is

$$u(t) = Ri(t) + L\frac{\mathrm{d}i(t)}{\mathrm{d}t} + \frac{\mathrm{d}\phi(t)}{\mathrm{d}t}, \qquad (9)$$

where u denotes terminal voltage, R resistance of circuit, L the inductance of circuit. The flux linkage ϕ is expressed as

$$\phi = \int_V \mu \boldsymbol{K} \cdot (\boldsymbol{T}_0 + \boldsymbol{T} - \nabla\Omega)\mathrm{dv}\ . \qquad (10)$$

C. Magnetic field and electric circuit coupled equations

Field-circuit coupled model is obtained from field equation and circuit equation. It can be expressed as

$$\begin{bmatrix} \boldsymbol{S} & 0 \\ 0 & \boldsymbol{R} \end{bmatrix} \begin{Bmatrix} \boldsymbol{T}_{i_s} \\ \boldsymbol{I} \end{Bmatrix} + \begin{bmatrix} \boldsymbol{M} & \boldsymbol{C} \\ \boldsymbol{C}^{\boldsymbol{T}} & \boldsymbol{P} \end{bmatrix} \frac{\mathrm{d}}{\mathrm{d}t} \begin{Bmatrix} \boldsymbol{T}_{i_s} \\ \boldsymbol{I} \end{Bmatrix} = \begin{Bmatrix} 0 \\ \boldsymbol{U} \end{Bmatrix}. \qquad (11)$$

APPLICATIONS

The $\boldsymbol{T}$-$\boldsymbol{T}_0$-Ω method has been used calculating short-circuit transient process of a 240000kVA/500kV single-phase power transformer. Fig.2 shows meshes of the transformer. Short-circuit current by the method together with that by $\boldsymbol{A}, V$-$\boldsymbol{A}$ method [1] is shown in Fig.3. The results show the validity of the $\boldsymbol{T}$-$\boldsymbol{T}_0$-Ω method.

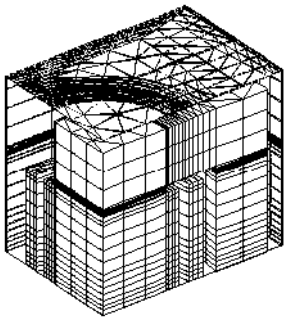

Fig.2. Meshes of the core, windings and tank (1/8 of a transformer)

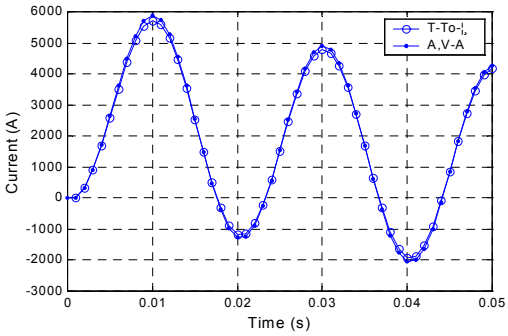

Fig.3. Short-circuit currents of high voltage winding

The method is used in the computation of a 40000kVA/110kV three-phase transformer. Fig.4 shows winding currents of the transformer when suffering three phase short-circuit. A transformer may suffer complex faults in operation. In the case of suffering two-phase short-circuit at 0 ms then three-phase short-circuit at 5 ms, the variations of winding currents are shown in Fig.5. The maximum current is 15% larger than that of three-phase short-circuit.

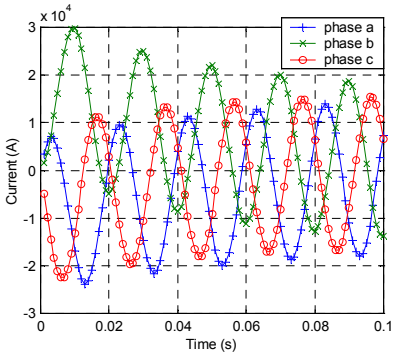

Fig.4. low voltage winding currents when suffering three-phase short-circui

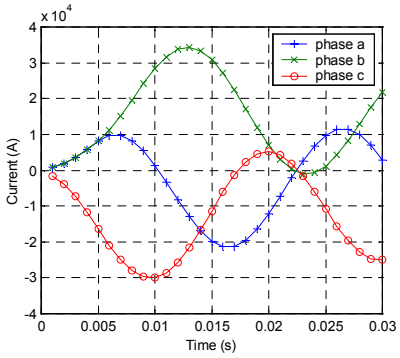

Fig.5. low voltage winding currents when suffering two-phase short-circuit

CONCLUSIONS

3D field-circuit coupled model based on $\boldsymbol{T}$-$\boldsymbol{T}_0$-Ω formulation has been studied. It's used in computing of a three phase transformer. Calculation results of fault processes reveal that maximum current of complex faults can exceed that of direct three-phase short circuit. It's important when analyzing a transformer's safe operation.

REFERENCES

[1] T.Renyuan, W.Shenghui, L.Yan, W.Xiulian and C.Xiang, "Transient Simulation of Power Transformers Using 3D Finite Element Model Coupled to Electric Circuit Equations," *IEEE Transactions on Magnetics*, Vol. 36, pp.1417-1420, July 2000.

[2] S.Bouissou and F.Piriou, "Numerical Simulation of a Power Transformer using 3D Finite Element Method Coupled to Circuit Equation," *IEEE Transactions on Magnetics*, Vol. 30, pp.3224-3227, Sept. 1994.

[3] L.Zhenguang, T.Renyuan, W.Chuncheng and H.Yan, "Study of Power Transformers Using 3D Finite Element Model Coupled to Electric Circuit Equations," *Proc. ICEF 2000, Tianjin, China*, pp.279-281, 2000.

A Direct Field-Circuit-Motion Coupled Modeling of Switched Reluctance Motor

Xie Dexin, Yan Xiuke, *Zhang Yihuang, Tang Renyuan

School of Electrical Engineering, Shenyang University of Technology,
Shenyang, Liaoning 110023, P.R.CHINA E-mail:xiebaiy@mail.sy.ln.cn
* North Jiaotong University, Beijing, 100044

***Abstract*— A direct field-circuit-motion coupled model combined with finite element analysis is presented to simulate the steady operation of switched reluctance motors (SRM) and to calculate the dynamic currents and torques of the motors. The torques are calculated with nodal-force and Maxwell stress tensor methods. The comparison of the numerical and measured results indicates the validity of the method proposed in this paper.**

INTRODUCTION

The switched reluctance motor has a simple and robust structure as well as high reliability and low lost. The evolvement in power electronic circuit technology has promoted the research on the performance simulation of SRM [1]-[3]. Most of the published papers used the calculation model based on the analysis of electric circuit and magnetic circuit or their coupling, in which the mutual inductances between phase windings are ignored. In fact, the electromagnetic procedure in SRM strongly depends on the coupling of field, circuit and motion. Reference [3] made a new start, presenting a model with coupled field-circuit method, in which the circuit-equation and field-equation were solved separately, and an iterative process was needed to find the winding current. However, a simple iterative process of the computation for magnetic field and electric circuit could not converge satisfactorily to obtain the circuit-variable, or even can not find the results at all for the problems with multi-circuit-variables in certain conditions. But the calculation of SRM is just this case.

A direct field-circuit-motion coupled modeling is proposed in this paper to analyze the dynamic currents and torques in the steady operation of SRM. The multi-circuit-variables and field-variables are solved simultaneously with the method described, and the controlling patterns to the motor by the circuit systems can be implemented easily.

DESCRIPTION OF THE PROPOSED METHOD

A. Governing equations

The 2D magnetic field governing equation of SRM for magnetic vector potential A_z is given by

$$\frac{\partial}{\partial x}\left(\nu\frac{\partial A_z}{\partial x}\right)+\frac{\partial}{\partial y}\left(\nu\frac{\partial A_z}{\partial y}\right)+J=0 \tag{1}$$

with the end effect neglected, where

$$J=\begin{cases}\dfrac{N_j i_j}{S_j} & \text{for current regions}\\ 0 & \text{for non - current regins}\end{cases} \tag{2}$$

The circuit equation can be expressed as

$$R_j i_j+\frac{d\psi_j}{dt}=u_j \tag{3}$$

according to the circuit configuration shown in Fig. 1. In (2) and (3) the subscript $j=1,2,\cdots,n$, n is the number of branches of the multi-phase winding of SRM; i_j, u_j, ψ_j, R_j, N_j and S_j are the stator current, source voltage, flux linkage, resistance, number of turns and the area occupying by the coil for branch j in the case of Fig. 1, respectively.

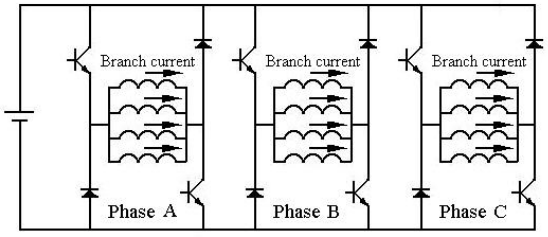

Fig.1 Main circuit configuration of a SRM

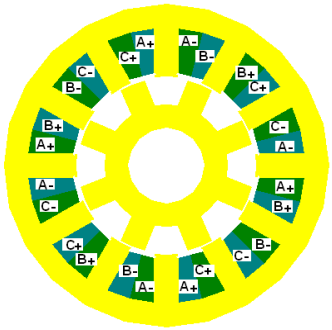

Fig.2 Distribution of the phase windings

In order to simulate the time differential in (3), the backward difference method is employed. Noting that the angle speed of SRM, ω, is constant for the steady status, so that we can transform (3) into

$$\psi_j^{k+1}+\frac{\Delta\theta}{\omega}R_j i_j=\frac{\Delta\theta}{\omega}u_j+\psi_j^{k} \tag{4}$$

where $\Delta\theta$ is the angle increment of the rotor, k denotes the number of time step.

Solving (1) and (4) simultaneously with finite element method for k = 0, 1, 2, …, in which the flux linkages are computed in terms of the difference between the magnetic vector potentials at two sides of per coil, we obtain the discretized equation in matrix form,

$$\begin{bmatrix} \mathbf{K} & \mathbf{P} \\ \mathbf{Q} & \mathbf{R} \end{bmatrix} \begin{bmatrix} \mathbf{A} \\ \mathbf{I} \end{bmatrix} = \begin{bmatrix} \mathbf{0} \\ \mathbf{U} + \boldsymbol{\Psi} \end{bmatrix} \tag{5}$$

where **K** is the submatrix integrated from the element coefficient matrix of the ordinary 2D finite element analysis; **Q** and **R** could be given as

$$\mathbf{Q} = \begin{bmatrix} q_{g+1,1} & \cdots & q_{g+1,g} \\ \vdots & q_{st} & \vdots \\ q_{g+n,1} & \cdots & q_{g+n,g} \end{bmatrix}, \quad \mathbf{R} = \begin{bmatrix} R_{g+1,g+1} & \cdots & R_{g+1,g+n} \\ \vdots & R_{st} & \vdots \\ R_{g+n,g+1} & \cdots & R_{g+n,g+n} \end{bmatrix}$$

in which

$$q_{st} = \sum_{l=1}^{n_1+n_2} \frac{N_s \Delta_l}{3 S_s}, \quad R_{st} = \frac{\Delta\theta R_s}{\omega L_{fe}}$$

where n_1 and n_2 denote the number of elements corresponding to the two sides of each phase winding respectively, Δ_l the element area, N_s and S_s the number of turns and the total area for branch s respectively, R_s the branch resistance, L_{fe} the length of iron core, g the number of nodes of the FE mesh; $\mathbf{P} = \mathbf{Q}^T$; the element of **U**,

$$U_j = \frac{\Delta\theta\, u_j}{\omega\, L_{fe}}$$

in which u_j is the source voltage across the branch j; and the element Ψ_j of $\boldsymbol{\Psi}$ is the flux linkage for step k, **A** is the sub-unknown vector of A_z and **I** the sub-unknown vector of branch currents. It is worth noting that to make the coefficient matrix symmetrical, the circuit equations involved in (4) are divided by L_{fe}.

B. Determination of the initial values and Computation of the Torques

It could be imagine that the motor started by another mechanical power from rest to its rating speed, then we apply the source voltages to the phase windings according to the controlling strategy of the circuit system. After a number of electromagnetic periods, the operation of the motor will reach its rating status. Therefore, the zero initial values are proper for the simulated procedure.

The computation of torques are implemented by two methods, the nodal-force and Maxwell stress tensor methods, to check the precision of the results.

NUMERICAL RESULTS

The numerical results are shown as follows.

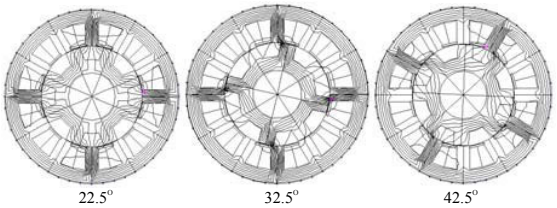

Fig. 3 Flux distribution for different rotary angles of rotor

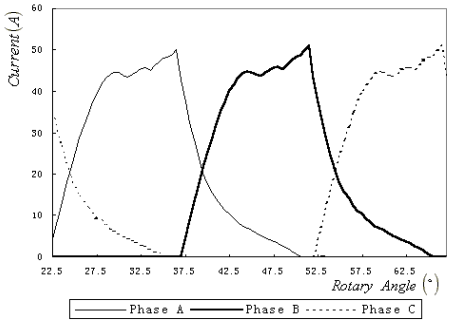

Fig.4 Current waveform of phase A, B and C by calculation

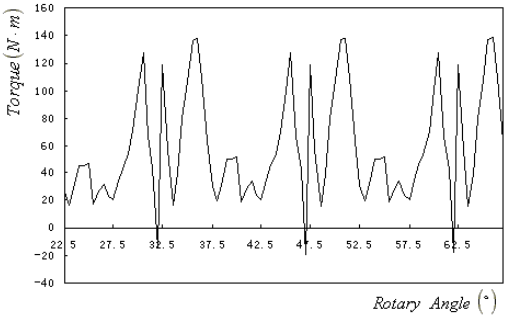

Fig.5 Torque waveform by calculation

TABLE I. RATING DATA WITH MEASURED AND CALCULATED RESULTS

Torque rating	60 N-m	Rotor speed	1200 rpm
Voltage	514 V	Output power	51.10 kW
Measured current	81.57 A	Calculated current	83.20 A
Measured torque	393.30N-m	Calculated torque	380.14N-m

CONCLUSIONS

A direct field-circuit-motion coupled model of SRM is presented. With this model, several key points, such as the directly simultaneous solution of field and circuit variables, the incorporation of mutual inductances, the current-wave-cutting control strategy, could be implemented satisfactorily. More experimental results will be included in the extended paper to prove the precision of the model.

REFERENCES

[1] P.J. Lowrenson et al., "Variable-speed switched reluctance motors," *IEE Proc.* Pt. B, Vol. 127, No.4, pp. 253-265, July 1980

[2] O. Ichinokura et al., "A new calculation model of switched reluctance motor for use on spice," *IEEE trans. On Magnetics*, Vol. 37, No. 4, pp. 2834-2836, July 2001

[3] Longya Xu et al., "Direct modeling of switched reluctance machine by coupled field-circuit method," *IEEE trans. On Energy Conversion*, Vol. 10, No. 3, pp. 446-452, September 1995

Integrated AI–EM Approach for the Characterization of AC Actuators

A.A. Arkadan N. Al Aawar M.J. J. Vander Heiden
Department of Electrical and Computer Engineering
Marquette University
Milwaukee, WI 53201
E-mail: **a.a.arkadan@marquette.edu**

Abstract– The performance characteristics of electromagnetic AC Actuators are predicted using an integrated Artificial Intelligence – Electromagnetic, AI - EM, approach. The approach makes use of electromagnetic field solutions in conjunction with AI fuzzy logic, FL, based models. This approach is applied to a prototype AC actuator under static and motion conditions. Furthermore, the results are compared to test data for verification.

INTRODUCTION

Although AC actuators are simple in construction, the coupled nature of their electromagnetic and mechanical forces in the actuator system require a simultaneous solution of the governing electrical and mechanical equations if one needs to accurately predict its performance [1]. In a recent paper, coupled structural and electromagnetic Finite Element, FE, analysis using voltage excitation was used to predict the behavior of AC actuators [2]. However a draw back with this approach is that it is relatively slow. In addition, one needs to repeat the analysis for any change in the system excitation or loading conditions. In the present work, an integrated AI electromagnetic approach is developed. This approach makes use of two major building blocks. The first is a nonlinear finite element electromagnetic model which is used to account for the nonlinear magnetic behavior of the actuator. The electromagnetic field solutions, are used to calculate the parameters of a state space model which generates data that will be used in setting up a fuzzy logic model. The fuzzy logic, FL, model, using Adaptive Network based Fuzzy Inference Systems, ANFIS, is applied to model the performance characteristics of AC actuators. The proposed FL approach exploits the large degree of uncertainty in AC actuators to achieve accurate, robust, low cost solution based on some knowledge of the system.

FUZZY LOGIC MODEL

The idea of the FL approach is to develop Adaptive-Network-based Fuzzy Inference System, ANFIS, to accurately replace the AC Actuators. The ANFIS consists of [3]: fuzzification inference that transforms the crisp inputs into degree of match, rule base containing a number of IF-THEN rules, database that defines the membership functions, decision-making unit that performs the inference operations, and defuzzification interface that transforms the fuzzy results to crisp output as illustrated in Fig. 1. In order to train ANFIS a hybrid learning algorithm based on least square estimation coupled with gradient descent is used to identify the parameters of the membership functions.

INDIRECTLY COUPLED FE-SS SPACE MODEL

The nonlinear electromagnetic and structural nature of AC actuators makes it difficult to accurately predict its performance. The nonlinear structural behavior is due to the actuator mechanical springs which are characterized by nonlinear stiffness that varies with load. The nonlinear electromagnetic behavior arises from the fact that AC actuators are often made of nonlinear magnetic material; thus their flux linkages and corresponding inductances are function of currents in the main coil and associated shading rings as well as the armature's position. The system nonlinear behavior is captured by using an iterative indirectly coupled Finite Element-State Space, FE-SS, approach, Fig. 2. This iterative approach results in the data sets needed to construct and train the FL model. The governing equations for the state space model of Fig. 2 are as follows:

$$\dot{\bar{I}} = -\bar{L}^{-1}\left(\bar{R} + \mathrm{v}\frac{d\bar{L}}{dx}\right)\bar{I} + \bar{L}^{-1}\bar{V} \qquad (1)$$

where $\bar{\mathrm{L}}$ represents the system inductance matrix in Henries; $\bar{\mathrm{R}}$ represents the resistance matrix in Ohms; v is the velocity in m/s, and $\bar{\mathrm{I}}$ is the current array in Amperes.

In addition, the mechanical equation governing the velocity is given by:

$$\mathrm{v}=\dot{\mathrm{x}}=\int_0^t \frac{F_{mag} + mg - F_D - \mathrm{Kx} - F_o}{m} + \mathrm{v}_0 \qquad (2)$$

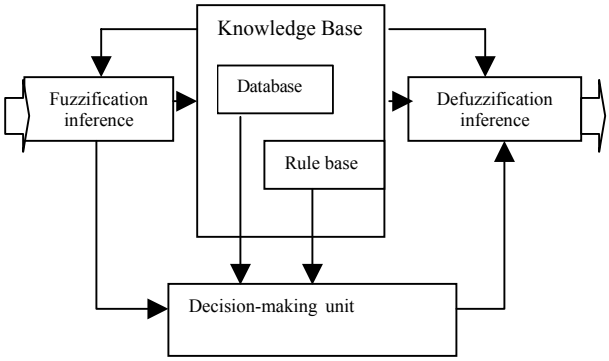

Fig.1: Block Diagram of the ANFIS Structure

In equation (2), F_{mag} is the magnetic force; F_D is the damping force; g is the gravitational constant; m is the mass of the armature; K is spring stiffness, and x is the spring displacement.

The approach uses the following convergence criterion :

$$\max\left(\left(I_n - I_{n-1}\right)/I_n\right) < \varepsilon \qquad (3)$$

where n is the iteration number, and ε is a preset tolerance.

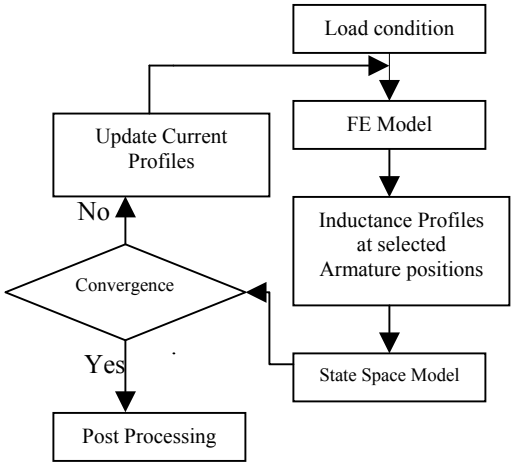

Fig.2: Fl Iterative Process Between FE and SS Models

ANFIS RESULTS

This approach was applied to a prototype AC actuator, Fig.3. In this work, static cases where the armature is held at fixed position, as well as motion cases where the armature is free moving, are considered. Sample results are presented below. In Fig. 4, the magnetic force is shown for an excitation voltage of 120V rms. Each data point along the position axis corresponds to a possible static armature position. The computed average and maximum errors of the results in Fig. 4, with respect to measured data, were found to be 3.9% and 6.57%, respectively. The static case of armature position at 6.096mm is shown in Fig. 5. Furthermore, Table1 shows a summary of results as obtained in a motion case. As demonstrated by these results, good agreement exists between the AI-EM model and test data. Full details and further results will be given in the full paper.

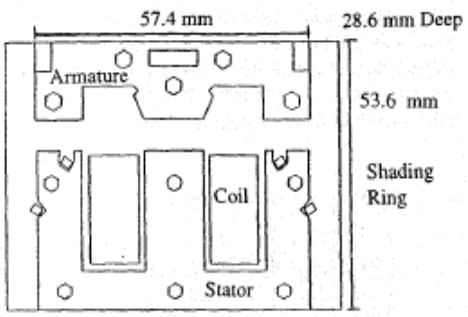

Fig.3: Outline of AC Actuator

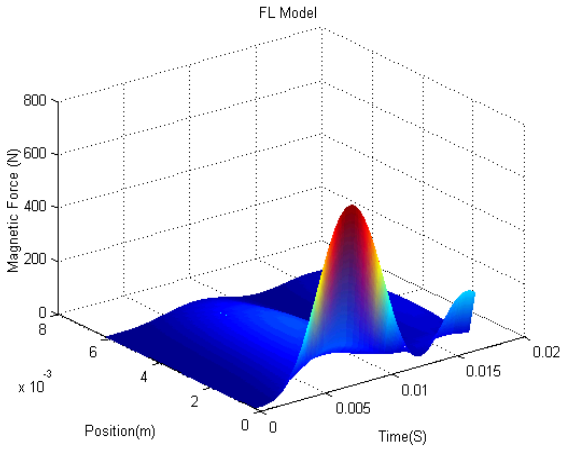

Fig. 4: FL Force Results at 120V RMS

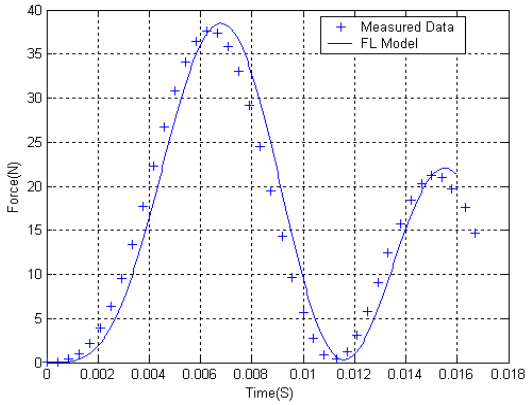

Fig. 5: FL Force Results at 6.096 mm and 120V RMS

Data	Measured	FL
Main current peak (A)	3.12	3.91
Time Ipeak (ms)	6.7	6.90
Magnetic force Peak (N)	47.10	56.77
Time Fpeak (ms)	7.56	8.40
Time to seal	16.50	14

Table 1: Motion Results for 120V RMS Case

ACKNOWLEDGMENT

This work was supported by a grant from U.S. Office of Naval Research to Marquette University.

REFERENCES

[1] H.C. Roters, "Electromagnetic Devices, "John Wiley & Sons, New York, 1941.

[2] A.A. Arkadan, M.J.J VandeHeiden, and J.R. Brauer, "The Coupled problem in Electromagnetic AC Contactors," IEEE Transactions on Magnetics, Vol. 33, No.2, pp. 1630- 1633, March, 1997.

[3] J. Shing and R. Jang, "Adaptive-Network-Based Fuzzy Inference System" IEEE Transactions on System, Man and Cybernetics, Vol. 23, No. 3, pp. 665- 685, May/June, 1993.

Vibration Reduction in Switched Reluctance Motor by Experimental Transfer Function and Response Surface Methodology

Kyung-Ho Ha, Young-Kyoun Kim, Geun-Ho Lee and Jung-Pyo Hong, *Senior Member*, *IEEE*
Dept. of Electrical Eng., Changwon National University
#9 Sarim-dong, Changwon, 641-773, Kyungnam, Korea
e-mail: agdokebi@cosmos.changwon.ac.kr, ensigma@hitel.com, motor@nc.namhae.ac.kr and jphong@sarim.changwon.ac.kr

***Abstract*—This paper deals with the vibration analysis and the optimal control for the vibration reduction in a Switched Reluctance Motor (SRM). To predict the vibration, the experimental transfer function coupled with the electromagnetic Finite Element Method (FEM) is proposed. Based on the proposed analysis method, the Response Surface Methodology (RSM) is applied to the optimal point for reducing the mechanical vibration according to switching angles. The experimental transfer function is obtained by the response of vibrations to harmonic components of electromagnetic forces. The electromagnetic and vibration characteristics are compared with the measured data.**

INTRODUCTION

The practical use of SRMs in industrial applications is limited by their higher vibration and torque ripple. The interaction of electromagnetic forces and mechanical structure is the major cause of noise and vibration [1-3]. The existing research on how to reduce the vibration can fall into two categories: drive strategies and geometric design. The former approach includes current waveform, turn-off and on angle, and duty cycle, etc. [2]. The second approach is a mechanical design to suppress the vibration against magnetic forces and to avoid resonance frequencies excited by harmonic magnetic forces [3].

It is necessary to predict the vibration level caused by the electromagnetic phenomenon under control techniques. Generally, the vibration characteristics are evaluated by the coupled electromagnetic and structural analysis based on the numerical method. For the prediction of mechanical vibrations by the structural FEM, a 3D analysis model and accurate mechanical properties are needed to obtain reliable estimates [3]. Hence, it takes a large time to compute and the process is complicated. Therefore, a more simple method is required to analyze the effects of changing the operating parameters of the power electronic controller on the vibration.

In this paper, the experimental transfer function instead of the structural FEM is coupled with the electromagnetic FEM to predict the vibration. The experimental transfer function is defined as the vibration response versus harmonic magnetic force components. This function is measured by the response of acceleration to harmonic components of magnetic force. It represents the inherent properties of the tested SRM. Based on this function, the vibration level is calculated very easily, accurately and simply by the magnetic force that is obtained from the electromagnetic FEM. From the proposed method, the electromagnetic and vibration characteristics according to switch on and off angles are investigated.

And this paper deals with the optimization to minimize the vibration. An optimization technique by the response surface methodology is applied to find the optimal switching angle. The response surface provides the designer with an overall perspective of the vibration response according to the behavior of the switching angle within a control space. It can be leading to great savings in time without very large repetition and computations [4]. The computation of the vibration response concerning the switching angle is achived by using the proposed analysis method. The various analysis results are compared with measurments.

ANALYSIS PROCEDURE

Fig. 1 presents the analysis process to find the optimal switching angle. The experimental transfer function coupled with electromagnetic FEM helps to evaluate the mechanical and electromagnetic performances of the SRM controlled by the switching angle. The response surfaces of the vibration and the magnetic torque is obtained from the RSM. The tested motor is a 6/4 SRM with three phases winding.

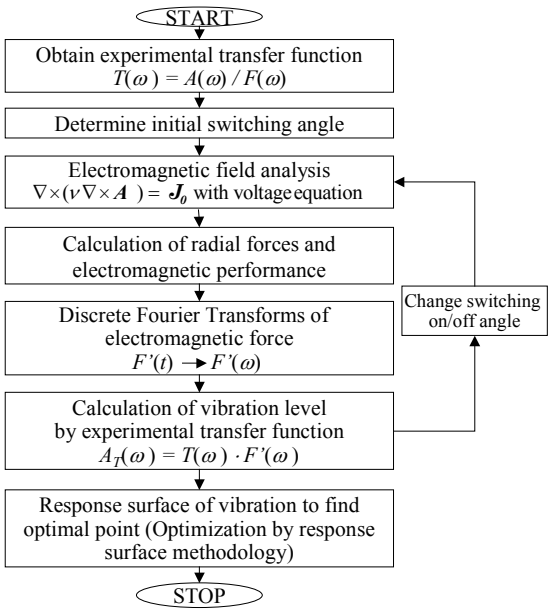

Fig. 1. Analysis procedure to find the optimal switching angle

ANALYSIS METHOD

A. Experimental Transfer Funciton

The experimental transfer function is defined as the output response of acceleration versus the input of magnetic force. The acceleration response $A(\omega)$ is measured when only one phase of three phases is excited. The electromagnetic radial force acting on the stator pole $F(\omega)$ is calculated by the electromagnetic FEM. The experimental transfer function $T(\omega)$ in the frequency domain is determined as follows:

$$T(\omega) = \frac{A(\omega)}{F(\omega)} \tag{1}$$

B. Vibration Analysis

The vibration according to the variation of switching angles can be easily calculated by above the experimental transfer function $T(\omega)$and the radial force $F'(\omega)$ obtained by the electromagnetic FEM. The vibration response $A_T(\omega)$ by three phase excited is the sum of the vibration responses emitted from the sequential excitation of each phase, which is expressed as:

$$\begin{aligned} A_T(\omega) = {} & T(\omega)\times F_A^{'}(\omega) + T(\omega)\times F_B^{'}(\omega)\cdot e^{j\omega\Delta t} \\ & + T(\omega)\times F_C^{'}(\omega)\cdot e^{j\omega 2\Delta t} \end{aligned} \tag{2}$$

C. Response Surface Methology

The response surface methodology procedures seek to find the relationship between the switching angle and the vibration response through statistical fitting method [4], which is based on the observed data obtained from the proposed analysis method. We suppose that the true response can be written as

$$\eta = F(\zeta_1, \zeta_2, \cdots, \zeta_k) \tag{3}$$

where, the variables ζ_1, ζ_2,…, ζ_k in (1) are expressed in natural variables, such as switch-on and off angle. Because the form of the true response function F is unknown and perhaps very complicated, we must approximate it. In many cases, the approximating function is normally chosen to be either a first-order or a second-order polynomial model, which is based on Taylor series expansion.

ANALYSIS RESULTS AND CONCLUSIONS

Fig. 2 shows the experimental transfer function of the tested SRM that is obtained by the measeured acceleration response to the calculated magnetic force in the frequency domain. The transfer function in the dwell angle 20 degrees is almost identical to that in 30 degrees. Therefore, the change of the switching angle has no influence on the experimental transfer function, because this function results from the material properties and the dimensions. Fig. 2 represents the inherent characteristic of the SRM structure. The effects of the switching angles on the vibration level and the electromagnetic torque are investigated by using the experimental transfer function of Fig. 1. The analysis results, as shown in Fig. 3., are similar to the experimental values. Based on the proposed analysis method, the results related to optimal control by the RSM to minimize vibrations will be reported in extended paper in detail.

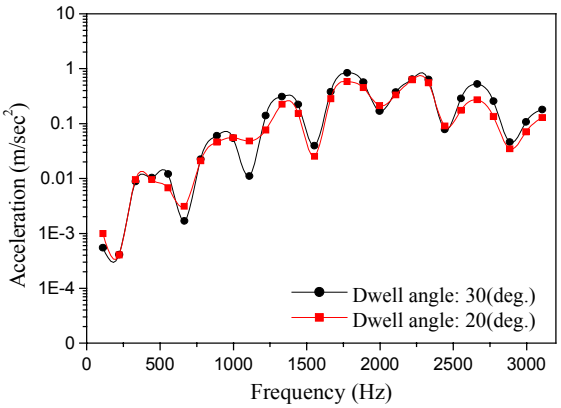

Fig. 2. Experimental transfer function of the tested SRM

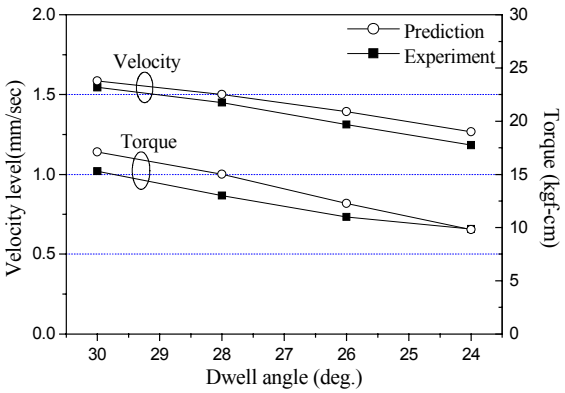

Fig. 3. Comparison of analysis results and measurements of the mechanical vibration and magnetic torque

REFERENCES

[1] D. E. Cameron, J. H. Lang and S. D. Umans, "The origin and reduction of acoustic noise in doubly salient variable reluctance motors," *IEEE Trans. Industry Application*, Vol. 28, No, 6, pp. 1250-1255, 1992.

[2] C. Pollock and C. Y. Wu, "Acoustic noise cancellation techniques for switched reluctance drives," *IEEE Trans. Industry Application*, vol. 33, pp. 477-484, March/April 1997.

[3] J. P. Hong, K. H. Ha and J. Lee, "Stator pole and yoke design for vibration reduction of switched reluctance motor," *IEEE Trans. on Magnetics,* vol. 38, pp. 929-932, 2002.

[4] Y K. Kim, Y S Jo, J P Hong, J Lee, "Approach to the Shape Optimization of Racetrack Type High Temperature Superconducting Magnet Using Response Surface Methodology," *Cryogenics*, vol. 41/1, pp.39-47, 2001.

Consideration of moving and forming of heating body in induction heating calculation.

Keisuke Fujisaki
Environment & Process Technology Center, Nippon Steel Corp., 20-1 Shintomi, Futtsu, 293-8511 Japan.
fujisaki@re.nsc.co.jp

Takahiro Yamada
Nittetsu Plant Designing Corp., 20-1 Shintomi, Futtsu, 293-8511 Japan.
yama@re.nsc.co.jp

Abstract — In numerical analysis of induction heating, it is difficult problem to consider moving and forming of the heating body simultaneously. In case of calculating such a model by using conventional method, it requires much calculation time. Therefore, we suggested the calculation method that expresses the moving and forming of the heating body by using 2-D section model, and applied to the induction heating of small-diameter pipe in steel making process.

INTRODUCTION

Induction heating is the technology that is used to various purposes widely in these days. In order to doing these design and development, the numerical calculation by means of finite element method is often used. Especially, induction heating against motionless heating body has ever been calculated frequently.

However, in case of calculating the model that is processed with moving, it is difficult problem to consider these phenomena simultaneously [1].

The conventional calculation method is shown in Fig.1. In case of moving with processing, the joule heat distribution and temperature distribution varies from moment to moment. Thus, we must calculate electromagnetic field calculation and temperature field calculation repeatedly in conventional method. This is the cause to increase calculation cost.

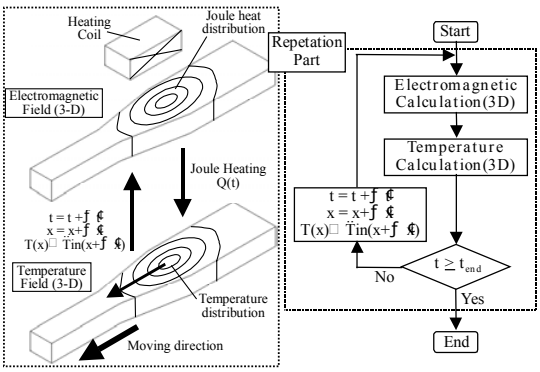

Fig. 1. Conventional calculation method

This model requires that it move temperature distribution with moving of heating body. In such case, the interpolation method is used frequently.

However, the interpolation in conventional 3-D model is very complicated, because it is not possible to slide the temperature distribution to only one direction at the place where the heating body is formed. Thus, conventional method is not effective method, because it has some problems.

On the other hand, the calculation method that is suggested this time is shown in Fig.2.

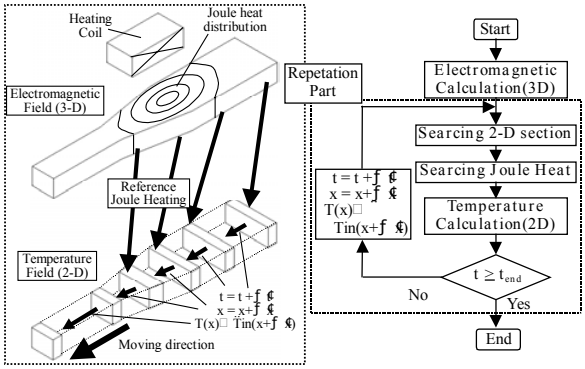

Fig. 2. Suggested calculation method

By considering a precondition that the moving speed of heating body is high speed, it is possible to calculate temperature filed by 2-D section model that is shown in Fig.2. The reason is considered as follows.

In case of moving with high speed, the temperature variation of heating body by virtue of joule heat is more dominant than the temperature variation by virtue of the thermal conduction of heating body. Therefore, the effect of the thermal conduction to progress direction can be ignored. And, the boundary of each 2-D section is treated as heat insulation condition.

In this calculation method, the movement method of temperature distribution is easy, because the calculated temperature at the 2-D section is given as initial

temperature of the next section.

Therefore, by using this calculation method, it is considered that we can calculate induction heating model efficiency.

CALCULATION RESULT

Calculation model is shown in Fig.3. We used induction heating of the small-diameter pipe as calculation model. The small diameter pipe is used as gas pipe, water pipe and boiler plumbing. Steel sheet that is origin of small diameter pipe is called “skelp”.

In making process of the small diameter pipe, the temperature at the contact point is very important [2]. Therefore, in order to obtain high temperature at this point, the skelp edge is heated before forming by the induction heating.

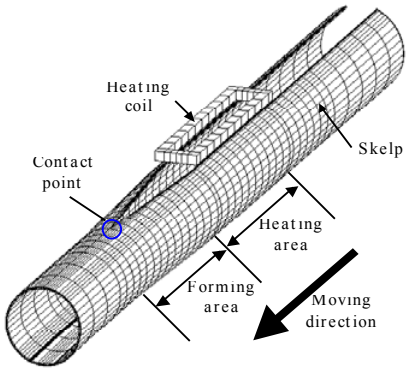

Fig. 3. Small diameter pipe model

The calculated joule heat distribution is shown in Fig.4. Because of high frequency, the skelp edge has high joule heat distribution right under the coil.

The temperature distribution contours at each section are shown in Fig.5. And, the temperature history plot at the skelp edge is shown in Fig.6. At first, the temperature of skelp-edge increases by the joule heat. After passing the heating area, the temperature decreases gradually by virtue of heat removal.

These results indicate that the suggested calculation method is available to apply to the real equipment with moving and forming of the heating body.

REFERENCE

[1] Z. Hu and J.Q.Li, “*Computer simulation of pipe-bending processes with small bending radius using local induction heating*,” Journal of Materials Processing Technology, Vol. 91, Issues 1-3, 30 June 1999, Pages 75-79.

[2] The Iron and Steel institute of JAPAN, *Steel-making process, Vol.3,* Maruzen Publishers, 1972.

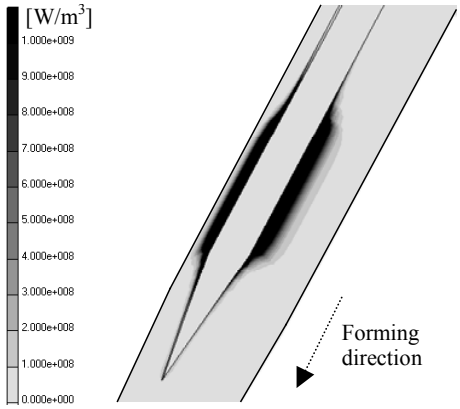

Fig.4. Joule heat distribution contour

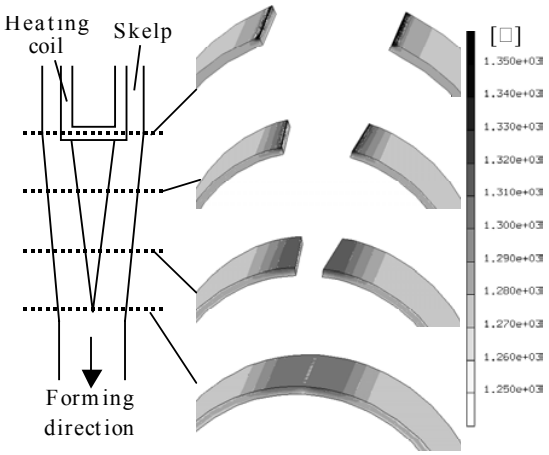

Fig.5. Temperature contour at 2-D section

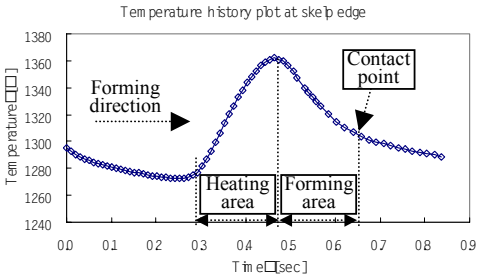

Fig.6. Temperature history plot at the skelp edge

Modeling of Multipole Magnetization of Sensor Disc Magnet

Y. Zhilichev
MAGNEQUENCH INTERNATIONAL
Technology Center – 9000 Development Drive – P.O.Box 14827
Research Triangle Park – NC 27709-4827 – USA
e-mail: yzhilich@mqii.com

***Abstract* — The paper describes a pulse magnetization of isotropic permanent magnet disc to provide a precise multipole structure with different magnet pole widths. The magnetization problem coupled with the discharge electrical circuit is solved for different cross sections of the magnet located in the magnetizing fixture. The magnetization vector then is imported into the static model of the sensor magnet. Based on finite element analysis the magnetizing fixture has been build and tested. The flux measurement shows that the precision of magnetization is in the range of +/-0.5 degree.**

INTRODUCTION

Multiple magnetization of a disc magnet is a straightforward problem when poles of the equal angular size are required to create on the magnet surface. The uniformly spaced trapezoidal coils embedded in the magnetic or non-magnetic disc-type fixture is a common way of magnetization. The precision of magnetization is mainly depends in this case only on the mechanical tolerances of positioning of magnetizing coils in the fixture slots (Fig.1). The problem of precise magnetization becomes complicated if a multi-peak waveform with non-equal width of positive and negative portions is specified for the sensor output (Fig.2). Normally, the sensor is located at some distance from the magnet. Therefore, first we have to project the pole distribution from the sensor location onto the magnet surface. This inverse problem can be solved in several iterations by specifying different pole angles and calculating the magnetic field of the disc magnet at the sensor location. Secondly, a position of slots in the magnetizing fixture should be determined to provide the magnetic poles of the determined angular width. In these cases, both these problems are interrelated and can be solved together step by step.

PULSE MAGNETIZATION PROBLEM

Accurate analysis of pulse magnetization is a complex nonlinear problem, in which determination of the transient magnetic field is coupled with a pulse current in the discharge electrical circuit. The problem has been under consideration for many years [1-3] A specialized magnetization solver accounting for hysteresis, eddy currents and field-circuit coupling has been developed and validated on designs of several magnetizing fixtures for isotropic permanent magnets [4-5]. The solver uses the first and

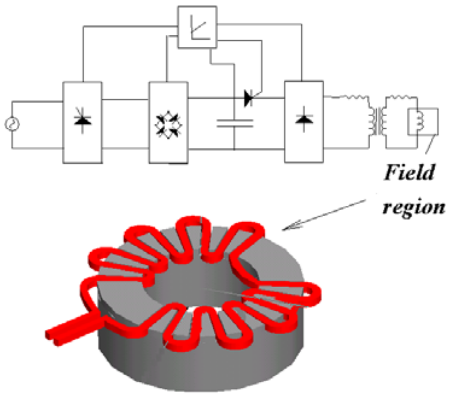

Fig. 1 Coupling of electromagnetic field region to discharge electric circuit

second quadrant portions of a magnet material's hysteresis loop. This loop consists of a virgin curve for the permanent magnet material when the field intensity increases and a demagnetization curve when the field decreases. A table is

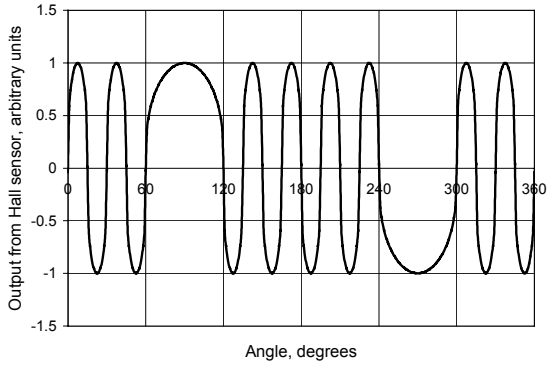

Fig. 2. Target output from the Hall sensor

used to define the virgin curve, and a series of curves are used to represent the major and minor demagnetization curves in the first and second quadrants. Although the solver accounts for major physical effects during magnetization process it can solve only 2D transient problems. To employ the solver, the disc magnet and magnetizing fixture are subdivided by several cylindrical cross-sections (ZOΦ) at different fixed radial coordinates (*r=const*) into a set of 2D

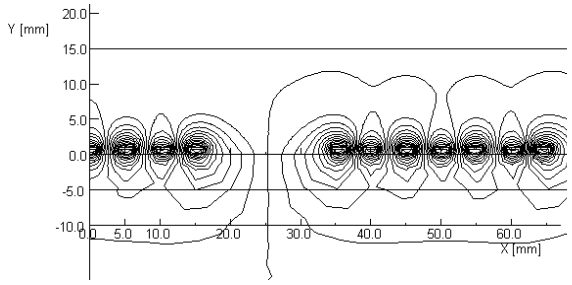

Fig. 3 Transient analysis in the unwrapped cross-section of the magnetizing fixture

models. The problem of pulse magnetization is solved in each section separately (Fig. 3). A contribution from the end parts of the winding can be taken into account via appropriate increase of the peak current in the discharge circuit. This is achieved by the adjustment for the charging voltage in the electrical circuit of the model.

PERMANENT MAGNET FIELD PROBLEM

A 3D magnetic field problem of the isotropic disc magnet is solved using a finite element model (Fig. 4). A distribution of magnetization vector over the magnet volume is imported from a finite element model of magnetizing fixture. The field is calculated at the sensor location . The zero points of B_z - component over angular coordinate are compared against the specified magnet pole widths, amd the appropriate corrections are made for the positions of conductors in the model of magnetizing fixture. The pulse magnetization problem and permanent magnet field problem are solved consequently untill the specified tolerance on the pole widths is achieved

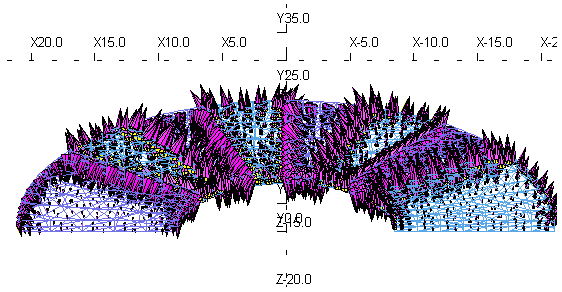

Fig. 4 Static model of disc magnet

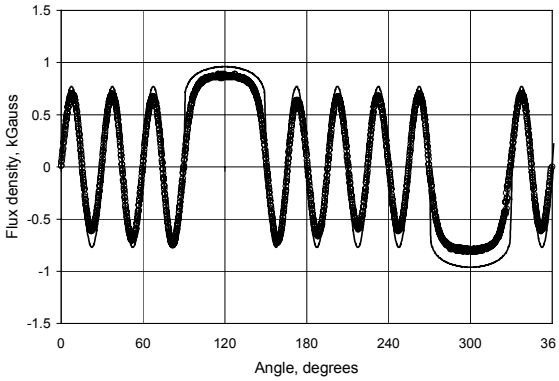

Fig. 5 Measured output from Hall sensor (dotted line) vs predicted flux density (solid line) from the finite-element analysis.

RESULTS

Based on the solution of two described above interrelated magnetic field problems angular distances between the slots of the magnetizing fixture have been determined. A prototype fixture has been built and tested. Figure 5 shows the output from the Hall sensor placed at 1 mm from the disc magnet. The magnetic field is sensed with the resolution of 1000 points per one degree. Based on the sensor output a precision of magnetization is detected as +/- 0.5 degree per pole.

REFERENCES

[1] T. Nakata, N. Takahashi, Numerical analysis of transient magnetic field in a capacitor-discharge impulse magnetizer, IEEE Trans. on Magnetics, vol. 22, No. 5, pp.526-528, 1986.

[2] G.W. Jewell., D. Howe, T.S. Birch, Simulation of capacitor discharge magnetisation, IEEE Trans. on Magnetics, vol. 26, No. 5, pp.1638-1640, 1990.

[3] R.H. Vander Heiden, A.A. Arkadan, J.R.Brauer, Nonlinear Transient Finite Element Modeling of a Capacitor-Discharge Magnetizing Fixture, IEEE Trans on Magnetics, vol.29, No. 2, pp.2051-2054, 1993

[4] P. Campbell, D. Miller, J. Simkin, Y. Zhilichev, Improved representation of the magnetization and resulting field in isotropic NdFeB, Proc. of 16th Int'l Workshop on Rare Earth Magnets and their Applications, The Japan Institute of Metals, pp. 955 -961, 2000

[5] P.Campbell , Y.Zhilichev, A Multi-Axis Model of Magnetization for Isotropic Permanent Magnets, IEEE Trans on Magnetics, vol.37, No. 4, pp.2634-2636, 2001

COMPUMAG Saratoga Springs, New York USA
July 13 - 17, 2003

Modal Analysis for the Transient Internal Voltage of a Transformer

Seunghyun Song*, Hyeong-Seok Kim**, Tae-Kyung Chung**, Song-yop Hahn***

*System LSI Division, Samsung Electronics, Yongin, 449-711, Korea
**School of Electrical and Electronics Engineering, Chung-Ang University, Seoul, 156-756, Korea
***School of Electrical Engineering, Seoul National University, Seoul, 151-742, Korea

***Abstract*—This paper deals with a method for obtaining the transient internal voltage distribution of a transformer. It is essential to consider the frequency-dependent effects of internal capacitance, inductance and resistance in order to analyze the transient characteristics of a transformer. Frequency-dependent inductance and resistance are obtained from analytic method and the values match well with the experimental ones. The numerical results of internal transient voltage of a transformer show good agreement with the experimental results from the literature.**

I. Introduction

Generally, transient internal voltage distribution should be considered in order to design high-voltage transformer effectively. It is essential to take into account of capacitance, inductance and resistance for analyzing a transient characteristics of a transformer. These circuit parameters are generally functions of frequency, which makes frequency-domain analysis more convenient than time-domain analysis. Especially, the variation of inductance and resistance according to frequency is large due to the eddy-current effect in a transformer core. The inductance and resistance are obtained from an analytic solution of Maxwell equations with appropriate boundary conditions. The eddy current has an effect on these values [1]. The fundamental difficulty in analyzing a transformer is due to the complexity of coupling between the windings. In this paper, this problem is treated by modal analysis which is usually adequate for lossless circuit and can be used effectively in lossy circuit as well [2].

II. The Calculation of Frequency-dependent Impedance

A. The analytic solution of impedance

After converting Maxwell equations into spectral domain through Fourier transformation along the axis of core, the electric fields are obtained from ordinary differential equations with appropriate boundary conditions for the structure in Fig. 1. The induced voltage in the winding is obtained through line integral of the electric field which results from inverse Fourier transform of the spectral domain electric field.

In real situation, the core is closed form as in Fig. 2. This closed core is modelled by infinite number of image windings placed along a core of infinite length.

Dividing the voltage in the ith winding by the current in the jth winding gives impedance Z_{ij} between the windings

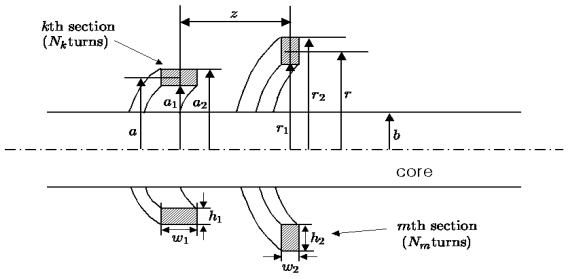

Fig. 1. A general winding structure for the calculation of impedance.

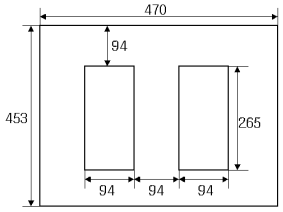

Fig. 2. The core structure for the calculation of impedance.

i and j. The impedance calculation procedure used in this paper will be described in the extended paper.

B. An example of Impedance calculation

In the case of a=r=81mm, a_1=r_1=71mm, a_2=r_2=91mm, b=47mm, h_1=h_2=20.2mm and w_1=w_2=10.4mm with the core structure in Fig. 2, the calculated inductance and resistance according to frequency are compared with the experimental results [1] in Fig. 3. The resistivity ρ is 0.0103[Ωm] and μ_r equals 843.

III. Mode Analysis of a Transformer

The voltage variation at the point x on the ith winding is as follows.

$$\frac{dV_i(x)}{dx} = -\sum_{j=1}^{N} \int_0^{\lambda_j} Z_{ij}(x,\beta) I_j(\beta) d\beta, \quad (i = 1, 2, \ldots, N) \qquad (1)$$

where $I_j(\beta)$ represents the current at the point β on the jth winding. $Z_{ij}(x,\beta)$ is the mutual impedance between the point x of ith winding and β of jth winding and λ_j represents the length of j-th winding. $V_i(x)$ and $I_j(\beta)$

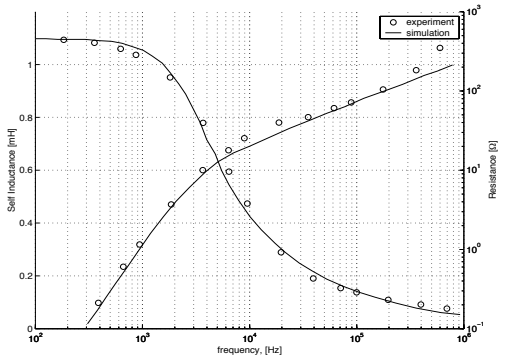

Fig. 3. Inductance and Resistance according to frequency.

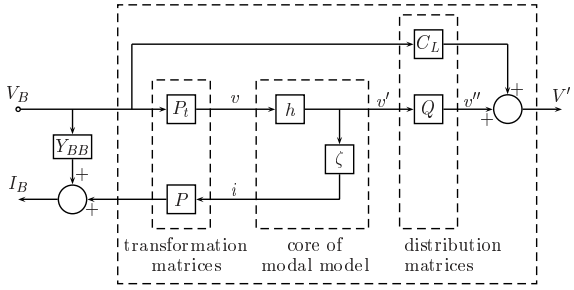

Fig. 4. Block diagram of modal model.

represent the Laplace transform of $v_i(x,t)$ and $i_j(\beta,t)$, respectively. The current variation takes a similar form like the following;

$$\frac{dI_i(x)}{dx} = -\sum_{j=1}^{N}\int_0^{\lambda_j} Y_{ij}(x,\beta)V_j(\beta)d\beta. \tag{2}$$

After sectioning the windings into small cells and discretizing the equations (1) and (2), the following modal equation is obtained through some calculations.

$$\begin{bmatrix} I_B \\ V' \end{bmatrix} = \begin{bmatrix} A & B \\ C & D \end{bmatrix} \begin{bmatrix} V_B \\ V' \end{bmatrix}, \tag{3}$$

where A, B, C, D are functions of impedance and admittance of the equivalent circuit, V_B represents voltage at the end point of the winding, I_B is the current entering into the port and V' represents the internal voltage at each small cell. Solving equation (3) for V' and I_B obtains the followings;

$$V' = (1-D)^{-1}CV_B \tag{4}$$

$$I_B = \{A + B(1-D)^{-1}C\}V_B. \tag{5}$$

The modal form of solution is obtained by diagonalizing the matrix D like the following;

$$D = Q\alpha Q^{-1}, \tag{6}$$

where α is a diagonal matrix whose elements are eigenvalues of D and Q is a matrix comprised of its eigenvectors. Substituting $C' + C_L$ for C and rearranging equations (4) and (5) result in the following modal equations which represent the overall structure of modal analysis as shown in Fig. 4.

$$V' = C_L V_B + QhP_tV_B \tag{7}$$

$$I_B = Y_{BB}V_B + XhP_tV_B, \tag{8}$$

where $P_t = Q^{-1}(C_L - C_H)$, $Y_{BB} = A + BC_L$, $C_H = -D^{-1}C'$ and $X = BQ$. The modal transfer function matrix h is $\mathrm{diag}(h_1, h_2, \ldots, h_n)$ and its element h_j equals $\alpha_j/(1-\alpha_j)$.

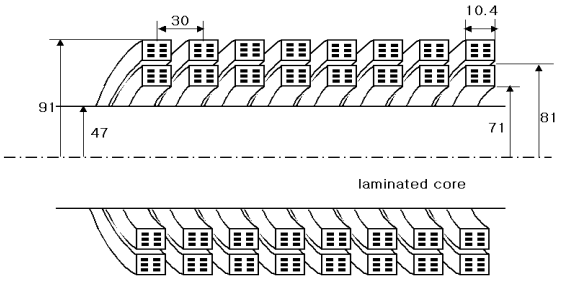

Fig. 5. The structure of a real transformer $[mm]$.

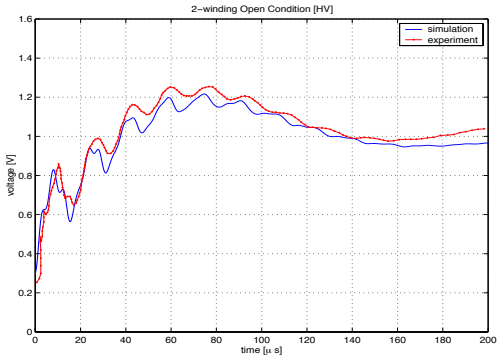

Fig. 6. Transient voltage in HV winding with all ports open.

IV. Numerical Results

The internal transient voltage of a transformer in Fig. 5 is obtained through inverse Fourier transformation of the results of the modal analysis with step input voltage. The result shows good agreement with the experimental one from the reference [2] as in Fig. 6 with all ports open. The numerical results from the test example have demonstrated that modal analysis is effective to the calculation of transient voltage response of a system whose parameters are frequency-dependent.

References

[1] D.J. Wilcox, M. Condon and W.G. Hurley, "Calculation of self and mutual impedances for coils on ferromagnetic cores," *IEE Proceedings*, Vol. 135, Pt. A, No. 7, pp. 470–476, Sept. 1988.

[2] D.J. Wilcox, M. Condon, D.J. Leonard and T.P. McHale, "Time-domain modelling of power transformers using modal analysis," *IEE Proc.-Electr. Power Appl.*, Vol. 144, No. 2, pp. 77–84, March 1997.

A Weak Coupling of a Nonlinear Semiconductor to the Finite Element Method

Silvio Ikuyo Nabeta
LMAG - Laboratório de Eletromagnetismo Aplicado -
PEA - EPUSP
Av. Prof. Luciano Gualberto, trav. 3 - n.158
05508-900 - São Paulo - Brazil
nabeta@pea.usp.br

Kay Hameyer
Katholieke Universiteit Leuven
ESAT/ELEN
Kasteelpark Arenberg 10
B-3001 Leuven-Heverlee – Belgium
kay.hameyer@esat.kuleuven.ac.be

Abstract – **The aim of this work is to present a weak coupling of a nonlinear diode model and the Finite Element Method (FEM). The coupling was accomplished by using a FEM package and HSpice, a circuit analyzer program. That coupling is applied to a time-stepping simulation of an inductor fed by a sinusoidal voltage source through a rectifier. The influence of the non-linearity is analyzed and the results are compared to other methods.**

Index Terms **– Weak Coupling, Diode, Semiconductor, Electric Circuit Coupling, Finite Element Method**

I. Introduction

One of the major achievements in the electromagnetic fields computation was the electric circuit and the finite element method coupling. Among the many benefits it brought one can point out the consideration of semiconductors in the numerical analysis.

In general, there are two different approaches to couple the Finite Element Method (FEM) with electric circuits. In the first approach, namely Strong or Direct Coupling, the equations from the FEM and the electric circuit analysis are assembled together and the system is solved simultaneously. In the second approach, known as Weak or Indirect Coupling, the FEM and the electric circuit systems are separate and the solution is achieved by an iterative method.

The aim of this work is to couple a nonlinear model of a diode with the Finite Element Method by a Weak Coupling and apply it to a Time-Stepping Finite Element Analysis of an inductor fed by a sinusoidal voltage source through a rectifier. In this work the Finite Element package used is the *Olympos* [1] and the circuit analyzer package is the *HSpice* [2].

In order to compare the influence of the non-linearity of the diodes model the simulation results were compared to the results of other three methods:

1. The FEM simulation coupled to a *On-Off* model for the diodes;
2. The simulation performed by *HSpice* only;
3. Analytical solution.

Moreover, the non-linearity is also evaluated regarding the voltage source amplitude.

This work was partially supported by FAPESP-Fundação de Amparo à Pesquisa do Estado de São Paulo under the Grant 00/08790-0

II. Diode Modeling

In this work two models for a diode are presented namely the *On-Off model* and the *nonlinear model*. For each model a Time-Stepping FEA is carried out and the results of the current are compared

On-Off Model

In the *On-Off* model the diode is considered as a perfect switch as presented in Fig. 1. No voltage drop is considered in the switch.

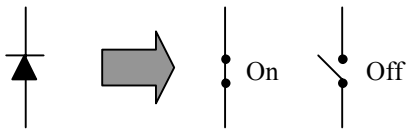

Fig. 1: On-Off Model

Nonlinear Model

The nonlinear model takes into account the nonlinear relation between the voltage and the current in the diode as presented in (1) [3].

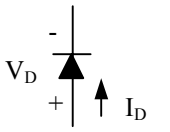

$$V_D = V_T \ln\left(\frac{I_D}{I_S} + 1\right) + R_S I_D \qquad (1)$$

Where: V_T is the thermodynamic voltage;
I_S is the reverse saturation current;
R_S is the internal resistance.

In this work the non-linearity of the diodes is taken into account by the *HSpice* package.

III. The Problem Under Analysis

The problem under analysis consists of an inductor fed by a sinusoidal voltage source through a rectifier as shown in Fig.2.

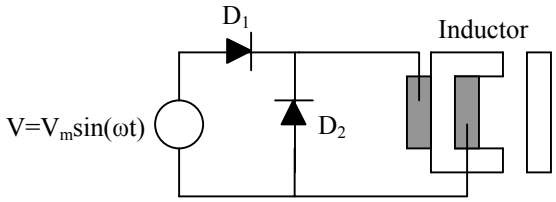

Fig. 2: FEM and Circuit Coupling Problem

The inductor has a coil with 100 turns and a linear ferromagnetic core with μ_r = 1000. The inductance and the resistance of the coil are L=13.96 mH and R=0.17 Ω, respectively.

The diodes D_1 and D_2 are modeled, in the nonlinear case, by (1) with parameters of the commercial type MBR4015 CTL [4].

The sinusoidal voltage source has amplitude of 24 V and frequency of 50 Hz.

IV. Diode Model and FEM Coupling

In order to accomplish the *Olympos* and *HSpice* weak coupling a manager is necessary to establish the file exchanging between the programs. In this work this task is done by *Matlab* [5], as presented in Fig.3.

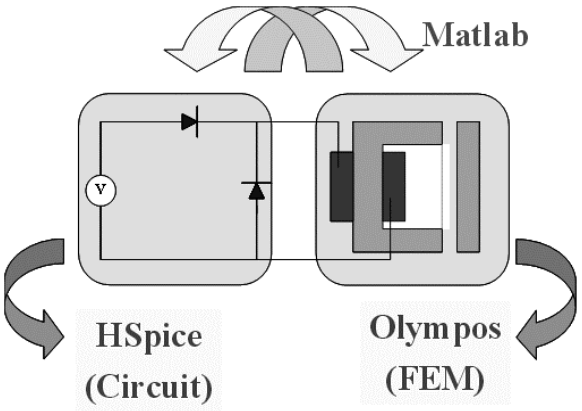

Fig. 3: Weak Coupling Scheme

The FEM provided a mesh with 342 nodes and the time-stepping analysis was carried out considering a time-step of 0.5 ms.

V. Results

Fig. 4 presents the results comparison.

Considering the results obtained from HSpice as the reference, one can observe that the numerical simulation with the nonlinear model provided results in a good agreement. It suggests that Eq.(1) represents fairly well the diode performance.

By the other hand, the results provided by the *On-Off* model indicate that this kind of modeling is not well suited in certain cases when the voltage is low.

Fig.5 shows the currents results for the analysis of the influence of the non-linearity of the diodes with higher voltages.

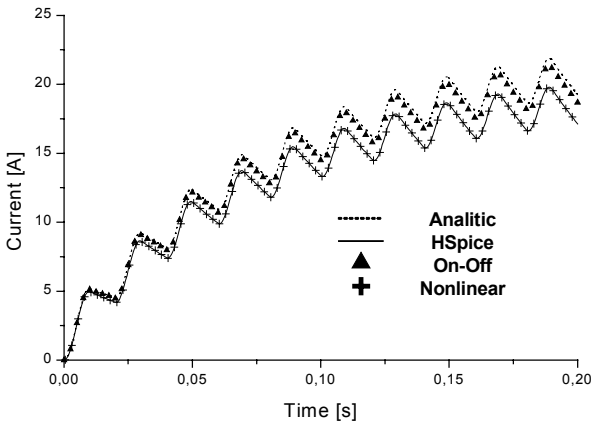

Fig. 4: Results Comparison

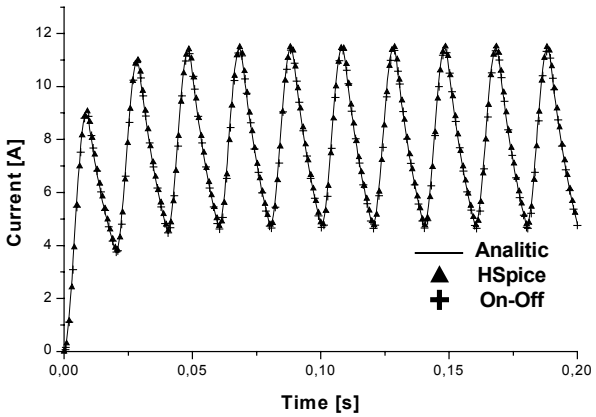

Fig. 5: Influence of the non-linearity with higher voltage

VI. Conclusions and Perspectives

A time-stepping analysis of an inductor fed by a sinusoidal voltage source through an inverter was performed. To accomplish this task a weak coupling FEM and electric circuit was proposed and a nonlinear model for the diodes was used.

In the four-page version a more detailed scheme of the weak coupling will be presented as well as an commented analysis of the influence of the non-linearity in problems with higher voltages.

References

[1] *Olympos*, Finite Element Package, ESAT/ELEN, 2001, http://www.esat.kuleuven.ac.be/elen/research/software-development
[2] *Star-HSpice*, HP platform, 2000
[3] P. Antognetti, G. Massobrio, *Semiconductor Device Modeling with SPICE*, New York, McGraw Hill, 1987.
[4] ON Semiconductors, http://www.onsemi.com
[5] *Matlab* v. 6.0, Mathworks, 2000

Researches of the Coil Geometry of TFIH Equipment with Numerical Analysis

Yang Xiaoguang, Wang Youhua
Hebei Univ. of Technology, Dept. of Electrical Engineering
Dingzigu 8, Guangrong Street, Hong Qiao District
Tianjin 300130, People's Republic of China
Email: xgyang@mail.hebut.edu.cn

Abstract: In this paper researches of the coil geometry of transverse flux induction heating (TFIH) equipment for continuously moving thin-strips are described. Taking advantage of the relation between the eddy current distribution and the coil geometry suitable coil geometry can be designed, which contributes to a uniform temperature distribution on the surface of the strip cross-section at the inductor outlet. With such a coil geometry numerical studies on the problem of transverse flux induction heating are presented. The eddy current field and its coupled thermal field are computed through three dimensional (3D) finite element method (FEM).

Key words: TFIH; coil geometry; 3D FEM; coupled fields;

1 Introduction

Compared with longitudinal flux induction heating equipments the TFIH equipments have considerable advantages, due to the need of lower frequencies, less reactive power and being suitable for continuously processes. The main disadvantage of the TFIH is the resulting inhomogeneous temperature distribution on the surface of the strip, which is mainly influenced by the coil geometry and the position of the coil edges relative to the strip width. In the last few years big research efforts have been done in different countries for the optimization in order to achieve the uniformity of temperature required. It is particularly important to analyze the effect of the main parameters on the power density distribution at the surface of the strip. In this paper taking advantage of the relation between the eddy current distribution and the coil geometry a TFIH inductor was designed.

2 The Design of Coil Geometry

To get a homogeneous temperature at the inductor outlet the heat source integrated along the velocity direction from the inductor inlet to outlet should be equal. For heat loss at the edges is more, more heat source should be inducted in the inductor design. Numerical investigations into transverse flux inductors revealed that in rough approximation, the distribution of eddy current or joule heat source in the strip is the projection of coil geometry onto the strip surface [1]. According to the relationship, the projection area of the coil geometry integrated along the velocity direction from the inductor inlet to outlet should be also equal in order to get a uniform temperature distribution on the surface of the strip cross-section at the inductor outlet.

According to that a new type of coil geometry is designed, which is square. But the edges of coil are not parallel to those of the strip, intersecting with an angle of forty-five degrees. Another fact is that long coils protruding beyond the strip edge lead to edge overheating, and short coils result in a temperature decrease. The optimal design methods, such as orthogonal experiment, allow the designer to minimize the influence of the position of the coil edges relative to the strip width. With this coil geometry by optimizing coil to strip width ratio it can result in a completely uniform temperature across the entire strip width at the inductor'exist.

3 Numerical Analysis Procedure

The mathematical model for this sinusoidal quasi-static eddy current problem results from the Maxwell equations and is described by the complex magnetic vector potential $\underline{\vec{A}}$ and an electrical complex scalar potential $\underline{\phi}$ with Coulomb Gauge [2]:

$$rot\frac{1}{\mu}rot\underline{\vec{A}} - grad(\frac{1}{\mu}div\underline{\vec{A}}) + j\omega\kappa\left(\underline{\vec{A}}+grad\underline{\phi}\right)=\kappa\underline{\vec{E}}_S \quad (1)$$

$\underline{\vec{E}}_s$ is the electric field strength impressed by the power source, μ the permeability, k the conductivity and ω the power angular frequency.

The requirement of a zero divergence condition of current density must be fulfilled:

$$div\left(\kappa \underline{\vec{A}} + \kappa grad \underline{\phi}\right) = 0 \tag{2}$$

The expression for currents is

$$\underline{\vec{J}} = -j\omega\kappa\left(\underline{\vec{A}} + grad \underline{\phi}\right) + \kappa \underline{\vec{E}}_S \tag{3}$$

And it determines the heat source:

$$p_v = \left|\underline{\vec{J}}^2\right| / k \tag{4}$$

The temperature field $\vartheta(x, y, z)$ is computed based on the Fourier's thermal conduction equation:

$$\frac{\partial(c\rho\vartheta)}{\partial t} = div\left(\lambda grad\,\vartheta\right) + p_V - \vec{v}\,grad\left(c\rho\vartheta\right) \tag{5}$$

where c is the specific heat, λ the thermal conductivity coefficient, ρ the mass density and $\vec{v}$ the strip velocity. The temperature ϑ depends on both the location (x, y, z) and the time t.

The solution of this coupled problem is possible by 3D FEM with Galerkin procedure. The necessary boundary and symmetrical conditions are taken into account. The calculation procedure starts from the solution of the eddy current problem, which gives as result the induced power losses distribution in the work piece. This power distribution is then used as the input of the temperature field problem, whose solution gives the temperature distribution.

4 Results

The considered strips are that their width varies from 0.2m to 0.4 m, thickness from 0.2 to 0.4mm, and speed from 10 to 60m/min. The working frequency is 3000Hz. The results presented below relate to one specific example which is one of many modifications. In Fig. 1. the calculated distribution of eddy current on the surface of the strip is illustrated. Fig. 2. gives the distribution of heat sources density. Fig. 3. shows the temperature distribution resulted from the computation.

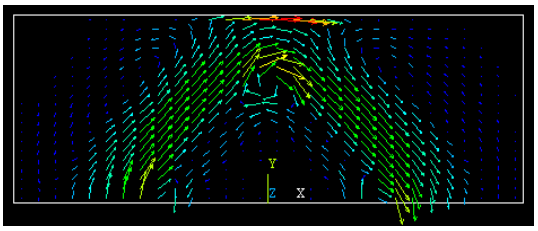

Fig. 1. Eddy current distribution on the 1/2 thin strip surface

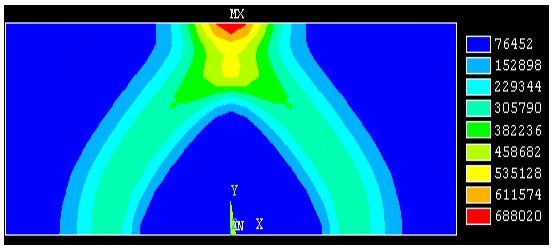

Fig. 2. Distribution of heat source density in half thin strip surface

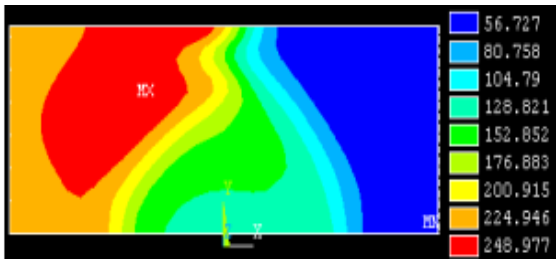

Fig. 3. Distribution of temperature on the half thin strip surface

Reference

[1] Zanming Wang, Xiaoguang Yang, Youhua Wang"Eddy Current and Temperature field Computation in Transverse Flux Induction Heating Equipment". IEEE Transaction on MAGNETICS, vol. 37, No. 5, pp. 3437-3439, SEPTEMBER 2001.

[2] Biro, K. Preis, "On the use of the magnetic vector potential in the finite element analysis of three-dimensional eddy currents, " IEEE Transaction on Magnetic, vol. 25, No. 4, pp. 3145-3159, July 1989

Passive and Active Magnetic Shielding of Induction Heaters

P. Sergeant[1], U. Adriano[2], L. Dupré[1], O. Bottauscio[2], M. De Wulf[1], M. Zucca[2], J. Melkebeek[1]

1. Department of Electrical Energy, Systems and Automation, Ghent University
Sint-Pietersnieuwstraat 41
Ghent B-9000, Belgium
peter.sergeant@rug.ac.be

2. Istituto Elettrotecnico Nazionale *Galileo Ferraris*
Strada delle Cacce 91
Torino I-10135, Italy
botta@ien.it

***Abstract*—In induction heaters, a metallic workpiece is heated by eddy currents, induced by strong alternating magnetic fields. Using numerical models, proper active and passive shields are designed in order to mitigate the stray field of the induction heater. Two models are presented: an axisymmetric Finite Element (FEM) and a hybrid Finite Element - Boundary Element (FEM – BEM) model. Results of both numerical methods are compared and verified with measurements on an archetype of an induction heater. A good correspondence is observed.**

INTRODUCTION

Induction heater equipment is exploited for a thermal treatment of metallic specimen. This thermal treatment is obtained by huge eddy currents, induced in the conductive specimen. The eddy currents result from the time dependent magnetic field, generated by the excitation coil.

The excitation coil creates also a magnetic field in the whole surrounding region. This gives rise to magnetic field levels ranging from several hundreds of μT up to some mT at a distance from the source in the range 0.1 m - 1 m. The operator of the equipment as well as electronic devices may be exposed to magnetic fields, significantly higher than the reference levels indicated by the ICNIRP [1]. Thus, the magnetic field should be mitigated using three techniques:

1. reconsideration of the induction heater design
2. passive shielding, using suitable materials to limit electromagnetic losses within the shield [2]
3. active shields: proper currents in a number of compensation coils generate counter fields opposite to the main one to be reduced.

Only the two last techniques are considered in this paper.

The modification of the thermal treatment of the metallic specimen by the reduction of the magnetic environmental pollution using passive and active shielding, must be limited to a minimum. Moreover, the area in which shields can be added is constrained, as the accessibility of the induction heater must be guaranteed.

Two numerical models are developed with geometry as shown in Fig.1. The geometry is axisymmetric, and symmetric to the $z = 0$ axis. To reduce the stray field in the subdomain D, the position of the passive shield is chosen as shown in Fig.1, taking into account the accessibility of the workpiece. The positions and the number of turns of the 'distributed 'compensation coils of the active shield as well as the optimal current in the active shield must be identified from a proper inverse problem in an iterative way [3]. Here, a least squares algorithm minimizes the average of the B-field norms in the P points of the regular grid defined in the subdomain D.

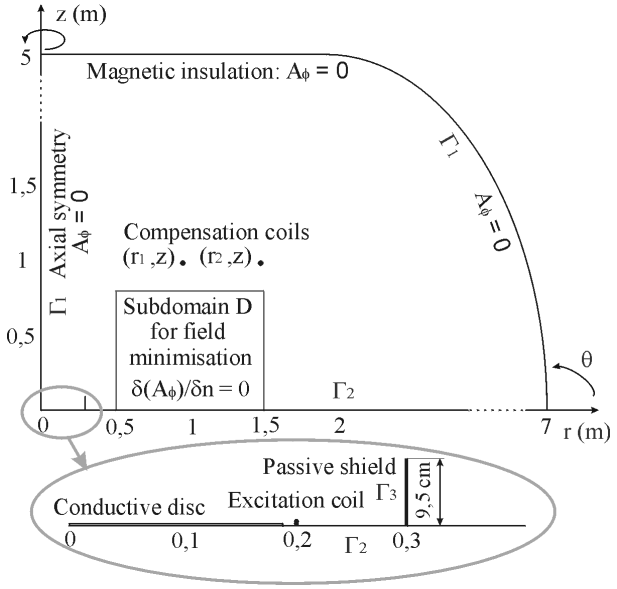

Fig. 1. Finite-element layout, scales in meter

AXISYMMETRIC 2D FINITE ELEMENT MODEL (FEM)

The Finite Element model (FEM) is linear, axisymmetric, quasi-static and time-harmonic. The domain Ω is defined by the induction heater, the passive and active shields, and the air surrounding the induction heater. In the numerical field calculation, the known current density in the compensation coils is denoted by $\mathbf{J_e}=J_e(r,z)\mathbf{1}_\phi$. In the domain Ω, the magnetic induction is written as $\mathbf{B}=\mathrm{rot}\mathbf{A}$, with the vector potential $\mathbf{A}=A_\phi(r,z)\mathbf{1}_\phi$. $A_\phi(r,z)$ obeys a second order boundary value problem (BVP) in Ω, i.e.

$$\left[\frac{\partial}{\partial r}\left(\frac{1}{r\mu}\frac{\partial}{\partial r}\left(rA_\phi\right)\right)\right]+\left[\frac{\partial}{\partial z}\left(\frac{1}{r\mu}\frac{\partial}{\partial z}\left(rA_\phi\right)\right)\right]-i\sigma\omega A\phi=-J_e \quad (1)$$

For frequencies higher than 6 kHz, however, the regions of the conducting passive shields are excluded in the FEM model. Then, impedance boundary conditions are used (Γ_3 in Fig. 1) [4]:

$$\frac{1}{r}\frac{\partial}{\partial r}\left(rA_\phi\right)\cdot n_r+\frac{1}{r}\frac{\partial}{\partial z}\left(rA_\phi\right)\cdot n_z=iA_\phi e^{-i\pi/4}\sqrt{\sigma_p\mu_p\omega} \quad (2)$$

wherein ω is the angular frequency, i the imaginary unit, μ_p the permeability of the passive shield and σ_p its conductivity.

HYBRID 3D FINITE ELEMENT-BOUNDARY ELEMENT MODEL (FEM-BEM)

In the second numerical procedure, taking into account that the passive shield has prevalent dimensions (19 cm high) with respect to its thickness (0.65 mm), the thin-shield approximation is employed, introducing suitable interface conditions [5]. Having defined a local reference system (Fig. 2) on the shield $\{\boldsymbol{t_1}, \boldsymbol{t_2}, \boldsymbol{n}\}$, defining surfaces (a) and (b) with respect to normal $\boldsymbol{n}$, the following interface conditions can be introduced:

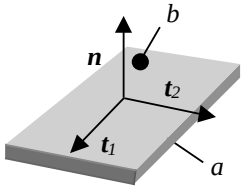

Fig. 2. Scheme of the passive shield structure in the hybrid 3D Finite Element-Boundary Element model

$$H_{m,n}^{(b)}+H_{m,n}^{(a)}+2H_n^{(s)}=\frac{i\zeta}{\omega\mu_o}div_S\left(grad_S\varphi^{(b)}-grad_S\varphi^{(a)}\right)$$

$$H_{m,n}^{(b)}-H_{m,n}^{(a)}=\frac{i\eta}{\omega\mu_o}div_S\left(2\mathbf{H}^{(s)}+grad_S\varphi^{(a)}+grad_S\varphi^{(b)}\right) \quad (3)$$

where μ_o the permeability of the surrounding region (air), and $\boldsymbol{H^{(s)}}$ is external source field (computed by the Biot-Savart law) and $\boldsymbol{H_m}$ is the reduced curl-free field, whose tangential component on the plane of the shield can be expressed introducing the reduced scalar potential φ. The terms ζ and η include the characteristics of the shield material, such as μ_p, σ_p and the thickness (d). Equations (3) are discretized introducing a 2D finite element mesh (M triangular elements) on the shield surface; they are completed with the 3D integral equations describing the field in the open-boundary air region where the sources are placed.

EXPERIMENTS

Due to the laboratory limitations for the excitation current, a sinusoidal excitation current reduced to 40 A (reduction factor ~500 with respect to the actual equipment) is used both in the simulation and in the experiment. In the experimental setup, the PC based data acquisition system measures the current in the excitation coil and calculates the required current in the active shield. The magnetic induction near the induction heater is measured by a 3D probe with sensitivity 1V/10μT and frequency range 50 Hz - 100 kHz.

RESULTS

Fig. 3 compares the measurements with the numerical results obtained by the two numerical procedures described above. It is shown that the deviations of both the FEM and the FEM-BEM curve to the measurements are of the same magnitude, which means that both models suffer from similar discretization errors. With only a passive shield, the average relative error to the measurements is 8% for FEM, and 10% for FEM-BEM. With passive and active shield, this error is 31% resp. 26%. Resulting average B_{avg} in subdomain D is 27.5 nT, about 20 dB less than B_{avg} without shields (261 nT).

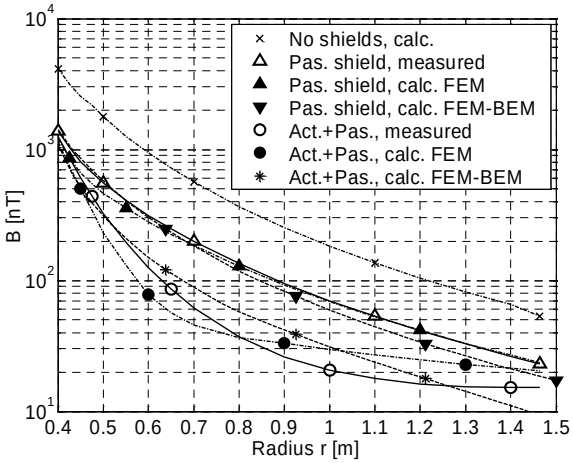

Fig. 3. Simulation and experimental results, 1 kHz

REFERENCES

[1] ICNIRP-Guidelines, "Guidelines for limiting exposure to time-varying electric, magnetic, and electromagnetic fields (up to 300 GHz)," *Health Physics*, Vol. 74, pp. 494-522, 1998.

[2] R.B. Schulz et al., "Shielding theory and practice," *IEEE Trans. Electromagn. Comp.*, Vol. 30, pp. 187-201, 1988.

[3] P. Girdinio and M. Nervi, "Techniques for the automatic optimization of active shields," *COMPEL*, Vol. 20, pp. 732-739, 2001.

[4] I. Mayergoyz, "Nonlinear Diffusion of Electromagnetic fields," Academic Press, London, 1998.

[5] L. Krahenbuhl and D. Muller, "Thin layers in electrical engineering. Example of shell models in analyzing eddy currents by boundary and finite element methods," *IEEE Trans. Magn.*, Vol. 29, No. 2, pp. 1450-1455, 1993.

Finite Element Models for Superconductive Cables with Finite Inter-Wire Resistance

Herbert De Gersem, Thomas Weiland

Technische Universität Darmstadt, Computational Electromagnetics Laboratory (TEMF),
Schloßgartenstraße 8, D-64289 Darmstadt, Germany
Email: degersem/weiland@temf.tu-darmstadt.de

Abstract— **Time-varying magnetic fields penetrate superconductive coils due to the finite inter-wire resistance, causing eddy currents and losses. Such effects are considered in finite element magnet models without meshing the detailed coil geometry. Particular current distributions due to the twisting of the cable are considered.**

Introduction

To reduce operation costs, superconductive magnets are planned for the new accelerator facilities at the 'Gesellschaft für Schwerionenforschung' (GSI) in Darmstadt, Germany. During the ramping of the magnetic field, significant eddy current effects are generated in the coils of the magnet, causing additional losses. This paper introduces the eddy-current effects in superconductive cables due to the finite inter-wire resistance into finite element (FE) magnet models.

Cable Geometries

The considered dipole magnets contain sets of conductors arranged between the aperture and the iron yoke. Two superconductive cable types are considered. In the Nuclotron-type cable, the strands are twisted around an iron tube (Fig. 1), whereas in the Rutherford cable, the strands are arranged in two layers, twisted around the border of the cable and keystoned to provide a good fit to the magnet geometry (Fig. 2). Each strand is a copper wire in which superconductive filaments are embedded. Unless the filaments are saturated or eddy currents appear, all current flows through the superconductive filaments. Persistent currents arising in the filaments due to time-varying fields are simulated as in [1]. The configuration is protected against quenching by implementing a wire coating with relatively low resistance such that current can redistribute between adjacent wires. Due to this limited insulation, however, eddy currents migrate between different wires when submitted to an external time-varying magnetic field. The insulation of the windings is of a substantially higher quality and prevents current migration between different windings.

Due to the large differences in size, resolving the individual strands within a FE model of the magnet would lead to too large and ill-conditioned models. Though occurring at microscopic scale, cable eddy-current effects can not be neglected in the simulation of ramped superconductive magnets. In this paper, FE cable models are developed which accurately describe the cable behaviour and avoid the cable geometry to be considered in full detail.

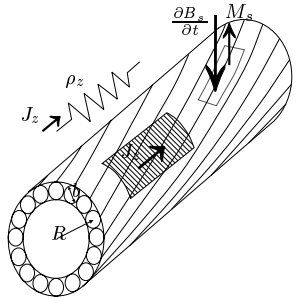

Fig. 1. Geometry of the Nuclotron-type cable.

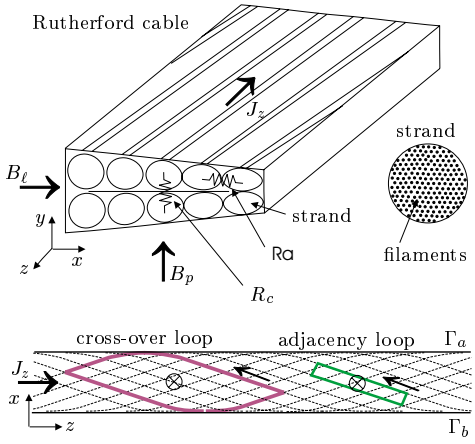

Fig. 2. Geometry of the Rutherford cable.

Finite Element Magnet Model

2D FE models of the superconductive dipole magnets are constructed based on

$$-\frac{\partial}{\partial x}\left(\nu\frac{\partial A_z}{\partial x}\right)-\frac{\partial}{\partial y}\left(\nu\frac{\partial A_z}{\partial y}\right)+\sigma\frac{\partial A_z}{\partial t}=J_s \qquad (1)$$

where A_z is the z-component of the magnetic vector potential, ν the reluctivity, σ the conductivity and J_s the source current density. The third term in (1) represents the eddy current effects and is further specified below. The discretization of (1) by linear FE shape functions $N_i(x,y)$

H. De Gersem is working in the cooperation project "DA-WE1 (TEMF/GSI)" with the "Gesellschaft für Schwerionenforschung (GSI)", Darmstadt.

reads

$$\sum_j k_{ij} u_j + \sum_j l_{ij} \frac{\partial u_j}{\partial t} = f_i \tag{2}$$

where k_{ij}, l_{ij} and f_i follow from applying the Galerkin approach to (1) and u_j denote the FE degrees of freedom.

Cable Eddy Current Model

An equivalent resistivity ρ_z of the wire-insulation composite can be determined based on measurements and homogenization techniques [2]. Cable eddy currents are incorporated in the FE model

$$\sum_j k_{ij} u_j + \sum_j l_{ij} \frac{\partial u_j}{\partial t} + g_{iq} \Delta V_q = f_i \tag{3}$$

where the unknowns ΔV_q represent the induced voltage drops across the wire coating in the z-direction, $1/\rho_z$ is introduced for σ,

$$g_{iq} = \int_{\Omega_q} \frac{\sigma_z}{\ell_z} N_i \, \mathrm{d}\Omega \, , \tag{4}$$

ℓ_z is the magnet length and Ω_q denotes the cross-sections of one of the n_w windings. Since there is no current migration between different windings, the netto eddy current through each winding vanishes, which corresponds to n_w constraints

$$\int_{\Omega_q} \left(\frac{\sigma_z}{\ell_z} \Delta V_q - \frac{1}{\rho_z} \frac{\partial A_z}{\partial t} \right) \mathrm{d}\Omega = 0 \tag{5}$$

added to (3). Although the modeling of the individual strands is avoided, each winding has to be meshed to resolve ΔV_q. The constraints (5) can also be applied in a weak form avoiding the modelization of individual windings [3]. In the magnet coils, an additional, non-matching FE mesh is built with elements which are larger than Ω_q but have the same form. The voltage drop $\Delta V(x, y)$ is discretized in terms of FE shape functions defined on the additional mesh instead on the individual windings. This procedure offers a sufficient accuracy at a substantially lower computational cost.

Cable Magnetization Model

The cable eddy current effect can also be represented analytically by a magnetization

$$\mathbf{M} = -\tau_{\mathrm{cable}} \frac{\partial \mathbf{B}}{\partial \mathbf{t}} \tag{6}$$

which depends on the incident magnetic field $\mathbf{B}$ and a time constant τ_{cable} determined by ρ_z and the cable geometry [2]. The magnetization due to the induced eddy currents is introduced as a current sheet at the surfaces Γ_p where the representative incident time-varying magnetic fields are considered:

$$\sum_j k_{ij} u_j + \sum_j m_{ij} \frac{\partial u_j}{\partial t} = f_i \tag{7}$$

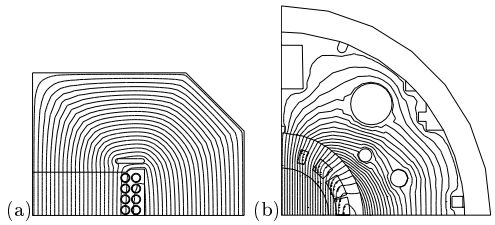

Fig. 3. (a) Dipole magnetic fields in (a) the Nuclotron magnet and (b) the $\cos\phi$-type magnet.

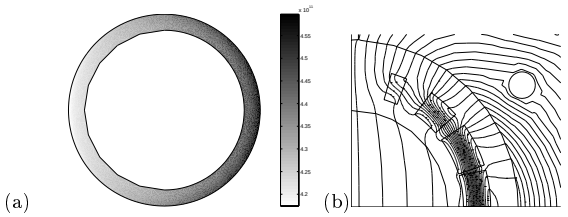

Fig. 4. (a) Eddy-current distribution of the Nuclotron cable and (b) magnetization due to cross-over eddy currents in the Rutherford cable.

with the integrals

$$m_{ij} = \int_{\Gamma_p} \frac{\nu \tau_{\mathrm{cable}}}{d_{\mathrm{strand}}} N_i N_j \, \mathrm{d}\Gamma \tag{8}$$

and d_{strand} a characteristic strand diameter. Cross-over eddy currents, occurring in the case of multi-layer windings, follow closed loops spanning the entire cable cross-section (Fig. 2). As a consequence, they are coupled to a global incident magnetic flux rather than to a local field distribution. This effect can not be modeled by a local eddy-current model but is simulated by a cable magnetization model considering the control contours Γ_a and Γ_b.

Simulation Results

The eddy-current and magnetization cable models are applied to the magnets of the SIS100 and SIS200 synchrotrons, planned at the GSI (Fig. 3). Typical eddy-current distributions and resulting magnetizations are shown in Fig. 4. The cable models developed in this paper allow to compute the additional losses and the deterioration of the aperture field during the ramping of the magnets.

Conclusions

Eddy currents induced by time-varying magnetic fields in superconductive cable can be modeled in a overall FE magnet model without meshing the individual windings.

References

[1] C. Völlinger, M. Aleksa, and S. Russenschuck, "Calculation of persistent currents in superconductive magnets," *COMPEL*, vol. 20, no. 2, pp. 562–569, 2001.

[2] A.P. Verweij and H.H.J. ten Kate, "Coupling currents in Rutherford cables under time varying conditions," *IEEE Transactions on Applied Superconductivity*, vol. 3, no. 1, pp. 146–149, Mar. 1993.

[3] H. De Gersem and K. Hameyer, "A multi-conductor model for finite element eddy current simulation," *IEEE Transactions on Magnetics*, vol. 38, no. 2, pp. 533–536, Mar. 2002.

Optimal Parameters of Transversal Flux Inductors

Fireteanu V.[*], Paya B.[**], Popa M.[***], Tudorache T.[*]
[*]POLITEHNICA University of Bucharest , 313 Splaiul Independenței,
Bucharest, Romania, E-mail adress: firetean@electro.masuri.pub.ro
[**] Electricite de France - R&D Division, Route de Sens-Ecuelles,
France, E-mail adress: Bernard.Paya@edf.fr
[***] University of Oradea, 5 Armatei Romane, Oradea, Romania
E-mail adress: mpopa@uoradea.ro

***Abstract* — This paper deals with the evaluation of optimal values of main parameters of transverse flux inductors, able to ensure a compromise between the system efficiency and the transversal uniformity of sheet heating.**

The decrease of frequency and pole pitch length and the increase of air-gap thickness determine the improvement of transversal heating uniformity, but the efficiency of the induction heating decreases. Optimal values of frequency, pole pitch length and air-gap thickness are evaluated, using both deterministic and stochastic optimization methods.

Introduction

Optimal design in engineering supposes a good understanding of optimization methods and of the phenomena involved in the device operation [1]. The optimizations of transverse flux induction heating systems (TFIH) have been mainly focused on the transversal non-uniformity of temperature across the sheet width [2].

This paper proposes the evaluation of optimal parameters of the inductor that ensure a compromise between a high value of induced power and a reduced non-uniformity of transversal profile of power density.

Transversal Profile of Power Density. Parameters of Influence

The power volume density in a sheet heated in transverse flux, Fig. 1, is very non-uniform, vanishing in three zones of the sheet on a pole pitch length. The mean value of this density, *pjmean*, characterizes the heating efficiency in the sense that if this density increases, the TFIH dimensions for imposed value of total inductor power decrease.

If *pjint* is the integral of the volume density over a pole pitch length along Ox coordinate, Fig. 1, the transversal profile of the induced power is defined by the function:

$$P(y/b)=[pjint(y/b)-pjint(0)]/pjint(0) \qquad (1)$$

This function, Fig. 2, provides an image of the transversal temperature non-uniformity of the sheet at the end of the heating. This non-uniformity can be characterized by the criterion:

$$ecart = max\{P(y/b)\} - min\{P(y/b)\} \qquad (2)$$

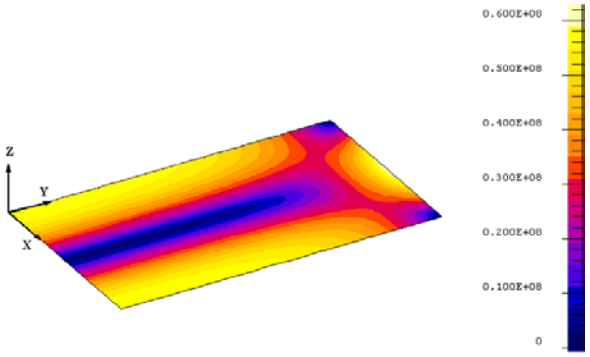

Fig. 1. Color shaded plot of eddy currents on a pole pitch length

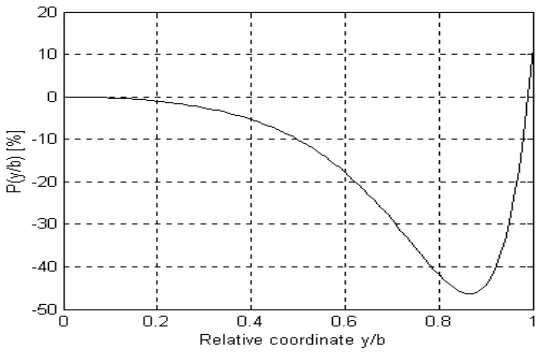

Fig. 2. Transversal profile of induced power density

A simple model of eddy current computation in reference [3] offers the expressions of the transversal profile *P(y/b)* and of the *pjmr* criterion that is the relative value of *pjmean* with respect to the reference value for $b \to \infty$.

The criteria *pjmr* and *ecart* depend on the three parameters characterizing the sheet, thickness *a*, width *2b*, and resistivity ρ and on the other three parameters, characterizing the inductor, pole pitch length τ, frequency f, and air-gap thickness *g*. The product $(a \cdot f)$ between the sheet thickness and the frequency is an invariant of the function *P(y/b)*.

For given values of parameters *a*, *2b* and ρ, the heating uniformity increases (the criterion *ecart* decreases) if: pole pitch length decreases, frequency decreases and air-gap thickness increases. In this case the criterion *pjmr* decreases,

and also the TFIH efficiency, so that for a given power level, the dimensions of the inductor increase. Consequently, the variations of the *ecart* and *pjmr* criteria with respect to the parameters of the inductor are contradictory.

Optimal Values of Inductor Parameters

The optimization of the TFIH inductor with respect to τ, f and g parameters in this section uses the following objective function:

$$Fobj\gamma(f, \tau, g) = \gamma \cdot Fecart + (1-\gamma) \cdot Fpj \ , \quad \gamma \in [0, 1] \qquad (3)$$

The quantities:

$$Fecart = (ecart - ecart\_min)/(ecart\_max - ecart\_min),$$
$$Fpj = (pjmr\_max - pjmr)/(pjmr\_max - pjmr\_min),$$

are dependent on the minimum and maximum values of *ecart* and *pjmr* criteria in the optimization domain of $Fobj\gamma$.

A small value of weighting coefficient γ means that a higher mean value of induced power is more important than a more uniform transversal profile of heating.

For $a = 2\ mm$, $2b = 1.0\ m$ and $\rho = 0.035\ \Omega mm^2/m$, optimizations were performed with Simplex (SS) and Random Search (RS) methods for $\tau \in \{0.2, 1.5\}\ m$, $g \in \{0.05, 0.2\}\ m$ and $f \in \{50, fls\}\ Hz$, where $fls = 8855\ Hz$ is an upper limit defined by the known condition $a/\delta < 2$.

The minimum of *Fobj0* (objective function for $\gamma = 0$) corresponds to maximum values of frequency and pole pitch length and to minimum value of air-gap thickness. For the most uniform heating, the minimum of the objective function *Fobj1* is reached to the opposite limits of the searching domain of parameters.

The two minima of the objective function *Fobj0.6* are very close to each other, but the two "optimum points" are however different: $f_{o1} = 3.52\ kHz$, $\tau_{o1} = 1.5\ m$ and $g_{o1} = 0.2\ m$ with SS method and $f_{o2} = 3.44\ kHz$, $\tau_{o2} = 1.5\ m$ and $g_{o2} = 0.195\ m$ with RS method; at least one, if not both solutions, are local minima. Two iso-value lines very close to each other and to the global minimum are represented in Figure 3. Several minima, e.g. A, B, C, D, Fig, 3, placed along a line, for which the values of the objective function differ only at the seven digit, were obtained with RS method. The function *Fobj0.6* has a large number of local minima, very close to the global one. In such cases, it is important that the optimization process emphasizes this property of the objective function. The use of stochastic methods, respectively of combinations between deterministic and stochastic methods is more adequate than the optimization with only one deterministic method.

Two minima of *Fobj0.9* were found: $Fobj\_min1 = 0.0999$, for $f_{o1} = 0.21\ kHz$, $\tau_{o1} = 0.2\ m$ and $g_{o1} = 0.12\ m$, with SS method and $Fobj\_min2 = 0.0976$, for $f_{o2} = 0.066\ kHz$, $\tau_{o2} = 1.5$ and $g_{o2} = 0.146\ m$, with RS method.

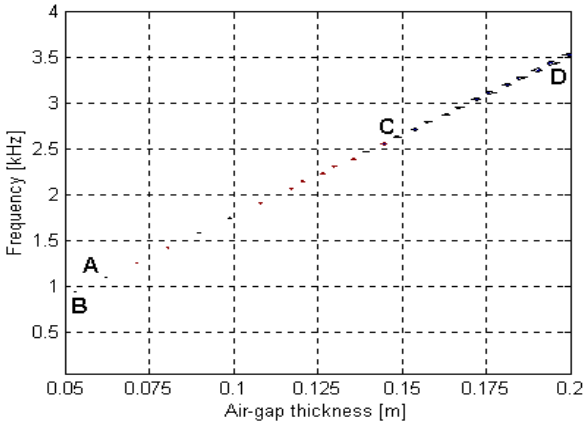

Fig. 3. Iso-value lines of objective function *Fobj0.6* for $\tau = 1.5\ m$

On the iso-value lines graph of *Fobj0.9* for $g = 0.3\ mm$, Fig. 4, were pointed the SS solution, a local minimum for $\tau = 0.2\ m$, and the better RS solution, to the other extremity, *1.5 m*. Consequently, when the objective function has many local minima with values close to one another, the optimization with stochastic methods is more appropriate.

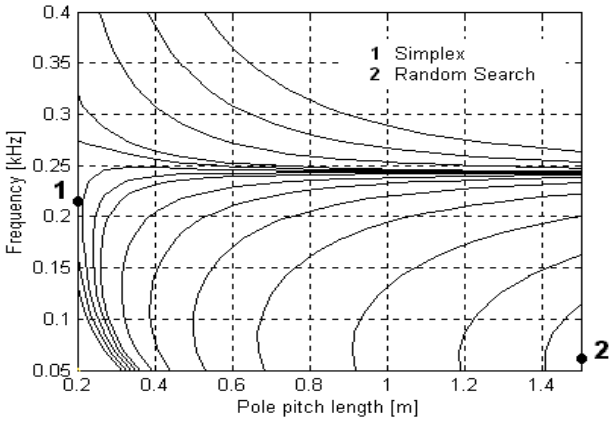

Fig. 4. Iso-value lines of objective function *Fobj0.9* for $g = 0.13\ m$

The extended version of the paper will include the study on the non-uniformity of transversal profile as effect of transversal variation of the air-gap and other optimization results.

References

[1] P. Neittaanmaki, M. Rudnicki and A. Savini, *Inverse Problems and Optimal Design in Electricity and Magnetism*, Clarendon Press, Oxford, 1996.

[2] P. Di Barba, F. Dughiero, S. Lupi and A. Savini, "Optimal shape design of devices and systems for induction heating: methodologies and applications", *Proc. of HIS–01 Seminar*, Padua, September 2001.

[3] V. Fireţeanu, Y. Neau, B. Paya and T. Tudorache, "Parameters of transversal non-uniformity of induced power in transverse flux induction heating", *Proc. of OPTIM'2002 Conference,* Brasov, May 2002

Three-dimensional Optimization of Modular Toroid-type SMES

Chang-Hwan Im*, Hyun-Kyo Jung*, Ji-Hoon Kim*, Song-Yop Hahn*, Sung-Chin Hahn**
*School of Electrical Engineering, Seoul National University, San 56-1, Shillim-dong, Kwanak-gu, Seoul, 151-742, KOREA
**Department of Electrical Engineering, Dong-A University, Pusan, 604-714, Korea
e-mail : ichich2@snu.ac.kr

***Abstract* — In this paper, modular toroid-type SMES was optimized based on 3-D magnetic field analysis technique. Stored magnetic energy was calculated by a recent flux linkage calculation technique developed by the authors. The affection of the mesh size on the accuracy of the calculated flux linkage was also investigated. (1+1) evolution strategy was applied to the optimization, and the optimized results were verified by 3-D finite element calculation.**

INTRODUCTION

Superconducting magnetic energy storage (SMES) has been attracted much interest to improve power quality issues. Generally, there are three types of SMES – solenoid, multiple solenoid, and toroid [1]-[3]. Each shape has its pros and contras. Solenoid type coils are simple to design and easy to manufacture, but there is nothing to prohibit or confine stray fields. Multiple solenoid coils show very good characteristics on stray field, but it has very poor energy density. Toroid-type can be an alternative proposal for this problem. A perfect toroid coil makes no stray field. The field is confined inside the coil, but it is very hard to realize such kind of coil. Instead, coils wound in pancake or stacked pancake coils can be configured to simulate similar effect. Toroid coils require more wire than solenoid coils but less wire than multiple solenoid coils [4]. In this research, the toroid-type was selected in consideration of its installation environment with very strict restriction of stray field emission.

To design the modular toroid-type SMES, 3-D magnetic field analysis is unavoidable. Biot-Savart's law with line element modelling can be a possible solution, but then it is very hard to calculate stored magnetic energy accurately. Hence, in this paper, real coil geometry was modelled solidly, and 3-D automatic mesh generator was used to generate tetrahedral elements. A recent flux linkage calculation technique developed by the authors was used to calculate self- and mutual- inductances of each module [5]. Especially, in this paper, the influence of the mesh size on the accuracy of the calculated flux linkage was investigated, which was not considered systematically in the previous study. Stray magnetic field and critical magnetic flux density were calculated by directly applying Biot-Savart's law.

(1+3) evolution strategy (ES) was used for the coil optimization, of which the objective was to minimize the total conductor length. The total scheme was applied to 100-kJ HTS SMES system with 8 modules, and the results were verified by 3-D finite element method (FEM).

METHODS

A. Flux Linkage Calculation for Solidly Modeled Coil

In this section, only resultants are dealt with and a detailed induction will be contained again in the full paper. The flux linkage in a solidly modeled coil can be calculated by

$$\lambda = \sum \mathbf{A}^{(e)} \cdot \mathbf{I}^{(e)} \, V^{(e)} \, N / S_{cross} \qquad (1)$$

where $\boldsymbol{A}^{(e)}$ is average vector potential of an element (e), $\boldsymbol{I}^{(e)}$ the current direction vector in the element, $V^{(e)}$ volume of the element, N is the total number of turns, and S_{cross} uniform cross-sectional area [5].

Fig. 1(a) shows a model to investigate the influence of mesh size on the accuracy of the flux linkage calculation. When compared to an analytic solution, it was verified that the calculated flux linkage was very accurate with just 1.5% error, even when the coarsest mesh in Fig. 1(b) was used. Detailed results will be shown in the full paper.

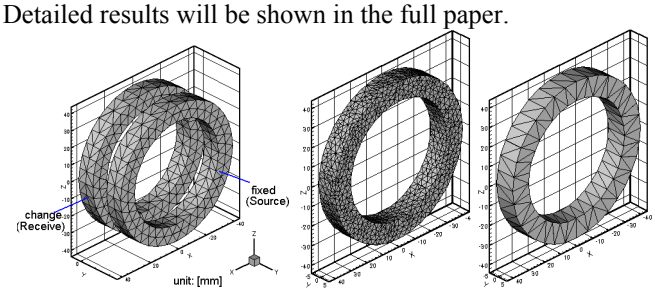

(a) Model (b) Finest and coarsest mesh

Fig. 1. Model to check influence of mesh size on the calculation accuracy

B. Calculation of Objective Function and Constraints

The objective function and constraints are defined as

$$F = w_1 \, l_c + w_2 \, | E - E_{ref} \, | \qquad (3)$$

$$B_t \le 5T \;,\; B_p \le 1T \;,\; B_s \le 10^{-4} \, T \qquad (4)$$

where l_c is total conductor length, E stored magnetic energy, E_{ref} targeted energy, B_t tangential magnetic field, B_p perpendicular magnetic field, B_s stray field at 5m from center axis, and w_1 and w_2 are weighting factors to normalize two different objective functions. The limit values of tangential and perpendicular magnetic field are determined considering

given condition (current 150 ~200A, temprature 20K). Stored magnetic energy is calculated by using self and mutual inductances of each module which can be calculated by applying (1). Magnetic flux density and magnetic vector potential are calculated by using Biot-Savart's law.

C. Optimization Strategy

To design a 100kJ SMES system, 3 design variables were considered as shown in Fig. 2 – current of a conductor, inner radius of the module, and the number of conductor turns. Because the width and thickness of a superconducting tape has a fixed value (32.1mm and 0.4mm), outer radius of a module can be evaluated using the number of turns.

Fig. 3 shows a flow chart of whole optimization process. As seen in the figure, (1+3) ES was used for the optimization strategy. If calculated magnetic field at some critical points violate constraints, penalty terms are imposed on the objective function to exclude those solutions.

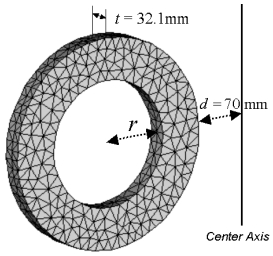

Fig. 2. Design variables of SMES coil. The distance of a module from a center axis is fixed as 70mm, considering supporting structure.

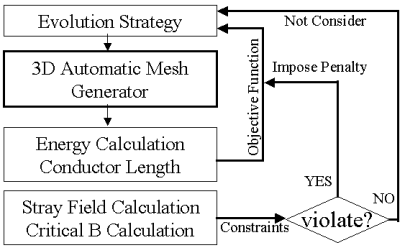

Fig. 3. Flowchart for whole optimization process

OPTIMIZATION RESULTS

Table I shows upper and lower limits of design variables and the optimized ones. Table II shows the optimized physical quantities. Fig. 4 shows the optimized SMES. The optimized quantities were verified by using 3-D FEM. The stored energy calculated by FEM was 102.5kJ, which agrees well with optimized one. Fig. 5 shows the perpendicular magnetic field distribution of a module obtained by FEM calculation, which also coincide with the pridicted result.

TABLE I. LIMITED AND OPTIMIZED VALUES OF DESIGN VARIABLES

Variables	Maximum	Minimum	Optimized
I [A]	200	150	157
r [mm]	150	100	129.7
N (×6)	150	220	189

TABLE II. OPTIMIZATION RESULTS

Stored energy [kJ]	999.85
Conductor length [km]	9.536
Maximum tangential field [T]	2.316
Minimum perpendicular field [T]	0.997
Stray field at 5m from center axis [T]	6.7×10^{-8}

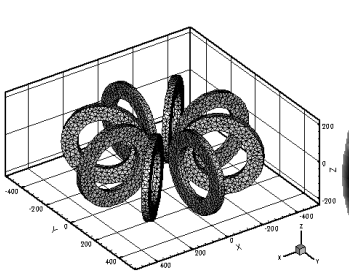

Fig. 4. Optimized SMES

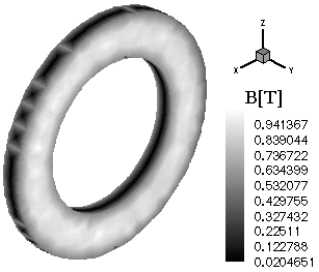

Fig. 5. Pependicular field (FEM)

CONCLUSION

In this paper, modular toroid-type SMES was optimized using 3-D magnetic field analysis technique and constrained optimization algorithm. Stored magnetic energy was calculated by new flux linkage calculation technique. Optimized results were verified by 3-D FEM.

ACKNOLOGEMENT

This work was supported by KEPCO as the part of 'Development of Customized Power Quality Service Systems for 21st Century.'

REFERENCES

[1] G. Schonwetter, "SMES solenoids with reduced stray field, " *IEEE Trans. Magn.*, vol. 30, pp. 2636-2639, July 1994.

[2] M. K. Abdelsalam, "Micro SMES magnet configuration for reduced stray field applications," *IEEE Trans. Appl. Superconduct*., vol. 5, pp. 333-336, June 1995.

[3] U. Brammer and H. W. Lorenzen, "Magnetic shielding of small high power SMES," *IEEE Trans. Appl. Superconduct*., vol. 5, pp. 329-336, June 1995.

[4] Ji-Hoon Kim, Seung-Yong Hahn, Chang-Hwan Im, Jae-Kwang Kim, Hyun-Kyo Jung, and Song-Yop Hahn, "Design of a 200kJ HTS SMES System," *IEEE Trans. Appl. Superconduct*., vol. 5, pp. 329-336, 1995.

[5] Chang-Hwan Im, Hyun-Kyo Jung, and Hong-Kyu Kim, "Novel Method to Calculate Flux Linkage for 3-D Finite Element Analysis, " *The Tenth Biennial IEEE Conference on Electromagnetic Field Computation (CEFC 2002)*, pp. 5, Perugia, Italy, 2002.

Application of Conformal FIT for Eddy Current Calculation in Coils of a Superconducting Magnet System

Jacek Junak[1], Ursula van Rienen
Rostock University, Institute of General Electrical Engineering
Albert-Einstein-Str. 2
D-18051 Rostock, Germany
jacek.junak@etechnik.uni-rostock.de, ursula.van-rienen@etechnik.uni-rostock.de

***Abstract* - The stellarator Wendelstein 7-X is a steady-state fusion experiment being built at the Greifswald Branch Institute of the Max-Planck-Institut für Plasmaphysik (IPP). During an emergency discharge of the superconducting magnet system eddy currents are generated in the steel case of the coils. Knowledge of the eddy currents' distribution is important for a reliable operation of the system. We apply a method of calculating the eddy currents based on the Finite Integration Technique with Perfect Boundary Approximation Technique. A description of the magnet system, of principles of the applied method, the model and example results are presented in the paper.**

INTRODUCTION

Intensive research on thermonuclear fusion led to the construction of stellarator type reactors. The stellarator should demonstrate the steady-state operation in contrast to previous constructions of tokamak type. The new stellarator Wendelstein 7-X is being built at the Greifswald Branch Institute of IPP [1] to prove the suitability for power plants. This current large fusion experiment results from investigations leading to a new concept for an optimal distribution of the magnetic field inside the plasma vessel [2].

The required distribution of the magnetic field is achieved by a set of non-planar coils – Fig. 1. During an emergency discharge of the magnet system eddy currents are generated in its metal parts. This concerns the steel case of the coils and also the plasma vessel and the shields. The generated eddy currents result in additional mechanical stresses and also in local overheating. In order to assure the reliability of the overall system the knowledge on the eddy current distribution is extremely important.

Fig. 1. Sketch of the non-planar coils of the Wendelstein 7-X stellarator (courtesy of IPP)

[1] Work supported by Max-Planck-Institut für Plasmaphysik, Germany

Due to the non-planar construction of the magnet system computations of the eddy currents by means of analytical methods or complete conventional numerical methods are hardly possible. There are examples of a numerical approach for eddy current computation in the plasma vessel [3]. The aim of our work is to calculate the eddy current distribution along the steel case of the coils. Herein we present a method based on Finite Integration Technique (FIT) [4]. According to the non-planar construction of the magnet system additional advantages can be achieved combining FIT with the Perfect Boundary Approximation Technique (PBA), also denoted as Conformal FIT (CFIT) [5]. This method presented here is one of several numerical approaches being in the scope of our project.

DESIGN OF THE MAGNET SYSTEM

The superconducting magnet system of the Wendelstein 7-X stellarator is presented in Fig. 1. It consists of 50 non-planar coils and 20 planar coils [2]. The major radius of the coil system is 5.5 m. The averaged coil radius is approx. 1.5 m. The system has a fivefold symmetry, which in consequence leads to five different types of the non-planar coils. The system is designed to generate a magnetic flux of 3 T at a current flow of 16 kA in each coil.

The coil's cross-section is presented in Fig. 2.a. Each coil embraces winding pack, the steel case and the intermediate embedding. A winding pack contains 108 conductor turns. The conducting wire of litz type is wound by 243 copper stabilized NbTi strands of 0.57 mm diameter.

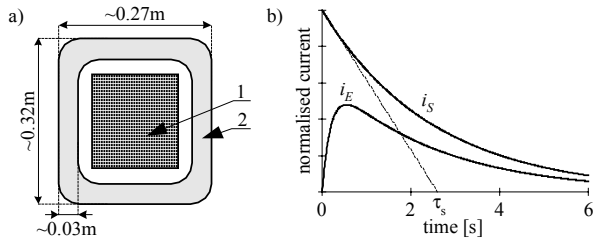

Fig. 2. Cross-section of the coil (a): winding pack (1) and steel case (2); Imposed current in coil i_S and eddy current in steel case i_E over time (b)

EMERGENCY TURN-OFF OF THE SYSTEM

Due to the special construction of the winding pack the eddy currents in the coil need not to be investigated. The eddy currents flow only in the steel case of the coil.

During emergency turn-off of the system (quench protection) the current in the coil decays exponentially as it is depicted in Fig. 2.b. The time constant τ_s varies from 2 to 5 seconds.

Changes in the eddy current value i_E over the time are illustrated in Fig. 2.b. Generally, due to decreasing changes in the driving current i_S the value of eddy currents i_E also decreases over time. However, in order to satisfy the continuity condition, at the beginning of the process the value of the eddy currents rises. Most important is the maximal value of the eddy currents. Since it is a very slowly varying process, the skin depth is always larger than the thickness of the steel case and therefore the skin effect could be neglected.

PRINCIPLES OF THE METHOD

Ampère's and Faraday's law for quasistatic magnetic fields are given by equations (2) and (3), respectively.

$$\operatorname{curl} \mathbf{H} = \mathbf{J}_S + \mathbf{J}_E, \tag{2}$$

$$\operatorname{curl} \mathbf{E} = -\frac{\partial \mathbf{B}}{\partial t}, \tag{3}$$

where $\mathbf{J}_S$ is the impressed current density and $\mathbf{J}_E$ is the current density of conducting regions (eddy currents).

The material relations are expressed as follows:

$$\mathbf{B} = \mu \mathbf{H}, \quad \mathbf{J}_E = \sigma \mathbf{E}. \tag{4}$$

The Finite Integration Technique (FIT) is a discretisation scheme for Maxwell's equations in their integral form applied for elementary volumes named grid G and dual grid $\widetilde{G}$ - Fig. 3.a [4]. As a result of this method equations (2) and (3) can be written in discrete form:

$$\tilde{\mathbf{C}}\hat{\mathbf{h}} = \hat{\tilde{\mathbf{j}}}_S + \hat{\tilde{\mathbf{j}}}_E, \tag{5}$$

$$\mathbf{C}\hat{\mathbf{e}} = -\frac{\partial \hat{\tilde{\mathbf{b}}}}{\partial t}. \tag{6}$$

The discrete material relations are expressed by:

$$\hat{\tilde{\mathbf{b}}} = \tilde{\mathbf{M}}_\mu \hat{\mathbf{h}}, \quad \hat{\tilde{\mathbf{j}}}_E = \mathbf{M}_\sigma \hat{\mathbf{e}}. \tag{7}$$

Substituting (7) into (5), next differentiating (5) and taking into account (6) yields:

$$\mathbf{M}_\sigma \frac{\partial \hat{\mathbf{e}}}{\partial t} + \tilde{\mathbf{C}}\tilde{\mathbf{M}}_\mu^{-1}\hat{\mathbf{e}} = -\frac{\partial \hat{\tilde{\mathbf{j}}}_S}{\partial t}. \tag{8}$$

Equation (8) can be solved numerically. Using (7) the distribution of eddy currents is achieved.

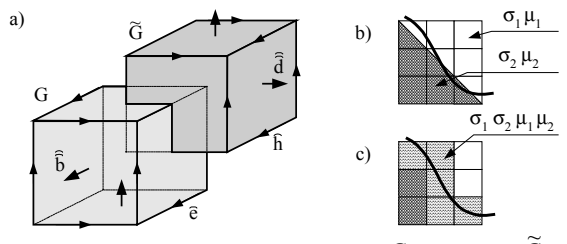

Fig. 3. Elementary volumes of classical FIT: grid G and dual grid $\widetilde{G}$ (a); Boundary approximation in classical FIT (b) and CFIT (c)

FIT is most widely used on Cartesian grids. Such grid is generally not too suitable for a complicated 3D geometry like non-planar coils. The grid does not exactly reflect the shape of the model as it is shown in Fig. 3.b. To overcome that problem Conformal FIT has been introduced [5]. This technique uses sophisticated algorithms to improve the grid approximation in non-homogeneous material – Fig. 3.c.

THE MODEL AND EXAMPLE RESULT

Calculations were done for one coil of the magnet system. The mesh including CFIT matrices was prepared in CST MicrowaveStudio™ [6] and next the transient analysis was carried out using MAFIA's TL3 module [6]. The shape of the coil was approximated by a polygon as it is shown in Fig. 4.a. The conductor is modelled by a filament centrally situated in the cross-section of the steel case. Fig. 4.b presents an arrow plot of the eddy currents in a cross-section of the coil.

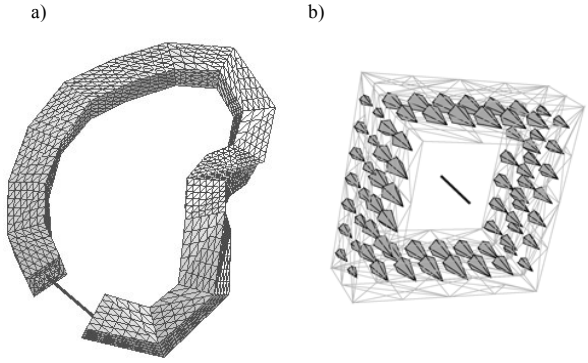

Fig. 4. The model of the coil (a) and an arrow plot of the eddy currents in a cross-section of the steel case (b)

CONCLUSIONS

Conformal FIT can be used for calculation of the eddy current distribution in non-planar coils of a magnet system. Our further work focuses on introducing the influence of other coils on the eddy current distribution in the examined coil. Due to the low impact of eddy currents on the magnetic field distribution inside the stellarator an indirect method based on Biot-Savart's law can be applied.

REFERENCES

[1] http://www.ipp.mpg.de

[2] J. Sapper and W7-X team, "The superconducting magnet system for the Wendelstein 7-X stellarator", *Superconducting Sci. Technology,* No. 13, pp. 516-518, 2000.

[3] A. M. Miri, N. A. Riegel, C. Meinecke, C. Sihler and F. Schauer, „Investigation of the transient processes and forces in metallic environments of large superconducting magnets by an optimised finite element approach", *IEEE Transactions on Energy Conservation*, vol. 15, No. 4, pp. 464-469, December 2000.

[4] T. Weiland, "Time domain electromagnetic field computation with finite difference methods", *International Journal on Numerical Modelling: ENDF*, vol. 9, pp. 259-319, 1996.

[5] M. Clemens and T. Weiland, "Magnetic field simulation using conformal FIT formulations", *IEEE Transactions on Magnetics*, vol. 38, No. 2, pp. 389-390, March 2002.

[6] CST GmbH, Bad Nauheimer Str.19, D-64289 Darmstadt. Germany.

Analysis and Optimized Design of Magnet for Micro SMES with Multiple Parallel Solenoids

K. R. Shao, S. L. Hung, L. R. Li
R & D Center for Electric Power Superconductivity, Huazhong Univ. of Sci. & Tech., Wuhan, 430074 China
J. D. Lavers
Department of Electrical & Computer Engineering, University of Toronto, Toronto, M5S 3G4 Canada

***Abstract*—Micro Superconducting Magnetic Energy Storage (SMES) system is becoming a powerful tool for application in power system. Nowadays, devices include active shielding system instead of passive ferromagnetic shields. This calls for sophisticated analysis and design techniques able to provide satisfactory performance in terms of stored energy efficiency, reduced stray field and/or minimal superconductor's volume. In this paper the features of an actively shielding system, the multiple parallel solenoid configurations, for superconducting magnets are analyzed and the results of their corresponding stray fields are compared. Two optimization strategies are briefly presented. The results using the proposed optimization strategies for magnet systems of energy capacity of 1MJ, 5MJ and 10MJ are given, respectively.**

INTRODUCTION

Typical applications of micro scale SMES in power system are protection of critical user facilities against voltage drops or short-term power delivery interruption. The most critical constraints on their design are the level of the stray field in the surrounding region. This is not only for the human and apparatus safety considerations, but also for the superconductor quench conditions. Because the micro scale SMES system often operates under dynamic state the transient stray field will induce eddy currents in the cryostat walls and other metallic parts, which produce additional Joule losses.

Previous investigations on active shielding of large scale SMES system have proved to be successful in reducing the stray field. It was shown that the stray field of a solenoidal SMES could be diminished by adding shielding solenoids under the condition that the sum of the magnetic dipole moments of all coils equals zero.

In this paper, the features of actively shielding systems, the multiple parallel solenoid configurations, for superconducting magnets are analyzed and the results of their corresponding stray fields are compared. Two optimization strategies are presented, one of which is to optimize the structure parameters for the coils to minimize the volume of the superconductor. The other one is to optimize the efficiency of the storage energy and minimize the stray field under a given amount of energy capacity. As an example, the field distribution for a magnet system of an energy capacity of 10MJ is analyzed in detail. The results using the proposed optimization strategies for magnet systems of energy capacity of 1MJ, 5MJ and 10MJ are given, respectively.

ANALYSIS OF THE STORED ENERGY AND THE STRAY FIELD

A. Single solenoid

Fig. 1 sketches the section of simplest kind of solenoid, the notations are indicated in the figure and its shape factors are defined as follows: [1]

$\alpha = R_o / R_i$, $\beta = l / R_i$.

The superconductor's volume $V = 2\pi \cdot R_i^3 \beta \cdot (\alpha^2 - 1)$, and at first sight it would appear that the best choice of α and β would be that which minimizes winding volume and thus the quantity of superconductor required. However this would neglect the influence of α and β on field uniformity, which is an important factor in determining the current-carrying capacity of the superconductor. The maximum field on the winding $\mathbf{B_m}$ determines the critical current density $\mathbf{J_c}$ in the winding, due to the quench condition that can be approximated by the equation in this work using NbTi superconductor: [2].

$$|\mathbf{J_c}| = (-6.4|\mathbf{B_m}| + 54.0)\ \mathrm{A/mm^2}. \quad (1)$$

The stored energy $E = 1/2 \cdot LI^2$, where L is the self-inductance of the coil, which can be readily calculated using numerical method and $I = J_c \cdot A$, where A is the area of cross-section of the coil. The stray field outside a solenoid coil can be expanded in a series of Legendre polynomials in cylindrical coordinate, and it will drop as R_p^{-3} (the observation point in Fig.1). [3] In this paper, we use a single integration method to calculate the stray field, since no ferromagnetic materials are present in the surrounding space.

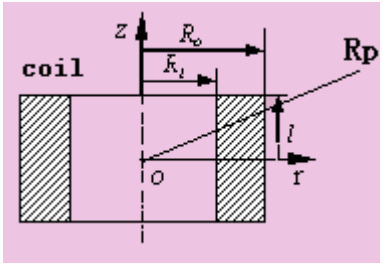

Fig. 1. Section of a single solenoid

B. Multiple parallel solenoids

The multiple parallel solenoid configurations are schematically shown in Fig. 2. Even number coils with same size are arranged in alternative magnetic moment direction.

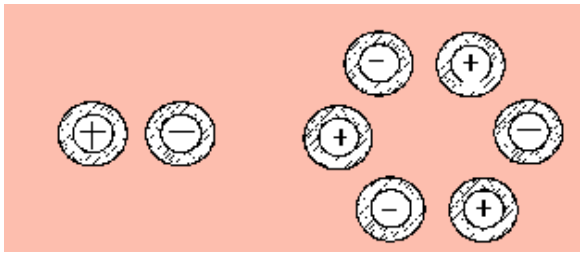

(a) Two-solenoid (b) Six-solenoid

Fig. 2. Multiple parallel solenoid configurations

The analysis in this circumstance is same as the single solenoid case except that:

- The superconductor's volume $V = 2\pi \cdot n \cdot R_i^3 \beta \cdot (\alpha^2 - 1)$, where n is the number of solenoids.
- The stored energy of whole system is sum of one for each individual coil which can be now expressed by:

$$E = 1/2 \cdot LI^2 + 1/2 \cdot I^2 \cdot \sum_{i=1}^{n-1} Mi, \quad (2)$$

where M_i denotes the mutual inductance between it and the surrounding coil.

- The maximum field B_m now is due to the coil's own current and that of the surrounding coils.

For comparison reason we analyze and calculate the field distributions of magnet system of an energy capacity of 10 MJ for single, two-solenoid and four-solenoid. The results shown in Fig. 3 clearly indicate that the multiple parallel solenoid configurations can greatly reduce the stray field outside the windows.

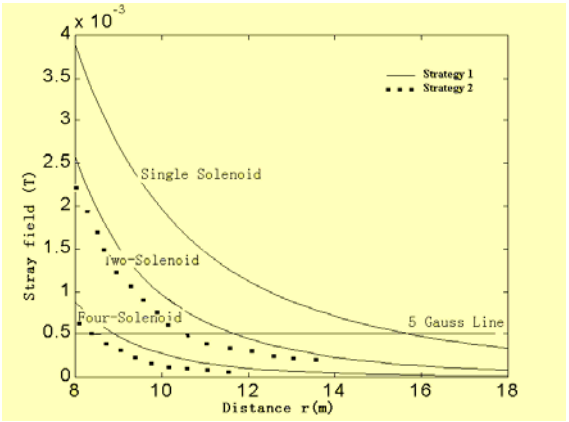

Fig. 3. Comparison of range 5 Gauss for different solenoid configurations

Optimization Strategies

Two possible strategies, both of which belong to the stochastic algorithm [4], could be pursued to design an optimized shielded micro SMES magnet.

A. Strategy 1-- Conjugate Gradient Strategy

The first search was evaluated using the Fibonacci section search along the direction of the gradient of the objective function. The subsequent search directions are found to be the conjugate direction. This optimization strategy is aimed to minimize the superconductor's volume, namely to optimum the magnet cost.

The objective function of this strategy is:

$$OF = 2\pi \cdot nR_i^3 \beta(\alpha^2 - 1) = \min., \quad (3)$$

subject to the following constraints:

- The stored energy in whole system should be rated capacity.
- The magnetic field must not violate the quench condition of superconductor.

The design variables are as follows:

$$(\alpha., \beta, G_{ap}[m], R_i[m], V[m^3], J_c[A \cdot m^{-2}])$$

B. Strategy 2-- Evolution Strategy

A (1+1) evolution strategy [4] with a maximum of 350 generations was applied to improve the quality and convergency of the solutions. This optimization strategy is aimed to improve the stored energy efficiency and to reduce the stray field of the system.

The multi-objective function is proposed as: [2]

$$OF = \frac{B_{stray}^2}{B_{norm}^2} + \frac{|E - E_{rate}|}{E_{rate}} = \min., \quad (4)$$

where E_{rate} denotes stored energy of the rated capacity, $B_{norm} = 0.5E - 3(T)$, indicates the stray field on the 5-gauss line shown in Fig. 3 and

$$B_{stray}^2 = \sum_{i=1}^{22} \left| \mathbf{B}_{\mathbf{stray_i}} \right|^2 / 22, \quad (5)$$

B_{stray_i} is evaluated along 22 equidistant points along line a and line b in [2].

Results

The results using the proposed optimization strategies for magnet systems of energy capacity of 1MJ, 5MJ and 10MJ will be given in detail in the full manuscript, where a novel conclusion different from the literature [5] will be presented.

References

[1] Maritin N. Wilson, *Superconducting Magnets*, Oxford: Clarendon Press, 1983, pp. 20-27.

[2] Ch. Maglel, G. Fuerntratt, I. Bardi, K.R. Richter, G. Schoenwetter, P. Alotto, G. Molinari, M. Repetto, "SMES Optimization Benchmark (Preliinary TEAM Workshop Problem 22)", Internet Edition: http://www-igte.graz.ac.at/team

[3] T. Hamajima, M. Shimada, S. Hanai, Y. Wachi, M. Tezuka and H. Takano, "SMES Coil Configurations with Reduced Stray Field", *IEEE Transactions on Applied Superconductivity,* Vol. 9, No. 2, pp. 346-349, June, 1999.

[4] Fletcher R. *Practical Methods of Optimization,* New York: J. Wiley & Sons, 1990

[5] M. K. Abdelsalam, "Micro SMES Magnet Configurations for Reduced Stray Field Applications", *IEEE Transactions on Applied Superconductivity,* Vol. 5, No. 2, pp. 333-336, June, 1995.

Current Distribution in a High Frequency Induction Coil

Bernard PAYA
Électricité de France, R & D Division
Centre des Renardières
F-77818 Morêt sur Loing CEDEX – France
bernard.paya@edf.fr

***Abstract*— This paper presents an efficient way to compute current distribution in a high frequency induction coil, using a surface impedance and magnetic reduced scalar potential formulation. This formulation naturally respect the Ampere's law. The validity domain is determined by comparing the skin depth to the other geometrical dimensions of the coil cross section. The current distribution computed using this method is compared to other classical approaches. Finally, we proved the impact of the current distribution in some industrial processes, specially when the load is closed to the coil.**

INTRODUCTION

When simulating an induction heating device, we often assume that the current distribution is uniform inside the coil region. We do not take into account the number of turns and the space between them. Sometimes, we only consider that the active part thickness is equal to the skin depth. The coil resistance is analytically evaluated. These assumptions are relevant if the heated load is far enough from the coil. In surface heat treatment such as contour hardening, the high frequency induction coil is so closed to the load that it may affect the current distribution in the coil and the load at the same time.

The paper presents a convenient way to compute current distribution in the coil using a surface impedance and reduced scalar potential formulation. We first examine the used formulation and evaluate its validity range. We then compare this approach with other 2D and 3D computations. Finally, we study a gear-wheel hardening to determine the effect of the non uniform current distribution on the induction heating.

THEORY

At high frequency level, the surface impedance is a convenient way to solve eddy current problems because it avoids very thin meshes just under the surface to take into account the skin effect. To control the total current I_0 flowing through each coil turn, we first design a current wire inside the coil cross section and evaluate the generated Biot and Savart magnetic field H_0. We then describe the surface impedance formulation using the reduced magnetic scalar potential ϕ_{red}. The magnetic field to be computed can so be written as :

$$\vec{H} = \vec{H}_0 + \overrightarrow{\text{grad}}\,\phi_{red} \tag{1}$$

This magnetic field naturally respects the Ampere's law. Indeed, if you consider a closed loop around a coil turn (Fig. 1), the magnetic field circulation can be calculated as :

$$\oint_\Gamma \vec{H}\cdot\vec{dl} = \oint_\Gamma \vec{H}_0\cdot\vec{dl} + \oint_\Gamma \overrightarrow{\text{grad}}\,\phi_{red}\cdot\vec{dl} = I_0 \tag{2}$$

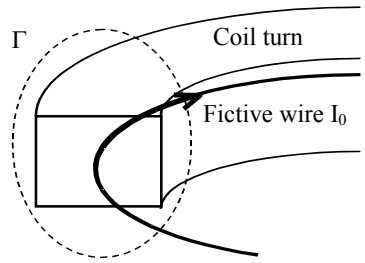

Fig. 1 : Fictive wire I_0 and loop Γ for Ampere's law

VALIDITY DOMAIN

The surface impedance model can be used only for a semi-infinite planar domain. Induction coils are made with a cylindrical or a rectangular copper tube for the water cooling. Validity domain with finite thickness or corner can be defined by comparison with the skin depth δ. Considering the finite thickness limitation, Aymard [1] shows that the error on the surface impedance and on the dissipated power is below 5 % when the thickness is larger than 2δ.

To describe the right angle corner behaviour in transverse magnetic problems, Deeley [2] introduced a modified surface

impedance $Z(x/\delta)$ which depends on the distance x from the corner. At the corner, its value is 2 times the infinite one Z_0. When moving along the edge, the difference between the two decreases (Fig. 2) and becomes less than 5 % at the distance of 3δ from the corner. We will show in the full paper that the error on dissipated power when using infinite model is less then 5 % when the edges dimensions are larger than 40δ.

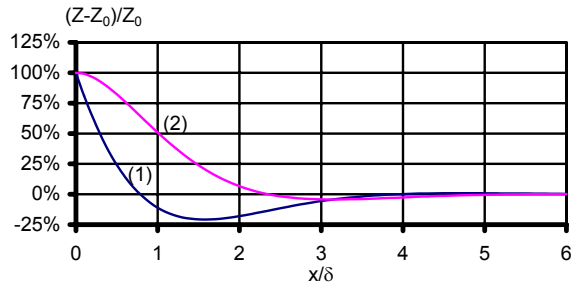

Fig. 2 : Comparison between modified ant infinite surface impedance real part : (1) - imaginary part : (2)

COMPARISON WITH OTHER MODELS

We have tested our approach on a rectangular one-turn coil used for a gear-wheel hardening. The working frequency is 160 kHz which leads to a skin depth of 0.18 mm. As shown earlier, we are allowed to use the surface impedance formulation. We have solved the same problem with the same geometry and the same meshing but with two other formulations : a 3D A-V and a 2D A_θ formulation. Naturally, in the two last cases, we also meshed the inner part of the coil, with a refined mesh where the skin effect occurs.

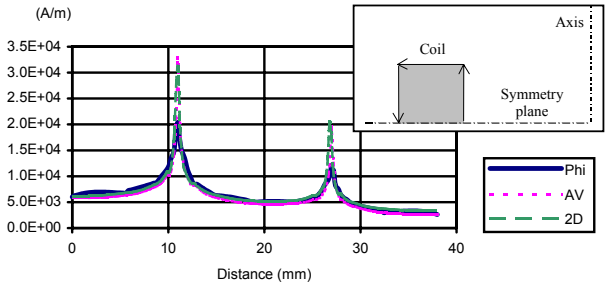

Fig. 3 : Surfacic current distribution on the tube surface.
Z_s-ϕ_{red} : solid line – A-V : dotted line – 2D-A_θ : dashed line

We have plotted (Fig. 3) the surface current distribution along the periphery of the tube evaluated either directly in the surface impedance formation or by integration in the normal direction in the other formulations. Each peak corresponds to a corner. We observe a good agreement between the three methods.
In the same way, we have calculated the total active and reactive power dissipated in the coil. Results are summarized in the table I. Here also, we can see that they are very closed.

TABLE I : TOTAL ACTIVE AND REACTIVE POWER IN THE COIL

Formulation	Active Power (W)	Reactive Power (VAr)
Z_s-ϕ_{red}	70.91 W	78.39 VAr
A-V	82.59 W	75.10 VAr
2D-A_θ	78.39 W	71.21 VAr

EXPLOITATION

We have used the proposed formulation to simulate the gear-wheel hardening at 160 kHz. Because of the high frequency, we also used the surface impedance formulation for the gear-wheel. To point out the impact of the current distribution on the heating, we have compared the results with a computation with a uniform current distribution in the coil. We observe that the total power dissipated in the load is 10 % higher in the real non uniform case than in the approximate uniform case. We will also present in the full paper the different power density distributions along the wheel teeth.

CONCLUSION

We have developed an improved method for calculating the current distribution in a high frequency induction coil. This approach has been validated by comparison with other numerical techniques. Finally, we have proved the impact of this distribution on the induction heating process when the load is closed to the coil.

REFERENCES

[1] N. Aymard, "Étude des phénomènes magnétodynamiques pour l'optimisation de structures 3D de chauffage par induction", *Ph'D dissertation*, Université de Nantes, November 20, 1997

[2] E. M. Deeley, "Surface impedance near edges and corners in three-dimensional media", *IEEE Trans. Magn.*, vol. 26, no. 2, pp. 712-714, March 1990.

A Novel Approach to Deal with Rotationally Symmetrical Boundary Conditions of 3D Eddy Current Field Problems

Shiyou YANG[1], Yongjie ZHANG[2],Xiangyong CHEN[2], Peihong NI[1], Yuhuai WANG[1]

[1]EE College, Zhejiang University, China
[2]Baoshan Iron &Steel Co. LTD, Shanghai, 201900, China

Abstract—To alleviate the excessive requirement for computer resources of the numerical methods such as the finite element analysis when they are applied to solve high frequency 3D eddy current problems, a novel iterative procedure to deal with the rotationally symmetric boundary conditions is proposed in this paper. Numerical results on computations of 3D eddy current fields of a cold crucible are reported to demonstrate the robustness and feasibility as well as the advantages of the proposed algorithm for solving practical 3D eddy current problems.

I. FORMULATIONS

The vector potential based finite element method is one of the most robust numerical tools for solving 3D eddy current problems. However, the demand for computer resources of this kind of methods will become excessively large when the skin depth of the conducting materials is very small compared to the dimension of the solution domain since the minimum size of the meshes must be a fraction of the skin depth. To alleviate this problem, a novel iterative procedure to reduce the solution domain in a relatively simple way for solving 3D eddy current problems with rotational symmetries is proposed in this paper.

To facilitate the understanding of the proposed procedure, one considers the 3D eddy current problems of a cold crucible (Fig. 1) with the rotational symmetry. A cold crucible is a high frequency induction melting furnace in which the conductive wall is segmented by longitudinal slits and each electrically isolated segment is internally or externally cooled by water [1]. According to the rotational symmetry of the problem, the solution domain can be reduced to one segment region as shown in Fig. 2. Moreover, by using the specific coordinate system of Fig. 2, the symmetrical boundary conditions of the vector potential based finite element models are

$$\frac{\partial \dot{A}_x}{\partial x}|_{S_{12}} = 0, \dot{A}_y|_{S_{12}} = \dot{A}_z|_{S_{12}} = 0 \tag{1}$$

$$\frac{\partial \dot{A}_n}{\partial n}|_{S_{23}} = 0, \dot{A}_\tau|_{S_{23}} = \dot{A}_t|_{S_{23}} = 0 \tag{2}$$

$$|\dot{\mathrm{A}}_\mathrm{n}|_{S_{23}} = |\dot{\mathrm{A}}_\mathrm{x}|_{S_{12}} \tag{3}$$

where, n is the outward normal direction of the specified surface, t and τ are the two tangential directions of the specified surface.

Obviously, since surface S_{12} is coincided with plane *yoz*, condition (1) is a natural boundary one, and no additional technique is required to tackle it. For condition 2 and condition 3, due to the arbitrariness in the segments, some specific technology must be designed to enforce them. Of course, one can use the well known coordinate transformation technique to address this problem. In this paper, a novel simple and efficient iterative approach is proposed to deal with this kind of Rotational Symmetrical Boundary Conditions (RSBC) and will be detailed in the next section.

II. A NOVEL APPROACH TO ENFORCE RSBCS

Actually, the proposed approach is an iterative one in nature and can be described as:

Initialization: Give initial values of the vector and scalar potentials $\dot{A}^k, \dot{V}^k$, respectively;

Step 1: The potential values at nodes of surface S_{23}, i.e., $\dot{A}|^{k'}_{S_{23}}$, are determined from (4);

Step 2: Resolve the 3D eddy current problem by taking the just determined $\dot{A}|^{k'}_{S_{23}}$ as known first kind of boundary conditions, letting the new solution be $\dot{A}^{k+1}, \dot{V}^{k+1}$;

Step 3: Compare the error of solutions between the two consecutive iteration steps, i.e., $\dot{A}^k, \dot{V}^k$ and $\dot{A}^{k+1}, \dot{V}^{k+1}$. If the error is with a threshold value predefined by the user, stop the iterative procedure; otherwise, go to Step 2 for the next iteration.

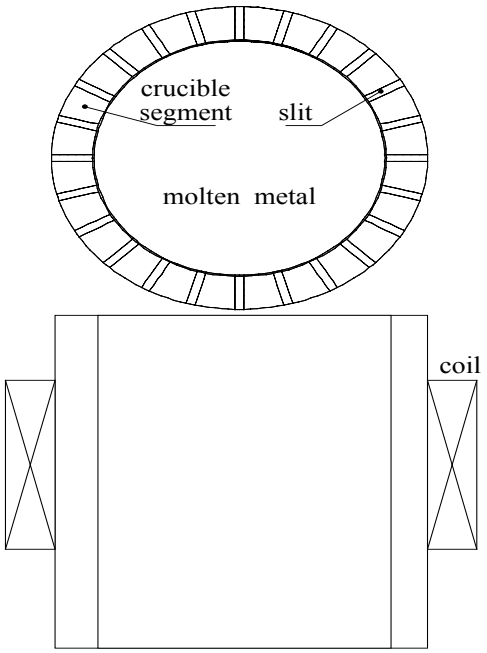

Fig. 1. Schematic diagram of a cold crucible

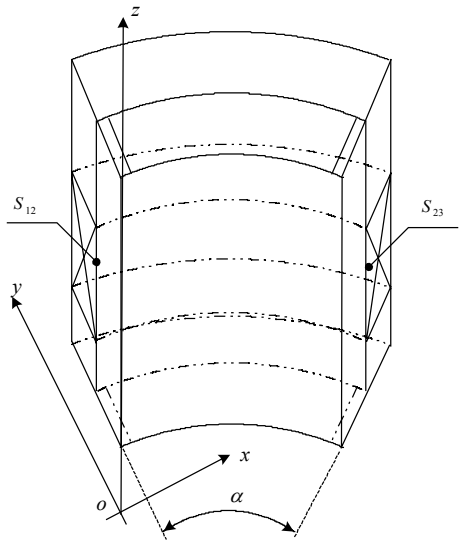

Fig. 2. The reduction of the solution domain (one segment)

Moreover,

$$\dot{A}_x \mid_{S_{23}} = \dot{A}_x \mid_{S_{12}} \sin(\alpha), \dot{A}_y \mid_{S_{23}} = -\dot{A}_x \mid_{S_{12}} \cos(\alpha) \quad (4)$$

where α is the central angle corresponding to one segment region of the crucible as shown in Fig. 2.

Since the ICCG method is used in the proposed method to solve the complex linear equation set, it will be preferable if the values of the predefined precision parameter to terminate the iterative process of ICCG method is set to a large one in the begging of the aforementioned iterative process and small enough in the end of the iterative process in sense of reducing the number of total iterations. In view of this point, an adaptive regulation scheme for determining the precision parameter of ICCG method is proposed as

$$\varepsilon^{k+1} = c \mid \dot{A}^k - \dot{A}^{k-1} \mid \varepsilon \quad (5)$$

where, ε^{k+1} is the precision parameter used in the $k+1^{th}$ step to stop the ICCG iteration, c is a constant coefficient, $\dot{A}^k, \dot{A}^{k-1}$ are, respectively, the solution of the vector potential at step k and step $k-1$, ε is a predefined precision parameter.

III. Numerical Results

To validate the proposed method, a closed slit mold with 48 crucible segments as reported in [2] is analyzed. Fig. 3 illustrates the distribution of the computed magnetic flux density on a predefined path when a 20 kHz harmonic current is applied to the coils. The path is defined as a circle which lies on the surface of the molten metal corresponding to the center position of the coil along the circumferential direction. Fig. 4 demonstrates the distribution of the computed magnetic flux density at points of the slit center which are on the surface of the molten metal along z-coordinate direction under the same operation condition. The performance comparison of the proposed method with the traditional ones is given in Table 1. It should be pointed out that these numerical results shown good agreement with those of [2]. Thus the numerical results positively confirmed the feasibility and the robustness as well as the advantages of the proposed algorithm for solving practical eddy current problems with rotational symmetry boundary conditions.

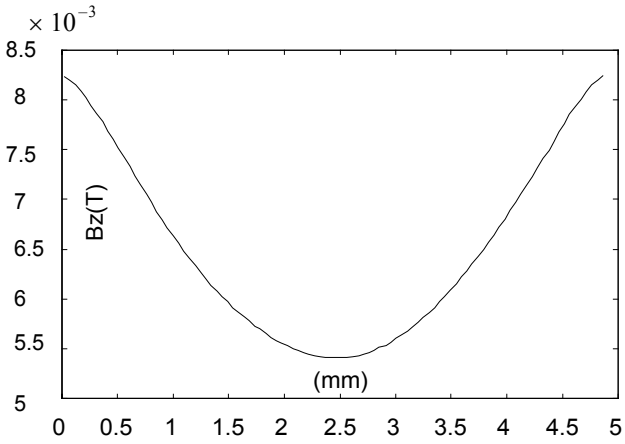

Fig. 3. The distribution of the computed magnetic flux density on the surface of the molten metal along the circumferential directions in the center position of the coil under a 20 kHz harmonic current

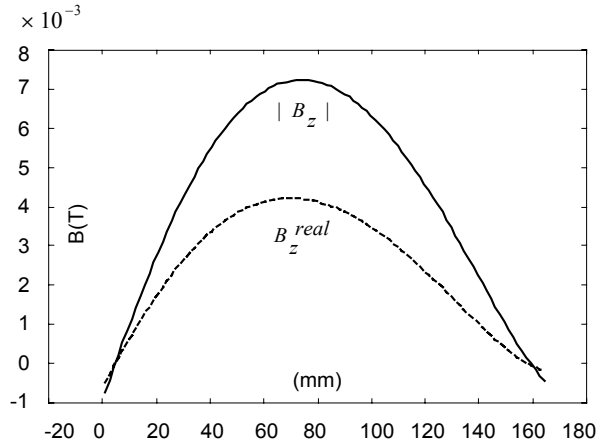

Fig. 4. The distribution of the computed magnetic flux density at points of the slit center which are on the surface of the molten metal along z-coordinate directions under a 20 kHz harmonic current

TABLE 1 Performance Comparison Of The Proposed And The Traditional Approaches

	Nodes	Meshes	No. of total DOF
Proposed	16000	18641	54188
Traditional	84000	100846	328600

References

[1] H. MAKINO, M. Kuwabara, S. ASAI, "Process analysis of non-contact continuous casting of materials using cold crucible," *ISIJ International*, vol. 36, pp. 380-387, 1996.

[2] N. Yoshida, S. Furuhashi, T. Tanka, "Newly designed stiff EMC mold with imposition of super-high frequency electromagnetic field," *Proceedings of the 3rd International Symposium on Electromagnetic Processing of Materials*, pp. 388-391, 2000.

Modeling of Superconducting Levitation System with Finite-Element Using the Magnetic Vector potential-Electric Field Formulation

Hassane MOHELLEBI, Djamel AMRANI, Mounir KEBBAS

Département d'Electrotechnique, Université Mouloud MAMMERI, Tizi-Ouzou BP17RP,Algerie.

e-mail : mohellebi@yahoo.fr

Abstract --- In this paper, a coupled magnetic-electric model with magnetic vector potential-electrical field formulation, in a superconducting levitation system composed of an association of permanent magnet and superconductor is proposed. The Maxwell equations are solved by the finite element method in axisymetrical case. The permanent magnet moves is taken account by re-meshing techniques. The results obtained are compared with existing experimental results , and shows a good agreement between them. This allows us to validate our coupled model.

INTRODUCTION

In recent years, great efforts have been made to establish superconducting levitation systems, such as magnetic bearing, flywheel or system for transportation[1].

In electromagnetism, the magnetic vector potential is used to deducts all others electromagnetic sizes. But because of non linearity of the current density [2], the computation of this size require choosing of an adequate method of computation. A coupled model between an equation in terms of magnetic vector potential $\vec{A}$ and the one in terms of electric field $\vec{E}$ is proposed.

The coupled method presented is executed by an equation told " power law " [2]. The equation obtained so, thus resolved by finite element method in axisymetrical case . The movement are taken into account by re-meshing for different positions of magnet.

The coupled model proposed allows to obtains an evolutions in function of time and displacement of different electromagnetic size like a force and magnetic induction . The results obtained are compared with a results given in reference [1], and shows a good agreement between them**.**

The coupled process are carrying out by writing a program who uses PDETOOL functions under MATLAB environment.

ELECTRIC AND MAGNETIC EQUATIONS

The computational domain are given by Fig. 1. Radius and thickness of the superconductor are respectively 10.5 mm and 10 mm, and those of magnet 11 mm and 20 mm [1].

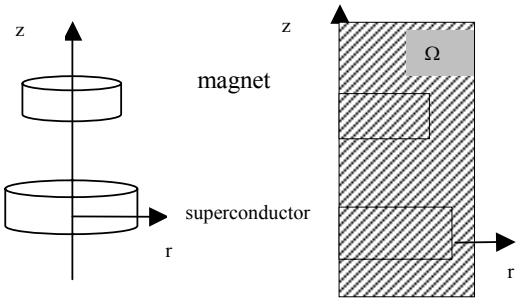

Fig. 1. The computational domain Ω

In our case, the electrical field can be described as follows[4] :

$$\overrightarrow{\text{curl}}\,(\upsilon\,\overrightarrow{\text{curl}}\,\vec{E})+\sigma_1(E)\frac{\partial\vec{E}}{\partial t}=0 \qquad (1)$$

The transient electromagnetic equation in term of magnetic vector potential is given by[4]:

$$\overrightarrow{\text{curl}}\,(\upsilon\,\overrightarrow{\text{curl}}\,\vec{A})+\sigma_1(E)\frac{\partial\vec{A}}{\partial t}=\vec{J} \qquad (2)$$

Finite element formulation of equations (1) and (2) using Galerkin method, allow to obtain two systems of algebraic equations given by :

$$\left\{[M]+\frac{[N]}{\Delta t}\right\}[A]^{t+1}=[K]+\frac{[N]}{\Delta t}[A]^{t} \qquad (3)$$

$$\left\{[P]+\frac{[Q]}{\Delta t}\right\}[E]^{t+1}=\frac{[Q]}{\Delta t}[E]^{t} \qquad (4)$$

[M], [P] :Mass matrix
[N] , [Q] : Dynamic matrix
[K] : Matrix of source term.

Solving coupled problem constituted by the systems (3) and (4), is done at first with the computation of electrical field $\vec{E}$ by solving the system (4), and the current density is deduced from equation (5). This equation is introduced in the system (3) for the computation of magnetic vector potential $\vec{A}$.

CURRENT DENSITY VERSUS LECTRICAL FIELD

The model given next deal with a relation between the electrical field E and the current density J.

Those two parameters are linked by a law told " power law " given as follows [2,3] :

$$J=J_c\left(\frac{E}{E_c}\right)^{\frac{1}{N}} \quad (5)$$

Avec : Ec=50 μ V/m.

Ec : Critical electrical field [V/m].

Jc : Critical current density [A/m²].

N : Coefficient.

The law J(E) is numerically hard to used in this form. It is modified slightly by introducing a good conductivity σ_0 more than $100\frac{J_c}{E_c}$ [2,3].

Then the power law is as follows [2,3] :

$$J=\sigma_1(E).E \quad (6)$$

with:

$$\sigma_1(E)=\frac{\sigma(E).\sigma_0}{\sigma(E)+\sigma_0} \quad (7)$$

$$\sigma(E)=Jc\frac{E^{\frac{1}{n}-1}}{E^{\frac{1}{n}}} \quad (8)$$

APPLICATION AND RESULTS

This practice consist to take the magnet an initial position at 0.5 mm above the superconductor ,after to move away the magnet in vertical motion.

To validate our model we have compared the results obtained with the results given in reference [1], comparison was effected to consider the relatives values, then we obtain follows paces:

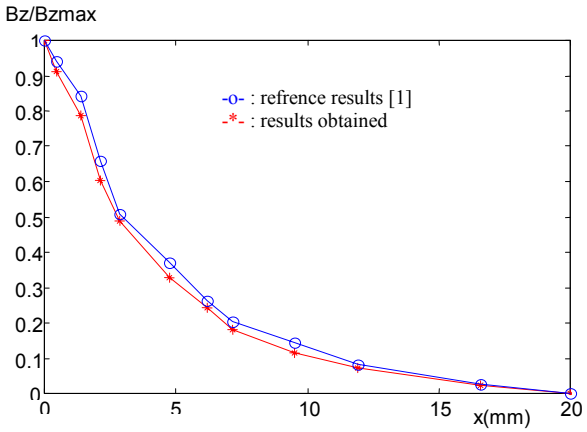

Fig. 2. axial force in fonction of the magnet motion.

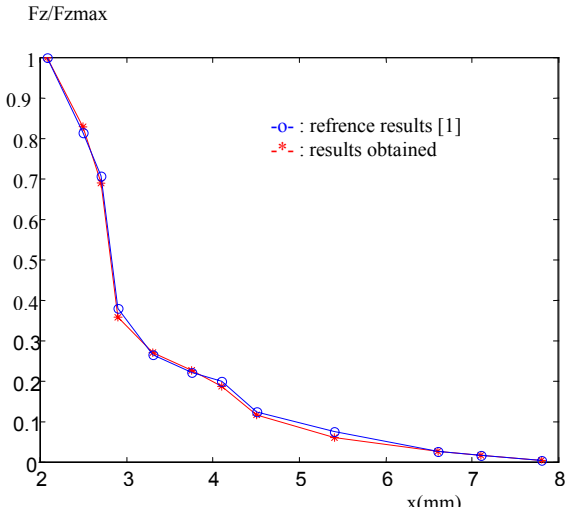

Fig. 3. induction in function of the magnet motion.

The results of the comparison show a good agreement between the results obtained and the existing experimental results given in reference [1].

CONCLUSION

In this study a coupled numerical model between magnetic and electric equations using magnetic vector potential-electrical field formulation is proposed.

The model presented is used for a computation of the behaviour of superconducting levitation system composed of an association of permanent magnet and superconductor. This model allow to more convenient calculation and induces advantages in the deduction of all others electromagnetic sizes.

The results obtained are in a good agreement with the existing experimental results and allows us to validate the proposed coupled model. The next is more convenient when introducing temperature effects.

REFERENCES

[1] S . Ho Tam Fou , A . Erraud , and F . Bouillault, " Numerical Modeling of the Association of Magnet and HTS Superconductors,". IEEE Transaction on Magnetics.Vol. 36 , N°.4 , July 2000.

[2] E . Vinot, " Modélisation des supraconducteurs HTC , Application au calcul des pertes AC, " , Thèse de docteur de L'INPG, Avril 2000, France.

[3] E . Vinot , G .Meunier , P . Tixador," Modélisation des pertes en alternatifs dans les supraconducteurs, " LEG and CRTBT , 2000.

[4] D. Amrani, M. Kebbas, " Modeling of Superconducting Levitation System with Finite Element Using the Magnetic Vector potential-Electric Field Formulation , " Ingineer Theses , Tizi-Ouzou University, October 2002, ALGERIA.

GUI Design of HFDSC

Zhenhai Shao, Zhongxiang Shen, *Member, IEEE,*
School of Electrical and Electronic Engineering, Nanyang Technological University
Singapore 639798 (e-mail: ezhshao@ ntu.edu.sg).

Wei Hong, *Member, IEEE*
State Key Lab. of Millimeter Waves, Southeast University, Nanjing, P.R . China, 210096

Abstract-- **In this paper, a software package named as HFDSC, which is based on the time domain discrete singular convolution method, is introduced. Using the OpenGL graphic technology and Class TList of Borland C++ Builder, the structural parameters can be defined graphically and all parameters can be viewed by TreeView control. Based on the multi-thread computer technology, we can control the program's running, resuming, suspending, stopping and post-processing electromagnetic field data on time. Furthermore, combining OpenGL and multi-thread technology, the time domain electromagnetic fields distribution can be generated in every time step and in every mesh layer.**

***Index Terms*—FDTD, Discrete Singular Convolution, PML, OpenGL.**

I. INTRODUCTION

THE time domain discrete singular convolution method (TDDSC) [1] has been introduced to the analysis of complicated electromagnetic problems. Compared with the standard FDTD [2, 3] method and MRTD [4] method, the TDDSC method not only attains higher accuracy and saves computer memory, but also reduces CPU time by choosing suitable meshes.

Recently, many commercial software packages, such as Ansoft HFSS, HP HFSS, ADS, IE3D and XFDTD etc., have been used to analyze various 3-dimensional electromagnetic problems. Among them, HFSS, IE3D and ADS are based on the frequency domain methods, and XFDTD is based on the FDTD method.

In this paper, we introduce a software package, named as HFDSC, which stands for High Frequency Discrete Singular Convolution Simulator. It is based on the time domain discrete singular convolution method. OpenGL has been used in CAD/CAM widely as a 3D graphic industrial standard. OpenGL has been used in HFDSC to define geometrical model and to display 3D electromagnetic field distribution in every mesh layer and every time step. With the development of operating systems, such as Windows 2000, Unix and Linux, it is possible to construct a multi-thread, multi-process and parallel program. In HFDSC, the multi-thread technology has been used to control processing time-domain electromagnetic fields, 2D, 3D graphic display, program running, resuming, suspending and stopping. Depending on the powerful Class library of Borland C++ Builder, such as TList Class, visual control library (VCL), HFDSC can be effectively developed.

This paper is organized as follows. In Section II, the TDDSC method is briefly reviewed. In Section III, some computer visualization technologies are introduced. In Section IV, a crosstalk example and its visual interfaces of HFDSC are given.

II. TIME DOMAIN DISCRETE SINGULAR CONVOLUTION METHOD

The TDDSC [1] is a time domain method, in which discrete singular convolution (DSC) is used to discretize the spatial difference, the sympletic integrator propagator (SIP) scheme is used to discretize the time difference. In every time step, the electric fields are calculated firstly as follows

$$E_x^{n+l+1/5}\big|_{(i-\frac{1}{2},j,k)} = A_{(i-\frac{1}{2},j,k)} \cdot E_x^{n+l}\big|_{(i-\frac{1}{2},j,k)}$$
$$+ B_{(i-\frac{1}{2},j,k)} \cdot \Bigg\{ \Big[\sum_{s=-M}^{-1} \delta^{(1)}_{\sigma,\Delta_y}\Big|_{(s+\frac{1}{2})\Delta_y} H_z^{n+l}\Big|_{(i,j+s+\frac{1}{2},k)}$$
$$+ \sum_{s=1}^{M} \delta^{(1)}_{\sigma,\Delta_y}\Big|_{(s-\frac{1}{2})\Delta_y} H_z^{n+l}\Big|_{(i,j+s-\frac{1}{2},k)} \Big] - \Big[\sum_{s=-M}^{-1} \delta^{(1)}_{\sigma,\Delta_z}\Big|_{(s+\frac{1}{2})\Delta_z} H_y^{n+l}\Big|_{(i,j,k+s+\frac{1}{2})}$$
$$+ \sum_{s=1}^{M} \delta^{(1)}_{\sigma,\Delta_z}\Big|_{(s-\frac{1}{2})\Delta_z} H_y^{n+l}\Big|_{(i,j,k+s-\frac{1}{2})} \Big] \Bigg\} \tag{1}$$

When all electric fields are calculated in the l-th step, the magnetic fields can be obtained from previous electric fields as

$$H_x^{n+l+1/5}\big|_{(i,j-\frac{1}{2},k-\frac{1}{2})} = \widetilde{A}_{(i,j-1/2,k-\frac{1}{2})} H_x^{n+l}\big|_{(i,j-\frac{1}{2},k-\frac{1}{2})}$$
$$+ \widetilde{B}_{(i,j-1/2,k-1/2)} \Bigg\{ \Big[\sum_{s=-M}^{-1} \delta^{(1)}_{\sigma,\Delta_z}\Big|_{s\Delta_z} E_y^{n+l+1/5}\Big|_{(i,j-1/2,k+s)}$$
$$+ \sum_{s=1}^{M} \delta^{(1)}_{\sigma,\Delta_z}\Big|_{(s-1)\Delta_z} E_y^{n+l+\frac{1}{5}}\Big|_{(i,j-\frac{1}{2},k+s-1)} \Big] - \Big[\sum_{s=-M}^{-1} \delta^{(1)}_{\sigma,\Delta_y}\Big|_{s\Delta_y} E_z^{n+l+\frac{1}{5}}\Big|_{(i,j+s,k-\frac{1}{2})}$$
$$+ \sum_{s=1}^{M} \delta^{(1)}_{\sigma,\Delta_y}\Big|_{(s-1)\Delta_y} E_z^{n+l+1/5}\Big|_{(i,j+s-1,k-1/2)} \Big] \Bigg\}. \tag{2}$$

where $l = 0, 1/5, 2/5, 3/5, 4/5$. $\delta_{\sigma,\Delta}^{(1)}$ is the DSC coefficient of the first order.

III. Software Design of HFDSC

The software flow chart is shown in Fig. 1. In model-draw interface, the structural parameters of the model are entered by OpenGL. At the same time, boundary conditions, incident planes and reference planes are defined. When the initial parameters are specified, we can calculate the field distribution. In the field calculation interface, by using multi-thread and daemon threads technology, the program can be run, resumed and suspended at any time by setting the starting, resuming and suspending time. For every time step, 3D electromagnetic real-time distribution can be generated in any plane by OpenGL and multithread technologies. When the time domain information is enough to obtain the frequency domain information, time domain computation is terminated. By FFT, DFT or AR model, frequency-domain results, such as the S-parameter, impedance or effective dielectric constant, can be shown by curves in the frequency information interface.

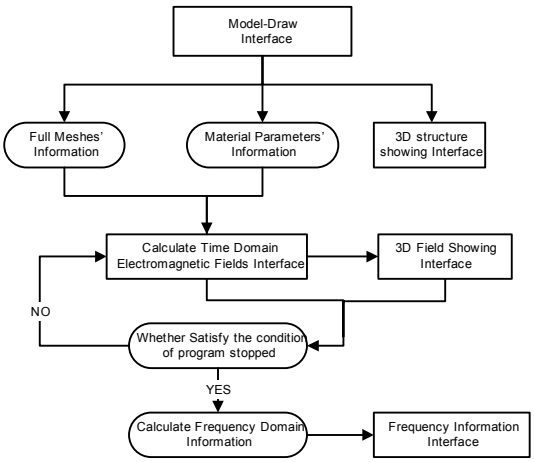

Fig.1. Flow chart of software design.

IV. Software Interface and Numerical Example

In order to demonstrate HFDSC's usage, the problem of crosstalk between two microstrip lines on the same substrate ($\varepsilon_r = 9.8$) is analyzed. The width and separation of two microstrip lines are the same as the substrate thickness 0.2mm. For Δt £½0.01/c_0 and spatial increment $\Delta x = \Delta y = \Delta z$ =0.04mm, the interface for model drawing, 2D and 3D time domain field distribution are illustrated in Fig.2, when time is at 150 Δt . Its transformed S-parameters are shown in Fig. 3.

HFDSC can be used to analyze not only crosstalk problems, but also radiation of antennas, periodic structures, filters, planar microwave circuits, scattering by electrically large dielectric and conductive objects and high-frequency MMIC interconnections. By a single run in the time domain, the S-parameters, impedance, effective dielectric constant, surface electric/magnetic current distribution or truncated-plane field distribution can be obtained.

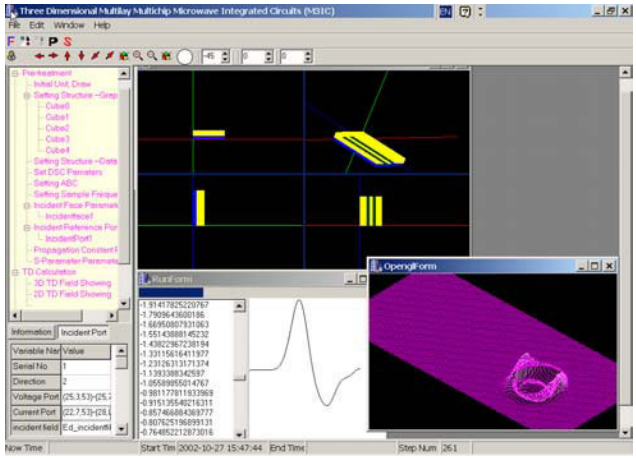

Fig. 2. Software interface for analyzing the crosstalk between two striplines

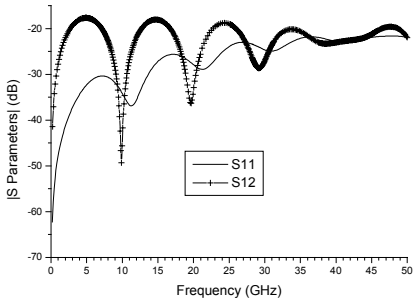

Fig. 3 S parameters for the crosstalk between two striplines

V. Conclusion

In this paper, the software package HFDSC has been introduced. Compared with many commercial packages, HFDSC is easy to use, can deal with complicated EM problems and has higher-order accuracy. However, because it is newly developed, it needs more time to improve its stability, flexibility and user interface.

References

[1] Z. H. Shao and Z. Shen, "A generalized higher-order finite difference time domain method and its application in guided-wave problems," to appear in *IEEE Trans. Microwave Theory Tech*., March 2003.

[2] K. S. Yee, "Numerical solution of initial boundary value problems involving Maxwell's equations in isotropic media," *IEEE Trans. Antennas Propagat.*, vol. AP-14, pp. 302-307, May. 1966.

[3] Z. H. Shao and W. Hong, "Generalized Z-domain absorbing boundary conditions for the analysis of electromagnetic problems with finite difference time domain method," *IEEE Trans. Microwave Theory Tech*., to appear in Jan. 2003.

[4] M. Krumpholz and L. P. B. Katehi, "MRTD: new time-domain schemes based on multiresolution analysis," *IEEE Trans. Microwave Theory Tech*., vol. 44, pp. 555-571, Jan. 1996.

[5] Z. H. Shao, Z. Shen and G. W. Wei, "DSC solution of 3D guided wave problems," *The Tenth Biennial IEEE Conference on Electromagnetic Field Computation (CEFC 2002)* in Perugia, Italy, pp. 164, in 16-19 June 2002.

[6] Z. H. Shao, Q. Y. He and Z. Shen, "An improved PML ABC for microstrip line problems," *The Tenth Biennial IEEE Conference on Electromagnetic Field Computation (CEFC 2002)* in Perugia, Italy, pp. 163, in 16-19 June 2002.

A Texture Method for Imaging Planar Magnetic Vector Field

ZHAO Yu, CHAI Jianyun
Department of Electrical Engineering, Tsinghua University
Beijing 100084, China
chaijy@tsinghua.edu.cn

Abstract - **A new concept of texture image method for displaying planar magnetic fields is presented. Field vectors are mapped to a grayscale image through its magnetic vector potential modulated with a sine function. The image visualizes a soft appearance of flux tubes instead of flux lines, whose orientation and width reflect the direction and amplitude of field vectors respectively. An illuminated model based on this concept is further discussed. The images created by the new algorithms show some unique properties that are rather different from others.**

I. INTRODUCTION

Visualization of the vector field distribution by graphics and images is an indispensable approach in interpreting of electromagnetic fields. Compared with the graph methods, the texture methods developed in the last decade are able to express more detailed features of the field vectors. Spot Noise [1] and LIC [2] are two typical texture methods, based on the convolutions along the direction of field vectors on a white noise image. These methods, however, are difficult to reflect the amplitude of field vectors on the image without using extra color resources.

II. SINUSOIDAL MODULATED POTENTIAL MAP

According to the Maxwell equations, the flux density **B** can be expressed by the curl of a vector potential **A**. It has been approved that using the function of vector potential with only one space component $\mathbf{A}=A\mathbf{k}$ is sufficient to represent any planar magnetic field $\mathbf{B} = B_x\mathbf{i} + B_y\mathbf{j}$. One advantage of replacing the flux density by the potential is that the contours of the potential on the field plane will always coincide with the flux lines of the field.

If we create an image called a potential map, which the pixels with same potential values are rendered to a same color, then the directions of the field vectors can be distinguished from the variance of pixel colors. This concept has been used in some commercial software. Although it is good for reading the potential values, the potential map with continuous full color tones, however, is not suitable for displaying the vector fields, because its colorful pattern weakens the observer's interpreting to the field directions.

In this paper, we develop a new kind of potential map. First, in order to save the color resources, we render the potential map in grayscale form; and then, the potential function A is modulated by a periodical function, e.g. a sine function, before mapped to the grayscale ranks. Such an image of vector field is called Sinusoidal Modulated Potential Map (SMP).

The algorithm can be expressed as follows: In a bounded region of 2D magnetic field, a gray mapping function g for the vector potential $\mathbf{A}=A\mathbf{k}$ can be chosen as:

$$g = g_{av} + g_m \sin(\omega A + \psi) \qquad (1)$$

Where: g_{av} is the average gray; g_m is the variation range of the gray; ω is the gray angular frequency determined by the potential period T, namely $\omega = 2\pi/T$; And ψ is the initial phase angle. T is an adjustable parameter by the observer, which means the flux in each tube of the field in physical. If A_{max} and A_{min} are the maximal and the minimal value of A in the region, and n is the number of the tubes to be showed, then $T= (A_{max}-A_{min})/n$. Fig. 1 illustrates such a SMP image of the magnetic field excited by a current filament.

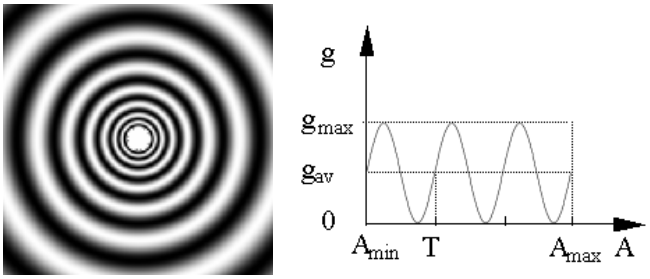

(a) (b)

Fig.1. A field image created from modulated potential map
(a) SMP image
(b) Sinusoidal Modulating function

The SMP images have some advantages over the traditional ones. It is a dense sampling of the field, being sequential and smooth modulation. It impresses a clear pattern of the soft flux tubes on the observers, whose orientation and width reflect the direction and amplitude of field vectors respectively. The variance of the pixel gray along the vertical direction of the field vector caused by the modulating function greatly enhances the capability of the image to display the field details. Thank to its straightforward mapping method, the SMP images of magnetic field can be fast rendered in real time.

Other periodical functions can also be chosen as the modulating function, for example, triangular wave function. If the periodic Dirac's function is used, the flux tubes in the image will degenerate into flux lines.

III. ILLUMINATED MODEL OF SMP

If we consider the SMP images discussed above as some kind of height fields, then we can apply the illuminated rendering techniques in computer graphics to the visualization of magnetic field. That is similar to "*Bump Mapping*" [3]. The kernel of the illuminated model of SMP is to determine of the virtual normal direction of each pixel. We define the normal direction by two directional angles α and β, showed in Fig.2.

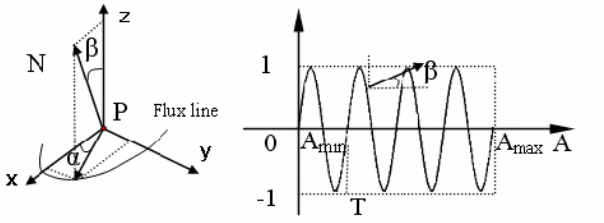

(a) (b)

Fig.2. Virtual normal direction of illuminated model of SMP
(a) Definition of the normal direction
(b) Calculation of the angle β

The angle α can be calculated from the gradient of A on the field plane, that is:

$$\cos\alpha\,\mathbf{i} + \sin\alpha\,\mathbf{j} = \nabla\mathbf{A}/|\nabla\mathbf{A}|;$$

and the angle β is determined by the sinusoidal modulating function $f = f_m \cos(\omega A + \psi)$. Then

$$\cos\beta = \frac{f}{\sqrt{1+f^2}}; \qquad \sin\beta = \frac{1}{\sqrt{1+f^2}}$$

Once a light source for illuminating the SMP model is given, we can render an image of the magnetic field by using Phong's formula.

IV. EXAMPLES

The algorithms of the proposed texture method for displaying planar magnetic fields have been implemented and tested. The images created by these algorithms show some features that are rather different from others. And the input data of the algorithms come from a set of analytical formulae, or the numerical solutions of, for example, finite element method.

In Fig.3, we show two SMP images with (b) and without (a) illumination of the magnetic field excited by a pair of current filaments with opposite flow directions. Because of the constant flux of each flux tube, the shrinking of flux tubes at the central of image means the higher flux density there.

Fig. 4 shows the images of the magnetic field in a permanent magnet motor, without (a) and with (b) illumination. The field is computed by a standard finite element solver, in which linear triangle elements are used.

The conception of SMP has also been approved very effective and efficient in creating high quality animation sequences of time varying magnetic fields. Fig.5 shows images in the animation of a rotating magnetic field excited by a set of three-phase AC winding currents.

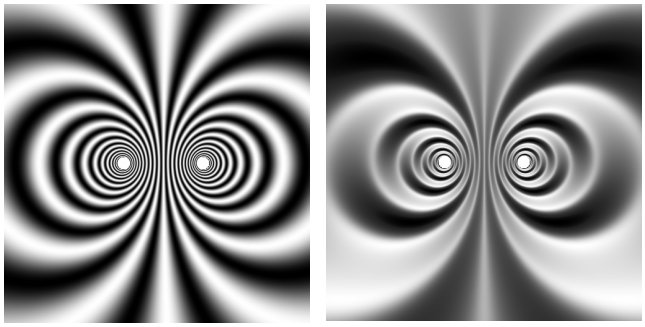

(a) (b)

Fig.3. SMP images of the magnetic field excited by 2 opposite currents

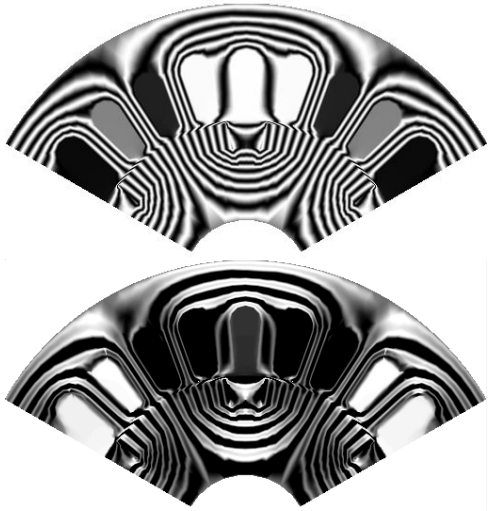

(a)

(b)

Fig.4. SMP images of the magnetic field in a PM motor

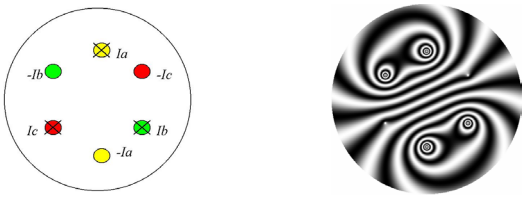

(a) (b)

Fig.5. 3-phase winds and SMP animation of rotating magnetic field

V.CONCLUSION

A novel texture method for imaging planar magnetic fields has been proposed. The SMP images created by the algorithms show a soft appearance of flux tubes instead of flux lines, whose orientation and width reflect the direction and amplitude of field vectors respectively. The illuminated model of SMP has been further constructed to enhance the visual effect of the field images.

REFERENCES

[1] J.J. Van Wijk. " Spotnoise: texture synthesis for data visualization," *Computer Graphics*, 25(1991) no.4, pp. 309-318.

[2] B. Cabral, L. Leedom. " Imaging vector fields using line integral convolution," *Proceedings of the ACM SIGGRAPH '93 Conference on Computer Graphics*, 1993, pp. 263-270, Aug 1993.

[3] Donald D. Hearn. *Computer graphics, C version, 2/E.* New Jersey, Prentice-Hall Inc., 1997.

A New Interactive Visualization System with Force Feedback Device in 3D Electromagnetics

Yutaka Matsubayashi[1], So Noguchi[1], Hideo Yamashita[1], Vlatko Cingoski[2]
1) Graduate School of Engineering, Hiroshima University, 1-4-1 Kagamiyama, Higashihiroshima 739-8527, JAPAN
2) Electric Power Company of Macedonia, 11 October, No. 9, 91000 Skopje, Macedonia
E-mail: yama@eml.hiroshima-u.ac.jp

***Abstract*— This paper describes the interactive visualization system with force feedback device in 3D electromagnetics. Previously, we developed the interactive system that can not only visualize some kinds of field distribution, but make a user feel the magnetic force in 2D electromagnetics simultaneously. The aim of the previous system is mainly education because physical behaviour in 2D electromagnetics is simpler than that of 3D. However, the 3D interactive visualization system with force feedback is required for design and so on, since the realistic model is necessarily used. Therefore, we have developed the 3D interactive visualization system with force feedback device.**

I. Introduction

In the common electromagnetic field visualization systems, the magnetic force is represented by the size and orientation of arrows or cones. However, in reality, we surely feel and recognize forces through a part of our body, such as hand. It is why we have developed the system that makes a user feel the magnetic force in 2D electromagnetic field by using the haptic interface for an educational tool [1]. The previous system can visualize the field distribution and make a user feel the magnetic force at the same time even if the movable ferrite is moved to an arbitrary position in 2D. The previous system helps us to understand the physical behaviour in 2D electromagnetic field. However, an actual or realistic electromagnetic field should be represented in 3D, whose physical behaviour is more complicated than that of 2D. Therefore, we have to consider the 3D electromagnetic field in order to make more practical tool for education and design.

In this paper, we propose a 3D interactive visualization system with force feedback device based on the previous 2D system [1], due to dealing with more realistic models. Surely, the newly proposed system can not only visualize the field distribution map, but also make a user feel the magnetic force in 3D electromagnetics simultaneously. We are sure that the proposed system becomes more useful and more effective for education and design.

II. Interactive Visualization System with Force Feedback

The proposed system consists of two major parts; one is to display the field distribution map, and another is to feed back the force to a user by using the haptic interface (see Fig. 1). In this paper, the haptic interface is the PHANToM while the library to control the PHANToM is the GHOST SDK [2]. The procedure of the proposed system is below:

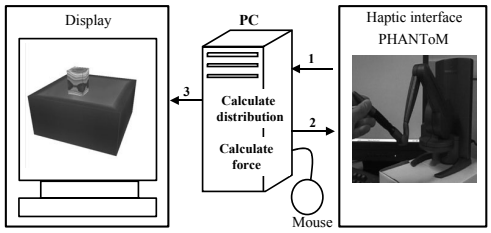

1. Coordinates of movable object 2. Information of magnetic force
3. Field distribution map (magnetic flux density)

Fig. 1. Construction of proposed system.

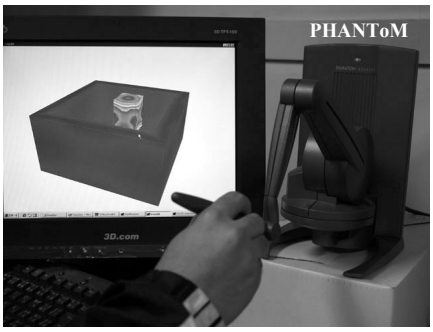

Fig. 2. Field distribution map and haptic interface (PHANToM).

At first, a user decides the position of movable object by the stylus pen of PHANToM. Second, after the field distribution map is visualized on the case of the user-defined position of movable object, the magnitude and orientation of the magnetic force are immediately computed by the tri-linear interpolation. And then, the user can feel the magnetic force through the stylus pen of PHANToM without feeling delay. An example, which the proposed system was applied to, is shown in Fig. 2.

By using a simple 3D model shown in Fig. 3(a), the processes of the proposed system are explained. And, the interpolation procedure to obtain the unknown distribution and magnetic force for an arbitrary position of movable object is briefly summarized below:

Pre-processing Step:

Step 1: Define the display area for each of the pre-computed configurations. Decompose the display area into some blocks for each of the pre-computed configurations (see Figs. 4 and 5). We call these blocks *"corresponding blocks"*.

Step 2: Decompose each *corresponding block* into 3D *i*j*k* grids and compute the physical value (for example,

magnetic flux density) at each grid point from the pre-computed results by FEM. The magnetic force, which works for the movable object, is computed utilizing the nodal force method [3].

Step 3: Utilizing Delaunay algorithm, make some tetrahedrons using the pre-computed position. These tetrahedrons are necessary for interpolation in the processing step (*Step 6*).

Processing Step:

Step 4: Move the movable object inside the area, which is surrounded by the pre-computed positions, by using the stylus pen arbitrarily.

Step 5: Decompose the display area into a set of blocks as in *Step 1*, and decompose these blocks into the 3D *i*j*k* grids as in *Step 2*.

Step 6: By using tetrahedrons constructed in the pre-processing step (*Step 3*), search the tetrahedron which the arbitrary position is included in.

Step 7: Calculate the physical value at each grid point of *corresponding blocks* by interpolation of the pre-computed physical value and the area coordinates. For all grid point the above procedure is executed, and then we obtain the distributions for arbitrary position of the movable object.

Step 8: Calculate the magnetic force working for the movable object by interpolation of the pre-computed magnetic force and the area coordinates.

After above steps, we can obtain the distribution map and the magnetic force working for the movable object for an arbitrary position in short time. In the previous system [1], to decompose corresponding block in *Step1* and to display the distribution map were simple. However, these of the proposed 3D system are complicated. Accordingly, we have to decompose corresponding blocks by using the geometry decided from the model configurations.

III. Application Model

The newly proposed visualization system was applied to a simple 3D model, where a movable ferrite existed inside a coil (see Fig. 3(a)).

The obtained field distribution for an arbitrary position of the movable ferrite is shown in Fig. 3(b). Figure 3(b) shows the magnetic flux density distribution map on surfaces of the ferrite and the coil. These physical value and distribution are calculated in less than 0.1s by the interpolation method described above (CPU: Pentium 4 1.8GHz, RAM: 512MB, Graphic Card: NVIDIA GeForce3). Such short computation time enables real time interaction between the user and the proposed system.

IV. Summary

We propose a new interactive visualization system with force feedback in 3D electromagnetic field. By using the visualization system with force feedback device (haptic interface), a user can observe the field distribution map, such as the magnetic flux density distribution, and can feel the magnetic force simultaneously.

This proposed system using the haptic interface makes us understand deeper in 3D electromagentics than only the graphical visualization. Furthermore, the proposed system serves as a powerful tool for education and design by using the special device, such as 3D display.

References

[1] Y.Matsubayashi, S.Noguchi and H.Yamashita, "A New Interactive Visualization System with Force Feedback for Education in Electromagnetics", *IEEE CEFC 2002 Conference Digests*, P.89, 2002.

[2] http://www.sensable.com.

[3] A.Kameari, "Local force calculation in 3D FEM with edge elements", *Int. jour. of App. elec. in Mat*, vol. 3, pp.231-240, 1993.

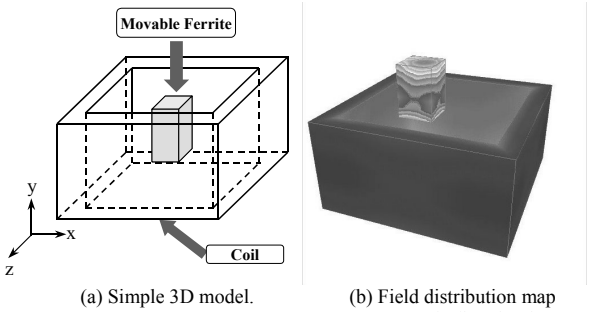

(a) Simple 3D model. (b) Field distribution map (Magnetic flux density).

Fig.3. Simple 3D model and field distribution map.

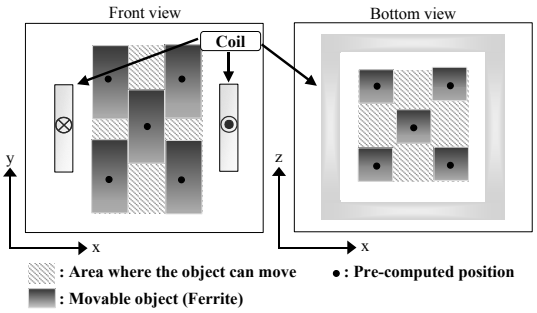

Fig. 4. Pre-computed positions and the area where ferrite can move.

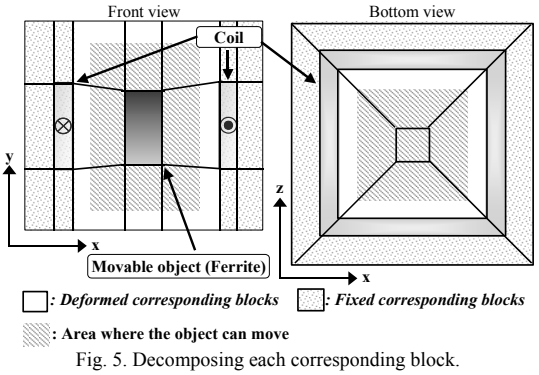

Fig. 5. Decomposing each corresponding block.

A Methodology and Tools for Worst-Case Tolerance Design

David Magot(♦Θ), Frédéric Wurtz(♦), Bruno Cogitore(Θ), Benoît Delinchant(♦), Jean-Pierre Keradec(♦)

(♦) Laboratoire d'Electrotechnique de Grenoble, INPG/UJF
CNRS, ENSIEG BP 46
38402 St Martin d'Hères cedex, France

(Θ) Microspire S.A
16 Parc d'activités du Beau Vallon
57970 Illange, France

***Abstract*—Optimization techniques are efficient to deal with sizing steps that designers have to perform. However, their industrial usefulness is also subject to their ability to deal with tolerance issues. A solution has been devised, based on optimization process encapsulations inside sizing models. It is believed to be fully independent of both the optimization and modeling methods. Its efficiency and capabilities are shown here on an industrial test example.**

INTRODUCTION

A new design methodology has been developed, based on the idea that merging in a friendly way a device model, a specification sheet and an optimization algorithm would increase design process efficiency. Thus, several sizing tools have successively been developed at our lab (Fig. 1)[1], becoming eventually a commercial product. Even if they have proved to be efficient for design, the industrial usefulness of this kind of tools would be increased if they were able to deal with tolerance issues, caused by all kind of uncertainty sources. The designer had therefore to perform a sensitivity analysis a-posteriori from the optimization results to take robustness into account, which is time consuming.

An efficient method along with tools is thus proposed here to deal with worst-case tolerance design. This involves taking into account uncertainties on some of the designed system parameters, while producing a system that match all the specification sheet requirements, for all the worst-case combinations of those uncertainties. This method is different from already existing ones [2][3][4]. In particular, [4] would not allow processing the industrial example given below. For clarity reasons, the method will first be detailed on a simple example, before being described on an industrial example to show its capabilities and efficiency.

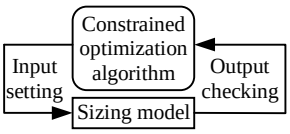

Fig. 1: Sizing tool principle

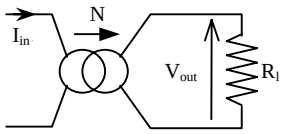

Fig. 2: Current measurement transformer

METHODOLOGY

Be {S} a system. Be *P* a parameter of {S}, computed as $P=F(x_i)$, $i \in I=\{1,\ldots,n\}$. Notice that function *F* can be computed in various ways, such as using equations or finite element modeling. A tolerance problem would be to quantify the effects on *P* of some uncertainties on x_j, $\forall j \in J \subset I$. Assuming that the uncertainty on parameter x_j can be bounded by a positive number tol_j, it is possible to compute the maximum deviation of *P*, caused by those uncertainties. This involves minimizing and/or maximizing function *F*. For instance, the maximization would give (1):

$$F_{\max}(x_i, tol_j) = \max_{y_j \in [x_j - tol_j,\, x_j + tol_j]} F(x_k, y_j) \quad , k \in I \backslash J \tag{1}$$

It is then possible to model {S} using functions F_{min} and/or F_{max}. Tolerance issues are thus transparently managed in the sizing model, tol_j parameters becoming then standard parameters of {S}. This involves therefore computing F_{min} and/or F_{max} inside {S} sizing model. It is sometimes easy, when it is possible to derive an explicit equation for F_{min} and/or F_{max} from function *F*. Else, it is necessary to use unconstrained optimization algorithms.

A SIMPLE EXAMPLE

This example is fully described in [4]. It involves minimizing a function *F* defined as below (2):

$$F(x_1, x_2) = \sum_{i=1}^{2} (0.01((x_i + 0.5)^4 - 30{x_i}^2 - 20x_i)) \tag{2}$$

A tolerance on parameter x_1 can additionally be considered for $x_1<0$. Then, parameter x_1 has to be considered as a stochastic parameter y_1, this one possibly ranging in $[X1_{min}, X1_{max}]$, with (3):

$$\begin{cases} X1_{\min} = x_1 - tol \\ X1_{\max} = x_1 + tol \end{cases} \text{, with } \begin{cases} tol = 0 & if \;\; x_1 \geq 0 \\ tol = \dfrac{|x_1|}{3} & if \;\; x_1 < 0 \end{cases} \tag{3}$$

To deal with tolerance issues, the goal is then to minimize function *G* defined below (4), instead of function *F*:

$$G(x_1, x_2) = \max_{y_1 \in [X1_{\min}, X1_{\max}]} F(y_1, x_2) \tag{4}$$

The computation of *G* is thus achieved using sizing model composition (Fig. 3). A visual composition tool has been used for that purpose. Using it, the user first loads the involved sizing models. Then, he connects the parameters together, the remaining tasks being automated. Thus, a first sizing model, named "X1 bounds", computes $X1_{min}$ and $X1_{max}$ using (3). The second sizing model, named "Max F", is more complex (Fig. 4). It has been automatically produced using another visual tool, which works as follow. First, the user loads a sizing model (function *F* here) and an unconstrained optimization algorithm ([5] here). For each input of this sizing model, the user selects which parameter has a tolerance (only x_1 here). He has also to configure the optimization algorithm. Then, both this model and algorithm are packaged by the tool as a new sizing model (Fig. 4).

Minimizing functions *F* and *G* using [5], it can be seen in Table I that the global minimum has moved (Fig. 5, Fig. 6). Due to tolerance issues, function *F* global minimum would therefore not be the best one for design.

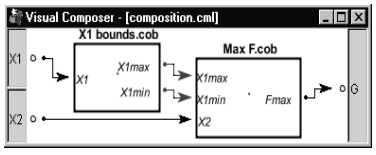

Fig. 3: Sizing model with tolerance

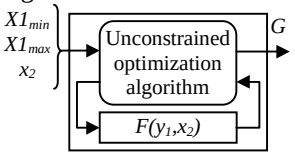

Fig. 4: "Max F" block internals

Table I. Global Minimum Position and Value of Functions *F* and *G*

	x_1	x_2	Value
F	-4.453792612914698	-4.453792612914698	-5.232758004115192
G	3.286761841860149	-4.453792612914698	-4.458341077241458

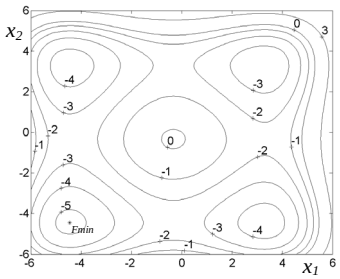

Fig. 5: Function *F* contour lines

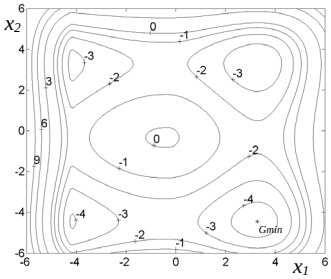

Fig. 6: Function *G* contour lines

AN INDUSTRIAL TOLERANCE PROBLEM

The tolerance problem described in the following comes from Microspire current measurement transformer design method (Fig. 2). A strong tolerance issue coming from a specified measurement precision had to be managed. It involved to compute reliably some parameters related to the deviation from nominal operation, caused by temperature changing and manufacturing tolerances. Minimization and maximization of a complex equation given below is thus required (6). This is then used to calculate the measurement precision *P* of the transformer, at each sizing model computation. This relative precision *P*, in %, is defined as below (5):

$$P = \frac{G_{\max} - G_{\min}}{G_{\max} + G_{\min}} \times 100 \qquad (5)$$

With G_{min} and G_{max} being respectively the minimum and maximum of the transformer gain *G*, defined as below (6):

$$G = \left| \frac{V_{out}}{I_{in}} \right| = F(f, R_l, x_i) \quad , i \in \{1,\ldots,4\} \qquad (6)$$

With:

- *F*, a scalar function of six parameters, not given here for space and industrial reasons
- *f*, the frequency, the input current being sinusoidal
- R_l, the transformer load resistor (Fig. 2)
- x_i, $i \in \{1,\ldots,4\}$, which are four parameters coming from the transformer equivalent circuit [6]. They are computed from the transformer geometry, among other parameters.

Thus, the computation of G_{min} and G_{max} was required, every parameter of function *F* ranging in a given interval, such as $[f_{min},f_{max}]$ for the frequency *f*, or $[Rl_{min},Rl_{max}]$ for the load resistor R_l (Fig. 2). However, function *F* was far too complex to be able to get an explicit equation for G_{min} and G_{max}. Indeed, this function is the square root of a rational fraction, with a polynomial denominator of degree six for *f*, with every of its coefficients depending on the other five parameters of function *F*. Moreover, G_{min} and G_{max} depend on all the six intervals over which function *F* is defined, each one being subject to change during the transformer optimization process.

To deal with the tolerance problem described above, two optimization processes have been encapsulated inside the transformer sizing model (Fig. 7). It has been done as for the previous example. To keep it simple, the "Transformer geometry" block computes function *F* parameter bounds from some input parameters, such as the transformer size. Those bounds are then input in the two parallel blocks named "G_{min}" and "G_{max}" (Fig. 8). Then, those two values are input in the fourth block named "Electro-magnetic properties", where precision *P* is computed along with other parameters.

Such a sizing model can be processed in the sizing tool using any non-linear constrained optimization algorithm, such as an SQP algorithm [7]. The tolerance problem is then transparently managed, simply by applying standard constraints on the corresponding parameters during the problem setting step. As an example, if a measurement precision of 5% is required for the transformer, such a constraint could be $0\% < P < 5\%$, or $P = 5\%$ at designer's choice for precision *P* (5). Applied to an industrial specification sheet provided by Microspire, the design time of such a transformer has been decreased by a factor ten. Microspire staff has also validated the design made using the sizing tool. It is quite similar to the product designed "by hand" by Microspire staff.

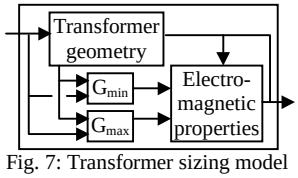

Fig. 7: Transformer sizing model

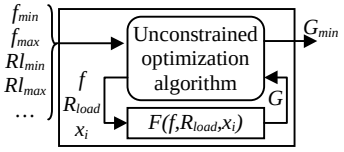

Fig. 8: "G_{min}" block internals

CONCLUSION

Sizing model composition and unconstrained optimization process encapsulations as sizing models have allowed to easily test a new methodology for worst-case tolerance design. It is believed to be quite generic. Indeed, it should be able to manage lots of tolerance problems. It is also independent of both the modeling and optimization methods. The results coming from an industrial example have shown its efficiency and capabilities. Future work will address the automation of the whole sizing model creation.

REFERENCES

[1] E. Atienza, J. Bigeon, F. Wurtz, V. Leconte, "EDEN : A generic integrated component software for constraint optimization", *COMPUMAG*, July 2-5, 2001, Evian, France, pp.232-233

[2] S.B Yoon, I.S Jung, D.S Hyun, "Robust Shape Optimization of Electromechanical Devices", *IEEE Transactions on Magnetics*, Volume 35, N°3, May 1999, pp 1710-1713

[3] B. Forouraghi, "Worst-Case Tolerance Design and Quality Assurance via Genetic Algorithms", *Journal of Optimization Theory and Applications*, Volume 113, N°2, May 2002, pp 251-268

[4] P. Alotto, P. Molfino, G. Molinari, "Optimization of electromagnetic devices with uncertain parameters and tolerances in the design variables", *COMPEL*, Volume 20, N°3, pp 808-812, 2001

[5] J.M Gablonsky, *Direct version 2.0 User's guide*, Center for Research in Scientific Computation, Department of Mathematics, North Carolina State University, 18th April 2001

[6] A. Schellmanns, K. Berrouche, J.P. Keradec, "Multi-winding transformers: a successive refinement method to characterize a general equivalent circuit", *IEEE Transactions on Instrumentation and Measurement*, October 1998, Volume 47, N°5, pp 1316-1321

[7] C.T Lawrence, J.L Zhou, A.L Tits, *User's guide for CFSQP version 2.5*, Electrical Engineering Department and Institute for Systems Research, University of Maryland, 1997

iMOOSE - An Open Source Environment for Finite Element Calculations

D. van Riesen, C. Monzel, C. Kaehler, C. Schlensok, G. Henneberger
Department of Electrical Machines (IEM)
Institute of Technology Aachen (RWTH)
Schinkelstrasse 4, D-52056 Aachen, Germany
e-mail: riesen@iem.rwth-aachen.de

***Abstract*—Implementing Finite Element solvers for new formulations is often a tedious task, as many common parts are coded again and again. Also, commercial codes are often expensive and therefore difficult to include in e. g. a teaching environment. iMOOSE is an open-source software package for Finite Element calculations which tries to solve these issues. It is a general purpose class library that allows for an easy implementation of new FE solvers or FE related tools. Also included are ready-to-use solvers for electromagnetic calculations and a powerful post-processing tool. Due to it's open-source nature, the source code can be examined, modified and extended to fit the user's needs.**

Introduction

iMOOSE [1] is an open-source environment for Finite Element calculations. It has been developed over the past years out of the necessity of redesigning and reimplementing the same procedures and data structures over and over when a new solver of formulation was developed. Using iMOOSE as an object-oriented class library, it is now possible to reuse all the basic building blocks of an FEM program.

The class library includes element classes for different 2D and 3D element shapes and types, problem definition classes and equation solving methods. For specialized tasks, interfacing to external libraries is implemented.

Object-oriented software development methods have acquired some popularity in the last years, and the Finite Element Method is well suited for this kind of technique. Different approaches are described in [2]–[4]. In contrast to some more academic decompositions of the F.E. procedure from the mathematical point of view, iMOOSE takes a more practical approach, paying also attention to the usability of the class library for practical applications and and to producing performant solvers, capable of handling large problems [5].

Using the provided class library, a number of solvers for electromagnetic, structural-dynamic and thermal computations has been implemented. Of general interest, and therefore included in the open-source release, are the solvers for 2D static and transient and 3D static electromagnetic calculations.

The open-source idea is considered by the authors to be a very important contribution to the development and distribution of software. Most of the external libraries, e. g. for equation solving or mesh partitioning used by the iMOOSE, are open-source products. iMOOSE has been also released under an open-source library. This allows other users in the scientific community to use the provided programs, review the design and implementation of the library, or use it as a base for own programs.

This paper will give an overview of the class library and present the released solvers. The example of parallel execution of a 3D static electromagnetic solver will demonstrate how some functionality is delegated to external libraries.

Class Library Design

The class library is divided in four main areas (Fig. 1). One is a complex comprising nodes and elements. Implemented element shapes include 2D triangles and quads, and 3D tetrahedra, pyramids, prisms and brick elements. For nodebased approaches both first and second order elements are available. Edgebased approaches use only first order tetrahedra at the moment. These elements and nodes are linked to the other parts via the concept of a Finite Element mesh. The other parts include a problem definition and solving area, where system matrices are built and equation systems are solved. For the i postprocessing of the solution, classes representing physical fields and quantities are available. Helper classes, that e. g. interface with external mesh generation tools, complete the class library.

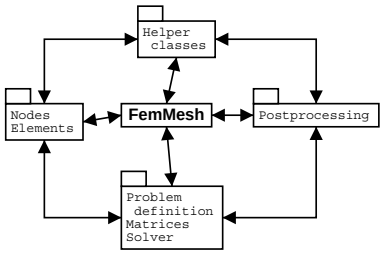

Fig. 1. Overview of the class library

Available Solvers

In the open-source release, the solvers are included which were most tested and of general interest. A 2D solver (iMOOSE.stat2d) for static electromagnetic calculation uses a nodal based magnetic vector potential. For 3D electromagnetic calculation, an edgebased approach with the magnetic vector potential is taken. Additionaly, this solver features a pre-processing stage with an electric vector potential for arbitrarily shaped source current regions. Examples of calculations using this solver are depicted in Fig. 2.

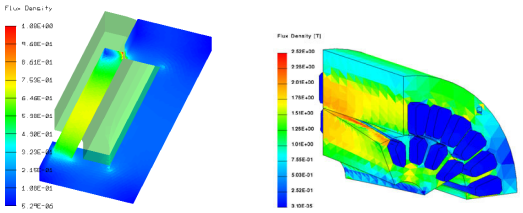

Fig. 2. Team 20 problem and a 3D induction machine calculated with 3D static solver iMOOSE.stat3d

A 2D solver for transient calculation is also included. With this solver, it is possible to take into account excentric rotor position and external circuits. An example of the use is shown in Fig. 3 and 4.

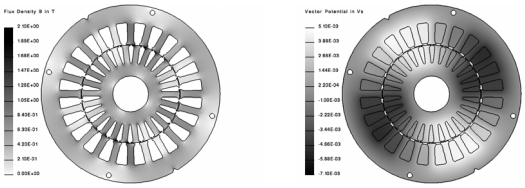

Fig. 3. Flux density and vector potential distribution in an induction machine calculated with iMOOSE.asm2d

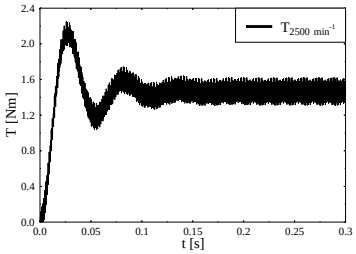

Fig. 4. Time depending torque behaviour of an induction machine

Parallel Execution In order to accelerate computation, the solvers provided by iMOOSE can easily be parallelized. By doing so, cheap clusters of standard personal computers can be used to achieve high speed-ups. To implement parallel execution, heavy use of open-source libraries and components has been made. Mesh partitioning is done by Metis [6], the equation system is solved by the PetSC-library [7] and the whole program runs in a MPI environment (LAM [8]).

The above shown examples for 3D, static calculation (Team 20 Problem, and an induction machine) have been calculated on a cluster of up to 6 PCs, each with an AMD Athlon 900 MHz processor and 1 GB Memory. Fig. 5 shows the achieved speed-up and the per-processor efficiency.

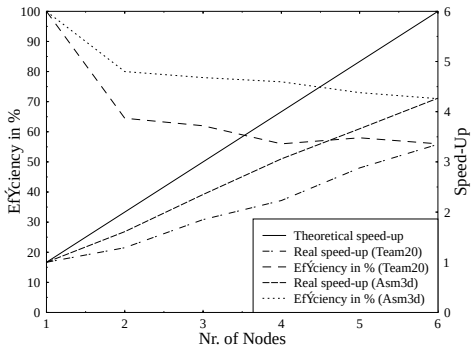

Fig. 5. Efficiency and speed-up with parallel execution

Conclusion

An object-oriented class library and program package for Finite Element computations has been presented. It is released as an open-source project available to everyone.

References

[1] G. Arians, T. Bauer, C. Kaehler, W. Mai, C. Monzel, D. van Riesen, and C. Schlensok, "Innovative modern object-oriented solving environment - iMOOSE." Available: http://imoose.sourceforge.net. [Online].

[2] R. C. Mesquita, E. J. Silva, R. L. Braga, M. A. Matias, C. R. S. Nunes, J. A. Vasconcelos, C. Jr., A. M. de Oliveira, J. P. A. Bastos, M. C. Costa, L. Lebenzstajn, A. B. Dietrich, J. R. Cardoso, and S. S. S. Melnikoff, "An object-oriented application framework for the computation of electromagnetic fields," in *Proceedings of the CEFC'02*, (Perugia, Italy), p. 256, 2002.

[3] S. Giurgea, T. Chevalier, J. L. Coulomb, and Y. Marechal, "Unified physical properties description in a multi-physics open platform," in *Proceedings of the CEFC'02*, (Perugia, Italy), p. 253, 2002.

[4] F. Henrotte, B. Meyes, A. Genon, and W. Legros, "An object-oriented decomposition of the f.e. procedure," *IEEE Trans. on Magnetics*, vol. 32, pp. 3403–3406, May 1996.

[5] G. Arians, D. van Riesen, and G. Henneberger, "Innovative object oriented environment for designing different finite element solvers with various element types and shapes," in *Proceedings of the 13th Compumag*, pp. 218–219, 2001.

[6] G. Karypis *et al.*, "Metis - family of multilevel partitioning algorithms." http://www-users.cs.umn.edu/ karypis/metis/. [Online].

[7] Various, "Petsc - the portable, extensible toolkit for scientific computation." http://www-fp.mcs.anl.gov/petsc/. [Online].

[8] Lam Team, "LAM / MPI parallel computing." http://www.lam-mpi.org. [Online].

Implementation of Boolean and Assembly Operations in a Solid Modeler

C. R. S. Nunes, R. C. Mesquita, A. L. C. C. Magalhães, C.L.L. Mol, H. F. M. Samora and T. S. Falqueto
Departamento de Engenharia Elétrica – Universidade Federal de Minas Gerais (UFMG)
Av. Antônio Carlos 6627, Pampulha, Belo Horizonte, 31270-901, Brazil
cassiasn@cpdee.ufmg.br, renato@cpdee.ufmg.br, analiddy@uol.com.br, mol@cpdee.ufmg.br, humberto@cpdee.ufmg.br, tiagofalqueto@yahoo.com.br

Abstract – **The main ideas used in the implementation of the Boolean operations and the assembly operation in a solid modeler designed to solve electromagnetic problems are presented. These operations provide an increase in the descriptive power of the modeler, making possible the generation of a larger number of 3D solid models well suited to solve electromagnetic problems.**

INTRODUCTION

This work explains the main ideas used in the implementation of the Boolean operations as well as the assembly operation in a solid modeler. It is part of a project under development at our research group, which involves the development of a multi-representational solid modeler (Gopac Solid Modeler - GSM). The GSM architecture was already presented in other papers [1] [2]. Its main goal is the generations of superficial meshes over 3D solids, which are used as input data for volumetric finite element mesh generators.

The main representation schemes used for the definition of objects by users are the Constructive Solid Geometry (CSG) and Sweep. From these schemes, a boundary evaluation is performed, so that the Boundary Representation (B-Rep) is obtained. The main contribution of GSM for the solution of electromagnetic problems by the finite element method is the inclusion of a special data structure definition that enables inner boundaries representation [1].

In this work, we describe the implementation of Boolean and assembly operations in GSM. The Boolean operations are part of an essential class of solid manipulation. They allow users to perform operations like addition, subtraction and intersection over simple models to generate new models with high complexity. Assembly is a new operation introduced in GSM [1]. To our knowledge, at this moment, there is no other geometric modeler that can directly represent and manipulate assemblies.

Assemblies are very important in electromagnetic problems where objects are composed of parts with different materials in direct contact. When the finite element method is used to solve these problems, it is necessary to interpret the common boundary between the parts as a single piece, even when we use the parts separately to perform other CSG operations. Doing that, the compatibility of the generated finite element mesh can be guaranteed. GSM makes this possible by the representation of inner boundaries on CSG and B-Rep structures [1].

Consider, for instance, the air that involves an electrical device. This air region can be easily shaped using the assembly operation performed in a box assembled to an electrical device located in its interior (for an example, please consult the results in Fig. 7). A model for an assembly reflects its important geometric properties: the shape, the arrangement and the individual characteristic of its components [3].

The process for accomplishment of Boolean and assembly operations has four steps, as shown in Fig. 1: (i) mesh generation over primitives; (ii) intersection of primitives, with calculation of all the intersection points; (iii) classification of elements – vertexes and edges as *in*, *on* or *out*, and faces as *in*, *on shared*, on *anti-shared* or *out*; (iv) Boolean evaluation and elimination of all undesired elements, as presented in Fig. 1. The three first steps are common to all operations. Only Boolean evaluation and elimination of undesired elements is specifically done, according to the operation being executed.

To perform step (iv) for the assembly operation a new Euler Operator [1] named AR (*Assemble Region*) was created. AR creates a common boundary between the two assembled regions for every identical and coincident face that occur in both regions. In the result of Fig. 6, two prisms of different sizes share a boundary. The larger prism has its boundary modified by step (ii) and the AR operator so that the part shared with the small box becomes the same.

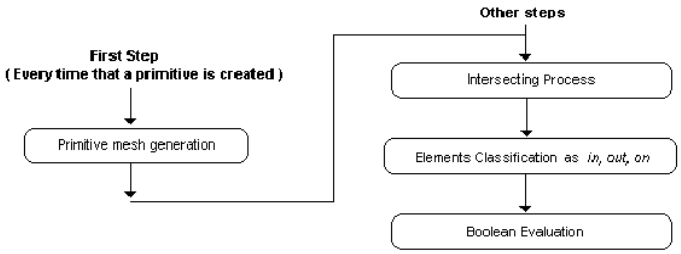

Fig. 1 – Flowchart of the boundary evaluation steps

INTERSECTING PROCESS DESCRIPTION

The execution process of Boolean operations and assembly operation can be divided into three parts: (i) determination of the intersection points; (ii) inclusion of the intersection points located at face's boundary, into B-rep structure; (iii) inclusion of the intersection points located at faces, into B-rep structure. These steps are presented in the flowchart of Fig. 2.

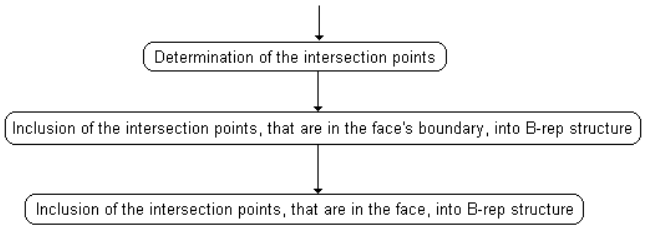

Fig. 2 – Flowchart of the intersection process steps

Determining the intersection points is the first step in the intersection process. In order to accomplish this, first the convex hull of each object is tested; second, if intersections exist, all components of one object need to be compared in relation to each other to identify the intersection points. The inclusion of the intersection points into B-rep structure is accomplished by using new Euler Operators [1] that guarantee GSM data structure integrity.

RESULTS

The implementation of the intersecting process has been done with special care. Each kind of intersection needs to be contemplated by a special calculation method to guarantee a correct mesh over the primitive.

In Figs. 3, 4 and 5 some results are presented, generated by the application of subtraction, addition and intersection operations over different kinds of models.

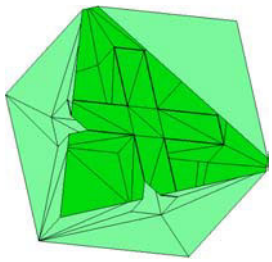

Fig. 3 – Result of the subtraction a cross from a prism

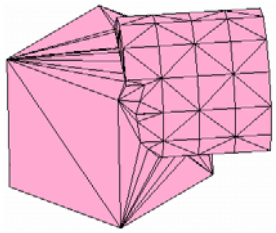

Fig. 4 – Result obtained from the union of a cylinder and a block

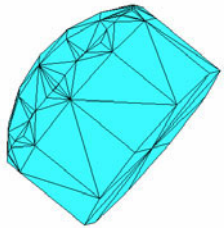

Fig. 5 – Result obtained from the intersection of a sphere and a cylinder

The result of an assembly is shown in Fig. 6. The different shading degrees of the prisms emphasize that their individual characteristics remain, as previously explained for the assembly operation. It is important to notice again that the generated meshes in both prisms are compatible, as well as the meshes presented in all other figures.

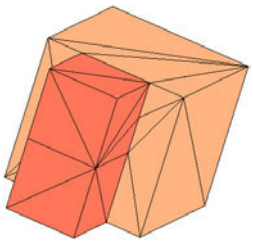

Fig. 6 – Result of an assembly of two prisms

Fig. 7 presents an example of an electrical device, a transformer, which is modeled, with the application of Boolean operations and the assembly operation. The air is modeled as a box that involves the transformer.

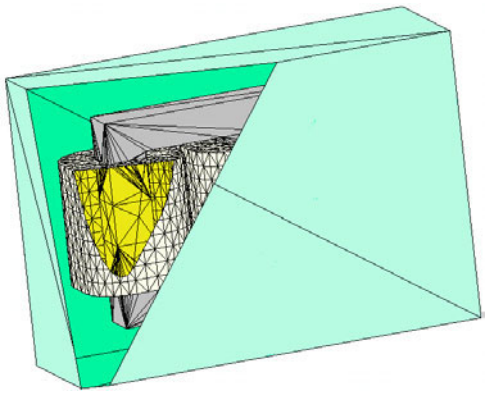

Fig. 7 – A view of a three-phase transformer

The meshes presented in the previous examples are used as input data to a finite element volumetric mesh generator [4]. This generator adds new points to the surface mesh improving its quality. So, the final quality of the finite element mesh is much better than the presented surface element quality.

CONCLUSIONS

The Boolean and the assembly operations make possible the creation of complex objects using any kind of pre-existent model, increasing the GSM descriptive power. In particular, the assembly operation, which, to our knowledge, is an exclusive feature of GSM, improves the representation of electromagnetic problems, making their description much easier than using other solid modelers.

REFERENCES

[1] A. L. C. C. Magalhães and R. C. Mesquita, "Exploring Inner Boundaries in Solid Modelers Applied to Electromagnetic Problems". IEEE Transactions on Magnetics, pp. 1682-1686, July 2000.

[2] A. L. C. C. Magalhães and R. C. Mesquita, "Requirements for a solid modeler coupled to a finite element mesh generator". IEEE Transactions on Magnetics, pp. 3347–3350, Sept. 1998.

[3] F. Arbab, "Set models and Boolean operations for solids and assemblies". IEEE computer graphics and applications, Los Alamos, p. 76-86, November 1990.

[4] S. Hang, "Tetgen: Quality Tetrahedral Mesh Generator", site <http://tetgen.berlios.de/>, e-mail: <sihang@mail.berlios.de>, Zhejiang University, China.

Static and dynamic consistency checking for numerical simulation: a mixed logic and object oriented programming approach.

Olivier Defour [1], Philippe Massé [2], Yves Maréchal [1]
[1] Laboratoire d'Électrotechnique de Grenoble - INPG/UJF-CNRS UMR 5529 ENSIEG, BP 46, 38402 Saint Martin d'Hères - France
[2] Laboratoire des Matériaux et du Génie Physique - INPG/UJF-CNRS UMR 5628 ENSPG, BP 46, 38402 Saint Martin d'Hères - France

***Abstract* - This paper presents a decision-making system based on Object Constraint Language formalism. This system ensures internal coherency of any object oriented simulation tools considering both static and dynamic behavior of the simulation tool. It has been implemented with a Java-Prolog coupling and we illustrate its capacities on several examples.**

INTRODUCTION

While the hardware performances tends to make simulation tools more and more affordable in terms of time consumption, the complexity of the simulation process has undoubtedly increased during the past few years.

There are several main reasons for that. First, the complexity of the numerical simulation formulations and methods themselves has increased. Because of a better understanding of what are the limits of today's methods as well as a higher level of requirements regarding the quality and the cost of the solution, we usually need to use hybrid methods and formulation giving the best solution at the best cost. Second, since numerical simulation in electromagnetism has proved to provide fairly good results, the industry has moved to more complex problems, corresponding to the always more complex devices is has to design.

Thus, not only the user spends a large time in modeling, but also in some cases the resolution fails because of inconsistencies in problem specifications. These errors are due to a bad modeling of the problem by the user. For instance, he is not fully aware neither of validity domains of models implemented by developers, nor the constraints on the coupling between them. On the contrary, knowing this kind of information provides great help for a successful modeling.

Of course, all this complexity is not wanted by the end user, and therefore, developers of commercial simulation packages in particular have to find ways to make the internal complexity more and more transparent to the end user, while in the same time guarantying the quality of the solution. This may become such a heavy constraint on the development process that it may even forbid integration of new functionalities.

This paper describes an Decision Making System that helps the end user to achieve a correct simulation at one go. It provides consistency checking, proposes valid choice, and explains why some input of the user are not accepted. The decision making system we have designed relies on a set of rules, expressing physical or numerical domains of validity. We will first see the state of art concerning Object Oriented Modeling techniques. Then, we will consider both static and dynamic consistency paradigm. Last, we will propose some examples of application of this system and consider the implementation requirements.

OBJECT ORIENTED MODELING STATE OF ART

It is well recognized that Object Oriented Programming (OOP) provides a powerful approach for designing and managing complex data models like the ones that are commonly used in any simulation environment. One step further in OOP technology consists in modeling the static and dynamic behavior of applications before their actual implementation using the Unified Modeling Language (UML™) ISO standard.

Considering the static modeling aspect, UML in itself does not provide full control on object associations. Object Constraint Language (OCL™) [1] is an important extension of UML that is dedicated for this job. It allows to express so called *class invariant rules*, i.e. constraints that should be verified at any time and for the full set of instances of a class.

The dynamic modeling side is not as developed as the static one. However, OCL still provides a *pre-condition* and *post-condition rules* formalism that enables the designer to define the necessary conditions before and after any method call.

OBJECT CONSTRAINT LANGUAGE

In order to illustrate our matter, let us consider an example of a simplified simulation software (Fig. 1).

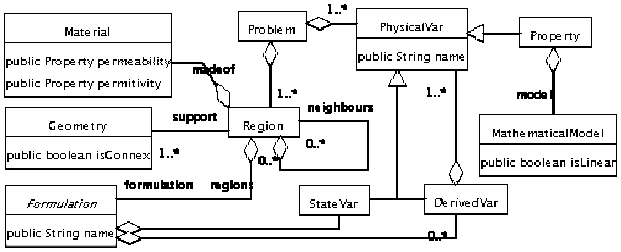

Fig. 1 – light UML diagram of simulation software

Let ScalarPotential be a formulation, developed under this specific constraint: «ScalarPotential formulation is valid only in a simply connected region R which permeability is linear ». This constraint may be translated into OCL invariant associated to the Region class:

```
context Region inv :
```

```
self.formulation.name = "ScalarPotential" implies
( self.support.isConnex and
  self.madeof.permeability.model.isLinear)
```

where the keyword self denotes an instance of the class Region. A similar syntax applies for pre and post conditions.

STATIC AND TRANSIENT ANALYSIS

In a static analysis context, we used the class invariant formalism to express all physical or numerical validity domains. The simulation environment is responsible for ensuring the validity of these constraints at any time. On the end user point of view, knowing that all theses constraints are verified is the guaranty that all known conditions of a successful simulation are met.

Considering transient analysis, ensuring the quality of the solution is a much more complex task, since it involves not only the validity of the initial numerical model, but also the validity of all numerical models at any time. For illustration purpose, consider for instance a typical induction heating problem. Geometry, mesh, numerical methods and formulations are closely related to the final level of temperature during the transient simulation. If, for any reason, the temperature rise becomes higher than the initial guess of the designer, the behavior of the materials may change considerably, and its choice of formulation, mesh or even geometry may become invalid. Thus, for transient analysis, even if the initial problem is correct, its evolution in time may get out the domain of validity of the chosen numerical model.

So, a first step towards the quality insurance of transient analysis consists in verifying the validity of all numerical models (i.e. verifying all available class invariant rules) at any time step. However, considering the end user point of view, this approach is limited since the only answer to rules violation is to stop the simulation process.

In our system, we tried to overcome this situation of system failure : of course, it detects the rules violation but also automatically adapts the numerical model of the device so as to become valid for the new time step. To achieve this, the designer has to provide additional information : first he needs to describe not only the initial numerical model of its device but also all potential models that may be encountered, to his point of view, during transient simulation. Second, the system needs to know what are the domains of validity of each potential model and how to move from one model to another. This needs are fulfilled by extending the simulation environment data model and by extensive use of OCL formalism, as explained in the full version of the paper.

FROM OCL TO PROLOG RULES

In this work, we implemented and extended the OCL approach in a simulation oriented Decision-Making System (DMS), using a mixed Java / Prolog programming

In order to standardize semantics, rules used in our DMS are strongly inspired by UML/OCL. So, the previous constraint is translated in this rule following the ISO-Prolog syntax [2]:

```
?- ocl_inv ( region, Self) :-
        instance ( Self, region),
        attribute ( Self, Form, formulation),
        attribute ( Form, "ScalarPotential", name), […] .
```

Thus, the semantic structure of the OCL expression is preserved in the DMS rule. The major difference is the presence inside rule of unknown variables (Self, Form). The answer of the DMS to a user query is the list of tuple of objects that satisfy the rule. For example, the previous rule applied to an instance of Region class, which known attributes are a simply connected geometry and a material with a linear permeability, determines that a possible formulation is ScalarPotential. The same rule applied to an other instance of Region class, which known attributes are a simply connected geometry and ScalarPotential formulation, determines that every instance of Material class with a linear permeability can be used as 'madeof' attribute.

DECISION-MAKING SYSTEM

Our Decision Making System provides three kinds of facilities : validity checking, proposal of valid solutions, and explanations of invalid choices.

The choice of a Java-Prolog coupling for implementing the DMS is natural. On the one hand, Java is a programming language respecting UML specifications. It also affords capabilities of dynamic method call (reflection), that are essential for rules verification. On the other hand, Prolog is dedicated to design DMS. The main issue of the coupling lies in the double representation of the data structures. The coupling uses Java Native Interface [3].

CONCLUSIONS

We have presented a Decision-Making System based on UML/OCL semantic. The DMS helps user to make coherent and valid choices. It is implemented by a Java-Prolog coupling.

REFERENCES

[1] OMG Documents : "UML 2.0 OCL RFP" (ad/2000-09-03), and "Response to the UML 2.0 OCL RFP" (ad/2001-08-01).

[2] ISO/IEC 13211-1, "Information technology -- Programming languages -- Prolog -- Part 1: General core" :1995.

[3] Liang S., "The Java™ Native Interface: Programmer's Guide and Specification" : Addison-Wesley Pub Co, 1999.

Random coupled gradient optimization of power busbars using PEEC method, Merging within finite element method

J.M. Guichon*, E. Clavel*, J. Roudet* and V. Mazauric**

* Laboratoire d'Electrotechnique de Grenoble
INPG/UJF – CNRS UMR 5529, ENSIEG, BP 46
38402 – Saint Martin d'Hères, France
edith.clavel@leg.ensieg.inpg.fr

** Schneider Electric
Research Center A2, 4 rue Volta
38050 – Grenoble Cedex 9, France
vincent.mazauric@mail.schneider.fr

***Abstract* – The modeling of connections using electrical equivalent circuit allows the evaluation of current or losses. Hence, the semi-analytical PEEC method is shown to be suitable to optimize geometry of conductors in order to reduce losses. To explore the space of solutions, an random method is coupled. At last, FEM allows taking into account magnetic shielding on the final design.**

I. INTRODUCTION

The design of power busbars is a compromise between several considerations:

- the per unit voltage drop;
- the geometrical constraints of the connections, volume and security;
- the optimization of copper volume versus carried power;
- the reduction of the number of shapes and references entering in the manufacturing process;
- the behavior to the electrodynamic strains;
- the respect of operating temperature;
- the Joule effect losses cutback;
- the Electro-Magnetic Compatibility.

The first two points are dominating constraints and are first looked up in the design process. The other points are adjusted to fit as well as possible the economic and normative constraints, given in the standard IEC 439-2 [1]. Usually, engineering and design centers use analysis tools based on Finite Element Method [2]. However, using such methods, the air must be meshed although it is one of the major adjustment means to the above mentioned constraints. Improvements are then reduced to "try and error" methods – with tedious re-meshing procedures at each check – or to determine behavior trends using a design of experiments.

In order to provide a parameterized design with arrangement of the bars, we have thought about an alternative method that "locates" the electromagnetic energy in conductors. The Partial Electrical Element Circuit (PEEC) method carries out this objective [3]. This method allows to obtain an electrical equivalent circuit of the problem directly linked to its geometry using analytical formula [4].

Hence, it is possible to optimize the geometry of the structure considering electrical criteria such as a low loop inductance, a balanced current sharing or a reduction of Joule losses induced by proximity effects... This may be done by gradient algorithm for a convex function. However, local minimum points are expected and a coupling with random procedure is described to catch other solutions.

As PEEC method does not allow to take into account magnetic materials, the final geometry of bars is introduced in a FEM software in order to analyze the impact of magnetic shielding on global Joule losses.

II. RANDOM COUPLED GRADIENT ALGORITHM FOR GLOBAL OPTIMIZATION

An example of investigated structure (Fig. 1) consists in a three-phases power bars structure in which it is important to control losses to limit temperature.

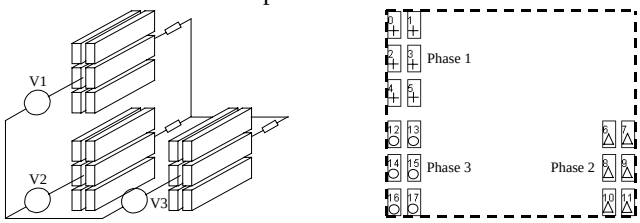

Fig. 1: Present structure to optimize (P = 663 W)

A gradient algorithm is a convenient procedure to optimize the geometry of the structure because calculations of equivalent circuit element lay on analytical formula, and then gradient of the objective function with respect of the position of the bars too. It has already given attractive results for our kind of problem [5].

However, the solution depends on the initial condition because it is based on the search of local minimum point only. Hence, for non-suitable initial point, such procedure may reach to a poor solution.

In order to circumvent such limitations, one idea is to start from several initial points. Their generation is obtained with random algorithm, which generates random numbers with non-uniform density. This density is modified during the optimization process according to the best points found. The algorithm keeps the n best initial conditions (n is chosen by the user). Therefore, for each of those initial conditions, the gradient optimization process is run to find the best local point.

At this step, the n local best points are known. Then it is just a choice to retain the better compromise between low costs, realistic solution, performances, and standards... This approach allows optimization of discrete problems (if only the random part is used). According to the considered case,

the objective function could not be better but a new technological solution can be reached and lead to a new design. This is the good way to innovate.

For example, Fig. 2 shows two optimized solutions providing approximately the same value of the objective function and obtained with this approach from the geometry presented at Fig. 1. While the second geometrical agency is realistic, the first one is not.

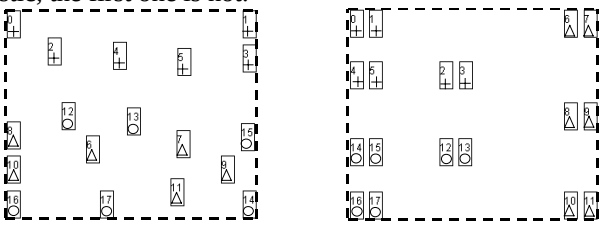

Fig. 2: Two optimizations (respectively P = 495 W and P = 511 W)

III. FEM SIMULATION

Thanks to the PEEC approach, it is possible to obtain global and local currents in the conductors taking into account skin and proximity effects. These values are introduced within a finite element approach to describe the inductors.

The basic idea of the FEM is to build an approximate variational formulation of divergence-free flux density and Maxwell-Faraday equations with a finite number of degrees of freedom. In this case, it is convenient to chose as degrees of freedom a magnetic scalar potential Φ along with an electrical vector potential $\vec{T}$ in the conductors at the nodes of the mesh [6], so that:

$$\vec{H} = \vec{T} - \overrightarrow{\text{grad}}\Phi \qquad (1)$$

obeys the Maxwell-Ampere equation.

Table 1 gives a summary of formulations used in various regions. While $\vec{Js} = \overrightarrow{\text{rot}}\vec{T_0}$ is given by Biot and Savart's law from PEEC calculations, the eddy current correction $\vec{Jf} = \overrightarrow{\text{rot}}\vec{T_1}$ provided by the ferromagnetic reaction of the shield is given by FEM.

TABLE I: SUMMARY OF FORMULATIONS PROVIDING H ACCORDING TO (1)

Busbar	Conductor	Air	Shield
Without shield (PEEC)	T_0	T_0	0
Without reaction of shield (PEEC - FEM)	T_0,Φ		T_1,Φ
With reaction of shield (PEEC - FEM)	T_0+T_1,Φ	T_0,Φ	T_1,Φ

The busbar structure, within its magnetic shield, has been modeled with a FEM software before and after optimization (table 2). Results on the optimized structure remain better when magnetic materials are considered.

Moreover, thanks to FEM, it is also possible to yield eddy current density in magnetic materials, and so point out regions where losses and temperatures may be critical (Fig. 4).

TABLE II: RESULT OF FEM SIMULATION

	Geometry		Losses (W)
Before optimization	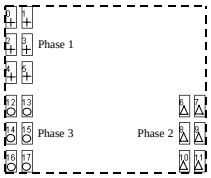	Without shield	Ptotal = 663
		With shield	Ptotal = 885 Pconductor = 735 Pshield = 150
After optimization	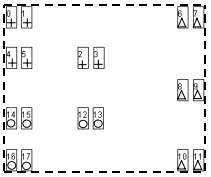	Without shield	Ptotal = 511
		With shield	Ptotal = 654 Pconductor = 561 Pshield = 93

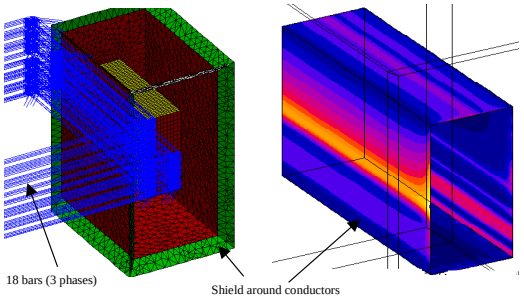

Fig. 4 : left : FEM meshing – right : Eddy currents in shielding part

IV. CONCLUSIONS

In this article, an optimization process is detailed. It consists in evaluating several initial points using random approach and to select the best design with respect of the objective function. Hence, the solution is introduced in FEM in order to analyze the magnetic behavior of the shield. Earning on Joule losses for the studied power busbar with its shield is about 26 %.

[1] "Low-voltage switchgear and controlgear assemblies - Particular requirements for busbar trunking systems", in IEC Standard 439-2. Geneva, Swiss.

[2] O. Bottauscio, E. Carpaneto, M. Chiampi, D. Chiarabaglio, and I. Panaitescu, "Numerical and experimental evaluation of magnetic field generated by power busbar systems", *IEE Proceedings - Generation, Transmission and Distribution*, 143 (1996) pp. 455 – 460.

[3] J.-M. Guichon, E. Clavel, J. Roudet, and V. Mazauric, "Method to compute current density in power distribution bars", presented at Biennal IEEE Conference on electromagnetic field computation (CEFC2k), Milwaukee, Wisconsin USA, 2000.

[4] C. Hoer, C. Love, "Exact Inductance Equations for Rectangular Conductors With Applications to More Complicated Geometries", *Journal of Research of the national Bureau of Standards – C. Engineering and Instrumentation*, Vol. 69C, No 2, pp. 127 – 137, 1965.

[5] N. Piette, Y. Maréchal, E. Clavel, "Optimization of Interconnection Inductances with a Coupled PEEC-Quasi-Newton Method", IEEE – CEFC'98, Tucson, Arizona, pp 453, June 1998.

[6] O. Biro, K. Preis, G. Vrisk, F.R. Richter, "Computation of 3D magnetostatic fields using a reduced scalar potential", *IEEE Transaction on Magnetic*, Vol. 29, No. 2, pp. 1329-32, March 1993.

A Framework for Collaborative Engineering Design and Analysis

Z. Xie, Z.J. Liu, T.C. Chong, and H. Zhou

Data Storage Institute, DSI Building, 5 Engineering Drive 1
Singapore 117608
xie_zhao@dsi.a-star.edu.sg

Abstract **-Engineering design is complex and highly iterative activity that may involve a number of designers who are geographically separated. The need for a design environment that allows collaboration among multiple designers to resolve the design conflicts at the early design stage is becoming apparent. This paper presents a framework for collaborative design and analysis, and, using an electromagnetic design of electric motors by way of example, demonstrates the structure of the environment through which multiple designer can work collaboratively with support from engineering design tools.**

INTRODUCTION

The need for engineering design collaboration arises from time to time across the production chain of manufacturing enterprises. Over 50% of the components manufactured by OEM are out-sourced to external supplier [1]. Resolving design issues in the early design stage reduces product lead-time and cost to a large extent [2].

The ever evolving network technology lead to several collaborative design efforts. Collaborative Solid Modeling system (CSM) proposed by Chan et al.[3] is a web-based collaborative modeling system for CAD with a client/server architecture. NetFEATURE presented by Lee et al.[4] is claimed to be a collaborative, web-based feature modeling system. This paper discusses a framework for collaborative engineering design and analysis. Using an electromagnetic design case relating to electric motors, we demonstrate the structure of the environment through which multiple designer can work collaboratively with support from engineering design tools over the network.

.

ARCHITECTURE AND DESIGN CONSIDERATIONS

Collaborative engineering design system is distributed system that allows multiple designers geographically separated to conduct design activities cooperatively, concurrently and synchronously. There are several crucial issues when designing such a system.

1. Three -tiered client/server architecture

Collaborative engineering design requires a good level of interactivity between client and server, thus an engineering design specific user interface is necessary as compared to an extremely ideal thin client for web-based applications. Moreover, due to the network limited bandwidth, putting all the functions on the server will cause more rounds of interaction between client and server and consequently decrease the performance. Nevertheless, putting more data and functionality on the client is not a good solution either, as synchronizing the design data among the clients in the same session will become another critical problem. However, installation of a complex thick client application is tedious. Therefore, finding a compromising solution to balance the activities of client and server is a challenge.

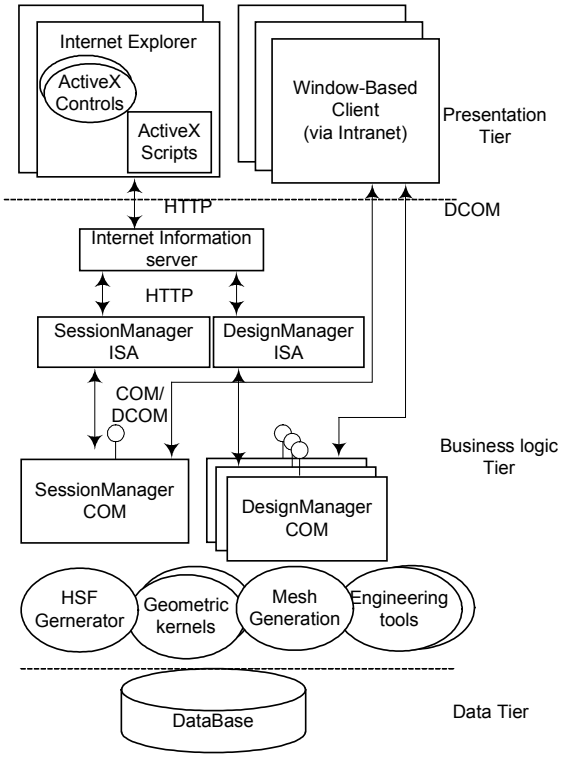

Fig. 1 Architecture of collaborative CAE framework

For the proposed framework, a three-tiered client/server architecture is adopted, as shown in Fig.1. The business logic tier contains a series of COM components that can be divided into two categories by their responsibilities, component managing the collaboration sessions and components dedicating to engineering functions that can be found in a typical standalone CAE system. For the presentation tier, two kinds of clients are built. Native Windows client written in C++ can access the server through DCOM via Intranet. The other one is Internet Browser client with a downloadable

ActiveX control embedded that can access server services across the Internet. The data ties can be databases or file systems. To be simplified, a file system is used in this framework as a demonstration.

2. Model data management

In the framework, the product geometric model, data intensive and the computationally expensive functions can be managed at server side. A 3D compact visualization representation, Hoops Streaming Format (HSF), which is specifically tailored to the needs of displaying engineering data is adopted for client side visualization. In the collaborative mode, product geometric model is never modified directly by the client application, instead a message containing the operation command will be sent to the server. Consequently, server parses the message and connects to the corresponding tools to execute the operation.

3. Concurrency, synchronization and session management

Since the design activities could be conduct on the same entity at the same time by multiple users in a session, a concurrency control mechanism is needed to resolve operation conflicts. In the framework, a control token is passed among the clients in one design session to grant the operation right to the holder. This can ensure that only one client at a single moment has the right to manipulate the product design. Furthermore, when the central design is modified by any of the client in a session, the updated model representation data should be sent back to all other session participants as well. Several sessions could be proceeded in parallel on the server. Once connect to the server, the client can join an ongoing collaborative design session or open a new design session. In the framework, all the information about sessions is handled by session management component on the server. When a new session starts, the Session Manager creates a new instance of the DesignManager component, register it with its mapping list and then pass the interface to the client. Thus, the connection between client and session is established.

4. Client/Server Communication

Two possible types of connection may be used to access the server, connection via Intranet and connection via Internet. For the first type connection, the client just uses TCP/IP to communicate with the server. To the second type, HTTP is only the available/acceptable protocol. Thus, a layer built on ISAPI is also developed to serve as a gateway between HTTP protocol and the server side COM component.

5. A collaborative design case using the framework

In this section, an electromagnetic design case relating to electric motors is presented to demonstrate how the framework can be utilized as a collaborative design environment, as shown in Fig 2.

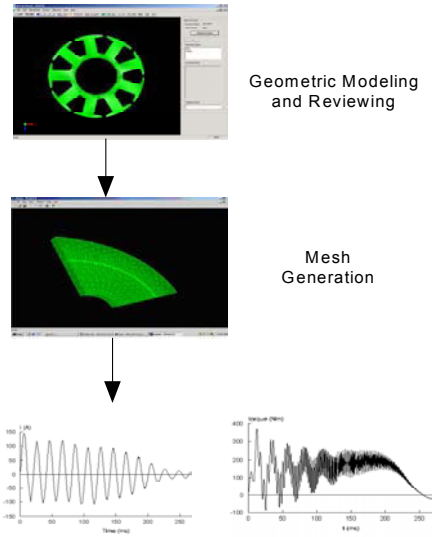

Fig 2. Electromagnetic Design of a electric motor

- Create a session. Client A (CA) connects to the server, initiate a design session, and send a request to the server to load the product geometry into the session. Server returns HSF representation format of the rotor to CA. CA calls Client B (CB) to join this design session.
- Join a session. CB connects to the server, finds and joins the session. B receives the HSF representation of the same model. B's view is also synchronized as A's.
- Work collaboratively. CA and CB discuss on the model, mark up on it. If one modifies the model, the server component connects geometric kernel and executed the operation. They can decide, for example, the correct way for meshing and numerical techniques to choose for the analysis, and to discuss on the computational results.

CONCLUSIONS

This paper introduces a framework using COM technology that can provide not only the engineering design tools but also the collaborative functionality that support collaboration among design engineers over the Internet. As the .Net technology evolves, the .Net framework provides more choices for communication between distributed parts of an application. It is expected that a much easier yet powerful framework can be build up with the COM interoperability feature of .Net framework.

REFERENCES

[1] Rezayat M. The enterprise-web portal for life-cycle support. Comput Aided Des 2000:32(2):85-96.
[2] Ullman DG.The mechanical design process. New York: McGraw Hill,1997.
[3] Chan, S., Wong, M. and Ng, V. (1999) Collaborative solid modeling on the WWW. Proceedings of the 1999 ACM Symposium on Applied Computing, San Antonio, CA, pp. 598-602.
[4] Lee J. Y., Kim, Han, S.B. and Park, S.B. (1999) Network-centric feature-based modeling. Proceedings of Pacific Graphics'99, Kim, M.-S. and Seidel, H.-P (Eds.), IEEE computer Society, CA, pp. 280-289.

Nanometer-Scale Electric Field Analysis by Sub-Window Zooming-In Technique

Sang-Joon Han, Se-Hee Lee, Joon-Ho Lee, and Il-Han Park
School of Information and Communications Eng., Sungkyunkwan Univ., Suwon 440-746, KOREA
E-mail: sangjhan@yahoo.co.kr

Abstract —**This p aper presents a numerical technique of local scaling of sub-windows that is for electric field calculation in nanometer-scale dimension system. To show validity of this sub-window zooming-in technique, the analytic solution of a spherical electrode problem is compared to its numerical solution, which is obtained by using the finite element method of electric scalar potential variables. This technique is applied to a real model of ferroelectric thin film recording by scanning probe microscopy.**

INTRODUCTION

Today various scanning probe microscopy (SPM) technologies are actively being developed. Among them, the next generation high-density data storage seems to be one of the most prominent applications [1]. This paper deals with one of the SPM technologies of following characteristic. A conductive atomic force microscope (AFM) tip above the film surface is supplied with a voltage to polarize ferroelectric domain for a bit data recording. The recorded bit is then read by electrostatic force microscopy (EFM) technique. The electric field distribution inside the ferroelectric film is necessary for analyzing and predicting the bit size. The size varies according to the tip radius and the gap size between the PZT film and the tip. The EFM makes use of electrostatic force between the AFM tip and the PZT film. Therefore, precise analysis of electric field distribution and force density is required for evaluating the characteristics of reading and writing process of ferroelectric data storage [1]. The critical problem in geometrical modeling for the system analysis lies in the fact that the tip and the air gap is too small compared with the total system to analyze that system only with one numerical modeling.

ZOOMING-IN TECHNIQUE USING SUB-WINDOW

The sub-window zooming-in technique is a method to precisely analyze the significant part of nano-systems by using zooming-in window of multi-steps. The basic procedure of this sub-window zooming-in technique is explained below.

First, the electric field is analyzed for the original system with a relatively coarse mesh density. Next, to close up a concerned smaller region a sub-window inside the original system is taken. The electric field for the sub-window region is also analyzed using the boundary condition obtained from the potential values of the original system. This above basic analysis procedure is repeated until the concerned region has fine mesh density that gives reasonable field distribution as shown by Fig. 1.

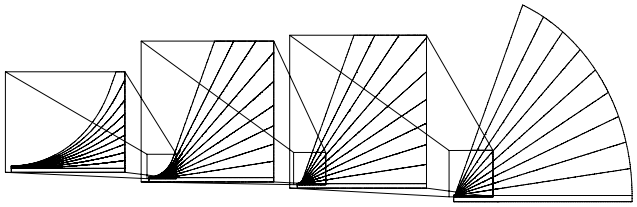

Fig. 1. Closing up by sub-windows

VALIDITY OF SUB-WINDOW ZOOMING-IN TECHNIQUE

To validate the proposed algorithm, we tested a spherical electrode doped with dielectric material as shown by Fig. 2. This model has a simple spherical conductor whose radius is 1(nm). The dielectric material covered the conductor has the thickness of 1(nm) and relative dielectric constant of 10, respectively. The radius of outer boundary is 1000(nm), which is sufficiently large compared to the electrode. 1V was applied to the conductor surface and 0V, the outer boundary surface.

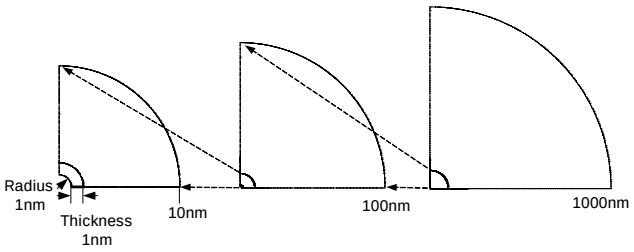

Fig. 2. A quarter part of simple test model in three steps

In this example, to compare the values between analytic and numerical solutions, the electric field intensity was tested between the radius of 1 and 2(nm) from the center of spherical conductor. The exact solution of electric field intensity in this dielectric region is obtained as follows [2].

$$\mathbf{E} = \frac{10^{-7}}{549}\left(\frac{1}{r^2}\right)\hat{a}_r \qquad \text{[V/m]} \qquad (1)$$

where, r is radius from the center of conductor, and $\hat{a}_r$ the unit vector of radius direction. This model was numerically analyzed to third step by using finite element method [3]. Fig. 3 shows the relative errors of electric field intensity between

the analytic solution (1) and numerical solutions, which are obtained in each step. As we can see in this Fig. 3, there was a significant difference of electric field intensity in the first step but the trend of error was a rapid decrease toward final step. In the final step, the error was below 0.1%.

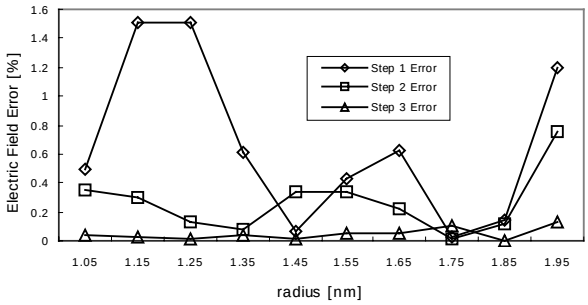

Fig. 3. Comparison with electric field intensity errors in each step

For a better result, boundary value data of each step must be obtained from 50%±10% region in current step. If the boundary value data is obtained from below 40% window size of current step region, the final results will become incorrect.

Therefore, we conclude that the sub-window zooming-in technique is useful method and is applicable to the analysis of nanometer-scale systems.

APPLICATION TO FERROELECTRIC DATA STORAGE DEVICE

On the basis of the above verification, we applied this sub-window zooming-in technique to calculating electric field intensity in ferroelectric data storage device using PZT film. The ferroelectric data storage using PZT film is the next generation high-density data storage has the basis structure.

Fig. 4 shows a type of the ferroelectric data storage using PZT film. The memory disk, PZT plate, was doped with the ferroelectric material with a thickness of 30~100(nm) on the surface [1]. While the size of the total system is in the order of micrometer, the tip radius is 20(nm) and the air gap between the PZT film surface and the tip is 0.8(nm) as in Fig. 4.

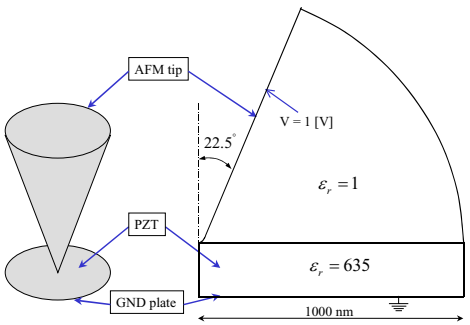

Fig. 4. Model description of electrode tip in ferroelectric data storage

This model was analyzed by the sub-window zooming-in technique with four steps. Fig. 5 shows the result of electric scalar potential distribution in the PZT by the round shape electrode tip at final step. Through the precise calculation of electric field, we compute the bit size evaluation and electrostatic force microscopy in ferroelectric thin film recording.

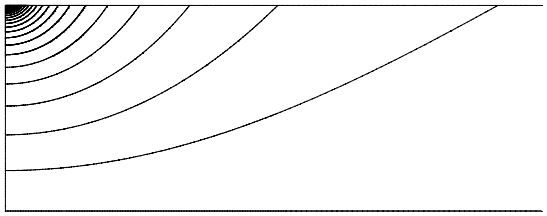

Fig. 5. Equi-potential lines in the PZT at final step

CONCLUSION

In this paper we presented the sub-window zooming-in technique for calculating accurate electric field of very small part such as in micro-electromechanical system and scanning probe microscopy technology. An analysis problem with an exact solution was tested and compared with the numerical values obtained by the sub-window zooming-in technique. Its results showed its validity that the technique gives sufficiently accurate values in nanometer-scale field analysis. In addition, the analysis procedure was also applied to a ferroelectric device of PZT film for data storage, where the bit size was analyzed and predicted. The detailed explanation and numerical data will be presented in the extended full version of paper.

REFERENCES

[1] C.H. Ahn et al., "Local, nonvolatile electronic writing of epitaxial $PbZr_{1-x}Ti_xO_3/SrRuO_3$ heterostructure," Science, vol.276, pp.110-113, 1997.

[2] Reitz, Milford, and Christy, Foundations of electromagnetic theory, Addison-Wesley publishing Co., 1993.

[3] Sheppard J. Salon, Finite element analysis of electrical machines, Kluwer academic publishers, 1995.

The Application of Sensitivity Analysis in the Design Process for Electromagnetic Devices

A. Cowan, D. Lowther
Department of Electrical and Computer Engineering
McGill University
3480 University Street, Montreal, Quebec Canada
e-mail: lowther@ece.mcgill.ca

***Abstract*—The paper describes the background to the determination of the sensitivity of the performance of a device to changes in its design parameters. Examples are given of the use of sensitivity analysis to indicate how the performance might change as a result of errors in manufacturing and how a knowledge of the variation of performance as a function of changes in parameter values can be used to accelerate optimization processes.**

INTRODUCTION

The process of designing an electromagnetic device or system consists of several stages beginning with the creation of a set of requirements (or specifications) which define the performance of the device and the constraints being imposed; and moving through synthesis, analysis and optimization until the desired solution is found or the process results in failure.

The design process itself is subject to a cost constraint: the more iterations used (or the longer it takes to find a solution in the design space) the higher the cost. In setting up a design system, then, a major goal is to minimize cost of the design process itself. Often, this is directly proportional to the time taken in the process and can be a major component of the final cost of the device being designed.

Advances in computational capability over the last three decades have provided the ability to replace physical test models with computer based equivalents. These are, usually, more flexible than the physical models and can provide results and insights into a design much faster and at lower cost. At this point in time, while analysis can always be improved, it has become almost a routine process for an electromagnetic device and, in the hands of a reasonably skilled designer, can deliver results which are certainly within the measurement tolerances for the physical device.

However, in creating an appropriate solution for a problem, there are two major issues facing the designer. The first relates to optimizing the device to try to match the requirements; the second to understanding how manufacturing errors (or tolerances in dimensions and properties) can affect the performance of the optimized design, i.e. will it still perform as required by the specifications?

There are several ways in which the optimization process can be approached from a fully automatic system based around zero or first order deterministic systems or stochastic methods through to manual modifications of the design in an attempt to improve the performance.

For both the automatic and manual approaches, considerable information can be developed by applying sensitivity analysis to the current design with the intention of determining which parameters in the design have the greatest effect on the desired performance. Once a design has been completed, the sensitivity information can then be used again to examine the effects of tolerance ranges on the optimum device performance.

The intention of this paper is to demonstrate the use of sensitivity analysis in the design process for both optimization and tolerancing.

SENSITIVITY ANALYSIS

The concept of determining the effect on the performance of a system of a small change in a particular parameter can be traced back to Tellegen's theorem [1] for electrical circuits and Lorenz's Reciprocity Theorem for distributed electromagnetic systems [2]. Tellegen's theorem has become a cornerstone in electronic circuit design for determining the effects of small variations in components on the performance of a circuit and several design systems use this to provide feedback on problem areas to a designer.

Sensitivity analysis, however, is not restricted to discrete systems such as electrical circuits, it can be developed for continuous systems such as those encountered in structural engineering or electromagnetics and over the last decade work in this area has been reported by several authors, for example [3], [4], [5].

The goal of a sensitivity analysis is to determine the sensitivity of an objective (cost) function, F, to variations in the design parameters, P. If the cost function is expressed as a function of the design parameters and the magnetic vector potential, A, as F(P, A), then the sensitivity with respect to the design parameters is given by:

$$\frac{dF}{dP} = \frac{\partial F}{\partial P} + \frac{\partial F}{\partial A} \cdot \frac{\partial A}{\partial P} \tag{1}$$

While $\partial F/\partial P$ and $\partial F/\partial A$ can be derived from F, $\partial A/\partial P$ must be obtained via the finite element representation of Poisson's equation:

$$SA = TJ \tag{2}$$

After some manipulation and the introduction of an adjoint vector, λ,

$$\lambda S = \frac{\partial F}{\partial A} \tag{3}$$

The final sensitivity equation is

$$\frac{dF}{dP} = \frac{\partial F}{\partial P} + \frac{\partial F}{\partial A} \cdot \frac{\lambda \partial (TJ - SA)}{\partial P} \tag{4}$$

From (4) above, the sensitivity of the performance of a particular device to any change in its design parameters can be determined. Thus a designer can be presented with a view of the design which shows those areas of the design which are most sensitive to a change in a particular parameter for a specified output quantity. For example, consider the inductance of a simple C-Core device. The designer is interested in where changes in the basic shape or material properties would have the most effect on the inductance. Fig.1. shows a shaded plot of the "sensitivity map" of the inductance as a function of the material of the structure. The picture clearly shows that small shape (material) changes near the outer edge of the air gap (where there is a magnetic insert) would have a large effect on the inductance value. If a designer was looking at the effect on the inductance of small changes to the device, it is evident from the display that these could be critical if they occur in the air gap area. Thus, if the question being asked relates to manufacturing tolerances, the solution makes it clear that any errors in manufacturing in the region of the air gap could have significant effects on the performance of the device.

Similar maps can be produced for any output parameter which can be expressed as a function of the currents and magnetic fields in the device.

SENSITIVITY ANALYSIS FOR OPTIMIZATION

Probably the most obvious use of sensitivity analysis is to improve the performance of optimization systems. Rather than showing a designer where to change the device in order to maximize the value of a cost function, the system can use this information to guide an optimizer. The ability to produce the gradient information for the cost of a single linear solution following the computation of the field can significantly reduce the time taken to optimize the performance of a device. The system discussed above for tolerancing has been used to guide a standard optimization process on the TEAM 25 problem – the Die Press Model. The time taken to optimize this device when sensitivity information is added is estimated at about 30% of the time taken with a conventional deterministic approach (11.9 seconds per iteration compared with 41 seconds). The convergence of the problem is shown in Fig. 2.

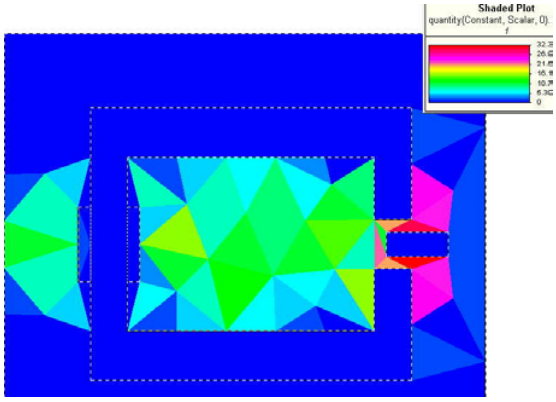

Fig. 1. Sensitivity of Inductance Value to Material Property Changes.

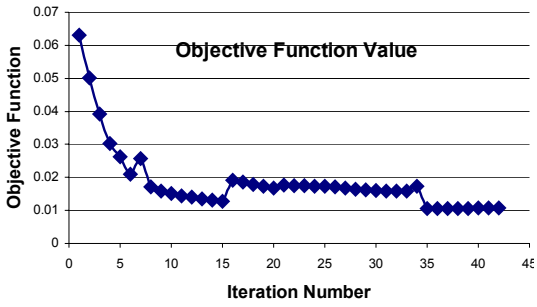

Fig. 2. Convergence of TEAM 25 using sensitivity.

CONCLUSIONS

The ability to compute the sensitivity of the performance of a device to changes in its design parameters can provide the designer with a large amount of information concerning the manufacturability and stability of a particular design. It also provides an effective method for implementing deterministic optimizers and deriving significant speed gains. In addition, quantities such as forces can be re-expressed in terms of the sensitivity of the energy stored to changes in shape and thus some force calculation methods can be seen as special forms of a generalized sensitivity approach.

The final paper will expand on most of the areas described above and will include a larger range of examples.

REFERENCES

[1] B.D.H.Tellegen, "A general network theorem, with applications," *Philips Research Reports*, Vol. 7, pp. 259-269, 1952.

[2] H.A.Lorentz,,"Vorslagen van de gewone vergadring der wis- en natuurkundige afdeeling," *Verslagen der Koninklijke Akademie van Wetenschappe*n, (Amsterdam), Vol. 4, p. 176-, 1896.

[3] S.Wang, S.Jeong, H.Yoon, "Continuum shape design sensitivity analysis of magnetistatic field using finite element method," *IEEE Transactions on Magnetics*, Vol. 35, May 1999, pp. 1159-1162.

[4] S-H.Lee, D-H.Kim, J-H.Lee, B-S.Kim, I-H.Park, "Shape design sensitivity for force distribution of magnetic systems," *IEEE Transactions on Applied Superconductivity*, Vol. 12, March 2002, pp. 1471-1474.

[5] J.A.Ramirez, E.M.Freeman, C.Chat-uthai, D.A.Lowther, "Sensitivity analysis for the automatic shape design of electromagnetic devices in 3D using FEM," *IEEE Transactions on Magnetics*, Vol. 33, March 1997, pp. 1856-1859.

A Sensitivity-Driven Parametric Electromagnetic Design Environment

P. Weicker, D. Lowther
Department of Electrical and Computer Engineering
McGill University
3480 University Street, Montreal, Quebec Canada
e-mail: lowther@ece.mcgill.ca

***Abstract*—The paper describes a design environment for electromagnetic devices and systems which links the concepts of variational geometry with sensitivity analysis. The goal is to allow a designer to explore a potential set of solutions to a design problem which has been posed through a rough, parameterized geometric sketch of the desired device.**

INTRODUCTION

While the creation of the virtual electromagnetic laboratory has become possible with the advances in numerical analysis systems and the gains in computational power over the past half century, attention has only recently shifted to using these capabilities in the synthesis phase of the design process. The tools available to assist the thought processes of the designer have actually progressed relatively slowly and the result is that pencil and paper and rough sketches are still a major component of developing design solutions. It is a well established fact that computer tools are only accepted by users when they can either provide more capability than existing methods or do the same job faster. The question to be addressed, then, is "how early in the design/thought process is it now possible to introduce computational electromagnetic tools?" Can the pencil and paper sketch plus rule of thumb field estimation be replaced and to what extent can it be enhanced?

In fact, all the components exist to create an effective replacement for the pencil and paper "sketch" paradigm. Such a system should allow a designer to enter a rough diagram of the proposed device and to parameterize this both in terms of its topology and its geometric quantities. If the system is limited, at least initially, to two-dimensions, then the various computational algorithms can be expected to operate fast enough that significant information can be provided to the designer in "real time".

In addition to working with the user in parameterizing the structure, future developments of the system could allow an interface to a case based reasoning system [1] which can be used to match the user's concepts onto an existing database of designs. These can then be presented to the user as he/she is working, thus enhancing the current "pencil and paper" paradigm.

VARIATIONAL GEOMETRY AND OPTIMIZATION

In handling a rough description of a device, there are two issues of importance in its physical shape. The first is its topology and the second the geometric structure. In creating a sketch, a user is generally creating a topological definition of the problem, i.e. the number of lines and arcs and the connections between them are specified. The geometric structure is generally a secondary consideration and leads to the concept of "parameterization". However, there is a third relationship – one which links the geometric parameters in some way. This third structure places constraints on the parameters and can actually reduce the number of parameters in the problem [2], [3]. Thus a line in a drawing might be constrained to be vertical, i.e. implying that the horizontal coordinate ("x") of both ends of the line should be the same. Or a line could be specified such that its ends are tangent to two circles. These constraints result in a reduced parameter set and lead to the concepts embedded in variational geometry.

In the first phase of creating a device, the user can specify the topology of a device by a largely freehand sketch. Each of the primitives used can be parameterized and the parameters linked to maintain the topology. These parameters can also be constrained so that particular geometric structures are enforced. These parametric constraints and relationships form the basis of the variational geometry approach and, when a device is optimized, serve to both limit the size of the parameter space as well as to control the changes in the geometric structure which an optimizer might attempt to make.

Once the constraints have been imposed and an initial set of values have been allocated to the parameters, a set of materials and excitations can be added and the problem solved.

The next step involves the use of sensitivity information to indicate how a geometry might be altered in order to optimize a cost function (e.g. the inductance of a permeable core with a winding).

SENSITIVITY AND OPTIMIZATION

A conventional deterministic optimizer (as opposed to stochastic systems such as genetic algorithms) tries to use information concerning the shape of the design space in the region around the current solution in an effort to improve the solution. This can be slow since each solution to a parameterized problem produces a single value in the search space. Recent work in shape optimization, [4], [5], has demonstrated that it is possible to set up a simple post-processing solution based on a finite element representation of the problem which can produce the variation of any desired

performance parameter with respect to a change in any input parameter. The basic form of this work expects a set of parameters (and typical of this is the set of endpoints of geometric primitives) to be linked to the geometry. It is then possible to determine if a slight variation in a geometric parameter, i.e. in the shape of the device, will have a large effect on the performance. The variational geometry approach described above sets constraints on how the sensitivity is derived and part of the work to be described in this paper is related to the merging of the variational geometry constraints with the sensitivity analysis. The information produced by the combination of these two pieces of work can significantly increase the speed of the optimization process since the deterministic optimizers can function much more effectively with the slope information while maintaining certain geometric constraints.

A System Design

Taking the above into account and using a standard commercial finite element package [6] as the core solution engine, a typical structure for the proposed system would be similar to that shown in Fig.1. In this model, once the user has produced a preliminary drawing and entered the constraints on the geometric primitives, the problem is solved and a sensitivity analysis with respect to the geometric parameters performed. This can provide fast feedback to the designer of critical points in the design and allow interactive geometric modifications to improve the performance. Fig.2. shows the basic parametric drawing system. The scrollable window on the right hand side shows an editable area for geometric parameters and allows the constraints to be set up. As these are entered, the initial sketch drawing is adjusted to impose the constraints.

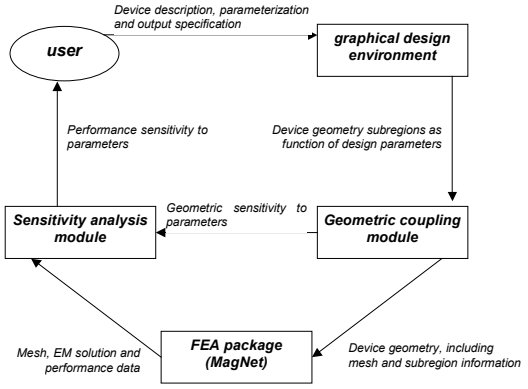

Fig. 1. System Architecture.

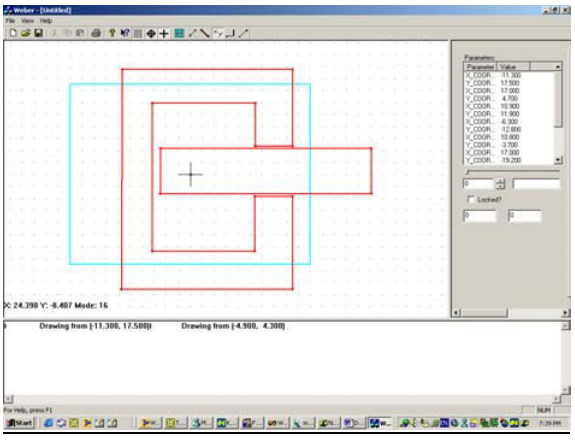

Fig. 2. Parametric drawing system.

Previous Design Experience

The system can be significantly enhanced by the inclusion of a Case Storage and Identification System which keeps a record of previous designs. The designs are stored based on their topologies and hence the sketched topology can be used to identify previous designs which may be of use in solving the current problem. These are displayed for the user as the design proceeds.

Conclusions

The paper has discussed the creation of a two-dimensional tool which can assist in the design of an electromagnetic device by taking initial topological descriptions of a device and allowing geometric constraints to be imposed. These constraints are then combined with a sensitivity analysis to provide information either to an optimizer or as visual feedback to the designer. By using the topological and geometric constraint information with a case based reasoning system, a set of previous designs which might be applicable to the current problem can be presented as the design progresses. The final paper will expand on the above and include experimental measurements made on the system.

References

[1] R.Rong, D.A.Lowther, "Adapting design using dimensional models of electromagnetic devices," *IEEE Transactions on Magnetics*, Vol. 32, May 1996, pp. 1437-1440.

[2] C.F.Parker, J.K.Sykulski, S.C.Taylor, C.S.Biddlecombe, "Parametric environment for EM computer aided design," *IEEE Transactions on Magnetics*, Vol. 32, May 1996, pp. 1433-1436.

[3] C.S.Biddlecombe, J.K.Sykulski, S.C.Taylor, "Design Environment Modules for Non-Specialist Users of EM Software", *IEEE Transactions on Magnetics*, Vol. 30, Sept. 1994, pp. 3625-3628

[4] S.H.E.Choi, D.A.Lowther, D.N.Dyck, "Determining boundary shapes from the optimized material distribution system," *IEEE Transactions on Magnetics*, Vol. 34, Sept 1998, pp. 2833-2836.

[5] S-H.Lee, D-H.Kim, J-H.Lee, B-S.Kim, I-H.Park, "Shape design sensitivity for force distribution of magnetic systems," *IEEE Transactions on Applied Superconductivity*, Vol. 12, March 2002, pp. 1471-1474.

[6] "The MagNet User's Guide", Infolytica Corporation, 2002.

Sensitivity Matrix Calculation for Fast Electrical Capacitance Tomography (ECT) of Flow Systems

Q. Marashdeh and F. L. Teixeira
ElectroScience Laboratory and Department of Electrical Engineering
The Ohio State University
Columbus, OH 43210, USA
marashdeh.1@osu.edu

***Abstract* — We describe an efficient approach to calculate the sensitivity matrix for three-dimensional (3-D) image reconstruction problems using electrical capacitance tomography (ECT). The sensitivity matrix calculation is used in conjunction with a neural-network based multi-criterion optimization image reconstruction technique (NN-MOIRT). The system is designed towards real time imaging of two-phase (gas-liquid) and three-phase (gas-liquid-solid) flow systems.**

I. INTRODUCTION

Electrical capacitance tomography (ECT) is being increasingly adopted in both laboratory and industry as an efficient tool to analyze multiphase flow systems. One of the most important issues in real time tomography of flow systems is the speed of capturing the data. ECT is considered to be the fastest among competing techniques, being able to capture as much as 100 frames per second. In terms of resolution capabilities, ECT has attained a good accuracy when using neural network based multi-criterion optimization image reconstruction technique (NN-MOIRT) [1]

The inverse problem (reconstruction) in electrical capacitance tomography is non-linear. Therefore, commonly used and/or commercially available techniques for linear tomography based on electromagnetic radiation (as the ones widely employed in medical fields), are not directly applicable to the nonlinear problem in ECT. A highly accurate reconstruction technique is needed for use in complex, multiphase flow systems. In this paper, we describe a finite-element based approach for the calculation of the mutual capacitances in the electrode sensor system of an ECT measurement apparatus (the sensitivity matrix of the direct or forward problem) for use with the NN-MOIRT.

II. ECT SYSTEM DESCRIPTION

Tomography can be divided into two steps: the global measurement and the image reconstruction technique [1–2]. In our ECT problem, the global measurement is a forward problem which maps the permittivity distribution $\varepsilon(x,y)$ into the a set of capacitance measurements according to the Poisson's equation for the electrical potential $\phi(x,y)$ between various plates placed around the flow system to be measured, as depicted in Fig. 1. The measured quantities are the capacitances C_{ij} between each plate capacitor pair.

In the inverse problem, $\varepsilon(x,y)$ is reconstructed for the measurement of the C_{ij} . This relation can be expressed as

$$\mathbf{C} = \mathbf{SG} \qquad (1)$$

where **C** is the measured capacitance matrix, **G** is the image vector (permittivity distribution) and **S** is the so-called sensitivity map [2]

III. SENSIVITY MATRIX CALCULATION

S in Eq. (1) is a $M \times N$ matrix, where M is the number of electrode pair combinations possible and N is the number of pixels adopted in the flow region. In our case, $M = n_e(n_e-1)/2$, where n_e is the number of electrodes as shown in Fig. 1. The capacitance between electrodes is calculated after filling an individual pixel with a high permittivity value. This process is repeated for every pixel in the domain. In the case of two-phase flow systems, the sensitivity matrix is formed by filling the n-th pixel with high permittivity, measuring all capacitance pairs, and normalizing the values according to:

$$N_{(ij)n} = \frac{n_{(ij)n} - e_{ij}}{f_{ij} - e_{ij}} \qquad (2)$$

Here $N_{(ij)n}$ is the normalized value for the ij capacitance pair and n-th pixel, $n_{(ij)n}$ is the measured value, e_{ij} is the measured value without filling the pixel with high permittivity, and f_{ij} is the measured value when filling all the pixels with high permittivity.

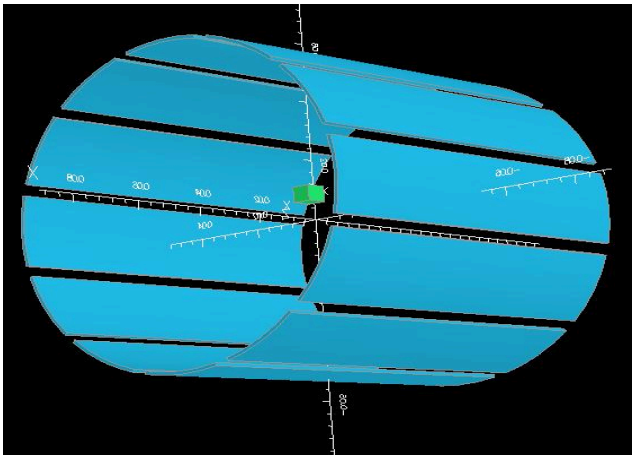

Fig.1 – The model involved in this study with 12 electrodes. An individual high-permittivity pixel is shown close to the center.

For the capacitance calculation, the first step is to obtain the electric field (potential) distribution, which is done via the finite element method (FEM). The size of FEM mesh is chosen accordingly to the necessary imaging resolution. In our typical problems, the FEM mesh is constructed by dividing the space domain in 400 pixels. Because the variation in the capacitance values resulting from an individual pixel change is very small, high accuracy is needed to determine capacitance values. Moreover, a trade-off exists between the accuracy on the computed electric field (which increases with the mesh refinement), and the accuracy needed to calculate the capacitance values from individual pixel changes (which increases with the mesh refinement). In order to decrease the susceptibility to local errors on the computation of the electric field, the capacitances values are obtained by calculating the difference in the total energy in the system. Fig.2 shows the variance on the capacitance values between two electrodes as a function of the high-permittivity pixel location. As expected, the capacitances are more sensitive to variations on the near pixels.

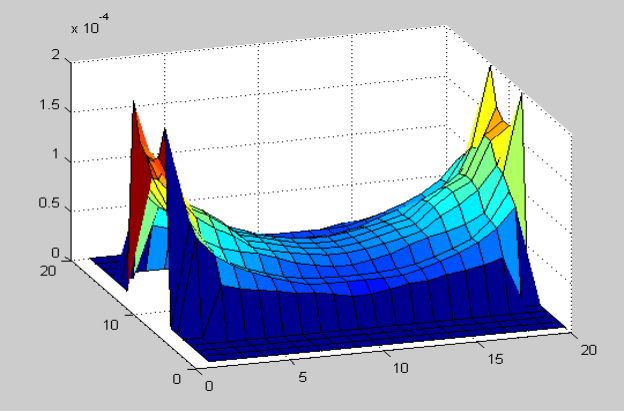

Fig. 2 – This image represents a grid where the location represents the pixel with high permittivity and the color/height represent the value of the capacitance for this pixel for a 2-parallel electrode system.

IV. NUMERICAL RESULTS

The sensitivity matrix thus formed is used as a basis to reconstruct the flow image by combining different pixels in different locations. Because of approximations on the model (including the finite mesh size) and measurement uncertainties, Eq. (1) needs to be modified by adding a *M*-dimensional error vector **E**:

$$\mathbf{C} = \mathbf{SG} + \mathbf{E} \qquad (3)$$

Notice that a linear back projection, $\boldsymbol{G} = \boldsymbol{S}^{-1}\boldsymbol{C}$ does not produce satisfactory results, even in the absence of errors, due to blurring effects. The error can be minimized in the reconstruction technique by finding the image vector such that the value of a set of objective functions, $f_i(\mathbf{G})$, are minimized simultaneously. In our case, $i=3$, representing (1) an entropy function, (2) a smoothness function, and (3) the least square error. These functions are combined to form a network energy function that is minimized using a Hopfield dynamic neural network, as described in detail in [1] (NN-MOIRT algorithm). Fig. 3 contains an example of a reconstructed image from the calculated capacitance value from a 12 plates of sensors. Fig. 5 (Left) in this figure represents the original 2-D permittivity distribution. The sensitivity matrix generated for this model is based on two parallel plates of sensors. The reconstructed results are shown in Fig. 5 (Right).

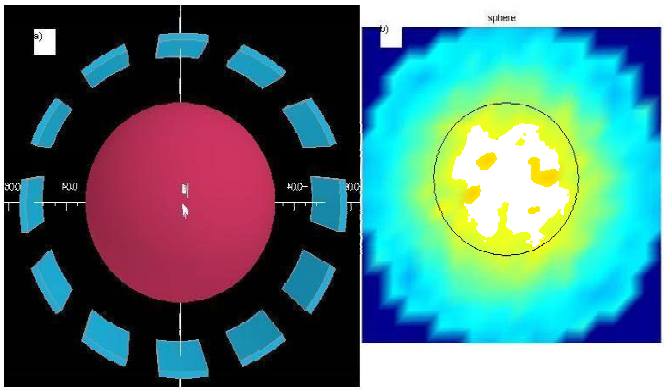

Fig. 3 – Result of reconstruction based on 3-D NN-MOIRT using a single capacitance data from 12 plates sensor: (Left) Original image with center zone representing higher permittivity region. (Right) Reconstructed flow image.

V. CONCLUSIONS

A finite element based approach to calculate the mutual capacitance between capacitor sensors in an ECT system was described. The capacitance values are used to represent the sensitivity matrix for real-time image reconstruction of flow systems using ECT. The sensitivity matrix acts as a basis for forming the 3-D image from the measured capacitances using a multi-criterion optimization image reconstruction technique.

ACKNOWLEDGMENTS

QM thanks W. Warsito for providing the NN-MOIRT algorithm [1] for use in the inverse calculation.

REFERENCES

[1] W. Warsito and L.-S. Fan, "Neural network based multi-criterion optimization image reconstruction technique for imaging two- and three-phase flow systems using electrical capacitance tomography", *Meas. Sci. Technol.*, vol. 12, pp. 2198-2210, 2001.

[2] C. G. Xie et al., "Electrical capacitance tomography for flow imaging system model for development of image reconstruction algorithms and design of primary sensor," *IEE Proc. G* , vol. **139**, pp. 89-98, 1992.

Design of Coil Ends for Superconducting Magnets Applying Differential Geometry Methods

Bernhard Auchmann, Stephan Russenschuck

Abstract— **An integrated design process has been adopted at CERN for the design of superconducting magnets, with the ROXIE program package as the key tool. Besides the essential tasks of determining optimal coil and yoke shapes in the cross-section, the adequate layout of the coil ends has proven to be the limiting factor for the magnets' quench performance. The objectives are to minimize mechanical stress on the cables, to optimize the multipole content of the integrated field and to limit the peak field enhancement. This paper introduces a new approach based on differential geometry methods for the ROXIE coil end routine that allows for the geometrical optimization of coil ends in the framework of the integrated magnet design.**

Keywords— **Superconducting Magnets, Differential Geometry, Optimization**

I. Introduction

THE coil shapes of high field magnets of mulitpole order n for the LHC (Large Hadron Collider) at the CERN were designed as to reproduce a $\cos n\theta$ current distribution in a shell around the magnet aperture with blocks of up to 20 slightly trapezoidal (keystoned) conductors of the Rutherford type. For the magnet design, an integrated approach has been adopted, with the ROXIE program package as the key tool. It combines a coupled finite element/boundary element method (BEM-FEM), [3], with a variety of optimization algorithms and CAD/CAM intefaces. After the optimization of the coil cross-section and the shape of ferromagnetic yoke, the geometry of the 3d coil end has to be determined according to the objectives of minimizing mechanical stress on the cables, optimizing the multipole content of the field and limiting the peak field enhancement. In the coil ends, the cables are wound around so-called end-spacers, made of glass epoxy material (G11). They must be carefully designed since the coil ends cannot be mechanically confined as rigidly as the straight sections. Any abrupt movement of the coils can cause the magnet to quench. This paper will present a new approach to coil end design, relying on differential geometry methods. The so-called theory of strips treats the mathematical analogon of a strip of paper which represents the rectangle-shaped Rutherford cable. An automatic geometric optimization process is being implemented, that aims at limiting the strain energy in the cable blocks while keeping the peak curvatures of the conductors below critical values. The mechanical forces on the conductors are calculated as well. The geometric design is followed in the ROXIE routine by a 3d field-quality optimization in the end region, which is decoupled from the geometric design, in that it varies only the position of the individual block turns along the magnet's axis. Eventually, the impacts of dynamic effects such as persistent currents and quench behavior on the magnet operation are investigated. The implementation of CAD/CAM standards yields interfaces for drawings and for the machining of end-spacers.

II. The Flexible Strip

A mathematical description of a strip that is bent along a *baseline* $\mathbf{r} : \mathbb{R} \to V^3$, $s \mapsto \mathbf{r}(s)$, a space curve with s as the parameter value, is to be derived. Without loss of generality, s shall subsequently denote the arclength on the space curve from a starting value $s_0 = 0$. The s-dependency of all vectors and differential forms shall be omitted in the notation. *Bending* is the act of continuous deformation of a surface under the constraint that arclengths of arbitrary curves in the surface be preserved. A surface is called *developable* if it can be (un)bent into a plane. Developable surfaces are described by a field over $\mathbf{r}$ of straight lines, the *generators*. For a strip to model a cable, one edge lies on $\mathbf{r}$. The position vector $\mathbf{p}$ of any other point on the strip can then be given as $\mathbf{p} = \mathbf{r} + t\mathbf{g}$, where $\mathbf{g}$ has the direction of the respective generator and t is a parameter. The *edge of regression* is the locus of the intersections between two consecutive generators. It constitutes the limitation for the width of a bent strip.

A trihedral, an orthonormal set of basis vectors $\{\mathbf{a}_1, \mathbf{a}_2, \mathbf{a}_3\}$, is assigned to every point on the space curve. A set of differential forms (one-forms or Pfaff-forms) σ^j and ω^{jk} is introduced to characterize a general one-parameter set of trihedrals, [1]:

$$\mathrm{d}\mathbf{r} = \sum_{\mathrm{j}=1,2,3} \mathbf{a}_\mathrm{j}\sigma^\mathrm{j}, \qquad \mathrm{d}\mathbf{a}_\mathrm{j} = \sum_{\mathrm{k}=1,2,3} \mathbf{a}_\mathrm{k}\omega^{\mathrm{jk}}. \tag{1}$$

Let $\mathbf{a}_1$ equal $\frac{\mathrm{d}\mathbf{r}}{\mathrm{ds}}$, which has magnitude one due to the choice of the arclength as the parameter. Further, with $\mathbf{a}_j \cdot \mathbf{a}_k = \delta^{jk}$ and, thus, $\omega^{jk} + \omega^{kj} = 0$, we write $\sigma^1 = \sigma$, $\sigma^2 = \sigma^3 = 0$, $\omega^{23} = \omega^1 = -\mathbf{a}_2 \cdot \mathrm{d}\mathbf{a}_3$, $\omega^{31} = \omega^2 = \mathbf{a}_1 \cdot \mathrm{d}\mathbf{a}_3$, $\omega^{12} = \omega^3 = \mathbf{a}_2 \cdot \mathrm{d}\mathbf{a}_1$. Finally, assume that $\mathbf{a}_3$ is the normal vector to the strip in every point of $\mathbf{r}$. The differential forms $\sigma, \omega^1, \omega^2, \omega^3$ contain all information about the geometric properties of the strip: The ω^j represent the differential increments $\frac{\partial \vartheta^j}{\partial s}\mathrm{ds}$ of the polar twist angles ϑ^j around the trihedral axes along the space curve, following the right-hand rule; σ is the differential arclength ds. Consequently, $\frac{\omega^1}{\sigma}$ represents the torsion of the strip, $\frac{\omega^2}{\sigma}$ the curvature over the broad side of the strip and $\frac{\omega^3}{\sigma}$ the curvature over its edge (the narrow side of the cable).

From the condition that the generators be the lines of intersection of two consecutive tangential planes $F(s)$ and $F(s + \mathrm{ds})$, [5], it can be derived that the generator vectors equal $\mathbf{g} = \frac{\omega^1}{\sigma}\mathbf{a}_1 + \frac{\omega^2}{\sigma}\mathbf{a}_2$. To determine the outer edge of

the strip with a given width, the inner theory of surfaces suggests to determine the geodesic that, from the point $\mathbf{r}$, thrives towards the outer edge on the bent strip with $\mathbf{a}_2$ as a tangential vector on $\mathbf{r}$.* This computationally challenging task can be avoided by making use of two *bending invariances*: (a) The angle between the $\mathbf{a}_1$ and $\mathbf{g}$; (b) The curvature $\frac{\omega^3}{\sigma}$, which, in the planar strip, determines the curvature of the inner edge with $\rho_3 = \frac{\sigma}{\omega^3}$ as the local curvature radius. In the unbent strip, the parameters t for points on the outer edge can then be determined by fundamental geometric operations from $\mathbf{p}_{\text{edge}} = \mathbf{r} + t\mathbf{g}$.

The application of additional twist around the tangent vector $\mathbf{a}_1$ can shift the edge of regression towards allowing for higher widths, or reduce critical curvatures according to:

$$\begin{aligned} \omega^{1*} &= +\omega^1 + \mathrm{d}\vartheta^1, \\ \omega^{2*} &= +\cos\vartheta^1\omega^2 + \sin\vartheta^1\omega^3 \\ \omega^{3*} &= -\sin\vartheta^1\omega^2 + \cos\vartheta^1\omega^3. \end{aligned} \qquad (2)$$

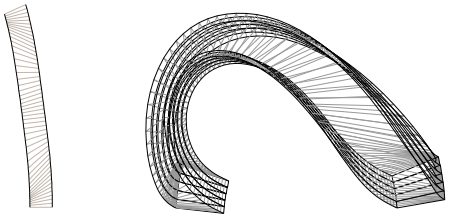

Fig. 1. Left: Innermost cable unbent into a plane. Right: A coil end block of 5 cables. The corresponding ω^j values can be seen in Fig. 2. The generators are represented in light gray.

III. Integrated Coil End Design

To apply the above theory, an initial set of differential forms σ and ω^j must be supplied: The *Frenet frame* is chosen as a field of trihedrals

$$\mathbf{a}_1 = \frac{\mathrm{d}\mathbf{r}}{\mathrm{ds}}, \quad \mathbf{a}_3 = \frac{1}{\rho_2}\frac{\mathrm{d}\mathbf{a}_1}{\mathrm{ds}}, \quad \mathbf{a}_2 = \mathbf{a}_3 \times \mathbf{a}_1, \qquad (3)$$

and, given a baseline $\mathbf{r}$, the forms are derived from (1). The baseline $\mathbf{r}$ is chosen as a hyper-ellipse $\frac{x^n}{a^n} + \frac{y^2}{b^2} = 1$ of order n and ellipticity $f = \frac{b}{a}$ on the cylinder-shaped winding mandrel. For the Frenet frame, $\omega^3 = 0$ and bending this *geodesic strip* onto a plane yields a straight strip. This initial configuration is often inadequate due to three shortcomings: (a) The geodesic strip is generally not developable for the required width of, e.g., 15 mm for LHC dipole cables. (b) The geodesic strip on $\mathbf{r}$ does not match a general coil cross-section. (c) Winding several cables onto each other induces negative ω^3 in the outer cables, thus, requiring positive ω^3 on the innermost conductor, in order to reduce the maximum curvature.

Before optimization can be carried out, a model of the entire block has to be computed, taking the keystoning of the conductors and optional wedges to be inserted after every cable into consideration. The objective is then to minimize the *strain energy* of an entire block,

$$E = \frac{1}{2}\sum_{i=1}^{I}\int_0^{s_i}\left(f_1\frac{\omega_i^1}{\sigma}\omega_i^1 + f_2\frac{\omega_i^2}{\sigma}\omega_i^2 + f_3\frac{\omega_i^3}{\sigma}\omega_i^3\right), \qquad (4)$$

where i denotes the cable number in a block of I cables and the coefficients f_j are the *flexural rigidities* that are still to be determined by measurement for every cable type, [2]. Moreover, the ω_i^j must be confined to values below the mechanical limits and intersections of generators must be ruled out. The new coil end routine simultaneously optimizes the torsion of the strip and the baseline on the winding madrel. ROXIE provides a variety of optimization algorithms, [4]. The design variables are constituted by a set of knots on a cubic spline function that models the additional twist ϑ^1, compare (2). The ellipticity f and the order of the hyper-ellipse n complete a set of 7 design variables. The problem of intersecting generators can be implemented by applying high penalty terms. Figures 1 and 2 show results obtained with the new algorithm for a block of 5 conductors. The baseline starts from an angle of 20 degrees on the winding mandrel and has ellipticity 1.2 and order 2.75. The cable block is turned by -5 degrees at $s = 0$ from a position perpendicular to the mandrel.

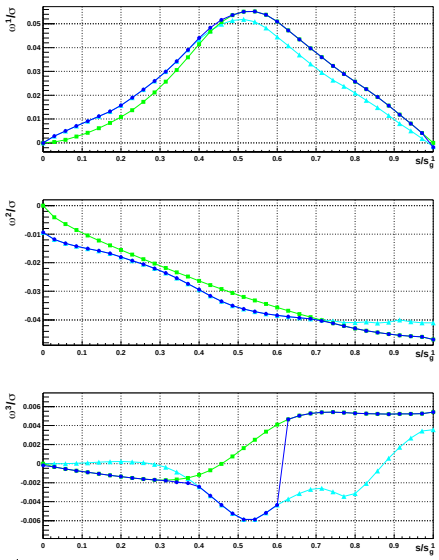

Fig. 2. ω^j values of the coil shown in Fig. 1. Marker styles - Squares: Innermost cable; Triangles: Outermost cable; Circles: Maximum over the block.

References

[1] W. Blaschke, *Einführung in die Differentialgeometrie*, 2. Auflg., Springer-Verlag, Berlin 1960

[2] "Strain Energy Minimization in SSC Magnet Winding", *IEEE Transactions on Magnetics*, Vol. 27, No. 2, March 1991

[3] S. Kurz and S. Russenschuck, "The Application of the BEM-FEM Coupling Method for the Accurate Calculation of Fields in Superconducting Magnets", *Electrical Engineering*, 1999

[4] S. Russenschuck and T. Tortschanoff, "Mathematical Optimization of Superconducting Accelerator Magnets", *IEEE Transactions on Magnetics*, Vol-Mag 30, No. 5, 1994, LHC-Note 246, CERN Geneva

[5] C. E. Weatherburn, *Differential Geometry of Three Dimensions*, University Press, Cambridge 1961

*A geodesic is the shortest path that connects two points on a surface. Given a parameter representation $\mathbf{p}(s,t)$ of the surface, the geodesic is found by the means of variation calculus.

Optimal Design of an Electromagnetic Longitudinal Levitator

F. Dughiero, S. Lupi and E. Tittonel
Università degli Studi di Padova
Via G. Gradenigo 6/A - 35131 – Padova (Italy)
e-mail: fabrizio.dughiero@unipd.it

Abstract – In the present paper an optimisation procedure based on a deterministic method (direct search method) has been used in order to analyse optimal configurations for Longitudinal Electromagnetic Levitators. The aim of the optimisation problem is to maximise the electrical efficiency but in the same time to obtain a stabilising lifting force behaviour. The cost function evaluation has been made by means of ad hoc analytical solution for a six conductors configurations and two promising optimal solutions have been deeply analysed both by a FEM procedure and by experimental results.

INTRODUCTION

The high-frequency electromagnetic levitation is a well known melting process for producing high-pure metals without contact with the crucible's walls. Maximisation of the levitating mass is a fundamental task for the development of this technology and different inductor geometries have been proposed for this purpose. Among them, the longitudinal levitator (LEL) appears to be the most promising since it gives the possibility to increase the melt volume by the increase of the inductor length [1,2]. This geometry is not yet fully investigated; in this paper an optimisation of a three "poles" longitudinal electromagnetic levitation system of the type shown in Fig. 1, is presented.

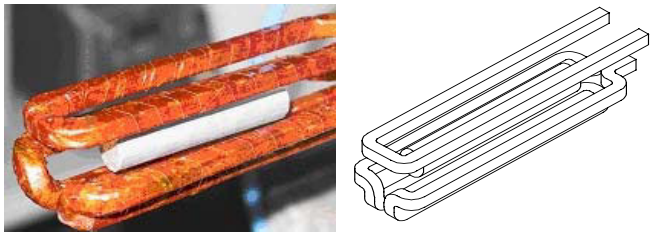

Fig. 1. Levitation system and 3D geometry

INVERSE PROBLEM AND OPTIMIZATION RESULTS

In order to improve the levitation melting process, the physical quantities which must be optimised are the electrical efficiency and the lifting force. As regards the latter, the lifting equilibrium is reached when the total electromagnetic force counterbalances the gravity force. But this condition can be obtained at different vertical positions of the workpiece, when the exciting current and/or the levitator geometry are changed. Moreover, of fundamental importance is the horizontal and vertical stability of the molten workpiece. The stability of the system is guaranteed when to a minimal movement of the load in a chosen direction, a corresponding value of the force in the opposite direction is present. For this reason the objective function related to the lifting force has been considered through a constraint which takes into account not only the value of the force itself but also the stability conditions.

The other basic parameter for the melting process is the total power P_{work} developed in the workpiece; this is why an objective function has been introduced, related to the electrical efficiency η as follows:

$$f(\bar{x}) = 1 - \eta = 1 - \frac{P_{work}}{P_{work} + P_{losses}} \qquad (1)$$

As design variables the (x,y) coordinates of the six linear conductors constituting the LEL and its exciting current and frequency values have been assumed.

The optimisation algorithm used is based on the direct search method (Hooke and Jeeves), the calculation of the electromagnetic quantities has been performed by an analytical method which substitutes the real conductors with current filaments whose position is placed in its barycentre [1], while the temperature field is calculated by means of a code using the finite difference method. The starting configuration is described by figure 2 and the data of Table I.

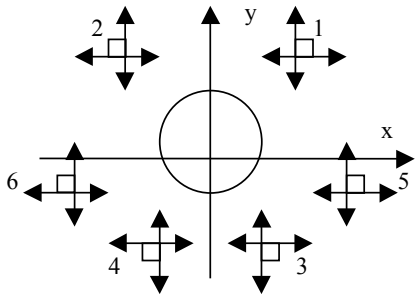

Fig. 2. Basic configuration of LEL with geometrical design variables represented.

TABLE I

Conductor coordinates	x [m]	y [m]
Conductor 1	+ 0.0125	+ 0.010
Conductor 2	- 0.0125	+ 0.010
Conductor 3	+ 0.0050	- 0.0125
Conductor 4	- 0.0050	- 0.0125
Conductor 5	+ 0.0140	- 0.0025
Conductor 6	- 0.0140	- 0.0025
Workpiece barycentre	0.000	-0.00037

The workpiece is constituted by an aluminium cylinder with 0.012 m diameter, 0.1 m length and 0.0305 kg weight. The system is supplied by a current I=2000 A at frequency f=10 kHz. Starting from this basic configuration different optimisation runs have been performed taking into account different groups of design variables.

The following two cases related to optimisations obtained moving jointly couples of conductors will be discussed in the following:

Case a

In this case only the vertical position of conductors 1 and 2 has been optimised; the corresponding optimal geometry is given in Table II together with the electrical efficiency and power transferred to the workpiece.

TABLE II

	Initial	Optimal
Y (1,2) [m]	+ 0.010	+ 0.099
Workpiece barycentre	0.000	+ 0.0743
Efficiency [%]	0.0065	0.0204
Load power [w]	53	174

Case b

In this second case only the variation of the vertical position of the couples of conductors 3,4 and 5,6 has been considered. The corresponding optimal configuration is shown in Table III together with the electrical efficiency and the power transferred to the workpiece.

TABLE III

	Initial	Optimal
Y (3,4) [m]	- 0.0125	- 0.0102
Y (5,6) [m]	- 0.0125	- 0.0224
Workpiece barycentre	0.000	+ 0.00013
Efficiency [%]	0.0065	0.0602
Load power [w]	53	536

These two cases are represented in figure 3 with reference to the original configuration described in Table I.

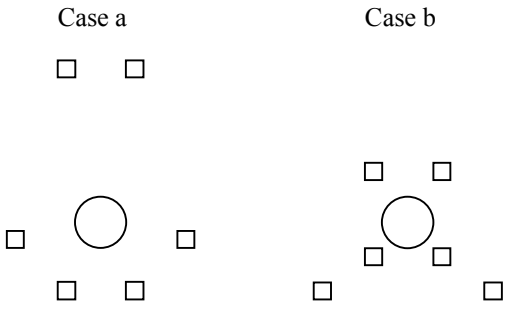

Fig. 3. Schematic of the optimal poles positions for cases a and b

For these cases, the behaviour of the vertical component of the lifting force is shown in figure 4. It should be pointed out that the equilibrium position (where the lifting force is zero) is stable in both cases.

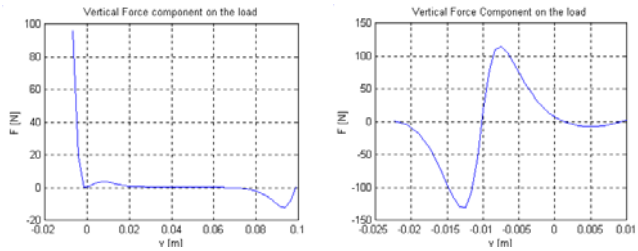

(a) (b)

Fig. 3. Lifting force as a function of y for cases a and b.

NUMERICAL AND EXPERIMENTAL RESULTS

In order to check the results of the optimisation procedure a FEM model has been implemented which takes into account the real dimensions of the exciting conductors (5x5x0.8 mm) and, moreover, is able to calculate the thermal transient in the levitating load. The solution is obtained by an iterative coupling between the electromagnetic and thermal problems solutions. The horizontal and vertical stability is calculated too, by the analysis of the behaviour of the lifting and transversal electromagnetic forces. For the case a) in addition an experimental test has been done and in table IV a comparison among optimal, numerical and experimental results is presented.

TABLE IV

	Optimal	FEM	Experiment *
Time to fusion	190 s	175 s	200 s
Load power	174 w	165 w	160 w **

(* at current I=1973 A r.m.s., frequency f=9800 Hz.
** value estimated from the theoretical heat content at 660 °C and surface thermal losses)

CONCLUSION

In the paper a direct search technique has been applied to the design of LEL for melting of metals. The calculation of the objective function has been done by means of an analytical code. Some interesting configurations can be recognised by the different optimal configurations. Two promising optimal systems case a) and b) have been analysed and the comparison with numerical and experimental results have demonstrated the powerfulness of the method.

REFERENCES

[1] R. Shampine and Y. Bayazitoglu: "Analysis of the Longitudinal Electromagnetic Levitator", *IEEE Transactions on Magnetics,* Vol. 33, pp. 4427-4433, Nov. 1997

[2] Xiaoyan Zhong, Yildiz Bayazitoglu: "Electromagnetic Fileld and Lifting Capacity for Longitudinal Electromagnetic Levitator", *IEEE Trans. On Magnetics*, Vol. 36, N. 5, September 2000, pp. 3746-3753.

[3] Yildiz Bayazitoglu, Xiaoyan Zhong:"Thermal Electromagnetic Levitation", *3rd Int. Symposium on Electromagnetic Processing of Materials,* 2000, Nagoya (Japan), pp.345-351

OPTIMIZATION OF AUTOMOTIVE ELECTROMAGNETIC DEVICES

Rodolfo Palma Fatma Kocer
Visteon Corporation

Abstract – Automotive components need to be small, deliver high performance, be mass produced and have low cost. Practical production methods to optimize the electric, magnetic and thermal performance of various electromagnetic devices, including inductors, fuel injectors, ignition coils, solenoids, electromagnetic brakes, and valve actuators are described. Results are included.

INTRODUCTION

In the automotive business customers demand superior performance and low cost. Regulators require adherence to strict norms. Automotive styling imposes tight restrictions on available space and geometries. Mass production of these devices require reliable designs. In this increasingly complex environment the only way to successfully satisfy these often contradictory demands is by using an automatic design process that ensures that all requirements are satisfied. In particular, to obtain reliable results the electromagnetic design needs sophisticated field computations. In the past it has been difficult to establish field computational processes that can automatically modify the geometry, sources, and materials such that specifications are satisfied while the performance is maximized.

OVERALL CONSIDERATIONS

The purpose of this project was to develop optimization methods that are generic enough to be applied to a variety of electromagnetic devices and specific enough to provide accurate, meaningful designs and design guidance for particular devices. For this, we selected commercial software codes [1,2] that are flexible and that excel in the computation of electromagnetic fields and in optimization.

This generic, electromagnetic FEA process allows us to develop common script interfaces between the optimization and FEA codes that are re-usable for the optimal design of most electromagnetic devices. There are only a few ad-hoc processes that are special for each electromagnetic device. Re-use and common procedures are the key attributes for a fast, efficient and reliable optimization development process. Fig. 1 shows the standard process for the optimization of automotive components.

The first step is to develop reliable and accurate math models of the component and/or system to be analyzed. This includes the electromagnetic FEM representation of the component and its surrounding. Similarly, thermal, mechanical and other math or FE models may be required. These models need to be parametric so that the optimization code can modify: dimensions, mesh, circuit connections, sources, loads, material properties, boundary conditions, etc.

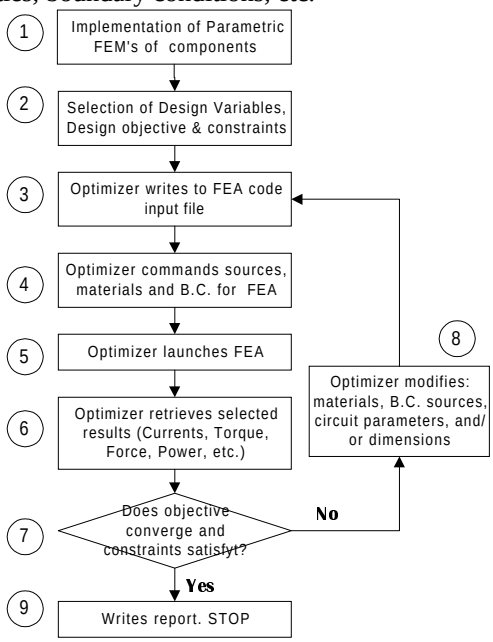

Fig. 1. Optimization procedure for automotive components

Step two: "Selection of Design Variables and Formulation of the Objectives and Constraints" is probably the most critical and difficult step of the whole optimization process. The selection of the parameters that affect the design and that can be modified in a given manufacturing and assembly environment should be done with the participation of manufacturing and plant engineers. The proper formulation of objectives and constraints separates a good optimization approach from others. Constraints should reflect specifications and limitations on design variables, performance and manufacturing capabilities. The objective function needs to reflect the goodness of the design, which is normally a combination of cost, size, weight, manufacturability and performance. In addition, the formulation of the design variables, constraints and objectives need to be done in a way that results in an effective and efficient numerical computation.

In the third step, the optimizer code, which controls the whole process, writes FEA input files formatted for the particular code being used. These input files include the dimensions, materials, loads, circuits, sources, etc. for the electromagnetic, thermal, and mechanical math models of all the design attributes that are considered in the constraints and/or objective function.

In the fourth and fifth steps the controlling code launches the execution of the math models that compute the electromagnetic and other attributes of the design. This can be done sequentially on one computer or it can be implemented as a distributed, parallel process across a computer network.

In steps six and seven, the significant results are retrieved from the math models and compared with the constraints and objectives. If the constraints are met and the objectives converge a report is written and the process stops (step 9). If not, the design variables are recomputed by the optimization algorithm in use, and the process is continued from step 3.

RESULTS FOR FUEL INJECTOR OPTIMAL DESIGN

The procedure described in fig. 1 was used for the design of a fuel injector. The design variables were the dimensions and the number of turns in the injector. Constraints include the range of the dimensions, current density, voltage source characteristics, limitations on the wire gauge, and acceleration of the armature. The objective was to minimize the closing time of the armature when a voltage source is applied to the coil. Fig. 2a) shows some of the design variables Fig. 2b) shows the field distribution at a particular time step.

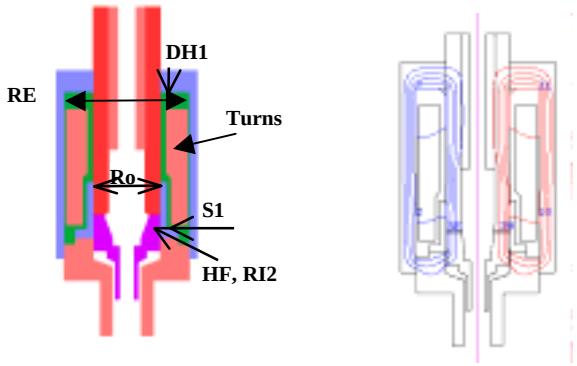

Fig. 2 a) Some of the fuel injector design variables b) Magnetic field distribution at 1.2msec.

OPTIMAL DESIGN OF ELECTROMAGNETIC RETARDERS

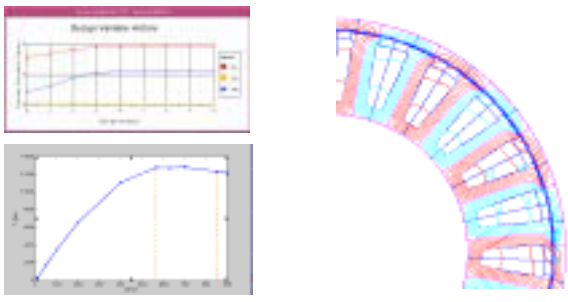

Fig. 3 a) Optimization history and **T-ω** curve b) Magnetic field distribution in a "retarder" section.

Electromagnetic brakes serve as non-contact brakes for trucks and cars. The objective is to design a brake that provides braking action over a wide range of speeds. Fig. 3 a) shows the design variable history and the **T-ω** characteristic. Fig. 3b) shows the magnetic field in one of the concepts tried.

OPTIMAL DESIGN OF INDUCTORS

An inductor for a choke with specifications of a minimum and a maximum inductance and maximum temperature rise was designed. Fig. 4 shows a cross section of the inductor and the evolution of the inductor's optimal design.

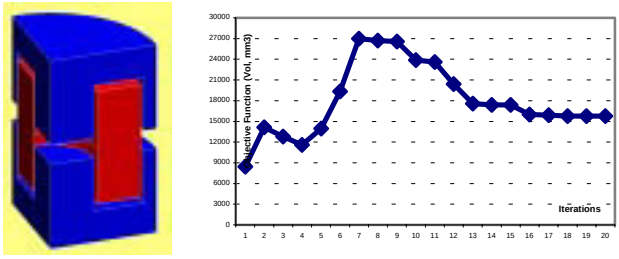

Fig. 4. Inductor's cross section and optimization evolution

OPTIMAL DESIGN OF AUTOMOTIVE VALVE ACTUATORS

To increase engine efficiency, reduce weight and emissions, cam shafts will be replaced with electromagnetic valve actuators, EMVA's [3]. The optimization of the EMVA requires that electric, magnetic, thermal and mechanical issues be considered together. Fig. 5 shows the magnetic field distribution in an optimized EMVA.

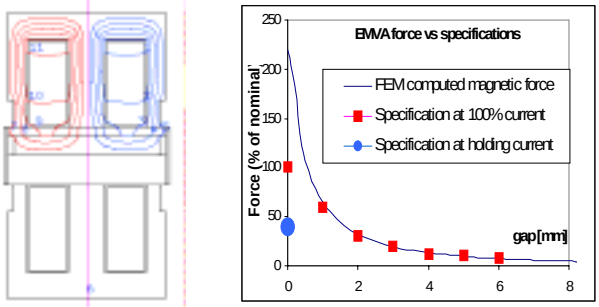

Fig. 5 a) Magnetic field distribution in an optimal EMVA design. b) Force vs. gap requirements

CONCLUSIONS

A multi-attribute optimization method for automotive electromagnetic components has been developed and implemented. The method uses re-usable procedures making the development of optimization for other components shorter and more reliable. The method has been used for the optimal design of several automotive components. Performance, cost and/or weight have been improved in each of them. From our experience in optimizing diverse automotive components, we have concluded that the problem formulation, the fine tuning of the optimization and analysis parameters are crucial for the success of the optimization process.

REFERENCES

[1] Magsoft v7.0 Users Manual, CEDRAT, 2001.
[2] iSight v6.0 Users Manual, Engineous Software, 2002.
[3] Wang, Yan; Stefanopolou (2000), "Modelling of EMVA for a camless engine", Proceedings of AVEC 2000.

3D Shape Optimization of Nonlinear Electromagnetic Device using Parameterized Sensitivity Analysis

Jae Seop Ryu, Yingying Yao*, Chang Seop Koh, and Pan-Seok Shin**

School of Electrical and Computer Engineering, Chungbuk National University, Chungbuk 361-763, KOREA E-mail) jsryu@vod.chungbuk.ac.kr, kohcs@chungbuk.ac.kr.
* School of Electrical Engineering, Shenyang University of Technology, Shenyang, Liaoning 110023, P. R. China. E-mail) yaoying62@hotmail.com
* Department of Electrical Engineering, Hongik University, Chochiwon, Chungnam 339-701, Korea

***Abstract*— In this paper, a 3D shape optimization algorithm which guarantees a smooth optimal shape is presented using parameterized sensitivity analysis. The design surface is parameterized using Bezier spline and the control points of the spline are taken as the design variables. The parameterized sensitivity for the control points are found from that for nodal points. The design sensitivity and adjoint variable formulae are also derived for the 3D non-linear problems. Through an application to the shape optimization of 3D electromagnet to get a uniform magnetic field, the effectiveness of the proposed algorithm is shown.**

INTRODUCTION

The aim of shape optimization of electromagnetic devices is not only to reduce the object function but also to make it possible to manufacture in real applications. Especially when the sensitivity analysis is used, unrealistic design having saw-tooth shape is often obtained because the nodal points are usually taken as the design variables and allowed to move independently. For this reason, in 2D shape optimal design, a geometric parameterization is often combined with sensitivity analysis to get a smooth design contour [1,2]. For 3D shape optimization, some algorithms are presented using sensitivity analysis for the linear magnetostatic problems and linear eddy current problems [3,4]. However, a method for smooth shape is still required.

In this paper, 3D parameterized sensitivity analysis is developed by combining sensitivity analysis and geometric parameterization using Bezier spline to guarantee a smooth design result. The mesh relocation method is also used to modify the finite element grid without changing of the mesh topology after the design surface changes.

PARAMETERIZED SENSITIVITY ANALYSIS

A. Non-linear Sensitivity Analysis

The 3D non-linear magnetostatic problems are governed by the following equation

$$\nabla \times \nu \nabla \times A = J \tag{1}$$

where the symbols have their usual meanings. Applying the Galerkin's approach, the residual vector can be obtained as

$$[G] = [K][A] - [Q]. \tag{2}$$

The objective function for non-linear problem can be expressed as follows:

$$F = f([p],[A(\nu, p)]) \tag{3}$$

where $[p]$ and $[\boldsymbol{A}]$ are the design variable and state variable that makes the residual in (2) zero, respectively.

The design sensitivity is computed as

$$\frac{dF}{d[p]^T} = \frac{\partial F}{\partial [p]^T} + \frac{\partial F}{\partial [A]^T}\frac{d[A]}{d[p]^T} \tag{4}$$

where $d[A]/d[p]$ can be obtained by differentiating the both sides of (2) with respect to $[p]$ as follows:

$$\frac{d[A]}{d[p]^T} = -\left([K]+[\bar{K}]\right)^{-1}\left([M]+[\bar{M}]\right) \tag{5}$$

where the matrices are defined as

$$[M]+[\bar{M}] = \left.\frac{\partial [G]}{\partial [p]^T}\right|_{\nu=c} + \frac{\partial [G]}{\partial \nu}\frac{\partial \nu}{\partial B^2}\frac{\partial B^2}{\partial [p]^T}, \tag{6-a}$$

$$[K]+[\bar{K}] = \left.\frac{\partial [G]}{\partial [A]^T}\right|_{\nu=c} + \frac{\partial [G]}{\partial \nu}\frac{\partial \nu}{\partial B^2}\frac{\partial B^2}{\partial [A]^T}. \tag{6-b}$$

Introducing adjoint variable $[\lambda]$, the design sensitivity can be computed as follows:

$$\frac{dF}{d[p]^T} = \frac{\partial F}{\partial [p]^T} - [\lambda]^T\left([M]+[\bar{M}]\right), \tag{7}$$

$$[K+\bar{K}]^T[\lambda] = \frac{\partial F}{\partial [A]}. \tag{8}$$

B. Parameterized Sensitivity Analysis

If the design surface is parameterized using the Bezier spline, the coordinates of the nodal points on the design surface can be expressed with control points as follows [5]:

$$[p] = [J][C], \tag{9}$$

where, $[J]$ is the Jacobian matrix made of Bezier spline blending functions, and $[C]$ is the control points.

The parameterized design sensitivity for the control points can be expressed as follows

$$\frac{dF}{d[C]} = \frac{dF}{d[p]}\frac{d[p]}{d[C]} = \frac{dF}{d[p]}[J]. \tag{10}$$

After the control points are updated using optimization algorithm, the coordinates of the nodal points on the design surface can be calculated using (9).

For initial design surface, which consists of the movable nodal points, the best surface fitting control points can be found using least square method so that the fitting error be minimized [5].

NUMERICAL EXAMPLE

The pole surface of 3D nonlinear electromagnet, shown in Fig.1, is optimized to obtain a uniform magnetic field B_z = 0.23T at the target region in the air gap. The initial shape of the pole face is flat. The nodal points on the pole face(104 nodes in the numerical example) are allowed to move in z direction. The exciting coil has 12,240[AT] in order to saturate the yoke partially.

The objective function is defined as follows:

$$F = \sum_{e=1}^{Ne} \left| B_{cal}^{e} - B_0 \right|^2 \tag{3}$$

where N_e is the number of element at the target region, B_{cal}^{e} and B_0 are the computed and desired magnetic flux densities, respectively.

During the optimization process the finite element mesh is modified using the mesh relocation method [4]. The shape optimization is carried out for the different numbers of the control points. Fig. 2 shows the effects of the geometric parameterization and number of control points. Compared with the optimized shape with sensitivity analysis without parameterization, the parameterization with (5x3) control points simplify too much, and that with (9x5) control points gives quite reasonable result. It can be also seen that the mesh topology does not change during optimization process due to the mesh relocation method. Fig. 3 compares the magnetic field distributions for initial and optimized shapes. It can be seen that at the objective region, almost uniform field distribution is obtained. Fig. 4 shows the convergence rates, where the parameterized sensitivity analysis with (5x3) control points gives little bigger objective function value

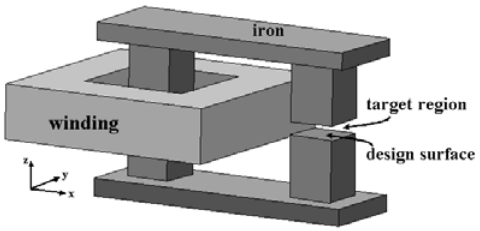

Fig. 1. 3D non-linear electromagnet model.

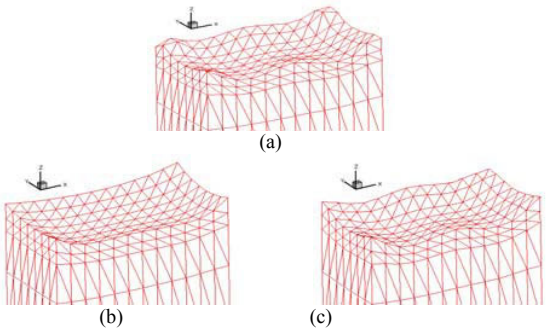

(a) (b) (c)

Fig. 2. Comparison of the optimized shapes. (a) sensitivity analysis, (b) parameterized sensitivity analysys with (5x3) control points, (c) parameterized sensitivity analysis with (9x5) control points.

CONCLUSIONS

A 3D shape optimization algorithm, which guarantees a smooth optimal shape, is presented. The method combines geometric parameterization of the design surface using Bezier spline with sensitivity analysis based on finite element method. An application to the 3D non-linear electromagnet design shows the effects of the parameterization.

REFERENCES

[1] H.B.Lee,I.H.Park, and S.Y.Hahn, "Optimum shape design of electromagnetic devices by Bezier spline parameterization of sensitivity," IEEE CEFC2002, Perugia, Italy, pp.21, June 16-19, 2002

[2] K.Weeber and S.R.H.Hoole, "Geometric Parameterization and Constrained Optimization Techniques in the Design of Salient Pole Synchronous Machines", *IEEE Trans. on Magn.*, vol.28, pp.1948-1960, 1992

[3] J.A.Ramirez, E.M.Freeman, C.Cat-uthai, D.A.Lowther, "Sensitivity Analysis for the Automatic Shape Design of Electromagnetic Devices in 3D Using FEM", *IEEE Trans. on Magn.*, vol.33, pp.1856-1859, 1997

[4] Y.Yingying, C.S.Koh, and X.Dexin, "3D shape optimization of electromagnetic devices including eddy currents by using design sensitivity analysis," IEEE CEFC2002, Perugia, Italy, pp.292, June 16-19, 2002

[5] D.F.Rogers and J.A.Adams, *Mathematical Elements for Computer Graphics*, McGraw-Hill, 1990

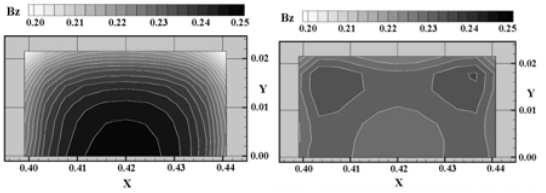

(a) (b)

Fig. 3. Magnetic field distribution at the symmetric plane. (a) with initial shape, (b) with optimized shape obtained using (9x5) control points parameterized sensitivity analysis.

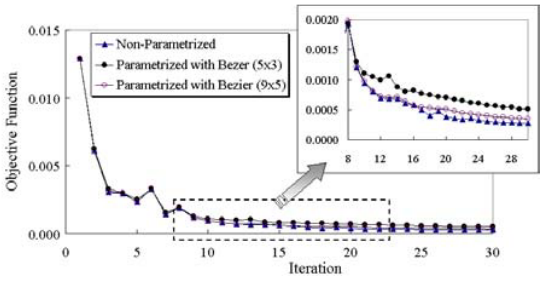

Fig. 4. The convergence rates of the objective function

Robust 3D Shape Optimization of Electromagnetic Devices by Combining Sensitivity Analysis and Adaptive Spline

Yingying Yao, Jae Seop Ryu*, Chang Seop Koh*, Dexin Xie
School of Electrical Engineering, Shenyang University of Technology, Shenyang, Liaoning 110023, P.R.China. yaoying62@hotmail.com
* School of Electrical and Computer Engineering, Chungbuk National University, Cheongju, Chungbuk, 361-763, Korea. kohcs@chungbuk.ac.kr

***Abstract*—New robust 3D shape optimization algorithms, which utilize parameterized sensitivity analysis and adaptive surface fitting method, are developed by combining sensitivity analysis and adaptive spline method. In the former the control points of spline are used as the design variables, while used to smooth the design surface in the latter. Through an application to the optimal shape design of electromagnetic device including eddy current, it is shown that both the algorithms give reasonable results.**

INTRODUCTION

For 3D shape optimization of the electromagnetic devices, gradients-based methods with sensitivity analysis is considered as a good choice because it reduces the computing time greatly compared with the zero-order deterministic methods and the non-deterministic methods [1]. In the shape optimization using sensitivity analysis, the nodal coordinates of a finite element mesh are usually chosen as design variables. If the design variables are allowed to move independently, the optimal shape may be often jagged and unrealistic[1,2].

In order to overcome the problem of jagged shapes, some algorithms such as linear constraints method[2], geometric parameterization using spline function[1,3] are developed for 2D shape optimization. However, for 3D shape optimal design, a reliable algorithm, which guarantees a robust design against jagged shapes, is not presented yet.

The geometric parameterization using spline functions, such as Bezier spline and B-spline, in 2D shape optimization problem can be extended to 3D problems. However, it is very difficult to determine the proper number of control points and their positions, because we don't know the optimum shape before the optimization. Furthermore, during the optimization, the side constraints for design variables are hardly converted into those for control points.

In this paper, two algorithms are developed for robust 3D shape optimization by combining the sensitivity analysis and adaptive parameterization.

SENSITIVITY ANALYSIS AND ADAPTIVE SPLINE PARAMETERIZATIONS

A Parameterized Sensitivity Analysis

The design surface, composed of the nodal points allowed to move, is parameterized using Bezier(or B)spline with proper control points. Using the control points, the coordinates of the nodal points on the design surface can be computed as follows:

$$[p]=[J][C], \tag{1}$$

where $[p]$ and $[C]$ are the coordinates of the nodal points on the design surface and the control points, reaspectively, and $[J]$ is the Jacobian matrix made of the basis functions of the spline.

The parameterized sensitivity for the control points are computed as follows:

$$\frac{dF}{d[C]^T}=\frac{dF}{d[p]^T}\frac{d[p]}{d[C]^T}=\frac{dF}{d[p]^T}[J] \tag{2}$$

where F is the objective function, and $dF/d[p]$ is the sensitivity for the nodal points. After parameterized sensitivity is found, the control points are updated to give new coordinates of the nodal points on the design surface. If any nodal point violates the side constraints, the acceleration factor in updating the control points is reduced.

If the final optimized shape does not meet the desired performance, the number of control points is increased and the optimization process is repeated.

B. Adaptive Surface Fitting Algorithm

The design surface, which is built up by the nodal points on the design surface, may not be smooth during the optimization process if the nodal points on the design surface are taken as the design variables and allowed to move independently. Just to make the design surface smooth, the spline methods such as Bezier and B-splines, are used.

With a initial number of control points, of which the (u,v) positions are fixed, as shown in Fig.1, the best surface fitting control points, C_{ij}, are determined using least square method to minimize the surface fitting error defined as follows[4]:

$$\varepsilon=\sum_{k=1}^{N_p}(z_k-s_k)^2 \tag{3}$$

$$s_k=\sum_{i=0}^{M}\sum_{j=0}^{N}B_{iM}(u_k)B_{jN}(v_k)C_{ij} \tag{4}$$

where N_p is the number of nodal points on the design surface, z_k and s_k are computed and splined coordinates of the k-th nodal point, M and N are the orders of the spline functions along u and v directions, respectively, and B is the basis function of the spline. Using the best fitting control points, we assign each region a score equal to the sum of the distance between the computed and splined coordinates whose (u,v) are within it. The new control points are inserted so that the region

with the largest score is split. This process is illustrated in Fig.1, where region R is split into R_1, R_2, R_3, and R_4.

Using this method, a set of new control points are inserted until a desired surface fitting is reached. The two optimization algorithms are summarized in Fig.2.

III. Numerical Results and Discussion

An electromagnetic shield model, excited by 40000[AT] with power frequency, is shown in Fig.3(a). The design target is to obtain an optimum shape of the shielding steel plate so that magnetic field should be as low as possible at the observation area while keeping the volume of plate less than 1.6e-2[mm^2]. The 169 nodal points on the upper surface of the shielding plate are allowed to move in $\hat{z}$ direction in the range from -5[mm] to 20[mm].

The magnetic field distribution is computed by using A, $\phi - A$ finite element method. The objective function is defined as follows:

$$F = \sum_{k=1}^{Ne} \dot{B} \cdot \dot{B}^* \tag{5}$$

where N_e is the number of elements on the observing region, and $\dot{}$ denotes the complex. The design sensitivity for nodal points can be expressed as follows:

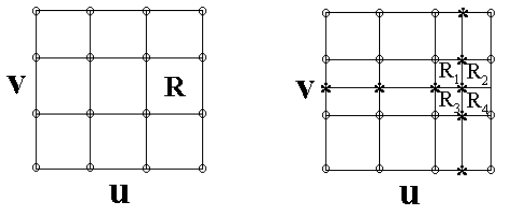

(a) (b)

Fig. 1 Insertion of the control points, (a) the region with largest error is found, (b) control points are inserted and the region R is divided into 4 regions.

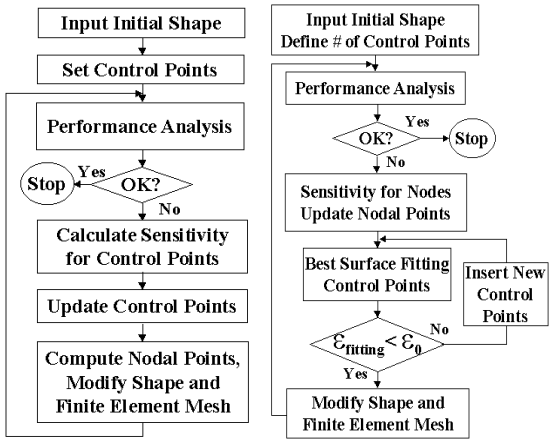

(a) (b)

Fig. 2. Summaries og the two algorithms, (a) parameterized sensitivity analysis, (b) adaptive surface fitting method.

$$\frac{dF}{d[p]^T} = \frac{\partial F}{\partial [p]^T} + 2\mathrm{Re}\left(\lambda^T \frac{\partial}{\partial [p]^T} \left[[\dot{Q}] - [S][\tilde{X}] \right] \right) \tag{6}$$

where $[p]$ is the coordinates of the nodal points on the design surface, $\tilde{X}$ and λ are the state and adjoint variables which satisfy the following discretized matrix equations, respectively.

$$[\dot{S}][\dot{X}] = [\dot{Q}], \tag{7}$$

$$[\dot{S}]^T \dot{\lambda} = \frac{\partial F}{\partial \dot{X}}. \tag{8}$$

Fig. 3(b) shows the optimized shape of the shielding plate obtained using the adaptive surface fitting method with Beizer spline. It can be seen that reasonable smooth surface is obtained. Fig. 4 compares the convergence rates for the design sensitivity analysis without parameterization, parameterized sensitivity analysis with (5×5) control points and adaptive surface fitting method. From the figure, it can be seen that (5×5) control points are not enough to get enough small objective function value. On the other hand the adaptive surface fitting method gives almost same objective function value as the design sensitivity analysis with unsmooth surface.

References

[1] K.Weeber, S.R.Hoole, "Geometric parameterization and constrained optimization techniqyes in the design of salient pole synchronous machines," IEEE Trans. On Magn., Vol.28, No.4, pp.1948-1960, July 1992

[2] S.Subramaniam, A.A.Arkadan, S.R.Hoole, "Optimization of a magnetic pole face using linear constraints to advoid jagged contours," IEEE Trans. On Magn., Vol.30, No.5, pp.3455-3458, September 1994

[3] V.Braibant, and C.Fleury, "Shape optimal design using B-spline," Computer methods in Applied Mechanics and Engineering, Vol.44, pp.247-267, 1984

[4] D.F.Roges and J.A.Adams, *Mathematical Elements for Computer Graphics*, McGraw-Hill, 1990

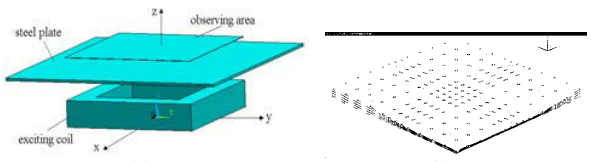

(a) (b)

Fig.3. Magnetic shield model. (a) model configuration, (b) optimized shape using adaptive surface fitting method with Beizer spline.

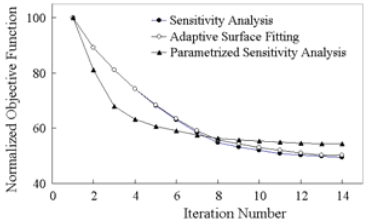

(a) (b)

Fig.4. Convergency rates of the optimization algorithms. (a) using parameterized sensitivity analysis, (b) using the adaptive surface fitting method.

Reducing sensitivity analysis time cost of compound model

B. Delinchant, F. Wurtz, E. Atienza
Integrated Design and Diagnostic Team
Laboratoire d'Electrotechnique de Grenoble (L.E.G.)
ENSIEG - BP 46 – 38402 Saint Martin d'Héres cedex - France
e-mail: benoit.delinchant@leg.ensieg.inpg.fr

***Abstract*—The present paper deals with the sensitivity analysis of compound models in the case of gradient based optimization. MDO (Multidisciplinary Optimization) may use time consuming analysis such as FEM resolution, their sensitivity analysis must then be managed efficiently in order to limit their evaluations. A composition model implementation based on differential propagation mechanism has been used. Different solutions of sensitivity analysis based on forward finite difference are proposed at the level of each inner models. These solutions have been implemented for the design of a transformer, using mixed modeling (FEM + analytic). It has led to a reduction by a factor 2 then 3 of an optimization iteration time cost.**

INTRODUCTION

Optimization of numerical models is a great challenge for the computer aided design, but has still to be improved. The cost-fidelity tradeoff has to be managed to face the increasing design variable number and disciplinary coupling. System design leads engineers from single analysis optimization to MDO (Multidisciplinary optimization). An MDO optimization is based on a *compound model* which can be seen as *black boxes* composition. A black box (called *inner model* in the following) can be a parameterized FEM resolution as well as an analytical model.

Two pieces of information are needed to perform an optimal gradient based sensitivity analysis of a compound model. First is composition information (what is the information exchanged between inner models). Second is the global sensitivities which will be studied (depending on optimizable inputs, constraints outputs and objective function). If both are known, a Global Sensitivity Equation [1] can be used to perform an optimal sensitivity analysis. Unfortunately, some optimization structures do not necessarily know both, as the one used in this paper.

The paper highlights some generic implications of model composition for sensitivity analysis. It proposes several techniques, trying to reduce the analysis number for each inner model. Some results are then presented, corresponding to the optimization (with *Pro@Design™* [1] software) of a model composed of FEM resolution (*Flux2D™* [2] software) and analytical equations.

[1] http://www.designprocessing.com/
[2] http://www.cedrat.com/

SENSITIVITY PROPAGATION INSIDE A COMPOUND MODEL

When composing models based on different analysis software, we are facing with the implementation of the *glue*, which enables communication with other models and with the optimization software. Sensitivity evaluations being time consuming, several methods may improve the global analysis. Coding sensitivity at the level of inner models allow specific sensitivity analysis, like adjoint field technique for magnetic field problems solving [2]. But in the case of compound model, an efficient analysis is not sufficient if it is called unnecessarily. This paper proposes different solutions to improve the global time cost of compound model sensitivity analysis.

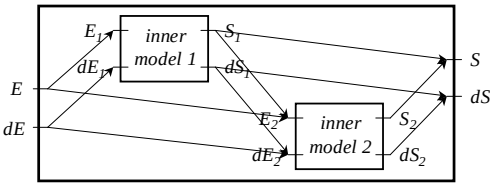

Fig 1 : A compound model based on differential propagation

As studied in [3], two kind of propagation mechanism can be considered: the partial derivative transmission and the differential transmission. In the aim of composing models, the choice of differential propagation (see fig.1) has been made (in *Pro@Design™* [1] software) to build a network which "*only depends on local information*". This means that adding a model in the beginning of the propagation process does not affect following connections. Taking this property into account, three sensitivity analysis implementations are proposed in the following, using a finite difference method.

Property 1 : partial derivative computation call from the global model may lead to more than one partial derivative computation call in an inner model (*see fig 2*).

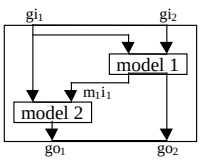

In this figure, the global partial derivation leads to the computation of two partial derivation inside of inner model 2:

$$\left.\frac{dgo_1}{dgi_1}\right|_{global} = \left.\frac{\partial go_1}{\partial gi_1}\right|_{model2} + \left.\frac{\partial go_1}{\partial m_1 i_1}\right|_{model2} \cdot \left.\frac{\partial m_1 i_1}{\partial gi_1}\right|_{model1}$$

Fig 2 : model composition issue due to derivative propagation

SENSITIVITY ANALYSIS USING PARTIAL DERIVATIVES

To perform the sensitivity analysis during an optimization iteration, an inner model is evaluated several times. The key to an optimized analysis is then to remember some information between each evaluations along an iteration.

A First significant improvement is to remember the computation point (list of input values). Indeed, using sensitivity method such as forward finite difference requires only one extra model evaluation per derivative. This allows function evaluation reduction from *2n* to *n+1* (*n* : optimizable parameter number). The differential is made of the sum of **systematic partial derivation**, which are built with a finite difference method (*see table 1, col.1*).

$$dS = \frac{\partial S}{\partial I_1} dI_1 + \cdots + \frac{\partial S}{\partial I_n} dI_n$$

$$\frac{\partial S}{\partial I_i} = \frac{S(I_1, \cdots, I_i + \Delta_i, \cdots, I_{n+p}) - S(I_1, \cdots, I_i, \cdots, I_{n+p})}{\Delta_i}$$

But as a consequence of *property 1*, for each global partial derivative computation, local partial derivatives can be computed several times.

A second improvement is then to remember these local partial derivatives. The solution consists of **memorizing the local Jacobian** along the construction of the global one. When partial derivatives are needed, if they are not in the local Jacobian, they are computed and put in it. Thus, partial derivatives of the inner model are only computed once, reducing dramatically model evaluations (*see table 1, col.2*), depending on the coupling with other inner models.

SENSITIVITY ANALYSIS USING DIFFERENTIALS

An other method may take advantage of the differential propagation mechanism. In the previous section, the number of evaluation was depending on the linkage between inner models. Differentials bring a sensitivity analysis independently of this linkage. The following expression of the output differential, based on a **differentials finite difference**, requires only one extra model evaluation.

$$dS = \left(S(I_1 + \frac{dI_1}{p}, \ldots, I_n + \frac{dI_n}{p}) - S(I_1, \ldots, I_n) \right) \cdot p$$

Parameter *p* is a normalization parameter which can be as following : $p = \sqrt{dI_1^2 + \ldots + dI_n^2}$ or $p = \sum \left| \frac{dI_i}{I_i} \right|$ or …

This solution reduces the model evaluation number to the optimizable input number (*see table 1, col.3*), but decreases the differentiation robustness by mixing all input differentials together.

APPLICATION ON A TRANSFORMER DESIGN

A compound model (FEM + analytic) of a transformer has been realized. 5 specification sheets were applied on it to study convergence of such a model [4]. All the proposed methodologies were applied to perform sensitivity analysis of the FEM model. The final paper will also develop this application which gave us significant results:

		systematic partial derivation	Jacobian memorization	differential finite difference
Spec 1	Iterations	18	18	12
	time (s)	8183	3835	1875
	time/iter (s)	454	213	156
Spec 2	Iterations	12	12	12
	time (s)	5300	2558	1822
	time/iter (s)	441	213	151
Spec 3	Iterations	11	11	10
	time (s)	5000	2305	1423
	time/iter (s)	454	209	142
Spec 4	Iterations	8	13	7
	time (s)	3100	2716	960
	time/iter (s)	387	208	137
Spec 5	Iterations	7	7	7
	time (s)	3100	1453	1000
	time/iter (s)	442	207	142

table 1 : transformer optimization of 5 specification sheets with three sensitivity analysis implementations for the FEM computation.

CONCLUSION

This work has highlighted issues and given solutions to reduce the time cost taken by compound model sensitivity analysis, during an optimization process. This time cost has been reduced in a particular study by a factor 2 with local Jacobian reminding, then by 3 with the differentials method. Naturally, total optimization time depends on the sensitivity quality, so these methodologies can not be applied without checking this sensitivity evaluation quality.

The final paper will develop further the problem of compound model sensitivity analysis. The transformer application will be detailed giving a concrete support for understanding all encountered issues.

REFERENCES

[1] Sobieszczanski-Sobieski, J., "Sensitivity of Complex, Internally Coupled Systems," *AIAA Journal*, Vol. 28, No. 1, January 1990, pp. 153-160

[2] Ioan, D.; Munteanu, I.; Ciuprina, G. Magnetics "Adjoint field technique applied in optimal design of a nonlinear inductor", *IEEE Trans. Mag., vol.* 34, no. 5, pp. 2849 -2852 Septembre 1998.

[3] E. Atienza, J. Bigeon, F. Wurtz, B. Belhabib "Steps to an Electrical Design ENvironment", IEEE-IECON'99, San Jose, CA, USA, November 29th - December 3rd, 1999.

[4] B. Delinchant, F. Wurtz, J. Fandino, "Mixing of FEM and Analytical Modeling for the Preliminary Design of a Transformer", OIPE'02, 7th International Workshop on Optimisation and Inverse Problems in Electromagnetism, Lodz, Poland, September 12-14 2002.

Kriging: a useful tool for electromagnetic devices optimization

Luiz LEBENSZTAJN Carina A. RONDINI MARRETTO Maurício CALDORA COSTA
LMAG-EPUSP, Laboratório de Eletromagnetismo Aplicado, 05508-900 – São Paulo/SP – Brazil
leb,carinarm,caldora@pea.usp.br

Jean-Louis COULOMB
LEG: Laboratoire d'Électrotechnique de Grenoble - INPG/UJF- CNRS UMR 5529 ENSIEG, BP 46, 38402
Saint Martin d'Hères France
Jean-Louis.Coulomb@leg.ensieg.inpg.fr

***Abstract*-- This paper deals with the use of the Kriging method for approximations and its use on optimization for electromagnetic devices. The method is compared with some radial basis function neural networks and with the diffuse element method. The comparative tests are done on an analytical function and on the TEAM workshop problem 25.**

***Index Terms*— Approximation techniques, Kriging, optimization, finite element method.**

I. INTRODUCTION

Electromagnetic device optimization often demands some procedures for replacement of the objective function with a very reliable performance, a low computational cost and good accuracy. One of those methods is named Kriging, one of the main tools of Geostatistics.

Kriging exploits the spatial correlation of data in order to build interpolations, thus the correlation function choice highly affects the quality of the approximation. Two different approaches to build Kriging models will be presented in this work. The first one is the classical Geostatistics approach [1] and the second one is based on Maximum Likelihood Estimates (MLE), and is more suitable to Design and Analysis of Computer Experiments (DACE)[2].

Kriging is a general term used for a family of methods for minimum error variance estimation. In this work, Kriging will replace the objective function during the optimization process. It will be compared with other three methods: the first-order diffuse elements and two kinds of radial basis functions (RBF): the MultiQuadrics RBFs and the Averaged Gaussian RBFs [3].

II. KRIGING MODELS

Kriging models have two different approaches, both based on random functions.

A. The Geostatistics Approach

Our goal is to estimate a function z(x) based on N sampling points $[x_1\ x_2 \ldots x_N]$. On the Geostatistics classical approach, we suppose that z(x) is a realization of a random function Z(x). This function is also supposed stationary of second order, i.e., both expectation and covariance function exist and do not depend on x.

The interpolation could be then performed, based on a estimate random function Ω(x), defined as a linear combination of the values of Z(x) on the N sampling points:

$$\Omega(x) = \sum_{i=1}^{N} w_i(x) Z(x_i) \tag{1}$$

So, in order to compute the estimate random function Ω(x), it is necessary to evaluate the values of all weight functions $w_i(x)$. The random function Ω(x) must be a good estimator of Z(x), so to evaluate $w_i(x)$, two conditions are imposed:

1. the expectation of the error between Z(x) and Ω(x) must be zero;
2. the error between Z(x) and Ω(x) must be minimized.

The mean is supposed unknown for every x, so the first condition allows us to write:

$$\sum_{i=1}^{N} w_i(x) = 1 \tag{2}$$

The second condition is equivalent to the minimization of the variance of (Z(x) - Ω(x)), for every x:

$$Var(\Omega(x) - Z(x)) =$$
$$= \sum_i \sum_j w_i(x) w_j(x) \operatorname{cov}(x_i, x_j) - 2\sum_i w_i(x) \operatorname{cov}(x_i, x) + \operatorname{cov}(x, x) \tag{3}$$

So, (3) must be minimized with respect to $w_i(x)$, constrained by (2). The solution to this minimization problem is given by:

$$\begin{bmatrix} \mathbf{C} & \mathbf{B} \\ \mathbf{B^t} & \mathbf{0} \end{bmatrix} \begin{bmatrix} \mathbf{w} \\ \lambda \end{bmatrix} = \begin{bmatrix} \mathbf{A} \\ 1 \end{bmatrix} \tag{4}$$

Equation (4) shows a linear system with N+1 equations and N+1 unknowns $[w_1\ w_2\ \ldots w_N\ \lambda]^T$. The general term of matrix **C** is the covariance function $\operatorname{cov}(x_i, x_j)$ and its dimension is N. **B** is a Nx1 vector filled by ones and λ is a Lagrange multiplier. **A** is also a Nx1 vector and its general term is $\operatorname{cov}(x, x_i)$.

Thus, if the covariance function is defined, the problem could be solved. A good choice of a covariance function is the great challenge on Geostatistics. One of the most popular covariance functions is the thin elastic plates model (TEPM):

$$\operatorname{cov}(x, y) = |x - y|^2 \log|x - y| \tag{5}$$

where |x-y| is a distance between the points x and y:

The value of the Kriging interpolation is, using (4) and (5):

$$z_{calc}(x) = \sum_{i=1}^{N} w_i(x) z(x_i) \tag{6}$$

B. The Maximum Likelihood Estimate Approach

In this approach it is possible to "control" some parameters on the correlation function. The Kriging model is defined as follows:

This wok was supported by CAPES-COFECUB and FAPESP

$$y(x) = f(x) + Z(x) \quad (7)$$

where y(x) is the interpolation function, f(x) is a known function (usually polynomial) and Z(x) is the realization of a random process with mean zero, variance equals to σ^2 and covariance non-zero. On (7), f(x) could be understood as a global model and the localized deviations are created by Z(x). In this work, f(x) will be adopted constant and equals to β.

The covariance matrix of Z(x) could be written as:

$$\mathrm{Cov}[Z(x_i), Z(x_i)] = \sigma^2 \mathbf{R}\,(R(x_i, x_i)) \quad (8)$$

where **R** is the correlation matrix and $R(x_i, x_i)$ is the correlation function. There are several correlation functions, but on general a Gaussian correlation function is adopted:

$$R(x_i, x_j) = e^{\sum_{k=1}^{N_{par}} -\theta_k (|x_i - x_j|_k)^2} = \prod_{k=1}^{N_{par}} e^{-\theta_k (|x_i - x_j|_k)^2} \quad (9)$$

Some important remarks on (9): $|x_i-x_j|_k$ is the difference between the coordinates of the points x_i and x_j on k-direction. The optimization problem is a multidimensional problem (N_{par} parameters) and the correlation function is defined as a product of correlation functions (different in each k-direction). The *positive* parameter θ_k is a constant on k-direction and it measures how the data are correlated this direction: a high valued θ_k reflects a low correlated set data on k-direction.

If the global model β and $\theta = [\theta_1\ \theta_2 \ldots . \theta_N]$ are fixed, then the best linear unbiased predictor (BLUP) of y(x) is:

$$y_{calc}(x) = \beta(\theta) + \mathbf{r}^t(x,\theta) \times \mathbf{R}(\theta)^{-1} \times (\mathbf{y} - \mathbf{f}\beta(\theta)) \quad (10)$$

where $y_{calc}(x)$ is the estimated value at x, **y** is a Nx1vector filled with the sampled values, **f** is a Nx1 vector filled by ones (because f(x) was assumed constant). The vector $\mathbf{r}^t(x)$ is equal to the correlation between x and the N sample points:

$$\mathbf{r}^t(x) = \left[\mathrm{R}(x, x_1) \quad \mathrm{R}(x, x_2) \quad \ldots\ldots\ \mathrm{R}(x, x_N)\right]^t \quad (11)$$

So, (10) shows us a family of interpolating curves, that depend on the parameters β, θ and σ^2. If θ are fixed, the MLEs of β and σ^2 have an explicit expression. The *estimated* global model β is:

$$\beta(\theta) = (\mathbf{f^t}\,\mathbf{R}(\theta)^{-1}\mathbf{f}^{-1})(\mathbf{f^t}\,\mathbf{R}(\theta)^{-1}\mathbf{y}) \quad (12)$$

and the *estimated* variance σ^2 between the global model β and y is:

$$\sigma^2(\theta) = [\mathbf{y} - \mathbf{f}\,\beta(\theta))^t\,\mathbf{R}(\theta)^{-1}(\mathbf{y} - \mathbf{f}\,\beta(\theta)]/N \quad (13)$$

The MLE of θ is then obtained by maximizing:

$$-(N \ln(\sigma^2(\theta)) + \ln(|\mathbf{R}(\theta)|))/2 \quad (14)$$

The solution of this unconstrained non-linear problem gives the value of θ and (10) allows us to evaluate the function for any x.

III. Results

Table I shows the unconstrained optimization of the analytical function $f = 0.01 * \sum_{i=1}^{2} (x_i + 0.5)^4 - 30x_i^2 - 20x_i$. It was analyzed on a square domain [-5.12,5.12]*[-5.12,5.12] and discretized by 9 equidistant points in each direction.

TABLE I
UNCONSTRAINED OPTIMIZATION OF AN ANALYTICAL FUNCTION

Approximation	x_1	X_2	f
Exact values	-4.4538	-4.4538	-5.2328
Averaged Gaussian RBF (σ=2)	-4.4123	-4.4123	-5.1680
Multiquadrics RBF	-4.3670	-4.3670	-5.1068
Kriging TEPM	-4.3147	-4.3210	-5.2689
Kriging MLE	-4.4215	-4.4216	-5.2856
Diffuse Element Method	-4.0864	-4.0864	-4.9185

The methods were also applied to TEAM Workshop problem 25 [4]. The magnetic field computations were done with finite elements [5]. Several geometric parameters can be varied [4], but the significant parameters showed to be R1, L2 and L4 [3]. Three-dimensional response surfaces were then constructed on the parallelepiped [5, 9.4]*[12.6, 18]*[4, 19].

On Table II, D is the deviation between each approximation and a finite element calculation on a regular 13x13x13 grid, f_{TEAM} is the approximation of the objective function and g_{TEAM} is the objective function calculated by finite element method[5].

TABLE II
TEAM25: OPTIMIZATION OBJECTIVE FUNCTION REGULAR GRID 7X7X7

Approximation	R1	L2	L4	10^3 D	10^3 f_{TEAM}	10^3 g_{TEAM}
Averaged Gaussian RBF	7.20	14.40	14.20	5.5	0.19	0.22
Multiquadrics RBF	6.76	13.03	14.81	7.4	-4.4	4.4
Kriging TEPM	6.78	13.06	14.87	4.0	3.6	2.7
Kriging MLE	7.20	14.40	14.00	47	0.278	0.280
Diffuse Element Method	7.17	14.06	14.35	5	-0.43	0.11

IV. Conclusions

Kriging models were applied and compared as approximations of the objective function. On the unconstrained optimization of an analytical function, the best solution was the Kriging MLE. It accurately found both the minimum coordinates as its value. For the optimization of TEAM 25, all of the studied methods localized an approximate solution in the same area. Although the true objective function is always positive, some approximation values are negative, due to the flatness of the actual function. Kriging TEPM is one of the easiest methods to implement and Kriging MLE seems to be very accurate for optimization purposes.

References

[1] Host, G. , "Kriging by local polynomials", Computational Statistics & Data Analysis vol. 29, 295-312, 1999.

[2] Simpson, T. W. et alli "Comparison of Response Surface and Kriging Models for Multidisciplinary Design Optimization", 7th Symposium on Multidisciplinary Analysis & Optimization, St. Louis, MO, September 2-4, AIAA, 1 (381-391) AIAA-98-4755. 1998

[3] Kobetski, A. et alli "Comparison of radial basis function approximation techniques", IGTE 2002 : 10th International IGTE Symposium on Numerical Field Calculation in Electrical Engineering September 16-18, 2002 Graz, Austria

[4] N. Takahashi et alli "Investigation of simulated annealing method and its application to optimal design of die mold for orientation of magnetic powder", IEEE Transactions on Magnetics, vol. 32, no.3, 1996.

[5] Flux, Cedrat, 10, Chemin de Pré Carré – ZIRST, 38246 Meylan, France. http://www.cedrat.com

Optimal Design of Thrust Characteristics of Permanent Magnet Type Linear Motor Using L9 Orthogonal Table and Multi-Regression Analysis

T. Ishikawa, C. Chen, S. Hashimoto, and M. Matsunami
Dept. of Electronic Engineering, Gunma University
1-5-1 Tenjin-cho, Kiryu, Gunma, 376-8515 Japan
e-mail: ishi@el.gunma-u.ac.jp

Abstract—**This paper proposes an optimization method using L9 orthogonal table of experimental design method and multi-regression analysis coupled with 2-D FEM. A linear synchronous motor with permanent magnet (PMLSM) is designed to develop a large trust and a small force ripple.**

INTRODUCTION

Linear synchronous motors with permanent magnet have been used in a wide variety of industrial applications such as robotics and high-precision position control equipments. They are currently being developed to implement better performance. We have designed a PMLSM to develop a large thrust by considering two design variables [1]. In the present paper, we design the PMLSM to develop a large thrust and a small force ripple by considering four design variables.

PROPOSED METHOD

The proposed method bases on the experimental design method and multi-regression analysis of multivariate analysis coupled with 2-D finite element method. In this paper, we choose four parameters as design variables, which define the shape of the motor with some assumptions. We design a PMLSM to develop a large thrust and a small force ripple. Then, the objective function is defined as follows,

$$f = f_{ave} + \alpha / f_{rip} \tag{1}$$

where, f_{ave} is the average thrust, f_{rip} is the force ripple and α is a constant. If $\alpha = 0$, the objective function takes into account the average thrust only. Fig.1 shows the flow chart of the proposed method. In the experimental design method, L9 orthogonal table usually uses three-level design variables, $x(i)(1-dx(i)), x(i), x(i)(1+dx(i))$. As there are 9 data in L9 table, we assume the following regression model,

$$f_{reg} = c_0 + c_1 x(1) + \cdots + c_4 x(4) + c_5 x^2(1) + \cdots + c_8 x^2(4) \tag{2}$$

The candidate of optimal design variables is calculated using above equation. When the objective function f calculated by using FEM with the candidate is greater than the last one $f^{(n-1)}$, we set the candidate as the optimal design variables at iteration n. When $f < f^{(n-1)}$, The coefficient with the smallest variance, c_i, is set to be 0, and the new candidate is obtained. We iterate the above process by setting dx to be a small value.

DESIGNED RESULTS

Fig.2 shows a schematic structure of an experimental PMLSM. Three-phase current of the motor is controlled by the position of stator. We choose the width of permanent magnets $x(1)$, the width of teeth $x(2)$ and lengths of teeth edge $x(3)$ and $x(4)$ as the design variables. In the optimization process, we assume that the volume of permanent magnets, the size of outside frame of stator, the size of outside frame of rotor and the area of armature coil are constant. Moreover, we assume the air gap length, pole pitch and slot pitch are constant. Fig.2 is discretized to a mesh, where the numbers of nodes and elements are about 3700 and 7300, respectively. Fig.3 shows the thrust characteristics of the experimental PMLSM. A good agreement is obtained between the computed thrust using the Maxwell's stress tensor method and the measured one.

Fig.4 shows the optimized results considering the average thrust only. In this figure, the thrust is divided by the area of stator, and variables are normalized by pole pitch. We set two starting positions, namely, one is the shape of the experimental motor, and the other is the center of the changeable range. The iteration process staring from the experimental motor converged at the 7-th iteration. The approximately same thrust and design variables are obtained for both staring positions. Fig.5 shows the optimize results considering the average thrust and the force ripple. When staring from the experimental motor, thrust is improved by 1.01 times, and force ripple is reduced by 0.51 times. When starting from the center, thrust is improved by 1.34 times, and force ripple is reduced by 0.38 times.

CONCLUSIONS

The present paper has proposed the optimization method using L9 orthogonal table of experimental design method and multi-regression analysis. The linear synchronous motor with permanent magnet has been designed to develop the large average trust and small force ripple. We have obtained the approximately same result when starting from different initial positions.

REFERENCES

[1] T.Ishikawa, C.Chen and M.Matsunami: "Design of Permanent Magnet Type Linear Synchronous Motor", The 10th biennial IEEE conference on Electromagnetic Field Computation, P2-6, 2002

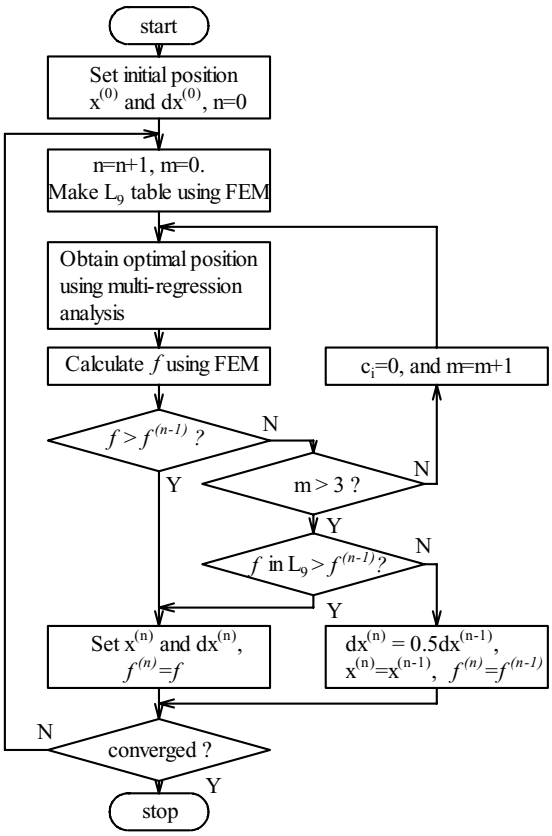

Fig.1. Flow chart of the proposed method.

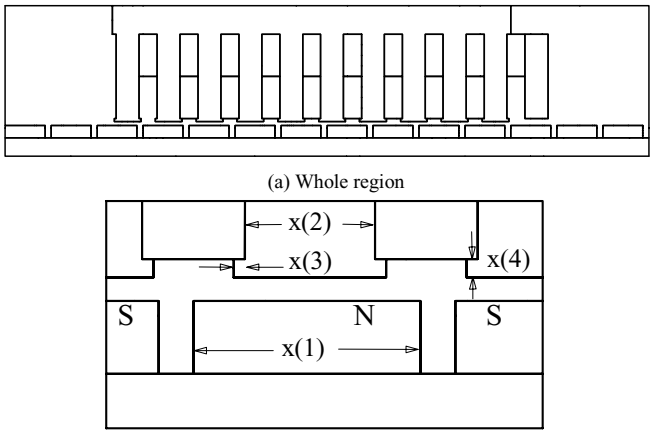

(a) Whole region

(b) Enlarged region

Fig.2. A target model of PMLSM.

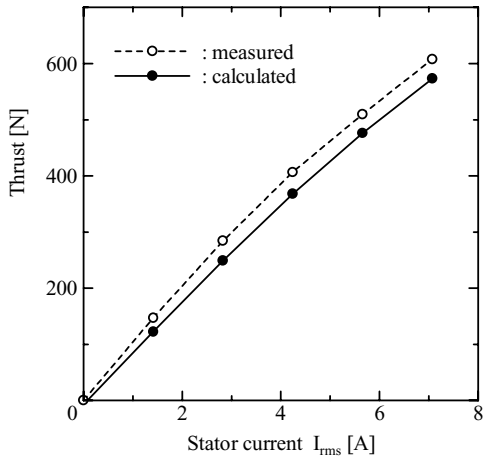

Fig.3. Thrust characteristics of the experimental PMLSM.

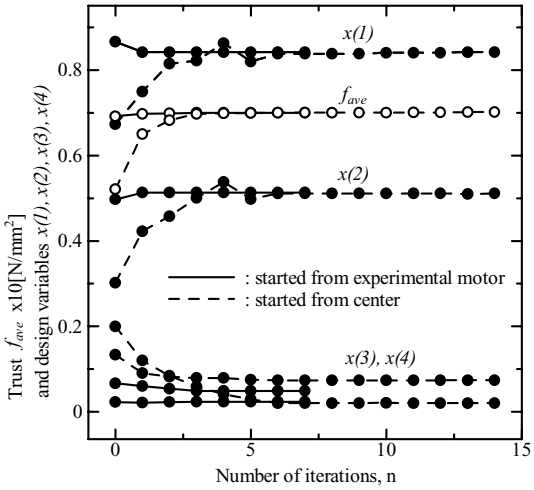

Fig.4. Optimization considering thrust.

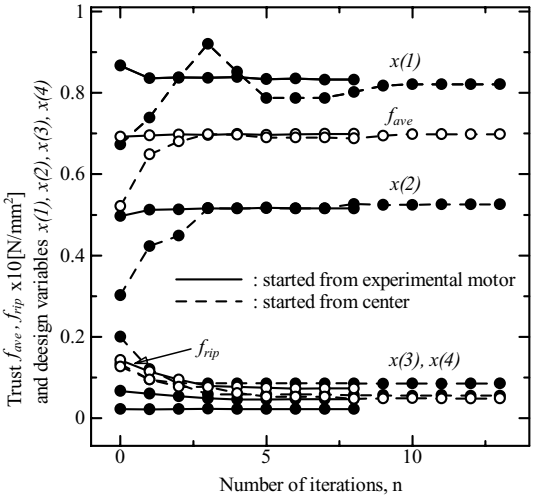

Fig.5. Optimization considering thrust and force ripple.

Optimization of Single-Phase Induction Motor for Reciprocal Compressor Using Response Surface Method

S. Wang, J. Kang, H. Shim, C. Kim, and T. Jung*
Dept. of Mechatronics, Kwangju Institute of Science and Technology , and LG Electronics*
1 Oryong-dong, Buk-ku, Kwangju, 500-712, Korea
e-mail: smwang@kjist.ac.kr

***Abstract*—The response surface method (RSM) became a popular meta modeling technique, but it always contains the approximation error. Instead of the conventional RSM, the moving least squares method (MLSM) was used to get more accurate models. The characteristics of a single-phase induction motor for the reciprocal compressor are analyzed by using the lumped method program (LMP). The proposed method is applied to a single-phase induction motor for increasing the efficiency.**

INTRODUCTION

Even though the single-phase induction motor is not considered as precision electric machine, it is almost certain that the single-phase induction motor has been used widely due to affordable price [1]. For this reason, the single-phase induction motor has been taken on as a subject by many researchers.

The torque and efficiency properties of the single-phase induction motor are calculated by using the lumped method program (LMP) which is developled by LG electronics.

The Response surface methodology is frequently used for the approximation and optimization of the complicated systems. Because of its several advantages, recently, this method became a popular tool for designing in many fields such as mechanical, electro-magnetic, chemical, and biological engineering. However, due to its approximation errors, this method may not give us accurate solutions.

The conventional RSM is based on the approximation of the scattered function data, so it could be easily obtained using the least squares method (LSM). Since the LSM can find only one function that fits the given data through the whole domain, some points should be sacrificed for the best-fitting response surface (RS) model. The weighted LSM calculates the least squares function as the weighted sum of the squared errors, and more advanced method, moving LSM, was adopted to get high accuracy models in this research [2].

The obtained meta models are used for analysis in the optimization process instead of the original system, so the accurate reconstruction is very important in this methodology.

The developed program has been verified with the single-phase induction motor of reciprocal compressor. A single-phase induction motor is optimized to increase the efficiency by using RSM.

RESPONSE SURFACE METHODOLOGY

Concept of Moving Least Squares Method

An advanced method for regression is the MLSM [2]. This is explained as a weighted LSM that has various weights function with respect to the position of approximation. Therefore, the coefficients of the RS model are the function of the location and they should be calculated for each position. This procedure is interpreted as a local approximation and the main concept is explained by Fig. 1.

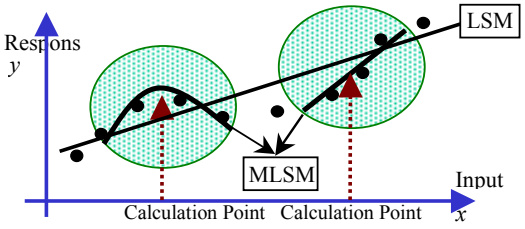

Fig. 1. Concept of LSM and MLSM

Numerical Expression of MLSM

Suppose we have n-response values, y_i, with respect to the changes of x_{ij}. We can express the relationship between the response and the variables like the following equation.

$$\mathbf{y} = \mathbf{X}\boldsymbol{\beta} + \boldsymbol{\varepsilon}_y \tag{1}$$

where $\mathbf{y}$ is an $n \times 1$ vector of the observations, $\mathbf{X}$ is an $n \times p$ matrix of the level of the independent variables, $\boldsymbol{\beta}$ is a $p \times 1$ vector of the regression coefficients, and $\boldsymbol{\varepsilon}_y$ is an $n \times 1$ vector of random errors.

The least squares function L_y could be defined as the following equation when we consider the weighted errors.

$$L_y(\mathbf{x}) = \sum_{i=1}^{n} w_i \varepsilon_i^{\,2} = \boldsymbol{\varepsilon}^T \mathbf{W}(\mathbf{x})\boldsymbol{\varepsilon} = (\mathbf{y} - \mathbf{X}\boldsymbol{\beta})^T \mathbf{W}(\mathbf{x})(\mathbf{y} - \mathbf{X}\boldsymbol{\beta}) \tag{2}$$

Now, we have to note that the diagonal weight matrix, $\mathbf{W}(\mathbf{x})$, is not a constant matrix in the MLSM. In other words, $\mathbf{W}(\mathbf{x})$ is a function of position and it can be obtained by weight shape functions.

From minimizing $L_y(\mathbf{x})$, the coefficients of the RS model, $\mathbf{b}(\mathbf{x})$, can be obtained by matrix operation

$$\mathbf{b}(\mathbf{x}) = (\mathbf{X}'\mathbf{W}(\mathbf{x})\mathbf{X})^{-1}\mathbf{X}'\mathbf{W}(\mathbf{x})\mathbf{y} \tag{3}$$

Note that the procedure to calculate $\mathbf{b}(\mathbf{x})$ is a local approximation and the moving process performs the global approximation through the whole design domain.

Even though the sensitivity is not available on this stage, if cheap sensitivities are available, we can apply more efficient method by defining a new least squares function [2].

NUMERICAL EXAMPLE

In this paper, the single-phase induction motor of the rotary compressor is analyzed by using LMP. The geometry of the stator and rotor are shown in Fig. 2 and 3, respectively.

The input voltage and frequency are 220 [V] and 60 [Hz]. The outer diameter of stator is 133 [mm], the outer radius of rotor is 59.98 [mm], and the stacked height of motor in the vertical direction is 48 [mm]. And this motor has the 34 slots of rotor and the 24 slots of stator.

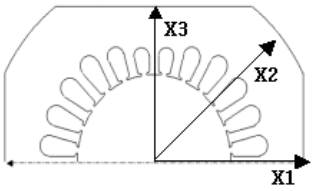

Fig. 2. Geomtry of Stator

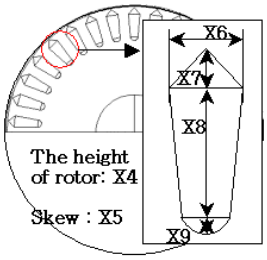

Fig. 3. Geomertry of Rotor

The objective function is to find the shape of stator and rotor that could produce maximum efficiency of motor at 3550 [rpm].

$$\begin{aligned} &obj.\ efficiency\ at\ 3550\ rpm \\ &s.t.\ a)\ T_{st} \geq T_{\text{int}} \times 0.95 \\ &\quad b)\ \Delta eff \leq \Delta eff_{\text{int}}\ @\ 75 \sim 115\%\ Load \\ &\quad c)\ V_t \leq V_{\text{int}} \end{aligned} \tag{4}$$

where T_{st}, Δeff, and V_t, are starting torque, variance of efficiency between 75% and 115% load, and total volume of stator, respectively.

Stator has three design variables, and rotor has six design variables as shown in Fig. 2 and 3. The side limits of each design variable are shown in TABLE I.

To find the optimal values of design variables, three sets of optimization are defined. Case A is when there is no constraints, Case B is when constraint of a) and b) in (4) are considered, and Case C is when all constraints are considered.

In TABLE II, the results of optimization are shown according to each case. From RSM, the efficiency of the induction motor can be increased about 1~ 2% and the starting torque and volume of motor are nearly maintained.

The results of optimization using LSM and moving LSM are compared in TABLE III. From TABLE III, we can know that the moving LSM can reduce the errors between result of optimization and one of re-analysis.

TABLE I
SIDE LIMIT OF DESIGN VARIABLE

	X_1	X_2	X_3	X_4	X_5	X_6	X_7	X_8	X_9
upper	65	60	70	60	7	3	2	7	1.2
lower	55	50	65	48	6	2	1	5	0.6

TABLE II
RESULTS OF OPTIMIZATION

	Initial	LSM			Moving LSM		
		Case A	Case B	Case C	Case A	Case B	Case C
Obj.	86.88	89.857	89.7	88.2	89.5	89.7	88.23
X_1	59	65	65	58	65	65	58
X_2	66.5	65	65	66.5	65	65	66.5
X_3	54	56.98	55	54.85	56.25	55	54.85
X_4	48	60	60	56.37	60	60	56.37
X_5	6.5	7	6	6.4	6.45	6	6.3
X_6	2.775	3	2.867	2.695	3	2.85	2.695
X_7	1.465	2	2	1.326	2	2	1.3
X_8	5.47	6.63	6.73	6.39	6.87	7	6.39
X_9	0.8868	0.896	0.94	1.02	0.889	0.94	1.02

TABLE III
COMPARISON BETWEEN LSM AND MOVING LSM

Efficiency [%]	CASE	Opt.	Re-analysis	Error [%]
LSM	Case A	89.857	88.98	0.985
	Case B	89.7	88.95	0.843
	Case C	88.2	88.37	0.192
Moving LSM	Case A	89.5	89.03	0.527
	Case B	89.7	89.01	0.775
	Case C	88.23	88.34	0.124

CONCLUSION

In this paper, to increase the efficiency, the optimization of a single-phase induction motor for reciprocal compressor is carried out by using the conventional and moving LSM. Lumped method program is used for electromagnetic analysis.

The moving LSM is implemented as a computer program and applied to a numerical example to verify its accuracy.

ACKNOWLEDGEMENT

This work was supported by Center for Innovative Design Optimization Technology(iDOT) and Brain Korea 21.

REFERENCES

[1] G. R. Slemon, Electric machines and Drives, Addison-Wesley publishing company, Inc., 1992

[2] C. Kim, S. Wang, and K. Choi, "Efficient Response Surface Modeling using MLSM and Sensitivity", WCSMO4, June 2001.

Node-based Distribution of Material Properties for Topology Optimization of Electromagnetic Devices

Jin-kyu Byun*, Joon-Ho Lee and Il-han Park
School of Information and Communication Eng., Sungkyunkwan University
Chunchun-dong 300, Jangan-gu
Suwon, Kyunggi-do, 440-746, Korea
*e-mail: aiolia@dreamwiz.com

Abstract — **In this paper, a new node-based material distribution scheme is proposed for TO (topology optimization) of electromagnetic devices. Electromagnetic properties of material such as permeability and current density are given on the nodes of FE (finite element) mesh, and within each element, they are interpolated using the nodal values. The proposed method can be used to alleviate the coarse layout of final device, which occurs frequently in conventional topology optimization. Numerical examples are given to show the effectiveness of the proposed method.**

INTRODUCTION

In general FE analysis, material properties are distributed based on FE element, and it has the same value within one element. This element-based distribution of material property is adequate when there is a clear boundary between different materials, but it displays a few problematic characteristics in TO (topology optimization) where material property can vary continuously element by element. That is, final device designed by TO has somewhat coarse layout because it is represented by on-and-off pattern or gray-scale pattern of regular rectangular grid [1]. (Fig. 1.) Increasing the number of meshes will improve the resolution of device, but computational cost becomes an issue then. The motive for starting this work was finding solutions to these problems, i.e., finding a way to obtain smooth layout with moderate number of meshes.

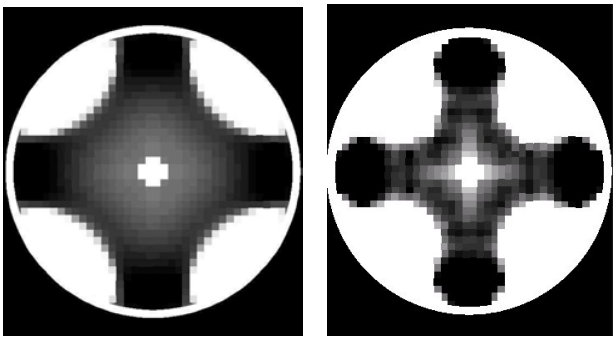

(a) Electrostatic MEMS actuator (b) Rotor of switched reluctance motor

Fig. 1. Examples of coarse layout of final device designed by topology optimization.

In this paper, we suggest a new node-based material distribution scheme that can be used in TO to alleviate these problems. In this scheme, material properties are distributed on the FE nodes, and within each element, they are interpolated by shape function using the nodal values. The proposed scheme is applied to numerical examples to show its validity and effectiveness.

NODE-BASED MATERIAL DISTRIBUTION

Material property within one finite element can be interpolated using its nodal values as:

$$\chi_e = \sum_{ie} \chi_{ie} N_{ie} \tag{1}$$

where χ_{ie} is nodal value of electromagnetic material property, χ_e is material property within one element and N_{ie} is element shape function. FE system matrix has to be assembled with this interpolated value of material property.

If suggested node-based distribution of material is used in TO, the calculation of sensitivity has to consider its effect. From now on, we derive equations for sensitivity assuming that material property χ, which is distributed node-wise, is current density J.

If we assume axis-symmetry magnetostatic system, one component of element forcing term $[Q]_e$ can be written as:

$$Q_{je} = \int_e J_e N_{je} 2\pi r \, dr dz \tag{2}$$

where current density J_e is given by:

$$J_e = \sum_{ie} J_{ie} N_{ie} \, . \tag{3}$$

Now, since we are dealing with TO, we assume that current is carried by microscopic filament. Then, nodal value of current can be represented by density method as [2]:

$$J_{ie} = J_0 \rho_{ie}^n \tag{4}$$

where J_0 is maximum current density, $\rho_{ie} (0 \le \rho_{ie} \le 1)$ is normalized density of microscopic filament at i th node, and n is a penalty factor for intermediate density. Substituting (3) and (4) into (2), we get:

$$Q_{je} = \sum_{ie} \int_e J_0 \rho_{ie}^n N_{ie} N_{je} 2\pi r \, dr dz \, . \quad (5)$$

In sensitivity calculation, the differentiation of $[Q]$ as to design variable is often required. In this case, design variable is nodal density ρ_{ie}, so that $\partial Q_j / \partial \rho_{ie}$ term can be calculated as:

$$\frac{\partial Q_{je}}{\partial \rho_{ie}} = \int_e J_0 n \rho_{ie}^{n-1} N_{ie} N_{je} 2\pi r \, dr dz \, . \quad (6)$$

Similar procedures can be applied when other material properties such as μ or ε are distributed.

NUMERICAL EXAMPLE AND DESIGN RESULTS

The suggested node-based distribution scheme is applied to the design of MRI solenoid. One quadrant of initial MRI model is shown in Fig. 2 with design domain and objective region. The design goal is to achieve uniform magnetic flux density in shell-shaped objective region, and the objective function to be minimized is:

$$F = \int_{\Omega l} \left\{ (B_r - B_{r0})^2 + (B_z - B_{z0})^2 \right\} d\Omega$$

where B_{r0} and B_{z0} are desired values of flux density in the objective region Ωl. The coil is made of superconducting material (Bi-2223/Ag) and nonlinear characteristic of $J_c - B_m$ curve is considered in sensitivity analysis [3].

To observe the effect of finite element mesh, we use 3 different meshes (Table I) and perform both node-based method and element-based method in each mesh. Fig. 3 shows the design results for each mesh. Surprisingly, node-based methods did not yield smooth layout of solenoid compared to the results of element-based method. However, in terms of objective function and performance, node-based method performed much better, its objective function being smaller than that of element-based method (Table I).

It should be also noted that the result of node-based method exhibit checkerboard-like pattern. The origin of this phenomenon is unclear, but it resembles the checkerboard pattern which often appears in TO in the structural engineering field. Strategies to suppress this checkerboard pattern and obtain smooth layout will be explored in the full paper.

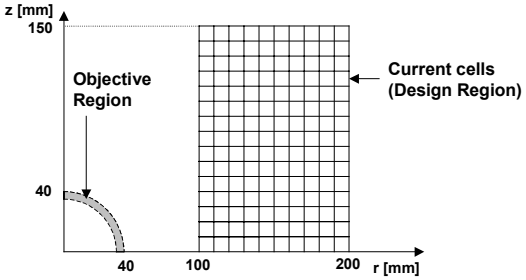

Fig. 2. Initial model for MRI solenoid design.

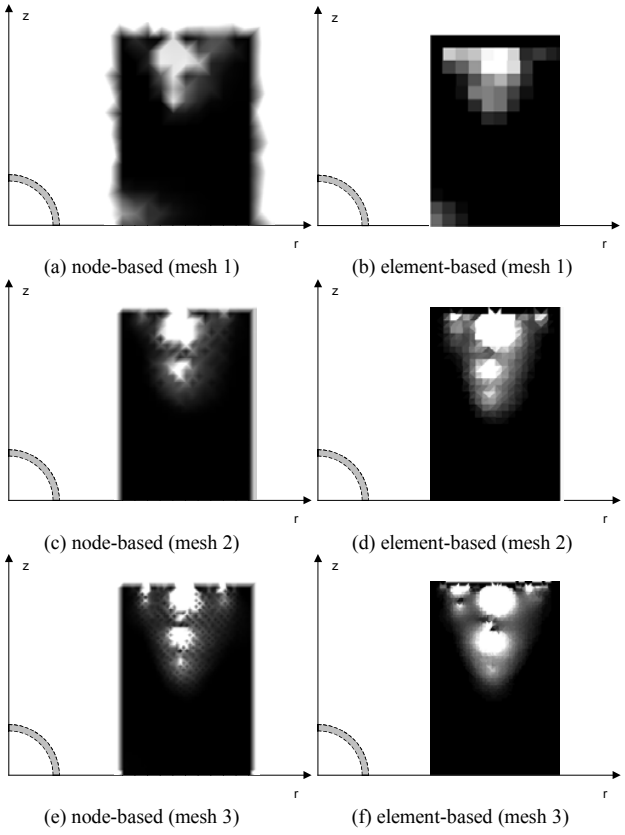

Fig. 3. Design results of node-based method and element-based method in various meshes.

TABLE I. TYPE OF FE MESHES FOR MRI DESIGN AND ITS RESULTS

Type of mesh	Mesh 1		Mesh 2		Mesh 3	
Number of FE meshes	1454		3643		7526	
Design method	Node-based	Element-based	Node-based	Element-based	Node-based	Element-based
Objective Function×1.0e-8	1.08	1.75	2.13	4.94	1.86	7.36

REFERENCES

[1] D. N. Dyck and D. A. Lowther, "Automated design of magnetic devices by optimizing material distribution," *IEEE Trans. Magn.*, vol. 32, no. 3, pp. 1188-1193, May 1996.

[2] R. J. Yang, "Multidiscipline topology optimization," *Computer & Structures*, vol. 63, no. 6, pp. 1205-1212, 1997.

[3] J. K. Byun, J. Kang, W. Nah and I.H. Park, "Topology optimization for superconducting coil distribution with critical current constraint," in *proc. IEEE CEFC 2002*, Perugia, Italy, p. 194, June 2002.

New Design Method Applied to a Linear Actuator

L. El Amraoui [1,2], F. Gillon [1], S. Vivier[1], P. Brochet [1] and M. Benrejeb[2]
[1] L2EP - Ecole Centrale de Lille, Cité Scientifique B.P. 48, 59651 Villeneuve d'Ascq, France
[2] LA.R.A. Automatique - Ecole Nationale d'Ingénieurs de Tunis, B.P. 37, le Belvédère 1002 Tunis, Tunisia
E-Mail: *lilia.el_amraoui@ec-lille.fr or gillon@ec-lille.fr*

***Abstract* — An optimization process of a linear actuator and an axi-symmetric finite element model, built and used for a direct optimization of the actuator starting force, are presented in this paper. The design space exploration is carried out by the use of trellis designs, offering a significant covering of the domain and a considerable decrease of simulation number. An adaptation step is performed to comply to the need analysis.**

INTRODUCTION

Nowadays, the available modern tools of numerical simulation allow complex electromagnetic system design and optimization. However, the optimization stage is often much more complicated than it appears! The mathematical tools generally offered to the designer are more or less adapted to the problem. In fact, the first stage of an optimization problem resolution consists on the mathematical formulation of the problem so that it becomes understandable by a computer. Then, the designer should make the choice of the model that represents, as well as possible, the device and the phenomenon that he wants to study. Finally, the obtained result depends on the combination of the precision and the pertinence of all these elements.

In order to achieve a linear tubular switched reluctance actuator optimization, a direct method is used. The main advantage of this method is that it carries out the optimization process directly from Finite Element simulations. Moreover, in order to minimize the number of these simulations, which are time consuming, a method based on experimental designs, allowing to consider at once discrete and continuous factors, is adopted.

Firstly, a shift strategy [1] is developed using completely new and original designs, named trellis designs. These designs have attractive properties like a large study domain covering, a high factor level and also the low number of simulations they require.

In a second step, once this algorithm has converged, an adaptation step is performed to comply to the need analysis and the structure is homothetically shrunk.

OPTIMUM DESIGN

The design objective is the maximization of the actuator starting force. The used Maxwell stress tensor method, for force computation from finite element results, requires a dense and regular mesh for accurate results. The air-gap of the machine is small and equals 0.1mm.

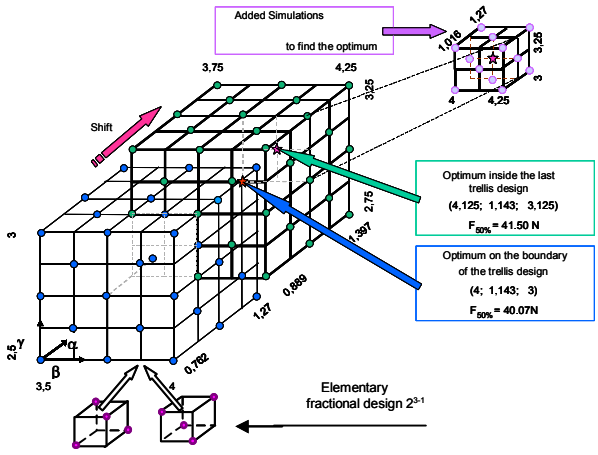

Fig. 1. Optimization process with discrete and continuous factors

Trellis Experimental Design

The proposed trellis design is built starting from a judicious assembly of fractional designs. It is strongly related to response surface designs (RSM), due to the high number of levels per factor, which allows an accurate representation of the system. It uses, at the same time, a juxtaposition of fractional designs, which are normally dedicated to screening analysis. The trellis design is particularly interesting because it offers the possibility of reducing considerably the simulation number while keeping very important statistical properties such as orthogonality.

Trellis designs appear as global experimental designs built from the study domain meshing into elementary two level fractional designs; so that each two adjacent designs share a maximum number of simulations (Fig.1).

The trellis design interest grows with the number of factors and factor levels. Indeed, for an optimization with six factors and five levels per factor, the most economic elementary design is a 2^{6-3} fractional one. Hence, the trellis design comprises 1900 experiments, instead of 15625 experiments with a full design, so with a reduction of more than 8 times. This tool allows to build analytical multidimensional models on which optimum search or inverse problem can be quickly achieved. Moreover, since the experimental matrix is known in advance, the calculations can be distributed on several

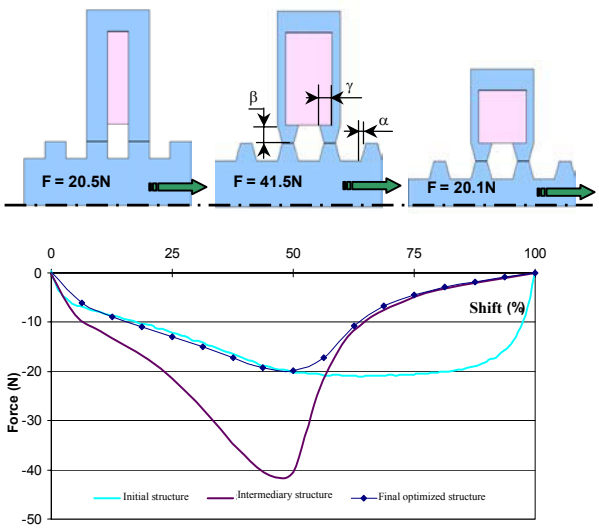

Fig. 2. Static force versus position for 3 design steps

computers in order to reduce the simulation time, which can be relatively long for this kind of problems [2].

Optimization Problem

The Finite Element model is completely parameterized, so that more than 6 geometrical factors can be handled. All of them are not necessarily pertinent for the considered problem. A selection is carried out in a screening stage which will keep only the 3 most influent factors, α, β and γ. In order to keep a regular mesh, the proposed method offers the possibility to chose discrete values for the factor β multiple of the displacement step during all the optimization stage.

The optimization problem is formulated as follows:

$$\begin{cases} \text{Maximize Starting Force} \\ \text{With constraints:} \\ \Delta T = 43°C \qquad 2\text{mm} \le \alpha \le 4.25\text{mm} \\ R_{out} = 46\text{mm} \qquad \beta = \dfrac{\text{step}}{100} \cdot i \text{ mm with } i = 1...30 \\ R_{in} = 15.05\text{mm} \qquad 0\text{mm} \le \gamma \le 3.25\text{mm} \end{cases} \quad (1)$$

where ΔT is the temperature rise, calculated by an analytical formula.

The optimization method using the shift of 5 level trellis designs is used in order to sweep as well as possible the study domain. Thus, only 63 experiments are needed with the first trellis design. The constraints are not directly taken into account by the algorithm, but introduced into the model building.

The optimization starts by a trellis design on a part of the study domain. If the best response is reached on the domain face, then a new design is created and centered around this best response. This process is repeated until the optimum becomes strictly inside the trellis design or reaches a limit of the design domain. At each shift, a significant experiment number is recovered by the new design. When the optimum becomes strictly inside the trellis design, a full three level factorial design is built around this point. In order to achieve this, the experiments already carried out are recovered and complementary simulations performed.

Figure 1 presents the optimum search progression on the two last trellis designs and also the full design carried out around the found optimum.

The optimum linear actuator is developing a starting force of 41.5N, compared to the initial structure developing a force of 20.5N. This result required six trellis design shifts, so approximately 300 evaluations, requiring a total CPU time of about 45 hours. The static characteristic of force developed by the optimum structure is presented on Fig.2.

Adaptation to Need Analysis

Because of the important improvement of the actuator performances, it is necessary to adapt the optimized structure to the need analysis, which imposes a starting force of 20N. Hence, a homothetic coefficient is calculated in order to reduce the radial dimensions of the actuator [3]. Figure 2 shows the reached optimum. Normally the whole process is restarted but as the need requirement is obtained, the work is already done.

For the building of an industrial prototype, this optimization work is not sufficient; it is necessary to test the robustness of the result obtained. This work is described in a companion paper [4].

CONCLUSION

The proposed method: screening, optimization and adaptation has proved to be efficient and a new experimental design, trellis design, allowing a global optimization at low cost has been presented. The quality of the obtained result shows the efficiency of the proposed method, which has allowed to reduce the actuator outline in a proportion of 51%.

REFERENCES

[1] S. Brisset, F. Gillon, P. Brochet "Optimization with experimental design: an approach using Taguchi's methodology and finite element simulations", *IEEE Trans. On Magnetics* , September 2001, Vol. 37, N°5, pp 3530-3533.

[2] S. Vivier, F. Gillon, M. Hecquet, P. Brochet "A design optimization manager", *Compumag*, Evian 2001, pp. 228-229.

[3] L. El Amraoui , F. Gillon, S. Vivier, P. Brochet, M. Benrejeb "Optimal design and experimental tests of linear tubular switched reluctance machine", *IEEE SMC 02*, IEEE International Conference on Systems Man and Cybernetics, Hammamet 2002.

[4] L. El Amraoui , F. Gillon, P. Brochet, M. Benrejeb "Robust electromagnetic optimization using signal-to-noise models", proposed to *Compumag*, Aratoga 2003.

Robust Electromagnetic Optimization using Signal-to-Noise Models

L. El Amraoui [1,2], F. Gillon [1], P. Brochet [1] and M. Benrejeb[2]
[1] L2EP - Ecole Centrale de Lille, Cité Scientifique B.P. 48, 59651 Villeneuve d'Ascq, France
[2] LA.R.A. Automatique - Ecole Nationale d'Ingénieurs de Tunis, B.P. 37, le Belvédère 1002 Tunis, Tunisia
E-Mail: lilia.elamraoui@enit.rnu.tn or gillon@ec-lille.fr

***Abstract*— The paper discusses robust optimization for electromechanical devices starting from finite element models and signal-to-noise analysis. The robustness study considering modeling and building noises is applied to the optimal structure of an axi-symmetric actuator.**

INTRODUCTION

Economic competition is being increasingly hard, thus it becomes necessary to optimize the industrial products diffused in great series or requiring high performances. For the study of electromechanical systems, the Finite Element Method is current and optimization tools are increasingly popularized. Nevertheless, once the optimum is found, the designer work is not terminated, it is necessary to test the robustness of the achieved model and to analyze the results obtained using this model. Without robustness analysis, the designed product remains a laboratory's one, unable to operate correctly in a less controlled industrial context.

Indeed, the precision of the mathematical model as well as the employed calculation method is not infinite. Moreover, the elements constituting the industrial equipments are manufactured or provided with a specific tolerance. Hence, the precision of the result presented by the computer requires deep thought.

As the mathematical model used and the optimal dimensions found can be disturbed by different noises. In this paper, a robust design methodology based on signal-to-noise ratio analysis is developed. Some small disturbances are voluntarily introduced into the finite element model in order to simulate numerical modeling errors and manufacturing dispersions. This robustness analysis is applied to a switched reluctance axi-symmetric actuator optimized in order to increase its starting force.

FORCE OPTIMIZATION

The static starting force performance developed by the axi-symmetric actuator is chosen as the quantity to be optimized in this study. This force is computed from the Maxwell stress tensor which requires a dense and regular mesh quality to obtain accurate results. A mesh of the air-gap with right-angle isosceles triangles at a rate of 100 nodes per tooth is carried out. In this air-gap, the Maxwell stress tensor integration is computed over 10000 points on the center line.

The achieved Finite Element Model is implemented into an optimization process using experimental design method [1].

Three geometrical dimensions α,β and γ, shown in Fig.1, are selected as design variables. The optimization algorithm converges to the optimal geometrical variables providing the maximum starting force as detailed in a companion paper [2].

In order to test the sensitivity of the optimum found, a full three level factorial design is built around it. The finite element result analysis shows that the computed force values on this factorial design are closed to each other and that other configurations of this design are candidates to become optimal. In fact, on this micro domain the mean response is of 19.04N, with a standard deviation of 0.62N. For this weak variation, what is the influence of the modeling noises, which are small variations in the model building process, and what is the representativeness of this variation in comparison to industrial manufacturing dispersions?

To answer these questions, modeling uncertainties and manufacturing dispersions are studied and used for the determination of robust and optimal actuators. Hence, the signal-to-noise ratio is used and the disturbances are introduced into the Finite Element Model and analyzed using the Taguchi's product designs [3].

ROBUSTNESS ANALYSIS

Modeling uncertainties are firstly introduced with three factors regarded as the modeling noise. The node number per tooth, the position of the Maxwell tensor integral line and the number of points considered on this line are chosen to depict this noise.

A global design is built as a product of two experimental designs. The first one: the main design, is a full three level design 3^3, built for the physical controllable factors (α,β,γ) and the second one: the noise design, is a two level fractional design 2^{3-1} built for the noise factors.

The product design consists on repeating the experiments of the main design for each configuration of the noise factors; so, 27x4 finite element simulations are achieved to obtain a product design. Then, the signal-to-noise ratio is used to analyze the noise effect on the starting force, so that the so defined actuator stays an operational optimum, even if disturbed by small design discrepancies or small deviations in realization. Each controllable factor can take three levels represented in reduced centered form by –1, 0 and 1, while the noise factors are referenced by levels 0 and 1. Table I gives the controllable and noise factor values.

TABLE I. DESIGN FACTORS

Controllable factors	-1	0	1
α (mm)	1.016	1.143	1.27
β (mm)	4	4.125	4.25
γ (mm)	3	3.125	3.25

Modeling noise factors	0	1
Node number/tooth	90	110
Line position	1/4	3/4
Point number	9900	10100

Building noise factors	0	1
Tooth thickness (mm)	5.07	5.09
Air-gap depth (mm)	0.09	0.11
B-H curve (%)	-5	+5

The signal-to-noise ratio, expressed on dB scale, is computed for each configuration of the mean design and for the considered combinations of noise factors [4].

Secondly, manufacturing dispersions are introduced with three factors regarded as the building noise. The tooth width, the air-gap thickness and the magnetic materiel proprieties are chosen to depict this noise. A tolerance of 1 hundredth of millimeter is taken on the geometrical dimensions and a variation of 5% is introduced on the magnetic properties of the materials. A second product design is achieved in order to study the influence of the building noise.

The modeling signal-to-noise ratio as well as the building signal-to-noise ratio are modeled over the controllable factor variation domain using a second order model given by (1) :

$$\hat{v} = a_0 + a_{11}\alpha^2 + a_{22}\beta^2 + a_{33}\gamma^2 + a_1\alpha + a_2\beta + a_3\gamma + a_{12}\alpha\beta + a_{13}\alpha\gamma + a_{23}\beta\gamma + a_{123}\alpha\beta\gamma \quad (1)$$

where a_0, a_{11}, a_{22}, a_{33}, a_1, a_2, a_3, a_{12}, a_{13}, a_{23} and a_{123} are the model coefficients.

Using these models, two regions are selected, the first one is limited by a modeling signal-to-noise ratio isosurface and the second one by a building signal-to-noise ratio isosurface. The levels of tolerated signal-to-noise ratios are chosen by the designer. Figure 2 presents the isoresponse surfaces corresponding respectively to a level of 26.75dB for the modeling signal-to-noise ratio and a level of 25.8dB for the building signal-to-noise ratio.

The intersection of the two selected regions corresponds to a robustness zone on which the choice of the controllable factors α, β and γ allows to build optimal and robust structures. Indeed, this robustness zone gives the optimum values of the controllable factors for which the force is maximum and also the least sensitive to modeling and building noises. Figure 3 presents this zone delimited by the intersection of the two isoresponse surfaces.

CONCLUSION

Optimal structures, combining maximum of force and robustness to noises can be defined by the choice of optimization factor combinations (α,β,γ) inside the robustness zone. The determination of this zone has allowed to enlarge the punctual optimum concept to the optimal zone one on which all the geometries are equivalent and robust to noises.

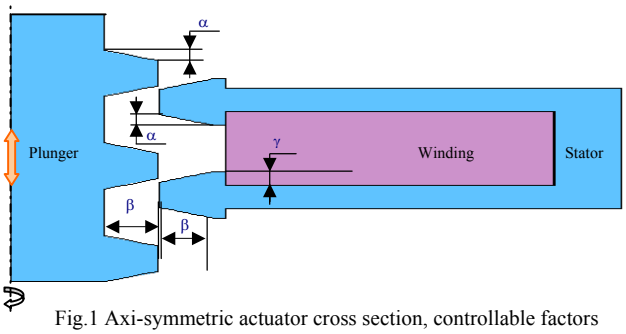

Fig.1 Axi-symmetric actuator cross section, controllable factors

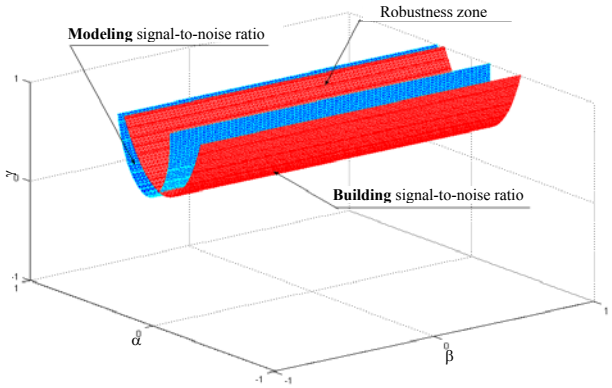

Fig.2 Three dimensional representation of noise ratios

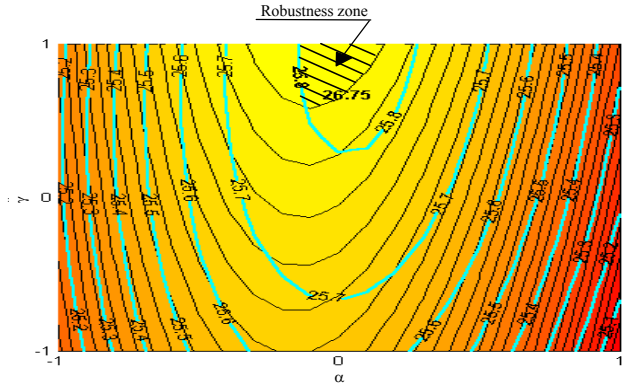

Fig.3 Noise-to-signal ratio (dB), Cross-section at level 0 of β

REFERENCES

[1] L. El Amraoui, F. Gillon., S. Vivier, P. Brochet and M. Benrejeb "Optimal design and experimental tests of linear tubular switched reluctance machine", *IEEE SMC 02*, IEEE International Conference on Systems Man and Cybernetics, Hammamet, 2002.

[2] L. El Amraoui, F. Gillon, S. Vivier, P. Brochet and M. Benrejeb "New design method applied to a linear actuator", proposed to *Compumag*, Aratoga 2003.

[3] G.E.P. Box and N.R. Draper "Empirical model building and response surfaces", Wiley series in probability and mathematical statistics, USA, 1987.

[4] X.K. Gao, T.S. Low, S.X. Chen, Z.J. Liu "Robust design for torque optimization using response surface methodology", *Compumag*, Vol. 3, pp.42 - 43, Evian 2001.

Numerical analysis of magnetic shielding efficiency of multilayered screens

O. Bottauscio, A. Manzin
Istituto Elettrotecnico Nazionale *Galileo Ferraris*
Strada delle Cacce 91, I-10135 Torino, Italy
e-mail: botta@ien.it, manzin@ien.it
M. Chiampi
Politecnico di Torino, Dipartimento di Ingegneria Elettrica Industriale
Corso Duca Abruzzi 24, I-10129 Torino, Italy
e-mail: chiampi@polel1.polito.it)

***Abstract*—An extension of the thin shell formulation for the analysis of the shielding efficiency of multilayered passive shields is presented here. After a validation of the proposed approach by comparison with analytical results, the model is applied to the analysis of shielding configurations of practical interest.**

INTRODUCTION

Magnetic field mitigation is often achieved by means of passive screens, whose shielding efficiency is strongly influenced by the shielding shape and position, and by the electromagnetic characteristics of the material. It is well known that magnetic and conductive amagnetic screens show complementary behaviours, so that a coupling between the two material categories can produce advantageous effects [1]. This goal can be achieved by employing multilayered screens, where some layers of different materials are composed to obtain a single sheet. The evaluation of the best configuration can be done employing a reliable numerical model for an extensive analysis of the shielding efficiency of all the possible combination of layers.

This paper presents a numerical model for the analysis of multilayered screens, allowing a deep comparison between different material combinations. The proposed approach represents an extension of the thin shield formulations based on interface boundary conditions [2,3], which overcomes the problems introduced by the presence of thin screens.

The model has been first validated by comparison with analytical results, obtained for simple geometries. Successively, it has been applied to the analysis of multilayered configurations, considering different shielding geometries and source characteristics.

NUMERICAL MODEL

Shielding structures are conveniently handled in numerical field formulations by means of the thin shell approximation. This is based on the introduction of interface conditions between the two faces of the shell, allowing the discretisation of the shield by means of surface elements instead of volume elements. These relationships can be generalized to the case of N layer shells (Fig. 1).

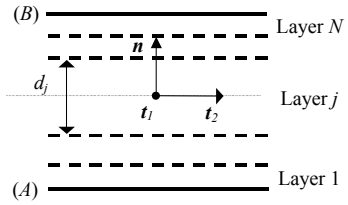

Fig. 1 Scheme of the screen with N layers

For the generic layer j, having electrical conductivity σ_j, magnetic permeability μ_j and thickness d_j, the following interface conditions, written in the matricial form, hold:

$$\begin{bmatrix} B_{n,j}^{(B)} \\ div_S \boldsymbol{H}_{t,j}^{(B)} \end{bmatrix} = \begin{bmatrix} T_{11,j} & T_{12,j} \\ T_{21,j} & T_{22,j} \end{bmatrix} \begin{bmatrix} B_{n,j}^{(A)} \\ div_S \boldsymbol{H}_{t,j}^{(A)} \end{bmatrix} \quad (1)$$

with

$$T_{11,j} = T_{22,j} = \frac{\zeta_j + \eta_j}{\zeta_j - \eta_j}; T_{12,j} = i\frac{1}{\omega}\frac{2\zeta_j\eta_j}{\zeta_j - \eta_j}; T_{21,j} = -i\frac{2\omega}{\zeta_j - \eta_j}$$

$$\zeta_j = \gamma_j / \left[\sigma_j tgh(\gamma_j d_j/2)\right]; \qquad \eta_j = i\omega\mu_j tgh(\gamma_j d_j/2)/\gamma_j$$

$$\gamma_j = (1+i)\sqrt{\omega\mu_j\sigma_j/2}$$

being ω the angular frequency, μ_o the permeability of the surrounding region (air), i the imaginary unit and div_S the surface divergence. Connecting in cascade all the layers, the following interface conditions between sides (A) and (B) of the global shell are deduced:

$$H_{m,n}^{(B)} + H_{m,n}^{(A)} + 2H_n^{(s)} = \frac{1}{\mu_o}\left[\frac{T_{11}+1}{T_{21}}\right] div_S\left(grad_S\varphi^{(B)} + \boldsymbol{H}_t^{(s)}\right) +$$
$$\frac{1}{\mu_o}\left[\frac{T_{12}T_{21} - T_{11}T_{22} - T_{22}}{T_{21}}\right] div_S\left(grad_S\varphi^{(A)} + \boldsymbol{H}_t^{(s)}\right)$$
$$H_n^{(B)} - H_n^{(A)} = \frac{1}{\mu_o}\left[\frac{T_{11}-1}{T_{21}}\right] div_S\left(grad_S\varphi^{(B)} + \boldsymbol{H}_t^{(s)}\right) + \quad (2)$$
$$\frac{1}{\mu_o}\left[\frac{T_{12}T_{21} - T_{11}T_{22} + T_{22}}{T_{21}}\right] div_S\left(grad_S\varphi^{(A)} + \boldsymbol{H}_t^{(s)}\right)$$

where

$$\begin{bmatrix} T_{11} & T_{12} \\ T_{21} & T_{22} \end{bmatrix} = \begin{bmatrix} T_{11,N} & T_{12,N} \\ T_{21,N} & T_{22,N} \end{bmatrix} \cdots \begin{bmatrix} T_{11,j} & T_{12,j} \\ T_{21,j} & T_{22,j} \end{bmatrix} \cdots \begin{bmatrix} T_{11,1} & T_{12,1} \\ T_{21,1} & T_{22,1} \end{bmatrix}$$

In Eqns. (2) $\boldsymbol{H}^{(s)}$ is external source field (computed by the Biot-Savart law) and $\boldsymbol{H}_m$ is the reduced curl-free field, whose tangential component on the plane of the shield can be expressed as the surface gradient of the scalar potential φ.

Eqns. (2), discretized introducing a finite element mesh (M elements) on the shield surface, are completed by the integral equations describing the field in the open-boundary air region where the sources are placed. For closed shields, dividing volumes $V^{(1)}$ and $V^{(2)}$, we have:

$$\tilde{\varphi}_l^{(A)} = \sum_{k=1}^{M} H_{m,n\,k}^{(A)} \int_{\Omega_k} \Psi ds - \sum_{k=1}^{M} \int_{\Omega_k} \varphi^{(A)} \left(\nabla\Psi \cdot \boldsymbol{n}_k\right) ds \qquad (3a)$$

for volume ($V^{(1)}$) on shield side (A), and

$$\tilde{\varphi}_l^{(B)} = -\sum_{k=1}^{M} H_{m,n\,k}^{(B)} \int_{\Omega_k} \Psi ds + \sum_{k=1}^{M} \int_{\Omega_k} \varphi^{(B)} \left(\nabla\Psi \cdot \boldsymbol{n}_k\right) ds \qquad (3b)$$

for volume ($V^{(2)}$) on shield side (B), where $\tilde{\varphi}_l$ is the mean value on the considered l element, Ψ is the Green function, Ω_k is the surface of the generic element.

For open shields, the integral equations are:

$$\frac{1}{2}\left(\tilde{\varphi}_l^{(A)} + \tilde{\varphi}_l^{(B)}\right) = \sum_{k=1}^{M} \left(H_{m,n\,k}^{(A)} - H_{m,n\,k}^{(B)}\right) \int_{\Omega_k} \Psi ds - \sum_{k=1}^{M} \int_{\Omega_k} \left(\varphi^{(A)} - \varphi^{(B)}\right) \left(\nabla\Psi \cdot \boldsymbol{n}_k\right) ds \qquad (4a)$$

$$\frac{1}{2}\left(H_{m,n_l}^{(A)} + H_{m,n_l}^{(B)}\right) = \left\{ -\sum_{k=1}^{M} \left(H_{m,n_k}^{(A)} - H_{m,n_k}^{(B)}\right) \int_{\Omega_k} \nabla\Psi ds - \sum_{k=1}^{M} \left[\left(\boldsymbol{n}_k \times \boldsymbol{H}_{m_k}^{(A)}\right) - \left(\boldsymbol{n}_k \times \boldsymbol{H}_{m_k}^{(B)}\right)\right] \times \int_{\Omega_k} \nabla\Psi ds \right\} \cdot \boldsymbol{n}_l \qquad (4b)$$

VALIDATION WITH ANALYTICAL SOLUTIONS AND APPLICATIONS

The model has been validated with analytical solutions available, for multilayered screens, for simple geometries. The magnetic field values inside a cylinder, placed in a uniform magnetic field of intensity equal to 1 A/m (from 50 Hz to 10 kHz), are reported in Table I, considering two materials: (A) amagnetic with 30 MS/m conductivity and (B) non-conductive with 15000 relative permeability. A good agreement between numerical and analytical results has been found also for plane shields.

The model is applied to the analysis of different multilayered shield configurations, considering plane, U-shaped and closed screens, in presence of a field source constituted by a system of parallel conductors in a range of frequency from 50 Hz to 10 kHz. The combination of three different materials is considered:

(A) Aluminum (conductivity=30 MS/m)
(B) Fe (relative permeability=200, conductivity=10 MS/m)
(C) GO Fe-Si (relative permeability=15000, conductivity = 2 MS/m)

The distribution of the magnetic flux density modulus along the observation line parallel to the plane shield is reported in Fig. 2, considering different combinations of materials (A) and (B), keeping fixed the total thickness of the shell (2 mm).

TABLE I – COMPARISON BETWEEN NUMERICAL AND ANALYTICAL RESULTS

Freq.	Layer Config.	H (A/m) (real, imaginary)	
		Numerical model	Analytical
50 Hz	A-B	(0.182E-2, -0.1057E-1)	(0.182E-2, -0.1059E-1)
	A-B-A	(-0.174E-2, -0.617E-3)	(-0.174E-2, -0.618E-3)
	B-A-B	(0.313E-5, -0.351E-3)	(0.328E-5, -0.354E-3)
	A-B-A-B	(-0.594E-4, -0.108E-4)	(-0.596E-4, -0.108E-4)
10 kHz	A-B	(-0.200E-4, -0.489E-4)	(-0.201E-4, -0.489E-4)
	A-B-A	(-0.318E-7, 0.314E-7)	(-0.319E-7, 0.314E-7)
	B-A-B	(-0.648E-6, -0.158E-5)	(-0.654E-6, -0.159E-5)
	A-B-A-B	(-0.112E-8, 0.102E-8)	(-0.102E-8, 0.102E-8)

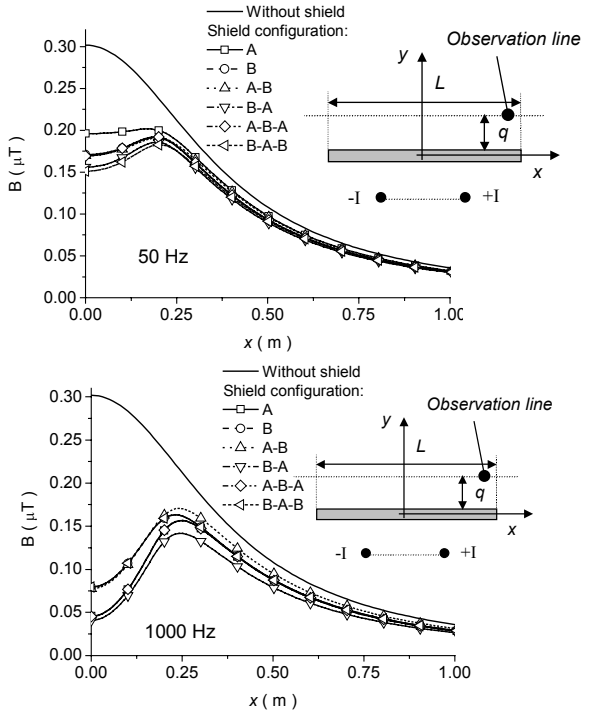

Fig. 2 Diagram of the magnetic flux density along an horizontal line for a plane multilayered shield (L = 0.4 m, q = 10 cm) for two frequencies

REFERENCES

[1] O. Bottauscio et al., "Role of magnetic materials in power frequency shielding: numerical analysis and experiments", IEE Proc. Generation, Transm. and Distribution, Vol. 148, No. 2, 2001, pp. 104-110.

[2] L. Krahenbuhl, D. Muller, "Thin layers in electrical engineering. Example of shell models in analysing eddy-currents by boundary and finite element methods", IEEE Trans. on Magn., 1993, 29 (2), pp. 1450-1455.

[3] H. Igarashi, T. Honma, A. Kost, "A three-dimensional analysis of magnetic shielding with thin layers, 7th IGTE Symp. on Numerical Field Calculation in Electrical Engineering, Graz, Austria, 1996, pp. 230-233.

Use of a Finite-Elements Method to characterize a Multiconductor Transmission Line problem on a tram ground-powered system.

E. Morin, D. Cornic
ALSTOM Transport Systems
23, Av. de la République
92506 Rueil-Malmaison, France
eric.morin@leg.ensieg.inpg.fr

G. Meunier, N. Retière, J. Roudet
Laboratoire d'Electrotechnique de Grenoble
ENSIEG-INPG BP 46
38402 Saint Martin d'Hères, France
james.roudet@leg.ensieg.inpg.fr

Abstract–This paper deals with the modeling of a ground-powered system for trams. After a quick presentation of the system, key points of our study-methodology are highlighted. The structure of the system is then described precisely in order to be modeled with a finite-elements software. Finally, The accuracy and the significance of this original modeling will be discussed.

General Information

Urban transport is a major concern these days. Railway markets, broadly speaking, have been ballooning lately. More and more cities are now equipped with tram networks. Most of the time, power supply is provided by overhead lines. The aim of ground power supply for trams is twofold: first, for esthetical reasons (overhead lines degrade historical heritages of the cities), and then to avoid unearthing power cables, which tend to be buried now in European cities.

An accurate modeling of each power system is required to reflect precisely transients. In ground-powered structures for instance, the environment of the buried power feeders has an important effect on the system. Hence, a simple modeling of this tram power network, using linear parameters for feeders characteristics is not relevant for our studies. In other words, to permit precise dynamic analyses, the whole environment of the power network has to be taken into account.

The studied ground power system is based on different ground conducting sectors, which are switched on when the tram runs over them. No conducting sectors can be turned on outwards the tram dimensions: safety is the keyword in ground supply systems. A signal is emitted in the tram, and received by ground modules. This signal can be transmitted by the tram power collector.

The switching process can be made with mechanical switches (contactors) or with power electronics switches (IGBTs for example). The use of power electronic devices requires a good knowledge on voltage transient magnitudes. Indeed, semiconductors are rated to an inverse voltage, which can't be exceeded. Transitions of the power collector along the adjacent ground sectors lead to rapid changes in electric states of the system. These transients, inherent to ground power-supplied structures have to be taken into account accurately, because they may be the source of important voltage magnitudes. Again, the environment of the buried feeders is important. As voltage transients characteristics are linked with it, the key point of our study is to integrate the environment of the power network into the overall schematic.

Technical Information

The modeling of the specific structure for ground power supply could be seen as a Multiconductor Transmission Line (MTL) problem [1]. Basically, this method implies the construction of a per-unit-length equivalent circuit, related to the network (composed of different conductors). As it is not sufficient to model each conductor by an impedance, impedance matrices will be defined to describe reflections between each pair of conductors. Precisely, the goal of this method is to determine per-unit-length matrices of inductances and capacitances (***L*** and ***C***).

Different methods exist to describe electric characteristics of cables, like the Finite-Elements Method (FEM) or the Partial Element Equivalent Circuit method (PEEC), introduced by A. E. Ruehli [2]. However, as magnetic materials are not taken into account yet in PEEC, the FEM is the only way to achieve our goals.

Description of the system

First, self and mutual inductances of the system have to be computed under electromagnetism domains (magnetostatic and magnetodynamic). Then, capacitances between the different conductors can be evaluated with electrostatic analyses.

The conducting sector is located between the two rails, at the top of an iron case. This case contains power electronics systems and supports the positive and negative feeders. Fig. 1 is a side cut of the ground-powered-system.

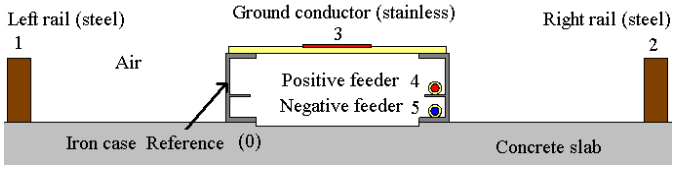

Fig. 1 **:** Ground power supply structure

Power cables run along a brace metal. As we will see, this iron case will have a great impact on the characterization of inductances. Magnetic field lines will be channeled through the metal case. They will thus reinforce the different inductances of the feeder cables.

Inductance matrices computation

To establish the inductance matrix, we will focus on the different magnetic fluxes between the six conductors. The

iron case will be the reference of our system. The matrix, containing self and mutual inductances between the different conductors will be a five-order matrix, as we have six massive conductors. To fill in the inductance matrix, every term has to be computed, based on the different fluxes between the conductors. Basically, the method consists in creating successively different current loops (by associating consecutively one conductor of the system to its reference). Every other non-supplied conductor has to be connected to a zero-current-source, so that global induced currents in each conductor are zero. The different fluxes equations have then to be computed:

$$\phi_k = \frac{D}{i_0}\iint_{\Omega_0}\mathbf{A}.\mathbf{J_0}.d\Omega_0 - \frac{D}{i_k}\iint_{\Omega k}\mathbf{A}.\mathbf{J_k}.d\Omega_k$$

$$\phi_k = L_{k1}\, i_1 \;\forall k \in [1,5] \quad (i_n = 0 \;\forall n \in [2,5])$$

where ϕ_k is the flux between the conductor 'k' and the reference, D is the depth of the system, i_k is the current in 'k', **A** is the magnetic vector potential, $\mathbf{J_k}$ is the current density in 'k', and L_{ij} is the inductance between conductors 'i' and 'j'. To calculate these different fluxes, we use a finite-element software: Flux2D, a Computer-Aided Design (CAD) software.

Each inductance determined using this method depends on the frequency of the currents injected in the different loops. The skin effect and the proximity effect are the sources of these phenomena. When the frequency increases, the currents are rejected to the periphery of the conductor. The geometry of the system is then different, leading to matrix changes. A few results are presented below, for two frequencies of the currents (0Hz and 1kHz).

f = 0 Hz *Unit: µH/m*

$$\boldsymbol{L} = \begin{pmatrix} 2.01 & 1.43 & 1.26 & 1.03 & 1.00 \\ 1.43 & 2.01 & 1.26 & 1.08 & 1.05 \\ 1.26 & 1.26 & 2.46 & 1.14 & 1.08 \\ 1.03 & 1.08 & 1.14 & 2.43 & 1.39 \\ 1.00 & 1.05 & 1.08 & 1.39 & 2.66 \end{pmatrix}$$

f = 1 kHz *Unit: µH/m*

$$\boldsymbol{L} = \begin{pmatrix} 0.75 & 0.25 & 0.12 & 0.05 & 0.04 \\ 0.25 & 0.79 & 0.13 & 0.06 & 0.06 \\ 0.12 & 0.13 & 1.30 & 0.10 & 0.08 \\ 0.05 & 0.06 & 0.10 & 0.87 & 0.17 \\ 0.04 & 0.06 & 0.08 & 0.17 & 0.94 \end{pmatrix}$$

As we can see in these two matrices, frequency is a key parameter in our studies. At first sight, in DC supply systems, harmonic disturbances may not seem to be very relevant. In reality, spectrums of tram-currents contain harmonics, for instance due to acceleration and braking phases, short-circuit faults, or closures of circuit-breakers. In other words, frequency has to be taken into account.

As far as the iron case is concerned, it also has a large influence on the inductance matrix. Fluxes flow in the magnetic case, thus reinforcing the inductances of the system. To compare the effect of the frequency or the influence of the material used for the case, we can compute the inductance of a loop, created by associating the positive feeder to the left rail :

$L_{0Hz,\ magnetic} = 2.43 + 2.01 - 2*1.03\ \mu H = 2.38\ \mu H$
$L_{0Hz,\ non\text{-}magnetic} = 0.80 + 1.48 - 2*0.40\ \mu H = 1.48\ \mu H$
$L_{1kHz,\ magnetic} = 0.87 + 0.75 - 2*0.05\ \mu H = 1.52\ \mu H$

The use of the iron material for the ground case gives 2.38 µH for the selected loop, whereas the use of a non-magnetic material leads to a smaller inductance (1.48 µH).

Capacitance matrix computation

As for the computation of the inductances of the system, a matrix of the capacitances between the conductors is established. The technique used to compute this matrix is different than the MTL method, because the MTL's formula linking the inductance and the capacitance matrices seems to be non-relevant in our study case. A method based on the energy is used in this paper. The procedure consists in defining consecutively a charge density (Q in Coulomb) on each conductor. By computing the global energy with the finite-elements software, a direct information on the capacitance is obtained by the well-known formula:

$$E_{global} = \frac{1}{2} C_{global} V^2 = \frac{1}{2}\frac{Q^2}{C_{Global}}$$

The capacitance matrix $\boldsymbol{C}$ is presented below: Unit : *pF / m.*

$$\boldsymbol{C} = \begin{pmatrix} 14.5 & 9.6 & 10.8 & 8.0 & 8.0 \\ 9.6 & 14.5 & 10.8 & 9.2 & 9.1 \\ 10.8 & 10.8 & 28.4 & 12.2 & 11.6 \\ 8.0 & 9.2 & 12.2 & 21.4 & 17.5 \\ 8.0 & 9.1 & 11.6 & 17.5 & 21.0 \end{pmatrix}$$

BASIC LINEAR APPROACHES, CONCLUSIONS

Comparisons of the FEM with linear approaches

Most of the time, values of line inductances of the cables, given by the manufacturer, are directly integrated in schematics. These values are usually computed at 50-60Hz in an open-area environment. For instance, if we compute the inductance of the loop between the two feeders, the manufacturer's approach gives 0.50 µH/m, whereas the FEM leads to 2.31 µH/m (at 50Hz). The difference between the results obtained is significant, and proves that an usual approach is not sufficient. Simulations of the overall modeling of tram networks are also very relevant.

Conclusions

Finite Elements Analyses permit to take into account the environment (proximity of the conductors, magnetic materials), in a MTL approach. This modeling of the power-grounded system for trams is important to further allow a better accuracy on transient analyses, leading to correct ratings of elements composing the system.

REFERENCES

1 Clayton, R. Paul. *Analysis of Multiconductor Transmission Lines.* Wiley Series in microwave and optical engineering, Kay Chang series editor, 1994, pp. 46-182.

2 E. Ruehli. *Inductance calculation in a complex integrated circuit environment.* IBM-Journal of research and development, Sept. 72, pp. 470-481.

Numerical Green's Function of a Point Current Source in Horizontal Multi-layer Soils by Utilizing the Vector Matrix Pencil Technique

J. Zou, J. L. He, R. Zeng
Department of Electrical Engineering, Tsinghua University, Beijing, 100084, China
zoujun@tsinghua.edu.cn

***Abstract*—A straightforward approach is developed to calculate Green's function of a point current source in horizontal multi-layer soils. The sampling value of the coefficient of Green's function is obtained in an iterative way in terms of the equation group satisfying the pertinent boundary value problem. Further, the closed-form expression of multilayered soil Green's function can be given by the vector matrix pencil technology. The numerical results are in agreement with those by other software. The approach proposed here is applicable to grounding problems with the structure of arbitrarily layered soil without needing the analytical expression of Green's function.**

INTRODUCTION

The study of grounding systems in horizontal multilayer soils has been the subject of considerable attention by many researchers in the past decades. The key point of the analysis of grounding system is to calculate Green's function generated by a point current source in the multilayer soil. However, there exist two basic difficulties. On one hand, the analytical expression of Green function is too complicated to derive when the number of soil layer is greater than 3. On the other hand, the calculation of Green's function involves the evaluation of the infinite integral including Bessel functions and is referred as computationally demanding in general. In this paper, a straightforward approach is developed to bypass above problems.

PRINCIPLE OF NUMERICAL GREEN'S FUNCTION

The cylinder coordinates system for the horizontal N-layer earth structure is shown in Fig.1, where h_i and ρ_i are the thickness and resistivity of layer i respectively. H_i is the distance between the layer i and the earth surface. By using the symmetrical property of problem concerned, Green's function $G_i(r,z)$ of the earth potential in the layer i satisfies the following boundary problem [1].

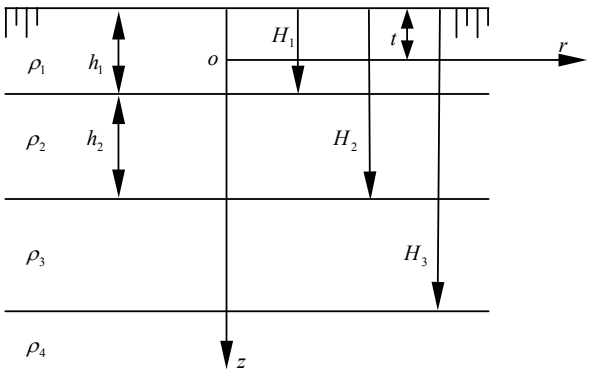

Fig. 1 Diagram of coordinates of multilayer soils

$$\begin{cases} \dfrac{\partial^2 G(r,z)}{\partial r^2}+\dfrac{1}{r}\dfrac{\partial G(r,z)}{\partial r}+\dfrac{\partial^2 G(r,z)}{\partial z^2}=0 \\ G_i(r,z)\big|_{z=H_i-t}=G_{i+1}(r,z)\big|_{z=H_i-t} \\ \dfrac{1}{\rho_i}\dfrac{\partial G_i(r,z)}{\partial z}\Big|_{z=H_i-t}=\dfrac{1}{\rho_{i+1}}\dfrac{\partial G_{i+1}(r,z)}{\partial z}\Big|_{z=H_i-t} \\ G_n(r,z)\big|_{z\to\infty}=0 \qquad \dfrac{\partial G_1(r,z)}{\partial z}\Big|_{z=-t}=0 \end{cases} \quad (1)$$

If the point source locates in the first layer, the formulation of Green's function can be expressed as follows.

$$\begin{cases} G_1(r,z)=\dfrac{\rho_1}{4\pi}\displaystyle\int_0^\infty\left[e^{-\lambda|z|}+A_1(\lambda)e^{-\lambda z}+B_1(\lambda)e^{\lambda z}\right]J_0(\lambda r)\,d\lambda \\ G_i(r,z)=\dfrac{\rho_i}{4\pi}\displaystyle\int_0^\infty\left[A_i(\lambda)e^{-\lambda z}+B_i(\lambda)e^{\lambda z}\right]J_0(\lambda r)\,d\lambda \qquad i\neq 1 \end{cases} \quad (2)$$

where $A_i(\lambda)$ and $B_i(\lambda)$ are the coefficient function in the layer i to be determined. J_0 is the Bessel function of the first kind of order zero. By matching the boundary condition in (1) with the expression in (2), one can obtain an equation group with respect to the variable λ, i.e.,

$$\boldsymbol{K}(\lambda)\cdot\boldsymbol{X}(\lambda)=\boldsymbol{Y}(\lambda) \quad (3)$$

where

$$\boldsymbol{K}(\lambda)=\begin{bmatrix} |e^{-2\lambda t} & 1 & 0 & 0 & 0 & \vdots & \cdots & \cdots & \cdots & \cdots \\ a_1 & 1 & \dfrac{-a_1}{k_1} & -1 & 0 & \vdots & \cdots & \cdots & \cdots & \cdots \\ -a_1 & 1 & a_1 & -k_1 & 0 & \vdots & \cdots & \cdots & \cdots & \cdots \\ \cdots & & \cdots & & & & \cdots & \cdots & \cdots & \cdots \\ 0 & 0 & 0 & 0 & 0 & \vdots & a_i & 1 & \dfrac{-a_i}{k_i} & -1 & 0 & \vdots \\ 0 & 0 & 0 & 0 & 0 & \vdots & -a_i & 1 & a_i & -k_i & 0 & \vdots \\ \cdots & & \cdots & & \cdots & & \cdots & & \cdots & & \cdots & \cdots \\ \cdots & & \cdots & & \cdots & & \cdots & & \cdots & & \cdots & \cdots \\ 0 & 0 & 0 & 0 & 0 & \vdots & \cdots & & \cdots & & \cdots & 1 \end{bmatrix}$$

$$\boldsymbol{X}(\lambda)=\left[A_1(\lambda)\quad B_1(\lambda)\quad A_2(\lambda)\quad B_2(\lambda)\quad\cdots\quad A_i(\lambda)\quad B_i(\lambda)\quad\cdots\quad B_n(\lambda)\right]^T$$

$\boldsymbol{Y}(\lambda) = \begin{bmatrix} -1 & -a_1 & a_1 & 0 & \cdots & 0 & 0 & \cdots & 0 \end{bmatrix}^T$. In addition, $a_i = \mathrm{e}^{-2\lambda(H_i - t)}$, $k_i = \rho_i / \rho_{i+1}$.Given that the integral in (2) can be truncated at $\lambda_{\max}$ determined according to the decay property of integrated function, the numerical limit of Green's function is evaluated by

$$\boldsymbol{X}_{\lim} = \boldsymbol{K}(\lambda_{\max})^{-1} \boldsymbol{Y}(\lambda_{\max}) \qquad (4)$$

Let the difference function of Green's function $\Delta\boldsymbol{X}(\lambda)$ be

$$\Delta\boldsymbol{X}(\lambda) = \boldsymbol{K}(\lambda)^{-1} \boldsymbol{Y}(\lambda) - \boldsymbol{X}_{\lim} \qquad (5)$$

Obviously, $\Delta\boldsymbol{X}(\lambda_{\max}) \to 0$. A series of sampling values of $\Delta\boldsymbol{X}(\lambda)$ are calculated by (5) in correspondence with the different λ in the interval $[0, \lambda_{\max}]$. Further, the difference function $\Delta\boldsymbol{X}(\lambda)$ can be approximated as a sum of complex exponentials by utilizing the vector matrix pencil technology [2] with above sampling data, as a result, the element i of $\Delta\boldsymbol{X}(\lambda)$ is

$$\Delta\boldsymbol{X}_i(\lambda) = \sum_{m=1}^{M} \alpha_{i,m} \mathrm{e}^{-\beta_m \lambda} \qquad (6)$$

where $\alpha_{i,m}$ and β_m are the coefficients determined by the vector matrix pencil technology and M is the rank of fitting model. The main novelty of this approach is that only one set of the exponential terms are shared by different element of $\Delta\boldsymbol{X}(\lambda)$, which is helpful to save computation time dramatically. It should be noted that $\alpha_{i,m}$ and β_m are usually complex numbers. In terms of (5) and (6), the coefficient function in (2) can be rewritten as

$$\boldsymbol{X}_i(\lambda) = \sum_{m=1}^{M} \alpha_{i,m} \mathrm{e}^{-\beta_m \lambda} \square \{X_{\lim} \qquad (7)$$

By substituting (7) into (2), the closed-form expression of the Green's function is obtained, that is,

$$G_i(r,z) = \sum_{m=1}^{M} \frac{\alpha_{i,m}}{\sqrt{(z+\beta_m)^2 + r^2}} \square \{ \frac{X_{\lim}}{\sqrt{z^2 + r^2}} \qquad (8)$$

The integral identical equation (9) is applied to (8) implicitly.

$$\int_0^{\infty} \mathrm{e}^{-\lambda|z|} J_0(\lambda r) \mathrm{d}\lambda = \frac{1}{\sqrt{z^2 + r^2}} \qquad (9)$$

NUMERCIAL EXAMPLES

The grounding system is 50×50 m^2 grid consisting of 25 mesh-grounding grids with uniform span. Four vertical rods are connected at the comer of the grounding system. All horizontal conductors are buried at a depth of 1 m. The soil is model as three-layered earth and its parameter are $h_1 = 5\ \mathrm{m}$, $\rho_1 = 1000\Omega \cdot \mathrm{m}$, $h_2 = 50\ \mathrm{m}$, $\rho_2 = 100\Omega \cdot \mathrm{m}$ and $\rho_3 = 1000\Omega \cdot \mathrm{m}$ respectively. The grounding resistance and the maximal touching voltages with 10 kA injecting current are calculated with the different length of vertical rods as shown in Tab. I & II. Moreover, the results and errors are also listed in Tab. I & II calculated by CDEGS [3] for the comparison purpose.

Tab.I Grounding resistance calculated by this paper and CDEGS

Length of the vertical rod (m)	Grounding resistance (Ω)		
	This paper	CDEGS	Error (%)
0	3.58	3.50	-2.29
5	3.15	3.09	-1.94
10	2.44	2.39	-2.09
50	1.19	1.15	-3.48
100	1.07	1.02	-4.90

Tab.II Maximal touching voltage calculated by this paper and CDEGS

Length of the vertical rod (m)	maximal touching voltage /V		
	This paper	CDEGS	Error (%)
0	16937.0	16539.0	-2.35
5	13513.2	13247.1	-1.97
10	9174.6	8971.8	-2.21
50	2514.2	2425.2	-3.54
100	2001.6	1902.5	-4.95

CONCLUSION

A straightforward and fast approach is presented to evaluate Green's function in the horizontal layered soils. The contributions of this paper lay the following aspects. First, the sampling value of Green's function is calculated in an iterative way without using the analytical expression. Second, a closed-form expression of Green's function is obtained by utilizing the vector matrix pencil method. The numerical results show good agreements indicating that the approach developed could be practically applied to grounding designs.

REFERENCES

[1] Sunde E.D. *Earth conduction Effects in transmission systems*, D. Van Nostrand Company, New York, 1949.

[2] Sarkar T K, Park S, Koh J and Rao S M. "Application of the matrix pencil method for estimating the SEM (Singularity Expansion Method) poles of source-free responses from multiple look directions", *IEEE Trans. on AP*, vol. 48, pp.612-618, April, 2000.

[3] Dawalibi F□ Donoso F., "Integrated analysis software for gounding, EMF and EMI", *IEEE computer application in power*, vol. 6, pp.19-24, June, 1993.

Measurement values used to compare the results of analytical and numerical methods (TLM) used to design the impulsive grounding system of a High Voltage Laboratory

Dias, Guilherme
PUCRS
gaddias@ee.pucrs.br

Marcos Telló
PUCRS
tello@ee.pucrs.br

José Nemetz
TRAFO
nemetz@trafo.com.br

Silveira, J. L.
CEFETSC
jony@cefetsc.edu.br

Ferreira, G. S.
CEFETSC
golberi@cefetsc.edu.br

Rizer, A.
UFSC
raizer@eel.ufsc.br

Flavio Neuls
TRAFO
neuls@trafo.com.br

***Abstract* – Grounding system of the high voltage impulse laboratory was designed using analytical method [1]. The performance of the related grounding system was evaluated using a numerical method, named the TLM (Transmission Line Model) [2].**

INTRODUCTION

Fig. 1 shows a view of high voltage impulsive laboratory installed in the TRAFO Electrical Equipments Inc.. Indeed, the impulsive grounding system of this laboratory was designed by analytical method. Considering that the used analytical method presents limitations [1] a numerical method (TLM) was applied to determine the behavior of grounding system when a surge impulse is applied in it. So, the grounding system measurements were done to compare the both methodologies.

Fig. 1. View of the High Voltage Laboratory

To better understand the electrical phenomena involved in a high-voltage laboratory, we must take in count about the fast voltage and current variation due to the chop of this quantities. In consequence, transient currents will appear in the grounding system and connections which can cause potential differences in the same magnitude order of the applied test voltages. The grounding system must be correctly design to assure the personal safety of the people that operates the laboratory measuring system.

Fundamentally, in high voltage laboratory, the total ground floor must be covered by the current return grounding system, which can of one of the three kinds: expanded metallic plate, solid metallic plates and metallic sheets. Due to cost questions, we use expanded plates instead of metallic plates.

DESIGN PARAMETERS

As design parameters, we used soil resistivity measurements and its two layer stratification, soil cover, and grounding systems materials.

- Soil type red clay
- Upper layer soil resistivity $\rho_1 = 230\ \Omega m$
- Thickness of upper layer soil resistivity $h_1 = 2{,}19$ m
- Second layer soil resistivity $\rho_2 = 41\ \Omega m$
- Cover material protruded concrete
- Concrete apparent resistivity $\rho_a = 90\ \Omega m$
- Return plane material :cooper expanded plate
- Ground mat material steel with 4 mm diameter

RETURN PLANE DESIGN

We evaluate the performance of the expanded plate as discharge return plane, comparing its performance with the performance of a solid plate. Its convenient explain that we intend to define the performance of the expanded plate as near as possible of that of a solid plate, in the most economic way. This evaluation was done considering the impedance value between two points in the return plane, as shown in Fig.2.

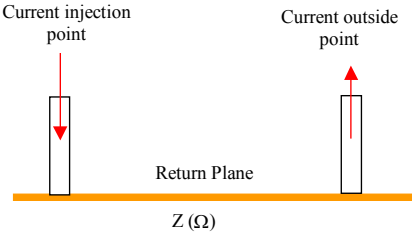

Fig. 2. Evaluation of return plane.

So, the calculated values were (see Fig. 3):

$\delta \cong 0{,}2 \times 10^{-4}$ m

δ Surge penetration depth in copper

$t = 2 \times 10^{-3}$ m

t Plate thickness ($t > 3\ \delta$)

We considered a copper expanded plate with the dimensions shown in the following Fig. 3.

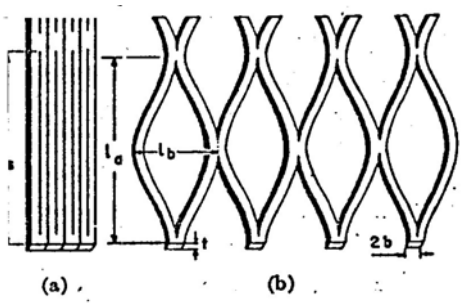

Fig. 3. Cooper expand plate: (a) original plate and (b) expanded plate

x ≅ 10
x Plate expansion factor (x < 15)
Zg = 0,005 + j 2,79 Ω
Zg Expanded plate impedance, referred to 1 m
Zp = 8,76 x 10^{-6} + j 0,02 Ω
Zp Solid plate impedance, referred to 1 m

$$\frac{U_g}{U_p} \cong 114 \qquad \frac{U_g}{U_p} < 500$$

Ug Voltage drop in 1m of expanded plate (V)
Up Voltage drop in 1m of solid plate (V)

GROUND MAT EVALUATION

We use a square ground mat of 10 x 10 m, with meshes of 0,20 m (20 cm) and steel conductor with cross section of 20 mm^2. The front of wave time of 0,10 0,10 μs was used, resulting in:

- Surge Impedance (high frequency) 7,27 Ω
- Resistance (low frequency) 4,08 Ω

SITE MEASUREMENTS

We prepare a grounding system test. To execute that evaluation, the proceed as follows:

- Put in short-circuit the low voltage part of Capacitive Potential Divider, keeping the measuring cable in the usual measuring position.
- Adjust the Osciloscope and the Impulse Peek Voltmeter, in the position of maximum sensitivity.
- Produce some impulses in the maximum charge voltage and record all the oscilograms.

TLM METHOD

TLM method has been successfully used to analyze problems related to electromagnetic compatibility (EMC). The Symmetrical Condensed Node (SCN), shown in Fig. 4, is used to model the entire volume.

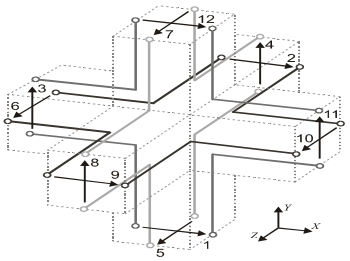

Fig. 4. The Symmetrical Condensed Node.

Each port of SCN is associated with two voltages and all the magnetic and electric variables are calculated from these voltages:

$$E_x = -\frac{2\cdot\left(V_1^i + V_2^i + V_9^i + V_{12}^i + \hat{Y}\cdot V_{13}^i\right)}{\Delta\ell\cdot(4+\hat{Y})} \quad (1)$$

$$H_x = \frac{2\cdot\left(V_4^i + V_7^i - V_8^i - V_5^i - V_{16}^i\right)}{Z_0\cdot\Delta\ell\cdot(4+\hat{Z})} \quad (2)$$

Where, E_x is the electric field component in the x-direction; H_x is the magnetic field component in the x-direction; $\Delta\ell$ is the length of the node; V_n^i is the incident voltage on port "*n*" and $\hat{Z}$ is the characteristic impedance of the background material, which is the air in this case. The calculation of the remaining field components follows the same trend. The stub voltages (V_{13} a V_{18}) allow the modeling of different characteristics, as electrical permitivity and magnetic permeability of the impulsive grounding system.

CONCLUSIONS

During the installation of TRAFO Electrical Equipments Inc. Hihg Voltage Laboratory, we expected an adequate performance of grounding system, due to the expanded plated have presented a similar theoretical behavior in the presence of surges as the one presented by a solid plate. Therefore, the impedances referred to remote earth, present reduced values, what tends to control earth potential rise, during tests. Up to now many equipment were tested in the TRAFO´s Laboratory indicating that the conceived grounding system "works".

REFERENCES

[1]. Silveira, J. L., Ferreira, G. S., Raizer, A., Telló, M. and Dias G. A. D. Transmission Line Modelling Applied In A Grounding System Installed Simultaneously In Soil And Water, EMC EUROPE 2002 - September 9-13, 2002 - Sorrento, Italy

[2] Devgan, S. S.; Whitehead, E. R., "Analytical Models for Distributed Grounding Systems", Paper T 73 182-3, recommended and approved by the Transmission and Distribution Commetee of the IEEE Power Engennering Society for apresentation at the IEEE PES Winter Meeting, New York, N.Y., January 28-February 2, 1973.

[3] Cavallius, N. R. H.; Giao, T. N.; "Floor Net Used as Ground Return in High-Voltage Test Areas", IEEE Trans. on PAS, Vol. PAS-88, No 7, July 1969, p. 996-1005.

ELF Magnetic Shielding by Global Formulation of Electromagnetic Field

A. Canova, G. Gruosso, M. Repetto
Politecnico di Torino, Dipartimento di Ingegneria Elettrica Industriale
Corso Duca Abruzzi 24, I-10129 Torino, Italy
e-mail: canova@polel1.polito.it, gruosso@polel1.polito.it, repetto@polel1.polito.it

***Abstract*— This paper presents the application of Global Formulation of Electromagnetic Field to the study of ELF magnetic shielding with conductive and ferromagnetic sheets. The shield, whose thickness is largely smaller than its other dimensions, is discretized by a system of surface dual grids. Maxwell laws are applied in the finite form and integral relations are used to apply proper boundary conditions. With this approach only the shield region must be discretized and far field boundary conditions are implicitly enforced. An outline of the formulation is presented and some results on test cases are discussed.**

INTRODUCTION

The problem of magnetic field shielding in the industrial or ELF frequency range has gained attention in the last few years both for electromagnetic compatibility reasons and for awareness to public exposure.

The study of this problem has some peculiarities which require a special formulation: presence of thin ferromagnetic or conductive regions, need for an accurate estimation of far field. Both these issues are not dealt properly by commercial Finite Element analysis codes. Several special formulations have been devised for this purpose, see for instance [1], [2]. In this paper two approaches for the analysis of thin ferromagnetic and conductive shields based on the Global Formulation of Electromagnetic Field (GFEF) proposed by Tonti [3] coupled to integral conditions are presented.

DOMAIN OF THE PROBLEM AND DISCRETIZATION

The domain of the problem under study is made up of three regions: source conductors region where current density is imposed by an external circuit; active region composed by ferromagnetic or conductive thin foils; air region surrounding the two previous domains. In most of engineering problems the shielding system is made of Aluminium whose relative permeability is equal to one or by ferromagnetic sheets whose thickness makes the eddy current effect usually negligible. In the following two cases will be discussed: ferromagnetic non conductive shields or amagnetic conductive ones. The presence of two kinds of shielding at the same time can be treated by crossing the magnetic effects but here, for sake of simplicity, has not been considered.

The thickness of the active region is at least two orders of magnitude smaller than its other dimensions thus a surface discretization is performed considering the thickness of the sheet as a material property.

The surface of the shield is discretized by a primal mesh made of quadrilateral cells. Due to the thickness of the shield each quadrilateral surface is actually a volume and its sides are the lateral faces of this volume. Starting by this primal mesh, a dual one is built keeping a strict duality relation between entities of the two grids: in the center of each cell a dual node is set and dual edges linking two dual nodes are built. Once dual meshes have been built each couple primal face-dual edge can be seen as a component with associated a flux flowing through it and a "voltage" across its terminals. Following this approach, each dual node can be seen as the node of a circuit and a tree can be defined along dual edges (Fig. 1). The only exception regards external primal faces, these faces have no dual edge crossing them so they will have to be treated differently from internal ones. Considering a mesh made of N_F primal faces $N_F^{(i)}$ of them are internal while the remaining $N_F^{(e)}$ are external.

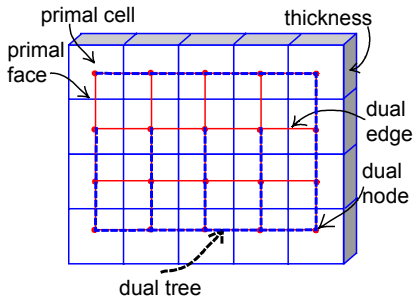

Fig. 1 System of dual meshes defined on the shield surface

SHIELDING PROBLEM FORMULATION

A. Ferromagnetic case

The ferromagnetic shield problem is formulated in terms of the magnetic flux ϕ on primal faces of the surface mesh. The magnetization of the material is considered to be parallel to the surface of the shield. This hypothesis is usually considered in the case of thin ferromagnetic sheets, see for instance [4]. The number of unknowns is equal to N_F. An equal number of constraints is obtained by imposing the following constraints:

- magnetic Gauss law on all cells except 1 (N_V-1 equations);
- Ampere law on all Fundamental loops defined by co-tree branches along dual edges ($N_F^{(i)} - N_v + 1$ equations);
- integral collocation equation on all external faces, in this case the flux is obtained by magnetization of the cells and source conductors one ($N_F^{(e)}$ equations).

This number of equations is thus equal to the number of unknowns and their independence is guaranteed by the well known network theorems.

Once the solution has been computed magnetic field is computed, in the post-processing phase, by means of integral formulas by the magnetization of the ferromagnetic sheet.

B. *Conductive case*

Conductive shield problem is formulated in terms of the current flowing along shield surface. Again, as in the ferromagnetic case it is considered that the current is flowing only parallel to the sheet surface. The problem is in this case naturally bounded by a null current flow on the external faces of the mesh. The $N_F^{(i)}$ current unknowns are set by an equal number of constraints:

- charge conservation of all but one cells (N_f-*1* equations);
- electromagnetic induction law on all fundamental loops on dual co-tree braches ($N_F^{(i)} - N_v + 1$ equations).

The electro-motive force involved in the second kind of equations is computed by means of the time derivative of the magnetic vector potential obtained by currents through Biot-Savart formula. The time variation of the variables can be handled by means of a time-marching scheme or by a time-harmonic formulation. More details about the method can be found in [5].

APPLICATION CASES

The two procedures have been validated versus a well established 2D hybrid FEM-BEM procedure using sufficiently long shields. A plane shield 1 m width and 6 m long placed over a two wire conductor systems carrying a unit current. The shield is placed at 0.25 m from the conductors and the field is compared along a line orthogonal to conductors axis at 0.25 m from the shield. Both procedures have shown good agreement with 2D codes even if discrepancies can be found locally and can be attributed to the discretization of the FEM mesh. Fig. 2a contains the data for the ferromagnetic shield considered a sheet 5 mm thick with a relative permeability of 1000 while Fig. 2b the ones for an Aluminum one with an electric conductivity of 35 MS/m.

A comparison between the two shielding techniques has then been performed along a line orthogonal to the shield surface. Results are presented in Fig. 3 where unshielded and shielded magnetic field values are reported. As it can be seen, ferromagnetic shield is quite effective in a region near to the shield while its efficacy is practically null far from it where magnetic field is almost equal to the unshielded one. On the contrary, the efficiency of the conductive shielding, relying on a source cancellation effect, is kept even at large distance from the shield.

More details on the formulations and on test cases will be presented at the Conference.

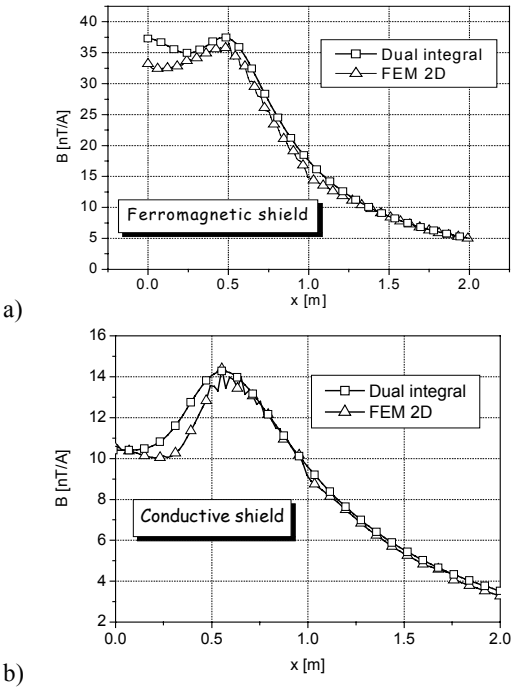

Fig. 2 Comparison between the proposed technique and 2D FEM-BEM code: a) ferromagnetic case, b) conductive case.

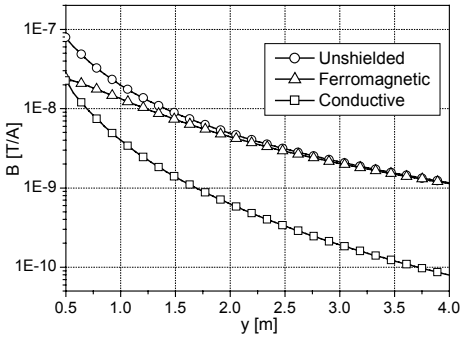

Fig. 3 Comparison between ferromagnetic and conductive shielding along a line orthogonal to the shield.

REFERENCES

[1] H. Igarashi, A. Kost, T. Honma, "A three dimensional analysis of magnetic fields around a thin magnetic conductive layer using vector potential", *IEEE Trans. On Magnetics*, vol. 34, No. 5 Part: 1 , Sept. 1998, pp. 2539 -2542

[2] O. Bottauscio, M. Chiampi, D. Chiarabaglio, M. Repetto, "A numerical approach to the design of conducting shields for ELF magnetic field reduction", *ETEP European Transaction on Electrical Power*, Vol.12, pp 111-116, 2002.

[3] E. Tonti, "Finite Formulation of Electromagnetic Field", IEEE Trans. Mag. Vol. 38, No. 2, March 2002, pp. 333-336.

[4] O. Chadebec, J.L. Coulomb, V. Leconte, J.P. Bongiraud, "Modeling of static magnetic anomaly created by iron plates", *IEEE Trans. On Magnetics*, vol. 36, Oct. 2000, pp. 677-671.

[5] A. Canova, GB. Gruosso, M. Repetto, "Quasi static integral formulation using duality and network equations", Proc. of Fourth-International-.-CEM-2002, 8-11 April 2002 Bournemouth, UK.

Analysis of the shielding effectiveness of a rectangular enclosure with apertures by TLM-TD

Jony L. Silveira
Gerência Educacional de Eletrônica
Centro Federal de Educação Tecnológica de SC
Av. Mauro Ramos, 950
88.020-300 Florianópolis – SC – Brazil
jony@cefetsc.edu.br

Lionel Pichon
Laboratoire de Génie Electrique de Paris
UMR 8507, CNRS, SUPELEC
Universités de Paris XI and Paris VI
91.192 Gif-sur-Yvette Cedex – França.
pichon@lgep.supelec.fr

Adroaldo Raizer
Departamento de Engenharia Elétrica
Universidade Federal de Santa Catarina
Caixa Postal 476
88.040-900 Florianópolis – SC – Brasil
raizer@eel.ufsc.br

***Abstract* – This paper presents a three-dimensional analysis of the shielding proprieties of a rectangular enclosure with multiple apertures. The numerical simulation uses a symmetric condensed node of TLM-TD (Transmission-line Modeling Method - Time Domain) and subsequent Fourier Transform. We obtain the shielding effectiveness response to an electric field impulsive excitation. A study of the influence of the number of aperture and aperture area is presented. The results obtained are compared with FE-TD (Finite Element - Time Domain) simulations and measurements results presented in other references.**

INTRODUCTION

The new rules in Europe as well as in other communities, regarding the electromagnetic immunity and electromagnetic interferences of the electronic devices, increase the importance of a careful design of shielding enclosures.

Apertures, slots, cable penetration, unused connector ports and others breaks in the shield can influence significantly the effectiveness of shielding enclosures. Thus, electromagnetic wave penetration into a cavity that presents apertures has been of considerable interest due to its relation with many practical problems involving EMC analysis.

The ability of the Finite-Difference Time-Domain (FD-TD) technique was investigated for the modeling of slots in shielding enclosures, recently, by Ma et al (1) and Li et al (2). A comparison between FD-TD and Method of Moments (MoM) in the study of the shielding effectiveness of a metallic enclosure was reported by Olyslager (3). Finally, a study of an enclosure with apertures using a Finite Element Time Domain (FE-TD) with a mass lumping technique was presented by Benhassine (4).

In this present contribution, a TLM-TD is applied to study the shielding effectiveness in a large frequency band. EMI coupling mechanism (slots resonances and cavity-mode resonances) and multiple apertures interactions are investigated in a rectangular enclosure.

SHIELDED ENCLOSURE

The studied unloaded 400×200×500mm rectangular cavity is shown in Fig. 1 and described in Park (5). All the walls of the cavity are made of 2 mm conducting sheet. The frontal panel is considered as an infinite conducting plane with different patterns of rectangular apertures depending on the desired comparison. Thus, for the validation of the TLM code, a single centered slot is used. In a second step, a set of different frontal panel configurations (Fig. 2) is used to evaluate the influence of the number of apertures in the shielding effectiveness. In this case, the total area of the aperture array remains constant and the distance between apertures is equal to the half of the side (a). Finally, in a last case, the number of apertures was kept constant and the total area was varied.

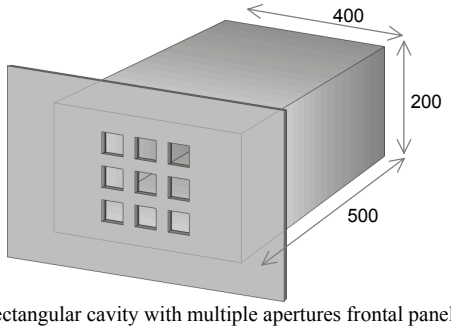

Fig. 1. Rectangular cavity with multiple apertures frontal panel

The shielding effectiveness (*SE*) of a barrier or a shield is defined in terms of the ratio of the observed field without shield ($\vec{E}$), to the observed field in the presence of the shield ($\vec{E}_s$). Thus, the shielding effectiveness can be expressed, in decibels, as:

$$SE_{dB} = 20 \cdot \log_{10} \left| \frac{\vec{E}}{\vec{E}_s} \right| \qquad (1)$$

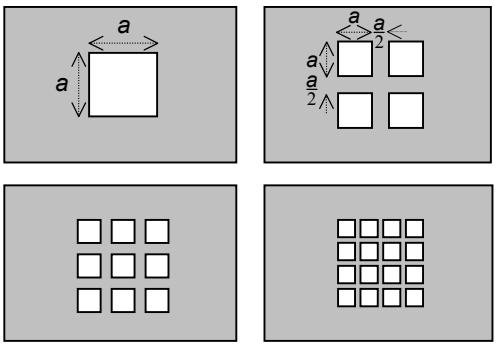

Fig. 2. Frontal panel with different number of apertures

SIMULATION RESULTS

The space is discretized by a regular grid with a node spacing of 5 mm. The walls of the cavity were considered as infinitesimally thin metallic walls.

In order to validate our simulations, Fig. 3 shows the *SE* in the central point of the cavity for a single slot (100×20mm) horizontally placed. The results are compared with those obtained by Park (5) and Robinson (6) and show a very good agreement, mainly below 0.5GHz. Above this frequency, the numerical results come close to measurements obtained in (6).

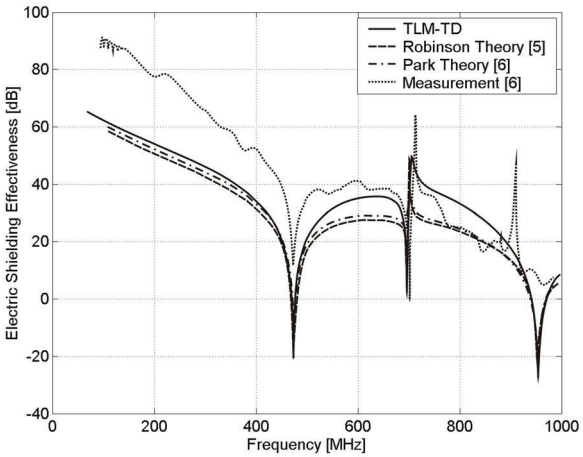

Fig. 3. Measurements and simulations results for the shielding effectiveness at the center of cavity with a single slot (100×20 mm)

Fig. 4 shows the computed spectrum below 2GHz, for a vertical and for an horizontal polarization. It can be observed that some resonance frequencies appear in the simulation results but do not correspond to any analytical cavity-mode resonances. These frequencies are of two types: the cavity-slot mode resonances, as also evidenced in (2), and the slot half-wavelength resonance.

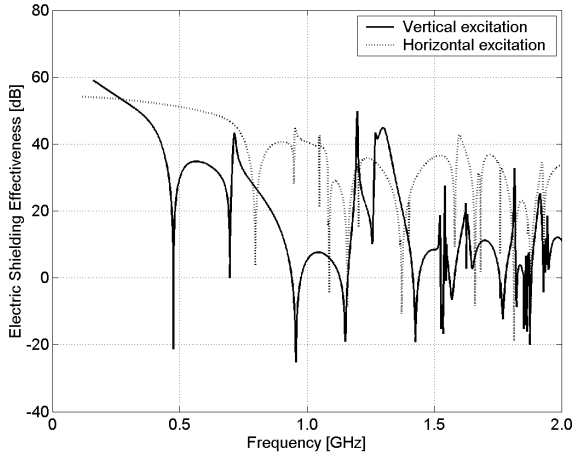

Fig. 4. SE at the center of cavity with a single centered slot

To illustrate the influence of the apertures topology in the *SE*, different simulations were achieved. Fig. 5 shows *SE* of the cavity versus frequency for the configurations of the front panel shown on Fig. 2. It clearly appears that *SE* is increased by increasing the number of apertures. This occurs because, despite the increase in the number of apertures, the total area of the aperture array is kept constant and consequently the area of each aperture is proportionally diminished.

We can also observe the appearance of a new resonance frequency, due to coupling between modes of the multiple apertures, as also evidenced in (3).

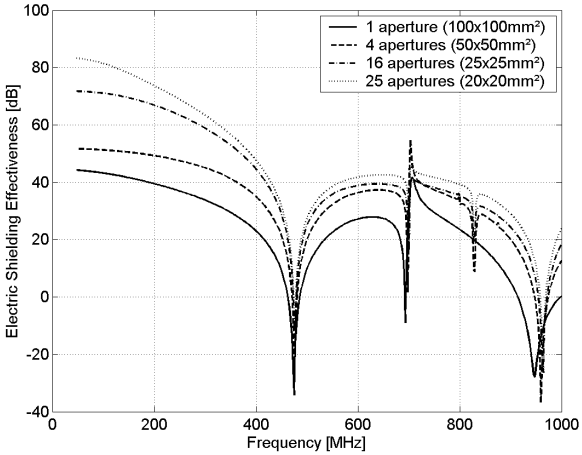

Fig. 5. SE at the center of cavity for various aperture numbers when the total area is kept constant

In a second series of computations, the number of apertures was kept constant and the total area of the apertures array was varied.

The problem of a cavity loaded with a computer motherboard (PCB) it was analyzed, considering a more complex and realist configuration of slots and apertures. Finally, a completely set of comparisons with the FE-TD results was obtained. These results will be presented at the conference.

REFERENCES

[1] K. P. Ma, M. Li, J. L. Drewniak, T. H. Hubing, and T. P. Van Doren, 1997, "Comparison of FDTD algorithms for subcellular modeling of slots in shielding enclosures", *IEEE Trans. on Electromagnetic Compatibility*, vol. 39, pp. 147-155, May 1997.

[2] M. Li, J. Nuebel, J. L. Drewniak, R. E. DuBroff, T. H. Hubing and T. P. Van Doren, "EMI from cavity modes of shielding enclosures – FDTD modeling and measurements," *IEEE Trans. Electromagnetic Compatibility*, vol. 42, pp. 29-38, Feb. 2000.

[3] F. Olyslager, E. Laermans, D. De Zuter, S. Criel, R. De Smedt, and A. De Clercq, "Numerical and experimental study of the shielding effectiveness of a metallic enclosure", *IEEE Trans. Electromagnetic Compatibility*, vol. 41, pp. 202-212, Aug. 1999.

[4] W. P. Carpes Jr., L. Pichon and A. Razek, "Efficient analysis of resonant cavities by finite element method in the time domain," *IEE Proc. Microwaves, Antennas and Propagation*, vol. 147, pp. 53-57, Feb. 2000.

[5] H. H. Park, and H. J. Eom, "Electromagnetic penetration into a rectangular cavity with multiple rectangular apertures in a conducting plane," *IEEE Trans. Electromagnetic Compatibility*, vol. 42, pp. 303-307, Aug. 2000.

[6] M. P. Robinson, T. M. Benson, C. Christopoulos, J. F. Dawson, M. D. Ganley, A. C. Marvin, S. J. Porter and D. W. P. Thomas, "Analytical formulation for the shielding effectiveness of enclosures with apertures," *IEEE Trans. Electromagnetic Compatibility*, vol. 40, pp. 240-248, Aug. 1998.

Transient Electromagnetic Field of Grounding Systems Considering Soil Ionization

J.L. He, J. Zou, Y.Q. Gao, J. Guo
Dept. of Electrical Engineering, Tsinghua University, Beijing 100084, China
hejl@mail.tsinghua.edu.cn

***Abstract*—A numerical calculation method is proposed to calculate the transient characteristic of grounding grids under lightning current, which takes into consideration the dynamic and nonlinear effect of soil ionization and the mutual-resistance and mutual-capacitance between conductors. The ionization phenomena in the soil are simulated by means of time-variable parameters under appropriate conditions. The influences of soil ionization and location of feed point on the transient characteristic of grounding grids are discussed. The generated electromagnetic fields in substation are analyzed by using electrical dipole theory and image theory. The influence of soil ionization on the electromagnetic fields is presented.**

INTRODUCTION

The lightning impulse performance of grounding systems plays an important role in the safe and reliable operation of power system. The lightning protection effects of substations or transmission lines are related to the transient characteristics of grounding systems.

There have been many papers on the performance of grounding systems [1,2]. However, the dynamic and non-linear ionization phenomenon is often omitted because this complicated phenomenon is too difficult to be modeled. Better electrical models are required to improve the studies of reliability and performance of grounding grids subjected to ionization of the surrounding soil.

A novel model is proposed to analyze transient characteristic of a grounding system, in which a combination of circuit theory and electromagnetic theory is utilized. The ionization phenomena in the soil are simulated by means of lumped time-variable parameters under appropriate conditions. The mutual-impedance between conductors is also considered. The generated electromagnetic fields in substation are also analyzed by using electrical dipole theory and image theory, when the lightning current flows into the grounding system.

EQUIVALENT CIRCUIT MODEL OF A GROUNDING SYSTEM

Model of non-linear soil ionization

When the electric field strength surrounding the grounding conductor exceeds the critical value of the electrical field strength (E_c), soil breakdown around the conductor will occur. It will convert the affected portion of the soil from an insulator to a conductor. The radius of the area of soil ionization surrounding the grounding electrode can be considered to be the equivalent radius of the electrode.

The actual shape of the ionized zone of the soil around a grounding conductor is not columniform but pyramidal. The paper proposes the model shown in Fig.1, in which the conductor is represented by a set of cylindrical zones. In Fig.1 r_i is the equivalent radius for the *i*-th segment, which is time-variable, and *a* is the radius of the metal conductor.

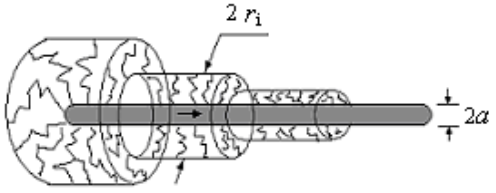

Fig.1 Modeling of equivalent radii for each segment

A grounding conductor can be considered as a distributed network (see Fig.2), which is composed of inductance, capacitance, conductance and resistance.

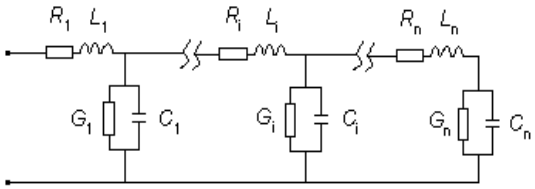

Fig. 2 Representation of a ground electrode with variable parameters

The unit length resistance, inductance, capacitance, and conductance of a grounding conductor are given in [3,4,5].

In order to simulate the ionization effects, the equivalent radius of the conductor is considered time-variable under appropriate conditions. The parameters of the conductor tied to the diameter of the conductor are also time-variable.

The equivalent radius can be obtained by

$$J_i = \frac{E_c}{\rho} = \frac{\Delta i_i}{2\pi r_i \Delta l} \tag{1}$$

Where, J_i is the current density leaked by the *i*-th segment; Δi_i is the current leaked into earth from the *i*-th segment; Δl is the length of the *i*-th segment. E_c is the critical electrical field.

In the model, a grounding grid is divided into elementary units represented by π-networks according to the non-linear trapezoidal algorithm.

Model of mutual-impedance

Assume that a square grounding grid is injected by lightning current from one corner. When the current flows along the conductor, it also leaks into the earth. The conductors are divided into a number of segments as described above. But here the grid is divided into only 4 segments for simplification.

Here we assume that the leakage currents are all from the midpoint of each segment. So we must add a node in the middle of each segment (Fig.3 a). The leakage current will give birth to potential on the surface of conductors, which can be considered there are mutual-impedances between conductors (Fig.3 b).

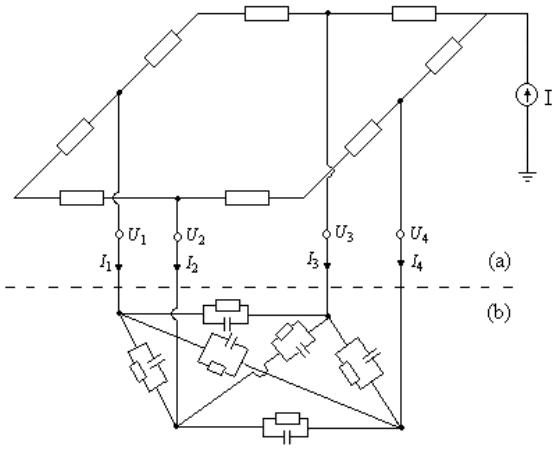

Fig.3 the equivalent circuit model of the grid

For the four leakage points in Fig.3b, we can get

$$I(\omega) = Y(\omega)U(\omega) \tag{2}$$

According to convolution theorem,

$$i(t) = Y(t) * U(t) \tag{3}$$

we can obtain the relation among 4 ports in time domain.

In (3) $\boldsymbol{Y}$ is the mutual-admittance matrix, which is the inverse matrix of the mutual-impedance matrix $\boldsymbol{R}$. The element of $\boldsymbol{R}$ is the average potential on one segment when a unit current leaks out of other one.

The mutual-impedance R_{ij} between two segments i and j can be determined by using (4).

$$R_{ij} = \frac{1}{4\pi(\sigma + j\omega\varepsilon_0\varepsilon_r)} \cdot \frac{1}{l_i l_j} \cdot \left[\iint_{l_i l_j} \frac{1}{d_{ij}} dl_i dl_j + \frac{\sigma_E + j\omega\varepsilon_0(\varepsilon_E - 1)}{\sigma_E + j\omega\varepsilon_0(\varepsilon_E + 1)} \iint_{l_i' l_j} \frac{1}{D_{i'j}} dl_i' dl_j \right] \tag{4}$$

The computations are made by using this mathematical model above. The impulse response of a grounding system can be obtained with the application of nodal analysis and a iterative algorithm, which takes into account the nonlinear soil ionization and the mutual-impedance between conductors.

TRANSIENT ELECTROMAGNETIC FIELDS

The grounding conductors are divided into segments, which are short enough to be considered to be Hertzian dipoles. The total radiated electromagnetic field is the sum of all the contributions from each constituent dipole.

When soil ionization is taken into consideration, the transient electromagnetic fields generated by lightning current will be different with those without considering soil ionization. Fig.4 illustrates the computation model.

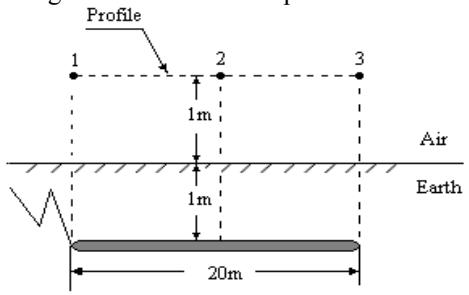

Fig.4 Model adopted for computations

When a lightning current mentioned above is injected in a grounding electrode with 20 meters length, which is buried at 1-meter depth under the earth, severe transient electric field will occur in air. From comparing the magnitudes of electromagnetic field at points 1, 2, and 3, we can get an idea of the influence of soil ionization on transient electromagnetic fields.

Fig.5 shows the magnitudes of electric field with and without soil ionization for point 1, 2, and 3 in Fig.4.

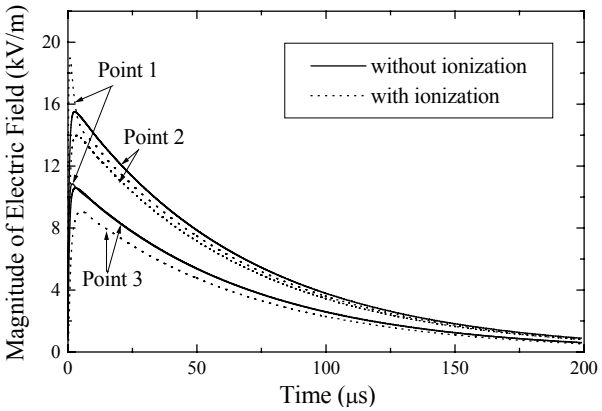

Fig.5 Magnitude of electric field at different points

From the curves in Fig.5, when soil ionization is taken into consideration, the electric fields in air near the position of feed point become severer. On the other hand, the electric fields in air far away the feed point become smaller. Similarly, it can be concluded that the magnetic fields in 3 points all become smaller.

CONCLUSIONS

A new model is proposed to calculate the transient fields of a grounding system under lightning current. The ionization phenomena around the ground conductors in the soil are simulated by means of time-variable parameters under appropriate conditions. The mutual-impedance between conductors is taken into consideration by appending an impedance network.

REFERENCES

[1] Oettle E E, "A new estimation curve for predicting the impulse impedance of concentrated earth electrodes, " *IEEE Trans. Power Delivery*, Vol.3, No.4, pp. 2020-2029, 1988.

[2] Leonid D G, Markus Heimbach, "Frequency dependent and transient characteristics of substation grounding systems," *IEEE Trans. Power Delivery*, Vol.12, No.1, pp. 172-178, 1997.

[3] Xiong W, Dawalibi F, "Transient performance of substation grounding systems subjected to lightning and similar surge currents," *IEEE Trans. Power Delivery,* Vol.9, No.3, pp.1412-1417, 1994.

[4] E. D. Sunde, "Surge characteristics of a buried bare wire," *AIEE transactions*, Vol. 59, pp. 987-991, 1940.

[5] A. Geri, "Behaviour of grounding systems excited by high impulse currents: the model and its validation," *IEEE Trans. Power Delivery*, Vol. 14, No, 3, July 1999.

.

Electromagnetic Field Sensor Based On Short Period Fiber Bragg Gratings

M. MAHMOUD
School of Engineering, Sheffield Hallam University
Pond Street, Sheffield S1 1WB, UNITED KINGDOM
E-mail: M.Mahmoud@shu.ac.uk

Abstract: - In the power production and distribution industry; there is a growing and continuous demand for increasing reliability and safety of electric current measurements, especially in high voltage application. Also the complexity of control systems used in the power transmission networks require more fixed points of measurement and a wider range of measurement situations. Magnetostriction is a property of ferromagnetic materials such as iron, nickel, and cobalt. When placed in a magnetic field, these materials change size and/or shape. Coating a short period Fiber Bragg Gratings (FBG) sensor with a ferromagnetic material makes the sensor sensitive to electromagnetic fields. In this paper an electromagnetic field sensor based on short period FBG is introduced and its mathematical model developed.

Key-Words: - Electromagnetic Field Sensor, Current sensor, Fiber Optic Sensors, Fiber Bragg Gratings, Sensor Arrays.

1 Introduction

Fiber optic sensor technology has been in a rapid development and displacing traditional sensors for many application such as rotation, acceleration, electric and magnetic field measurement, temperature, pressure, vibration , linear and angular position, strain, chemical measurements and a host of other sensor applications. The main advantages of fiber optic sensors are their ability to be light weight, of very small size, passive, low power, flexibility, high temperature tolerance, high sensitivity, wide bandwidth and environmental ruggedness. The major advantage of a fiber bragg gratings sensor is that the measurand information is wavelength-encoded (an absolute quantity), thereby making the sensor self-referencing and independent of fluctuating light levels and the system immune to source power and connector losses that plague many other type of optical sensors [1,2,3,4]. Fiber Bragg gratings are made by laterally exposing the core of a single-mode fiber to a periodic pattern of intense ultraviolet light. The exposure produces a permanent increase in the refractive index of the fiber's core, creating a fixed index modulation according to the exposure pattern. This fixed index modulation is called a grating; at each periodic refraction change a small amount of light is reflected. All the reflected light signals combine coherently to one large reflection at a particular wavelength when the grating period is approximately half the input light's wavelength. This is referred to as the Bragg condition, and the wavelength at which this reflection occurs is called the Bragg wavelength [2, 3], only those wavelengths that satisfy the Bragg condition are affected and strongly back-reflected into the same core of the fiber. The grating spacing and index of refraction are sensitive to strain and temperature effects, thus in sensing applications the shift in the reflected wavelength is proportional to the applied temperature and strain [2, 3]. Those shifts in the reflected wavelength are detected and interpreted at the end of the fiber by a process indicator or controller. Compared to most other fiber-optic components, fiber Bragg gratings are simple to manufacture, they are commonly between one millimeter and 25 millimeters long of uniform or chirp modulation, however longer gratings or custom design gratings are fabricated too, in some applications it is possible to use multiple gratings structure [2]. Selection of the grating length or design is dependent on the desired rangeability and bandwidth. An illustration diagram of a uniform fiber grating sensor is shown in figure (1) and its reflection spectrum is show in figure (2).

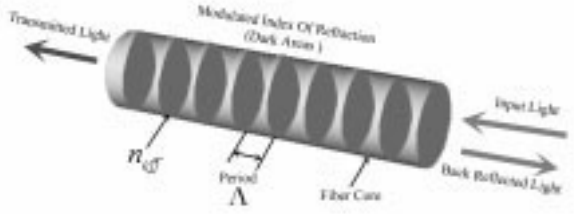

Figure (1) Uniform FBG Sensor

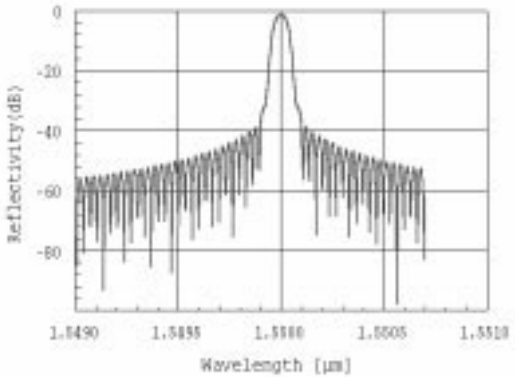

Figure (2) Reflection Spectrum of Uniform FBG Sensor

2 FBG Sensors Theory and Characteristics

For a uniform fiber Bragg gratings sensor on a single mode fiber the relationship between the Bragg wavelengths, period, and refractive index is represented as follows [2]:

$$\lambda_B = 2\Lambda N_{eff} \tag{1}$$

Where; λ_B = Bragg wavelength. It is the (reflected) free space center wavelength of the input light.

n_{eff} = Effective refractive index of the fiber core at the free space center wavelength.

Λ = The grating spacing (period).

Equation (2) represents the mathematical model of a uniform FBG temperature sensor [1].

$$\Delta\lambda_B = \lambda_{Bo}(\alpha_\Lambda + \alpha_n)\Delta T \tag{2}$$

Where; λ_{Bo} = the initial or FBG Bragg wavelength at reference temperature of T_o

$\Delta\lambda_B$ = the fractional wavelength shift in nm.

$\alpha_\Lambda = \frac{1}{\Lambda}\frac{\partial\Lambda}{\partial T} \approx 0.5x10^{-6}$ =The thermal expansion coefficient.

$\alpha_n = \frac{1}{n_{eff}}\frac{\partial n_{eff}}{\partial T} \approx 8.6x10^{-6}$ = thermo-optic coefficient for

ΔT = the temperature change in ^{O}C.

Equation (3) represents the mathematical model of FBG strain sensor.

$$\Delta\lambda_B = \lambda_{Bo}(1 - p_e)\varepsilon_z \tag{3}$$

Where; λ_{Bo} = the initial or the fabricated FBG Bragg wavelength at zero strain.

$\Delta\lambda_B$ = the fractional wavelength shift in nm.

$\varepsilon_z = \frac{\Delta L}{L}$ = longitudinal strain in $\mu\varepsilon$

p_e = effective strain-optic constant defined as

$$p_e = \frac{n_{eff}}{2}[p_{12} - \nu(p_{11} + p_{12})] \tag{4}$$

Where; p_{11}, p_{12} = the components of the strain-optic tensor (constant values).

ν = the Poison's ratio

n_{eff} = effective refractive index of the fiber core at the free space center wavelength.

Equation (3) may write as follows:

$$\Delta\lambda_B = \lambda_{Bo}(1 - p_e)\frac{\Delta L}{L} \tag{5}$$

Where; L is the length of FBG sensor and ΔL is the displacement in length due to strain.

3 The Magnetostriction property of ferromagnetic materials

Magnetostriction is a property of ferromagnetic materials such as iron, nickel, and cobalt. When placed in a magnetic field, these materials change size and/or shape. As illustrated in figure (3), a magnetising force H causes a dimensional change due to the alignment of magnetic domains. The physical response of a ferromagnetic material

Electric field shielding for reducing induced voltage under transmission lines

Mário Leite Pereira Filho
LAE - Laboratório de Avaliação Elétrica
IPT - Instituto de Pesquisas Tecnológicas
Cidade Universitária
05508-901 Sao Paulo, SP, BRAZIL
e-mail: mleite@ipt.br

Carlos A. França Sartori, Viviane Cristine Silva, José Roberto Cardoso
LMAG - Laboratório de Eletromagnetismo Aplicado
PEA - Universidade de São Paulo
Av. Prof. Luciano Gualberto - trav. 3, n. 158
05508-900 Sao Paulo, SP, BRAZIL
e-mail: sartori@pea.usp.br

Abstract: **This paper demonstrates the reduction in the voltage induced on persons working along an elevated railroad which crosses under a high-tension transmission line. The induced voltage was reduced by a shield formed by a mesh of cables. The efficiency of this shield was evaluated by means of a modified charge simulation method to take into account the 3D configuration as well as the huge dimension of the domain, and the interaction between the finite and semi-infinite segments of the model.**

INTRODUCTION

Urban structures are becoming ever increasingly closer to high voltage transmission lines, as in the case considered in this paper, which involves the crossing of an elevated section of railroad under a double-circuit, 345 kV TL, as shown in Fig. 1. Persons working along the walkway of the railroad have complained of electric discharges while on the stretch under the TL.

A shield mesh was constructed between the overhead ground wires of the railroad and the lowermost phase of the TL. Since the induced voltage was not measured prior to construction of the shield, a model was necessary to estimate the reduction of the induced voltage.

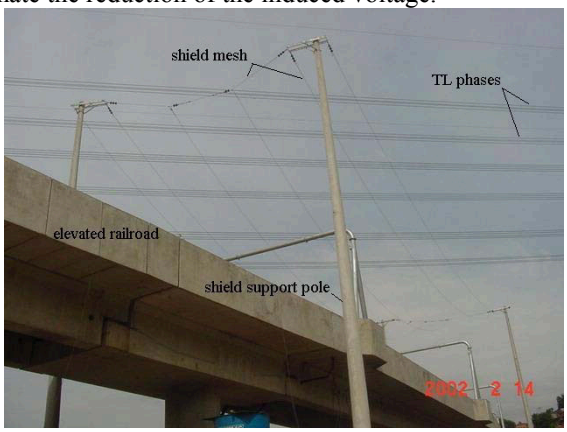

Fig. 1 View of the crossing

MODEL DESCRIPTION

The calculation of electric field on urban structures has aroused considerable interest due to environmental aspects [1] and regarding induced voltage in long objects [2]. The 3D configuration and huge dimension of the domain allowed an approach applying the Charge Simulation Model (CSM). The numerical method used in this work is based on the formulation proposed in [2], and it presents an important modification on assembling the Maxwell's matrix between the finite and semi-infinite segments of the model.

The basic principle of the CSM is that the potential ϕi at a given point, generated by a discrete set of n charges Qj can be found by:

$$\phi_i = \Sigma P_{i,j} \cdot Q_j \, , \; j = 1 \text{ to } n \qquad (1)$$

The coefficients Pi,j depend on the types of charge elements, such as line, ring etc., as described in the literature [3],[4]. In order to determine the charges Qj it is necessary to first find the value of ϕi at m points outside the space of the sources Qi and then resolve the matrix system:

$$[P] \cdot [Q] = [\phi] \qquad (2)$$

Once the charge vector Qj is known, (1) is applied to obtain the potential at any point.

In this specific case, the TL was modeled with one finite and two semi-infinite segments at the extremities, thus enabling alterations in the charge in the finite segments to reflect the presence of the railroad and shield mesh close to the TL. Fig. 2 shows an overhead view of the crossing between the railroad and the TL.

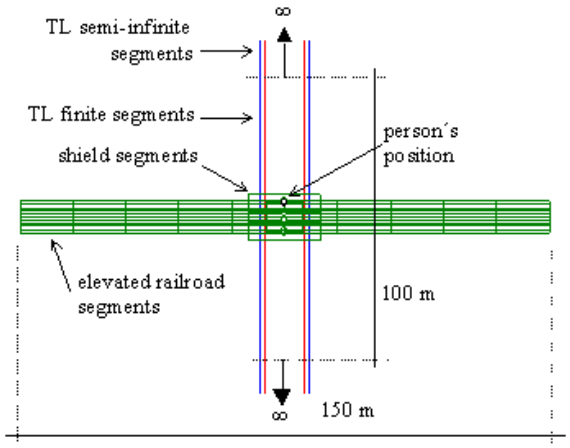

Figure 2. Overhead view of crossing

METHOD IMPLEMENTATION

The finite section of the transmission line was represented by 8 segments, subdivided into 10 parts. 79 segments represented the elevated structure, the person standing on the walkway was considered to be electrically isolated and was represented by 11 segments and eight

segments represented the shield. All the passive segments were subdivided into 10 parts.

In order to apply the CSM on [2] it was necessary to first tryout the position of boundary points Xi on the semi-infinite section, with a view to avoiding discontinuities in the value of the potential calculated for the TL phases. In the present article, imposing a null value for mutual capacitance between the finite and semi-infinite segments solved this problem, or that is, that the charges located in the finite segments could not alter the amount of charges in the semi-infinite segments, although the contrary is true. Table 1 shows the coefficients of a hypothetical case with four segments, in which the first and last are of the semi-infinite type and the remaining two are finite.

$$\begin{vmatrix} P_{11} & 0 & 0 & P_{14} \\ P_{21} & P_{22} & P_{23} & P_{24} \\ P_{31} & P_{32} & P_{33} & P_{34} \\ P_{41} & 0 & 0 & P_{44} \end{vmatrix}$$

TABLE 1 - MAXWELL'S MATRIX COEFFICIENTS

This solution meant that the Maxwell's matrix was no longer symmetrical, but eliminated the problem of discontinuity between the finite and semi-infinite segments of the TL. Complex variables were used to consider the phases of the 60 Hz, three-phase power line.

RESULTS

The voltage induced on a person standing in the walkway without the shield installed was 4530 Vrms. The capacitance between a person and earth was 220 pF. If someone came into contact with the earthed structure, while the tension was at its peak value, he would get a 6300 V electrostatic discharge. If this person was permanently earthed, the short-circuit current would be 0.38 mA. Fig. 3 shows the profile of the potentials over the elevated structure without the shield installed.

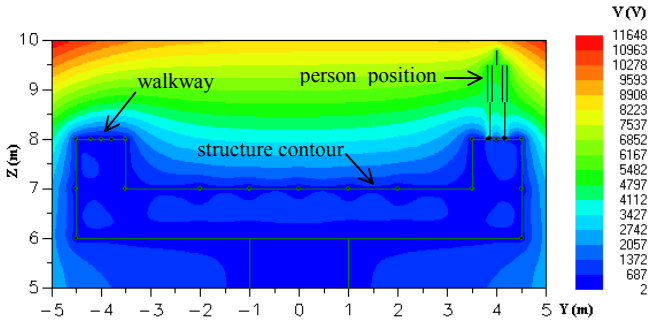

Figure 3. Profile of the potential without the shield mesh

With the shield mesh installed, the induced voltage on a person was reduced to 192 VRMS, representing a ratio of 23.6 in relation to a similar situation without the shield. This voltage value is insufficient to cause an electrostatic discharge, thereby eliminating the sensation of an electric shock among the railroad workers. Fig. 4 shows the profile of the potential on the elevated structure after installing the shield.

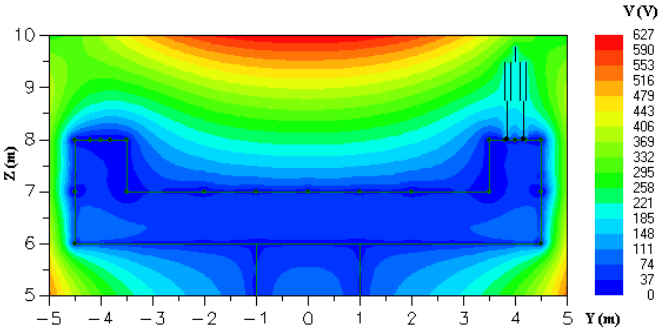

Figure 4. Profile of the potential with the shield mesh

Fig. 5 shows the values of the voltage variation along the lowermost phase conductor of the TL, 100 meters either side of the railroad. It can be seen that the greatest variation in the voltage in relation to the theoretical value was ± 0.8 % for all 10 sections.

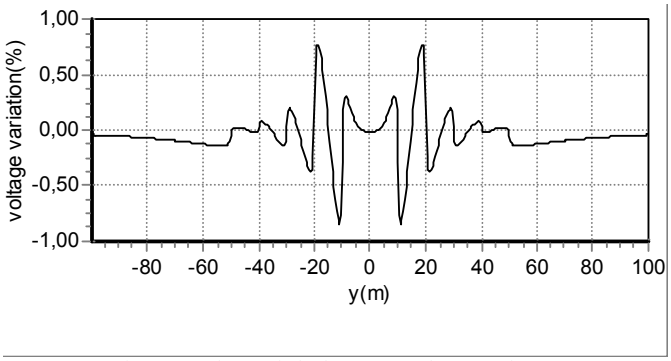

Figure 5 Voltage of the lowermost phase conductor

CONCLUSIONS

The modification to the construction of the Maxwell matrix enabled the elimination of difficulties presented in previous works [2]. Using the Charge Simulation Method it was possible to calculate the induced voltages on a person with and without the presence of a grounded shield mesh.

REFERENCES

[1] C. Saldafia, "Electric Field Calculation for Six-Phase Transmission Line", Paper presented at the 11ª COMPUMAG, November, 03-06, 1997, Rio de Janeiro - Brasil, p 171-172.

[2] M. Abdel-Salam, Al-Shehri, "Induced Voltages on Fence Wires and Pipelines by AC Power Transmission Lines", IEEE Trans. on Insdustry Applications, Vol 30, No 2, p 341-349, 1994.

[3] N. H. Malik, "A Review of the Charge Simnulation Method and its Applcations", IEEE Trans. on Electrical Insulation, Vol 24, No 1, p 3-20, 1989.

[4] H. Singer, H. Steinbigler and P. Weiss, "A Charge Simnulation Method for the Calculation of High Voltage Fields", IEEE Trans. on Power Apparatus & Systems, Vol 93, p 1660-1668, 1974.

COMPUMAG Saratoga Springs, New York USA
July 13 - 17, 2003

3D Finite Element Analysis and Experimental Validation for the Consequent Pole PM Machine

Juan A. Tapia
Dept. of Electrical Eng.
University of Concepcion
Casilla 160-C, Correo 3
Concepcion, CHILE

Franco Leonardi
Vehicle Electronic Syst. Dept.
Ford Research Labs
Dearborn MI 48120
Ph./fax 313-390-6923

Thomas A. Lipo
ECE Department
University of Wisconsin-Madison
Madison WI 53706 USA
Tel:(608) 265-0727

Abstract—
In this paper the Consequent Pole Permanent Magnet (CPPM) machine finite element analysis is presented. Due to the double excitation (PM and field winding) and inherent three-dimensional flux distribution an appropriate numerical analysis must be done so that operating conditions can be predicted. Using this analysis flux distribution, winding inductances, back-emf and other parameters of the magnetic structure are calculated. This work was carried out to obtain parameters and airgap flux control range for the CPPM machine. Experimental verification is made to verify the accuracy of the method when is applied to this type of machine configuration.

Index Terms —**Motor and Generator, Numerical analysis.**

I. Introduction

ACCURATE machine parameter calculation is required for high performance AC drives, where the operating range and control are highly interdependant [1]. For example, speed range and field weakening capabilities of the PM machine are defined by the inductances values and the back-emf [2] . Two and three-dimensional FEA allow one to calculate with adequate precision the airgap flux distribution under any operating condition.

It has been shown that the CPPM machine has attractive features for variable speed AC drives applications [3]. Due to the double excitation (PM and field winding) a wide range of airgap flux can be achieved with a modest amount of field MMF. In addition, there does not exist a demagnetization risk for the magnets because the control action is made over soft iron poles rather than over magnet as a regular PM machine. Slip rings, brushes or other mobile contact are not required to transfer energy to the field winding because it is located in the stator. However, the operation of the CPPM machine involves a three-dimensional flux distribution which increases the analysis complexity. In this paper a FEA is carried out to obtain the airgap flux control range, back-emf and *d-q axis* inductances. Maxwell 3D provides the ability to analyze volumetric structures and supplies tools to calculate local and integrals variables. In addition, experimental results are presented from a 3kW prototype built using the consequent pole configuration and field control strategy.

II. Analysis Domain

Figure 1 shows the magnetic structure of the CPPM machine. The machine consists of a rotor divided into two sections. One section has partial surface-mounted permanent magnets, which are radially magnetized, and the other has a laminated iron pole. The stator is composed of a laminated core, solid iron yoke, and a conventional AC three-phase winding allocated in slots around the periphery of the inner diameter. To complete the stator structure, a circumferential field winding is placed in the middle of the stator, which is excited by a DC current.The combination of the PM and field winding fluxes generate a demagnetizing or magnetizing effect on the machine airgap according with the magnitude and direction of the DC current.

III. FEA and Experimental Comparison

A. Flux per pole

The magnetization curve of the CPPM machine represents the relation between the AT field excitation and the flux per pole. This relation shows the airgap flux control range from the maximum subtractive effect of the field flux, (minimum airgap flux) up to a maximum additive effect (with maximum airgap flux). Figure 2 shows the flux per pole predicted by 3D-FEA and the experimental flux control capability of the prototype. It can be noted that the control provided for the DC field winding allows one the ability to control the airgap flux over a range of +/-40% with respect to zero field current conditions. Slight differences between the actual and predicted slope was found. In effect, 3D-FEA does not consider several practical manufacturing considerations which are present in the actual prototype, such as interlamination airgap and junction between stator lamination and solid core. These were not considered in order to reduce the complexity of the numerical analysis.

B. Back-emf waveform

From Faraday's law, the $back-emf$ induced in a full pitch coil is obtained from

$$e = \frac{\partial \lambda}{\partial t} \tag{1}$$

where λ is the coil flux linkage. Asumming constant speed, the induced voltage is calculated from the flux distribution at different rotor position and DC field current.

Figures 3, presents the calculated and actual $back-emf$ waveforms. In addition, fundamental harmonics component for the actual and predicted waveforms are also shown. Close

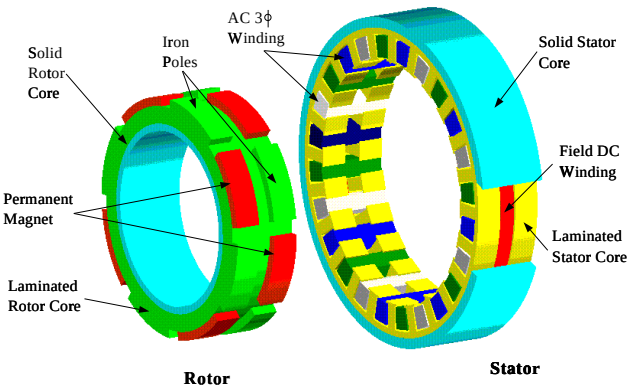

Fig. 1. Magnetic structure of the CPPM machine

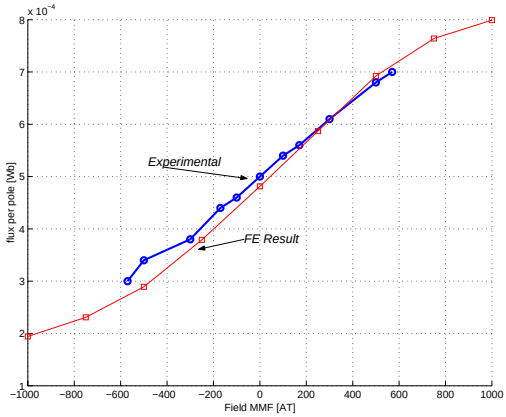

Fig. 2. Flux per pole: FEA and measured values comparison

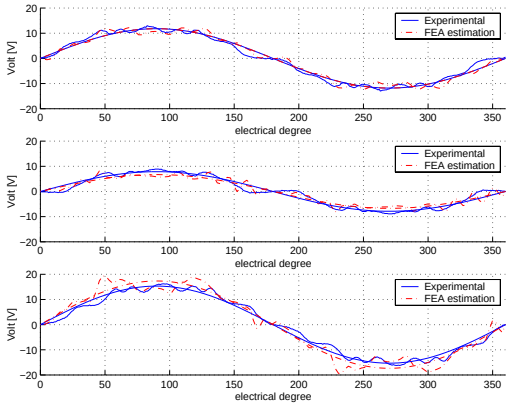

Fig. 3. Back-emf waveform (actual and predicted) as a function of field current

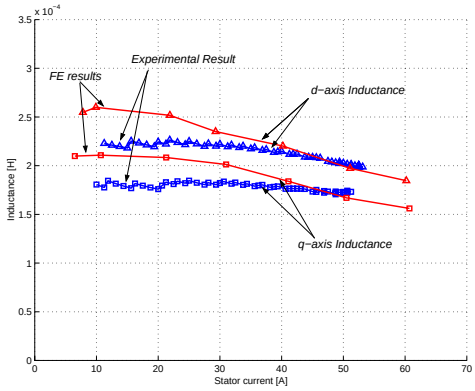

Fig. 4. Variation of $d-axis$ and $q-axis$ inductances under stator current variation.

agreement was found between experimental and 3D-FEA results. Fundamental components for no-field current match almost exactly with the actual $back-emf$. There are slight differences when field current is circulating, which is predicted from figure 2. In reality, underestimation for magnetizing and overestimation for demagnetizing effect of the field current are predicted from the flux per pole vs. field current characteristic. This disagreement is related with the FE model and the simplification utilized to reduce its complexity.

C. $dq-axis$ Inductances

In order to determine the $dq-axis$ inductances, the following equation are evaluated [4].

$$L_d = \frac{\lambda_d - \lambda_{pm}}{i_d} \quad and, \quad L_q = \frac{\lambda_q}{i_q} \tag{2}$$

Figure 4 summarize the $dq-axis$ inductance variation as the stator current changes. As predicted, the $d-axis$ inductance results higher than the $q-axis$ value. In general, PM machines present a lower L_d due to the high PM reluctance. However, for the CPPM machine, iron poles represent a very low reluctance path for the $d-axis$ flux, which results in the reverse relation between $d-axis$ and $q-axis$ inductances. Some disagreement was found for the inductance calculations. At low current, more flux is predicted than the actual values due to interlamination of the stator stack. In fact, solid stator iron has been assumed for the FEA model which presents lower reluctance. At high current, saturation makes the numerical results closer to the experimental values.

IV. Conclusions

Experimental tests demonstrate that the CPPM machine can control the airgap flux over a wide range. Over +/- 40% variations in emf with respect to the no-field current condition can be achieved using DC field current. It appears feasible to weaken the airgap flux by varying the field current in variable speed applications. Close agreement between actual and predicted back-emf waveform. The CPPM machine exhibits inverse relation between L_d and L_q, with respect to the traditional surface mounted PM machines, due to the presence of the iron poles used to create the consequent pole pattern.

References

[1] Z.Q. Zhu, G.W. Jewell, D. Howe, "Finite Element Analysis in the Design of Permanent Magnet Machines, " IEE Seminar on Current Trends in the Use of Finite Element (FE) in Electromechanical Design Analysis, 2000.

[2] R. F. Schiferl, T. A. Lipo, "Power Capability of Salient Pole Permanent Magnet Synchronous Motor in Variable Speed Drive Applications, " IEEE Transactions on Industry Applications. Vol 26, No. 1, January/February 1990, pp.115-123.

[3] J.A. Tapia, F. Leonardi, T.A. Lipo, "Consequent Pole Permanent Magnet Machine With Field Weakening Capability." IEEE International Electric Machines and Drives Conference, IEMDC 2001. Cambridge. pp 126-131.

[4] E.C. Lovelace, T.M. Jahns, J.H. Lang, "Impact of Saturation and Inverter Cost on Interior PM Synchronous Machine Drive Optimization ." IEEE T IA, Vol. 36, No. 3 May/June 2000 pp 723-729.

Instantaneous Torque Analysis of Spoke type BLDC Motor Considered Freewheeling Mode of Six-Switch Drives

Jin Hur[1] , Gyu-Hong Kang[2]
[1]Mechatronics Research Center, Korea Electronics Technology Institute, 451-865, Korea
[2]Dept. of Electrical Engineering, Changwon National University, Changwon, Kyungnam, 641-773, Korea
E-mail: jinhur@keti.re.kr, ipmsm@korea.com

***Abstract*— This paper represents the instantaneous torque performance of spoke type Brushless DC (BLDC) motor. In spoke type BLDC motor, the circuit parameters, self and mutual inductance vary with rotor potion that is spatial function. Its effect leads to instantaneous current and torque ripple. Therefore, analysis of spoke type BLDC motor should be considered to current dynamic performances. The instantaneous characteristics are analyzed coupled magnetic field analysis with voltage circuit equation of the conduction and freewheeling mode by controlling the excitation method..**

INTRODUCTION

PM excited motors such as IPM and SPM have gained increasingly interest in recent days due to the use of hard magnetic materials. A spoke type BLDC motor is of to have a rotor structure of interior type PM with higher saliency ratios as shown in Fig 1, which is to be concentrated the magnetic flux generated by PM. So, it is lead to increase the higher reluctance torque as well as torque ripple. However, the reluctance torque is induced torque ripple and vibration of machine but it could be contributed on the effective torque by control of current phase in inverter fed system. Therefore, the PM arrangement and driving control circuit have to be considered in the design stage of spoke type motor.

In this paper a new dynamic analysis method is developed for the force performance of spoke type BLDC motor and used as an efficient tool for design optimization. So the optimal current phase for the spoke type BLDC motor is proposed for maximization of generating torque per unit current. The method is coupled Finite Element Method (FEM) with and driving circuit considering controlled current phase angle in voltage source inverter to consider accurately the distributed characteristics. In the modeling of the inverter fed spoke type BLDC system, the current is analyzed by separated conduction considering freewheeling period. During this freewheeling period, the voltage equation should be modified.

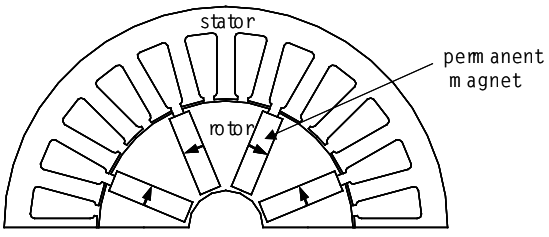

Fig. 1. Geometry of spoke type BLDC motor.

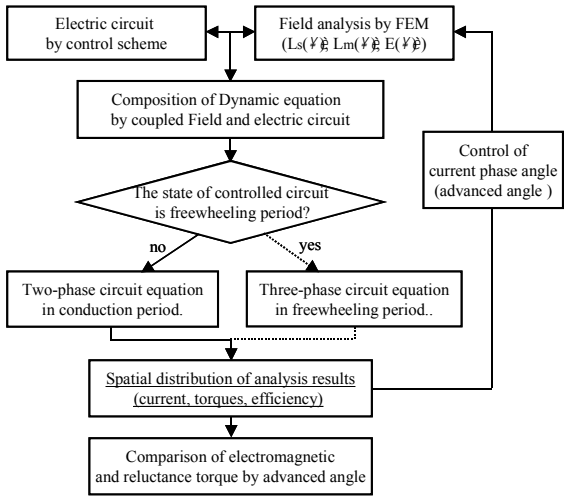

Fig. 2. Dynamic analysis process by coupled field and electric circuit.

METHOD OF ANALYSIS

The instantaneous torque analysis of the spoke type BLDC motor that has the rotor model as illustrated in Fig1is performed by developed method. In this work, the reluctance torque strongly influences the torque characteristics. Also, the driving circuit considering conduction and freewheeling period must be considered to exactly analyzed the characteristics. For the analysis, the back EMF, self and mutual inductances are calculated using FEM with a rotor moving line technique, and then there are applied to electric circuit analysis for the instantaneous current and torque controlled by current phase with advanced angle. Fig. 2 shows analysis process and Fig. 3 shows the current flow in conduction and freewheeling period at six-switched converter. In conduction period, two phases out of three phases are energized as shown by the solid line in Fig. 3.

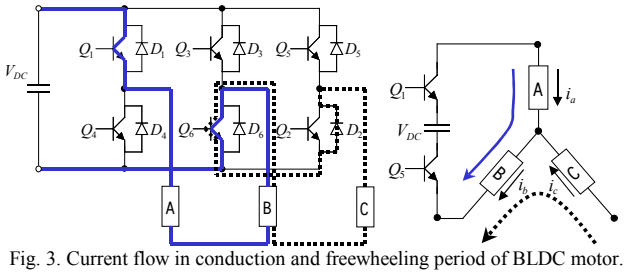

Fig. 3. Current flow in conduction and freewheeling period of BLDC motor.

The voltage equation for instantaneous current in conduction period is given by

$$V_a - V_b = R(i_a - i_b) + d/dt\,(L_a(\theta) - M(\theta))i_a + e_a - d/dt\,(L_b(\theta) - M(\theta))i_b + e_b \quad (1)$$

$$di_a / dt = (V_a - V_b - e_a - e_b - 2Ri_a)/(L_a(\theta) + L_b(\theta) - 2M(\theta))$$

However, when the phase commutates from C to B, A-B phases are conducted immediately after switching off the A-C phases and C phase current is freewheeling through diode D_2. The current freewheeling in commutation period is generated by inductance of the motor. So, the voltage equation should be reconstructed to three phases considering freewheeling current as follows:

$$\frac{d}{dt}\begin{bmatrix} i_a \\ i_b \end{bmatrix} = -\begin{bmatrix} 1 & 0 \\ 0 & 1 \end{bmatrix}\begin{bmatrix} R/(L_a(\theta) - M(\theta) \\ R/(L_b(\theta) - M(\theta) \end{bmatrix}\begin{bmatrix} i_a \\ i_b \end{bmatrix} + \begin{bmatrix} 1/3 & 0 \\ 0 & 1/3 \end{bmatrix}\begin{bmatrix} R/(L_a(\theta) - M(\theta) \\ R/(L_b(\theta) - M(\theta) \end{bmatrix}\begin{bmatrix} 2V_{ac} - V_{bc} - 2e_a + e_b + e_c \\ 2V_{bc} - V_{ac} + e_a - 2e_b + e_c \end{bmatrix} \quad (2)$$

RESULTS AND DISCUSSION

The self and mutual inductance of spoke type BLDC motor, which are varied by rotor position due to interior type PM in rotor, is described in Fig.4. Their effects lead to reluctance torque and increasing of current and torque ripple. The phase current and back EMF in steady state are shown in Fig. 5 with commutation phase voltage. The spatial distribution of back EMF and inductances make effect on phase current waveform then instantaneous torques distribution as shown in Fig. 6. The commutation torque ripple is generated by current ripple and the effect of reluctance torque is hardly. However, the phase current and torques distribution by advanced angle at 30 degree are shown in Fig. 7 and Fig. 8. The phase current is increased by advanced angle and it lead to increase of electromagnetic torque. Moreover, the reluctance torque has effect on effective torque in advanced angle. To accurate analysis and optimal design in spoke type BLDC motor, therefore, the characteristics by current waveform and controlled current phase angle should be analyzed and considered spatial distribution of back EMF and inductances for instantaneous current analysis. In the final paper, these points plus further results comparing the measured value and a detail of the new method will be given.

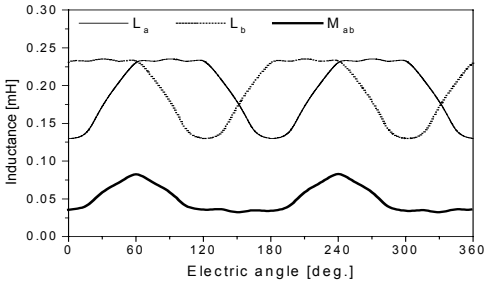

Fig. 4. Variation of self and mutual inductance by rotor position

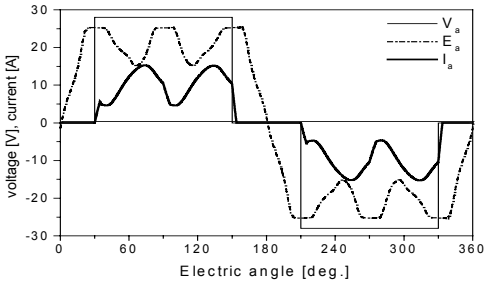

Fig. 5. Phase current and back EMF waveform on advanced angle 0^0.

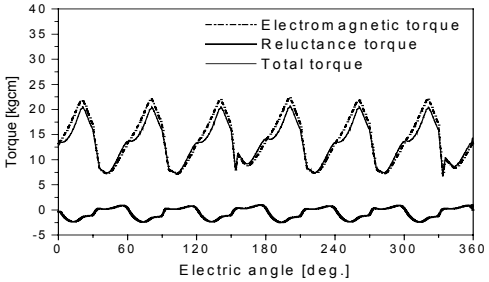

Fig. 6. . Commutation torques distribution on advanced angle 0^0.

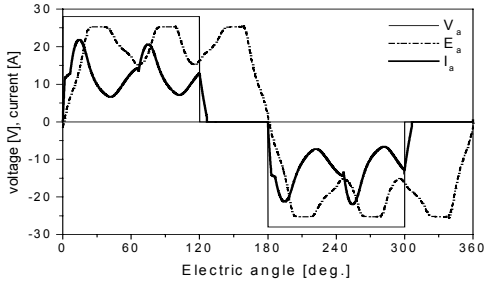

Fig. 7. Phase current and back EMF waveform on advanced angle 30^0

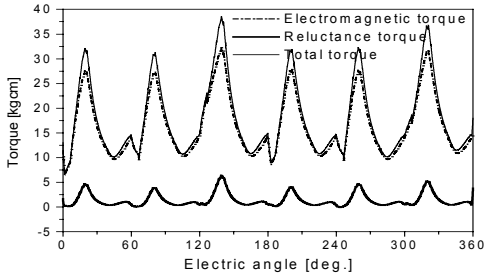

Fig.8. Commutation torques distribution on advanced angle 30^0

REFERENCES

[1] G. H. Jang, J. H. Chang, D. P. Hong and K. S. Kim "Finite-Element Analysis of an Electromechanical Field of a BLDC Motor Considering Speed Control and Mechanical Flexibility", IEEE Trans. on Mag., vol. 38. No. 2, pp. 945~948, Mar. 2002

[2] Motoya Ito, Kaoru Kawabata, Fumio Tajima and Naganori Motoi "Coupled Magnetic Field Analysis with Circuit and Kinematics Modeling of Brushless Motors" IEEE Trans. on Mag., vol. 33. No. 2, pp. 1702~1705, Mar 1997

Comparison of Irreversible Demagnetization Characteristics by Rotor Structure in Permanent Magnet type Brushless DC Motors

Gyu-Hong Kang[1], Jin Hur[2], Jung-Pyo Hong[1]
[1]Dept. of Electrical Engineering, Changwon National University, Changwon, Kyungnam, 641-773, Korea
[2]Mechatronics Research Center, Korea Electronics Technology Institute, 451-865, Korea
e-mail : ipmsm@korea.com, jinhur@keti.re.kr, jphong@sarim.changwon.ac.kr

***Abstract*— This paper deals with irreversible demagnetization characteristic of permanent magnet (PM) Brushless DC (BLDC) motor by rotor structure. The instantaneous currents in either starting or lock rotor condition are calculated from the current dynamic analysis by coupled electric and magnetic field with Finite Element Method (FEM). The currents are applied to the analysis of irreversible demagnetization field by FEM. In irreversible demagnetization analysis by FEM, the variation of residual flux density in PM is analyzed by nonlinear simultaneous with magnetic core on B-H plan.**

INTRODUCTION

In PM type BLDC motor, the instantaneous current at starting or locked rotor condition can cause the tremendous demagnetizing field in PMs. In the case of PM material, it is occurring the irreversible demagnetization due to the external demagnetizing field and this causes the residual flux density of PM is reduced and the performance of PM type BLDC motor is deteriorated. Therefore, the irreversible demagnetizing characteristics of PM must be considered for designing the rotor structure of BLDC motor.

This paper presents the analysis method to irreversible demagnetization phenomena of PM type BLDC motor by using FEM [1]. In irreversible demagnetization phenomena analysis, proposed FE analysis method is considered non-linearity of magnetic core simultaneous with B-H characteristics of PM in nonlinear analysis. When the irreversible demagnetization is occurred in partial of PM, the nonlinear analysis by FEM is iterated from the renewal residual flux density of such element. Their effects lead to changing of Electromotive Force (EMF) in BLDC motor [2].

The parameters due to irreversible demagnetizing effects are instantaneous current for external demagnetizing field, dimension of PM and structure of magnetic circuit. In this paper, the instantaneous current in either starting or lock rotor condition is calculated by coupled FE analysis and controlled electric circuit. Moreover, the irreversible demagnetizing effects are analyzed by several type rotor structures that are Surface mounted PM (SPM), Interior type PM (IPM) and spoke type PM rotor. The results of the proposed analysis are presented to compare EMF distribution by rotor structure.

METHOD OF ANALYSIS

The instantaneous peak current in starting or transient state is calculated from current dynamics analyses and the calculated instantaneous current is applied to irreversible demagnetizing FE analysis for external magnetic field computation. Fig. 1 shows the demagnetization curve of the ferrite type permanent magnet on B-H plane. When operating point p_1 moves to p_2 due to the external demagnetizing field, the residual flux density, B_r, is decreased to B_r', and the irreversible demagnetization is occurred [2].

Fig. 2 presents the process of irreversible demagnetization analysis of BLDC motor. As the magnetic flux density in each element of the permanent magnet region is less than the knee point by the external demagnetizing field, the residual flux density of the element renews in analysis process.

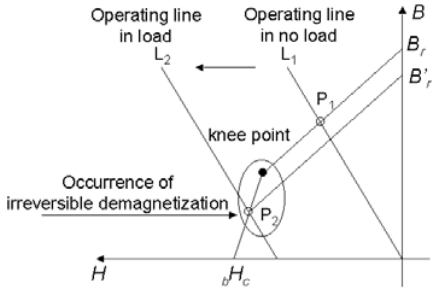

Fig. 1. Demagnetization curve of the ferrite type PM on B-H plane.

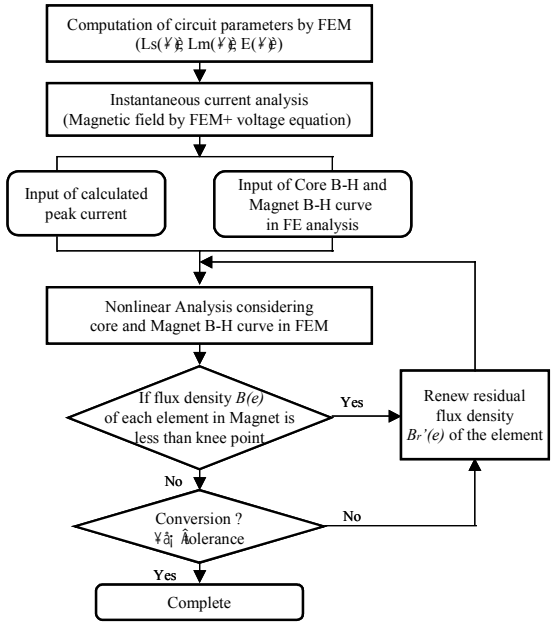

Fig. 2. Irreversible demagnetization analysis process of PM type BLDC motor

RESULTS AND DISCUSSION

From the irreversible demagnetization analysis, the results of residual flux density variation in PM are compared to several type rotor structures. Fig. 3 shows the variation of residual flux density comparison of each rotor structure in PM by (-) d-axis instantaneous peak current. In case of spoke type rotor, PM is demagnetized entirely by external field on the other hand the SPM type rotor occurred partial irreversible demagnetization. Moreover, IPM type rotor is hardly demagnetized so the regional irreversible demagnetization rate according to rotor structure is different.

Fig. 4 shows the back EMF distribution between initial condition that the PMs are fully magnetized and demagnetized condition that is induced external field on (-)d axis. The airgap flux of spoke type BLDC motor is concentrated so the back EMF is largest in three type rotor on the other hand it has weak external demagnetizing effect. The IPM type BLDC motor have robust demagnetizing field but back EMF is less then the other type rotor. Therefore, the design of PM type BLDC motor should be considered to airgap flux density and irreversible demagnetization effect by rotor structure.

REFERENCES

[1] S. J. Salon, *Finite Element Analysis of Electrical Machines*. Rensselaer Polytechnic Institute, Troy, New York. : Kluwer Academic, 1995.

[2] Gyu-Hong Kang, Jin Hur *et al.,* "Analysis of irreversible magnet demagnetization in line-start motors based on finite element method," in Proc. 10th CEFC 2002, pp. 132.

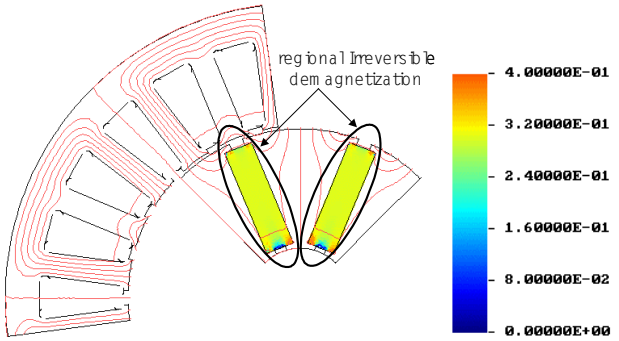

(a) spoke type BLDC motor

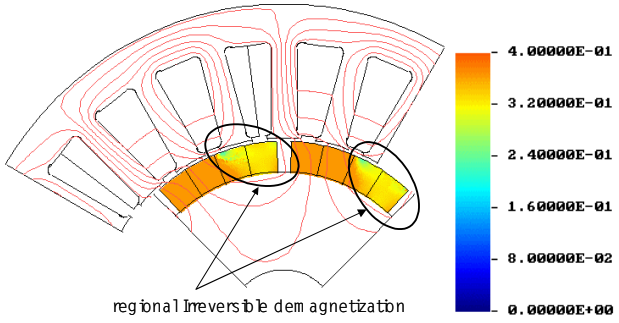

(b) SPM type BLDC motor

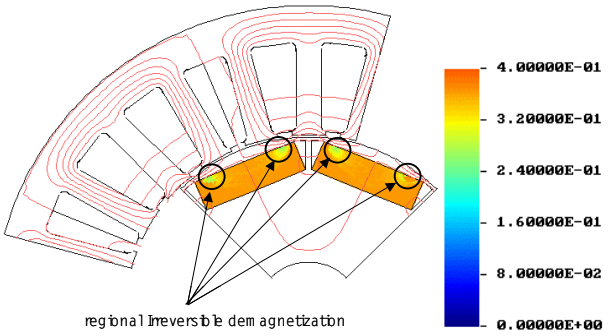

(c) IPM type BLDC motor

Fig 3. Comparison of residual flux density by external demagnetizing field.

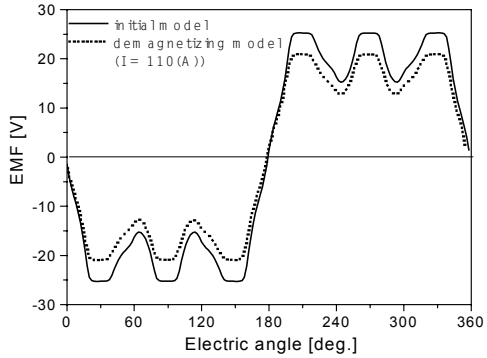

(a) spoke type BLDC motor

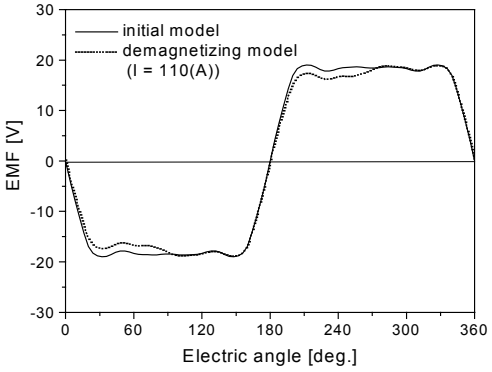

(b) SPM type BLDC motor

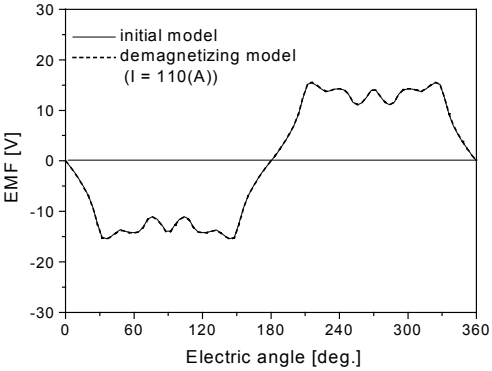

(c) IPM type BLDC motor

Fig4. Back EMF characteristics of initial versus demagnetizing model.

Design and Analysis of a Novel Inset Permanent Magnet Synchronous Motor for Industry Applications

C. C. Hwang, *Member*, *IEEE*, S. P. Cheng, X. Y. Chien and M. Y. Shiu
Department of Electrical Engineering
Feng Chia University, Taichung, Taiwan, R.O.C.
Email: cchwang@fcu.edu.tw

G. Chang
Energy Saving Tech. Corp.,
Taichung, Taiwan, R.O.C.

***Abstract*- This paper aims to introduce a permanent magnet synchronous motor with the magnets laid flush in slots let into the rotor surface, called inset-magnet rotor. The rotor configuration gives a rugged construction that is less dependent on banding for magnet retention. This design also produces a certain amount of reluctance torque which improves the constant-power speed range. Certain design for the salient iron interpoles is introduced to reduce the armature reaction. Experimental results obtained are in good agreement with the finite element analysis.**

I. INTRODUCTION

Permanent magnet (PM) synchronous motors have been widely used in industrial applications as variable speed servo drives for several years. They are often required to have a performance characteristic which exhibits constant torque to a base speed and constant power to an elevated speed. To extend the constant power speed range of these PM motor drives, flux-weakening control has been developed in recent years [1]. But this is difficult to achieve with the rectangular-fed PM brushless dc motors with surface-mounted rotor magnets since the *d*- and *q*- axes have essentially identical reactances. However, since the salient iron interpoles cause the *q*-axis reactance to be higher than the *d*-axis reactance with inset rotor configuration, and hence the power capability can be extended [2].

In this paper the design and construction of an inset magnet motor is described. A particular slot shape for magnet retention is designed to protect the magnets against centrifugal forces and to increase mechanical strength of the rotor [3]. To reduce the armature reaction, certain design for the salient iron interpoles is introduced [4,5]. Experimental results obtained are in good agreement with the finite element analysis.

II. MOTOR DESIGN

The cross section of the motor is shown in Fig. 1(a). It has twelve coils on the stator. The coils have concentrated windings. This construction allows a shorter end turn and a small coupling between phases. Also a flat-top type of flux distribution can be produced.

The eight rotor poles are made of Nd-Fe-B magnets and are magnetized radially. Since the torque ripple is strongly affected by the air gap flux density waveform. To have a minimize torque ripple, an empirical formula is used to guarantee that a required waveform is produced. The air gap flux density due to the magnet (B_m) is used [6,7].

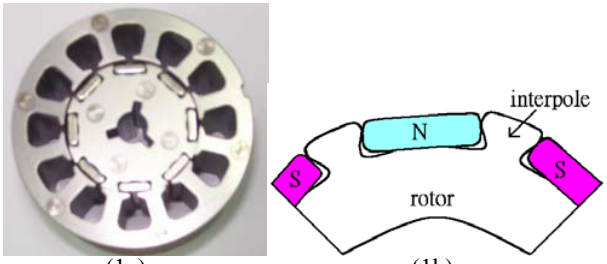

(1a) (1b)

Fig. 1. Cross section of the motor.

$$B_m = B_0\left[1 - e^{-\frac{2\theta}{\pi\gamma}} - e^{-\frac{2(\pi-\theta)}{\pi\gamma}} + e^{\frac{-2\theta}{\gamma}}\right], \quad B_0 = \frac{B_{\max}}{1 - 2e^{-\frac{1}{\gamma}} + e^{\frac{-2}{\gamma}}} \qquad (1)$$

where B_{max} is the peak value of the flux density, θ varies from 0 to π and parameter γ is used to adjust the waveform. The lower the value of γ the closer the flux density waveform approaches a square wave.

To reduce the effect of armature reaction, an eccentric surface on the salient iron interpoles is designed as shown in Fig.1(b). The technical data of the motor is given in Table I.

III. FINITE ELEMENT ANALYSIS

The finite element (FE) method is used to calculate the performance of the motor. The magnetic field is determined in terms of the magnetic vector potential A, which is governed by the well known equation [8]

$$\nabla \times (\nu \nabla \times A) = J_s + J_m \qquad (2)$$

where ν is the reluctivity, J_s is the source current density, and J_m is the equivalent current density corresponding to the coercive force of the magnet.

Table I MOTOR DATA

Rated power	500 W	Number of coils	12
Rated voltage	48 V	Turns per coil	16
Rated speed	2400 rpm	Resistance per phase	0.15Ω
Rated current	14.75 A	**Rotor**	
No. of phases	3	Outer diameter	42 mm
Stator		Inner diameter	5 mm
Outer diameter	78 mm	No. of poles	8
Inner diameter	42.6 mm	Magnet width	2.8 mm
Stack length	60 mm	Magnet height	10.1 mm
No. of slots	12	Magnet remanence	1.25 T

The midgap radial flux density waveforms can be calculated from the FE solution by plotting the radial flux density component, B_g of the elements in the air gap region of the motor versus the angular position of the centroids of these elements.

The induced EMF in a conductor with the axial effective length ℓ and the linear velocity υ with respective to magnet poles can be expressed as

$$e_n(\theta) = \ell \upsilon B_g(\theta) \quad (3)$$

The virtual work for computing torque is derived from the magnetic coenergy w' changes against space displacement. It is seen that the total torque in direction p is found by computing the change of the stored magnetic coenergy, when the component is displaced in this direction under the constant flux linkage λ, hence the torque is expressed as [8]

$$T = -\left.\frac{\partial w'}{\partial p}\right|_{\lambda=cons\tan t} \quad (4)$$

IV. RESULT AND VERIFICATION

An evaluation of the induced EMF waveform can provide the information on the torque generated by the motor. Fig. 2(a) shows the air gap flux density and (2b) shows the induced EMF waveform for the motor. Without the effect of slotting, the air gap flux density waveform in Fig. (2b) approaches a square wave with γ = 0.057 which is almost same as the number obtained for the data from FE analysis [9].

The theoretical current waveform is determined for an input of 48V at 2400 rpm. Fig. 3 compares the FE result with the experimental result with good agreement between them.

The steady state characteristic of torque versus rotor position changes with phase current as shown in Fig. 4. The corresponding positive and negative degree positions represent the rotor rotating clockwise and anticlockwise, respectively.

V. CONCLUSIONS

A novel inset PM synchronous motor has been developed. The particular form of the rotor makes magnets be easily assembled. The eccentric surface designed on the salient iron interpoles on the rotor can reduce the effect of armature reaction. The proposed motor is analyzed with FE method. Analysis results of the steady state and transient state performance are supported by experimentation.

REFERENCES

[1] Z. Q. Zhu, Y. S. Chen and D. Howe, "Maximising the Flux-weakening Capability of Permanent Magnet Brushless AC Machines and Drives," *PIEMC* 2000, Vol. 2, pp. 552-557, 2000.

[2] Z. Q. Zhu, D. Howe and Z. P. Xia, "Predication of Open-circuit Airgap Field Distribution in Brushless Machines Having an Inset Permanent Magnet Rotor Topology," *IEEE Trans. Magnetics,* Vol. 30, No. 1, pp. 98-107, January 1994.

[3] Energy Saving Tech. Corp., Deutschen Patent 202 02 161.0, April 2002.

[4] J. Gan, K.T. Chau, C.C. Chan and J.Z. Jiang, " A New Surface-Inset, Permanent-Magnet, Brushless DC Motor drive for Electric Vehicles," *IEEE Trans. Magnetics,* Vol. 36, No. 5, pp. 38103818, September 2000.

[5] R. Vyas, S. Muphy and T. Sebastian, "Evaluation of Brushless Permanent-Magnet Motor Rotor Configurations for Square Wave Current Excitation," *Proceeding of the 1996 International Conference on Power Electronics, Derives and Energy Systems for Industrial Growth*, Vol.2, pp. 895-899, 1996.

[6] Y. Murai, Y. Kawase, K. Ohashi, K. Nagatake and K. Okuyama, "Torque Ripple Improvement for Brushless DC Miniature Motors," *IEEE Trans. Ind. Appl.*, Vol. 25, No. 3, pp. 441-450, May/June 1989.

[7] T. Sebastian and V. Gangla, "Analysis of Induced EMF waveforms and Torque Ripple in a Brushless Permanent Magnet Machines," *IEEE Trans. Ind. Appl.*, Vol. 32, No. 1, pp. 195-200, Jan./Feb. 1996.

[8] S. J. Salon, *Finite Element Analysis of Electrical Machines*, Kluwer Academic Publishers, Boston, 1995.

[9] *Flux2D User's Guide*, Version 7.4, Magsoft Corporation, Troy, New York, U.S.A., 2000.

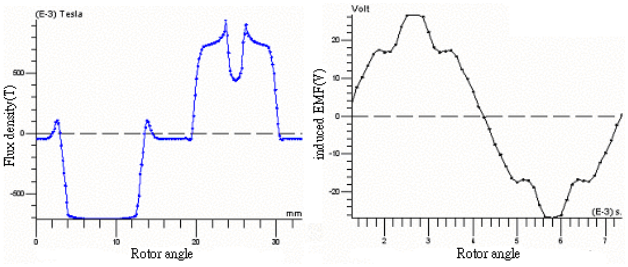

(2a) (2b) Induced EMF at 2400 rpm

Fig. 2. No-load characteristics: (2a) air gap flux density (2b) EMF

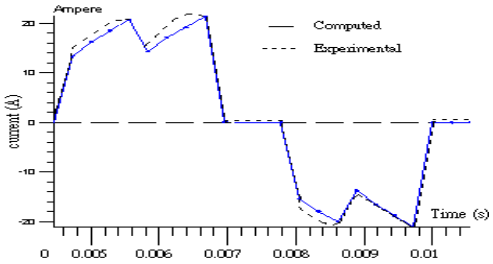

Fig. 3. Phase current waveform.

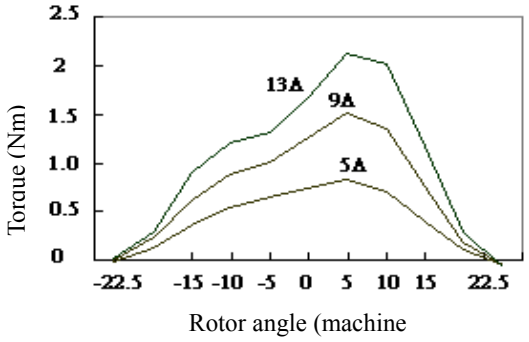

Fig. 4. Torque-angle curve

Magnetic Modeling of Synchronous Motors with Surface-Mounted Magnets

C. C. Hwang, *Member*, *IEEE,* S. P. Cheng
Department of Electrical Engineering
Feng Chia University, Taichung, Taiwan
E-mail: cchwang@fcu.edu.tw.

Song Chu Chang and His-Kuang Hsieh
Power Electronics Section, Electronics System Division
Chung-Shan Institute of Science &Technology, Taiwan

Abstract-- This paper aims to develop a magnetic circuit model for surface-mounted permanent magnet synchronous motors and to derive simple analytical expressions of the average flux densities within the air gap and the parameters, such as EMF and synchronous reactance. To verify the accuracy of the proposed model, 2D finite element analysis is conducted for the model motor. The comparison between the analytical prediction and numerical calculation shows that the present model is suitable for design purpose.

I. INTRODUCTION

There are two basic current control waveforms for high performance PM synchronous motor drives: rectangular current and sinusoidal current. Rectangular current control requires only incremental position information. Sinusoidal current control requires more refined rotor position information, and hence more expensive but results in small torque ripples. Several rotor configurations are proposed for PM synchronous motors. Of these, only surface-mounted magnet rotor motors are used, both rectangular and sinusoidal current control.

In this paper the magnetic circuit approach is used to analyze a surface-mounted magnet motor. This approach takes the flux leakage flux into account and yields the simple analytical expressions for the average flux densities within the air gap and the parameters, such as EMF and synchronous reactance. To validate the accuracy of the proposed model, 2D finite element analysis (FEA) is conducted for the model motor. The comparison between the analytical prediction and numerical calculation shows that the present model is suitability for design purpose.

II. MAGNETIC CIRCUIT MODEL

A simple representation of the main flux paths in an eight-pole motor is depicted in Fig. 1 and its equivalent magnetic circuit is shown in Fig. 2. In the figure, R_r and R_s are the reluctances of the rotor and stator back irons, respectively, $2R_g$ is the reluctance of the one-half of the air gap with compensation for slotting, $2R_{mo}$ is the reluctance of the one-half of a magnet and R_{mm} is the reluctance modeling the flux leakage.

In this analysis, the stator and rotor steel is assumed to be infinitely permeably everywhere. Hence R_r and R_s, are neglected. By flux division the air gap flux ϕ_g is related to the remanent magnet flux ϕ_r by

$$\phi_g = \frac{1}{1+\beta(1+4\lambda)}\phi_r \qquad (1)$$

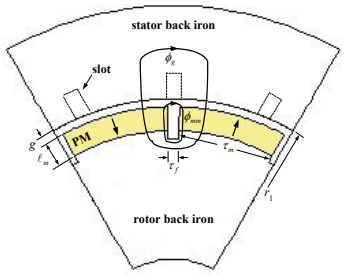

Fig. 1. Cross section of the motor.

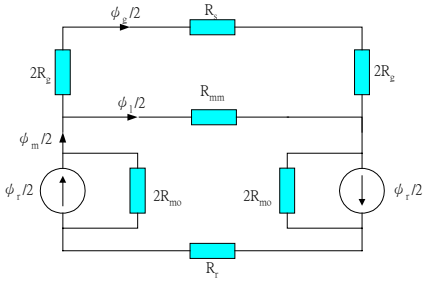

Fig. 2. A magnetic circuit model for the configuration in Fig. 1.

In this equation, $\beta = R_g / R_{mo}$ is the reluctance ratio [1-3], and $\lambda = R_{mo} / R_{mm}$ is the leakage flux ratio [4]. Eq. (1) states that the remanent magnet flux is reduced by the machine geometry given by the reluctance ratio and the leakage flux ratios. The average air gap flux density is given by

$$B_g = \frac{C_\phi}{1+\beta(1+4\lambda)} B_r \qquad (2)$$

where B_r is remeance of the magnet and A_g and A_m are the cross-sectional areas per pole of the air gap and magnet, respectively, and $C_\phi = A_m / A_g$ is the flux concentration factor [2,3]. The corresponding magnet flux density B_m in the magnet is determined as

$$B_m = \frac{1+4\beta\lambda}{1+\beta(1++4\lambda)} B_r \qquad (3)$$

The operating point of the magnet can be determined by calculating H_m from the equation describes the demagnetization characteristic:

$$B_m = \mu_{rec}\mu_o H_m + B_r \qquad (4)$$

where μ_{rec} is the recoil permeability of the magnet.

With reference to Fig. 1, the following expressions can be easily obtained 2,3],

$$R_g = \frac{k_c g}{\mu_o A_g}, \quad R_{mo} = \frac{\ell_m}{\mu_o \mu_{rec} A_m} \tag{5}$$

$$A_g = 2\pi(l_r + l_m + g/2)\ell / 2p, \quad A_m = \tau_m \ell \tag{6}$$

where μ_0 is the permeability of free space, ℓ is the stack length, ℓ_m and τ_m are the length and width of magnet, respectively, and p is the pole pair, g is the air gap length, k_c is the Carter coefficient.

Using the circular-arc straight-line permeance model, R_{mm} is approximated as[2]:

$$R_{mn} = \frac{\pi}{\mu_0 \ell} \frac{1}{\ln(1 + \pi g / \tau_f)} \tag{7}$$

and hence

$$\lambda = \frac{\ell_m \ell \ln(1 + \pi g / \tau_f)}{\mu_{rec} \pi A_m} \tag{8}$$

where τ_f is defined in Fig.1.

It is important to note that the expressions of B_g and B_m in Eqs. (2) and (3) can be inversely formulated to obtain the basic design of magnet dimension. From above equations, gives

$$\ell_m = \frac{\mu_{rec} k_c g}{(\frac{B_r}{B_g}) - 1 - \frac{\tau_f}{2\tau_m} - 4(\frac{k_c g}{\pi \tau_m}) \ln(1 + \frac{\pi g}{\tau_f})} \tag{9}$$

Multiplying l_m with τ_m gives the magnet volume per stack length (V_m).

The amplitude of the fundamental component of the air gap flux due to the magnet acting alone is

$$B_{M1} = k_1 B_g = k_1 \frac{C_\phi}{1 + \beta(1 + 4\lambda)} B_r \tag{10}$$

where

$$k_1 = \frac{4}{\pi} \sin \frac{\alpha \pi}{2} \tag{11}$$

α is the ratio of pole arc to pole pitch. Hence the amplitude of the fundamental flux per pole is

$$\Phi_{M1} = \frac{D\ell}{p} B_{M1} = \frac{4D\ell}{p\pi} \frac{C_\phi}{1 + \beta(1 + 4\lambda)} B_r \sin \frac{\alpha \pi}{2} \tag{12}$$

For a winding with N_{ph} series turns per phase and a winding factor K_{w1}, the open circuit EMF per phase is [4,5]

$$E_q = \frac{2\pi}{\sqrt{2}} K_{w1} N_{ph} \Phi_{M1} f \tag{13}$$

The synchronous reactance X_s can be written as

$$X_s = \frac{6\mu_o D \ell f}{p^2 g''} k_{w1}^2 N_{ph}^2 + X_\ell \tag{14}$$

where X_ℓ is the leakage reactance per phase and

$$g'' = k_c g + \ell_m / \mu_{rec} \tag{15}$$

III. RESULT AND MODEL VERIFICATION

To verify the model, the predictions are compared to FEA estimates for a SPM machines design. Table I shows the machine specifications that were analyzed. The stator of the motor is essentially the same as for the three-phase induction motor. Magsoft's Flux2D analysis software was conducted for the FEA results [4]. Table II shows the comparison between the predictions and the numerical calculations of B_g, B_m, E_q and X_s. They agree near perfectly for the two methods. This means that the proposed model is valid and suitable for the purpose of design.

IV. CONCLUSIONS

This paper presents a magnetic circuit model for SPM synchronous motors. The analytical expressions of the field quantities in terms of the reluctance ratio β and the leakage flux ratio λ provide the solutions in extremely short times. Each field quantity of the model can be evaluated directly from the dimensions and magnetic material properties and thus can be easily and suitably incorporated into the motor magnetic design. A prototype of SPM machine is in progress and the experimental evaluation of the prototype will be reported in the future paper.

References

[1] J. R. Hendershot Jr., T. J. E. Miller, *Design of Brushless Permanent-Magnet Motors*, Magna Physics Publishing, Hillsboro, OH, 1994.

[2] D. C. Hanselman, *Brushless Permanent-Magnet Motor Design*, McGraw-Hill, New York, 1994.

[3] C. C. Hwang and Y. H. Cho, "Effects of Leakage Flux on Magnetic Fields of IPM Synchronous Motors," *IEEE Transactions on Magnetics*, Vol. 37, No. 4, pp. 3021-3024.

[4] *Flux2D User's Guide*, Version 7.40, Magsoft Corporation, Troy, New York, 1999.

TABLE I MOTOR SPECIFICATIONS

Parameter	Symbol	Value
Stator bore radius	r_1	150 mm
Stack length	ℓ	70 .0mm
Air gap length	g	5.00 mm
Bridge width	τ_f	7.01 mm
Magnet width	τ_m	68.92 mm
Magnet length	ℓ_m	15.0 mm
Remanent flux density	B_r	1.12 T
Saturation flux density	B_s	1.684 T
Recoil permeability	μ_{rec}	1.05
Pole pairs	p	6

TABLE II COMPARISON BETWEEN PREDICTIONS AND FEA RESULTS

	Analytical results	FE results
B_g (T)	0.6698	0.6865
B_m (T)	0.7610	0.7856
E_q (V)	70.348	72.258
X_s (Ω)	1.95	2.03

Mathematical Modeling of Bonded Isotropic Magnet Magnetization for the Finite Element Design Analysis of Brushless DC Motors

Tan H. Pham, *Member, IEEE*

***Abstract*—A mathematical model and design methodology have been developed to simulate the Brushless DC motor using the finite element software analysis. The analysis is based on the characterization and measurement of magnetization patterns of bonded isotropic permanent magnets. This paper presents the derived mathematical model, the finite element simulation and the validation of the model and the methodology through correlation between the simulated results and motor performance measurements.**

***Index Terms*—Brushless DC motor, Finite Element Method, Bonded Magnet.**

I. Introduction

The isotropic bonded NdFeB magnets are increasingly used in the motor industry for servo applications primarily due to reduce cost resulting from simplified magnetization processes. With its isotropic characteristic, the bonded NdFeB magnet can be custom-magnetized [1] to meet the requirements of minimum torque ripples and vibrations for position control, speed control needs of servo applications.

Minimizing the torque ripples [2] [3] consists of minimizing the two main torque ripples components of the brushless DC (BLDC) motor:

- The reluctant torque or cogging torque that is generated by the tendency of the permanent magnet (PM) rotor to align with the slotted stator at positions where the permeance of the PM magnetic circuit is maximized.
- The electromagnetic torque ripples that originates from the interaction between the back EMF and the armature current.

In the case of a six step inverter DC driver, the electromagnetic torque ripples can be virtually eliminated if the motor back EMF is perfectly trapezoidal. In the case of a sine current driver, on the other hand, a perfectly sinusoidal back EMF is required.

For the motor engineer to achieve the above constraints during the design process, a detailed and accurate knowledge of the air gap flux density distribution of the magnets is needed, especially if the finite element analysis (FEA) is used as simulation tool to predict the designed motor performances. Generally, finite element design packages [4] either offer radial magnetization model or unidirectional model for the magnets to describe the air gap flux density distribution. However, in the case of bonded isotropic magnet, the flux density distribution is neither radial nor unidirectional but parabolic.

This paper describes a methodology to measure the air gap flux density distribution of bonded isotropic magnets, to develop its mathematical model for FEA. The methodology is validated by comparing the FEA simulation results with the motor performance measurements.

Manuscript received November 11th, 2002.

Tan H. Pham is with BEI Technologies, Kimco Magnetics Division, San Marcos, CA 92069 USA (telephone: 760-744-5671, e-mail: tpham@beikimco.com).

II. Methodology and Model

A. Proposed Methodology

The proposed methodology is subdivided in 4 main parts as follows:

- Measure the normal component of the air gap flux density (Bn) of the bonded magnet in a magnetic circuit which, has the same air gap as the designed motor air gap (as in Fig. 1). In many of the cases, the designed motor air gap is smaller than the thickness of the flux probe. Therefore, a magnetic test fixture must be designed with a sufficiently large air gap to facilitate controlled measurements with the flux probe. Experiences and measurements confirm that in such cases, the harmonic contents of the flux density waveform don't change much. Fig. 1 shows the FEA of a pole pair of bonded ring magnet (6 poles) in the magnetic test fixture.
- Perform the sine FFT of the measured waveform to extract the harmonic contents as shown in Fig. 2.
- Perform the FEA with the extracted sine FFT model of the bonded ring magnet with the magnetic circuit to validate the sine FFT model vs. the measurements. Fig. 3 displays the computed Bn of the bonded ring magnet in the magnetic test fixture vs. the measured Bn. Table 1 gives the per unit value of the FFT coefficients of the magnet mmf, the computed Bn and the measured Bn.
- Perform FEA of designed BLDC motor with the sine FFT model magnet to simulate motor performances

such as cogging torque, back emf and torque ripples.

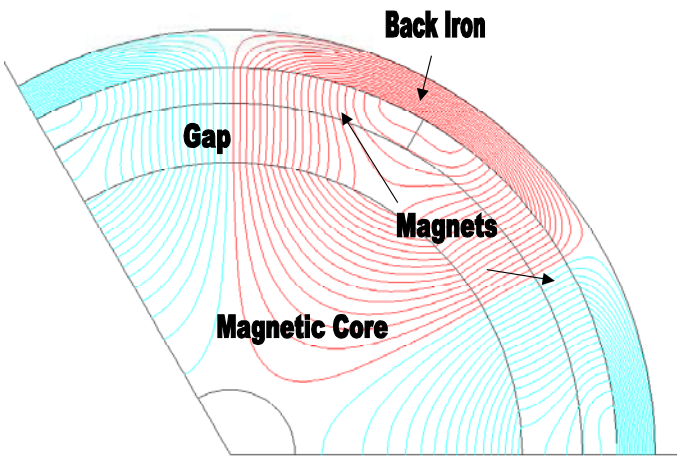

Fig. 1. Magnetic fluxes lines of 6 six poles bonded magnet in the magnetic circuit test fixture (a pole pair finite element model presented).

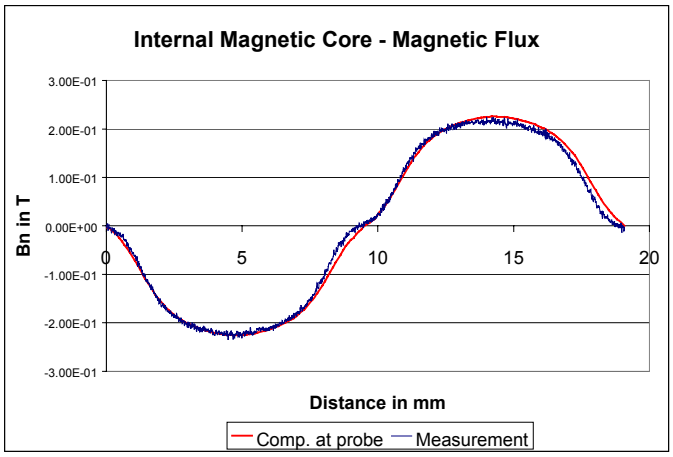

Fig. 2. Normal component of the air gap flux density (Bn) measured and Bn computed.

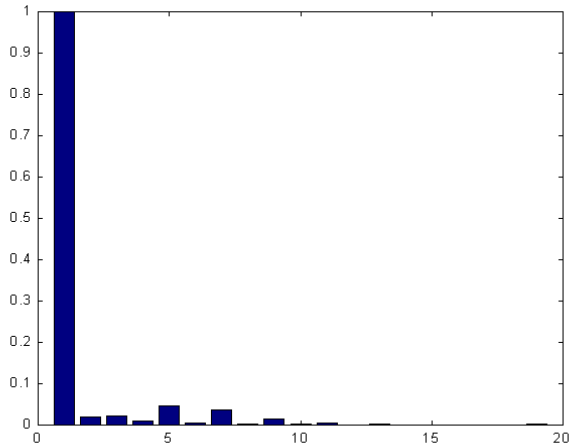

Fig. 3. Harmonic contents of the measured Bn.

Table 1: FFT coefficients – Internal magnetic core magnet flux test

FFT (p. u.) coefficients	Magnet MMF (FEA)	FFT of Bn (FEA)	FFT of Bn measured
Fundamental	1	1	1
3rd harmonic	0.0220	0.02178	0.0220
5th harmonic	-0.0459	-0.03774	-0.0459
7th harmonic	-0.0378	-0.02582	-0.0378
9th harmonic	-0.0141	-0.00783	-0.0141
11th harmonic	-0.0038	-0.00179	-0.0038

B. Motor Performances

An outside rotating bonded NdFeB ring magnet Brushless DC motor was tested and modeled to validate the methodology. The BLDC motor has 6 poles and 9 slots. It is 1' long and its OD is also 1'.

The cogging torque computed is 0.1 Oz-In vs. a measurement of 0.125 Oz-In.

The computed 5th harmonic of the back EMF is 1.6% vs. the measurement of 1.4%. The computed peak value of the back EMF is 4% lower than the measured value.

ACKNOWLEDGMENT

The author would like to thank P. Wendling, Magsoft Corporation, NY, USA and P. Lombard, Cedrat, France for their helps and collaborations in developing the user subroutine for the sine FFT magnetization model of the magnet.

REFERENCES

[1] S. P. Hong, H. S. Cho, H. S. Lee, and H. R. Cho, "Effect of Magnetization Direction in Permanent Magnet on Motor Characteristics," *IEEE Trans. Mag.*, vol. 35, no. 3, pp. 1231-1234, May 1999.

[2] C. A. Borghi, D. Casadei, A. Cristofolini, M. Fabbri, and G. Serra, "Minimizing Torque Ripples in Permanent Magnet Synchronous Motors with Polymer-Bonded Magnets," *IEEE Trans. Mag.*, vol. 38, no. 2, pp. 1371-1377, March 2002.

[3] S. M. Hwang, and D. K. Lieu, "Reduction of Torque Ripple in Brushless DC Motors," *IEEE Trans. Mag.*, vol. 31, no. 6, pp. 3737-3739, November 1995.

[4] Flux2D, User's Guide, Magsoft Corporation, Troy, NY, USA.

Detection of a Magnetically Unbalanced PM Rotor in an Assembled Motor

Alexander V. Kildishev
School of Electrical and Computer Engineering, Purdue University
1285 EE Building West Lafayette IN 47907-1285 U.S.A.
a.v.kildishev@ieee.org

***Abstract*— An analysis of a simplified finite element model of the external magnetic field due to a non-ideal PM rotor is presented. At first, accurate harmonic coefficients of a given PM rotor without a stator yoke are obtained for a range of non-ideal magnetizations and comparisons are made with the results of the FE simulation. It is found that the presence of the yoke may increase the error of both the location a defective PM pole and the pole deviation level. The specific cases presented here model the non-ideal pole magnetization in the radial direction and along the axis of rotation.**

INTRODUCTION

In naval applications the magnetic characterization of onboard equipment is commonly used. The aim is to achieve minimal magnetic signatures by limiting external magnetic fields in each component of a propulsion system. In particular, large PM motors are considered to be among the most critical magnetic sources. To control the magnetic signature of a PM motor, it is important to detect non-idealities of rotor magnets [1]. The core of the detection technique is to use spatial harmonic analysis to determine the location of an effective magnetic center (MC) of the rotor.

The classical approach defines the MC as the location of coordinate system origin that provides "the simplest to the second degree of approximation for the distant potential of a magnet having any irregular distribution of magnetism" [2]. With the same effect, later works [3, 4, 5] define the MC as the location of the origin that minimizes the zonal and two tesseral quadrupole coefficients of a spherical harmonic expansion of the magnetic scalar potential (U).

The spherical harmonic expansion of U is given by

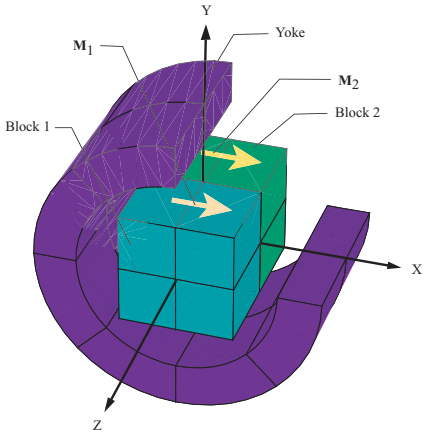

Fig. 1. An initial model of a non-uniformly magnetized bar magnet.

$$U = \sum_{n=1}^{\infty} \sum_{m=0}^{n} g_n^m F_c^{n,m} + h_n^m F_s^{n,m} \,, \quad (1)$$

where the harmonic coefficients g_n^m, h_n^m determine the multipole image (MI) of the source, and $F_c^{n,m}$, $F_s^{n,m}$ are the spherical harmonic functions of the n-th degree and m-th order.

For determination of the MC, the first eight coefficients (g_1, g_1^1, h_1^1, g_2, g_2^1, h_2^1, g_2^2, h_2^2) of a spherical harmonic expansion of the magnetic potential should be known. The MC coordinates $r_{MC} = \{x_{MC}, y_{MC}, z_{MC}\}$ are calculated according to known formulae [3, 4], which can be rewritten as the superposition of two orthogonal offsets:

$$\vec{r}_{MC} = 3\vec{t}\cdot\vec{m}_0 - \left(\left(\vec{t}\cdot\vec{m}_0\right)\times\vec{m}_0\right)\times\vec{m}_0 \,,$$

where $\vec{m}_0 = \vec{m}/|\vec{m}|$,

$$\vec{t} = \frac{\pi}{|\vec{m}|}\begin{pmatrix} \frac{2}{3}g_2 & h_2^1 & g_2^1 \\ h_2^1 & -2g_2^2 - \frac{2}{3}g_2 & 2h_2^2 \\ g_2^1 & 2h_2^2 & 2g_2^2 - \frac{2}{3}g_2 \end{pmatrix}, \text{ and } \vec{m} = 4\pi\begin{pmatrix} g_1 \\ h_1^1 \\ g_1^1 \end{pmatrix}.$$

An example of the experimental determination of the magnetic center of a simple source is shown in [6].

Previous spatial harmonic models of a PM rotor for characterization of the rotor as a set of magnetic multipoles have either been based on an idealized approximation of a non-ideal unshielded rotor [1], or have used the spherical harmonic analysis of the FE data of an ideal bar magnet [7] and a non-ideal PM multipolar rotor inside a yoke [8]. In all cases for the non-ideal rotor [1], [3] the deviation of the magnetization was assumed uniform for a given pole and the dependence of the field upon the random combinations of defective poles was examined. It has been confirmed that both the sectorial dipolar terms (g_1^1, h_1^1) and the significant zonal quadrupole (g_2) could appear due to the imperfection of the PM rotor.

In this work, the effect on the detection technique of shielding a PM rotor by a yoke is investigated. The dependence of the magnetic center of the non-ideal rotor inside the yoke upon different levels of non-uniform magnetization of a pole is examined and comparisons with the same but unshielded rotor are made.

MODELING OF A SHIELDED BAR MAGNET

In the initial case of the study, a single PM bar was placed inside a ferromagnetic yoke as in [7] and the effect of an asymmetric magnetization along the magnet was considered.

This model shown in Fig. 1, was for the bar magnet divided by

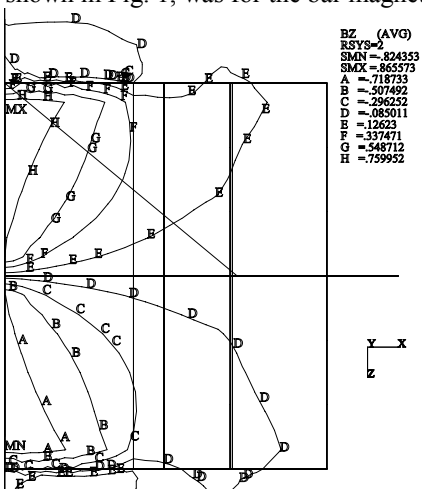

Fig. 2. Asymmetric B_z at the *xz*-plane due to 5% deviation of Block 2.

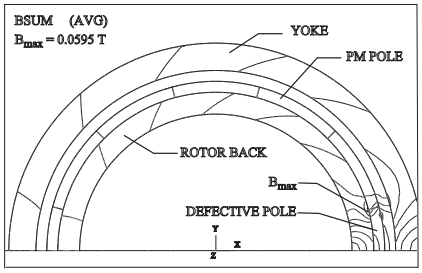

Fig. 3. A simplified 3D finite element model of 12-pole PM motor. The difference between normal and asymmetric total field is shown for the case of 5% less magnetized pole.

the *yx*-plane in two similar blocks ($0.4\times0.4\times0.3$ m^3) with two slightly different uniform magnetizations $\mathbf{M}_1$ and $\mathbf{M}_2$ in x direction. An example of asymmetric distribution of B_z in *zx*-plane due to 5% deviation of Block 2 is shown in Fig. 2.

The multipole image of the magnet with the yoke was restored using the approach of [7]. It was found that the MC of the magnet could not be accurately restored from the vector or scalar field data and influence of the shielding effect of the yoke should be eliminated in the detection technique.

Even though a single pole is assumed to be axis symmetrically placed inside the yoke, the results of direct application of (1) are catastrophic due to the significant difference in the locations of the MC of the magnet with the yoke and the MC of the magnet alone. The difference can be well understood for the particular case of Block 1 being at zero magnetization.

The core procedure is based on spatial harmonic techniques similar to [9], and [10] in the studies of multipolar sources inside a permeable shield with axial symmetry. Accordingly, the harmonic coefficients of the inducing magnetic field ($\mathbf{g}^m \quad \{g_m^m, g_{m\,1}^m \quad g_{m\,\max}^m\}$, $\mathbf{h}^m \quad \{h_m^m, h_{m\,1}^m \quad h_{m\,\max}^m\}$) and the harmonic coefficients of the total magnetic field ($\overline{\mathbf{g}}^m \quad \{\overline{g}_m^m, \overline{g}_{m\,1}^m \quad \overline{g}_{m\,-\max}^m\}, \overline{\mathbf{h}}^m \quad \{\overline{h}_m^m, \overline{h}_{m\,1}^m \quad \overline{h}_{m\,-\max}^m\}$) are connected by a shielding effect matrix T as $\overline{\mathbf{g}}^m \quad \ddot{T} \quad \mathbf{g}^m$ and $\overline{\mathbf{h}}^m = \ddot{T} \cdot \mathbf{h}^m$. The numerical evaluation of the matrix T is taken whereby any effects on the total field due to the yoke other than the presence of the inductor non-idealities are ignored. This permits the initial multipole image of the inductor to be retrieved as $\ddot{T}^{-1} \cdot \overline{\mathbf{g}}^m = \mathbf{g}^m$. (Since usually $\nu_{\max} > \overline{\nu}_{\max}$ pseudoinverse is used for $\ddot{T}^{-1}$). Once the inducing MI is restored, the MC detection by (1) is more accurate.

MODELING OF A MULTIPOLAR MOTOR

The detection accuracy for a more realistic magnetic system shown in Fig. 3 is examined. T of the yoke in 12-pole system of Fig. 3 is calculated from FEM models using 648-point spherical grid. This provides less than 8% MC detection error for pole deviations in 3% to 5% range. In addition, the use of the background field generated by the averaged uniform magnetization simplifies a numerical solution for non-linear permeability and realistic PM magnets. For this case, a linearized solution within limited variations of the inducing field is considered a first approximation. In particular, it has been confirmed that the shielding effect of the yoke for an individual multipole could be scaled linearly to achieve errors less than 10% within ±5% deviation of pole intensity.

Future studies will be focused on multiple pole defects.

ACKNOWLEDGMENT

This work was supported by the ONR under the Grant N000140310127. For this study, typical magnetic characteristics of compression molded, fully dense, hot extruded and sintered PM samples were provided by Magnequench, Inc.

REFERENCES

[1] A. V. Kildishev, J. A. Nyenhuis and Y. N. Zhilichev, "Extended multipole image of a non-ideal PM rotor", accepted for publication in the Journal of Applied Physics, May, 2003.

[2] W. Thomson, *Reprint of papers on electrostatics and magnetism by Sir William Thomson*, 2nd edition, Macmillan, London, 1884, pp. 372-374.

[3] A. Schmidt, "Der magnetische Mittelpunkt der Erde und seine Bedeutung," Gerlands Beit. Geophis., Bd. 41, pp. 346-358, 1934.

[4] J. P. Wikswo and K. R. Swinney, "Scalar multipole expansions and their dipole equivalents," Journal of Applied Physics, Vol. 57, No 9, 1985, pp. 4301-4308.

[5] Y. Sano, "A Best-fit eccentric dipole and the invariance of the earth dipole moment," Journal of Geomagnetism and Geoelectricity, Vol.43, No 10, pp. 825-837, 1991.

[6] A.V. Kildishev, *et al*, Application of magnetic signature processing to magnetic center pinpointing in marine vehicles, OCEANS '99 Proceedings, Vol. 3 , 1999, pp. 1532 –1536.

[7] A. Kildishev, S. Salon, M. V. K. Chari, and O.-M. Kwon, "The spatial harmonic analysis of FEM results in magnetostatics," to be presented at the INTERMAG 2003, Boston, USA, March 30-April 3, 2003.

[8] S. Salon; O.-M. Kwon, K. Sivasubramaniam, "Effects of asymmetry in far fields of permanent magnet motors," INTERMAG Europe 2002, Digest of Technical Papers, 2002, p. 294.

[9] M. A. Morgan, *et al* "Optimal Sensor Placement for Magnetic Signature Prediction", INTERMAG Europe 2002, Digest of Technical Papers, 2002, p. 293.

[10] A. V. Kildishev, M. A. Morgan, and J. A. Nyenhuis, "A permeable spheroidal shield of an almost uniform thickness," to be presented at the INTERMAG 2003, Boston, USA, March 30 - April 3, 2003.

Characteristic Analysis of Brushless DC Motor Considering Flywheel Diodes and DC Link Voltage Ripples

T. H. Kim, J. Lee
Dept. of Electrical Engineering
Hanyang University
Seoul 133-791, Korea
e-mail: ktheoung@dreamwiz.com

***Abstract*—This paper deals with the characteristic analysis of a brushless DC (BLDC) motor considering flywheel diodes and DC link voltage ripples by using time-stepped voltage source finite element method. By comparing with the experimental results, we show that the proposed analysis method is useful for the analysis and the design of a BLDC motor. We also examine the influence of flywheel diodes and DC link voltage ripples on the performance of a BLDC motor such as torque ripples and radial force on teeth.**

INTRODUCTION

In recent years, brushless DC (BLDC) motors have been adopted in home appliances for the purpose of an energy saving and a low noise. Especially application to direct-drive type washing machines (without mechanical system such as a gear) is considerably increasing.

BLDC motors in washing machines have a high input voltage, current and phase inductance to get a sufficient torque at a low speed and adopt a capacitor with a low capacitance in the rectifier of a drive circuit to decrease cost and size [1]. So, the commutation period becomes long and big DC link voltage ripples are generated, which have a bad effect on the performance of a motor such as torque ripples and a radial force on teeth. Therefore, these kinds of conditions must be considered in analysis.

In this paper, we present the analysis method of a BLDC motor considering flywheel diodes and DC link voltage ripples by using time-stepped voltage source finite element method and show that the proposed analysis method is suitable to analyze a BLDC motor by comparing the predicted and the measured phase currents and DC link voltage ripples. The performance of the motor when flywheel diodes and DC link voltage ripples are considered or not are also compared.

ANALYSIS MODEL AND DRIVE CIRCUIT

Fig. 1 shows the exterior-rotor type BLDC motor that drives washing machine. The motor is driven by 120° square wave voltage sources, and three hall sensors are used to detect the rotor position. Table 1 shows the specifications of the analysis model.

The drive circuit diagram is illustrated in Fig. 2. It is composed of the rectifier with capacitor and the inverter and the current limiter that protect over-current.

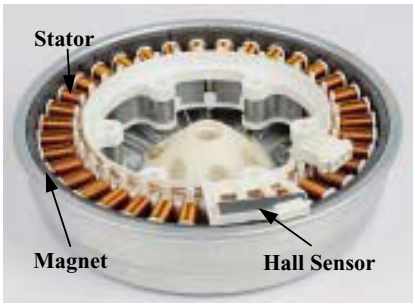

Fig. 1. Configuration of exterior-rotor brushless DC motor

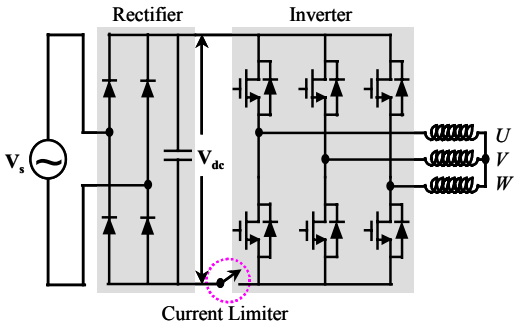

Fig. 2. Diagram of drive circuit

TABLE I. SPECIFICATIONS OF THE ANALYSIS MODEL

Section	Item	Value	(Unit)
Stator	Number of phases	3	
	Number of slots	36	
	Outer diameter	265	(mm)
	Stack width	36	(mm)
	Number of turn / phase / pole	110	(turn)
Rotor (PM)	Number of poles	48	
	Outer diameter	282	(mm)
	Radial thickness	8	(mm)
	Axial length	41	(mm)
	Residual flux density	0.4	(T)
Air gap	Mechanical air gap	1	(mm)
Drives	Current limit	6.35	(A)

FINITE ELEMENT FORMULATIONS

The system stiffness matrix can be constructed by combining circuit equations with discretized governing equation.

When capacitor is discharged and 2-phases (U and V) drive the motor as shown in Fig. 3(c), the system matrix can be expressed as (1).

$$\begin{bmatrix} [S] & [Q] & 0 \\ [F]/\Delta t & 2R+2L/\Delta t & -1 \\ 0 & 1/C & 1/\Delta t \end{bmatrix} \begin{bmatrix} A^{t+\Delta t} \\ I^{t+\Delta t} \\ V_{dc}^{\,t+\Delta t} \end{bmatrix} = \begin{bmatrix} 0 & 0 & 0 \\ [F]/\Delta t & 2L/\Delta t & 0 \\ 0 & 0 & 1/\Delta t \end{bmatrix} \begin{bmatrix} A^{t} \\ I^{t} \\ V_{dc}^{\,t} \end{bmatrix} + \begin{bmatrix} 0 \\ 0 \\ 0 \end{bmatrix} \quad (1)$$

When capacitor is discharged and the current is switched from phases UV to UW as shown in Fig. 3(d), the system matrix can be expressed as follows:

$$\begin{bmatrix} [S] & [Q_1] & [Q_2] & 0 \\ [F_1]/\Delta t & 2R+2L/\Delta t & 0 & -1 \\ [F_2]/\Delta t & 0 & 2R+2L/\Delta t & 0 \\ 0 & 1/C & 0 & 1/\Delta t \end{bmatrix} \begin{bmatrix} A^{t+\Delta t} \\ I_1^{\,t+\Delta t} \\ I_2^{\,t+\Delta t} \\ V_{dc}^{\,t+\Delta t} \end{bmatrix}$$

$$= \begin{bmatrix} 0 & 0 & 0 & 0 \\ [F_1]/\Delta t & 2L/\Delta t & 0 & 0 \\ [F_2]/\Delta t & 0 & 2L/\Delta t & 0 \\ 0 & 0 & 0 & 1/\Delta t \end{bmatrix} \begin{bmatrix} A^{t} \\ I_1^{\,t} \\ I_2^{\,t} \\ V_{dc}^{\,t} \end{bmatrix} + \begin{bmatrix} 0 \\ 0 \\ -V_d \\ 0 \end{bmatrix} \quad (2)$$

where V_d is the voltage drop in diode, C is the capacitance.

To make the system matrix in the case that capacitor is charged as shown in Fig. 3(a) and 3(b), the last row and column must be eliminated and the capacitor voltage (V_{dc}) should be replaced with the source voltage (V_s) in the equations (1), (2) because the capacitor voltage Vc is not unknown variable.

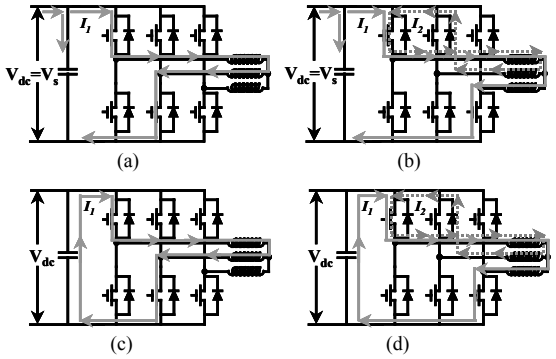

Fig. 3. Current flow in drive circuit

ANALYSIS RESULTS

Fig. 4 shows the calculated (a) and the measured (b) DC link voltage ripples and phase current at 100 rpm. We can see that the commutation period (when flywheel diode is on) is considerably long and big DC link voltage ripples (the difference between maximum and minimum value is about 90V) are generated. We also know that the experimental results closely match those obtained in the simulation of the proposed computational method.

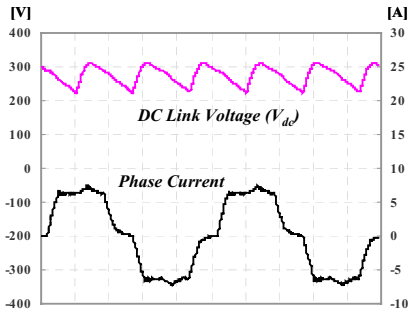

(a)

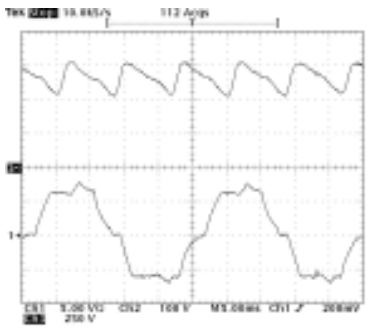

(b)

Fig. 4. Simulation (a) and experimental (b) DC link voltage ripples and phase current

CONCLUSION

In this paper, we analyzed the characteristics of a BLDC motor with a long commutation period and big DC link voltage ripples by using time-stepped voltage source finite element method. We also presented that the proposed analysis method is suited for the analysis of a BLDC motor by comparing the calculated and the experimental results.

We confirm that our analysis method is useful for the analysis and the design of a BLDC motor and drives with high input voltage, current and phase inductance.

REFERENCES

[1] S. Kitamura, "Magnetic field analysis of DC brushless motor considered volt-ampere characteristic of feedback diodes," *Inst. Electr. Engs. Japan,* vol. 12, pp. 1268-1275, 1996.

[2] T. J. E. Miller, *Brushless Permanent-Magnet and Reluctance Motor Drives.* Clarendon Press, 1989.

Utilization of 3D FEM to study and design a SMC Electrical Machine

[1]T. Henneron, [2]S. Clénet, [3]J. Cros, [3]P. Viarouge

[1]L2EP, USTL
Bat P2
59655 Villeneuve d'ascq, France
Francis.Piriou@univ-lille1.fr

[2]L2EP, ENSAM CER LILLE
8, Bd Louis XIV
59046 LILLE Cedex, France
Stephane.Clénet@lille.ensam.fr

[3]LEEPCI, Université Laval
Ste-Foy
Québec Canada G1K7P4 (PQ) Canada
cros@gel.ulaval.ca

Abstract – **In this paper, we test a 3D FEM model using Whitney's elements to study a permanent magnet machine made up soft magnetic composite (SMC) material . The model based on both magnetostatic potential formulations is briefly presented. To evaluate the accuracy of these formulations, theoretical fluxes are compared with fluxes measured on permanent magnet machine. For each potential formulation, a specific method of flux calculation is used in order to improve accuracy.**

INTRODUCTION

Electrical machines working at industrial frequencies are made up laminated steel to reduce eddy current losses. In this condition, the magnetic flux has to flow in the plan of the sheet. This induces some constraints on the machine structure. Nowadays, new soft magnetic composite (SMC) materials are available[1][2]. In this case, the magnetic flux can flow in three directions. Consequently, new concepts of electrical machines can be achieved [3]. But, to study and optimize their electromagnetic structures, the designer requires an efficient 3D field computation. In this communication, we propose to evaluate a 3D FEM model based on Whitney's elements to study electrical machines made up of SMC material. Special attention is paid on the calculation of fluxes flowing through windings or any surface. In fact, these kinds of information are very useful for a designer and it is well known that these quantities are difficult to calculate accurately.

First, the SMC machine is presented. Then, the model based on both potential formulations in magnetostatics is described. We compare measurements to fluxes obtained with different methods developed for each potential formulation.

PRESENTATION OF THE MACHINE

We propose to study a 22-poles permanent magnet machine with a 3-phase claw pole stator (Fig. 1). This stator structure is divided in 3 parts made of SMC material (Fig.2). The tooth tips are extending like claws to cover the air-gap surface with the rotor. There are three phase coils wound on the central part of the magnetic circuit (Fig. 2). When the mechanical assembly is achieved, these coils are surrounded by two-rings of teeth and the winding is perfectly enclosed in the stator yoke. The rotor is classical and is made with 22 sintered NdFeB magnets mounted on the surface of a magnetic steel yoke. The magnetic fluxes created by the permanent magnets and the stator windings flow in three dimensions.

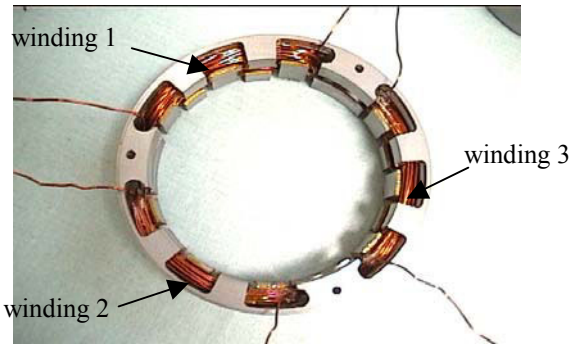

Fig. 1. Stator of a 3 phase claw pole stator

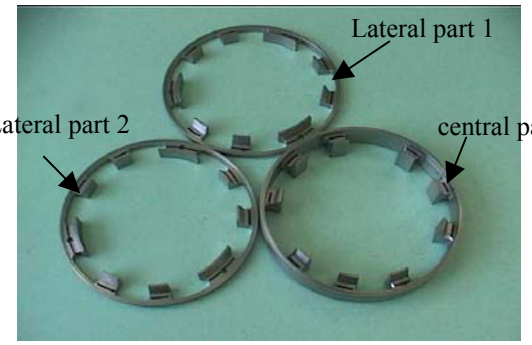

Fig. 2. Three parts of the stator magnetic circuit

PRESENTATION OF THE MODELS

We consider a domain D with a boundary Γ. In magnetostatics, the magnetic field **H** and the magnetic flux density **B** verify Maxwell's equations.

$$\mathbf{curl}\,\mathbf{H} \quad \mathbf{J} \text{ with } \mathbf{H}\times\mathbf{n}=0 \text{ on } \Gamma_H \qquad (1)$$

$$\mathrm{div}\,\mathbf{B} \quad 0 \text{ with } \mathbf{B}.\mathbf{n}=0 \text{ on } \Gamma_B \qquad (2)$$

with **J** the known current density flowing the inductors and Γ_H and Γ_B two complementary surfaces such as $\Gamma_H \cup \Gamma_B = \Gamma$ and $\Gamma_H \cap \Gamma_B = 0$. To take into account the behavior of the material, the fields **B** and **H** are linked by the constitutive relationship :

$$\mathbf{B} \quad f(\mathbf{H}) \qquad (3)$$

In the case of permanent magnet machine (huge air gap), the relation between **H** and **B** for SMC material is supposed to be linear. The relative permeability is quite low compared to the one of laminated steels and is equal to 150. For each phase j a vector $\mathbf{K}_j$ is introduced such as :

$$\mathbf{curl}\,\mathbf{K}_j \quad \frac{\mathbf{J}_j}{i_j} \text{ with } \mathbf{K}_j \times \mathbf{n} = 0 \text{ on } \Gamma_H \tag{4}$$

with $\mathbf{J}_j$ the current density and i_j the current flowing through the phase winding j. The vector $\mathbf{K}_j$ can be easily discretised in the edge element space using a tree technique [4,5]. Two formulations can be used to solve the magnetostatic problem. The **A**-formulation consist in introducing a vector potential **A** such as :

$$\mathbf{B} \quad \mathbf{curl}\mathbf{A} \text{ with } \mathbf{A} \times \mathbf{n} = 0 \text{ on } \Gamma_B \tag{5}$$

This potential is discretized in the edge elements space [4]. For the Ω-formulation, we find out a scalar potential Ω such as :

$$\mathbf{H} \quad \sum_{j=1}^{N} i_j \mathbf{K}_j \quad \mathbf{grad} \quad \text{with } \Omega = 0 \text{ on } \Gamma_H \tag{6}$$

with N the number of phase. The function Ω is discretised in the nodal element space [4]. The linkage flux of the winding j can be obtained by [5] :

$$\bar{j} \quad \int_D \mathbf{B}.\mathbf{K}_j \, dD \tag{7}$$

The vector **B** can be calculated using FEM either by the **A**-formulation or by Ω-formulation. To compute the flux Φ_s flowing through a surface S supported by facet elements of the mesh, the method can't be the same anymore. If ∂S is the set of edges of the boundary of S, the flux Φ_s can be obtained in the case of the **A**-formulation by :

$$\bar{s}^{A} \quad \int_S \mathbf{A}\,\mathbf{dl} \quad \sum_a A_a . \delta_a \tag{8}$$

with A_a the circulation of the vector potential along the edge a, δ_a is a sign function to take into account the relative orientation of the edge a with respect to the one of ∂S. For Ω-formulation, we introduce the vector **K** corresponding to the magnetic field created by a coil formed by the edges of ∂S and supplied by a current of one Ampere. This field is calculated by using the Biot and Savart law. From magnetic flux density **B** calculated with the Ω-formulation, the flux Φ_s is obtained by:

$$\bar{s} \quad \int_D \mathbf{B} \,.\mathbf{K}\, dD \tag{9}$$

APPLICATION

The mesh of the machine is composed by 180,000 tetrahedral elements and 33,062 nodes. The unknown number is about 200,000 for **A**-formulation and about 33000 for Ω-formulation. First, we compare the fluxes calculated by both formulations to the experimental flux of one phase that is supplied by a current of 1 A (Table I). Experimental and numerical results are close, we can note that both formulations give different results due to numerical errors. Second, fluxes flowing through three teeth have been measured by coils. The location of three coils is given in Fig. 3. In Table II, we have reported the local fluxes calculated by (8) for **A**-formulation and by (9) for Ω-formulation and the measurements.

Table I. calculated and experimental linkage fluxes

	A-form.	-form	measure
(μWb)	142	166	144

Table II. Fluxes through different teeth (μWb)

	A-form.	-form	Measures
Coil 1	1.34	1.44	1.7
Coil 2	1.3	1.41	1.66
Coil 3	0.46	0.52	0.39

In this case, the differences between measurements and theoretical results, already encountered when calculating winding fluxes, appear also with the local fluxes but with a more important gap. This ones from numerical errors but also from the experimental conditions. In fact, the actual coils are not perfectly match the teeth they wound on. But globally, the error remains acceptable for a designer of electrical machines. Moreover, we can see that **A**-formulation doesn't give the best results even if this one enforces naturally the conservation of the flux.

REFERENCES

[1] Quebec Metal Powder ltee, "Atomet EM-1 Ferromagnetic composite powder," *datasheet*, 2000

[2] L.P. Lefevre, S. Pelletier and C. Gélinas, "Effect of electrical resistivity on core losses in soft magnetic iron powder materials", *Journal of Magnetism and Magnetic Materials*, 176, pp 93-96, September 1997.

[3] J. Cros, and P. Viarouge, "New Structures of Polyphase Claw-Pole Machines", 37th Annual Conf. of Industrial Applications Society, IAS'02, Pittsburg, October 2002.

[4]A. Bossavit, Computationnal electromagnetism, Academic Press, Boston, 1998.

[5] Y. Le Menach, S. Clénet and F. Piriou, "Numerical Model to Discretize Source Fields in the 3D finite element Method", *IEEE Trans. Mag.*, vol. 36, No. 4, July 2000.

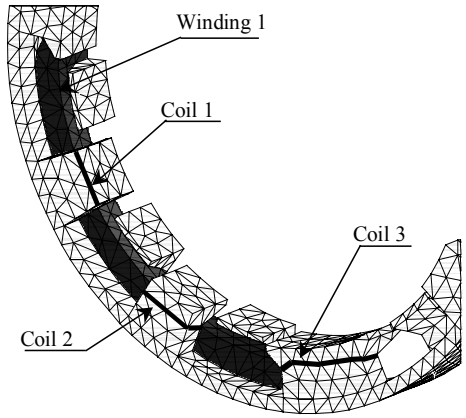

Fig. 3. Location of the coils use to measure and to calculate fluxes flowing through teeth

Effect of Pole to Slot Ratio on Cogging Torque and EMF Waveform in Fractional Slotted BLDC Motor

Kab-Jae LEE[1], Ki-Chan KIM[1], and Ju LEE[2]
(1) Electro-Mechanical Research Institute , Hyundai Heavy Industry Co., Mabook, Kuseong, Yongin, Kyunggi, 449-716, Korea (2) Dept. of Electrical Engineering, Hanyang University, Haengdang, Seongdong, Seoul, 133-791, Korea
e-mail: kjlee@hhi.co.kr

Abstract **Conventional integral slot design in permanent magnet motor tends to have a high cogging torque and large end turns, which increase copper losses. The fractional slot is effective compared to integral slot in the cogging torque and EMF waveform. The effectiveness of fractional slot can be maximized by selecting optimal pole to slot ratio. This paper presents the effect of pole to slot ratio on the cogging torque and EMF waveform in the fractional slotted PM motor. The effectiveness of the proposed design has been analyzed by finite element method.**

INTRODUCTION

The design technique of permanent magnet motor has been studied to improve power density and performance required as a controlled motor. However PM motor has cogging torque due to existence of permanent magnet. Particularly in case of using high-energy magnet, it is necessary to consider cogging torque as a design parameter. [1].

Cogging torque is caused by interaction between the harmonics of the mmf by permanent magnet and the air gap permeance harmonics that is generated in the slots. The cogging torque dose not largely influence to an effective torque of the motor but causes pulsating electromagnetic torque, and the speed ripple and vibration [2], [3]. Consequently it reduces the performance for high-performance control motor. In order to decrease cogging torque, skewing and auxiliary slot, increasing the air gap length, selection of fractional slot, increasing the number of slot, and minimization of slot opening can be considered. The skewing of one-slot pitch perfectly removes the cogging torque in ideal case. The skewing can minimize the cogging torque but it causes distortion of square wave back EMF in BLDC motor. Consequently the torque ripple is increased by commutation. Therefore, the skewing leads to the inferior performance.

Even if the general type of three-phase BLDC motors (model I) has 1:3 pole to slot ratio of lab winding with three-slot coil pitch. It usually has high cogging torque and disadvantage of having an end-turn, which causes big copper loss in the stator. The common fractional slot PM motor (model II) has a pole to slot ratio 3/2. The cogging torque of the motor has lower cogging torque motor, but the torque performance is not improved significantly compared to conventional motor. The new fractional slotted PM motor (model III) of which pole to slot ratio is 27/20 is proposed in this paper. The effects of pole to slot ratio on the performance such as cogging torque, torque ripple, and EMF waveform have been investigated in detail by finite element method.

ANALYSIS MODEL AND NUMERICAL METHOD

Table I shows the specification of the BLDC motor used in the analysis. Model I is the specification of a conventional model, which has pole to slot ratio 1:3. Model II is the specification of the first improved model. This type is widely used as BLDC motor that has pole to slot ratio 2:3. Also maximum power of it is 9.2Nm and maximum speed is 6000rpm. Stator coil is concentric winding. Model III is the proposed motor in this paper. Since this model has pole to slot ratio 20:27, it has asymmetric characteristic of pole-slot unlike 1:3 or 2:3 models. Therefore stator winding is different from conventional concentric winding. Although three models have different slot combination respectively, they have approximately equivalent size and torque.

TABLE I. SPECIFICATION OF BLDC MOTOR

Items	Model I	Model II	Model III
Max torque [Nm]	47	49	47
Max output [KW]	10	9.2	10
Number of pole	10	12	20
Number of slot	30	18	27
Number of phase	3	3	3
Permanent magnet	NdFeB	NdFeB	NdFeB

OBSERVATION OF THE RESULTS

Fig. 1 shows the analysis results of cogging torque of three models. Model I has a cogging torque frequency same as the slot number, which can be predicted by physical understanding. The cogging torque frequency of model II is 36, which is same to the least common multiple(LCM). The magnitude of cogging torque is decreased compared to model I. The period of cogging torque of model III is increased and its magnitude is decreasing significantly because LCM is 540. The magnitude of cogging torque of model III is 1/24.6 comparing with that of model I. Fig. 2 shows the back EMF of the three models. The magnitude of back EMF is highest in the model II but the waveform is not sinusoidal. The back

EMF waveform of model III is almost sinusoidal and the frequency is twice compared to model I. There is another torque ripple source, which is produced by commutating. So, the torque ripple has to consider in the high performance motor design. Fig. 3 shows the analysis result of total torque and torque ripple. The torque ripple of model III is the lowest. From this results, it is clear that the proposed fractional slot to pole ratio model is very effective in all respects.

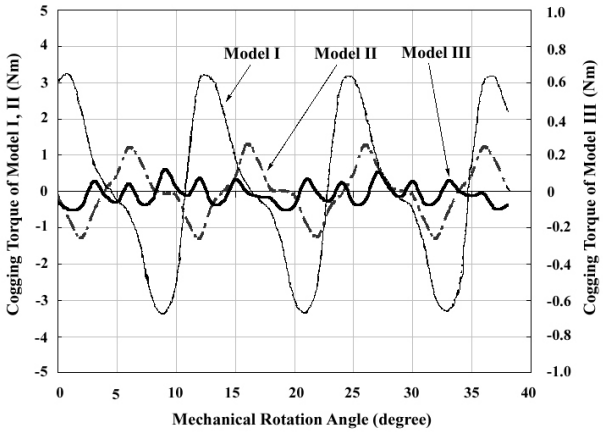

Fig. 1. Comparison of cogging torque of three models

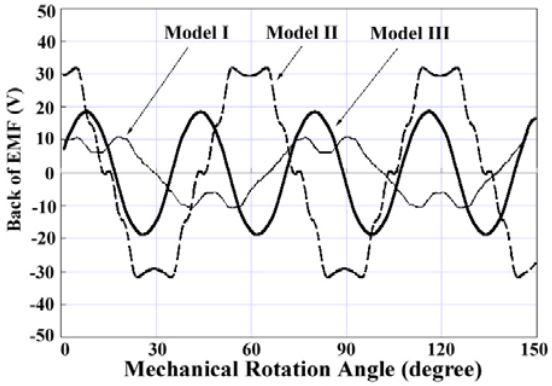

Fig. 2. Phase back-EMF waveform

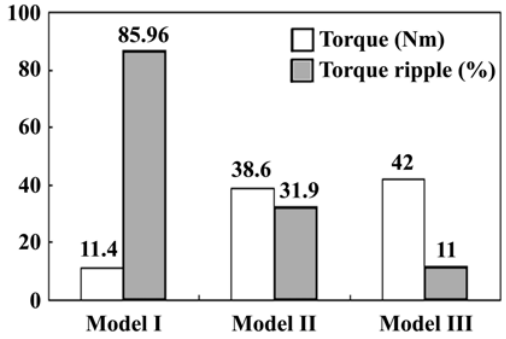

Fig. 3. Comparison of torque and torque ripple of three models

CONCLUSION

The effects of pole to slot ratio on back EMF and torque performance such as cogging torque, torque ripple, and torque density have investigated in detail. The frequency and magnitude of cogging torque in the various models can be predicted by cogging torque characteristic equation. From this prediction, we proposed the smallest cogging torque model of which pole to slot ratio is 20:27.

The effeteness of the proposed model has been confirmed quantitatively by numerical analysis approach. The other torque characteristics are also improved in the proposed model by the winding method. From these results, we can conclude that the well-designed fractional slotted PM motor can have an excellent performance. Since proper fractional slot design can avoid necessity of additional modification such as lamination and skewing after basic design, the proposed method may be certainly looks effectiveness in point of PM motor design.

REFERENCES

[1] J. R. Hendershot Jr. and T. J. E Miller, *Design of brushless permanent magnet motors*, Oxford, 1994

[2] T.M. jahns and W. L. Soong, "Pulsating torque minimization techniques for permanent magnet ac motor drives-A review," *IEEE Trans. on Power Electronics*, vol. 43, no. 2, pp. 321-330, 1996.

[3] R. P. Deodhar, D. A. Station, T. M. Jahns, and T. J. E. Miller, "Prediction of cogging torque using the flux-mmf diagram technique," *IEEE trans. on Industry Application*, vol. 32, pp.569-576, 1996.

Study in Post-assembly magnetization of Line Start Permanent Magnet Motor

C. K. Lee*, B. I. Kwon*, B. T. Kim**
*Graduate school of Hanyang University, Ansan 425-791
**LG Electronics Inc, Seoul 152-050
E-mail: bikwon@hanyang.ac.kr

Abstract **In this paper the study in post-assembly magnetization of LSPM(Line Start Permanent magnet Motor) is represented. There is a problem of post-assembly magnetization in the manufacturing process of LSPM, which is that the magnet is not magnetized enough by using its own stator coil when the capacity of LSPM is large. When the capacity of the LSPM is small, the magnet can be magnetized well by using its own stator coil. Hence another magnetizing fixture is necessary to magnetize the magnet of large capacitive LSPM.**

In order to magnetize the magnet of large capacitive LSPM, the author proposes the magnetizing fixture that have the large number of coil-turn and proposes the rotor that have the small dimension of rotor bar.

I NTRODUCTION

Recently, the LSPM(Line Start Permanent Magnet Motor) is noted as an alternative for an induction motor because it offers a very high efficiency and unity power factor. LSPM is an attractive choice with a constant velocity due to these attributes when applied to a high duty cycle motor.[1,2] However, high manufacture costs as compared to an induction motor is disadvantage comparing to an induction motor.

Thus, the post-assembly magnetization of the NdFeB magnet is considered as the way reducing the material and the manufacturing costs. In case of small capacitive LSPM the post-assembly magnetization is performed with its own stator coil. On the other hand, in case of large capacitive LSPM the post-assembly magnetization cannot be done by using its own stator coil. Hence, magnetizing fixture is required to be designed. But the eddy current occurring in the rotor bar during magnetization disturbs the magnetization of magnet. And if the magnetizing fixture is not designed properly, the magnet of LSPM will not be magnetized in post-assembly magnetization. Hence, the study of the design and analysis concerning post-assembly magnetization in LSPM is necessary. However, there is a paucity of research in this area.

So, in this paper the method of post-assembly magnetization of LSPM is presented. The characteristics of the magnetization are analyzed by time-stepping finite element method.

ANALYSIS MODEL

The magnetizing fixture and the rotor analyzed in this paper is shown in Fig. 1, when the 4-pole magnetizing fixture surrounds the rotor of LSPM. And the coil is located between the poles. And Fig. 1 shows also the FEM region. We use the 2-dimensional FEM(Finite Element Method) coupled with circuit equation in order to analyze the magnetizing state. The governing equation of FEM and circuit equation is shown in equation (1) and (2) respectively[3]. The M_x, M_y represent the magnetization of x direction and y direction respectively in FEM element.

$$\frac{}{x}\left(\frac{1}{}\frac{A}{x}\right)\quad\frac{}{y}\left(\frac{1}{}\frac{A}{y}\right)\quad J_0\quad\frac{1}{}\left(\frac{M_y}{x}\quad\frac{M_x}{y}\right)\quad\frac{A}{t}\qquad(1)$$

$$\frac{d}{dt}\quad(R\quad R_c)\frac{dQ(t)}{dt}\quad L_0\frac{d^2Q(t)}{dt^2}\quad\frac{Q(t)}{C}\quad\frac{Q_0}{C}\quad 0\qquad(2)$$

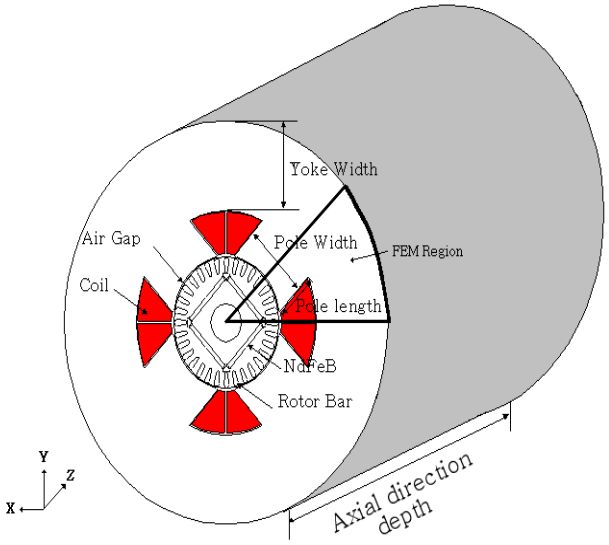

Fig. 1 Magnetizing Fixture and rotor

MAGNETIZING FIXTURE DESIGN

In case of small capacitive LSPM, the post-assembly magnetization fixture is usually its own stator. But in case of large capacitive LSPM, it is impossible to magnetize the magnet in post-assembly by its own stator because the stator winding is distributed and high leakage flux is produced. Hence, another magnetizing fixture is needed.

It is important to design magnetizing fixture because the magnetization of magnet is well affected by magnetizing

fixture. The important point of designing magnetizing fixture is that the magnetic flux flows sufficiently to magnet and the magnetic saturation must not be occurred in the fixture.

Usually the small number of coil-turn is made in post-assembly magnetization[4]. When the number of coil-turn is small, the magnitude of the impulse current increases and the magnitude of magnetic field intensity increases. However, eddy current occurred in rotor bars disturbs the permanent magnet in post-assembly magnetization of LSPM, where the magnet is located in the squirrel cage rotor.

Hence, it is important to reduce the eddy current of rotor bars. In this paper, we propose two methods of reducing the eddy current of rotor bars. One is to make the inductance of magnetizing fixture high by using large number of coil-turn. The other is to make the resistance of rotor bar high by using small rotor bar.

Fig. 2 shows the analysis result of magnetic field intensity in cases of the small number of coil-turn and the large number of coil-turn. From Fig.2, we know that the magnetic field intensity becomes much larger in large number of coil-turn than in small number of coil-turn. Fig. 3 shows the anlysis result of magnetic field intensity according to rotor bar dimension. From Fig. 3, we know that the magnetic field intensity increases as the rotor bar dimension decreases. The voltage and the capacitance of magnetizer are 3500 [V] and 3000[F] respectively when these analyses are simulated.

Finally, the magnetizing fixture that has large number of coil-turn and the rotor that has small bar are made. Fig. 4 shows the analysis results and the experimental results of the rotor surface flux density of magnetized LSPM. The experimetal results concur with analysis result. The difference between the analysis and the experiment is determined by experimental error.

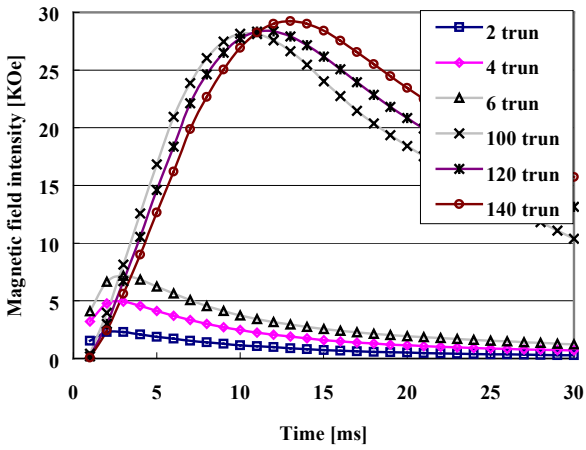

Fig. 2 The magnetic field intensity according to coil-turn

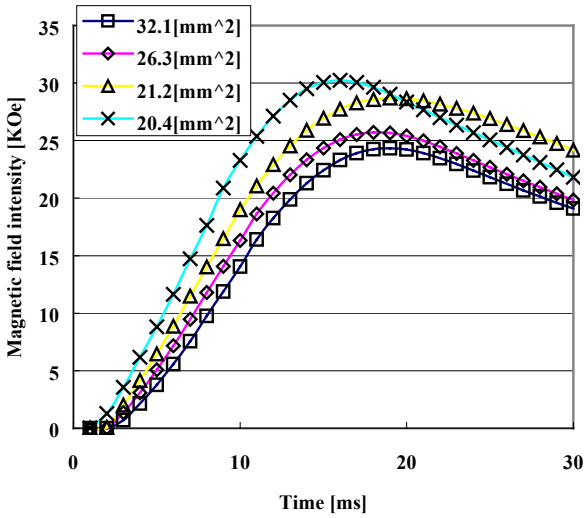

Fig. 3 The magnetic field intensity according to rotor bar dimension

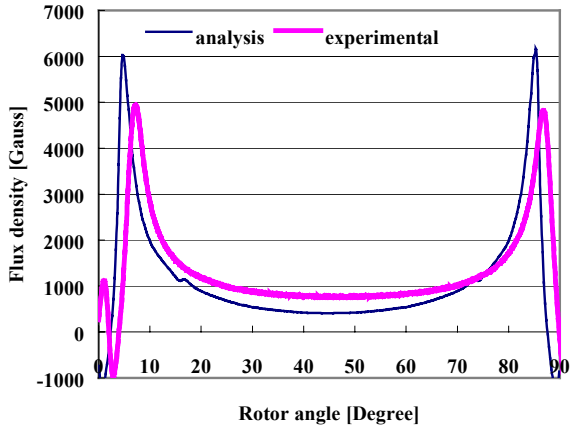

Fig. 4 The rotor surface flux density of manetized LSPM

REFERENCES

[1] Essam S. Hamdi, "Design of small electrical machines", JHON WILEY & SONS, pp.175, 1994.

[2] S. Williamson, A. M. Knight, "Performance of Skewed Single Phase Line-Start Permanent Magnet Motors", *IEEE Industry Applications Society Annual Meeting*, New Oleans, Louisiana, October 1997.

[3] T. Nakata and N.Takahashi, "Numerical Analysis of Transient Magnetic Field in a Capacitor-Discharge Impulse Magnetizer", *IEEE Transactions on Magnetics*, vol.22, no. 5, pp.526-528, 1986.

[4] G. W. Jewel, D. Howe, " Computer-aided design of magnetization fixtures for the post-assembly magnetizaion of rare-earth permanent magnet brushless DC motors", IEEE Transactions on Magnetics, vol .28, no.5, pp.3036-3038, 1992

Optimum Rotor Configuration of Interior Permanent Magnet Motor with Concentrated Winding for Sinusoidal Induced Voltage

Kab-Jae LEE[1], Ki-Chan KIM[1], and Ju LEE[2]
(1) Electro-Mechanical Research Institute , Hyundai Heavy Industry Co., Mabook, Kuseong, Yongin, Kyunggi, 449-716, Korea (2) Dept. of Electrical Engineering, Hanyang University, Haengdang, Seongdong, Seoul, 133-791, Korea
e-mail: kjlee@hhi.co.kr

Abstract **Permanent magnet (PM) motor is one of candidates in the application to the hybrid or electric vehicle. Minimizing PM motor size is an important requirement in the applications. This requirement has been satisfied by adopting high performance permanent magnet and concentrated winding. PM configuration is also one of the critical design points for this purpose. This paper presents the effect of PM configuration on the motor performance, especially sinusoidal induced voltage and demagnetization. The proposed design by finite element method has been confirmed by comparing EMF waveform, cogging torque and demagnetization between conventional and new model.**

INTRODUCTION

The design technologies of PM motor have been intensively researched to improve the performance, especially torque density. Maximum torque is an important performance in the application to the hybrid and electrical vehicles. We can maximize the maxim torque by using high-energy product PM or good magnet material. This approach is easy to accomplish, but has a limit to improve the performance because it depends on material performance. Winding method and PM configuration are other design techniques, which are difficult, but very useful. Especially, there are some design schemes in the PM configuration in the PM motor design. One of commonly used PM motor is surface mounted PM motor (SPM). Interior PM motor (IPM), outer rotor type motor are other choices. In addition, axial motor and transverse flux machines have also proposed.

Many engineers have researched for advantages and disadvantages various PM motors. P. Pillay and R. Krishnan pressed characteristic comparison between trapezoidal motor and sinusoidal motor[1], and Rich schiferl have reported that single layer interior permanent magnet synchronous motor is superior to surface permanent magnet synchronous motor in view of torque and speed characteristics[2]. Y. Honda reported that two-layer magnet IPM for electric vehicle had had high performance[3, 4]. Although T.J.E. Miller insisted spoke magnet type IPM that is same as embedded IPM had higher air gap flux density than lateral magnet type IPM[5], no research report for quantitative comparisons among spoke magnet type, lateral magnet type and outer rotor type has been published so far.

This paper presents quantitative comparison of representative for PM motors based on time stepped finite element analysis (FEA). The four BLDC motor models are embedded IPM(model I), lateral magnet type IPM(Model II), 1-layer IPM(model III) and new 1-layer IPM(modelm IV). The PM motors are analyzed in the condition that the volume of geometrical configurations and input current is identical.

CONVENTIONAL MODEL DESCRIPTION

Fig. 1 shows cross-section view and flux distributions of two representative IPM motors. These motors have a concentrating winding with 1.5 slot to pole ratio. Fig. 1 (a) shows flux distribution of IPM Motor with lateral magnet. This model can produce large reluctance torque, because there is reactance difference between d-axis and q-axis. There is local magnetic saturation on the rib structure. How to design the rib structure is important design factor. Fig. 1(b) shows circumferentially magnetized embedded PM motor with spoke magnet. The airgap flux density can be increased because the magnetic surface of permanent magnet can be made larger than pole-pitch. In addition, this model can produce a little reluctance torque because the reactance difference between d-axis and q-axis is small. But permanent magnet and magnetic barrier configuration have to be carefully designed to prevent the leakage flux. The magnetic barrier using non ferromagnetic material is used surrounding the shaft.

But Fig. 1 (a) and (b) have trapezoidal or not enough sinusoidal induced voltage characteristics because of concentric winding. New model presented in this paper is modified rotor magnet configuration from Fig. 1 (a). Therefor, it has good sinusoidal induced voltage and demagnetization characteristics.

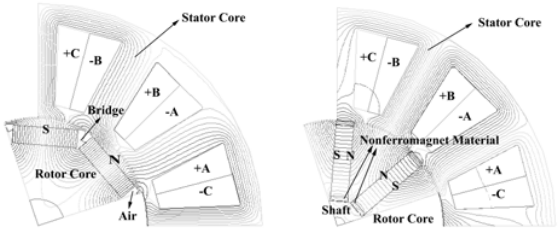

(a) Interior PM Motor (b) IPM Motor with spoke magnet
Fig. 1. Conventional IPM Motor

NUMERICAL ANALYSIS METHOD

If the magnetic vector potential and current density have only a *z*-axis component, the governing equation for PM motor can be expressed in a magnetic vector potential A as follows:

$$ / x \quad A/ x \quad / y \quad A/ y \quad J_o \quad J_m \quad 0, \qquad (1)$$

where is the inverse of permeability, A is the magnetic vector potential, J_0 is the input current density, and J_m is the equivalent magnetizing current density of permanent magnet.

After applying the Gelerkin method in (1), system matrix equation is defined in region of the total analysis as follows.

$$\sum_{e\ 1}^{n} S^{e} A^{e} \quad J_o{}^{e} \quad J_m{}^{e} \quad 0 \qquad (2)$$

The moving line technique is introduced to carry out the dynamic analysis[6]. The flux linkage can be calculated as follows:

$$\frac{Nh}{Z} \int_{s} A \quad A \quad dxdy, \qquad (3)$$

where A^+ and A^- are the magnetic vector potential in the same slot of one phase winding, Z is the area of one slot, and h is the stack width.

CONCLUSION

This paper analyzed effect of induced voltage and demagnetization of BLDC motor with variation of magnet configuration, and presented quantitative comparison of four models. Torque trend of four models was similar although discrepancy in number of poles, size, and salient ratio of models. These results provided guideline for determining current control methods and rotor configuration of permanent magnet motor for electric vehicle, hybrid electric vehicle, and electric motorbike applications.

REFERENCES

[1] P. Pillay and R. Krishman, IEEE IAS Annual Meeting, Atlanta, 380(2001).

[2] Rich Schiferl, Design considerations for salient pole, PM synchronous motors in variable speed drive applications, (Ph. D. thesis, University of Wisconsin-Madison, 1987).

[3] Y. Honda, T. Higaki, S. Morimoto and Y. Takeda, IEE Proc. Electr. Power Appl., 145, 119(1998).

[4]Yukio Honda, Tomokazu Nakamura. Toshiro Higaki and Yoji Takeda, IEEE IAS Annual Meeting, New Orleans, LA, 75(1997).

[5] T.J.E Miller, Brushless Permanent Magnet and Reluctance Motor Drives, (Clarendon, New York, 1989).

Three-Dimensional Finite Element Analysis of a Transverse Flux Permanent Magnet Motor

M. V. Ferreira da Luz[1], P. Dular[2], N. Sadowski[1], J. P. A. Bastos[1]

[1] Universidade Federal de Santa Catarina
GRUCAD/EEL/CTC - C.P. 476 – 88040-900
Florianópolis - SC – Brazil

[2] University of Liège - Dept. of Electrical Engineering
Institut Montefiore - Sart Tilman Bât. B28
B-4000 Liège - Belgium

e-mail: valencia@grucad.ufsc.br, Patrick.Dular@ulg.ac.be

Abstract **A finite element analysis of a transverse flux permanent magnet motor is presented in this work using the 3D magnetic vector potential magnetodynamic formulation. The rotor movement is modeled using the moving band technique for which a dynamic allocation of periodic or anti-periodic boundary conditions is performed. The carrier for the stator poles is made of aluminum alloy. Consequently, the investigation of eddy current losses in these areas is relevant for machine performance predictions.**

INTRODUCTION

The use of permanent magnets allows generating substantial air-gap magnetic flux without external excitation. Therefore, the efficiency characteristics of permanent magnet synchronous machines are, in general, quite good. The application of new magnet materials with high inherent energy in machines using a transversal flux configuration allows high force densities, which cannot be reached with machines using conventional longitudinal flux configurations [1].

In recent years, permanent magnet machines with transverse flux structure are attracting increased attention. The machine under investigation has a larger torque per units of volume and weight when compared to conventional machines [2]. A precise field evaluation for transverse flux machines requires 3D finite element analysis.

This paper presents the developed numerical techniques and their application for the 3D finite element analysis of this type of motor. The structure of one phase of the motor and the course of the magnetic flux are shown schematically in Fig. 1 and Fig. 2, respectively. Aluminum pieces are used between the stator U-shaped iron cores and the induced eddy currents effects on the functioning of the machine will be investigated (for visualization purposes, the aluminum pieces are not presented in Fig. 1 and Fig. 2).

METHODOLOGY

In this work, 3D finite element magnetodynamic calculation is performed using a magnetic vector potential formulation. As 3D calculations are usually very time consuming we reduced the calculation domain using periodic boundary conditions.

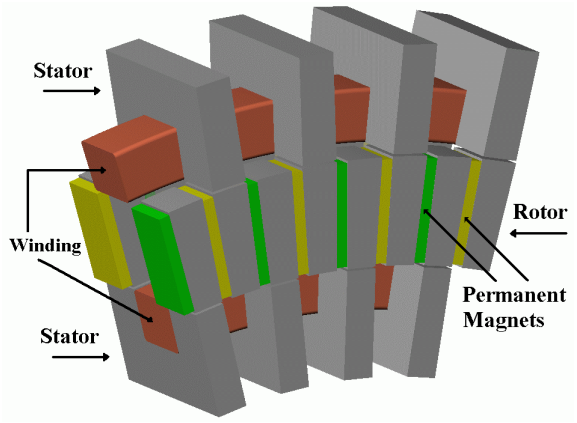

Fig. 1. One phase of the transverse flux machine prototype.

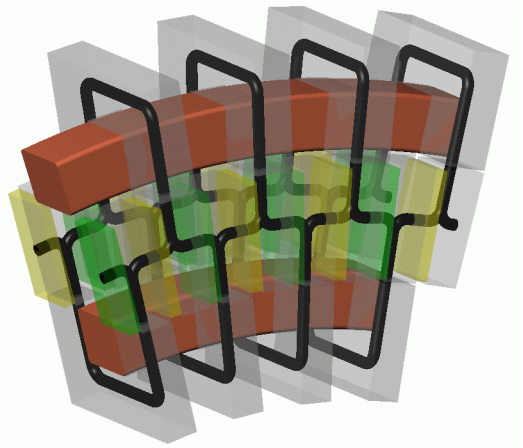

Fig. 2. Course of the magnetic flux in the transverse flux machine.

The movement is modeled using two 3D moving bands, where the connections between moving and stationary regions are considered with dynamic allocations of periodicity boundary conditions. With the magnetic vector potential formulation in 3D using edge elements, periodicity conditions have to be consistent with gauge conditions associated with trees of edges [3]. Such connection conditions have to be updated for each position during the movement. When the

calculation domain angle is exceeded, the moving part must be newly disposed in front of the stationary part and, if the study domain is anti-periodic, the rotor field sources must be inverted.

RESULTS AND DISCUSSIONS

The synchronous transversal flux prototype machine has been built by *Weg Industrias S.A. – Motores* and has the following design parameters:

Rated power: 10 KW
Rated phase voltage: 220 V
Rated phase current: 17.3 A
Rated speed: 200 rpm
Magnets: Nd-Fe-B
Number of pole pairs: 45.

The Nd-Fe-B permanent magnets on the rotor are magnetized with alternating polarity.

Considering the electromagnetic symmetries and using periodic boundary conditions, the smaller domain of study consists of an 8-degree sector of the whole structure. The 3D mesh without the air elements is shown in Fig. 3. In this figure we can see the stator, the coils, the rotor with the permanent magnets and the two moving bands (one inner and another external to the rotor). Each air gap was divided in three equal layers, being the moving band located in the central layer. Hexahedra in the moving band and prisms elsewhere have been used. The mesh of the structure has 40 divisions along the moving band.

Results are presented for a speed of 200 rpm and when the machine operates at no-load condition, i.e. only the permanent magnet excitation is considered. The simulation and measured results for the induced electromotive force (EMF) are shown in Fig. 4 and Fig. 5, respectively.

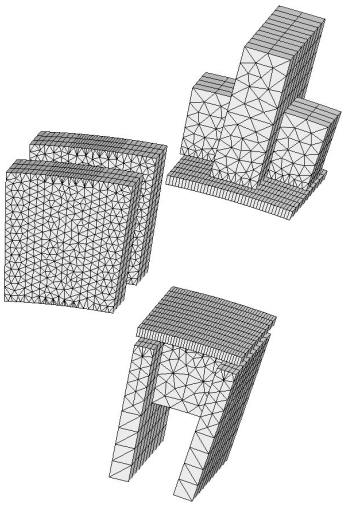

Fig. 3. The studied domain and 3D mesh.

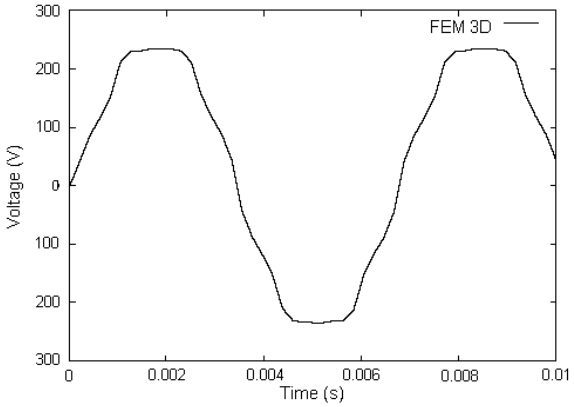

Fig. 4. EMF at 200 rpm – Simulation result.

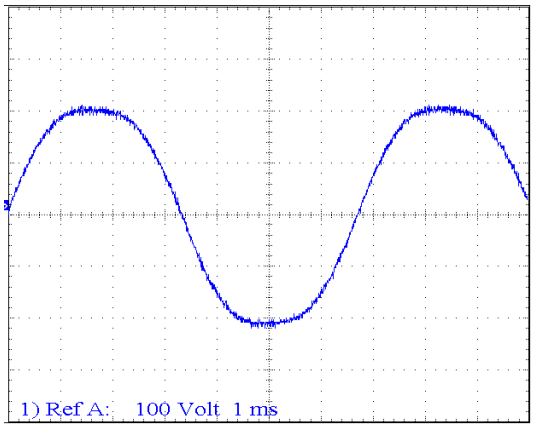

Fig. 5. EMF at 200 rpm – Measured result.

The agreement of calculated and measured electromotive forces is good in spite of some differences, which will be discussed in the extended paper. Others results will be also presented as, for example, eddy currents and associated losses. The advantages of the different numerical techniques used will be pointed out. The influence of iron non-linearities will be also studied.

REFERENCES

[1] H. Weh, H. Hoffmann, J. Landrath, "New permanent excited synchronous machine with high efficiently at low speed", *Proc. Int. Conference on Electrical Machines (ICEM)*, Vol. 3, pp. 35-40, 1988.

[2] M. Bork, R. Blissenbach, G. Henneberger, "Identification of the loss distribution in a transverse flux machine", *Proc. Int. Conference on Electrical Machines (ICEM)*, Vol. 3, pp. 1826-1831, 1998.

[3] M.V. Ferreira da Luz, P. Dular, N. Sadowski, C. Geuzaine, J.P.A. Bastos, "Analysis of a permanent magnet generator with dual formulations using periodicity conditions and moving band", *IEEE Trans. Magn.*, Vol. 38, No. 2, pp. 961-964, 2002.

Dynamics on Ferroresonance Circuit Exhibiting Chaotic Phenomenon

[1]Hisashi Endo, [2]Iliana Marinova, [1]Seiji Hayano, and [1]Yoshifuru Saito
[1]Graduate School of Engineering, Hosei University, [2]Technical University of Sofia, 1756 Sofia, Bulgaria
3-7-2 Kajino, Koganei, Tokyo 184-8584, JAPAN
E-mail: endo@ysaitoh.k.hosei.ac.jp

***Abstract*– This paper studies the chaotic phenomenon of ferroresonance circuit. At first, a state variable equation of the circuit is derived from a Chua-type magnetization model consisting of the nonlinear parameters. Second, the transient analysis of this system is carried out. Because of nonlinearity of the system, the characteristic values of the state transition matrix are calculated in each of iteration steps as well. Finally, it is clarified that the characteristic values trace on the same loci although exhibiting the chaotic phenomenon. This suggests that the changes of coercive forces are tightly related with the chaotic behaviors.**

INTRODUCTION

In the field calculation including ferromagnetic materials, we have to take into account magnetic hysteresis, saturation, aftereffects, frequency dependence, etc. at least [1]. For example, analyzing the ferroresonance circuits is difficult to work out due to such nonlinearity in dynamics. In the present paper, the nonlinear calculation with a Chua-type magnetization model, representing static as well as dynamics in ferromagnetism, carries out to a ferroresonance circuit analysis. To clarify the ferroresonance system, the characteristic values of the state variable equation are calculated in each of iteration steps. It reveals that they have no hysteretic properties even though exhibiting chaotic phenomenon.

FERRORESONANCE CIRCUIT ANALYSIS

Formulation

The Chua-type magnetization model gives the dynamic constitutive relation between magnetic field H (A/m) and flux density B (T) [2,3]:

$$H = \frac{1}{s}\frac{dH}{dt} + \frac{1}{\mu}B + \frac{1}{s}\frac{dB}{dt} \tag{1}$$

where μ, μ_r and s denote permeability (H/m), reversible permeability (H/m), and hysteresis parameter (Ω▪m), respectively. Fig.1 shows the typical curves giving the parameters of (1)[3]. Various phenomena in ferromagnetic materials, excepting for anisotropic materials, have been clarified by this model [4]. Apply (1) to the circuit shown in Fig.2, then the state equations (2) and (3) can be derived.

$$\frac{1}{s}\frac{d^2\varphi}{dt^2} + \frac{lR}{sAN^2}\frac{d\varphi}{dt} + \frac{lR}{AN^2} = \frac{1}{s}\frac{dv}{dt} + \frac{1}{sRC}v \tag{2}$$

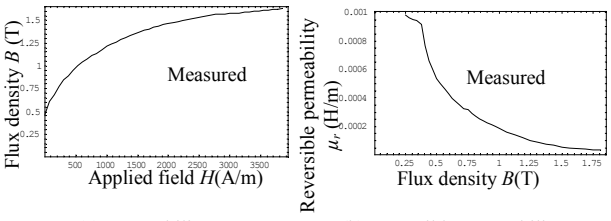

Fig. 1. Curves giving the parameters of Chua-type magnetization model (measured data of soft iron)

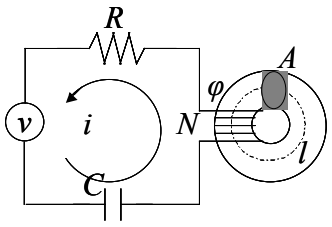

A : cross-sectional area (m²)
C : capacitance (F)
i : current (A)
l : flux path length (m)
N : number of coil turns
q : charge of capacitance (C)
R : resistance (Ω)
v : driving voltage (V)
φ : magnetic flux (Wb)
λ : linkage flux (Wb)

Fig. 2. Series ferroresonance circuit

$$\frac{dq}{dt} = \frac{1}{R}\frac{d\varphi}{dt} + \frac{1}{RC}q + \frac{1}{R}v \tag{3}$$

As a result, equations (2) and (3) are reduced into a state variable equation having 3×3 state transition matrix as in (4).

$$\frac{d}{dt}\begin{bmatrix} d\varphi/dt \\ \varphi \\ q \end{bmatrix} = \begin{bmatrix} 0 & 1 & 0 \\ a_{21} & a_{22} & a_{23} \\ 0 & a_{32} & a_{33} \end{bmatrix}\begin{bmatrix} d\varphi/dt \\ \varphi \\ q \end{bmatrix} + \begin{bmatrix} 0 \\ u_2 \\ u_3 \end{bmatrix} \tag{4}$$

Where the elements a_{21}, a_{22},…, u_2 and u_3 are determined by (2) and (3).

Results and discussions on chaotic phenomenon

Solving (4) with parameters listed in Table I yields a typical ferroresonance phenomenon shown in Fig.3. We calculate the characteristic values of the state transition matrix in each of iteration steps to clarify the nature of system.

TABLE I. CONSTANTS FOR CALCULATION OF FERRORESONANCE CIRCUIT

M : permeability (H/m)	Fig. 1(a)
μ_r : reversible permeability (H/m)	Fig. 1(b)
S : hysteresis parameter (Ω·m)	Fig. 1(c)
A : cross-sectional area (m^2)	48.6 x 10^{-6}
C : capacitance (F)	22.5 x 10^{-6}
L : flux path length (m)	78.3 x 10^{-3}
N : number of coil turns	180
R : resistance (Ω)	1.0

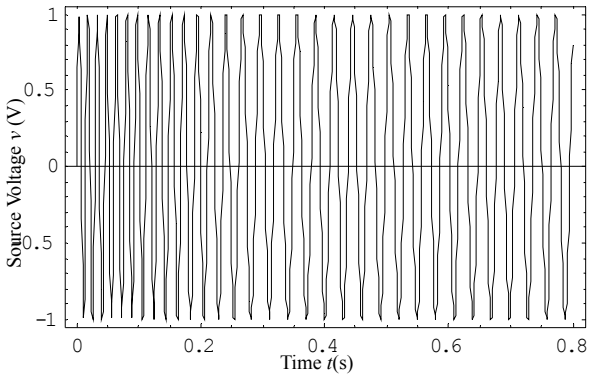

(a) Driving voltage v. Frequency is decreased from 70 to 33 Hz until t=0.29 s., then fixed.

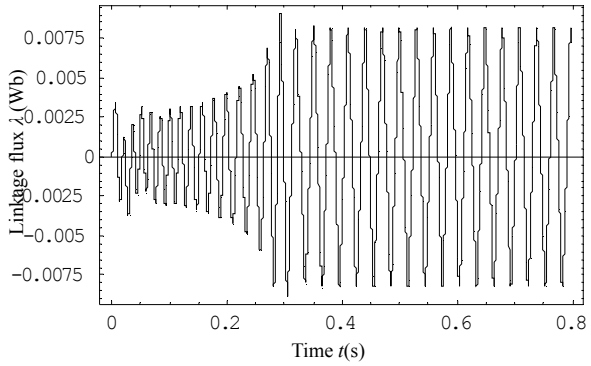

(b) Calculated linkage flux λ vs. time t

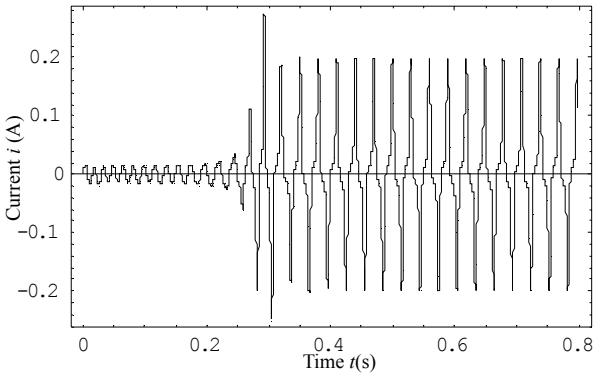

(c) Calculated current i vs. time t

Fig. 3. Transient analysis of the ferroresonance circuit

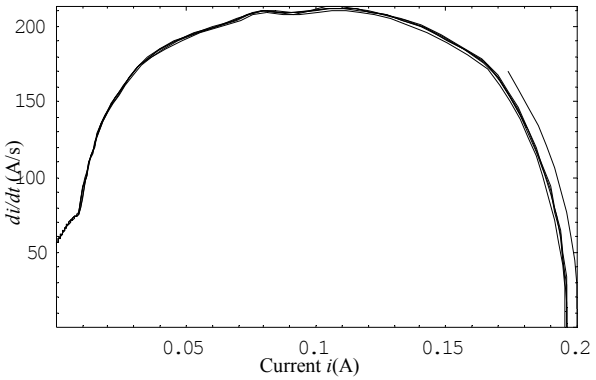

Fig. 4. Magnified trajectory of di/dt vs. i exhibiting a chaotic behavior (t=0.35~0.5s)

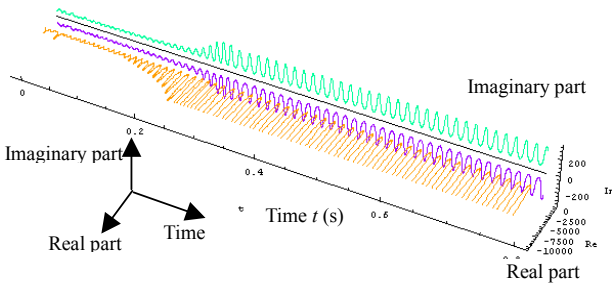

Fig. 5. Characteristic values changing of the state transition matrix

Fig.4 illustrates di/dt versus i, showing the chaotic behavior while the driving voltage frequency of is fixed. On the other hand, the characteristic values obtained from the state transition matrices in Fig.5 trace the same trajectory even though the chaotic phenomenon is exhibiting. This is because the parameters of the Chua-type magnetization model are independent of past history [3,4]. This means that the chaotic mode involves the right side terms of (2) in which coefficient μ_r/s is closely related to the coercive force [5].

REFERENCES

[1] Ivanyi, *Hysteresis Models in Electromagnetic Computation*, Budapest: Akademiai Kiado, 1997.

[2] L. O. Chua and K. A. Stromsmoe, "Lumped circuit models for nonlinear inductor exhibiting hysteresis loops," *IEEE Transactions on Circuit Theory*, vol.CT-17, no.4, pp.564-574, November 1970.

[3] Y. Saito, M. Namiki, and S. Hayano, "A magnetization model for computational magnetodynamics," *Journal of Applied Physics*, vol.69, no.8, pp.4614-4616, April 1991.

[4] Y. Saito, S. Hayano, and N. Tsuya, "Experimental verification of a Chua type magnetization model," *IEEE Transactions on Magnetics*, vol.MAG-25, no.4, pp. 2968-2970, July 1989.

[5] Y. Saito, S. Hayano, Y. Kishino, K. Fukushima, H. Nakamura, and N. Tsuya, "A representation of magnetic aftereffect," *IEEE Transactions on Magnetics*, vol.MAG-22, no.5, pp.647-649, September 1986.

The Magnetic Field Diffusion Equation Including Dynamic Hysteresis : Part 1: a linear formulation of the problem

M.A. Raulet, B.Ducharne, J.P.Masson, G. Bayada*
CEGELY, C.N.R.S. UMR 5005, Université Claude Bernard , Bât. Oméga
43 Bd du 11-11-1918, 69622 Villeurbanne Cedex., France.
*MAPLY, C.N.R.S. UMR 5585, INSA de Lyon, Bât. 401,
20, avenue Albert Enstein, 69621 Villeurbanne Cedex., France.

***Abstract*- the introduction of accurate material modeling such as hysteresis phenomenon in numerical field calculation leads to numerical problems induced by the non-linear properties of the initial system [1].**
We focus on the resolution of the magnetic field diffusion equation, which contains such problems.
This article presents a new formulation of the diffusion equation including dynamic hysteresis. The resulting formulation leads to a linear system to solve.
We submit a second article devoted to the numerical implementation of the problem.

INTRODUCTION

The resolution of the diffusion equation through the cross-section of an electrical sheet and taking into account the material hysteresis dynamic law leads to numerical problems involved in the non-linearity of the system.

We already implemented an hysteresis dynamic model in the diffusion equation of the magnetic excitation field [2]. The resolution of the whole diffusion model leads to accurate results but numerical problems of convergence appear in particular cases.

We present in this article how a new formulation of the diffusion problem coupled to an hysteresis dynamic material law leads to a linear system to be solved.

PROBLEM

Hypothesis

The diffusion equation is solved through a cross-section sheet of an Epstein frame. The design assumptions are those of the Epstein frame: unidirectional and homogeneous surface excitation field (according to the length of the sheet). The conductivity σ of the magnetic sheet is constant and homogeneous.

Taking into account dimensions of the studied sheets (width much more significant than the thickness), a 1D study according to the thickness of the sheet is carried out [3]. This 1D study also limits the number of the variables of the problem. This simplification constitutes a significant profit with the integration of an hysteresis model.

Material law

If a static reversible material law B(H) is considered in the diffusion equation, the resolution of this one is easy but leads to inaccurate results. In this case the dynamic effects related to the wall motions are neglected.

Previous work [2] has presented a property dynamic model (and hysteretic) of material. This model based on the resolution of a differential equation (1) was tested and integrated in a traditional way in the diffusion equation. This implementation was performed using the term of permeability $\mu = B/H$ with B obtained by the model of the material law.

This material law represents a statistical behavior of the wall motions. It can then be considered as isotropic and characteristic of the material.

$$\frac{dB}{dt} = \frac{1}{\beta}[H - Hstat(B)] \qquad (1)$$

B represents the magnetic field, H the magnetic resulting excitation field and Hstat(B) a fictitious value calculated from a static model of material law. The coefficient β is independent of the geometry of the studied sample and of its excitation. It is a coefficient characteristic of the material dynamic wall motions.

The whole model of diffusion leads to obtain a non-linear system, which is solved by the Newton Raphson's Algorithm. The resolution gives accurate results but sometimes presents numerical problems of convergence related to the non-linearity [4].

NEW FORMULATION OF THE DIFFUSION PROBLEM

Principle

The idea of the new formulation comes from the expression (1), which defines the law of the material dynamic property. The dB/dt term at the first member of the equation (1) constitutes also a part of the second member of the diffusion equation (2).

$$\frac{\partial^2 H(y,t)}{\partial y^2} = \sigma . \frac{\partial B(y,t)}{\partial t} \qquad (2)$$

It is natural to replace the dB/dt term of the equation (2) by the second member of the equation (1), which gives a new formulation of the diffusion equation (3):

$$\frac{\partial^2 H(y,t)}{\partial y^2} = \sigma.\frac{1}{\beta}.[H(y,t) - Hstat(B(y,t))] \qquad (3)$$

This equation coupled with the equation (1), which defines the material law, does not reveal any more the term of permeability μ, which is responsible of the non-linearity of the system to be solved.

Writing of the linear system

Taking into accounts the simplicity of the study domain (half thickness of the sheet illustrated on figure (1)), a formulation by finite differences method of the diffusion equation is carried out.

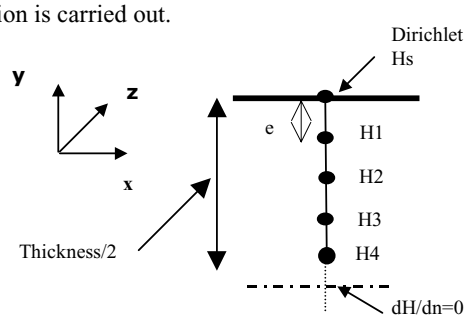

Fig. 1. One dimension problem

The new system obtained is:

$$\begin{bmatrix} \frac{\sigma e^2}{\beta}+2 & -1 & 0 & 0 \\ -1 & \frac{\sigma e^2}{\beta}+2 & -1 & 0 \\ 0 & -1 & \frac{\sigma e^2}{\beta}+2 & -1 \\ 0 & 0 & -2 & \frac{\sigma e^2}{\beta}+2 \end{bmatrix} \begin{bmatrix} H1 \\ H2 \\ H3 \\ H4 \end{bmatrix} = \begin{bmatrix} Hs \\ 0 \\ 0 \\ 0 \end{bmatrix} + \begin{bmatrix} \frac{\sigma e^2}{\beta}.H1_{stat}(B_1) \\ \frac{\sigma e^2}{\beta}.H2_{stat}(B_2) \\ \frac{\sigma e^2}{\beta}.H3_{stat}(B_3) \\ \frac{\sigma e^2}{\beta}.H4_{stat}(B_4) \end{bmatrix}$$

This system is linear; the stiffness matrix contains only constant terms. The second member can be divided into two terms:

- A term, which only depends on the excitation field Hs on the surface of the sheet and on the initial conditions.
- A term made up of values Hstat(Bi), which come from the model of the material law.

The numerical implementation of the problem is described in another submitted article.

EXPERIMENTAL VALIDATION – PERFORMANCES

In order to test the results of simulations corresponding to the new formulation of the whole diffusion equation, we carried out tests on Epstein frame sheets. These sheets are made of pure iron; the quality is M700P65, the thickness 0.65 mm, the width 30 mm. The σ conductivity is identified to the value of 0.033 $S.m^{-1}$. The resolution of the diffusion equation gives the local values of B(y, t), which can be used to calculate the whole flux. This value can be compared with experimental data.

Figure (2) shows the superposition of simulated and measured averaged dynamic loops when the surface excitation field Hs is 50 Hz frequency sine wave with 50 % of harmonic 3. We can note that the diffusion model is reliable.

This simulation case had been tested with the old formulation of the diffusion equation. The resolution, which had then raised some convergence difficulty, imposed the use of very high accuracy criterion [4].

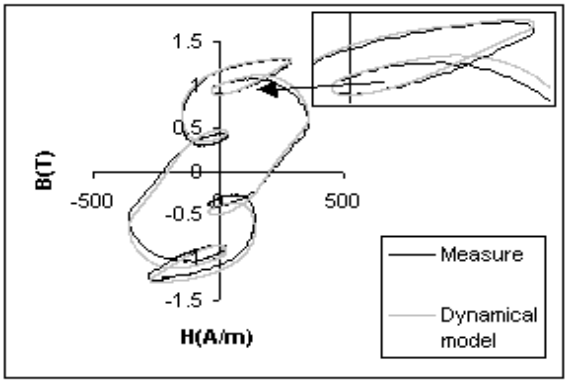

Fig. 2 : dynamical loops with 50 Hz sine wave excitation with harmonic 3

CONCLUSION

A new formulation of the diffusion equation including dynamic hysteresis is presented. This new formulation leads to the resolution of a linear system, which avoids many numerical problems. Local results are available. The global results are validated with experimental data.

The final article will detail this new formulation and will show the performances of the presented diffusion model.

REFERENCES

[1] F Henrotte "Modelling ferromagnetic materials in 2D finite element problems using Preisach's model".IEEE Transaction on magnetics, Vol. 28, n°5, September 1992.

[2] M.A. Raulet, J.P. Masson, D. Gaude. "Presentation and experimental validation of a behavioral model of dynamic properties for magnetic materials"J. Phys IV, France 8 (1998) Pr2-619-622.

[3] M.A. Raulet, J.P. Masson, A. Nicolas "Reduction of a 2D problem of magnetic field diffusion including dynamic hysteresis through the cross section of a magnetic lamination. COMPUMAG, Sapporo October 25-28 1999, Japan.

[4] Modélisation des pertes et du cycle d'hystérésis dynamique des tôles magnétiques Revue Internationale de Génie Electrique Vol. 5, N° 2/20

Comparison of Identification Methods for Stop Model with Input-Dependent Shape Function

T. Matsuo, Y. Terada and M. Shimasaki
Graduate School of Engineering, Kyoto University, Kyoto 606-8501, Japan
email : tmatsuo@kuee.kyoto-u.ac.jp

Abstract— **Representation ability of the stop model is improved by introducing an input-dependent shape function. Several identification methods for the stop model having the input-dependent shape function are compared. The comparison shows that improved stop models satisfactorily represent the hysteretic characteristics of a silicon steel sheet.**

Introduction

Since the stop model [1], [2] can provide a hysteretic output of H from an input of B, it can be an efficient tool for magnetic-field analysis using magnetic vector potential. A previous study [3], however, has shown that the stop model cannot sufficiently represent hysteretic characteristics of a silicon steel sheet. In order to improve the hysteretic representation of the stop model, the present paper proposes an input-dependent shape function.

Stop Model with Input-Dependent Shape Function

The stop model describes a hysteretic relation between B and H as

$$H = h(B) = \int_0^{B_s} g(\eta, s_\eta(B), B)\mathrm{d}\eta \qquad (1)$$

where B_s is the saturation magnetic flux density, s_η is the stop hysteron operator with height η, and $g(\eta, s, B)$ is the shape function.

This stop model has the property of equal vertical chords [2] if the shape function $g(\eta, s, B)$ is independent of the input B as

$$g(\eta, s, B) = g(\eta, s)\ . \qquad (2)$$

A previous study [3] has shown that the magnetic characteristics of a silicon steel sheet do not satisfy the property of equal vertical chords, and that accordingly the stop model cannot sufficiently represent hysteretic characteristics of the silicon steel sheet.

In order to improve the hysteretic representation of the stop model, the present paper introduces an input-dependent shape function that is given by

$$g(\eta, s, B) = g_0(\eta, s)w(B) \qquad (3)$$

where in the present paper $w(B)$ is called the weighting function. Equations (1) and (3) lead to

$$\frac{h(B)}{w(B)} = \int_0^{B_s} g_0(\eta, s_\eta(B))\mathrm{d}\eta\ . \qquad (4)$$

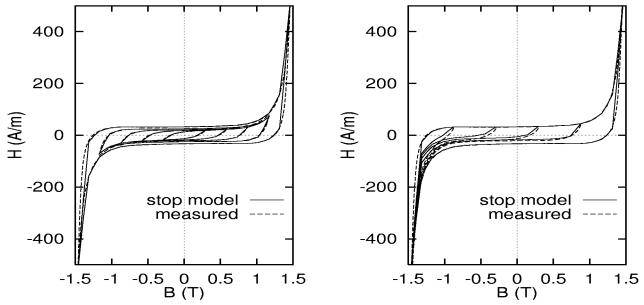

(a) symmetric loops (b) asymmetric loops

Fig. 1. Stop model identified from symmetric loops with Eq. (5).

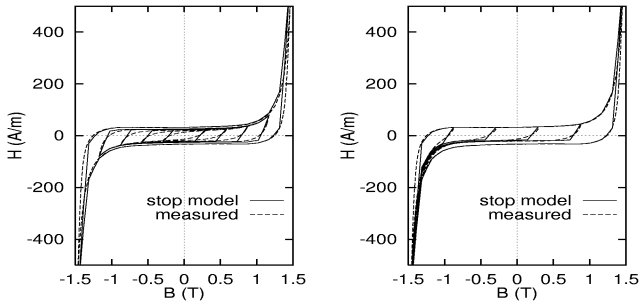

(a) symmetric loops (b) asymmetric loops

Fig. 2. Stop model identified from asymmetric loops with Eq. (5).

Since the right-hand side of (4) represents the stop model with an input-independent shape function, $h(B)/w(B)$ should have the property of equal vertical chords.

The present paper set the weighting function $w(B)$ as

$$w(B) = \max(h_{M+}(B) - h_{M-}(B), w_{\min}) \qquad (5)$$

where $h_{M\pm}(B)$ denotes the ascending and descending curves of the major hysteresis loop, respectively, and $w_{\min}$ is a small positive constant that prevents $w(B)$ from being 0. The hysteretic characteristics of $h(B)/w(B)$ with (5) have a major hysteresis loop that has a constant loop-width along the H-direction independently from B. Since the major hysteresis loop has the maximum loop-width among all the B-H loops, $h(B)/w(B)$ is expected to have the property of approximately equal vertical chords.

Hysteretic characteristics of a non-oriented silicon steel sheet (JIS: 50A290) are measured and represented by the stop model with the weighting function (5), where $g_0(\eta, s)$ is determined by the identification method in [2]. Figs. 1 and 2 show the B-H curves given by the stop model

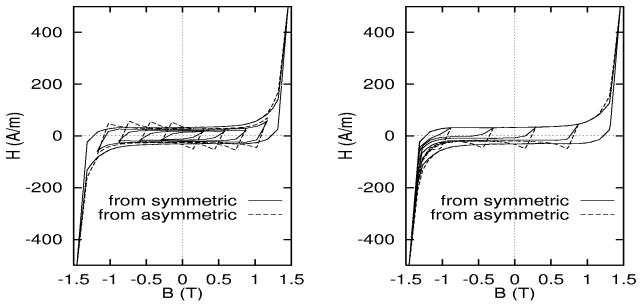

(a) symmetric loops (b) asymmetric loops

Fig. 3. Stop model with input-independent shape function.

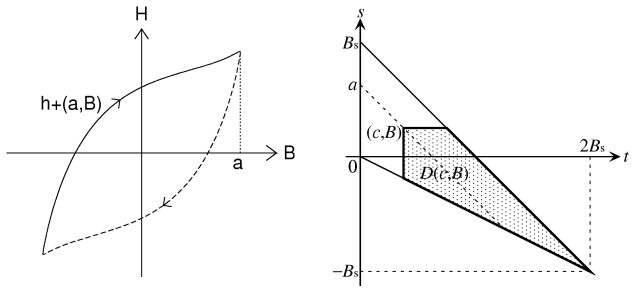

(a) $h_+(a,B)$ (b) integral domain for $D(c,B)$

Fig. 4. Ascending curve with amplitude a: $h_+(a,B)$.

identified from symmetric and asymmetric B-H loops [3], respectively. Fig. 3 shows the hysteretic characteristics represented by the stop model with the weighting function $w(B) = 1$.

Comparison of Figs. 1 and 2 with Fig. 3 shows that the weighting function (5) improves the representation of hysteretic characteristics.

A New Identification Method

The identification method proposed in [2] uses only loop-widths along the H-direction and does not use the shapes of B-H loops. The present paper proposes a new identification method that uses the shapes of symmetric B-H loops. By defining $\kappa(\eta, s) = \partial g_0(\eta, s)/\partial s$, $h(B)/w(B)$ is written as

$$\frac{h(B)}{w(B)} = \int_0^{B_s} \int_{-\eta}^{s_\eta(B)} \kappa(\eta, s) \mathrm{d}s\mathrm{d}\eta + \frac{h(-B_s)}{w(-B_s)} \ . \qquad (6)$$

The ascending curve of the symmetric B-H loop with amplitude a (see Fig. 4) is given by

$$\frac{h_+(a,B)}{w(B)} - \frac{h(-B_s)}{w(-B_s)} = \int_{\frac{a-B}{2}}^{B_s} \int_{-\eta}^{\bar{s}} \kappa(\eta, s)\, \mathrm{d}s\mathrm{d}\eta = D(c,B) \qquad (7)$$

$$D(c,B) = \int_c^{2B_s} \int_{-t/2}^{\min(B, -t+B_s)} \hat{\kappa}(t,s)\, \mathrm{d}s\mathrm{d}t \qquad (8)$$

where $\bar{s} = \min(B, \eta - a + B)$, $c = a - B$, $t = \eta - s$, and $\hat{\kappa}(t,s) = \kappa(\eta, s)$ $(-t/2 \le s \le -t + B_s, 0 \le t)$. Equation (8) leads to

$$\kappa(a,B) = \hat{\kappa}(c,B) = -\frac{\partial^2 D(c,B)}{\partial c \partial B} \ . \qquad (9)$$

Fig. 5 shows the hysteretic characteristics identified by the above method using (5), where smoother B-H curves are obtained than those in Figs. 1 and 2.

Identification by Least-Square Method

A least-square method can be applied to the identification of the stop model. The least-square method determines the shape function g_0 so as to minimize

$$\sum_i \left| \frac{H_0(B_i)}{w(B_i)} - \frac{h(B_i)}{w(B_i)} \right|^2 \qquad (10)$$

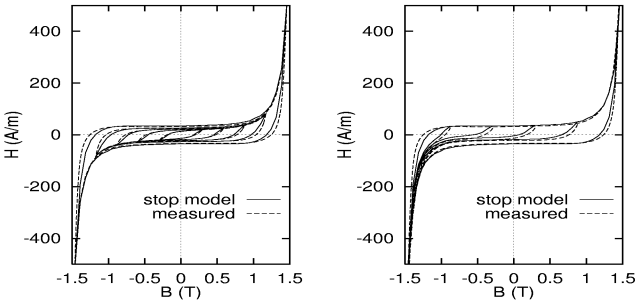

(a) symmetric loops (b) asymmetric loops

Fig. 5. Stop model identified by proposed method.

where B_i $(i = 1, 2, \ldots)$ is an input sequence and H_0 is a measured output sequence of the magnetic field. Fig. 6 shows the hysteretic characteristics identified by the least-square method using (5), where the input sequence is given by both the symmetric and asymmetric B-H loops. The least-square method achieves a more precise representation as seen in Fig. 6 than do the other identification methods as shown in Figs. 1, 2, and 5, at the cost of much longer computation time.

References

[1] S. Bobbio, G. Miano, C. Serpico and C. Visone, *IEEE Trans. Magn.*, vol. 33, pp. 4417-4426, 1997.

[2] T. Matsuo and M. Shimasaki, *IEEE Trans. Magn.*, vol. 37, pp. 3357-3361 and p. 3995, 2001.

[3] T. Matsuo D. Shimode, Y. Terada and M. Shimasaki, CEFC 2002, P6-6, p. 175, 2002.

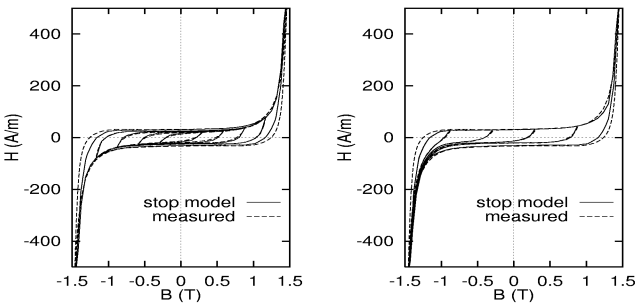

(a) symmetric loops (b) asymmetric loops

Fig. 6. Stop model identified by least-square method.

Increasing the Accuracy of the Numerical Identification of the Modified Scalar Preisach Model

E. Cardelli[1], G. Finocchio[2] and E. Pinzaglia[1]
1 University of Perugia, Department of Industrial Engineering
Via G. Duranti, 67, Perugia I-06125, Italy (e-mail: ermanno2@unipg.it)
2 University of Messina, Dipartimento di Fisica della Materia e Tecnologie Fisiche Avanzate
Salita Sperone 31, 98166 Messina, Italy

Abstract— In this paper we discuss in general the numerical problem of the identification of the Preisach function in the Modified Scalar Preisach Model (MSPM), for soft materials. We show that the solution of the inverse problem using a bilinear algebraic system approach introduces a numerical error: this error can be avoided, or greatly reduced, using a simple recursive technique explained in the paper. We show the results obtained for laminated magnetic steels, and in particular the shape of the functions of the MSPM.

INTRODUCTION

The numerical estimation of the Preisach function in the modeling of magnetic hysteresis for soft materials [1], [2], [3] has some numerical difficulties. One of them is the accurate calculation of the one-dimensional product function from the measured hysteresis loops. The use of bilinear algebraic equation systems, as suggested by some Authors [4] [5] introduces, in fact, large numerical errors in the computation of this function. These errors are not compatible with the physical meaning, even if, using a set of reconstructed first reversal curves, it is possible to estimate the complete form of the Preisach function with acceptable accuracy.

In this paper we present and discuss this numerical problem, and its possible solution using an iterative Successive Over-Relaxation (SOR) technique, in order to obtain with accuracy the shape of the one-dimensional product function for magnetic soft materials.

IDENTIFICATION PROCEDURE AND NUMERICAL ERROR

The MSPM is a type of so called product models of one dimensional hysteresis [5] [6], and has the following typical mathematical shape:

$$\frac{dM}{dH} = K(M)\left[W(H) + 2P_s(H)\int_{-H_s}^{H} P_s(-V)\,dV\right] \tag{1}$$

referred to the case of monotonic increasing of the applied magnetic field H. For decreasing fields MSPM has an analogous shape, In (1) H_s is the value of the applied magnetic field at saturation state, W is a the reversible component of the magnetization, and K is a function of M that introduces the non congruency for minor loops. The function P_s is the one-dimensional product function mentioned in the introduction section, defined as follows:

$$P(U,V) = P_s(U)P_s(-V) \tag{2}$$

where $P(U,V)$ is the Preisach distribution function.

In order to show as the numerical error can be generated during the identification procedure we take into account firstly the Classical Scalar Preisach Model (CSPM) that is a reduced case of the MSPM, with K=1 and W=0, but with a problem of identification of the same kind.

Starting from the differential formulation (1), if we know n values of magnetic field in the major loop (n must be even) we can rewrite (1) in the following discretized way:

$$\sum_{i=n-j+1}^{n} P_s(H_i) = \frac{\frac{dM}{dH}(H_j)}{2dHP_s(H_j)}, \quad j = 1,\ldots,n \tag{3}$$

The analytical solution of the bilinear system (3) can be found with these recursive formulas:

$$P_s(H_{n-i+1}) = k_{n-i}P_s(H_{n-i}), \quad for\, i = 1,\ldots,\frac{n}{2}-1 \tag{4}$$

$$P_s(H_i) = \frac{\frac{dM}{dH}(H_i)}{2dHk_iP_s(H_{n-i+1})}, \quad for\ i = 1,\ldots,\frac{n}{2} \tag{5}$$

where:

$$k_{n-i} = \frac{\frac{dM}{dH}(H_{n-i})}{\frac{dM}{dH}(H_{n-i-1})} - \frac{\frac{dM}{dH}(H_{i+1})}{k_{i+1}\frac{dM}{dH}(H_{n-i-1})},$$

$$for\ i = 0,\ldots,\frac{n}{2}-1 \tag{6}$$

$$k_i = 1 + k_{n-i+2}k_{i-1}, \quad for\, i = 2,\ldots,\frac{n}{2} \tag{7}$$

$$k_1 = 1 \tag{8}$$

The starting value of these recurrence formulas is:

$$P_s(H_{n/2+1}) = \sqrt{\frac{\frac{dM}{dH}(H_{n/2+1}) - \frac{1}{k_{n/2}}\frac{dM}{dH}(H_{n/2})}{k_{n/2}}} \tag{9}$$

A first problem of this numerical technique for the identification of P_s is in the expression (6). The value of the derivative of the major loop goes to zero for values of the magnetic field approaching to saturation, so in (6) the denominators are both nearly zero for i=1.

As from the value of k_{n-1} are calculated the others, using (6) and (7), so all the k_i are affected from this kind of numerical error.

Another source of numerical error is due to the expression (5). The value of $P_s(H_i)$ for $i<n/2+1$ is calculated with the expression (5) in function of the value of $P_s(H_i)$ for $i>n/2$. These last values go to zero as i goes n; so the value of $P_s(H_i)$

for $i<n/2+1$ goes to a positive, large value as i goes to 1. Note that the bilinear system above has no solution for asymmetric distribution respect to zero of $\frac{dM}{dH}$.

In figure 1 we can see a typical trend of the function P_s calculated with the above method, and the value corrected using the numerical technique described in the next section. The P_s obtained using the bilinear algebraic equation system approach has a large error and its shape has no physical meaning, but it can be employed in order to obtain the Preisach function.

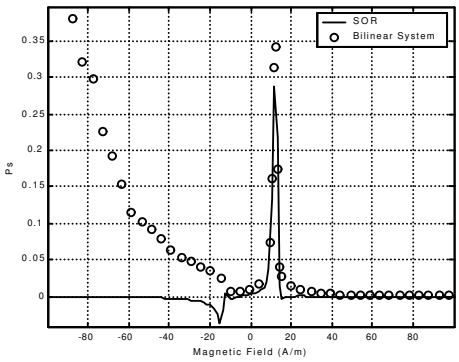

Fig.1 . Typical error in the identification of P_s using the bilinear equation system approach

In fact it is not difficult to calculate the reversal curves of first order (see Ref. [1] p. 18), and to use these curves to calculate $P(U,V)$ with the following expression:

$$P(U,V)=\frac{\partial^2 M}{\partial U\,\partial V} \tag{10}$$

The product function P_s can be calculated from the Preisach function only for positive values of H with the following formula:

$$P_s=\sqrt{P(H,-H)} \tag{11}$$

NUMERIC METHOD TO IMPROVE THE ACCURACY OF THE IDENTIFICATION PROCEDURE

The numerical technique we propose to calculate the one dimensional product function P_s is based on a SOR iterative method. This procedure is composed of the following steps:

1. we assume that:

$$P_s(H)=\frac{dM_l}{dH} \tag{12}$$

where M_l is the magnetization of the lower branch of the major loop.

2. We compute the following function of the magnetic field:

$$\Delta P_s(H)=\frac{dM_l}{dH}-2P_s(H)\int_{-Hs}^{H}P_s(-V)\,dV \tag{13}$$

3. If $\Delta P_s(H)$ has a small value we stop the process, or we go to the next point.
4. We recalculate the one dimensional product function with the following:

$$P_s(H)=P_s(H)+\alpha\Delta P_s(H) \tag{14}$$

and we come back to the point a).

The extension of the method presented from the case of the CSPM to the case of the MSPM is rather easy: in this case we must use in addition the measured virgin curve. So we can compute again the function W at each iteration with the following formula:

$$W(H)=\frac{1}{K(M)}\frac{dM_v}{dH}-2P_s(H)\int_{-H}^{H}P_s(-V)\,dV \tag{15}$$

where M_v is the magnetization along the virgin curve.

With this procedure we have obtained encouraging results, as shown in figure 2, where we report the values of the major loop calculated using the MSPM for a laminated magnetic iron, and the measured data.

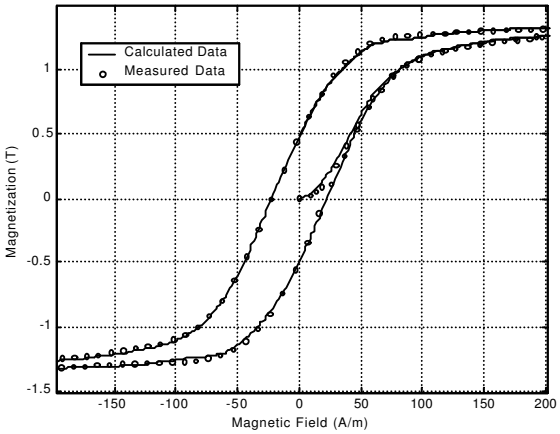

Fig.2 . Comparison between the measured major loop and virgin curve of a laminated not oriented grain magnetic steel cut at 90 degrees and the same data calculated with the proposed technique.

In the extended version of the paper we will show the numerical results obtained more in detail, and will discuss about the typical shape of P_s found.

REFERENCES

[1] I. D. Mayergoyz, Mathematical Models of Hysteresis, Springer- Verlag, 1991.
[2] G. Bertotti, *Hysteresis in Magnetism*, Academic Press, 1998.
[3] E. Della Torre, *Magnetic Hysteresis*, IEEE Press, 1999.
[4] G. Kadar, "On the Preisach function of ferromagnetic hysteresis", *J. of Applied Phys*., Vol. 61, No. 8, April 1987, pp. 4013-4015.
[5] E. Cardelli, E. Della Torre, G. Ban, "Experimental Determination of Preisach Distribution Functions in Magnetic Cores", *Physica B*, 275, pp.262-269, 2000.
[6] E. Cardelli, E. Della Torre, L. Fiorucci, "Identification of the Preisach Probability Function for Soft Magnetic Materials", *IEEE Transactions on Magnetics, vol.* 36, pp.3366-3369, September 2001.

COMPUMAG Saratoga Springs, New York USA
July 13 - 17, 2003

Time-Domain Simulation of Nonlinear Inductors Displaying Hysteresis

John Paul, Christos Christopoulos and David W. P. Thomas
School of Electrical and Electronic Engineering,
University of Nottingham, Nottingham, NG7 2RD, U.K.
E-mail: jdp@eee.nottingham.ac.uk

***Abstract*—A method for the time-domain simulation of nonlinear inductors displaying hysteresis is outlined. The technique is based on the incorporation of the Jiles-Atherton magnetization model into the Transmission-Line Modeling (TLM) method for lumped circuits. The approach was validated using a simple circuit containing a voltage source, a series resistor and a hysteretic inductor. Close agreements were obtained for the power lost to hysteresis and the series resistor compared with the power delivered by the source.**

Introduction

The major difficulty in the simulation of inductors having a ferromagnetic core is that the magnetization curve displays hysteresis, that is the relationship between the magnetic field intensity and the magnetic flux density is not a one-to-one function, but instead depends on the magnetic history of the sample. The approach developed by Jiles and Atherton (J-A) [1, 2] is well suited for inclusion in Transmission-Line Modeling (TLM) for lumped components because it is formulated in terms of a first-order differential equation.

In previous work, [3], the modeling of nonlinear dielectric materials using TLM has been presented. As an extension to the technique, the simulation of inductors by the inclusion of the J-A hysteresis model in the TLM method is described here. The paper is organized as follows: Firstly, the development of the TLM algorithm is described, next, an outline the J-A technique is given and it's incorporation into TLM is described. To validate the algorithm, a simulation is performed for a nonlinear inductor displaying hysteresis.

Formulation

Consider a nonlinear inductor carrying a current I_L with a voltage V_L dropped across it. The branch constraint for an inductor is $V_L = d\Psi/dt$ where Ψ is the total flux linkage. The flux ϕ is related to the total flux linkage by $\Psi = N\phi$, where N is the number of turns in the winding. The flux density is given by $B = \phi A$ where A is the area of the core. The constitutive relation for the flux density is $B = \mu_0(H + M)$ where μ_0 is the permeability of free-space, H is the magnetic field intensity and M is the magnetization intensity. From Ampère's law, the magnetic field intensity is given by $H = I_L N/l$ where l is the mean length of the magnetic path. By combining these relationships and defining $L_0 = \mu_0 N^2 A/l$ and $M = I_m N/l$ where I_m is the normalized magnetization, gives

$$V_L = L_0 \frac{dI_L}{dt} + L_0 \frac{dI_m}{dt} = V_0 + V_m \tag{1}$$

where V_0 is the voltage drop due to rate of change of I_L and V_m is the voltage drop due to the rate of change of I_m.

Inductor model The TLM model of (1) follows from the bilinear approximation of the time-derivative, i.e.,

$$\frac{d}{dt} = \frac{2}{\Delta t}\left(\frac{1 - z^{-1}}{1 + z^{-1}}\right) \tag{2}$$

where Δt is the simulation time-step and z^{-1} is the time-shift operator. Using (2) in (1) to obtain V_0 and V_m gives

$$V_0 = 2V_0^i + Z_0 I_L \qquad V_m = 2V_m^i + Z_0 I_m \tag{3}$$

where $2V_0^i = -z^{-1}(V_0 + Z_0 I_L)$, $2V_m^i = -z^{-1}(V_m + Z_0 I_m)$ and $Z_0 = 2L_0/\Delta t$. The voltage across the inductor is

$$V_L = Z_0 I_L + Z_0 I_m + 2V_0^i + 2V_m^i \tag{4}$$

For a circuit consisting of a voltage source V_s in series with a resistor R_s connected to the inductor,

$$V_s - V_L = I_L R_s \tag{5}$$

Using (5) to eliminate V_L from (4) gives

$$(Z_0 + R_s)I_L + Z_0 I_m - U_m = 0 = f(I_L, I_m, U_m) \tag{6}$$

where $U_m = V_s - 2V_0^i - 2V_m^i$. For an inductor with a ferromagnetic core, $I_m = I_m(I_L, I_m)$, so an iterative process is necessary to solve for $f = 0$ in (6).

Jiles-Atherton model In the J-A model, [1, 2], the magnetization is split into two parts, the anhysteretic magnetization and the irreversible magnetization. In normalized form, this is expressed by

$$I_m = \beta_c I_{an} + (1 - \beta_c) I_{irr} \tag{7}$$

where $0 \leq \beta_c \leq 1$, I_{an} is the normalized anhysteretic magnetization and I_{irr} is the normalized irreversible magnetization. The anhysteretic magnetization curve is given by a modified Langevin function, i.e.

$$I_{an} = I_s\left[\coth\left(\frac{I_L + \alpha I_m}{I_a}\right) - \frac{I_a}{I_L + \alpha I_m}\right] = I_s L(\gamma) \tag{8}$$

where I_s, α, I_a are positive constants, $L(\gamma)$ denotes the modified Langevin function and $\gamma = (I_L + \alpha I_m)/I_a$. In the J-A model, the change in irreversible magnetization is

$$\Delta I_{irr} = \left[\frac{\delta_M(I_{an} - I_{irr})}{\delta I_c - \alpha(I_{an} - I_{irr})}\right]\Delta I_L \tag{9}$$

In (9), $\Delta I_{irr} = I_{irr} - z^{-1}I_{irr}$, $\Delta I_L = I_L - z^{-1}I_L$, I_c is a positive coefficient and the migration flag δ_M is given by [2]:

$$\delta_M = \begin{cases} 1 & : \text{ if } \Delta I_L > 0 \text{ and } I_{an} > I_{irr} \\ 1 & : \text{ if } \Delta I_L < 0 \text{ and } I_{an} < I_{irr} \\ 0 & : \text{ otherwise} \end{cases} \quad (10)$$

Also in (9), the directional flag $\delta = 1$ for $\Delta I_L \geq 0$, otherwise $\delta = -1$.

Numerical Algorithm In the TLM model, the J-A equations (8—10) are solved as part of a Newton-Raphson (N-R) iteration to yield $f = 0$ in (6). To implement the N-R procedure, the derivative of the total magnetization curve with respect to the magnetic field is required, from (7),

$$\partial I_m/\partial I_L = \beta_c \partial I_{an}/\partial I_L + (1-\beta_c)\partial I_{irr}/\partial I_L \quad (11)$$

The derivative $\partial I_{an}/\partial I_L = [-\text{cosech}^2(\gamma) + 1/\gamma^2]/I_a$ and $\partial I_{irr}/\partial I_L = \Delta I_{irr}/\Delta I_L$ if $|\Delta I_L| > 0$, otherwise $\partial I_{irr}/\partial I_L = 0$. At iteration k, the N-R process is

$$\begin{aligned} {}_{k+1}I_L &= {}_kI_L - \frac{(Z_0 + Rs)_k I_L + Z_0\,{}_kI_m - U_m}{Z_0 + R_s + Z_0\,{}_k\partial I_m/\partial I_L} \\ {}_{k+1}I_m &= \left(U_m - (Z_0 + Rs)_{k+1}I_L\right)/Z_0 \end{aligned} \quad (12)$$

To aid convergence, the starting values for (12) are the values of I_L and I_m at the previous time-step. The algorithm described requires the storage of six real numbers, i.e. $\{V_0^i, V_m^i, I_L, \Delta I_L, I_m, I_{irr}\}$.

Results

As a simple example, consider an inductor consisting of $N = 230$ turns wound on a ferromagnetic core having a mean magnetic path length of $l = 75.4$mm and a cross-sectional area of $A = 45.4\text{mm}^2$. The material properties of the core were $M_s = 275$kA/m, $H_a = 14.1$A/m, $\alpha = 5 \times 10^{-5}$, $H_c = 17.8$A/m and $\beta_c = 0.55$ [2]. The voltage source was specified as $V_s = V_{s,pk}(1 - \exp(-\zeta t))\sin\omega_0 t$ where $V_{s,pk} = 5$V, $\zeta = 20\text{s}^{-1}$ and $\omega_0 = 2\pi f_0$, where $f_0 = 50$Hz. The resistor in series with the voltage source had a resistance of $R_s = 220\Omega$. The simulation time-step was $\Delta t = 100\mu$s and the number of time-steps was 2000. The convergence parameter of (12) was set at 10^{-8}A and an average of about 12 steps were required for convergence.

Fig. 1 shows the inductor voltage and current and Fig. 2 shows the $B-H$ relation of the core. To provide a check on the time-domain solution, the power lost to hysteresis and the power dissipated in the series resistor is compared with the power supplied by the source. The energy lost to hysteresis per cycle $T = 1/f_0$ is

$$w_h = \int_T H_z\, dB_z \simeq \sum_T H_z\, \Delta B_z \quad (13)$$

By evaluating numerically the summation in (13) over the final source cycle gave $w_h = 7.744\text{J/m}^3$, so the power lost in the inductor is $P_h = w_h\, A\, l\, f_0 = 1.325$mW. The power supplied by the source was obtained from $P_s = (1/T)\sum_T V_s I_L \Delta t$. The power dissipated in the inductor and resistor were found from similar expressions. Numerical evaluation of these summations gave $P_s = 50.02$mW, $P_r = 48.70$mW and $P_l = 1.324\text{mW} \simeq P_l$.

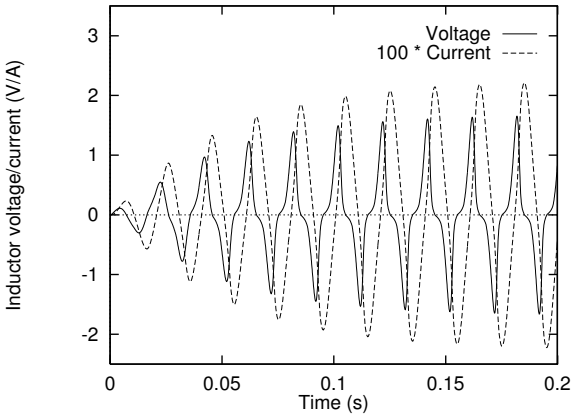

Figure 1: Inductor voltage and current

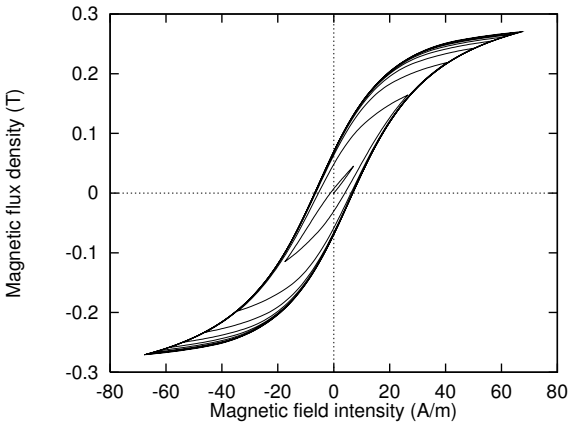

Figure 2: B–H relation of the inductor

Conclusion

A time-domain method for the simulation of nonlinear inductors displaying hysteresis was outlined. The approach was based on the incorporation of the Jiles-Atherton hysteresis model in TLM. The technique was validated by comparing the power dissipated due to hysteresis and the series resistance with the power supplied by the source. In future work, the method will be applied to magnetic circuit simulation, pulse problems and extended to deal with rate-dependent hysteresis.

References

[1] D. C. Jiles, J. B. Thoelke and M. K. Devine. Numerical Determination of Hysteresis Parameters for the Modeling of Magnetic Properties Using the Theory of Ferromagnetic Hysteresis. *IEEE Transactions on Magnetics*, 28(1):27–35, January 1992.

[2] J. H. B. Deane. Modelling the Dynamics of Nonlinear Inductor Circuits. *IEEE Transactions on Magnetics*, 30(5):2795–2801, September 1994.

[3] J. Paul, C. Christopoulos and D. W. P. Thomas. Generalized Material Models in TLM—Part 3: Materials with Nonlinear Properties. *IEEE Transactions on Antennas and Propagation*, 50(7):997–1004, July 2002.

COMPUMAG Saratoga Springs, New York USA
July 13 - 17, 2003

Feedback Control Systems for Micro-positioning Tasks with Hysteresis Compensation

A. Cavallo, C. Natale, S. Pirozzi, C. Visone

Abstract— **The paper proposes the analysis of a control loop system employing a Terfenol-D actuator driving a real mechanical load. The aim of the paper is to analyze the performances of such a system when a strategy of hysteresis compensation is employed. Such strategy has demonstrated its effectiveness in simpler feedback systems (with no mechanical load) by improving the tracking error, decreasing the control signal so as to avoid saturation and harmful stress to the actuator. As a consequence, the algorithm allows also to reduce energy losses in the actuator.**

Keywords— **Magnetostrictive actuators, Hysteresis, Compensation, Feedback.**

I. Introduction

Hysteresis is the effect of loss phenomena at the macroscopic scale taking place inside the material itself, basically due to the re-arrangement of magnetic domains [1] in response to assigned input magnetic field variations. These effects are in several cases important for the correct design of devices or apparatuses and require suitable modelling. In the design of smart devices employing active materials like Terfenol-D or SMA (Shape Memory Alloys) hysteresis is an undesired effect. Therefore, the design of any feedback control system requires, a correct modelling and subsequent compensation of hysteresis.

Generally speaking, even if the availability of the inverse (or compensator) hysteresis operator is guaranteed from the mathematical viewpoint, in very few cases such a compensator can be exactly formalized. In previous papers, a procedure for the approximation of the compensator and its identification, proposed in [2], has been applied in the description of an actual feedback control system employing a magnetostrictive actuator. The effects of hysteresis compensation were experimentally evidenced and analyzed in terms of both performance and energy efficiency for a tracking control problem. The hysteresis compensation algorithm is proven to reduce the tracking error and the energy losses in the material in the quasi-static case.

Magnetostrictive materials like Terfenol-D are widely known and used for the design of actuation devices [3]. At low frequencies, these actuators can be applied for micropositioning tasks or to move a mechanical load. Another recent application is the employment of these active materials to modify the dimensions of a mechanical structure like Superconducting Radiofrequency Cavity (SRF) used in particle accelerators [4]. In any of such applications, actuator should drive a mechanical load. Therefore, it is important to test the feedback system performances when the control variable is the force exerted on the load.

A. Cavallo, C. Natale and S. Pirozzi are with Dipartimento di Ingegneria dell'Informazione Seconda Università degli Studi di Napoli Via Roma 29, 81031 Aversa, Italy, E-mail: {albcaval,cinatale}@unina.it, salvatore.pirozzi@unina2.it

C. Visone is with Dipartimento di Ingegneria Università degli Studi del Sannio Piazza Roma 1, 82100 Benevento, Italy E-mail: visone@unisannio.it

II. Analysis of the feedback control system

In the present paper it is analyzed the effects of hysteresis compensation in a magnetostrictive actuator exerting a force on a real mechanical load, according to the scheme shown in Fig. 1, different from the control system studied in a previous paper [5]. The feedback system is constituted by two loops, the inner one performs the force control, the outer one is devoted to control the position of the mechanical load to be moved. Similarly to the procedure described in previous works, the analysis of such a system should be performed by preliminary defining a suitable hysteresis model able to describe accurately the hysteresis effects taking place inside the actuator. Afterward it is necessary to build up an exact or approximate version of its compensator which allows to improve the design of the control system. Specifically, the objective of the inner loop is twofold, first a compensation algorithm approximately linearizes the behavior of the hysteretic actuator, then a linear controller is designed to track a force reference profile provided by the outer loop. Thus, the inner loop operates so as to drive the actuator with a suitable feeding current such that the force exerted on the mechanical load follows a desired force profile. In turn, this force profile is computed by position controller in the outer loop, which compares the actual and the desired load position and generates a force profile in order to compensate for the tracking error.

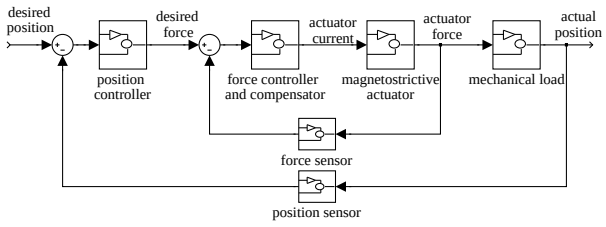

Fig. 1. Scheme of the control system

III. Preliminary definitions

The concept of inverse (or compensator) of a given hysteretic transducer has been tackled by several authors (see, e.g., [6]–[7]. A simplified version of Krasnoselskii's definition is as follows. A system Z is called the compensator (or inverse) of a system Y if, for any initial state y_0 of the

system Y, there is a state z_0 of the system Z such that, starting from the states y_0 and z_0, the series connection of the two systems gives the identity transformation independently of their order.

The definition of inverse can be applied to the classical Preisach model of hysteresis

$$y(t) \equiv \Gamma[x](t) = \iint_{\alpha \geq \beta} \mu(\alpha, \beta)\, \widehat{\gamma}_{\alpha\beta}\, x(t)\, \mathrm{d}\alpha \mathrm{d}\beta. \qquad (1)$$

In previous papers ([2],[5] and references therein) the problem of the construction of the compensator of an hysteresis operator or its numerical approximation by the definition of a new suitable operator, has been sufficiently addressed. For sake of the reader's commodity, we resume the idea of pseudo-compensator widely applied also in this paper as an effective tool for the design of the control algorithm of a real magnetostrictive actuator.

The idea of pseudo-compensator as the approximate version of the inverse of a Preisach hysteresis model (PM) has been tackled in previous cited papers is based on the following observation. Since PM fulfills congruency, its compensator is not a Preisach model. Nevertheless, it can be built up an hysteresis operator of Preisach type $\tilde{\Gamma}$ such that the condition $\tilde{\Gamma} \circ \Gamma = I$ holds on the first order reversal branches. Since this transducer cannot be a PM, a nonzero error in the compensation is expected on higher order reversals. The $\tilde{\Gamma}$ operator is defined as

$$x(t) \equiv \tilde{\Gamma}[y](t) = \iint_{\alpha \geq \beta} \nu(\alpha, \beta)\, \widehat{\gamma}_{\alpha\beta}\, y(t)\, \mathrm{d}\alpha \mathrm{d}\beta. \qquad (2)$$

where the role of input and output has been interchanged. A suitable identification procedure [2], allows to reconstruct the ν distribution function which guarantees, on the first order reversals, the condition specified above. The compensation results, shown in Fig. 2 appear to be good also for hysteresis branches of higher order.

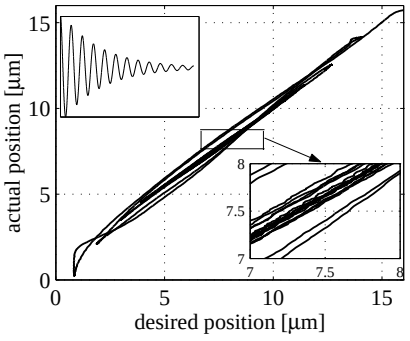

Fig. 2. open loop compensation results

IV. Experimental results

The experimental set-up used comprises a dSPACE rapid prototyping system and an Energen magnetostrictive actuator with its current amplifier.

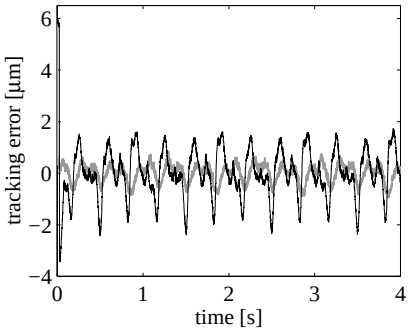

Fig. 3. tracking error with (gray) and without (black) compensation

In particular, for the controller implementation, we have considered a modular dSPACE system with a DS 1005 board, equipped with a Motorola PowerPC750 processor at 480 MHz, a DS 2001 ADC board with 16 bit channels and 5 μs sample time and a DS 2102 DAC board, with 16 bit channels and 2 μs settling time. The magnetostrictive device is a linear motion actuator produced by Energen, Inc. and equipped with displacement and current sensors, and with a current amplifier. Moreover, a PCB 208 C01 dynamic load cell has been employed as a force sensor. For the design and the simulation of the control algorithm we have used the MATLAB/SIMULINK software package.

The hysteresis compensation greatly simplifies the design of both the force and the position controllers, which can be selected as standard linear regulators due to the linearizing effect of the pseudo-compensator. In Fig. 3 preliminary results are shown, proving the effectiveness of the hysteresis compensation in terms of tracking error. Moreover, since compensation reduces the control signal to the actuator, also actuator's energy losses are reduced.

V. Conclusions

In this paper a control strategy for micro-positioning by means of a magnetostrictive actuator has been proposed. The control law is based on two nested feedback loops comprising two linear controllers and a nonlinear hysteresis compensation algorithm. Experimental results confirm the effectiveness of the proposed approach in terms of high tracking accuracy and good energetic efficiency.

References

[1] G. Bertotti, *Hysteresis in Magnetism*, Academic Press, 1998.

[2] C. Natale, F. Velardi, C. Visone, "Identification and compensation of Preisach hysteresis models for magnetostrictive actuators," *Physica B*, vol. 306, pp. 161–165, 2001.

[3] G. Engdhal (editor), *Handbook of Giant Magnetostrictive Materials*, Academic Press, 2000.

[4] C. Joshi, B. Bent, M. Drury, J. Preble, V. Nguyen, "A magnetostrictive tuning mechanism for SRF cavities," *Proceeding of the 1999 Particle Accelerator Conference*, New York, 1999.

[5] A. Cavallo, C. Natale, S. Pirozzi, C. Visone, "Effects of Hysteresis Compensation Feedback Control Systems," *IEEE Trans. on Magnetics*, submitted.

[6] M. A. Krasnoselskii, A. V. Pokrovskii, *Systems with Hysteresis*, Springer-Verlag, 1989.

[7] P.Krejci, "Hysteresis and periodic solutions of semilinear and quasilinear wave equations," *Mathematische Zeit.*, vol. 193, pp. 247–264, 1986.

Parallelogram Shaped Hysteresis Loops for Describing the Energetic Magnetic Behavior of Hysteretic Media

[1]E. Cardelli, [2]S. Di Fraia, [2]B. Tellini
(1) Dipartimento di Ingegneria Industriale, Università di Perugia
Via G. Duranti, 1-A/4, 06125 Perugia, Italy, e-mail: ermanno2@isten.ing.unipg.it
(2) Dipartimento di Sistemi Elettrici e Automazione, Università di Pisa
via Diotisalvi 2, 56126 Pisa, Italy, e-mail: bernardo.tellini@dsea.unipi.it

Abstract — **The characterization of the energetic magnetic behavior of hysteretic materials and the determination of the surface impedances are here proposed. A numerical model in time domain is adopted for the calculations. The use of parallelogram shaped hysteresis loops allows for simplifying the numerical formulation and for reducing the computation time with respect to more accurate models. Equivalent major loops have been defined starting from the measured ones. Comparison with the scalar Preisach model is presented and discussed.**

INTRODUCTION

Practical and industrial applications often need approximated formulas or models able of giving realistic and acceptable solutions to the required problem. This necessity can be in contrast with the accuracy of the obtained results. Anyway the possibility of handling simple analytical or numerical tools remains, in many cases, a valid compromise.

The numerical treatment of magnetic hysteresis represents a serious task. Accurate descriptions require both very complex numerical formulation and high computational efforts, therefore, a macroscopic simple hysteresis model can be very useful.

The magnetic power losses prediction is an important matter for industrial applications. In this paper we present the capabilities of the parallelogram shaped loops model for describing the energetic behavior of a hysteretic material.

A comparison with the Modified Scalar Preisach Model (MSPM) formulation is presented and discussed for the Mn-Zn soft magnetic ferrite.

HYSTERESIS MODEL

The model is based on the assumption that hysteresis loops have parallelogram shape. From the existing literature [1] [2] and in particular from the results obtained in a previous paper [3] we observed that any simpler hysteresis cycle form should have not only the same area but, also and more important, a very similar virgin curve to reproduce as better as possible the energetic magnetic behavior of the investigated material. In our opinion, the choice of parallelogram cycles can be a good compromise for simplifying the numerical treatment of hysteretic non-linearity because, for many soft magnetic materials, it is relatively easy to define an equivalent parallelogram family of hysteresis loops, close to the actual ones.

We have obtained the equivalent parallelogram major loop by first drawing the tangent line to the rising (lower) branch of the measured major loop at its intersection with the H-axis. The saturation region is described tracing the tangent line to the measured major loop in the positive saturation point. The second side of the equivalent parallelogram major loop is obtained tracing a third line from the intersection of the previous two tangent lines, and tangent to the measured major loop. The negative part of the equivalent parallelogram major loop is then completed taking into account the symmetry of the loop. Figure 1 shows the geometrical construction.

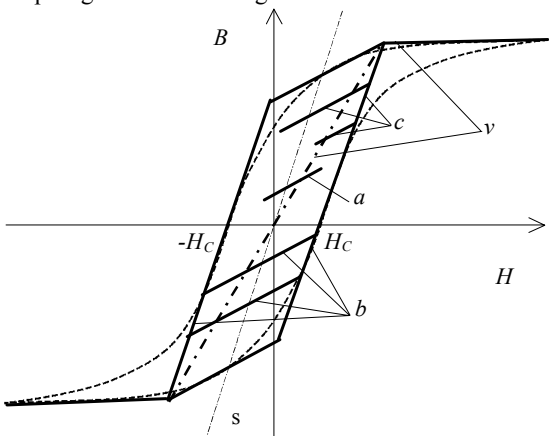

Fig.1. The equivalent parallelogram major loop, three generic equivalent minor non-symmetric loops (a, b, and c) and the virgin curve (v).

The first magnetization (virgin) curve (v in Fig. 1) is obtained by linking the upper right vertex and the lower left vertex of the parallelogram. The equivalent minor loops shape depends on the magnetic field variation behavior and, in some cases, the parallelograms can degenerate into linear or piecewise linear relation between the magnetic field and the magnetic induction (paths a and c of Fig. 1).

For more clearness we describe here the formation of different minor loops. With reference to Fig. 1, if we start from a generic internal point of the parallelogram major loop, and we vary the magnetic field without reaching the major loop only a segment will be formed (path a). Minor parallelogram loops creation is possible only if the path runs on a part of the major loop (path b). The algorithm can generate open polygons as again shown in Fig. 1 (path c). In addition, if the *H*-field reaches the saturation region, paths follow the major loop; in particular, if only the saturation region is interested, a straight line represents the corresponding loop.

NUMERICAL MODEL AND RESULTS

We have used the equivalent parallelogram loops model described in the previous section, applied to a numerical scheme in time domain and we show here the main results obtained with this formulation for the problem of the magnetic penetration in a half-space magnetic material. The diffusion equation we are dealing is:

$$\frac{\partial^2 H}{\partial z^2} = \left(\mu_0 + \frac{dM}{dH} \right) \frac{\partial H}{\partial t} \tag{1}$$

Equation (1), together with the initial and boundary conditions: $H(z,0)=0$, $M(z,0)=0$, $H(0,t)=H_0(t)$ is discretized and solved by means of a FDITD two-level/three-point scheme using a varying spatial step [4].

Numerical results are in the form of $H(m,n)=H(z(m),n\Delta t)$, where Δt is the constant time step while $z(m)$ is the spatial coordinate and it varies with the following law:

$$\begin{cases} z(m)=0 & m=0 \\ z(m)=q^m \Delta z_0 & m \geq 1 \end{cases} \tag{2}$$

where q has been chosen, experimentally, according to the speed up of the numerical calculation.

Once the diffusion equation has been solved, the electric field can be evaluated in the whole computation domain through the Ampere's law. The general expression for every spatial step is here reported:

$$E(m,n) = -(1/(\sigma\, \Delta z(m+1)))(H(m+1,n)-H(m,n)) \tag{3}$$

The knowledge of the electric field at the interface allows for evaluating the power entering the medium.

For preliminary results we used, as input sources, the magnetic field expression $H(t)=H_1\times(1-e^{-t/\tau})+H_2\sin(2\pi f t)$ directly applied at the interface of the half-space with the aim of involving non-symmetric hysteresis loops. The $H_A(t)$ and $H_B(t)$ sources have been defined, respectively, adopting the following parameter values H_1 = 25 A/m, H_2 = 50 A/m, and H_1 = 140 A/m, H_2 = 120 A/m. In both cases the frequency f is 20 kHz and $\tau = 10^{-5}$ s. Surface impedance and power flux density values are summarized in Table I.

TABLE I. SURFACE IMPEDANCE AND POWER FLUX DENSITY VALUES.

	$\lvert Z_S \rvert$ (Ω)	Phase (Z_S) (deg)	Power (W/m^2)
Input source: $H_A(t)$			
Preisach model	20.83	40.20	2.11×10^4
Parallelogram model	20.17	41.73	2.01×10^4
Input source: $H_B(t)$			
Preisach model	10.18	38.70	9.82×10^4
Parallelogram model	9.28	40.55	10.00×10^4

Fig. 2 reports a comparison between the total electric field waveforms and the corresponding fundamental harmonics, respectively, for the equivalent parallelogram model (dashed line), and the MSPM [5] (solid line). The amplitude of the observed fundamental harmonics differs about the 3 %. The $H_A(t)$ source has been used.

In Fig. 3 we report hysteresis cycles corresponding to the input source $H_A(t)$ related to the equivalent parallelogram model and to the MSPM at the interface and at about 7 cm from the interface metal-air. The picture shows also the capabilities of the parallelogram model of reproducing paths in the magnetic induction - magnetic field plane quite close to that obtained with the MSPM.

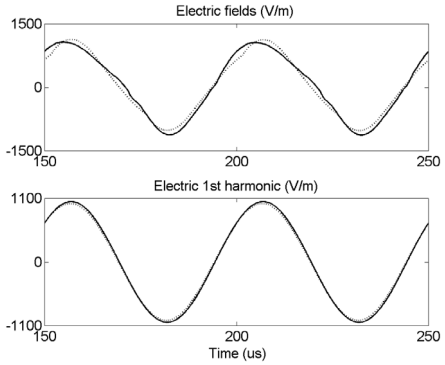

Fig. 2. Total electric field strength and its first harmonic vs. time.

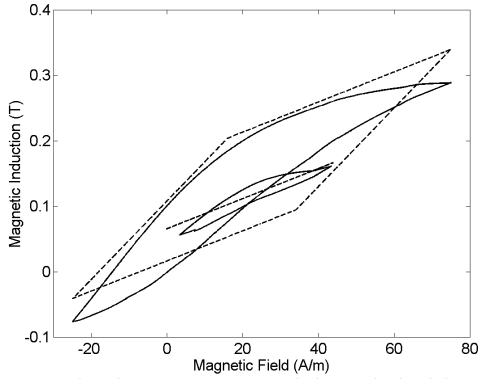

Fig. 3. Comparison between non-symmetric loops obtained through the parallelogram and the Preisach model. Input source $H_A(t)$.

REFERENCES

[1] I. D. Mayergoyz, "Mathematical Models of Hysteresis," New York, Springler Verlag 1991.

[2] I. Mayergoyz, *Nonlinear diffusion of electromagnetic fields*, Academic Press, USA, 1998.

[3] F. Bertoncini, E. Cardelli, S. Di Fraia, B. Tellini, "Evaluation of Surface Impedance of Hysteretic Materials," CEFC 16-19 June 2002, Perugia, Italy, p. 177.

[4] F. Bertoncini, F. Beux, E. Cardelli, S. Di Fraia, B. Tellini, "Stable FDITD Formulation for Electromagnetic Field Diffusion in soft magnetic materials, " CEFC 16-19 June 2002, Perugia, Italy, p. 78.

[5] E. Cardelli , E Della Torre, and B. Tellini, "Direct and Inverse Preisach Modeling of Soft Materials," *IEEE Trans. On Magn.* ,Vol. 36, No. 4, July 2000.

Application of the TLM Method for Simulation of Hysteresis Effects on Transformers

Sérgio H. L. Cabral[1,3] scabral@furb.br
Luiz H. Meyer[1,*] lhmeyer@engmail.uwaterloo.ca
D.W. P. Thomas[2] dave.thomas@nottingham.ac.uk
Adroaldo Raizer[3] raizer@eel.ufsc.br
Thair I.A.H. Mustafa[1] tim@furb.br

1 - Dept. de Eng. Elétrica – Univ. Regional de Blumenau - Caixa Postal 1507 - CEP 89010-971 Blumenau/SC BRASIL
2 - School of Electrical and Electronic Engineering, the University of Nottingham, Nottingham, UK, NG7 2RD
3 - Dept. de Eng. Elétrica – Univ. Fed. de Santa Catarina - Caixa Postal 476 - CEP 88040-900 Florianópolis/SC BRASIL

***Abstract* - This work presents the application of the numerical method Transmission Line Method-*TLM* to simplified modellings of hysteresis in view of allowing the ease prediction of the behaviour of transformers under several but practical conditions of voltage supply. Since the TLM is a very flexible method, its application facilitates the consideration of the most significant parameters of transformers that are usually neglected. The focus of this wok is directed to the comparison between experimental and computational results.**

INTRODUCTION

Magnetic hysteresis is a very important phenomenon that has been intensively studied and modelled since transformers have been put in use [1]. Nowadays, as a consequence, there are various models for hysteresis, each one with different applications and degrees of complexity [2,3]. Simplified modelling techniques allow fast and reasonable accurate evaluation of the transient response of magnetic devices, such as transformers subjected to voltage transients. Given the inherent simplicity, these techniques are very useful for engineers who deal with transformers, since field conditions can be quickly and easily simulated. For the sake of efficiency, numerical methods have been applied to solve the equations that govern these simplified modellings. The *Transmission Line Modelling* (TLM) method is a numerical method that has been successfully applied to the solution of several problems in electrical engineering, including the modelling of the magnetic saturation [4]. Thus, the aim of this work is to show how the TLM numerical method can be advantageously used in view of improving the efficiency of simplified modellings of hysteresis. An immediate consequence from this proposed application of the TLM method is that the simulation of important conditions of transformers in power systems becomes a simple task. Results from the simulation using the TLM method under different field conditions are presented in this work.

SIMPLIFIED MODELLINGS OF HYSTERESIS

Since there are different modellings for the hysteresis phenomena, each one with a different degree of complexity, their application depends on how much accuracy is needed. Usually, accurate models of hysteresis are indeed complex and most of them are intended for the evaluation of magnetic losses. On the other hand, the simplified models of hysteresis are relatively less accurate but their implementation is much simpler. Therefore, simplified models are directed towards the understanding of the behaviour and interactions of equipments and devices that present magnetic materials with hysteresis. Simplified models of hysteresis are frequently applied to the analysis of transformers under various abnormal conditions of supply voltage. For example; the presence of voltage harmonics, the interaction between transformers and capacitors when connected in parallel which is known as ferroresonance and also the inrush current that occurs when transformers are connected to their voltage supplies. In all of these cases, the application of the TLM method improves the use of these simplified models. To couple the TLM method with simplified modelling techniques, there are two basic requirements that facilitates significantly the use of the TLM method [5]:

a) The magnetisation curve of a transformer at no-load, with saturation, should be analytically fitted by an expression that represents the current as a function of the magnetic flux linkage, λ. Thus, the non-linear magnetisation inductance is substituted by a non-linear current source that is dependent on the flux linkage.

b) In parallel to the non-linear inductance, a resistive element, *Rp*, should be connected to represent the core losses within transformers. For the sake of simplicity, this resistive element can be considered as constant. The current of this resistive element is then added to that of the non-linear current source to which yield the total current of a given transformer at no-load.

Thus, in Fig.1 is shown the equivalent electric circuit that represents magnetisation branch of a transformer at no-load condition, in accordance with these two basic requirements.

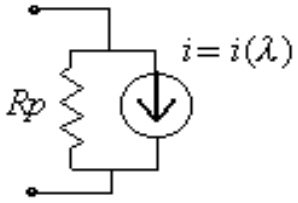

Fig. 1 - Equivalent circuit of the magnetisation branch of a transformer

* - L Meyer is currently with Univ. of Waterloo – Waterloo – ON – Canada, under a PhD program at E&CE Dept.

Fortunately, these requirements are inherently satisfied by most of the available simplified models of hysteresis, even for current transformers. Nevertheless, for those simplified models that apparently do not satisfy these requirements, some little additional algebraic manipulations are required. Thus, since the representation of the magnetisation branch of a transformer becomes simplified, the consideration of the leakage inductance can be easily done. Usually, this inductance is neglected because it is relatively small when compared to the magnetisation inductance and its presence implies an increase in the order of the system of equations. Nevertheless, if this inductance is neglected, differences between simulation and experimental results can be significant. On the other hand, the use of the TLM method allows the consideration of the leakage inductance in an simple way. Finally, the series resistance of the winding is added to the circuit that represents the transformer at no-load. Figure 2 shows the complete circuit of a transformer at no-load connected to a voltage source. The element *rs* represents the series resistance and *Ls* represents the leakage inductance.

Fig. 2 - Equivalent circuit of a transformer at no-load

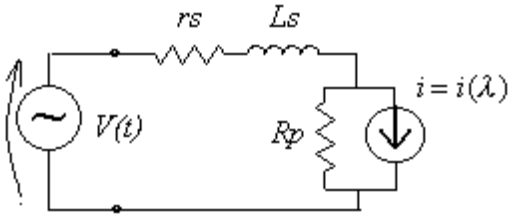

Thus, this equivalent circuit of a transformer, so obtained, can be used for the simulation of transformers at various types of abnormal conditions of voltage supply.

APPLICATION OF THE TLM METHOD

From what is above described, it can be concluded that the application of the TLM method to simplified modellings of hysteresis consists in the use of this method for the solution of the electric circuits that represent the transformer as well as the equivalent network to which the transformer is connected. One of the advantages of the use of this proposed methodology is that all of the passive electric parameters of the representative circuit of a transformer can be obtained from the AC steady-state regime. The proposed modelling is not only applicable to power transformers but also to current and potential transformers. Regarding potential transformers, the methodology is essentially the same as for power transformers. For current transformers, the most significant but obvious difference is that the input source should be a current source instead of a voltage source, in Fig. 2.

For illustrating the efficiency of the application of the TLM to simplified models of hysteresis Fig.3 shows a comparison between experimental and computational results for the maximum inrush current of a small single-phase transformer, 120 VA-220/380 V, switched on to a 220V/60 Hz voltage source. The computational simulation considered the magnetisation curve of this transformer as analytically fitted in a simple and practical form uses a hyperbolical function [5,6] :

$$i(\quad) \qquad \text{senh}(\quad) \qquad (1)$$

Where α = 63,08 mA and β = 2,30 Wb^{-1}. Referring to Fig. 2, the other parameters of this transformer are *rs* = 10 , *Ls* = 1 mH and *Rp* = 7,26 k , all of them referred to the 220 V side.

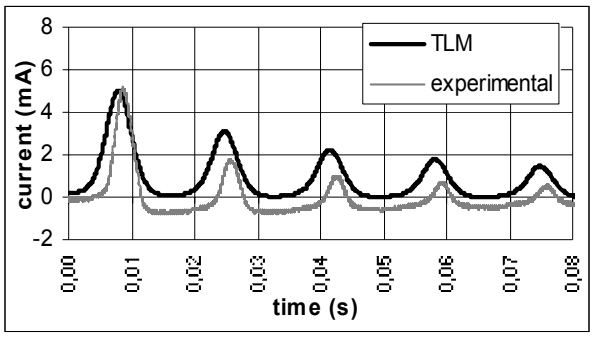

Fig. 3 - Comparison between experimental and computational results of the inrush current

The differences of the curves obtained by the TLM method and experimental results are due to the simple form of the function used for fitting the magnetization curve. Nevertheless, Fig. 3 shows a good simulation of the dynamic wave shape along a very good prediction of maximum inrush current, with a calculated error of less than 5%.

Similar comparisons for other conditions of the supply voltage, including the presence of harmonics, are presented in this work, for validating the proposed methodology.

REFERENCES

[1] - F. de León and A. Semlyen, "A Simple Representation of Dynamic Hysteresis Losses in Power Transformers", *IEEE Trans. on Power Delivery*, vol. 10, no. 1, pp. 315-321, 1995.

[2] - F. Preisach, "Über die magnetisch nackwirkung", *Zeitschrift für Physik*, vol. 94, pp. 277-302, 1935.

[3] - I. D. Mayergoyz, "Mathematical Models of Hysteresis", *Springer-Verlag* , New York, 1990.

[4] - C. Christopoulos, "The Transmission Line Modelling Method – TLM", *IEEE Press* , New York, 1995.

[5] - L.H. Meyer, S.H.L. Cabral and T.I.A.H. Mustafa, "Differential Modelling for Hysteresis Loops ", *Proceedings of the II International Symposium on Hysteresis Modelling and Micromagnetics - HMM'99* , pp. 1-2-6/1-2-11, June 6-8, Perugia.

[6] - S.H.L. Cabral , A. Raizer , L.H. Meyer and T.I.A.H. Mustafa, "Application of the TLM Method to Simplified Modeling of Hysteresis", CEFC 2002 - The Tenth Biennial Conference On Electromagnetic Field Computation, 16-19 of September of 2002, Perugia, Italy.

Orientation Correction in Ellipsoidal Magnetizable Material

G. R. Kahler and E. Della Torre
Institute for Magnetics Research
The George Washington University
Ashburn, VA 20147-2604

Abstract - **This paper presents computed and measured magnetization for anisotropic magnetic particle tape as the material rotates in an applied magnetic field. An orientation correction must be applied to the computed rotational magnetization. For isotropic materials, an orientation correction has been developed and presented. For anisotropic materials, an orientation correction is introduced.**

INTRODUCTION

This paper presents measurements and computations of the angle of magnetization for elliptically magnetized material rotated in an applied field. The material, magnetic particle (MP) tape, is saturated in an applied field of negative 1.3 T, which is then increased to an applied field between ± 1.0 T at which the material is rotated. The angle of rotation is 0° to 360° in 5° increments. A Preisach model has been presented which computes the angle of magnetization as a function of the angle of applied field for isotropic material [1]. The computation of the magnetization angle for isotropic materials requires an orientation correction. Likewise, an orientation correction is required for anisotropic materials.

RESULTS

The computed angle of magnetization for an applied field of 0.2 T is shown in Fig. 1, where the dashed line shows where the angles of magnetization and applied field are equal. Fig. 2 shows the angle of magnetization for an applied field of 0.2 T computed from measured x- and y-component magnetization data. The computed angle of magnetization equals the applied field angle at 0°and 360°; the curve displays a four-fold periodicity between 0°and 360°. Likewise, the measured angle of magnetization equals the angle of applied field at 0°and 360°, but the curve displays a two fold-periodicity.

The orientation correction applied to isotropic media removes the four-fold periodicity in the applied field angle-magnetization angle curves. The resulting vector plot of the magnetization due to a rotating applied field is a circle. For anisotropic media whose parameters are the same in the x and y directions except for the squareness, S, the plot of the normalized magnetization vector m will be a circle (see Fig.3.). Multiplying this normalized magnetization vector by the saturation, M_s, and the squareness, $S = (S_x, S_y)$ will make the plot of the unnormalized irreversible magnetization vector, M, into an ellipse (see Fig. 4.). This action effectively removes the four-fold periodicity in the applied field angle-magnetization angle curves and replaces it with two-fold periodicity.

The full paper will compare the results of the model with experiments on MP tape.

REFERENCES

[1] E. Della Torre and A. Reimers, " Isotropic media and the simplified vector Preisach model," *Physica B*, vol 306, pp. 72-77, December 2001.

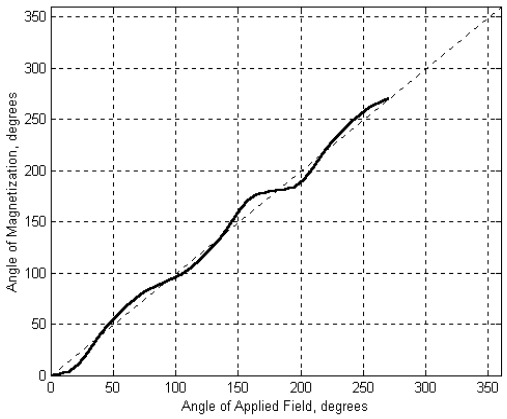

Fig. 1. Computed angle of magnetization as a function of applied field = 0.2T.

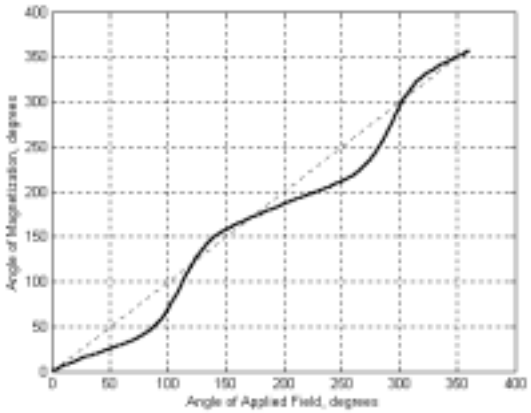

Fig. 2. Angle of magnetization as a function of applied field = 0.2T computed from measured x- and y-component magnetization.

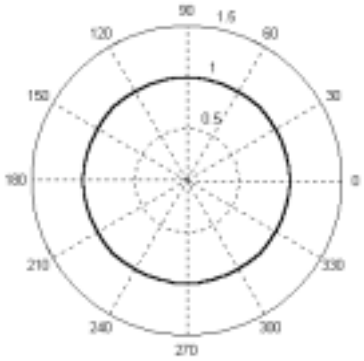

Fig. 3. Normalized magnetization vector for anisotropic media.

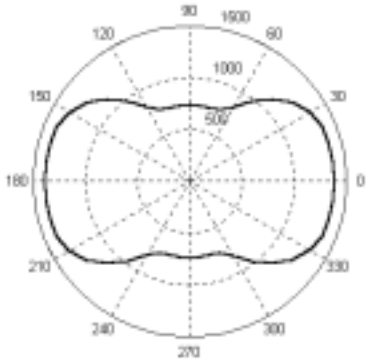

Fig. 4. Unnormalized irreversible magnetization vector for anisotropic media.

A Method of Magnetic Current for Magnetic Field Computation

[1]Hisashi Endo, [2]Iliana Marinova, [1]Seiji Hayano, and [1]Yoshifuru Saito
[1]Graduate School of Engineering, Hosei University, [2]Technical University of Sofia, 1756 Sofia, Bulgaria
3-7-2 Kajino, Koganei, Tokyo 184-8584, JAPAN
E-mail: endo@ysaitoh.k.hosei.ac.jp

***Abstract*– This paper proposes a new formulation employing the magnetic current corresponding to magnetomotive force (MMF) in classical magnetic circuits. The classical MMF can be introduced into modern magnetic field computation by our formulation. In our formulation, the rotation of electric fields represents the external magnetic field due to impressed voltage. We demonstrate magnetic field computation around troidal core inductor by finite elements. Comparison with experimental result verifies our formulation.**

INTRODUCTION

The concept of magnetomotive force (MMF) has been widely used to analyze magnetic devices in the classical magnetic circuits. However, it could not utilize in modern magnetic field computation, i.e., it is difficult to introduce MMF into magnetic field computation. To introduce MMF into magnetic field computation we propose a formulation employing magnetic currents [1].

The present paper has studied 2-dimensional magnetic field distribution with our formation. The equivalent source of MMF is derived from the rotation of electric polarization, i.e., magnetic current [2-4]. Stokes's theorem shows that the magnetic current is closely related with MMF. We demonstrate magnetic field computation around troidal core inductor by finite elements. Comparison with experimental result verifies our formulation [5-7].

METHOD OF MAGNETIC CURRENTS

Formulation

We considered the equivalent representation of MMF as the orthogonal component of the exciting current, as shown in Fig. 1. Namely, the rotation of electric field component is introduced as

$$\mathbf{D} \quad (\ _0\mathbf{E} \quad \mathbf{P})$$

or (1)

$$\mathbf{E} \quad \mathbf{J}_m \quad \frac{\mathbf{B}}{dt}$$

where $\mathbf{P}$ and $\mathbf{J}_m$ respectively denote the polarization and magnetic current given by

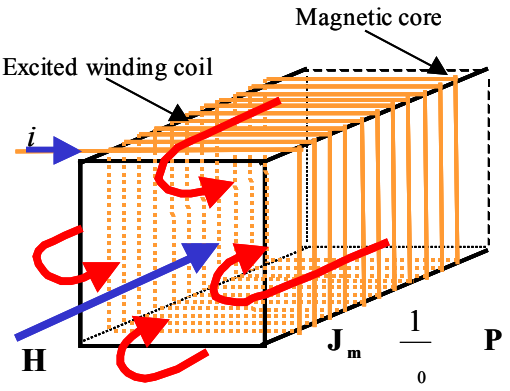

Fig. 1. Relationship between magnetic motive force and magnetic current

$$\mathbf{J}_m \quad \frac{1}{0} \quad \mathbf{P}. \qquad (2)$$

Apply the surface integral to (1), then the line integral along with the winding coil path l can be derived from Stokes's theorem.

$$\mathbf{E} \ d\mathbf{s} \quad \frac{1}{0} \quad \mathbf{P} \ d\mathbf{s} \quad \frac{\mathbf{B}}{dt} \ d\mathbf{s} \qquad (3)$$

$$\mathbf{E} \ d\mathbf{l} \quad \frac{1}{0} \ \mathbf{P} \ d\mathbf{l} \quad \frac{\mathbf{B}}{dt} \ d\mathbf{s} \qquad (4)$$

Since the first term on right side of (4) has dimension of voltage, then magnetic current $\mathbf{J}_m$ corresponds to voltage per unit area caused by magnetic charge moving. Thus, $\mathbf{J}_m$ times conductivity σ of the coil material is equivalent to MMF generating in volume surrounded by the exciting coils.

Result and discussions

As an example, we computed an axisymmetrical solution of a troidal ferrite material illustrated as in Fig. 2. Because of the magnetic current formulation, the problem is reduced into a 2-dimensional finite element analysis having open boundary[5]. The governing equation in terms of θ component becomes (5).

$$^2H \quad \mathrm{j} \quad (\ )H \quad J_m \qquad (5)$$

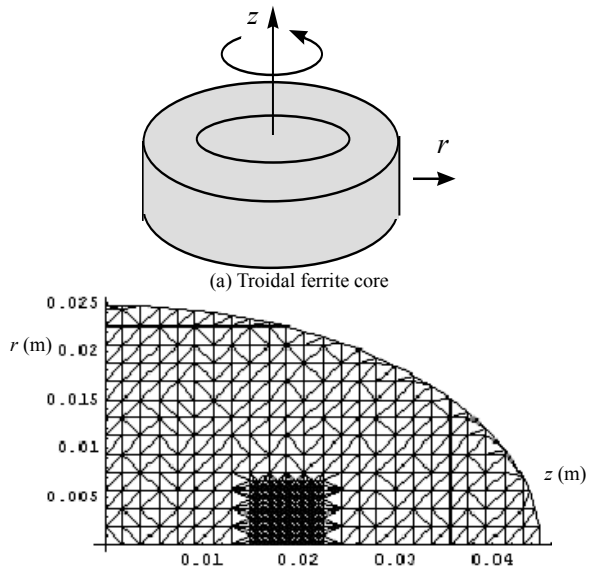

(a) Troidal ferrite core

(b) Mesh system used in computation

Fig. 2. Finite element analysis of troidal core inductor

where $\mu(\omega)$ is complex permeability based on the Chua type magnetization model[6,7]. Moreover, the magnetic current is characterized as voltage per unit area. Therefore, the exciting current relates to the right hand term in (5). As a result, (5) is rewritten as

$$^{2}H \quad \text{j} \quad (\ )H \quad \frac{Ni}{V} \qquad (6)$$

where V denotes volume surrounded by the exciting coils.

Fig. 3 shows calculated and experimented magnetization curves. The results support our formulation, suggesting that MMF can be represented by magnetic currents.

REFERENCES

[1] P. Silvester and R. L. Ferrari, Finite elements for electrical engineers, Cambridge University Press, Cambridge, England, (1983)

[2] P. Silvester, Modern Electromagnetic Fields, Prentice-Hall Inc., Englewood Cliffs, NJ (1968)

[3] J. Jin and J. L. Volakis, "A hybrid finite element method for scattering and radiation by microstrip patch antennas and arrays residing in a cavity," IEEE Transactions on Antennas and Propagation, vol. 39, no. 11, pp. 1598-1604, November 1991

[4] J. A. Stratton, Electro-magnetic theory, McGraw Hill Book Company, NY, (1941)

[5] Y. Saito, K. Takahashi and S. Hayano, "Finite element solution of unbounded magnetic field problem containing ferromagnetic materials," *IEEE Transaction on Magnetics*, vol. MAG-24, no.6, pp. 2946-2948, 1988

[6] Y. Saito, M. Namiki, and S. Hayano, "A magnetization model for computational magnetodynamics," *Journal of Applied Physics*, vol.69, no.8, pp.4614-4616, April 1991.

[7] Y. Saito, S. Hayano, and N. Tsuya, "Experimental verification of a Chua type magnetization model," *IEEE Transactions on Magnetics*, vol. MAG-25, no.4, pp. 2968-2970, July 1989.

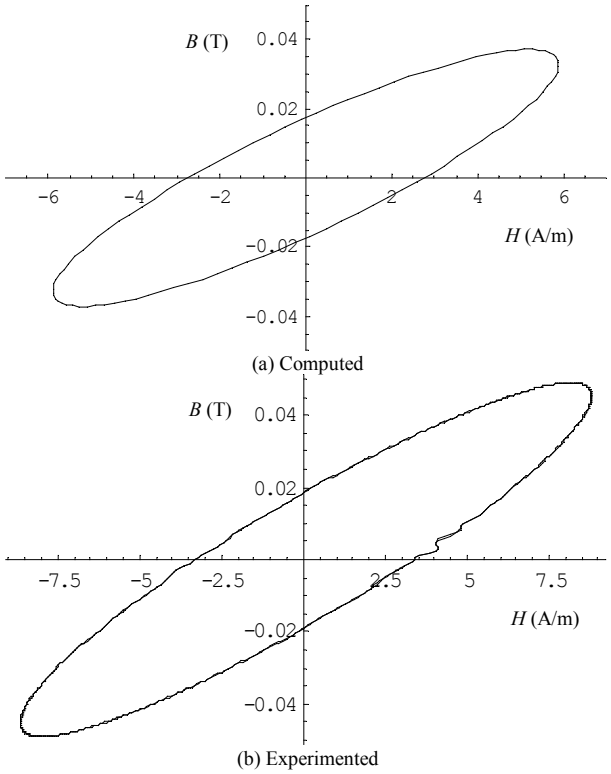

(a) Computed

(b) Experimented

Fig. 3. Comparison in magnetization curves

COMPUMAG Saratoga Springs, New York USA
July 13 - 17, 2003

Nonlinear magnetic field calculation with FEM

Peter Kis, Amalia Ivanyi

Abstract— **The ferromagnetic materials are investigated in numerical field calculations. The Finite Element Method (FEM) is applied to solve the nonlinear eddy-current problems. Two field computation problems are introduced in this paper. The first is the infinite ferromagnetic half-space, which is described in 1D. The second is a 2D arrangement, which contains a ferromagnetic bar with rectangular cross-section. The ferromagnetic properties are taken into account with the $\tan^{-1}$ nonlinearity in the first approach after that the Jiles–Atherton model of hysteresis is built into the FEM.**

Index Terms— **nonlinear problems, hysteresis**

I. Introduction

TWO numerical field computation problems are presented in this paper. Our goal is to combine the FEM with modelling the ferromagnetic material. Two types of nonlinearity are applied in FEM. A simply way is to take into account the material nonlinearity, namely the saturation, introducing an $\tan^{-1}$ type function between H and M, but this approach is not accurate enough in some practical cases. Usage of a hysteresis model in the FEM is more sophisticated description of the material. In this paper the Jiles–Atherton model is applied to describe the hysteresis. Nodal Finite Element Method is applied for solving numerical field computation problem and the Delaunay triangulation is used for 2D mesh generation [1].

The Jiles–Atherton model of hysteresis is based physical concepts, it can be extended to take into consideration the eddy current effect and the effect of the domain wall motion, which causes anomalous loss, but only the classical Jiles–Atherton model is applied in this paper. The model has been composed by energy terms. In classical case the external supplied energy is equal to sum of the internal magnetic energy changing and the hysteresis loss. The eddy current loss comes from the second Maxwell's equation and the loss from the domain wall motion during the magnetization process. The above mentioned energy-balance equation has to be extended by these two energy terms [2], [3], [4], [5], [6].

II. Governing equations of FEM

The numerical magnetic field computation is performed with H formulation. The following equation can be obtained form the Maxwell's lows

$$-\nabla \times \nabla \times \mathbf{H} - \mu_0 \sigma \left(\mathbf{1} + \frac{\partial \mathbf{M}}{\partial \mathbf{H}}\right) \frac{\partial \mathbf{H}}{\partial t} = 0. \qquad (1)$$

The weak form of (1) is the following, which is taking into account the material nonlinearity

$$-\frac{1}{\mu_0 \sigma}\left(\mathbf{1} + \frac{\partial \mathbf{M}}{\partial \mathbf{H}}\right)^{-1} \int_\Omega (\nabla \times \mathbf{H})\,(\nabla \times \mathbf{w}) \mathrm{d}\Omega - \int_\Omega \mathbf{w} \frac{\partial \mathbf{H}}{\partial t} \mathrm{d}\Omega = 0, \qquad (2)$$

where $\mathbf{w}$ is the applied weight function, $\mathbf{1}$ is an eigentensor, σ is the conductivity of the material.

The $\dfrac{\partial \mathbf{M}}{\partial \mathbf{H}}$ term is the differential susceptibility tensor. In this way the hysteresis and the nonlinearity can be built into the FEM.

III. Material models

A. The $\tan^{-1}$ type nonlinearity

If the saturation follows the curve

$$M = \frac{2M_s}{\pi} \tan^{-1} \frac{H}{H_0}, \qquad (3)$$

where M_s is the saturation magnetization and H_0 is the value of the magnetic field intensity at $M_s/2$, the expression of the differential susceptibility is as follows

$$\frac{\partial M}{\partial H} = \frac{2M_s}{\pi H_0 \left[1 + \left(\dfrac{H}{H_0}\right)^2\right]}, \qquad (4)$$

which can be directly built into (2).

B. Jiles–Atherton model of hysteresis

We equate the work done by an external source (battery) δW_{bat}, with the change in the internal energy of the material δW_{mag} and losses in the magnetization process δL_{mag}

$$\delta W_{bat} = \delta W_{mag} + \delta L_{mag}. \qquad (5)$$

The work done by the battery in changing the magnetization per unit volume, in one cycle, to be given by

$$\delta W_{bat} = \oint \mu_0 H \mathrm{d}M = -\oint \mu_0 M \mathrm{d}H_e, \qquad (6)$$

where

$$H_e = H + \alpha M. \qquad (7)$$

The last equation is of interest because in Weiss's molecular field theory for ideal ferromagnetic rods (no losses), $M_{an} = M$ is a function of

Manuscript received November 15, 2002. The research work is sponsored by the Hungarian Scientific Research Found, OTKA 2002, Pr. No. T 034 164/2002.

Péter KIS. Author is with the Budapest University of Technology and Economics, Budapest, H–1521, Hungary. He is now with the Department of Electromagnetic Theory (telephone: +36-1-463-1049, e-mail: kpeti@evtsz.bme.hu).

Amália IVÁNYI. Author is with the Budapest University of Technology and Economics, Budapest, H–1521, Hungary. She is now with the Department of Electromagnetic Theory (telephone: +36-1-463-2817, e-mail: ivanyi@evtsz1.evt.bme.hu).

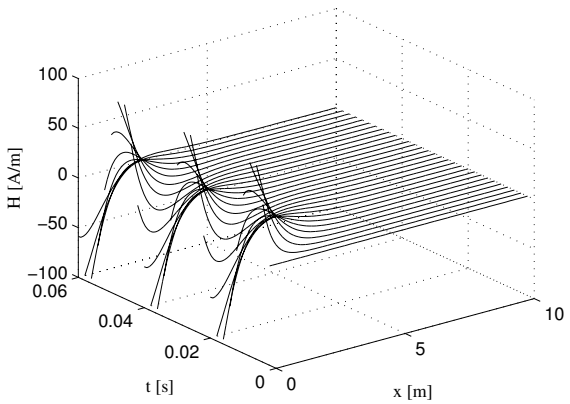

Fig. 1. Simulation results of the infinite half-space problem with sinusoidal excitation at $x = 0$

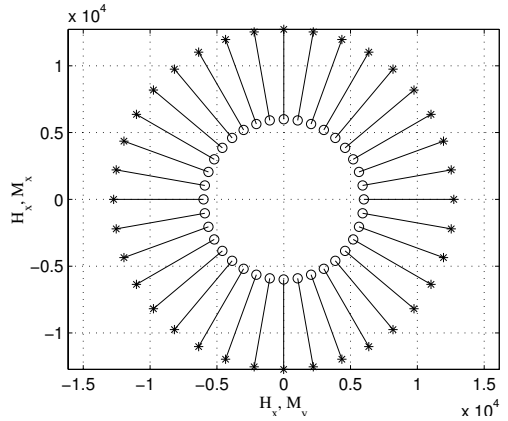

Fig. 2. Simulated $\mathbf{H}$ ($\circ$) and $\mathbf{M}$ ($*$) loci for vectorization of $\tan^{-1}$ scalar model, the coherent points connected with lines

and $\alpha > 0$ is the molecular field parameter. For an ideal ferromagnetic rod, M_{an} is given by the Langevin function [7]

$$M_{an} = M_S \left(\coth \frac{H + \alpha M}{a} - \frac{a}{H + \alpha M} \right), \tag{8}$$

where M_S is the saturation magnetization and a is a parameter that depends on the temperature of the specimen.

The average magnetic moment per unit volume M to be comprised of an irreversible component M_{irr} and a reversible component M_{rev}. M_{rev} is related to the anhysteretic or ideal magnetization by the following expression

$$\begin{aligned} M &= M_{rev} + M_{irr}, \\ M_{rev} &= c(M_{an} - M_{irr}), \end{aligned} \tag{9}$$

where $0 < c < 1$ is a parameter that depends on the material.

The following parameter has to be introduced

$$\delta_M = \begin{cases} 0 : \dot{H} < 0 \text{ and } M_{an} - M > 0 \\ 0 : \dot{H} > 0 \text{ and } M_{an} - M < 0 \\ 1 : \text{otherwise} \end{cases}, \tag{10}$$

for handling non-physical solutions. The differential susceptibility can be expressed as the following equation

$$\frac{dM}{dH} = (1 - c)\delta_M \frac{dM_{irr}}{dH} + c\frac{dM_{an}}{dH}. \tag{11}$$

The differential susceptibility can be shown after some manipulations that

$$\frac{dM}{dH_e} = \frac{\delta_M}{k\delta}(M_{an} - M) + c\frac{dM_{an}}{dH_e}, \tag{12}$$

Equation (12) describes the bulk ferromagnetic hysteresis model. There are five non-negative parameters in this model namely a, α, c, k, M_S, but $0 < c < 1$.

IV. Vector material models

The scalar models has been detailed in the previous sessions. Vectorized models is required in the 2D field computation problem, because the directions of the field quantities are important.

Vector models can be generated on similar way for the above mentioned $\tan^{-1}$ nonlinearity and the Jiles–Atherton model of hysteresis. The vector model of magnetic hysteresis is constructed as a superposition of scalar models in given directions $\mathbf{e}_\varphi$ [2], [8], [9]. Magnetization can be expressed in two dimensions as

$$\mathbf{M}(t) = \int_{-\pi/2}^{\pi/2} \mathbf{e}_\varphi \mathscr{H}\{H_\varphi\} \mathrm{d}\varphi, \tag{13}$$

where $M_\varphi = \mathscr{H}\{H_\varphi\}$ is the magnetization in the direction $\mathbf{e}_\varphi$, $H_\varphi = |\mathbf{H}| \cos(\theta_H - \varphi)$and θ_H is the direction of magnetic field intensity H [10].

The differential susceptibility can be formulated as

$$\frac{\partial \mathbf{M}}{\partial \mathbf{H}} = \frac{\pi}{2n} \sum_{k=1}^{n} \begin{bmatrix} \cos^2 \varphi_k & \sin \varphi_k \cos \varphi_k \\ \sin \varphi_k \cos \varphi_k & \sin^2 \varphi_k \end{bmatrix} \frac{d\mathscr{H}\{H_{\varphi_k}\}}{dH_{\varphi_k}}. \tag{14}$$

V. Results

The solution of the infinite half-space problem can be seen in Fig. 1. The changing of the magnetic field intensity can be observed as a function of the time and the place. The excitation is a sinusoidal function in H at $x = 0$.

The Fig. 2. shows the character of the magnetization M and the magnetic field intensity H in circular magnetic field excitation.

VI. Conclusion

The finite element method has been successfully merged with the nonlinear material models. The detailed results will be presented in the full paper.

References

[1] H. R. Schwarz, *Methode der finiten Elemente*. B. G. Teubner Stuttgart, 1991.
[2] A. Iványi, *Hysteresis Models in Electromagnetic Computation*. Akadémia Kiadó, Budapest, 1997.
[3] A. Iványi, *Magnetic Field computation with **R**-function*. Akadémia Kiadó, Budapest, 1998.
[4] D. Jiles, "Frequency dependence of hysteresis curves in conducting materials," *J. Appl. Phys.*, vol. 76, no. 10, pp. 5849–5855, November 1994.
[5] D. C. Jiles, "Modelling the effects of eddy current losses on frequency dependent hysteresis in electrically conducting media," *IEEE Transaction on Magnetics*, vol. 30, no. 6, pp. 4326–4328, November 1994.
[6] D. Jiles and D. Atherton, "Ferromagnetic hysteresis," *IEEE Transaction on Magnetics*, vol. 19, pp. 2183–2185, September 1983.
[7] S. Chikazumi, *Physics of Magnetism*. John Wiley an Sons, Inc., 1996.
[8] I. D. Mayergoyz, *Mathematical Models of Hysterezis*. Springer, 1991.
[9] C. Ragusa and M. Repetto, "Accurate analysis of magnetic devices with anisotropic vector hysteresis," *Physica B*, vol. 275, pp. 92–98, 2000.
[10] M. Kuczmann, J. Füzi, and A. Iványi, "Neural network based scalar and isotropic vector hysteresis model," *Proceedings of the 8th International Conference on Optimization of Electrical and Electronic Equipments*, pp. 57–62, May 16-17 2002.

E&S^2 model including higher harmonics component of the field strength waveform

Masato Enokizono, Hiroyasu Shimoji and Toyomi Horibe
Department of Electrical and Electric Engineering, Faculty of Engineering, Oita University
700 Dannoharu, Oita 870-1192 Japan
E-mail: horibe@mag.eee.oita-u.ac.jp

***Abstract*— This paper present the E&S^2 model including the high higher harmonic component of the field strength waveform. E&S^2 model can express the hysteresis, that is, relationship between the *H*-vector and the *B*-vector. The hysteresis modeling is improved by considering the n-th higher harmonics component in the simulation.**

INTRODUCTION

TWO -dimensional magnetic characteristics, the relationships between the measured magnetic flux density ***B*** and the magnetic field strength ***H*** as vector quantity can express the magnetic anisotropy and iron loss precisely. We have improved the modeling of the magnetic anisotropy and nonlinearity that have so far been considered difficult to do[1]. Thus the tendency that iron loss increases when the phase difference between ***B*** and ***H*** exists, is well expressed in this method. However, when the magnetic flux density becomes higher, the higher harmonic components of the magnetic field strength increase. The conventional method was limited to consider until the 5th higher harmonic component. We can see that the reproducibility of the magnetic field strength waveform is not good in the conventional method. However, the reproducibility of magnetic field strength can be improved, by considering any until n-th higher harmonics component. In this research Enokizono, Soda and Shimoji (E&S^2) modeling is expanded to a high magnetic flux density area.

E&S^2 MODELING

The vector (two-dimensional) magnetic hysteresis model can express the relationship between the ***H***-vector and the ***B***-vector in the formulation. In order to take into account this relation, we have developed the E&S^2 model to make the vector magnetic property technologically[2]. This model can be defined by the following relationship between the ***B***-vector and the ***H***-vector

$$\begin{cases} H_x = \nu_{xr} B_x + \nu_{xi} \int B_x d\tau \\ H_y^{\mathrm{I}} = \nu_{yr} B_y^{\mathrm{I}} + \nu_{yi} \int B_y^{\mathrm{I}} d\tau \end{cases} \tag{1}$$

where, the hat symbol expresses a waveform of one period. The variable τ is in a range from 0 to 2π. ν_{xr} and ν_{yr} are named as the magnetic reluctivity coefficients, then ν_{xi} and ν_{yi} are named as the magnetic hysteresis coefficients. ν_{xr} and ν_{xi} are written by

$$\begin{cases} \nu_{xr} = \dfrac{\sum_{n=1}^{N} R_{(2n-1)H_x} \cos(2n-1)\theta}{\cos\theta} \left(\dfrac{R_{B_x}}{R_{B_x}^{\,2} + I_{B_x}^{\,2}} \right) \\ \qquad + \dfrac{\sum_{n=1}^{N} I_{(2n-1)H_x} \sin(2n-1)\theta}{\sin\theta} \left(\dfrac{I_{B_x}}{R_{B_x}^{\,2} + I_{B_x}^{\,2}} \right) \\ \nu_{xi} = \dfrac{\sum_{n=1}^{N} R_{(2n-1)H_x} \cos(2n-1)\theta}{\cos\theta} \left(\dfrac{I_{B_x}}{R_{B_x}^{\,2} + I_{B_x}^{\,2}} \right) \\ \qquad - \dfrac{\sum_{n=1}^{N} I_{(2n-1)H_x} \sin(2n-1)\theta}{\sin\theta} \left(\dfrac{R_{B_x}}{R_{B_x}^{\,2} + I_{B_x}^{\,2}} \right) \end{cases} \tag{2}$$

where, the coefficients R_B,I_B , R_H and I_H are obtained from the measured data by using the two-dimensional magnetic measurement system[3].

Fig.1 shows the definition of the alternating and rotating flux condition. The alternating flux condition is expressed by the maximum magnetic flux density B_{max} and the angle θ_B from the easy axis direction. The rotating flux condition is also expressed by the axis ratio .(B_{min}/B_{max}) and the maximum magnetic flux density B_{max} and the angle θ_B from the easy axis direction.

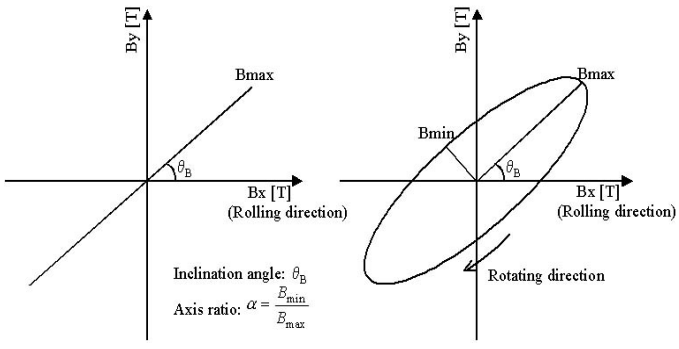

Fig.1. Representation of alternating and rotating flux condition.

THE MAGNETIC STRENGTH WAVEFORMS

Fig.2. shows the magnetic field strength waveforms when limited to 3rd, 5th and 15th harmonic wave. The sample was the silicon steel sheet, 35Z145 produced by Nippon Steel Corporation. It is evidence that it is able to express more accurately magnetic field intensity waveforms, by including the higher harmonic components.

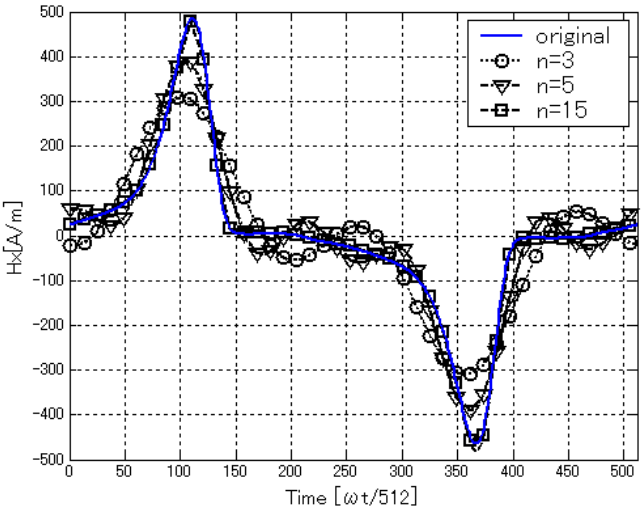

Figure 2: The magnetic field strength waveform considered until 3rd, 5th and 15th higher harmonic wave.
(Sample: 35Z145, Bmax=1.2[T], Axis=0.41, Inc=25[degree])

IRON LOSS

In this method, the iron loss P_t [w/kg] can be calculated directly by using the following equation without the loss database.

$$P_t = \frac{1}{\rho T}\int_0^T \left(H_x \frac{dB_x}{dt} + H_y \frac{dB_y}{dt} \right) dt \qquad (3)$$

where, ρ is the core material density, and T the period of the exciting waveform.

The iron loss depends on the phase angle between $\boldsymbol{B}$ and $\boldsymbol{H}$ in addition to the amplitude of $\boldsymbol{B}$. Therefore the iron loss does not always become large in proportion to B^2.

Fig.3. shows the hysteresis curves when limited to 3rd, 5th and 15th harmonic wave. The hysteresis curves can be also improved in comparison with conventional ones.

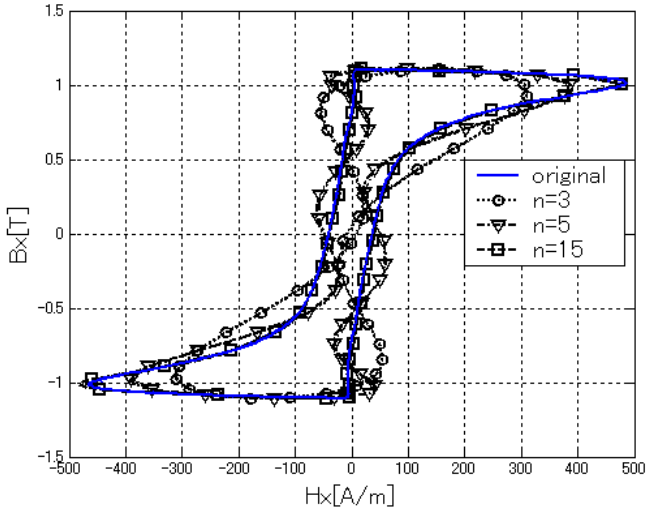

Fig.3 Hysteresis curves.
(Sample: 35Z145, Bmax=1.2[T], Axis=0.41, Inc=25[degree])

CONCLUSION

Conclusion paper, the E&S2 modeling has been improved by considering the higher harmonics component of the field strength waveform. The method can be applied to a problem, including high flux density regions. Because, the hysteresis curves can be also improved in comparison with the conventional one, this method is useful in evaluation of loss distributions.

REFERENCES

[1] M.Enokizono and N.Soda, "Direct Magnetic Loss Analysis by FEM Considering Vector Magnetic Properties", IEEE Trans. On Magnetics, Vol.34, No5, pp.188-195, 1998.

[2] M.Enokizono, "Two-dimensional Magnetic Properties", Trans. IEEE of Japan, Vol. 15-A, No. 1, Jan, 1995

[3] M.Enokizono edit "Two-Dimensional Magnetic Measurement and its Properties", Proceedings of the Second International Workshop on 2DMAG, JSAEM Studies in Applied Electromagnetic, 1 (1992)

Monte Carlo Simulation for Barkhausen Noise

Katsuhiko YAMAGUCHI, Shinya TANAKA, Hiroko WATANABE

Faculty of Education, Fukushima Univ., Kanayagawa 1, Fukushima 960-1296, JAPAN

Toshiyuki TAKAGI

Institute of Fluid Science, Tohoku University, Sendai, 980-8577, JAPAN

e-mail: yama@educ.fukushima-u.ac.jp

Abstract – **In this paper a new method is proposed for analyses of Barkhausen noise, which are expected for nondestructive evaluations for iron based materials, using Monte Carlo simulation. The results show typical properties of Barkhausen noise are well reproduced by this method.**

1. Introduction

Barkhausen noise is well known to be sensitive for states such as residual stress in magnetic materials [1]. The microscopic process and the method of the analyses for Barkhausen noise, however, don't seem to be studied sufficiently. For that reason nondestructive evaluation (NDE) using Barkhausen noise has not been made fit for practical use as yet, although it has been expected as a method of NDE for iron based materials. On the other hand, recently early detection for metal fatigue of iron based materials was strongly demanded to ensure our society against serious risk such as accidents of nuclear power generations. Therefore we tried to study more deeply for Barkhausen noise using Monte Carlo simulation with expectation that new powerful method for NDE can be developing in near future.

Figure 1 shows a typical result of Barkhausen noise for SS400, which is a steal with a soft magnetic property. Barkhausen noise detected by pick up coil appears for applied magnetic field formed into a triangle wave (frequency=15Hz) between –1A and +1A which are current flowing through an electromagnet. The noise intensity increases around a and b both which are points over 0A and rapidly decreases over the turning point of c and d. In this paper these properties of the phenomena will be reproduced by Monte Carlo method.

2. Numerical Method

Simulation was performed for a spin system composed of 31^3=29791 cells (0 x 30, 0 y 30, 0 z 30) arrayed as the single cubic lattice for simplicity, although iron metals take the body center cubic lattice actually. We use a simple spin Hamiltonian of a spin system describing magnetism for simplicity as below,

$$H \quad J_{ij} S_i S_j \quad B \quad S_i . \qquad (1)$$

Here S_i denotes the spin state of i-th cell, and J_{ij} stand for the effective exchange energy between i-th and j-th spins. B represents applied magnetic field. Now the first summation of Eq.(1) run over the nearest neighbor cells with a constant exchange energy *J*. On the conventional Monte Carlo method, after an initial spin arrangement is set, the local Hamiltonian of a focussed spin is calculated including thermal fluctuation effect. Then new arrangement is decided by comparison with the energy of other state of this spin. This cycle is repeated until getting stable state ordinarily. But now we stopped the repeating before getting stable state because of dealing with pseudo dynamic process for Barkhausen noise. One Monte Carlo step (1MCS) means to scan up to total cell number (31^3) of times and 1000MCS was carried out for one applied magnetic field. Under the constant field condition, the total spin is in an unequilibrium state and going to an equilibrium state with progress of the Monte Carlo steps. The applied magnetic field is given as a step function of Monte Carlo steps. The step width is taken to 0.001 and the field changes as a triangle wave between –0.1 and +0.1, overall. Figure 2(a) shows an example for the applied magnetic field and the change of magnetization in 5000 MCS, which are a part of more numerous Monte Carlo steps. In a few steps, magnetization has discrete changes, although it has a tendency to decrease as circle in Fig.2(a) in this region on the whole. Here we introduce an assumption that data less than 1000 MCS under the same condition, which is ordinarily discarded, reflect the medium state between the each result after 1000 MCS. Differential calculus dM/dt of the discrete components of the magnetic process including virtual state less than 1000 MCS for the applied magnetic field is performed as shown in Fig.2(b).

The simulation was carried out by the use of the super-computer, ORIGIN 2000 in the Institute of Fluid Science, Tohoku University. 1MCS took about 0.3 second and typical CPU time is 99900 sec.

3. Results and Discussions

Figure3 shows the calculated result for magnetic field dependence of magnetization (M-H curve). Magnetization is saturated over the magnetic field of 0.7. Along magnetic process a□b□c□d□e□f□a□b in Fig.3, dM/dt was calculated as shown in Fig.4. The behavior of dM/dt has good correspondence with experimental results of Barkhausen noise in some respects. The most notable point is the correspondence of the region with their peak intensities. And furthermore, in the region of suppressed noise between peak intensities, gradual increase of noise is seen for both them. Therefore we treat dM/dt as simulated Barkhausen noise. One of difference between Barkhausen noise and dM/dt is tail shape over the peak intensity of them. It may be caused by the difference of existence of voids and residual stress or saturation magnetic field. Moreover grain size dependence of dM/dt was calculated as shown in Fig.5. Original 31^3 spin cells cluster was divided into 2, 4, 8, 27, 64 clusters inserting void planes which could isolate both sides from exchange interaction. Then the relation between average of simulated Barkhausen noise and cluster size showed monotonous decrease as same as experimental results [2]. As the mentioned above, dM/dt calculated by Monte Carlo method well reproduces experimental Barkhausen noise and has possibility that it becomes a useful tool for analysis of NDE.

References

[1] R. L. Pasley, Mater. Eval., 28 (1970) 157.
[2] R. Hill, A. Cowking, J. Mackersie, NDT & E Int., 24 (1991) 179.

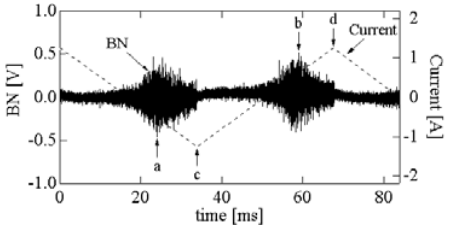

Fig.1 Experimental result of Barkhausen noise for a steal (SS400) under applied magnetic field formed into a triangle wave.

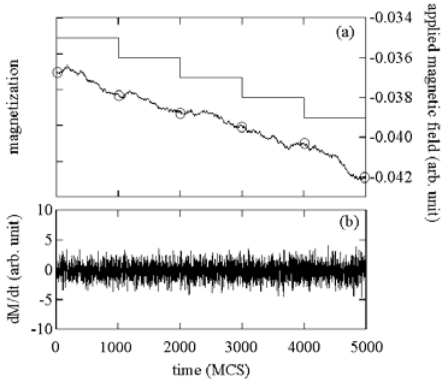

Fig.2 An example of Monte Carlo step dependence of (a) applied magnetic field and magnetization and (b) dM/dt.

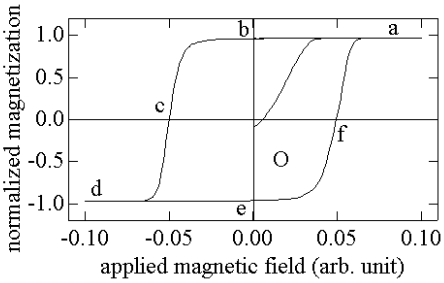

Fig.3 Calculated result for magnetic field dependence of magnetization (M-H curve).

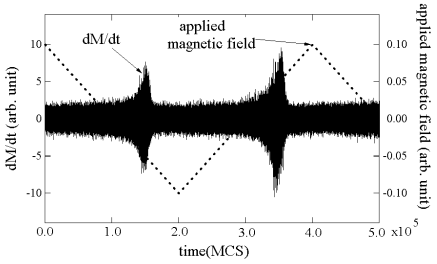

Fig.4 Differential calculus of the discrete components of the magnetic process under applied magnetic field formed into a pseudo-triangle wave.

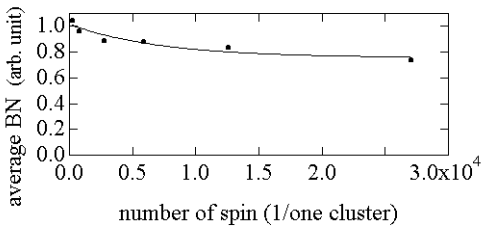

Fig.5 Relation between average of Barkhausen noise and spin cluster size.

Real Coding Genetic Algorithm for Jiles-Atherton Model Parameters Identification

J.V. Leite, S.L. Avila, N.J. Batistela, W.P. Carpes Jr., N. Sadowski, P. Kuo-Peng, J. P. A. Bastos
GRUCAD / EEL / CTC / UFSC
FlorianÛpolis, SC, P. O. Box 476, 88040-900, Brazil
jean@grucad.ufsc.br avila@grucad.ufsc.br

***Abstract* – The parameters set of the Jiles-Atherton (JA) hysteresis model is identified by using a real coded genetic algorithm. The parameters identification is performed by minimizing the mean squared error between experimental and simulated magnetic field curves. The procedure is validated by comparing experimental and simulated results.**

INTRODUCTION

Among the hysteresis models proposed in the last years for representation of nonlinear characteristics in magnetic materials the Jiles-Atherton (JA) model has been one of the most investigated. Compared to other models, the JA model has some advantages: it is formulated in terms of a differential equation; it uses only five parameters; and parameters identification is performed from a single measured hysteresis loop [1].

A modified JA model presenting the magnetic induction as independent variable was proposed in [2]. The main equation of this model is:

$$\frac{dM}{dB} = \frac{(1-c)\dfrac{dM_{irr}}{dB_e} + \dfrac{c}{\mu_0}\dfrac{dM_{an}}{dH_e}}{1+\mu_0(1-c)(1-\alpha)\dfrac{dM_{irr}}{dB_e} + c(1-\alpha)\dfrac{dM_{an}}{dH_e}} \qquad (1)$$

where M_{irr} is the irreversible components of total magnetization M; M_{an} represents the anhysteretic magnetization; δ is a directional parameter; H_e and B_e are the effective magnetic field and induction, respectively [1]; a, α, c, k and M_s are the five JA model parameters which have to be determined from a measured hysteresis loop [3][4].

This inverse model keeps the original advantages of the direct model and can be directly used in time-stepping finite element calculations using a formulation based on the vector potential.

PARAMETERS IDENTIFICATION

The mathematical model presented by Jiles and Atherton is based on physical considerations of the magnetic behavior of matter. As a result, the five parameters of the JA model have a physical significance.

Jiles and Thoelke [3] proposed the first methodology for JA parameters identification from an experimental B-H loop.

Several methods have been developed to achieve the best parameters set for the JA hysteresis model. Among them, some authors have proposed the use of optimization techniques to obtain a good representation of the hysteresis loops. For instance, [4] uses an optimization technique based on simulated annealing and [5] uses genetic algorithm with binary codification.

In this work we present an optimization methodology for the parameters identification using a real coded Genetic Algorithm (GA). The model parameters are obtained by fitting the simulated curve with the experimental one. This method is less time consuming compared to trial-and-error adjustment (as given in a previous work [6]) and, as it will be shown, the obtained parameters allow a good agreement between simulated and measured curves even for inner loops.

GENETIC ALGORITHMS

Genetic algorithms are optimization techniques based on the concepts of natural selection and genetics. Among the advantages of GAs, we can quote that they can optimize with continuous or discrete parameters and do not require information about gradients; the possible discontinuities present on the fitness function have little effect on overall optimization performance; they are resistant to become trapped in local optima; they work with numerically generated data, experimental data or analytical functions; and they can be employed for a wide variety of optimization problems [7].

Real coding is well suited to a large class of programming languages and to problems with a great number of variables. For this reason, modified genetic operators are being developed for a real coded GA that allow an effective exploration of the search space [8]. These modified genetic operators are used in this paper as well as the improvement tools presented in [9].

The GA was implemented with 30 individuals (each one with five variables corresponding to the parameters of the JA hysteresis model) and the maximum number of generations has been set to 50. The objective function to be minimized corresponds to the total mean squared error (*MSE*) between the experimental and simulated magnetic field curves.

SOME RESULTS

Fig. 1 shows the experimental and simulated hysteresis curves for a material A modeled with the set of parameters obtained with the methodology proposed here. Fig. 2 shows the experimental and simulated field curves of this material when submitted to a sinusoidal induction with a 1.24 T amplitude. Calculated and measured hysteresis loops for another material are also shown in Fig. 3; the corresponding field curves are presented in Fig. 4.

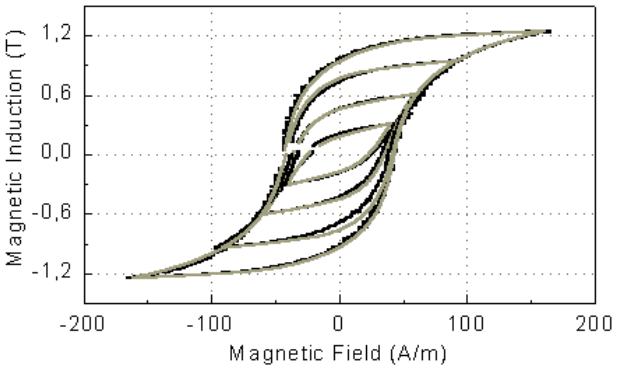

Fig. 1 ñ Hysteresis loops: measured and modeled for material A.

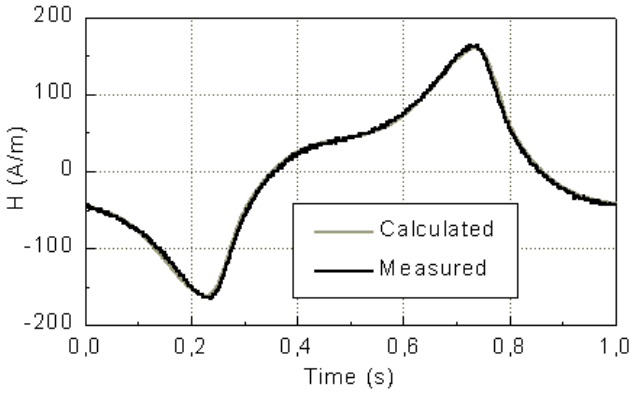

Fig. 2 ñ Field: measured and modeled for material A.

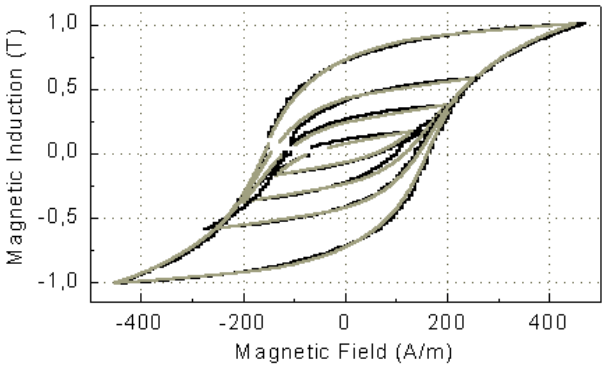

Fig. 3 ñ Hysteresis loops: measured and modeled for material B.

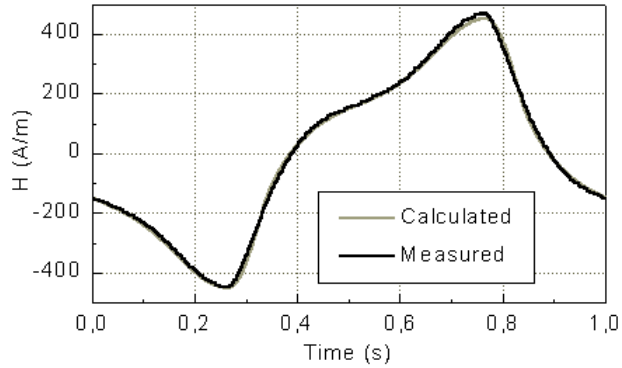

Fig. 4 ñ Field: measured and modeled for material B.

The comparison between these results shows a very good agreement.

Fig. 5 and 6 show, respectively, the evolution of the MSE for materials A and B. We observe that the error decreases quickly and the algorithm achieves an optimized set of parameters with little computational effort.

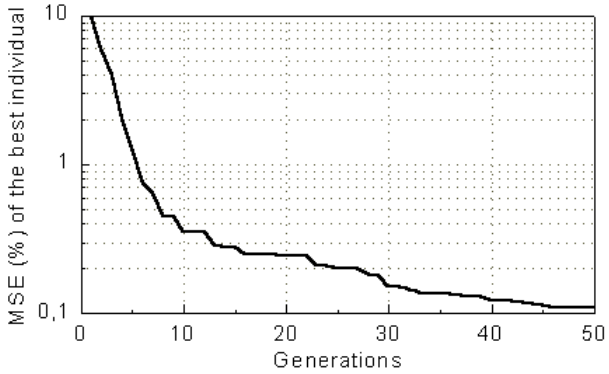

Fig. 5 ñ Evolution of the total error to material A.

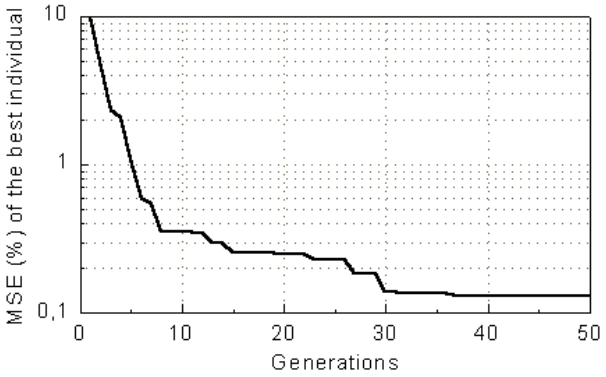

Fig. 6 ñ Evolution of the total error to material B.

REFERENCES

[1] D. C. Jiles, D. L. Atherton . ìTheory of ferromagnetic hysteresisî, *Magnetism Magn. Mater*., v. 61, pp. 48-60, 1986.

[2] N.Sadowski, N.J. Batistela, J.P.A.Bastos, M.Lajoie-Mazenc, ìAn Inverse Jiles-Atherton Model to Take into Account Hysteresis in Time Stepping Finite Element Calculationsî, *IEEE Trans. on Magn*., v. 38, n. 2, pp. 797ñ800, March 2002.

[3] Jiles, D.C.; Thoelke J.B. ìTheory of ferromagnetic hysteresis: determination of Model parameters from Experimental hysteresis loopsî. *IEEE Trans. Magn*. v. 25, n. 5, p.3928 - 3930, Sept 1989.

[4] Lederer, D.; Igarashi, H.; Kost, A.; Honma, T. ìOn the parameter identification and application of the Jiles-Atherton hysteresis model for numerical modeling of measured characteristicsî. *IEEE Trans. Mag*., v. 35, p. 1211 ñ 1214, 1999.

[5] Wilson, P. R.; Ross, J. Neil; Brown, A. D. ìOptimizing the Jilesñ Atherton Model of Hysteresis by a Genetic Algorithmî. *IEEE Trans Mag*, v. 37 n. 2 , p. 989 ñ 993, March 2001.

[6] Leite, J. V., Sadowski, N., Kuo-Peng, P. Batistela, N. J., Bastos, J. P. A. ìThe Inverse Jiles-Atherton Hysteresis Model Parameters Identificationî, *IEEE CEFC*, p. 261, 2002.

[7] Haupt, R. L. ìAn Introduction to Genetic Algorithms for Electromagnetics,î *IEEE AP-Mag.*, v. 37, n. 2, pp. 7ñ15, April 1995.

[8] Avila, S. L.; Carpes Jr. W. P.; Vasconcelos, J. A. ìGenetic Algorithms for Optimization of an Offset Reflector Antennaî, *to be submitted to COMPUMAG'2003*.

[9] Vasconcelos, J. A.; et al. ìImprovements in Genetic Algorithmsî, *IEEE Trans. on AP*, v. 37, n. 1, pp. 3414ñ3417, Sept. 2001.

COMPUMAG Saratoga Springs, New York USA
July 13 - 17, 2003

Use of barycentric dual grids for the solution of frequency domain problems by FIT

Lorenzo Codecasa, Vito Minerva, Marco Politi

Dipartimento di Elettronica e Informazione
Politecnico di Milano
Piazza Leonardo da Vinci, 32
20133 Milan, Italy
{codecasa, minerva, politi}@elet.polimi.it

***Abstract*—In this paper the Finite Integration Technique for the approximation of 3D electromagnetic boundary value problems is formulated in the hypothesis that the primal grid is composed of either (oblique) parallelepipeds or (oblique) triangular prisms or tetrahedra and that the dual grid is the barycentric subdivision of the primal grid. Novel constitutive relations are derived assuring solution matrices of symmetric and positive definite type.**

I. Introduction

The Finite Integration Technique (FIT) is largely used for the numerical solution of electromagnetic boundary value problems, both in the time and in the frequency domain [1], [2]. In particular, for electromagnetic boundary value problems in the frequency domain, the electromagnetic field is discretized using a primal grid $\mathcal{G}$ and a dual grid $\tilde{\mathcal{G}}$. The Maxwell's equations are formulated exactly in terms of the finite electromagnetic field quantities while the constitutive relations are only approximated.

In particular, constitutive equations can be naturally written when the dual grids are orthogonal. It results that the $\boldsymbol{v}$ vector, whose elements are the line integrals of the electric field $\mathbf{e}(\mathbf{r})$ along the edges of $\mathcal{G}$, is related to the $\tilde{\boldsymbol{\psi}}$ vector, whose elements are the fluxes of the electric displacement $\mathbf{d}(\mathbf{r}) = \varepsilon(\mathbf{r})\mathbf{e}(\mathbf{r})$ across the faces of $\tilde{\mathcal{G}}$, by the diagonal matrix $\mathbf{M}_\varepsilon$

$$\tilde{\boldsymbol{\psi}} \approx \mathbf{M}_\varepsilon \boldsymbol{v}. \tag{1}$$

This relation is approximate, being exact when the $\mathbf{d}(\mathbf{r})$ and $\mathbf{e}(\mathbf{r})$ fields are spatially uniform. Similarly the $\boldsymbol{\varphi}$ vector, whose elements are the fluxes of the magnetic induction $\mathbf{b}(\mathbf{r})$ across the faces of $\mathcal{G}$, is related to the $\tilde{\boldsymbol{f}}$ vector, whose elements are the line integrals of the magnetic field $\mathbf{h}(\mathbf{r}) = \nu(\mathbf{r})\mathbf{b}(\mathbf{r})$ along the edges of $\tilde{\mathcal{G}}$, by the diagonal matrix $\mathbf{M}_\nu$

$$\tilde{\boldsymbol{f}} \approx \mathbf{M}_\nu \boldsymbol{\varphi}. \tag{2}$$

Also this relation is approximate, requiring uniform $\mathbf{h}(\mathbf{r})$ and $\mathbf{b}(\mathbf{r})$ fields to become exact . Matrices $\mathbf{M}_\varepsilon$ and $\mathbf{M}_\nu$ are diagonal, positive definite, as is required for numerical analysis [3]. However, constitutive relations (1) and (2) can be written only if the electromagnetic media are isotropic and only if edges and faces of the primal grid $\mathcal{G}$ are orthogonal to the corresponding faces and edges of the dual grid $\tilde{\mathcal{G}}$, which imposes strict conditions over $\mathcal{G}$. Some attempts of removing these limitations of FIT have been presented in literature, mainly for staggered grids [4]. In these cases however, the proposed $\mathbf{M}_\varepsilon$ and $\mathbf{M}_\nu$ matrices, even if symmetric, are no longer assured to be positive definite. In this paper, constitutive relations (1) and (2) are written in the hypotheses that the primal grid $\mathcal{G}$ is composed of either (oblique) parallelepipeds or (oblique) triangular prisms or tetrahedra. Assuming that the dual grid $\tilde{\mathcal{G}}$ is built by the barycentric subdivision [5] of $\mathcal{G}$, which always exists, no other conditions are required to be satisfied by the primal grid $\mathcal{G}$. In this way the deduced $\mathbf{M}_\varepsilon$ and $\mathbf{M}_\nu$ matrices are symmetric and positive definite. The method is thus an extension of the standard FIT over orthogonal dual grids, reducing to it in the hypothesis that the grid $\mathcal{G}$ is composed of right parallelepipeds.

II. Constitutive relations

If the relation between $\tilde{\boldsymbol{\psi}}$ and $\boldsymbol{v}$ is approximated by (1) then the energetic quantity

$$\int_\tau \mathbf{e}(\mathbf{r}) \cdot (\varepsilon(\mathbf{r})\mathbf{e}(\mathbf{r}))^\star \, d\tau \tag{3}$$

is approximated by

$$\boldsymbol{v}^{\mathbf{T}} \cdot (\mathbf{M}_\varepsilon \boldsymbol{v})^\star. \tag{4}$$

In fact (4) converges to (3) for finer and finer discretizations, under mild assumptions, as proved in [6].

In order to guarantee the stability of the discretized electromagnetic boundary value problem, the converse approach is here considered: if matrix $\mathbf{M}_\varepsilon$ is such that (4) approximates (3), does (1) approximates the constitutive relation between $\tilde{\boldsymbol{\psi}}$ and $\boldsymbol{v}$? Hereafter a sufficient condition is given.

Let the primal grid $\mathcal{G}$ be composed either by (oblique) parallelepipeds or (oblique) triangular prisms or tetrahedra and let the dual grid $\tilde{\mathcal{G}}$ be the barycentric subdivision of $\mathcal{G}$. Further, let $\varepsilon(\mathbf{r})$ be uniform within each volume of $\mathcal{G}$ and let the electric field $\mathbf{e}(\mathbf{r})$ be approximated by

$$\mathbf{e}(\mathbf{r}) = \sum_1^l{}_i \, v_i \mathbf{w}_i^e(\mathbf{r}) \tag{5}$$

where v_i is the i-th element of the $l \times 1$ vector $\boldsymbol{v}$ and $\mathbf{w}_i^e(\mathbf{r})$ is the i-th weight function of $\mathbf{e}(\mathbf{r})$, defined as follows. The support of $\mathbf{w}_i^e(\mathbf{r})$ is the union of all the non-empty intersections of one volume of $\mathcal{G}$ with one volume of $\tilde{\mathcal{G}}$ that are adjacent to the i-th

edge of $\mathcal{G}$. In each of these intersections ρ, $\mathbf{w}_i^e(\mathbf{r})$ is a constant vector given by

$$\mathbf{w}_i^e(\mathbf{r}) = \frac{\mathbf{a}_j \times \mathbf{a}_k}{\mathbf{a}_i \times \mathbf{a}_j \cdot \mathbf{a}_k}$$

in which $\mathbf{a}_i$, $\mathbf{a}_j$ and $\mathbf{a}_k$ are three vectors that are tangent to the edges of $\mathcal{G}$ adjacent to ρ, having the same lengths of these edges (see Fig. 1). Using (5) for $\mathbf{e}(\mathbf{r})$, it results

$$\boldsymbol{v}^{\mathbf{T}} \cdot (\mathbf{M}_\varepsilon \boldsymbol{v})^\star = \int_\tau \mathbf{e}(\mathbf{r}) \cdot (\varepsilon(\mathbf{r})\, \mathbf{e}(\mathbf{r}))^\star \, d\tau$$

where the element at the i-th row and j-th column of $\mathbf{M}_\varepsilon$ is

$$\int_\tau \mathbf{w}_i^e(\mathbf{r}) \cdot (\varepsilon(\mathbf{r}) \mathbf{w}_j^e(\mathbf{r}))^\star \, d\tau.$$

This $\mathbf{M}_\varepsilon$ matrix, as easily proved, is symmetric and positive definite. Moreover, it approximates the relation between $\tilde{\psi}$ and $\boldsymbol{v}$. In fact the following necessary and sufficient condition is satisfied

$$\int_\tau \mathbf{w}_i^e(\mathbf{r})\, d\tau = \int_{\tilde{\sigma}_i} \mathbf{n}(\mathbf{r})\, d\sigma,$$

in which $\tilde{\sigma}_i$ is the i-th face of $\tilde{\mathcal{G}}$, of normal $\mathbf{n}(\mathbf{r})$.

Matrix $\mathbf{M}_\nu$ is deduced in a similar way. Let $\nu(\mathbf{r})$ be uniform within each volume of $\mathcal{G}$ and let the magnetic induction $\mathbf{b}(\mathbf{r})$ be approximated by

$$\mathbf{b}(\mathbf{r}) = \sum_1^f{}_i \, \varphi_i \mathbf{w}_i^b(\mathbf{r}) \qquad (6)$$

in which φ_i is the i-th element of the f-vector $\boldsymbol{\varphi}$ and $\mathbf{w}_i^b(\mathbf{r})$ is the i-th weight function of $\mathbf{b}(\mathbf{r})$, so defined. The support of $\mathbf{w}_i^b(\mathbf{r})$ is the union of all the non-empty intersections of one volume of $\mathcal{G}$ with one volume of $\tilde{\mathcal{G}}$ that are adjacent to the i-th face of $\mathcal{G}$. In each of these intersections ρ, $\mathbf{w}_i^b(\mathbf{r})$ is a constant vector given by

$$\mathbf{w}_i^b(\mathbf{r}) = \frac{\mathbf{b}_j \times \mathbf{b}_k}{\mathbf{b}_i \times \mathbf{b}_j \cdot \mathbf{b}_k}$$

in which $\mathbf{b}_i$, $\mathbf{b}_j$ and $\mathbf{b}_k$ are three vectors that are normal to the faces of $\mathcal{G}$ adjacent to ρ, having as lengths the area of these faces (see Fig. 1). Using (6) for $\mathbf{b}(\mathbf{r})$, it results

$$\boldsymbol{\varphi}^{\mathbf{T}} \cdot (\mathbf{M}_\nu \boldsymbol{\varphi})^\star = \int_\tau \mathbf{b}(\mathbf{r}) \cdot (\nu(\mathbf{r}) \mathbf{b}(\mathbf{r}))^\star \, d\tau,$$

where the element of $\mathbf{M}_\nu$ at the i-th row and j-th column is

$$\int_\tau \mathbf{w}_i^b(\mathbf{r}) \cdot (\nu(\mathbf{r}) \mathbf{w}_j^b(\mathbf{r}))^\star \, d\tau.$$

Also $\mathbf{M}_\nu$ matrix, as easily proved, is symmetric and positive definite and approximates the relation between $\tilde{\boldsymbol{f}}$ and $\boldsymbol{\varphi}$. In fact the following necessary and sufficient condition is satisfied

$$\int_\tau \mathbf{w}_i^b(\mathbf{r})\, d\tau = \int_{\tilde{\gamma}_i} \mathbf{t}(\mathbf{r})\, d\sigma,$$

where $\tilde{\gamma}_i$ is the i-th edge of $\tilde{\mathcal{G}}$, of tangent $\mathbf{t}(\mathbf{r})$.

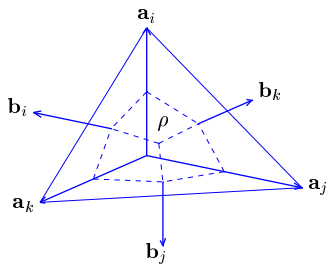

Fig. 1. Vectors $\mathbf{a}_i$, $\mathbf{a}_j$, $\mathbf{a}_k$, and $\mathbf{b}_i$, $\mathbf{b}_j$, $\mathbf{b}_k$, of the ρ region.

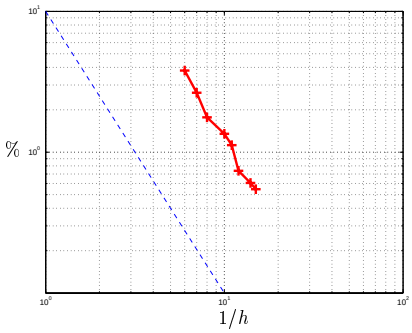

Fig. 2. Per cent error in the energy norm at $\omega/\omega_c = 1.5$ as a function of h.

III. Numerical Results

The field inside a short-circuited section rectangular waveguide, under TE_{10} excitation, has been evalued as a simple test case. The analyses have been performed at different normalized angular frequencies ω/ω_c, using a primal grid $\mathcal{G}$ composed of triangular prisms. The resulting error in the norm of the energy [6] is shown in Fig. 2, as a function of the maximum diameter h of the volumes of $\mathcal{G}$.

IV. Conclusion

In this paper the solution of electromagnetic boundary value problems by FIT has been extended to the case of primal grid composed of either (oblique) parallelepipeds or (oblique) triangular prisms or tetrahedra adopting as dual grid the barycentric subdivision of the primal one. Novel constitutive relations have been deduced leading to symmetric, positive definite matrices. This method can be easily extended to anisotropic media.

References

[1] T. Weiland, A Discretization Method for the Solution of Maxwell's Equations for Six-Component Fields, *Electronic and Communication (AEÜ)*, vol. 31, p. 116, 1977

[2] E. Tonti, "Finite formulation of electromagnetic field", *IEEE Trans. Magn.*, vol. 38, p. 333, 2002.

[3] R. Schuhmann, P. Schmidt, T. Weiland, "A New Whitney-Based Material Operator for the Finite-Integration Technique on Triangular Grids", *IEEE Trans. Magn.*, vol. 38, p. 409, 2002.

[4] R. Schuhmann and T. Weiland, "Stability of the FDTD algorithm on nonorthogonal grids related to the spatial interpolation scheme", *IEEE Trans. Magn.*, vol. 34, p. 2751, 1998.

[5] A. Bossavit, Computational Electromagnetism, Academic Press (Boston), 1998.

[6] L. Codecasa, M. Politi "Consistent Spatial Discretization of Electromagnetic Boundary Value Problems Through Augmented Dual Grids", submitted to *IEEE Tran. Antennas Propag.*

COMPUMAG Saratoga Springs, New York USA
July 13 - 17, 2003

A New Consistent Way to build Symmetric Constitutive Matrices within the Cell Method on arbitrary 2D Grids

Massimiliano Marrone
DEEI, University of Trieste,
Piazzale Europa 1, 34127 Trieste, Italy
e-mail: marrone@dic.univ.trieste.it

***Abstract*—Starting from the constitutive matrices built by the Microcell Interpolation Scheme we propose a general approach to symmetrize them in a consistent way. The resulting matrices, sparse and positive definite in most of the cases, are suitable to be utilized in the Cell Method in order to ensure stability in solving two dimensional time-domain problems on arbitrary unstructured grids.**

I. Introduction

The study of the mathematical structure common to many physical theories [1] provides a new discrete mathematical model of the electromagnetic field theory that gives rise to a new method for solving electromagnetic static and dynamic problems on unstructured grids [2][3]. This new method, called Cell Method (CM), is very similar to the Finite Integration Technique (FIT) [4] for the space part but different for the time part, that is continuous in FIT. CM is based on the followings tools:
1)Two oriented space-time cell complexes and a relationship of duality between them. A space cell complex, synonymous of three dimensional grid, is a structured collection of points, lines, surfaces and volumes whereas a time cell complex, synonymous of one dimensional grid, is a structured collection of instants and intervals [2].
2)The global (integral) variables (Electric V and Magnetic voltage F, Electric Ψ and Magnetic flux Φ, Electric current I, Electric charge content Q_c), in order to represent physical variables, and their physically coherent association with the oriented space and time cells [1][2].

Within CM the e.m. laws can be divided in two classes: **Topological equations** (field equations). Since they do not use metric concepts, they can be enforced on the cell complexes in an exact discrete form by using appropriate incidence matrices. If we denote with $\mathbf{G}$, $\mathbf{C}$, $\mathbf{D}$ and $\tilde{\mathbf{G}} = \mathbf{D}^{\mathbf{T}}$, $\tilde{\mathbf{C}} = \mathbf{C}^{\mathbf{T}}$, $\tilde{\mathbf{D}} = -\mathbf{G}^{\mathbf{T}}$, the incidence matrices [1][3][4] related to the primal and dual cell complexes respectively, which are the discrete counterparts of the differential operators *gradient*, *curl* and *divergence*, the topological equations can be expressed as follows:

-Faraday-Neumann law: $\mathbf{C}\mathbf{V}^{n+1/2} = -(\mathbf{\Phi}^{n+1} - \mathbf{\Phi}^{n})/\tau$
-Magnetic Gauss law: $\mathbf{D}\mathbf{\Phi}^{n} = 0$
-Maxwell-Ampère law: $\tilde{\mathbf{C}}\mathbf{F}^{n} = (\mathbf{\Psi}^{n+1/2} - \mathbf{\Psi}^{n-1/2})/\tau + \mathbf{I}^{n}$
-Electric Gauss law: $\tilde{\mathbf{D}}\mathbf{\Psi}^{n+1/2} = \mathbf{Q}_c{}^{n+1/2}$

where $\mathbf{V}^{n+1/2}$, $\mathbf{\Phi}^{n}$, $\mathbf{F}^{n}$, $\mathbf{\Psi}^{n+1/2}$, $\mathbf{I}^{n}$, $\mathbf{Q}_c{}^{n+1/2}$ are arrays of scalars, τ is the time step and the apexes n e $n+1/2$ denote the primal and the dual time instants respectively.
Constitutive relations. They use metric concepts and material parameters and can be enforced on the cell complexes only in an approximated discrete form by using suitable constitutive matrices. Let us denote with $\mathbf{M}_\varepsilon$, $\mathbf{M}_\mu$ the constitutive matrices that enter in the following algebraic constitutive relations:

Electric constitutive relation $\quad \mathbf{\Psi}^{n+1/2} = \mathbf{M}_\varepsilon \mathbf{V}^{n+1/2}$
Magnetic constitutive relation $\quad \mathbf{\Phi}^{n} = \mathbf{M}_\mu \mathbf{F}^{n}$

The desired features of the constitutive matrices are: (1)**Symmetry** and (2)**Positive definiteness**, in order to ensure stability [4][5], (3)**Sparsity**, to save memory and assure fast computations. Moreover they must ensure the (4)**Consistency** [5] and the (5)**Accuracy** of the numerical method employing these matrices. In this paper we propose a general way to build them, satisfying $(1)-(5)$ in *most of the cases*, for many kinds of two dimensional grids (triangular, quadrilateral, square grids with subgridding etc) starting from the constitutive matrices built by the *Microcell Interpolation Scheme* (MIS) [2].

II. A consistent symmetrization

In MIS an arbitrary constitutive matrix $\mathbf{M}_\varepsilon$ is built by composition of local constitutive matrices $\mathbf{M}_{\varepsilon a}$, one for each primal surface S_a in the 2D cases, that will be located along the main diagonal of $\mathbf{M}_\varepsilon$. Since the dimension of each $\mathbf{M}_{\varepsilon a}$ is equal to the number of edges of S_a then $\mathbf{M}_\varepsilon$ is sparse in general. In order to meet the other features it is enough to deal with the local constitutive matrices [5]. Given an arbitrary local constitutive matrix $\mathbf{M}$, such as $\mathbf{M}_{\varepsilon a}$ i.e., built by MIS, it is not symmetric in general, but it meets the feature (5) both in frequency domain [3] and in time domain applications [2]. Our goal is to find a new local constitutive matrix $\mathbf{M}_S$ such that:
(A) $\mathbf{M}_S$ is symmetric.
(B) $\mathbf{M}_S$ meets the feature about the consistency [5].
(C) $\mathbf{M}_S$ is as close as possible to $\mathbf{M}$ in a square mean.
The request (C) is formulated for two reasons based on empirical assumptions. The first is preserving the accuracy of the numerical method due to the original matrix

$\mathbf{M}$. The second is satisfying the positive definiteness, since $\mathbf{M}$ has most of the larger values on the main diagonal. From the requests (A) and (B) it is possible to build a linear system, whose unknowns x are the entries of the difference matrix $\mathbf{M}_S - \mathbf{M}$, that we represent in the usual form $Ax = b$. In all the tested cases we have verified that in the linear system the unknowns are more than the equations and that at least a solution x exists. In order to satisfy the request (C) we are interested in the minimum norm solution $\|x\|_2$ that is $x = A^+ b$ where $A^+$is the *Moore-Penrose pseudo inverse*[6] of A.
In order to check if the request (C) leads to the positive definiteness of the constitutive matrices, we have performed thousands of tests on symmetrized local constitutive matrices built for primal surfaces for each number of edges n=3,...,6. The percentages of non positive definite matrices, due to degenerate cells with very bad shapes, have been very low (Table I).

TABLE I
Percentages of failure in the positive definiteness tests

edges	3	4	5	6
%	0.074	0.000	0.004	0.526

III. Numerical results

In order to check the accuracy of CM with the new constitutive matrices we have performed two tests and in both of them we have compared the results using the old constitutive matrices built by MIS and the new symmetric ones (Symmetrized MIS). In the first test, using the exact solution $\varphi(x, y) = exp(x)cos(y)$ of the Laplace equation on a square domain [0,1]x[0,1], by the corresponding Dirichlet boundary condition, the numerical solution of the Laplace equation:

$$\mathbf{G}^T \mathbf{M}_\varepsilon \mathbf{G} \varphi = 0$$

has been calculated employing a primal triangular grid (Fig.1a) and a primal quadrilateral grid (Fig.1b). In the second test we have calculated the resonant frequencies of a $2D$ circular cavity with radius $R = 0.5$ by CM solving the following generalized eigenvalues problem for TEz modes:

$$\mathbf{C}^T \mathbf{M}_\mu^{-1} \mathbf{C} \mathbf{V} = \omega^2 \mathbf{M}_\varepsilon \mathbf{V}$$

The eigenfrequencies have been calculated employing a triangular primal grid (Fig.2a), a quadrilateral primal grid (Fig.2b) and a square grid with subgridding (Fig.3a).

IV. CONCLUSION

In this paper we have outlined a new consistent way to build symmetric sparse constitutive matrices within the Cell Method on arbitrary 2D grids. Numerical tests show that the constitutive matrices rarely fail to be positive definite and that the new approach is accurate.

References

[1] E. Tonti, "On the formal structure of physical theories", preprint of the *Italian National Research Council* 1975.

[2] M. Marrone, "Computational Aspects of Cell Method in Electrodynamics", *PIER monograph series*, vol.32, pp 317-356, 2001.

[3] M. Marrone, A.M.F. Frasson, H.E.H. Figueroa , "A Novel Numerical Approach for Electromagnetic Scattering: The Cell Method", in *Proc. IEEE AP-S/URSI*, 2002, Vol. 1,pp. 160-163.

[4] R. Schuhmann, P. Schmidt, T. Weiland, "A New Whitney-Based Material Operator for the Finite-Integration Technique on Triangular Grids", *IEEE Trans. Magn.*, vol.38, pp 409-412, March 2002.

[5] A. Bossavit, "Computational Electromagnetism and Geometry: Building a Finite-Dimensional "Maxwell's house"", *JSAEM* , July 1999.

[6] J. Stensby, "AX=b: The Minimum Norm Solution and the Least-Square-Error Problem", [Online]. Available: http://www.eb.uah.edu/ece/courses/ee448/chapter6.pdf.

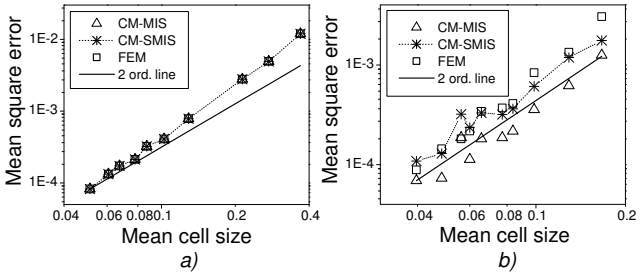

Fig. 1. Mean square error vs mean cell size in the solution of the Laplace problem on a square domain (a) using a triangular grid (b) using a quadrilateral grid.

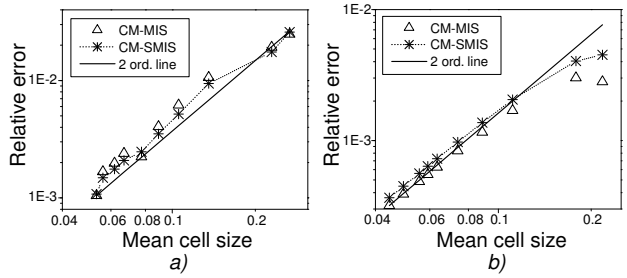

Fig. 2. Relative error vs mean cell size in the calculus of the resonant frequency of a circular cavity (a) using a triangular grid (b) using a quadrilateral grid.

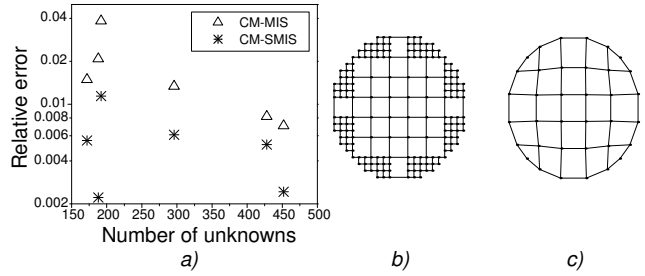

Fig. 3. (a) Relative error vs number of unknowns in the calculus of the resonant frequency of a circular cavity with a square grid and subgridding. (b) Primal square grid with subgridding. (c) Primal quadrilateral grid.

Stability and Fidelity of the Finite Element Time Domain Method with Distorted Mesh

Boguslaw Butrylo[(1)], Christian Vollaire[(2)], Laurent Nicolas[(2)]

[(1)] Bialystok Technical University
ul. Wiejska 45D
15-903 Bialystok, Poland
bogb@cksr.ac.bialystok.pl

[(2)] Ecole Centrale de Lyon
36, Avenue Guy de Collongue
69134 Ecully Cedex, France
{Christian.Vollaire, Laurent.Nicolas}@eea.ec-lyon.fr

Abstract – **Properties of the three-dimensional formulation of the finite element time domain (FETD) algorithm are analyzed. First order edge elements are implemented in the formulation. Several issues associated with deformation of the structured mesh and efficiency of the time integration scheme are presented. The convergence and stability of the time domain algorithm depending on the spatial discretization are discussed. The numerical accuracy of the simulation is studied.**

INTRODUCTION

The spatial discretization of a finite element model and quality of the mesh have an effect on the properties of the finite-element time-domain algorithm used for wave propagating problems. The value of the time step Δt for known FE grid must satisfy CFL restriction [1]:

$$\Delta t \le q \cdot \frac{\min(\Delta r)}{v}, \qquad (1)$$

where Δr is a dimension of an element, v is the speed of EM wave in a medium, and q is the Courant number. If the finite element mesh is distorted or locally refined, the value of the Courant number depends on quality of the mesh and method of integration in time domain. There is no clear rule to determine this value of the q coefficient. The objective of this paper is to analyze the stability and convergence of the FETD-edge element algorithm in order to estimate the minimum value of the Courant number.

TIME DOMAIN MODELING

Application of the Galerkin method to a typical wave equation, and spatial discretization of the analyzed model yield to a matrix linear ordinary differential equation (ODE)

$$\mathbf{T}\frac{d^2\mathbf{e}}{dt^2} + \mathbf{R}\frac{d\mathbf{e}}{dt} + \mathbf{S}\cdot\mathbf{e} + \mathbf{f}(t) = 0, \qquad (2)$$

where components of a mass matrix **T**, a stiffness matrix **S**, and a damping matrix **R** are stated by equations

$$t_{ij} = \int_{V_p} \varepsilon \mathbf{W}_i \mathbf{W}_j dV \;,\; s_{ij} = \int_{V_p} \frac{1}{\mu}(\nabla\times\mathbf{W}_i)(\nabla\times\mathbf{W}_j)dV \;, \text{(3a, b)}$$

$$r_{ij} = \int_{V_p} \sigma \mathbf{W}_i \mathbf{W}_j dV + \int_{S_{ABC,p}} \mathbf{W}_j \frac{1}{\mu c}(\mathbf{W}_i \times \vec{\mathbf{n}})dS \;. \qquad (3c)$$

The **f**(t) vector represents a dynamic load in the analyzed model. The numerical model is approximated by edge elements, therefore $\mathbf{W}_i$ and $\mathbf{W}_j$ are the edge-based vector shape functions. In the elaborated algorithm the first order **H**(*rot*, *Ω*) tetrahedral elements are applied. The first order Engquist-Majda boundary condition is implemented on the external surface to modelize an unbounded domain [2].

The ODE is transferred into linear algebraic equation by discretization of the time domain. Two unconditionally stable (backward Euler scheme, Newmark method [1]) and two conditionally stable (central Euler and mixed Euler) schemes are used in the algorithm. For example, the final matrix equation for central Euler scheme is stated by the form

$$\left(\mathbf{T} + \frac{\Delta t}{2}\mathbf{R}\right)\mathbf{e}_{n+1} = \left(2\mathbf{T} - \Delta t^2\mathbf{S}\right)\mathbf{e}_n + \left(\frac{\Delta t}{2}\mathbf{R} - \mathbf{T}\right)\mathbf{e}_{n-1} - \Delta t^2\mathbf{f}_n \quad (4)$$

while mixed time integration scheme (the backward Euler scheme for the first derivative and central Euler scheme for the second derivative of time) results in the following equation

$$\mathbf{T}\cdot\mathbf{e}_{n+1} = \left(2\mathbf{T} - \Delta t\mathbf{R} - \Delta t^2\mathbf{S}\right)\cdot\mathbf{e}_n + \left(\Delta t\mathbf{R} - \mathbf{T}\right)\cdot\mathbf{e}_{n-1} - \Delta t^2\mathbf{f}_n \,. \quad (5)$$

The preconditioned conjugate gradient algorithm (PCG) with the SSOR preconditioner is applied to solve the final, time dependent matrix equation $\mathbf{A}\cdot\mathbf{e}_{n+1}=\mathbf{b}_n$ [3]. The computational cost of the PCG algorithm is known to be approximately $N_{DOF}^{1.5}$, but the quality of the mesh has an effect on the total cost of the iterative solver.

RESULTS AND DISCUSSION

The presented time domain algorithm is used to calculate a test problem with a monochromatic plane wave propagating in a free space. Several 3D rectangular domains are meshed with the same number of elements (46305 tetrahedral elements, 20 nodes per wave-length) leading to several distorted mesh. The unequivocal information about distortion of the tetrahedral mesh is expressed by the Robert/Roux factor [4]:

$$Q_R = N \cdot \left(\frac{V_T}{V_S}\right)^{1/3}, \qquad (6)$$

where N - a normalization coefficient, V_T - the volume of a

tetrahedron, V_S - the volume of a circumscribed sphere. This factor can change from 0 (4 points lie in a plane) to 1 (ideal, regular tetrahedral element).

The created FE mesh is based on a cubic discretization of the 3D rectangular model. Two types of the tetrahedral mesh are used (fig. 1). The first mesh (A) has some elements (20%) with better Robert/Roux quality factor, while the second grid (B) consists of similar tetrahedral elements (uniform value of the Q_R). Both types of FE grids are described by the minimum value of the Q_R coefficient.

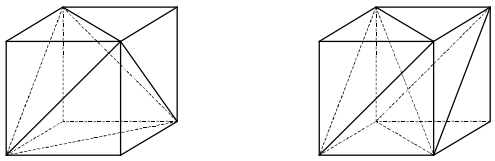

Fig. 1. Two types of tetrahedral grid inscribed into a single cubic element.

It is shown from the numerical results, that the value of the Courant number must be decreased when the distortion of the FE mesh increases (fig. 2). If the value of q factor is greater than the value presented on the figure, the central and mixed Euler schemes are not stable.

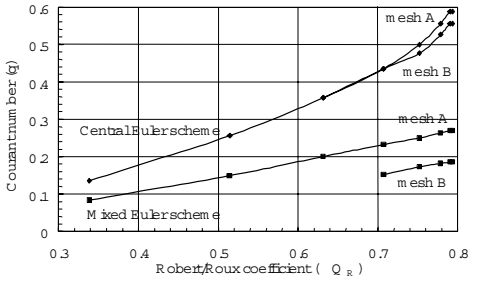

Fig. 2. Maximal value of q factor as a function of mesh deformation.

It is also shown that the difference between A and B meshes for central Euler scheme is perceptible only when the ideal FE mesh is created. If the value of Q_R factor is less than 0.7, the maximum q coefficient is equal for these types of the tetrahedral grid. Both conditionally stable schemes do not converge when the inferior mesh (B) is significantly distorted (Q_R<0.615 for central scheme, and Q_R<0.7 for mixed scheme). The set of tetrahedral elements with better characteristic of the shape (20%) improves the overall stability of the time domain algorithm for the A-type mesh. This essential factor of stabilization is lost for the B mesh.

The mixed time integration scheme needs lower q coefficient than the central scheme. It means, the value of time step Δt must be smaller, and computational cost of the FETD algorithm increases. However the mixed scheme is useful in explicit formulation of the algorithm, because the mass matrix has to be lumped solely.

The results of numerical simulation are compared to the analytical solution. The backward Euler method introduces the largest magnitude error (fig. 3). Its maximal value is about 20%. The fidelity of Newmark method is better than the backward scheme for both the ideal and distorted meshes. The maximum magnitude error for conditionally stable schemes is less than 5%. The value of the error for these schemes increases two times when the distortion is changed in a narrow scope $Q_R \in \langle 0.615, 0.8 \rangle$.

The good agreement between computational and analytical results demands enlargement of iterations in the PCG algorithm (fig. 4). In this way the efficiency of the PCG algorithm decreases, because more float-point operations in the PCG algorithm are required to find the final solution. When the distorted FE mesh is used the matrix **A** becomes worse conditioned and diagonally dominant. The components on the diagonal are constant while some non-diagonal components are equal to them. The second part of the off-diagonal components of **A** matrix goes to zero when the distortion increases.

These results indicate the tight relation between performance of the algorithm and the quality of FE mesh. The stability and accuracy of the algorithm with unstructured mesh depend on the local quality of the grid and the total statistic of the Q_R coefficient in the model.

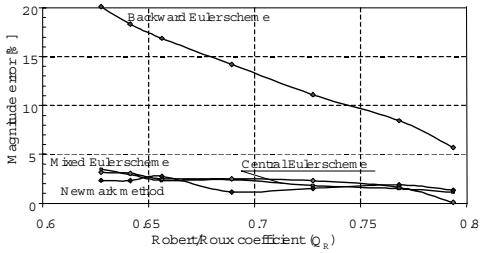

Fig. 3. Maximum value of magnitude error for uniform, distorted mesh.

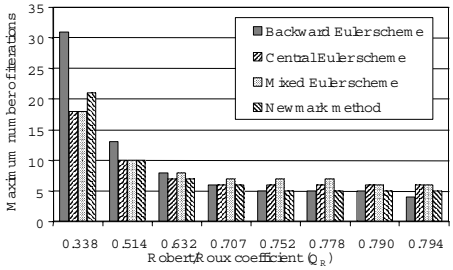

Fig. 4. Maximal number of iterations in PCG algorithm as a function of Q_R factor.

REFERENCES

[1] U. Navsariwala, S. Gedney, "An Unconditionally Stable Parallel Finite Element Time Domain Algorithm," *IEEE APS/URSI Symposium,* Baltimore, 1996.

[2] B. Engquist, A. Majda, "Absorbing Boundary Conditions for Numerical Simulation of Waves," Math. of Computation, vol. 31, No. 139, pp. 629-651, 1977.

[3] C. Vollaire, L. Nicolas, "Preconditioning Techniques for the Conjugate Gradient Solver on a Parallel Distributed Memory Computer," *IEEE Trans. on Magnetics*, IEEE, vol. 34, No 5, pp. 3347-3350, 1998.

[4] P. W. Daly, "The Tetrahedron Quality Factors of CSDS," Max-Planck-Institut, http://www.mpae.gwdg.de/~daly/tetra.html, 1994.

Investigation of Optimization Techniques for the Convergence Improvement of Higher-Order Whitney Element FEM in RF and Microwave Analysis

T. V. Yioultsis[(1)], I. T. Rekanos[(2)], and T. D. Tsiboukis[(1)]
[(1)] Dept. of Electrical and Computer Engineering, Aristotle University of Thessaloniki, GR-54124, Thessaloniki, GREECE
[(2)] Dept. of Informatics and Communications, Technological Educational Institute of Serres, GR-62124, Serres, GREECE

Abstract – A new concept based on optimization of convergence for higher order FEM is presented in this paper. The key feature is the existence of a multidimensional family of higher order vector finite elements which allows infinitely many choices of different basis functions providing the same accuracy but being different with respect to convergence properties. Several optimization schemes are investigated and proposed to trace the optimal element.

INTRODUCTION

A number of different generalizations of Whitney elements can be found in the literature [1]-[4] with significantly different convergence characteristics [5]. However, the majority of such elements actually belong to the same class since they are related to each other by a simple affine transformation. Therefore, an optimal, with respect to convergence element can be derived, if the transformation is defined such that the eigenvalues of the element matrix are as clustered as possible [6]. In this paper, we investigate several different optimization strategies to deal with problem-specific cases and the effect of this choice on the convergence rate. Several results have been considered results, including a 2-D scattering problem and a 3-D patch antenna analysis, which demonstrate a remarkable improvement of convergence, especially in the case of severely ill-conditioned matrices that arise due to the presence of different materials in the same problem. In a further level, we propose the use of different transformations in different regions and, despite the lack of a clear optimization criterion, an additional improvement is observed, again, in the case of the most ill-conditioned matrices. The study is ongoing and extends to elaborate optimization shemes, in a quest of improvement in some notoriously severe cases, like the presence of perfectly matched layers (PMLs) in FEM simulations.

OPTIMIZED WHITNEY ELEMENTS

Any second order Whitney element of the multidimensional class can be derived by appropriate transformations to a reference element [2], having two DoFs on each edge (i,j), and two on each facet $\{i,j,k\}$, or any other analogous existing element of the literature with a possible exception of [1] which is a marginal case, though having very good convergence properties. A consistent transformation of basis functions is, then, sought, which would provide optimal convergence. If the DoFs and basis functions for a single element are represented using column vectors **F** and **W**, respectively, we seek transformations of the form

$$\mathbf{F} \quad \mathbf{MF},\ \overline{\mathbf{W}} \quad \overline{\mathbf{W}}, \tag{1}$$

where **M** and are appropriate transformation matrices. These transformation matrices are, naturally, related to each other, since the unknown field in the new basis is given by,

$$\overline{F} \quad \mathbf{F}^T\overline{\mathbf{W}} \quad (\mathbf{MF})^T \quad \overline{\mathbf{W}} \quad \mathbf{F}^T(\mathbf{M}^T \quad)\overline{\mathbf{W}}. \tag{2}$$

We require that the field is invariant under (1), hence

$$= (\mathbf{M}^T)^{\ 1}. \tag{3}$$

What is of primary concern in this context is the transformation of the FEM matrices. Again, using column vector notation, the mass matrix, **T**, is transformed via the following congruence transformation

$$\begin{aligned} \mathbf{T} \quad T_{ij} \quad \langle \overline{w}_i, \overline{w}_i \rangle \quad \langle \overline{w}_i, \overline{w}_i \rangle \quad & \int_{V_e} \overline{w}_i \ \overline{w}_i \, dv \\ \int_{V_e} \overline{\mathbf{W}}\,\overline{\mathbf{W}}^T dv \quad & \int_{V_e} \overline{\mathbf{W}}\mathbf{W}^T \quad ^T dv \quad \mathbf{T} \quad ^T \end{aligned} \tag{4}$$

which also holds for the stiffness matrix, **S**.

The transformation matrices should, then, be defined such that the property of tangential continuity property is preserved. Therefore, **M** will include appropriate links of DoFs, shown in Fig. 1 for each facet of the tetrahedron. Other links, e.g. between edge degrees of freedom not being on the same edge or facet or facet degrees of freedom on different facets are not allowed, since they violate continuity.

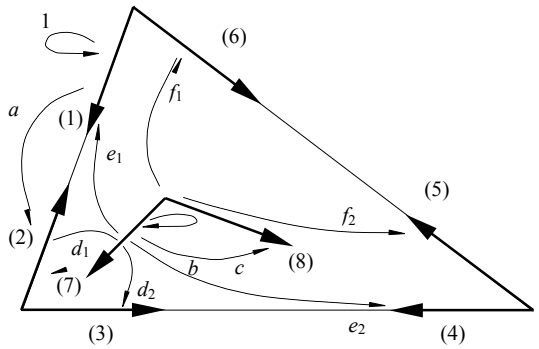

Fig. 1. Graphic representation of the transformation of DoFs #1 and #7 in a facet of a tetrahedral 2nd order Whitney element.

If the numbering of degrees of freedom is chosen in a sequential way as in [2] **M** takes the form of Fig. 2(a), in terms of a set of nine arbitrary parameters. This transformation can be easily included in an existing code.

Next, the transformation providing optimal convergence is sought by means of an eigenvalue clustering criterion for the local, element matrix. Although it is not well established which criterion actually provides best performance, it seems that minimization of the following measure of clustering,

$$F(\mathbf{p}) \quad \sum_{i=1}^{N_f} \left| \lambda_i(\mathbf{p}) \quad \max \lambda_i(\mathbf{p}) \right|, \qquad (5)$$

where $\mathbf{p} = [a\ b\ c\ d_1\ d_2\ e_1\ e_2\ f_1\ f_2]^T$ is the parameter vector and $\lambda_i(\mathbf{p})$ the eigenvalues of the transformed matrix, provides the best results, while a criterion based on the condition number fails, possibly due to the indefinite system matrices. The optimization is done by line search algorithms or gradient schemes. Other criteria like a measure of "diagonality", as well as multiobjective optimization have been also considered.

Finally, we investigate the effect of introducing different transformations in different materials. The use of appropriate parameters in each region does not provide any significant improvement, while if the optimization is performed for the main material only and the set of parameters for the other regions is adjusted such that the corresponding eigenvalues match, as closely as possible, the eigenvalues of the element matrix in the main region, an additional improvement is observed in the case of extremely ill-conditioned matrices.

COMPUTATIONAL RESULTS

We consider both 2-D and 3-D problems of scattering and radiation of a patch antenna. A PML is used for mesh termination, which makes the convergence in 3-D even slower, compared to other ABCs. For a uniform comparison, we solve the system by means of a conjugate gradient scheme with diagonal scaling. The optimizations are based on an arbitrarily chosen, badly-shaped element. In Fig 2(b), a characteristic graph of the convergence improvement is shown. A comparison of convergence for different problem sizes and values of the relative dielectric permittivity is shown in Table I. The most impressive results are observed in the case of the most severely ill-conditioned matrices due to active materials. In such cases, remarkable improvement is achieved by means of region-specific transformations, reaching a reduction to a number of iterations less than 4% of that in the case of the reference element.

In general, the ideas introduced in this paper could be considered a kind of geometric preconditioning that not only provides an optimally-conditioned approximation but is also open to further improvements, such as the **A**-V formulation, multigrid preconditioners or investigation of more general classes of Whitney elements [7].

REFERENCES

[1] J. F. Lee, D. K. Sun, and Z. J. Cendes, "Tangential vector finite elements for electromagnetic field computation," *IEEE Trans. Magn.*, vol. 27, no. 5, pp. 4032-4035, Sept. 1991.

[2] T. V. Yioultsis and T. D. Tsiboukis, "Development and implementation of second and third order vector finite elements in various 3-D electromagnetic field problems," *IEEE Trans. Magn.*, vol. 33, no. 2, pp. 1812-1815, Mar. 1997.

[3] R. D. Graglia, D. R. Wilton and A. F. Peterson, "Higher order interpolatory vector bases for computational electromagnetics," *IEEE Trans. Antennas Propagat.*, vol. 45, no. 3, pp. 329-342, Mar. 1997.

[4] L. S. Andersen and J. L. Volakis, "Hierarchical tangential vector finite elements for tetrahedral," *IEEE Microwave Guided Wave Lett.*, vol. 8, no. 3, pp. 127-129, Mar. 1998.

[5] Z. Ren and N. Ida, "Solving 3D eddy current problems using second order nodal and edge elements," *IEEE Trans. Magn*, vol. 36, no. 4, pp. 746-750, July 2000.

[6] T. V. Yioultsis and T. D. Tsiboukis, "Convergence-optimized higher order vector finite elements for microwave simulations," *IEEE Microw. and Wireless Comp. Lett.*, vol. 11, no. 10, Oct. 2001.

[7] I. Tsukerman, "General tangentially continuous vector elements" *CEFC 2002,* Perugia, 2002.

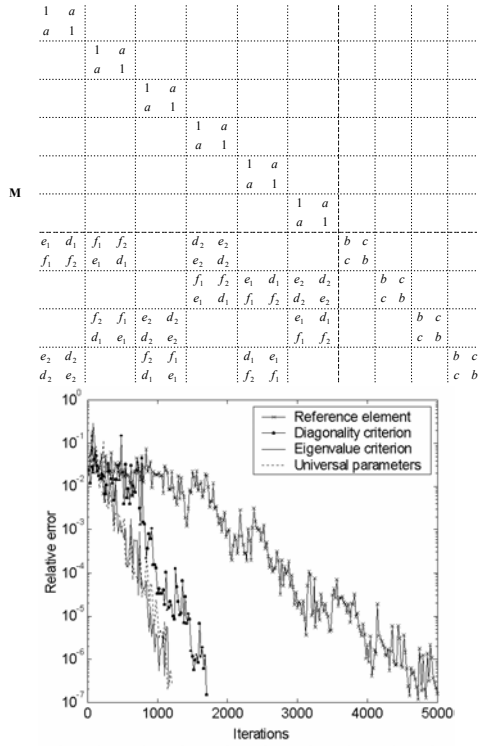

Fig. 2. (a) 3-D transformation matrix (b) Improvement of convergence rate

TABLE I
ITERATIONS FOR CONVERGENCE (2-D)

Total DOFs	ε_r	Ref. element	Optimized	Material-optimized
14288	4	3707	914(25%)	1221(33%)
14288	4-*j*10	2280	551(24%)	630(28%)
14288	4+*j*10	83447	5735(7%)	3347(4%)
22848	4	4970	1236(25%)	1439(29%)
22848	4-*j*10	2920	775(27%)	723(25%)
22848	4+*j*10	129249	7472(6%)	4235(3%)

P-adaptive Computation of the Scattering Parameters of 3D Microwave Devices

D. Nair and J. P. Webb
Department of Electrical and Computer Engineering
McGill University, 3480 University Street
Montreal, H3A 2A7, Canada
jon.webb@mcgill.ca

***Abstract*–A new error indicator is proposed to guide the *p*-adaptive finite element analysis of 3D microwave devices. The indicator makes use of the properties of hierarchal elements to target directly the error in the scattering parameters of the device. Results for two rectangular waveguide components – a U-bend and an impedance transformer – confirm that, with the new indicator, accurate scattering parameters are obtained more cheaply than with an earlier, cruder indicator.**

INTRODUCTION

P-adaption, or *hp*-adaption, has been shown to be an effective strategy for the accurate calculation of electromagnetic fields in 3D wave problems by the finite element (FE) method [1] [2]. The error indicators proposed in those papers, and used to guide the adaption, were designed to improve the accuracy of the electric or magnetic field as rapidly as possible. However, in analyzing microwave components the designer is generally interested not in the fields but in the behavior of the device as seen from its ports, i.e. in its scattering parameters. Is it possible to find an indicator that focuses on one of these, so that the error in the parameter is reduced more rapidly than it would be using a more general indicator based on field quality?

Targeted error indicators of this type have been applied to 2D low frequency electromagnetics problems [3], where they were shown to be superior to general indicators. More recently, a targetted indicator for scattering parameters was developed by Sun *et al*. [4] and used to guide *h*-adaption in 3D. The approach taken was first to obtain an estimate of field error in the element, and then to use this to estimate the element's contribution to the error in S_{11}. With the hierarchal elements used in *p*-adaption, a simpler and more direct approach is possible, which was explored in [5]. The coefficients of the highest order basis functions in the element are set to zero, and the contribution to S_{11} from the element is recalculated. The indicator is the change in S_{11}. But this method, corresponding to Scheme 1 of [3], is backwards. What we would really like to know is what the change in S_{11} would be from increasing the order of the element, i.e. *adding* basis functions of the next highest order, not *subtracting* those of the highest order [6]. In [3] such an approach was called Scheme 2, and was shown to outperform Scheme 1. In the present paper, Scheme 2 is applied to the computation of scattering parameters in 3D.

THE SCHEME 2 INDICATOR

In [7] it was shown that the scattering parameter S_{ij} can be calculated from

$$S_{ij} = \tfrac{1}{2} e^{(j)T} r^{(i)} - \delta_{ij} \tag{1}$$

where $r^{(i)}$ is the righthand side of the global FE matrix equation when a wave is incident on port i of the device and all the other ports are matched; δ is the Kroenecker delta; and $e^{(j)}$ is a solution vector representing the electric field, obtained by solving:

$$Ke^{(j)} = r^{(j)} \tag{2}$$

where K is the global FE matrix. When the order of an element is increased and degrees of freedom (DOFs) thereby added, the matrix system enlarges to:

$$\begin{pmatrix} K & K_{12} \\ K_{21} & K_{22} \end{pmatrix} \begin{pmatrix} e_1^{(j)} \\ e_2^{(j)} \end{pmatrix} = \begin{pmatrix} r^{(j)} \\ r_2^{(j)} \end{pmatrix} \tag{3}$$

Note that $e_1^{(j)} \neq e^{(j)}$. From (1) and (3) it can be shown that the change in S_{ij} resulting from the increase in order is:

$$\Delta S_{ij} = \tfrac{1}{2} \left(e_1^{(j)T} r^{(i)} + e_2^{(j)T} r_2^{(i)} - e^{(j)T} r^{(i)} \right) \tag{4}$$

This is an exact result, but unfortunately impossible to evaluate without solving (3), which is too expensive. However, we can get a rough solution to (3) quite cheaply, by *freezing* the original DOFs, i.e. by setting $e_1^{(j)} = e^{(j)}$ and using the second row of (3) to find the new DOFs:

$$K_{22} \bar{e}_2^{(j)} = r_2^{(j)} - K_{21} e^{(j)} \quad = \bar{r}_2^{(j)}, \text{ say} \tag{5}$$

Equation (5) is a small, local problem that can be solved to find an approximation, $\bar{e}_2^{(j)}$, to $e_2^{(j)}$. It is then possible to show, provided the global matrix is symmetric (i.e. reciprocal materials), that

$$\Delta S_{ij} = \tfrac{1}{2}\left(\bar{e}_2^{(j)T}\bar{r}_2^{(i)} + \Delta e_2^{(j)T}\bar{r}_2^{(i)}\right) \quad (6)$$

where $\Delta e_2^{(j)}$ is the error in $e_2^{(j)}$ introduced by this freezing approach:

$$\Delta e_2^{(j)} = e_2^{(j)} - \bar{e}_2^{(j)} \quad (7)$$

Equation (6) is still exact and still impossible to evaluate because we do not know $\Delta e_2^{(j)}$. But if we neglect this term, presumably small, we get an approximation for ΔS_{ij} that is cheap to compute and can serve as a targeted error indicator for S_{ij}:

$$\Delta S_{ij} \cong \tfrac{1}{2}\bar{e}_2^{(j)T}\bar{r}_2^{(i)} \quad (8)$$

RESULTS

Both Schemes 1 and 2 were applied to several microwave devices, analyzed with hierarchal, vector, tetrahedral finite elements of three different orders [5]. At each adaptive step, the 25% of the elements with the highest error indicators were increased in order. S_{11} was targetted, and the error in the return loss plotted against the cumulative computational cost. The error in the return loss is not an absolute error, since the exact value of S_{11} is not known. Rather, it is the difference between the return loss computed at some stage of the adaption to the return loss computed when all the elements were at the highest order, which presumably gives the most accurate value. The cumulative computational cost is obtained by summing the costs of the current and preceding adaptive steps, the cost per step being the number of floating point operations needed to solve the global matrix equation, (2).

Results are shown for two devices in Figs. 1 and 2. The first point (lowest order mesh) is omitted in both because it is identical for Schemes 1 and 2. Both figures show that Scheme 2 converges more quickly than Scheme 1. (In Fig. 2, there is just one early point for which Scheme 1 gives greater accuracy than Scheme 2, but this is obviously not a reliable result, because for the next point the Scheme 2 error is significantly higher.)

CONCLUSIONS

The new indicator for *p*-adaptive analysis, based on a forward-looking estimate of how the scattering parameter will change when the element order is increased, is clearly superior to the older indicator.

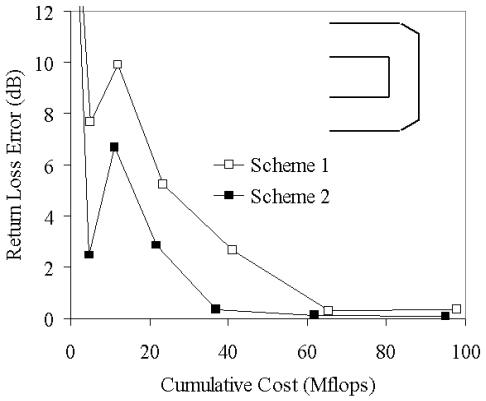

Fig. 1. Return loss at either port of a U-bend rectangular waveguide (cross section 1.905 x 0.508cm) , for two adaptive schemes. 850 tets, 12.5GHz.

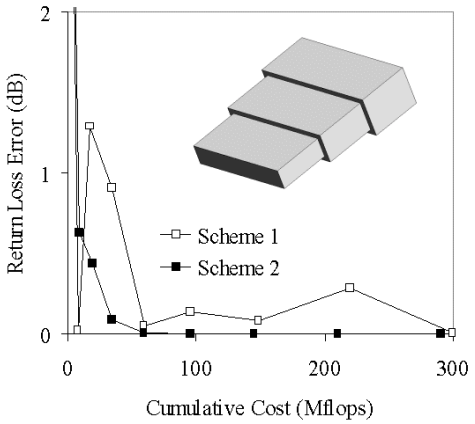

Fig. 2. Return loss at the larger port (2.4 x 0.8cm) of a waveguide transformer, for two adaptive schemes. 1350 tets, 10GHz.

REFERENCES

[1] L.S. Andersen, J.L. Volakis, "Adaptive multiresolution antenna modeling using hierarchical mixed-order tangential vector finite elements", *IEEE Trans. Antennas and Propagation*, vol. 49, no. 2, pp.211-222, February 2001.

[2] W. Rachowicz, L. Demkowicz, "An hp-adaptive finite element method for electromagnetics - part II: A 3D implementation", *Int. J. for Numerical Methods in Engineering*, 53 (1):147-180, Jan 10, 2002.

[3] M.M. Gavrilovic, J.P. Webb, "Targeted error indicators for use in finite-element p-adaption", *IEEE Trans. on Magnetic.*, vol. 34, no. 5, pp.3280-3283, Sep. 1998.

[4] D.K. Sun, Z. Cendes, J. F. Lee, "Adaptive mesh refinement, h-version, for solving multi-port microwave devices in three dimensions", *IEEE Trans. Magnetics*, vol. 36, no. 4, pp.1596-1599, July 2000.

[5] J. P. Webb, "P-adaptive methods for electromagnetic wave problems using hierarchal tetrahedral edge elements", *Electromagnetics*, vol. 22, no. 5, pp.443-451, July 2002.

[6] O. C. Zienkiewicz, R. L. Taylor, "The finite-element method," Vol. 1, Fourth Edition, McGraw-Hill, London, 1988, Chapter 14.

[7] H. Akel, J. P. Webb, "Design sensitivities for scattering-matrix calculation with tetrahedral edge elements", *IEEE Trans. on Magnetics*, vol. 36, no. 4, pp.1043-1046, July 2000.

Goal-Oriented Error-Estimation for S-parameter Computations

Pär Ingelström, Anders Bondeson
Department of Electromagnetics
Chalmers University of Technology
SE-412 96, Göteborg, Sweden
E-mail: pi@elmagn.chalmers.se, elfab@elmagn.chalmers.se

Abstract—**We derive goal-oriented error estimates, based on dual solutions, for the S-parameters of a waveguide cavity resonator and propose a cheap method to compute these. Numerical results show that the error estimators are relatively accurate, especially at high resolutions. Further, with adaptive mesh-refinement based on these estimators we recover optimal convergence rates for complete and incomplete, first and second order, curl-conforming finite elements of Nédélec-type, despite singularities at reentrant corners.**

Problem Description

The goal is to compute the S-parameters, S_{11} and S_{12}, of a two-dimensional model problem for a waveguide cavity resonator (shown in Fig. 1) together with error estimates for these. Further we need to compute well-working error indicators that can be used for adaptive mesh-refinement.

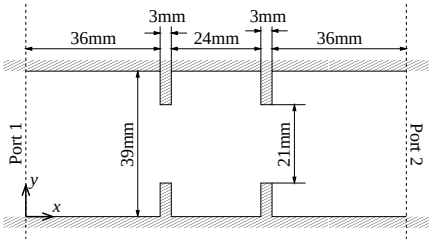

Fig. 1. Geometry of the two-dimensional waveguide resonator.

We use the finite element method to solve the curl-curl equation for the magnetic field inside the waveguide (Ω) with homogeneous Neumann boundary conditions at the metal walls (Γ_0) and Robin conditions at the ports (Γ_1 and Γ_2). On the boundary we define a normal unit vector $\hat{n}$ and a tangential unit vector $\hat{t}$ which has Ω on its left-hand side.

$$\nabla \times \nabla \times \boldsymbol{H} - k^2 \boldsymbol{H} = \boldsymbol{0} \qquad \text{in } \Omega \qquad (1)$$

$$\hat{n} \times \nabla \times \boldsymbol{H} = \boldsymbol{0} \qquad \text{on } \Gamma_0 \qquad (2)$$

$$\hat{n} \times \nabla \times \gamma \boldsymbol{H} + \hat{n} \times k^2 \boldsymbol{H} \times \hat{n} = A_1\, b\, \hat{t} \qquad \text{on } \Gamma_1 \qquad (3)$$

$$\hat{n} \times \nabla \times \gamma \boldsymbol{H} + \hat{n} \times k^2 \boldsymbol{H} \times \hat{n} = A_2\, b\, \hat{t} \qquad \text{on } \Gamma_2 \qquad (4)$$

Here γ is the (imaginary) propagation constant for the lowest (TE_{10}) mode in the waveguide, k is the wavenumber, A_1 and A_2 are the amplitudes of the inserted waves at port 1 and 2 respectively and the function b is defined as $b = -2k^2 \sin(\pi y/w)$, where $w = 39$mm is the width of the waveguide. The boundary conditions short-circuit all modes except for the TE_{10} mode at the ports. However, this is no problem if the waveguide is operated at a frequency where only the TE_{10} mode propagates and the ports are placed far enough from any discontinuities in the waveguide.

Finite Element Formulation

Setting $A_1 = 1$ and $A_2 = 0$, we derive a weak form from (1–4): Find $\boldsymbol{H}_h^p \in \mathcal{H}(\mathbf{curl}; \Omega)$ such that

$$a(\boldsymbol{H}, \boldsymbol{V}) = b_1(\boldsymbol{V}) \quad \forall \boldsymbol{V} \in \mathcal{H}(\mathbf{curl}; \Omega) \qquad (5)$$

where $a(\cdot,\cdot)$ and $b_1(\cdot)$ are defined from

$$a(\boldsymbol{H}, \boldsymbol{V}) = (\nabla \times \boldsymbol{H}, \nabla \times \boldsymbol{V})_\Omega - k^2 (\boldsymbol{H}, \boldsymbol{V})_\Omega - k^2 \gamma^{-1} \langle \boldsymbol{H} \cdot \hat{t}, \boldsymbol{V} \cdot \hat{t} \rangle_{\Gamma_1} - k^2 \gamma^{-1} \langle \boldsymbol{H} \cdot \hat{t}, \boldsymbol{V} \cdot \hat{t} \rangle_{\Gamma_2}$$

$$b_{1,2}(\boldsymbol{V}) = 2k^2 \gamma^{-1} \langle \sin(\pi y/w), \boldsymbol{V} \cdot \hat{t} \rangle_{\Gamma_{1,2}}$$

Here $(\cdot,\cdot)_\Omega$ and $\langle \cdot,\cdot \rangle_\Gamma$ are the *symmetric* inner products (i.e. no complex conjugates) on the domain Ω and the boundary Γ respectively, $\mathcal{H}(\mathbf{curl}; \Omega)$ is the space of functions where the functions themselves and their curls are square integrable. The functional $b_2(\cdot)$ corresponds to the source when a wave is inserted through port 2 and will be used for error estimates of S_{12}. We note that the S-parameters now can be expressed as $S_{11} = 1 - C b_1(\boldsymbol{H})$ and $S_{12} = C b_2(\boldsymbol{H})$, where $C = \gamma k^{-2} w^{-1}$.

Let $\mathcal{N}_h^p$ denote the space of curl-conforming functions of complete [2] or inomplete [3] order p on a triangulation of Ω. Restricting the solution to $\mathcal{N}_h^p$, we get the finite element formulation: Find $\boldsymbol{H}_h^p \in \mathcal{N}_h^p$ such that

$$a(\boldsymbol{H}_h^p, \boldsymbol{V}) = b_1(\boldsymbol{V}) \quad \forall \boldsymbol{V} \in \mathcal{N}_h^p. \qquad (6)$$

It is important that we use a hierarchical base for $\mathcal{N}_h^p$, and we will use basis-functions similar to those in [4].

Note that the errors for S_{11} and S_{12} are proportional to $b_1(\boldsymbol{e})$ and $b_2(\boldsymbol{e})$ respectively, where $\boldsymbol{e} = \boldsymbol{H} - \boldsymbol{H}_h^p$ is the error of the finite element solution.

Derivation of Error Estimates

We use the technique introduced by Becker and Rannacher (see [1] for a survey) to compute the error estimates for S_{11} and S_{12}. The error estimators are based on $\boldsymbol{G}_1$ and $\boldsymbol{G}_2$ respcetively, which are solutions of two dual problems. The first dual problem is identical to the original problem, hence $\boldsymbol{G}_1 = \boldsymbol{H}$, while $\boldsymbol{G}_2$ is the solution to the problem fed through port 2, i.e. where $A_1 = 0$ and $A_2 = 1$. In the following we let the

subindex n on $\boldsymbol{G}_n$ and $b_n(\cdot)$ represent either 1 or 2 depending on which dual problem we want to solve. The weak forms of the dual problems are

$$a(\boldsymbol{G}_n, \boldsymbol{V}) = b_n(\boldsymbol{V}), \forall \boldsymbol{V} \in \mathcal{H}(\mathbf{curl}; \Omega). \tag{7}$$

Now let $\boldsymbol{V} = \boldsymbol{e} = \boldsymbol{H} - \boldsymbol{H}_h^p$, use the symmetry of $a(\cdot,\cdot)$ and then use (5) to eliminate $\boldsymbol{H}$,

$$b_n(\boldsymbol{e}) = b_1(\boldsymbol{G}_n) - a(\boldsymbol{H}_h^p, \boldsymbol{G}_n).$$

Next we let $\boldsymbol{r}_h^p$ be an interpolation operator that projects $\boldsymbol{G}_n$ onto $\mathcal{N}_h^p$ and use (6) with $\boldsymbol{V} = \boldsymbol{r}_h^p \boldsymbol{G}_n$ to get final expressions for the errors in S_{11} and S_{12}

$$\begin{aligned} e_{11} &= -C\left(b_1(\boldsymbol{G}_1 - \boldsymbol{r}_h^p \boldsymbol{G}_1) - a(\boldsymbol{H}_h^p, \boldsymbol{r}_h^p \boldsymbol{G}_1)\right) \\ e_{12} &= +C\left(b_1(\boldsymbol{G}_2 - \boldsymbol{r}_h^p \boldsymbol{G}_2) - a(\boldsymbol{H}_h^p, \boldsymbol{r}_h^p \boldsymbol{G}_2)\right) \end{aligned} \tag{8}$$

For the adaptive mesh-refinement, we compute each elements contribution to e_{11} and/or e_{12} and use the magnitude of these contributions to determine which elements to split.

Computation of Error Estimates

To compute the error estimates, we need some approximation of the dual solutions. To be useful in practice these approximate solutions, which we will denote $\tilde{\boldsymbol{G}}_n$, should not be too expensive to compute. Initially we compute the dual solutions using the same mesh and same elements as for the original problem. This has the important advantage that we get the same matrix as for the original problem and only need to add an extra right-hand side. Also remember that $\boldsymbol{G}_1 = \boldsymbol{H}$, so when we compute $\tilde{\boldsymbol{G}}_1$ in this way we get $\boldsymbol{H}_h^p$ "for free". However, from (8) we see that the error estimates vanish if $\tilde{\boldsymbol{G}}_n \in \mathcal{N}_h^p$. Therefore we extend our dual solutions to the space of higher order elements – $\mathcal{N}_h^{p+1}$, based on the idea in [5]. We use the finite element solution in $\mathcal{N}_h^p$ as a starting guess for the solution in $\mathcal{N}_h^{p+1}$ and then make one single Jacobi iteration to obtain a better approximation. This is a very cheap operation, it is simple to implement using hierarchical basis functions and it has proven quite sufficient for this case. We also note that the interpolator $\boldsymbol{r}_h^p$ is trivial to implement for hierarchical basis functions – just put degrees of freedom associated with basis functions of order higher than p to zero.

Numerical Results

For the current geometry, where there are several right-angled reentrant corners, we get the convergence rate $h^{4/3} \propto (N_h^p)^{-2/3}$, *independent* of the order p of the elements if we use uniform mesh refinement. The optimal convergence rate is $(N_h^p)^{-p}$ for p:th order methods. Hence adaptive mesh refinement is very important, especially for higher order methods.

In Fig. 2 we show convergence results for S_{12} at the frequency 4.30 GHz. First and second order, complete and incomplete curl-conforming elements are used, and refinement is based on local contributions to e_{12}, e_{11} or both. We see that we recover optimal convergence using either refinement method, but that we get more accurate results for S_{12} when the refinement is based on e_{12} – as one would expect. The corresponding relation is also true for S_{11}. To get the reference solution S_{12}^{Ref} we extrapolated the results obtained using second order complete elements to zero element size. In Fig. 3 we show the efficiency index, defined as the ratio of the computed error and the actual error.

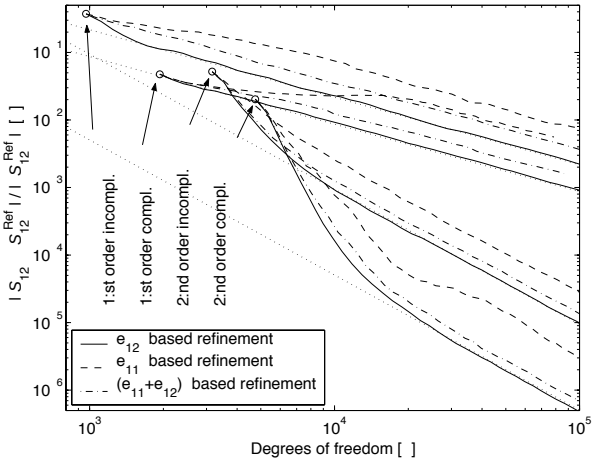

Fig. 2. Convergence rates for S_{11} at 4.30 GHz when the mesh refinement is based on error estimates for S_{11} only, S_{12} only and both.

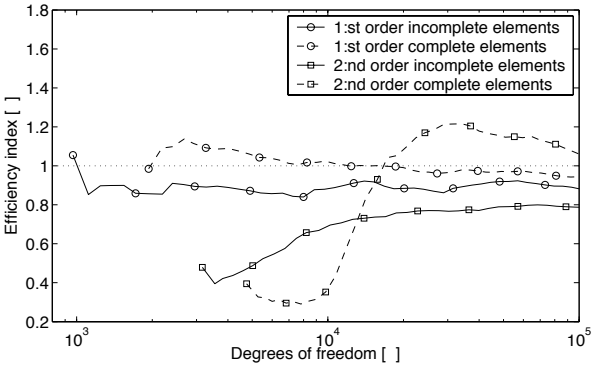

Fig. 3. Convergence rates for S_{11} at 4.30 GHz when the mesh refinement is based on error estimates for S_{11} only, S_{12} only and both.

References

[1] R Becker and R Rannacher, "An optimal control approach to a posteriori error estimation in finite element methods," *Acta Numerica*, vol. 10, pp. 1–102, 2001.

[2] J C Nédélec, "Mixed finite elements in R^3," *Numer. Math.*, vol. 35, pp. 315–341, 1980.

[3] J C Nédélec, "A new family of mixed finite elements in R^3," *Numer. Math.*, vol. 50, pp. 57–81, 1986.

[4] J P Webb, "Hierarchical vector basis functions of arbitrary order for triangular and tetrahedral finite elements," *IEEE. Trans. Antennas Propagat.*, vol. 47, no. 8, pp. 1244–1253, 1999.

[5] R Bank, "Hierarchical bases and the finite element method," *Acta Numerica*, vol. 5, pp. 1–43, 1996.

Author Index

Author Index

Author Index

Author Index

The 14th COMPUMAG Conference on the Computation of Electromagnetic Fields will be held in Saratoga Springs, NY USA, from July 13 to 18, 2003.

Previous COMPUMAG Conferences were held at
Oxford, UK · 1976
Grenoble, France · 1978
Chicago, USA · 1981
Genoa, Italy · 1983
Fort Collins, USA · 1985
Graz, Austria · 1987
Tokyo, Japan · 1989
Sorrento, Italy · 1991
Miami, USA · 1993
Berlin, Germany · 1995
Rio de Janeiro, Brazil · 1997
Sapporo, Japan · 1999
Evian, France · 2001

www.compumag2003.com

For more information, please e-mail the Secretariat for Compumag 2003 at secretariat@compumag2003.com

Chairman
Dr. Sheppard Salon,
Rensselaer Polytechnic Institute

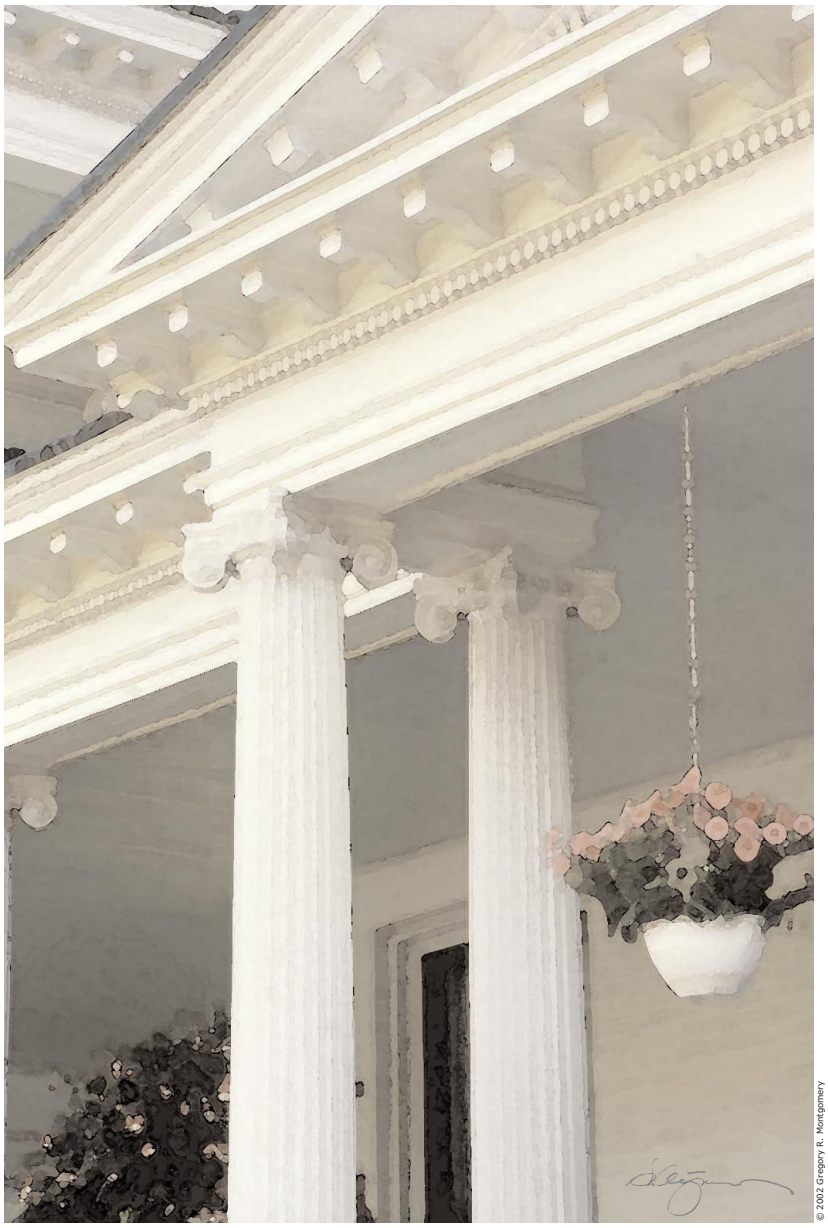

COMPUMAG 2003

Conference on the Computation of Magnetic Fields

Saratoga Springs, NY, USA

July 13–18, 2003